

# UNIVERSITÉ DE TOURS

## ÉCOLE DOCTORALE EMSTU

Laboratoire E.A. 6293 GéoHydrosystèmes Continentaux (GéHCO)

# THÈSE

 présentée par :

**Pierre LOICQ**

soutenue le : 20 avril 2018

pour obtenir le grade de : **Docteur de l'université de Tours**

Discipline/ Spécialité : Sciences de la Terre

## **Caractérisation et modélisation de la température des rivières sur le bassin de la Maine: influence de la végétation rivulaire et des échanges nappe-rivière**

**THÈSE dirigée par :**

**Florentina MOATAR**

**David HANNAH**

Professeur, Université de Tours

Professeur, Université de Birmingham, UK

**RAPPORTEURS :**

**Nicolas FLIPO**

**Eric SAUQUET**

Maître de Recherche, HDR, Mines ParisTech

Directeur de Recherche, IRSTEA

**JURY :**

**Nicolas FLIPO**

**David HANNAH**

**Florentina MOATAR**

**Gilles PINAY**

**Eric SAUQUET**

**Zahra THOMAS**

Maître de Recherche, HDR, Mines ParisTech

Professeur, Université de Birmingham, UK

Professeur, Université de Tours

Directeur de Recherche, IRSTEA, Lyon

Directeur de Recherche, IRSTEA, Lyon

Maître de conférences, INRA-AgroCampus, Rennes



## Remerciements

Je tiens à remercier Florentina de m'avoir accompagné durant ces 3 ans, de m'avoir fait confiance en me proposant ce sujet de thèse et de m'avoir ainsi permis de mettre un pied dans le monde de la recherche.

Thank you David for your helpful advices, for your encouragements and for making the bridge with the great English research in stream temperature and with the English-speaking hydroEco world.

Thanks a lot to Stephen Dugdale who was a great support in the writing of my first article.

Merci à Gilles Pinay et à Zahra Thomas d'avoir accepté d'examiner mon travail, ainsi qu'à Nicolas Flipo et Eric Sauquet d'avoir accepté d'en être les rapporteurs.

Un grand merci à Yann Jullian. Nos petites réunions spontanées de résolution de bug, d'implémentation de code ou de résolution d'intégrales doubles, ainsi que ton cours de calcul parallèle furent un réel plaisir !

Merci à Yves Lansac et Enrick Olive pour l'accès à la machine Neptune (16 cœurs 64 Gb de RAM) sur laquelle T-NET a tourné, ainsi qu'à nos chers informaticiens pour la maintenance de nos outils (Dimitri Dubé, Olivier Thibault et Romain Vallet).

Merci à toutes les personnes qui m'ont fourni des jeux de données et ont répondu à mes questionnements les concernant : Dominique Thiéry (EROS) ; Fulvia Baratelli (Eaudyssée) ; Pere Quintana Seguí et Denis Cendrier (Safran) ; Claire Thomas et Mathilde Marchand (Helioclim) ; Philippe Saunier et Thierry Blouin (LiDAR) ; Kamel Soudani (NDVI) ; Karl Kreutzenberger et Vincent Tamisier (Carhyce) ; Pierre Steinbach (ROE) ; Nicolas Lamouroux (Estimkart) ; André Chandesris et Thierry Tormos (taux de végétation).

Merci aux personnes qui gèrent les sondes de température au fil des saisons et les données résultantes : Cécile Broussard, Yvan Rouveure, Laurent Gigaud et Claire Magand (AFB) ; Edouard Onno et André Robert (DREAL Pays de la Loire) ; Pierre Fetter (Fédération de Pêche d'Eure-et-Loir).

Merci à Cyril Lombardot et Thibault Vigneron pour leur expertise concernant la faune piscicole du bassin de la Maine.

Merci à Bénédicte Augeard et à l'AFB d'avoir permis le financement de cette thèse.

Merci à tous les membres permanents et au flux de membres du GÉHCO (j'ai compté 15 personnes qui sont passées rien que dans "mon" bureau) pour avoir maintenu constante la bonne ambiance au labo ! Sans oublier les écologues de CITERES !

Un merci particulier à Cécile Poisvert, Camille Minaudo, Louis Manière, Antony Foucher, Aurélien Beaufort, Florence Curie, Célestine Delbart et Francesca Degan pour nos échanges technico-scientifiques, ainsi qu'à mes collègues directs Eric Lalot, Maud Diraison, Julien Gouillet et Boussad Lezoul qui ont contribué directement ou indirectement à ce travail.

Merci également à mon compagnon de thèse Nikita d'avoir égayé nos moments de vie lysimétriques (notre bureau étant à moitié enterré) !

Merci à ma Fannie pour les relectures et à sa famille pour son soutien.

Et enfin, merci à ma famille pour son soutien à distance.



Le Loir au niveau de Château-du-Loir, été 2016 (P. Loicq)

## Résumé

La température des rivières ( $T_w$ ) est un paramètre important de la qualité de l'eau, car elle impacte la solubilité de l'oxygène, les réactions chimiques, et les réactions métaboliques des êtres vivants. Elle influence le comportement de la faune aquatique, qui grandit, se nourrit et survit dans des plages de températures déterminées. Dans le contexte actuel des changements climatiques, on se doit de comprendre les processus qui régissent  $T_w$  afin de déterminer les meilleurs moyens pour réguler le réchauffement, ce qui permettrait de limiter la perte de biodiversité associée. Couplé à des modèles biologiques, la modélisation de  $T_w$  à l'échelle régionale est d'une importance majeure car elle permet de comprendre l'évolution de l'aire de répartition des espèces aquatiques.

Ce travail porte sur la caractérisation et la modélisation de la variabilité spatiale de la température des rivières du bassin de la Maine (22350 km<sup>2</sup>), où le climat est relativement homogène mais d'autres caractéristiques sont hétérogènes (géologie, végétation rivulaire, obstacles à l'écoulement). Celui-ci se compose de trois sous-bassins, avec d'ouest en est, la Mayenne, la Sarthe et le Loir.

La variabilité spatiale de la température des cours d'eau a été analysée à 44 stations de mesure localisées sur des ordres de Strahler allant de 2 à 7, et grâce à différentes métriques. Un grand nombre de métriques sont corrélées à la sensibilité thermique (TS), qui correspond à la pente de la régression de  $T_w$  en fonction de la température de l'air (moyennes hebdomadaires). TS varie de 0.42 à 1.17, ce qui démontre la diversité des habitats thermiques qui se trouvent au sein de ce bassin climatiquement homogène et les différentes réponses potentielles au changement climatique actuel et futur.

La variabilité de TS est la mieux expliquée par la distance des stations de mesure à la source et par le rapport entre le débit mensuel minimal et le débit mensuel maximal (moyennés sur plusieurs années), qui est utilisé comme proxy pour quantifier les flux de nappe. De là, un modèle empirique a été développé. Sur le bassin de la Maine, il peut prédire la température hebdomadaire de l'eau avec un RMSE (racine carrée de l'erreur quadratique) de 1,35 °C et un biais moyen de -0,13 °C. En période estivale, la moyenne de la température mensuelle du mois d'août, une variable importante pour les études écologiques, est estimée avec une bonne performance (RMSE = 1.42 °C, biais = -0.35 °C). Ce modèle permet de reconstituer  $T_w$  sur l'ensemble d'un réseau hydrographique, à partir du moment où les débits mensuels sont disponibles/reconstitués et qu'on ne s'écarte pas trop des conditions climatiques et hydrologiques prises en compte pour le calage du modèle.

Le modèle à base physique T-NET a été développé précédemment lors de la thèse d'Aurélien Beaufort (Beaufort, 2015) pour calculer  $T_w$  sur chaque tronçon de rivière d'un réseau hydrographique (réseau Carthage), à l'échelle régionale (bassin de la Loire) et au pas de temps horaire (Beaufort et al., 2016). Dans la présente thèse, ce modèle a été appliqué au bassin de la Maine afin de comprendre ses points forts et ses faiblesses et comment les résoudre. En hiver, la précision est bonne (RMSE de 1.6 °C sur les  $T_w$  moyennes journalières). En été, les biais sur les  $T_w$  modélisées sont corrélés à la sensibilité thermique, avec des biais positifs pour les stations possédant des TS faibles (proches des sources et/ou avec des flux de nappe importants ;  $TS < 0.6$ ) et des biais négatifs pour les stations possédant des TS élevées ( $TS > 1$ ). Toute l'année, les amplitudes journalières ainsi que les amplitudes

du signal thermique observées sur une à deux semaines sont surestimées à une majorité de stations. Les tests de sensibilité montrent que cela est très probablement lié à une sous-estimation généralisée des hauteurs d'eau, du fait d'une méconnaissance de la géométrie des rivières à l'échelle régionale.

De nombreuses études ont montré que l'ombrage porté par la végétation rivulaire pouvait diminuer significativement la température des petits cours d'eau en période estivale. Des études similaires sur des rivières plus grandes et à l'échelle régionales sont plus rares. Dans ce travail, l'impact de la végétation rivulaire sur le rayonnement solaire (direct et diffus) et infrarouge a été caractérisé à la résolution métrique grâce à des données LiDAR, sur 270 km du Loir (zone de disponibilité des données). L'effet de refroidissement de la végétation sur la température maximale journalière évolue de -2.8 °C (amont du Loir, largeur 15-25 m) à -1.1 °C (aval, largeurs 40-50 m), en moyenne sur la période 13-31 août 2009 (durant laquelle des mesures sont disponibles aux 4 stations localisées sur le Loir). La précision de T-NET est améliorée par rapport aux méthodes plus simples de caractérisation de l'ombrage. Les résultats montrent qu'une bonne caractérisation du taux de végétation rivulaire est nécessaire si on souhaite caractériser correctement l'impact de la végétation avec une méthode de complexité intermédiaire (là où il n'y a pas de données LiDAR). L'amélioration de ces données entrantes devrait donc être une priorité pour améliorer notre compréhension de l'impact de la végétation sur d'autres bassins.

Le modèle hydrogéologique distribué Eaudyssée a été appliqué au bassin de la Loire par Baratelli et al. (2016) à Mines ParisTech. Ce modèle est inédit car il a été conçu pour tourner à l'échelle régionale, mais aussi parce qu'il considère que les hauteurs d'eau des cours d'eau varient avec le temps. Il permet de modéliser les échanges nappe-rivières, qui ont un impact important sur  $T_w$ . En effet, la température des nappes phréatiques étant relativement constante tout au long de l'année, les flux de nappe (aquifère → rivière) ont un effet stabilisateur sur  $T_w$ , en la réchauffant en hiver et la refroidissant en été. Ainsi, les flux de nappe calculés sur le bassin du Loir à la résolution kilométrique et au pas de temps journalier ont été injectés dans le modèle T-NET. Comparé à la version initiale du modèle T-NET, les flux de nappe sont augmentés à environ 75% des stations. Les impacts thermiques peuvent être importants: jusqu'à  $\pm 2.5$  °C pour une station de la Beauce, en moyenne mensuelle sur 2008-2013. A cause des biais présents initialement dans T-NET, l'amélioration des performances de T-NET est mitigée, avec une amélioration pour 35% des stations et une dégradation pour 29% des stations. Comparé à un scénario sans flux de nappe, les flux de nappes fournis par Eaudyssée impliquent une diminution de la température maximale journalière qui évolue de -0.5 °C en amont du Loir à -1.3 °C en aval (avec un pic local à -2.8 °C tout à l'amont) (moyenne sur la période 13-31/08/2009). Cette utilisation combinée d'un modèle d'échanges nappe-rivière avec un modèle de température de rivière est inédit à ces résolutions et cette échelle régionale. Les résultats montrent l'importance d'une caractérisation précise des flux de nappe dans la modélisation de  $T_w$ .

Dans le contexte de l'analyse de l'adaptation des milieux au changement climatique, cette thèse apporte des éléments essentiels sur la capacité des modèles à restituer la température des rivières à une échelle spatiale fine et régionale.

## Abstract

Stream temperature (Tw) is an important water quality parameter because it impacts the solubility of oxygen, chemical reaction rates and the biological processes of living organisms. It influences the behaviour of aquatic fauna, which grow, feed and survive in defined temperature niches. In the current context of climate change, it is necessary to achieve a better understanding of the processes that govern Tw in order to determine appropriate management strategies to mitigate loss of biodiversity. Coupled with species distribution models, regional-scale Tw modelling is of major importance because of its ability to shed light on the response of aquatic species distribution to climate change.

This work focuses on the characterisation and modelling of spatial variability in Tw in the Maine catchment (22350 km<sup>2</sup>). Climate in the Maine basin is relatively homogeneous, while other characteristics (e.g. geology, riparian vegetation, presence of weirs) are more spatially-variable. The catchment consists of three sub-basins, with the Mayenne, Sarthe, and the Loir basins (from west to east).

The spatial variability of Tw was analysed at 44 measurement stations located on streams of Strahler orders 2 to 7, using a variety of different metrics. A range of metrics were found to correlate with the thermal sensitivity (TS), which corresponds to the slope of the regression of Tw as a function of air temperature (taken as weekly averages). TS ranged from 0.42 to 1.17, demonstrating the diversity of thermal habitats located within this climatically homogeneous catchment and the different potential responses to the current and forecasted climate change.

Variability in TS was best explained by the distance of the Tw measurement stations to the headwaters and by the ratio between the minimum and the maximum monthly flow (averaged over several years), which is as a proxy for groundwater flow. Based on these findings, an empirical model for water temperature was developed. On the Maine catchment, it is able to predict weekly Tw with a RMSE (root-mean-square error) of 1.35 °C and an average bias of -0.13 °C. In summer, the August mean monthly Tw, an important variable for ecological studies, is also estimated with good degree of accuracy (RMSE = 1.42 °C, bias = -0.35 °C). This model will allow for the reconstruction of Tw on a whole hydrographic network, as soon as monthly discharges are available or modelled and provided that climatic and hydrologic conditions are similar to those used for the model calibration.

In addition to this empirical model, the physically based T-NET model (previously developed during the thesis of Aurélien Beaufort; see Beaufort, 2015) was applied to the Maine catchment in order to understand its advantages and limitations and to propose potential solutions. T-NET computes reach-averaged Tw at regional scales and hourly timesteps as a function of input meteorological and physiographic data. Our findings indicate that model performance is good in winter (RMSE of 1.6 °C on the daily average Tw). However, in summer, biases in Tw correlate with the thermal sensitivity: biases are positive for stations with low TS (< 0.6) while they are negative for stations with high TS (> 1). Furthermore, on a yearly-basis, both the diel Tw amplitudes and the amplitudes of variations occurring with a wavelength of some weeks are overestimated at a majority of stations. Sensitivity analyses show that this shortfall in model performance is most likely related to a global

underestimation of the water level within the model, due to a lack of knowledge of the streams' channel geometry at the regional scale.

Many studies have shown that shade cast by riparian vegetation can significantly decrease  $T_w$  of small streams in summer. However, similar studies on larger streams and at the regional scale are scarce. In light of this knowledge gap, we parameterised the T-NET model with LiDAR-derived riparian shading information for 270 km of the Loir River, with a view to understanding the impact of riparian vegetation on solar (direct and diffuse) and longwave downward radiation, and thus on  $T_w$ . We observed that the cooling effect of vegetation on maximum daily temperature ranged from  $-2.8$  °C (upstream reaches of the Loir, channel width of 15-25 m) to  $-1.1$  °C (downstream reaches, channel widths of 40-50 m), on average over the 13-31 August 2009 period (period with concurrent measures at the 4 monitoring stations located on the Loir). We also found that T-NET performed better when parameterised using these LiDAR data, in comparison to simpler methods of shading characterisation. The application of an intermediate complexity method (applicable where there is no LiDAR data) shows that good characterisation of vegetation rate (percentage of vegetation in a buffer around the river reaches) is necessary to properly quantify the thermal impact of riparian tree cover. Hence, the collection of improved riparian vegetation data should be a priority to improve our understanding of the impact of tree cover on stream temperature in other catchments.

Finally, the outputs of the Eaudyssée distributed hydrogeological model (Baratelli et al., 2016) were integrated in T-NET, in order to further improve predictions of  $T_w$ . Eaudyssée permits the simulation of stream-aquifer exchanges at the regional scale. This model considers the variation of stream water depth with time. In catchments with high permeability like that of the Loir, these exchanges have a particularly important impact on  $T_w$ . Indeed, due to the relative annual stability of groundwater temperature, groundwater flows (aquifer to river) have a stabilising effect on  $T_w$ , warming it in winter and cooling it in summer. Groundwater flows calculated on the Loir catchment at a resolution of 1 km and at daily timesteps were injected into the T-NET model. Compared to the initial version of T-NET, groundwater flows are increased at about 75% of the stations. The thermal impacts of these groundwater inputs are significant (up to  $\pm 2.5$  °C for a station in the Beauce area, monthly average on 2008-2013). Because of the biases initially present in T-NET, the performance improvement of T-NET is limited, with improvement in simulated  $T_w$  RMSE at 35% of the temperature monitoring stations and degradation in simulated  $T_w$  at 29% of the stations. Compared to a scenario without groundwater flow, groundwater flows provided by Eaudyssée cause a reduction of daily maximum temperature ranging from  $-0.5$  °C (upstream of the Loir) to  $-1.3$  °C downstream, with a local peak at  $-2.8$  °C in the very upstream part of the catchment (average over the 13-31/08/2009 period). This coupling of a hydrogeological model with a stream temperature model has never before been conducted at the regional scale, and results highlight the importance of accurate groundwater flow characterisation for the modelling of  $T_w$ .

In the context of the adaptation of river communities to climate change, this thesis provides essential information on the ability of models to simulate stream temperature at the regional scale.

# Table of contents

|  |           |
|--|-----------|
| <b>Chapter 1: Introduction (français)</b> .....  | <b>21</b> |
| 1.1 Contexte.....  | 21        |
| 1.2 Objectifs et plan.....   | 22        |
| <b>Chapter 1: Introduction (English)</b> .....   | <b>25</b> |
| 1.1 Context.....   | 25        |
| 1.2 Aims and plan .....  | 26        |
| <b>Chapter 2: Study site of the Maine catchment</b> .....  | <b>29</b> |
| 2.1 Résumé en français.....  | 29        |
| 2.2 General description and elevation .....  | 29        |
| 2.3 Lithology and hydrogeology .....   | 30        |
| 2.4 Landuse and riparian vegetation .....  | 32        |
| 2.5 Climatic conditions.....   | 33        |
| 2.6 Hydrological conditions .....  | 35        |
| 2.7 Obstacles to flow .....  | 36        |
| 2.8 Conclusion.....  | 37        |
| <b>Chapter 3: Spatio-temporal variability of stream temperature in the Maine catchment</b> .....   | <b>39</b> |
| 3.1 Résumé en français.....  | 39        |
| 3.2 State of the art of stream temperature regime characterisation .....   | 40        |
| 3.3 Presentation of temperature monitoring stations.....   | 45        |
| 3.4 Method of spatio-temporal analysis of stream temperature .....   | 48        |
| 3.5 Contrasted variability of stream thermal metrics compared to air temperature metrics .....   | 51        |
| 3.6 Air-water temperature relationship.....  | 53        |
| 3.6.1 Global Tw-Ta regressions and performances .....  | 53        |
| 3.6.2 Interannual variations of thermal sensitivity .....  | 57        |
| 3.7 Can we predict thermal metrics based on hydrology and basin properties?.....   | 57        |
| 3.8 Discussion .....   | 61        |
| 3.9 Conclusion.....  | 63        |
| <b>Chapter 4: The T-NET model on the Maine catchment: standard configuration, sensitivity analysis and comparison with a hydraulic model</b> ..... | <b>65</b> |
| 4.1 Résumé en français.....  | 65        |
| 4.2 Context and objective .....  | 66        |
| 4.3 The standard version of the T-NET model.....   | 68        |
| 4.3.1 Heat fluxes.....   | 68        |
| Provided by the SAFRAN reanalysis.....   | 68        |
| 4.3.2 Principles and equations .....   | 68        |
| 4.3.3 River geometry .....   | 71        |
| 4.4 Input datasets.....  | 71        |
| 4.4.1 Meteorological reanalysis .....  | 72        |
| 4.4.2 Discharge.....   | 73        |
| 4.4.3 River network, topography and vegetation cover.....  | 76        |
| 4.5 Results with the standard version.....   | 77        |
| 4.5.1 Mean accuracy on the 44 stations .....   | 77        |
| 4.5.2 Annual cycle of the bias.....  | 77        |
| 4.5.3 Accuracy in summer .....   | 78        |
| 4.5.4 Comparison with the statistical model in August 2009.....  | 81        |
| 4.6 Sensitivity analysis with the standard version .....   | 83        |

|   |  |            |
|---|--|------------|
| 4.6.1   | Water velocity (isolated) .....  | 84         |
| 4.6.2   | Wetted width .....   | 86         |
| 4.6.3   | Depth.....   | 87         |
| 4.6.4   | Discharge.....   | 89         |
| 4.6.5   | Groundwater temperature.....   | 89         |
| 4.7   | Conclusion.....  | 91         |
| <b>Chapter 5: Thermal impact of riparian vegetation shading on solar and downward longwave radiation .....</b>                            |  | <b>93</b>  |
| 5.1   | <i>Résumé en français</i> .....  | 93         |
| 5.2   | <i>Introduction</i> .....  | 94         |
| 5.3   | <i>Modification 1: a variable albedo</i> .....   | 95         |
| 5.3.1   | Equations.....   | 95         |
| 5.3.2   | Tw results and performance with a variable albedo .....  | 95         |
| 5.4   | <i>Modification 2: an improved phenology</i> .....   | 96         |
| 5.4.1   | Method for phenology characterisation .....  | 96         |
| 5.4.2   | Tw results and performance with a variable transmissivity .....  | 97         |
| 5.5   | <i>Modification 3: using Helioclim global solar radiation in place of SAFRAN</i> .....                                       | 99         |
| 5.5.1   | Comparison of Helioclim radiation dataset with SAFRAN radiation .....  | 99         |
| 5.5.2   | Results in simulated Tw .....  | 101        |
| 5.6   | <i>Improving representation of riparian vegetation shading in a regional stream temperature model using LiDAR data</i> ..... | 102        |
| 5.6.1   | Introduction.....  | 102        |
| 5.6.2   | Methods .....  | 104        |
| 5.6.2.1   | Net solar radiation calculation .....  | 104        |
| 5.6.2.2   | Shadow factor and view factor calculations.....  | 105        |
| 5.6.2.3   | Study site and water temperature observations.....   | 106        |
| 5.6.2.4   | T-NET model implementation and criteria of model performance .....   | 108        |
| 5.6.3   | Results .....  | 109        |
| 5.6.3.1   | Characterisation of riparian vegetation cover .....  | 109        |
| 5.6.3.2   | Variation in riparian shading computed with the three methods.....   | 110        |
| 5.6.3.3   | Impact of riparian shading method on annual and seasonal river temperature simulations.....                                  | 112        |
| 5.6.3.4   | Impact of riparian shading method on summer maximum daily temperature long profile ..  | 113        |
| 5.6.4   | Discussion .....   | 114        |
| 5.6.4.1   | Discrepancies in computed SF and TVF .....   | 114        |
| 5.6.4.2   | Influence of shading routine on simulated river temperatures .....   | 115        |
| 5.6.4.3   | Performance of T-NET model on the Loir River .....   | 115        |
| 5.6.4.4   | Implications, shading methods limitations and perspectives.....  | 116        |
| 5.7   | <i>Impact of vegetation uncertainty of tributaries on the Loir thermal profile</i> .....                                     | 118        |
| 5.8   | <i>Additional results on <math>T_{mean}</math>, <math>T_{min}</math> and diel amplitudes</i> .....                           | 118        |
| 5.9   | <i>Improvement of the longwave downward radiation characterisation on the Loir River thanks to LiDAR data</i> .....          | 119        |
| 5.10  | <i>Validation with the thermal infrared imagery in summer and winter</i> .....   | 121        |
| 5.10.1  | Thermal infrared imagery acquisition and treatment.....  | 121        |
| 5.10.2  | Results of the comparison of the <i>lidar</i> method with TIR profile in summer and winter.....                              | 122        |
| 5.11  | Conclusion.....  | 123        |
| <b>Chapter 6: Impact of groundwater fluxes modelled with the hydrological-hydrogeological model Eaudyssée on the Loir catchment .....</b> |  | <b>125</b> |
| 6.1   | <i>Résumé en français</i> .....  | 125        |
| 6.2   | <i>Context and objective</i> .....   | 125        |
| 6.3   | <i>Methods</i> .....   | 126        |
| 6.3.1   | The Eaudyssée model and resulting data.....  | 127        |
| 6.3.2   | Eaudyssée stream-aquifer exchange data.....  | 127        |

|   |   |            |
|---|---|------------|
| 6.3.3   | Method to inject the Eaudyssée output into T-NET .....  | 130        |
| 6.4   | <i>Results in water temperature</i> .....   | 130        |
| 6.4.1   | Annual cycle at Tw stations .....   | 130        |
| 6.4.2   | Thermal impact in August 2009 .....   | 133        |
| 6.4.3   | Average accuracy.....   | 134        |
| 6.5   | <i>Conclusion</i> .....   | 135        |
| <b>Chapter 7: Conclusion and perspectives (English) .....</b>   |   | <b>137</b> |
| 7.1   | <i>Aims</i> .....   | 137        |
| 7.2   | <i>Characterisation of thermal regimes</i> .....  | 137        |
| 7.3   | <i>Empirical model</i> .....  | 137        |
| 7.4   | <i>The T-NET model</i> .....  | 138        |
| 7.4.1   | Performance of T-NET on the Maine catchment .....   | 138        |
| 7.4.2   | Fine scale characterisation on the Loir River and catchment.....  | 139        |
| 7.4.3   | T-NET performances on the Maine catchment with all modifications (applied where applicable).....                              | 140        |
| 7.4.4   | Perspectives for the T-NET model development.....   | 142        |
| <b>Chapter 7: Conclusion et perspectives (français) .....</b>   |   | <b>145</b> |
| 7.1   | <i>Objectifs</i> .....  | 145        |
| 7.2   | <i>Caractérisation des régimes thermiques</i> .....   | 145        |
| 7.3   | <i>Modélisation statistique</i> .....   | 146        |
| 7.4   | <i>Le modèle T-NET</i> .....  | 146        |
| 7.4.1   | Performances de T-NET sur le bassin de la Maine .....   | 146        |
| 7.4.2   | Caractérisation à résolution fine sur la rivière Loir et son bassin .....   | 147        |
| 7.4.3   | Performances de T-NET sur le bassin versant de la Maine avec toutes les modifications (appliquées où cela est possible) ..... | 148        |
| 7.4.4   | Perspectives pour le développement de T-NET .....   | 150        |
| <b>Bibliography .....</b>   |   | <b>153</b> |
| <b>Appendices .....</b>   |   | <b>163</b> |
| <i>Appendix A: Time series of observed discharges at the 3 downstream most gauging stations of each subcatchment .....</i>  |   | <i>163</i> |
| The Mayenne River at Chambellay .....   |   | 163        |
| The Sarthe River at Saint-Denis-d'Anjou .....   |   | 164        |
| The Loir River at Durtal.....   |   | 166        |
| <i>Appendix B: Availability of measured temperature and stations numbers .....</i>  |   | <i>168</i> |
| <i>Appendix C: Water and air temperature metrics in 2010.....</i>   |   | <i>169</i> |
| <i>Appendix D: Station characteristics (interannual average where appropriate) .....</i>  |   | <i>171</i> |
| <i>Appendix E: Time series of measured mean daily Tw.....</i>   |   | <i>172</i> |
| <i>Appendix F: Scatterplots of mean weekly water temperature as a function of mean weekly air temperature, using data available on the 08/2008-07/2015 period.....</i>                          |   | <i>189</i> |
| <i>Appendix G: Mean daily temperature modelled with the standard and the final version of T-NET, compared to observed values.....</i>   |   | <i>195</i> |
| <i>Appendix H: Article published in Sciences of the Total Environment: Improving representation of riparian vegetation shading in a regional stream temperature model using LiDAR data.....</i> |   | <i>228</i> |



## Table of figures

|   |    |
|---|----|
| Figure 2.1: The Maine catchment with the 3 subcatchments, elevation, the hydro-eco region boundary, river classified by Strahler order and the main cities .....  | 30 |
| Figure 2.2: Geology of the Maine catchment. Source: Alhaskeer et al. (2014), data from BRGM (1980). .....   | 31 |
| Figure 2.3: Landuse from Corine Land Cover 2012 .....   | 32 |
| Figure 2.4: Vegetation cover data computed by Valette et al. (2012) in a 10m buffer around their own river network and extrapolated on our river network .....  | 33 |
| Figure 2.5: Mean vegetation cover for each sub-catchment and by Strahler order .....  | 33 |
| Figure 2.6: Mean air temperature in July on 1981-2010 (Aurelhy data from Météo-France) .....  | 34 |
| Figure 2.7: Mean yearly precipitations on 1981-2010 (Aurelhy data from Météo-France).....   | 34 |
| Figure 2.8: Monthly air temperature deviations around the 08/1985-07/2015 monthly averages on the Maine catchment (SAFRAN data from Météo-France).....  | 35 |
| Figure 2.9: Interannual averages of specific discharge measured at the downstream most gauging stations of each sub-basin. Data are from the French hydrologic. Availability is 1965-2016 for the Mayenne, 1970-2016 for the Sarthe, 1960-2016 for the Loir. .... | 35 |
| Figure 2.10: Ratio of mean specific discharge in August on annual average. Stations with bigger symbols are located on the main rivers.....   | 36 |
| Figure 2.11: Tiering rate computed from each river reach all the way to the source of the corresponding river   | 37 |
| Figure 3.1: Spatial distribution of the 44 stream temperature monitoring stations and hydro-eco region boundary. Numbers are distance from source (km). Stations with bigger symbols are located on the main rivers.....  | 46 |
| Figure 3.2: Histogram of distances from source of the 44 stations .....   | 46 |
| Figure 3.3: Availability of data at the 44 Tw monitoring stations .....   | 47 |
| Figure 3.4: Number of stations with available data for each day on 2008 - 2015 .....  | 48 |
| Figure 3.5: Representation of the different metrics on the Tw time series of Jouanne 50 (a) 2010 (b) between 01/07 and 12/07/2010. ....   | 49 |
| Figure 3.6: Spatial distribution of the ratio between the minimum and maximum monthly mean discharge on 08/2008-07/2014 .....   | 50 |
| Figure 3.7: Criteria's for 2010 and the 44 stations ordered by increasing $Q_{min}/Q_{max}$ , the ratio between the minimum and maximum monthly mean discharge on 08/2008-07/2014. ....   | 51 |
| Figure 3.8: Duration plot for the 24 stations with full data in 2010, built on hourly Tw .....  | 52 |
| Figure 3.9: Tw-Ta weekly linear regression (a) Maine 328, with the highest TS (b) Boulon 23 with the lowest TS (c) Conie 27, (d) Yerre 47 .....   | 54 |
| Figure 3.10: Linear regressions fitted on data available between August 2008 and July 2015 for the 44 stations  | 54 |
| Figure 3.11: Spatial distribution of thermal sensitivities computed on weekly Tw-Ta regressions .....   | 55 |
| Figure 3.12: Relationship between intercept and slope of Tw-Ta weekly regressions .....   | 56 |
| Figure 3.13: Spatial distribution of stations classified thanks to the hierarchical clustering method .....   | 56 |
| Figure 3.14: Temporal evolution of thermal sensitivity .....  | 57 |
| Figure 3.15: Thermal sensitivity as a function of distance from source.....   | 58 |
| Figure 3.16: Modelled weekly Tw vs. observed weekly Tw (validation group of 22 stations, with a colour for each station) .....  | 58 |
| Figure 3.17: Biases of the statistical model on the validation stations, computed on data available on the 08/2008-07/2015 period .....   | 59 |
| Figure 3.18: Annual cycle of modelled weekly mean, averaged on 07/2008-08/2015 and for each group of stations on the 22 validation stations .....   | 59 |

|   |    |
|---|----|
| Figure 3.19: Mean temperature simulated with the empirical model on the 13-31/08/2009 period.....   | 60 |
| Figure 3.20: Thermal sensitivity computed on the whole river network.....   | 61 |
| Figure 3.21: Diel amplitude as a function of distance from source (a) As described in Caissie (2006) (b) observed on the Maine catchment (Sarthe River stations are in red) .....   | 62 |
| Figure 4.1: Principles of the T-NET model (Beaufort, 2015).....   | 70 |
| Figure 4.2: Tw computation scheme (Beaufort et al., 2016). Travel time in reach 1 is 3 hours, while it is 1 hour for reach 3. UN stands for upstream node, DN stands for downstream node. ....  | 71 |
| Figure 4.3: Summary of the use of the different input data (modified from Beaufort et al., 2016).....   | 72 |
| Figure 4.4: Principle of the EROS model (modified from Thiéry, 2005) .....  | 73 |
| Figure 4.5: Nash-Sutcliff coefficient computed on 1971-2015 (a) classic criterion (b) modified criterion focusing on low flows .....  | 74 |
| Figure 4.6: Simulated vs. observed discharges. Each cross is a sub-basin, averaged on the given season and on the 08/2008-07/2015 period.....   | 74 |
| Figure 4.7: Errors on modelled hydraulic parameters computed from the Estimkart equations, as a function of biases of modelled discharge. Both X and Y scales are ratio, so that a value of 2 means that the value relying on simulated discharge is twice bigger than the value related to the observed discharge. Each point is a sub-basin, averaged on the given season and on the 08/2008-07/2015 period. .... | 75 |
| Figure 4.8: Ratio between the baseflow and the total flow modelled on each sub-basin by EROS (08/2008-07/2015 average) .....  | 76 |
| Figure 4.9: Histogram of the reach lengths on the Maine basin .....   | 76 |
| Figure 4.10: Temporal evolution of bias on the 44 stations, averaged by classes of distance from source (2008-2015 average). Classes of increasing distance from source have 7, 13, 5, 11 and 8 stations respectively. (a) Tmean (b) Tmax (c) Tmin (d) diel amplitudes.....   | 78 |
| Figure 4.11: Histogram of biases computed on available observed mean daily temperature on the 2008-2015 period, displayed for each season and discriminated for the Loir River and the other rivers. ....   | 78 |
| Figure 4.12: Bias of mean daily temperature on July-August of the 2008-2015 period .....  | 79 |
| Figure 4.13: Bias (Tsim-Tobs) of mean daily temperature in July-August as a function of thermal sensitivity (2008-2015 average) (a) standard configuration (b) with no groundwater fluxes. Stations numbers are in appendix B. ....   | 79 |
| Figure 4.14: Simulated and observed mean daily temperature in 2010 (a) Yerre 47 (b) Merdereau 21 (c) Conie 40 .....   | 80 |
| Figure 4.15: Longitudinal profile of simulated daily mean temperature on the 4 main rivers of the Maine catchment, averaged on the 13-31/08/2009 period.....  | 80 |
| Figure 4.16: Bias of diel amplitudes ( $Ampli_{sim} - Ampli_{obs}$ ) as a function of the Qmin/Qmax ratio (2008-2015 average). Stations numbers are in appendix B.....  | 81 |
| Figure 4.17: Simulated and observed Tw in 2011 (a) Sarthe 5 (b) Aigre 25 (c) Conie 27 .....   | 81 |
| Figure 4.18: Mean temperature simulated with T-NET on the 13-31/08/2009 period .....  | 82 |
| Figure 4.19: Map of the difference $TW_{T-NET} - TW_{statistical\ model}$ (average on the 13-31/08/2009 period) .....   | 83 |
| Figure 4.20: Difference $TW_{T-NET} - TW_{statistical\ model}$ (average on the 13-31/08/2009 period). Boxplots over the 9998 reaches of the Maine catchment. ....   | 83 |
| Figure 4.21: Time to travel the whole Loir River (317 km) on the 09-10 hydrological year (a) the standard configuration of T-NET (b) with doubled travel time .....   | 84 |
| Figure 4.22: Longitudinal profile of altitudes for the four main rivers of the Maine catchment .....  | 84 |
| Figure 4.23: (a) water velocity and (b) travel time for the 4 main rivers of the Maine catchment, averaged between the 13 and the 31 August 2009 .....  | 84 |
| Figure 4.24: Water velocities computed from 42 Carhyce field measurements compared to the corresponding reach-averaged modelled velocities. Measurements were achieved on 40 stations located on 32 different streams of the Maine catchment between 2009 and 2014. ....  | 85 |

|   |     |
|---|-----|
| Figure 4.25: Difference of biases between a simulation where water is 2x slower and the standard simulation (a) mean daily temperature (b) diel amplitude .....   | 86  |
| Figure 4.26: Longitudinal profile of wetted width on the 4 main rivers, averaged on the 13-31/08/2009 period  | 86  |
| Figure 4.27: Wetted widths measured during 42 Carhyce field measurements compared to the corresponding reach-averaged modelled widths.....  | 86  |
| Figure 4.28: Difference of biases between a simulation with doubled wetted widths and the standard simulation (a) mean daily temperature (b) diel amplitude .....   | 87  |
| Figure 4.29: Longitudinal profile of water depth on the 4 main rivers on the 13-31/08/2009 period .....   | 87  |
| Figure 4.30: Water depths measured during 42 Carhyce field measurements compared to the corresponding reach-averaged modelled depth. ....   | 87  |
| Figure 4.31: Impact of doubling the water depth. (a) Difference with the standard simulation. SDE of mean daily temperature (continuous) and bias of diel amplitude (dashed) (b) Bias of diel amplitude with D*2 .....            | 88  |
| Figure 4.32: Bias of the diel amplitudes in July-August as a function of thermal sensitivity (2008-2015 average) with doubled river depth.....  | 88  |
| Figure 4.33: Difference of biases between a simulation where discharge is 2x smaller (continuous)/2x larger (dashed) and the standard simulation (a) mean daily temperature (b) diel amplitude.....                               | 89  |
| Figure 4.34: Water temperature at Aron 34 (a) daily means on 2010 (b) hourly values between 13 and 31 August 2009.....  | 89  |
| Figure 4.35: Difference of biases between a simulation where $T_g = T_g + 2\text{ }^\circ\text{C}$ (continuous)/ $T_g = T_g - 2\text{ }^\circ\text{C}$ (dashed) and the standard simulation .....                                 | 90  |
| Figure 4.36: Bias ( $T_{\text{sim}}-T_{\text{obs}}$ ) of mean daily temperature in July-August as a function of thermal sensitivity (2008-2015 average) with groundwater temperature decreased by $2\text{ }^\circ\text{C}$ ..... | 90  |
| Figure 4.37: Longitudinal profile of stream temperature averaged on the 13-31 august 2009, with standard configuration (continuous), $T_g + 2\text{ }^\circ\text{C}$ (dashed), $T_g - 2\text{ }^\circ\text{C}$ (dotted).....      | 91  |
| Figure 5.1: Variable albedo parameterisation as a function of solar elevation angle.....  | 95  |
| Figure 5.2: Bias of mean daily $T_w$ averaged by classes of distance from source and on 2008-2015. Comparison between the fixed and the variable albedo parameterisations. ....   | 96  |
| Figure 5.3: Bias of diel amplitudes averaged by classes of distance from source and on 2008-2015. Comparison between the fixed and the variable albedo parameterisations. ....  | 96  |
| Figure 5.4: Transmissivity parameterisation on ground-based NDVI measured from oak trees during 2008-2012 (Soudani et al., 2012).....   | 97  |
| Figure 5.5: Daily mean $T_w$ bias, averaged by Strahler order and on 2008-2015 (a) $\text{Bias}_{\text{Variable transmissivity}} - \text{bias}_{\text{Standard}}$ (b) Absolute values .....                                       | 98  |
| Figure 5.6: Comparison of RMSE computed on daily mean $T_w$ between the standard configuration and the configuration with a variable transmissivity. Averages on available observed data on 2008-2015. ....                       | 99  |
| Figure 5.7: Comparison between SAFRAN and Helioclim mesh.....   | 99  |
| Figure 5.8: Comparison of Helioclim and SAFRAN daily (24h) mean global radiation distributions on 08/2008-07/2015. A SAFRAN equivalent was attributed to each Helioclim cell.....   | 100 |
| Figure 5.9: Spatial distribution of Helioclim - SAFRAN differences in global radiation over 08/2008-07/2015 (a) mean difference (b) standard deviation of the difference .....  | 100 |
| Figure 5.10: Monthly mean differences between Helioclim and Safran global radiation on the Maine basin ( $\text{W}\cdot\text{m}^{-2}$ ) .....   | 101 |
| Figure 5.11: $T_{\text{mean}_{\text{Helioclim}}} - T_{\text{mean}_{\text{Standard}}}$ for each year on 2008-2015, averaged on the 44 stations .....   | 101 |
| Figure 5.12: Longitudinal profile of simulated $T_{\text{mean}}$ on the 4 main rivers of the Maine catchment, averaged on 13-31/08/2009. Standard simulation (continuous), simulation with Helioclim (dashed).....                | 101 |
| Figure 5.13: Comparison of RMSE computed on mean daily $T_w$ between the standard configuration and the configuration using Helioclim. Averages on available observed data on 2008-2015.....                                      | 102 |

|  |     |
|--|-----|
| Figure 5.14: Calculation of a sky view factor from measures of $\theta$ , the angle between the horizon and the highest vegetation seen from a water pixel and with an angular step $\phi$ of $10^\circ$ . R is the radius of the hemisphere   | 106 |
| Figure 5.15: Map of the Loir catchment, with stream temperature monitoring stations, gauging stations, watersheds used for discharge modelling, LiDAR area, geologic formations, Helioclim grid. ....  | 107 |
| Figure 5.16: Period of availability of stream temperature observation at the four logger stations located on the Loir River.....   | 108 |
| Figure 5.17: Characterisation of riparian vegetation for each T-NET reach (a) comparison of vegetation cover derived from the BD TOPO database (Valette et al., 2012) and LiDAR datasets (buffer of 10 m on both sides of the river polygons) (b) median and 3 <sup>rd</sup> quartile vegetation heights from LiDAR data .....                           | 110 |
| Figure 5.18: Longitudinal profile of shadow factor provided by the 3 methods on the Loir River at the summer solstice (21 <sup>st</sup> June) at 12h UTC.....  | 110 |
| Figure 5.19: Percentiles of the SF distribution obtained with the three methods on the 135 T-NET reaches (a) Annual cycles at noon (b) daily cycles at the summer solstice.....  | 111 |
| Figure 5.20: Longitudinal profile of tree view factor provided by the 3 methods on the Loir River. Values from the <i>variable</i> method are averaged on 08/2007-07/2014.....   | 111 |
| Figure 5.21: Monthly biases ( $T_{sim}-T_{obs}$ ) and standard deviation of errors of maximum daily temperature provided by the 3 methods at the 4 stations (averaged annual cycles computed on available observed data) .....   | 113 |
| Figure 5.22: Longitudinal profile of maximum daily temperature (averaged between the 13 and the 31 August 2009) provided by the 3 methods and by a vegetation-free simulation. The vertical dashed line depicts the start of LiDAR cover. Conie, Yerre and Aigre are the main tributaries.....   | 114 |
| Figure 5.23: Width obtained with 3 methods on the 13-31/08/2009 period. BD TOPO width was obtained by the ratio between the polygons area and the length of the river lines inside these polygons. ....  | 114 |
| Figure 5.24: Longitudinal profile of maximum daily temperature (averaged between the 13 and the 31 August 2009) provided by injecting the <i>variable</i> method with vegetation cover ( <i>vc</i> ) and median height from LiDAR data. The vertical dashed line depicts the start of LiDAR cover. Conie, Yerre and Aigre are the main tributaries. .... | 115 |
| Figure 5.25: Longitudinal profile of the maximum daily temperature on the Loir River averaged from 13 to 31 August 2009. WS are the subwatersheds, numbers are the distances from source (km), and names are the main tributaries .....  | 118 |
| Figure 5.26: Mean annual cycle of the impact of riparian vegetation on the longwave downward radiation at the 4 Loir's monitoring stations (2008-2014) (a) minimum daily temperature (b) diel amplitude. ....  | 120 |
| Figure 5.27: Longitudinal profile on the Loir and on average on the 13-31/08/2009 period with and without considering the impact of vegetation on the longwave downward radiation (a) on minimum daily temperature (b) on maximum daily temperature. SW = shortwave (solar) radiation; LW = longwave downward radiation. ....                            | 120 |
| Figure 5.28: Temporal evolution of the total (solar and longwave radiation) impact of riparian vegetation at the downstream-most Loir's reach of the LiDAR area. Vertical lines delimit the 13-31/08/2009 period. Moving average is over 21 days. ....   | 121 |
| Figure 5.29: Temperature modelled with the <i>lidar</i> method and observed on the thermal imagery the 10 September 2014 at 16h UTC .....  | 122 |
| Figure 5.30: Temperature modelled with the <i>lidar</i> method and retrieved from thermal imagery and in-situ observations on the 5 February 2015 at 11h UTC.....  | 123 |
| Figure 5.31: Total (solar and longwave radiation) impact of riparian vegetation on the Loir's maximum daily $T_w$ using the <i>lidar</i> method (average on 08/2007-07/2014).....  | 124 |
| Figure 6.1: Eaudyssée river network on the Maine catchment .....   | 126 |
| Figure 6.2: Mean stream-aquifer exchanges on 08/2008-07/2013. Values are negative when river is drained by the aquifer .....   | 128 |
| Figure 6.3: Histogram of the values on the Loir catchment and on the 08/2008-07/2013. Probability for the zero value are 0.36, 0.37, 0.42 and 0.44 in winter, spring, summer and fall respectively .....   | 128 |

|   |     |
|---|-----|
| Figure 6.4: Stream-aquifer exchanges at the 17 Tw monitoring stations linked to an Eaudyssée mesh on the 13-31 August 2009 period. ....   | 129 |
| Figure 6.5: Groundwater fluxes variability on the 2008-2013 period and at the 17 stations linked to an Eaudyssée mesh. Variable plotted is $Q_G/A$ where $Q_G$ is the groundwater flux ( $m^3.s^{-1}$ ) and A is the cross sectional area ( $m^2$ ). (a) EROS (b) Eaudyssée. ....   | 130 |
| Figure 6.6: Longitudinal profile of the groundwater fluxes averaged on the Loir River and on the 13-31 August 2009. Variable plotted is $Q_G/A$ where $Q_G$ is the groundwater flux ( $m^3.s^{-1}$ ) and A is the cross sectional area ( $m^2$ ).....   | 130 |
| Figure 6.7: $Bias_{Eaudyssée} - Bias_{Standard}$ on mean daily temperature on 08/2008-07/2013 for the 17 stations linked to an Eaudyssée cell.....  | 131 |
| Figure 6.8: Mean daily biases on 08/2008-07/2013 for the 17 stations linked to an Eaudyssée cell (a) $Bias_{Standard}$ (b) $Bias_{Eaudyssée}$ .....   | 131 |
| Figure 6.9: Comparison of RMSE computed on mean daily Tw between the standard configuration and the configuration using Eaudyssée. Averages on available observed data on 2008-2013. ....   | 132 |
| Figure 6.10: Mean daily temperature modelled and measured in 2010 at (a) Yerre 47 (n°44), where accuracy is improved (b) Yerre 27 (n°43), where accuracy is decreased.....  | 132 |
| Figure 6.11: $Bias_{Eaudyssée} - Bias_{Standard}$ of diel amplitude on 08/2008-07/2013 for the 17 stations linked to an Eaudyssée cell.....   | 133 |
| Figure 6.12: $T_{mean_{Eaudyssée}} - T_{mean_{EROS}}$ , on average on the 13/31/08/2009 period.....   | 133 |
| Figure 6.13: Longitudinal profile of mean daily temperature on the Loir River, averaged on the 13-31/08/2009 period .....   | 134 |
| Figure 6.14: Temporal evolution of the thermal impact of groundwater fluxes on maximum daily Tw as modelled by Eaudyssée at the downstream-most Loir's reach of the LiDAR area (for consistency with Figure 5.28), in comparison with a simulation with no groundwater flux. ....   | 134 |
| Figure 6.15: Thermal impact of groundwater fluxes as modelled by Eaudyssée on the Loir's maximum daily Tw (average on 08/2007-07/2013) .....  | 135 |
| Figure 7.1: Bias ( $T_{sim} - T_{obs}$ ) of mean daily temperature in July-August as a function of thermal sensitivity (2008-2013 average) (a) simulation including all modifications brought in the thesis (b) Standard simulation (configuration of Beaufort et al., 2016). Stations numbers are in appendix B.....                                 | 141 |
| Figure 7.2: Longitudinal profile of daily mean temperature on the 4 main rivers of the Maine catchment, averaged on the 13-31/08/2009 period, simulated by the most complete version of T-NET (continuous) and by the standard version of T-NET (dotted).....   | 142 |
| Figure 7.1 : Biàs ( $T_{sim} - T_{obs}$ ) de la température moyenne journalière en juillet-août en fonction de la sensibilité thermique (2008-2013) (a) simulation incluant toutes les modifications apportées dans cette thèse (b) version standard du modèle (Beaufort et al., 2016). Les références aux numéros de stations sont en annexe B. .... | 150 |
| Figure 7.2: Profils longitudinaux des températures moyennes journalières sur les 4 rivières principales du bassin de la Maine, moyennées sur la période 13-31/08/2009, simulés avec la version la plus complète de T-NET (lignes continues) et avec la version standard (pointillés) .....  | 150 |



## List of tables

|  |     |
|--|-----|
| Table 2.1: Repartition of obstacles on the different entities of the Maine basin .....   | 36  |
| Table 3.1: Summary of Tw metrics used by other authors .....   | 40  |
| Table 3.2: Methods previously used to compute the thermal sensitivity.....   | 42  |
| Table 3.3: Overview of statistical models built with landscape descriptors at the regional scale (adapted from Goullet, 2017).....   | 43  |
| Table 3.4: Number of stations on each sub-catchment and on the main rivers.....  | 46  |
| Table 3.5: Distribution of Tw monitoring stations by Strahler order .....  | 47  |
| Table 3.6: Number of stations with data available for each year .....  | 48  |
| Table 3.7: Correlation coefficient between landscape and hydrologic descriptors.....   | 50  |
| Table 3.8: Linear regression models resulting of a stepwise selection .....  | 52  |
| Table 3.9: Percentage of time that observed Tw (hourly data) exceed given threshold in 2010 .....  | 53  |
| Table 3.10: Correlation matrix for Tw metrics .....  | 53  |
| Table 3.11: Linear regression model resulting of a stepwise selection between the residuals of the slope-intercept and the descriptors.....  | 56  |
| Table 3.12: Linear regression models resulting of the stepwise selection.....  | 57  |
| Table 3.13: Empirical model at the weekly time scale fitted on the 22 stations (fit group among the 44 stations). .....  | 58  |
| Table 4.1 : Formulations of heat fluxes taken into account at the atmospheric and the riverbed interfaces (Beaufort et al., 2016) .....  | 68  |
| Table 4.2: Biases and RMSE of the 5 variables provided by SAFRAN at the hourly time step on 08/2001-07/2002, averaged on the 5 validations stations (Sarrebouurg, Bordeaux, Puechabon, Toulouse, Col de Porte) (Quintana-Seguí et al., 2008).....  | 72  |
| Table 4.3: Bias ( $T_{sim}-T_{obs}$ ), standard deviation of errors and root mean square error (°C) computed on maximum, mean and minimum daily Tw and diel amplitude .....  | 77  |
| Table 5.1: Difference of criteria with the standard simulation. Green and red denote .....   | 98  |
| Table 5.2: Bias, standard deviation of errors and root mean square error (°C) computed on maximum, mean and minimum daily Tw and diel amplitude. Green and red denote .....  | 102 |
| Table 5.3: Model performance criteria for maximum daily temperature, averaged for the 4 stations located on the Loir River from April to September and from October to March (°C).....   | 112 |
| Table 5.4: Model performance criteria for minimum daily temperature, averaged for the 4 stations located on the Loir River from April to September and from October to March (°C).....   | 118 |
| Table 5.5: Model performance criteria for mean daily temperature, averaged for the 4 stations located on the Loir River from April to September and from October to March (°C) .....   | 119 |
| Table 5.6: Model performance criteria for diel amplitudes, averaged for the 4 stations located on the Loir River from April to September and from October to March (°C) .....  | 119 |
| Table 5.7: Model performance criteria (raw and compared to a simulation where riparian vegetation impact on longwave downward radiation is null), averaged for the 4 stations located on the Loir River from April to September and from October to March (°C). Green denotes improvement by more than 0.1 °C. All methods rely on LiDAR data where available..... | 121 |
| Table 6.1: Performance criteria on available data on the 08/2008-07/2013 period (a) values for the Eaudyssée simulation (b) $Criteria_{Eaudyssée} - criteria_{Standard}$ .....   | 135 |
| Table 7.1: Two thermal metrics summarised by sub-catchment and by Strahler order (2010) .....  | 137 |
| Table 7.2: Accuracy criteria of a simulation including all modifications brought in the thesis, and compared with the standard configuration.....  | 140 |
| Tableau 7.1 (français) : Deux métriques de Tw résumées par sous-bassin et par ordre de Strahler (2010) .....   | 145 |
| Tableau 7.2 (français) : Performance d'une simulation incluant toutes les modifications effectuées durant la thèse, comparée à la version standard. Toutes les valeurs sont en °C. ....  | 149 |



# Chapter 1: Introduction (français)

## 1.1 Contexte

La température des cours d'eau ( $T_w$ ) est un paramètre important de la qualité de l'eau car elle contrôle la solubilité de l'oxygène (Moatar et al., 2001), les réactions chimiques (Haag et Westrich, 2002), et les processus physiologiques des organismes (Angilletta, 2009). Par conséquent, elle affecte le comportement et la survie des poissons (Magnuson et al., 1979) et de l'ensemble des communautés aquatiques (Woodward et al., 2010 ; Floury et al., 2013 ; Daufresne et al., 2004). Elle influence ainsi les aires de répartition de ces espèces ectothermes (Isaak et al., 2017).

Les changements climatiques et d'occupation du sol altèrent les échanges d'énergie, ce qui se traduit lors des dernières décennies par une augmentation de la température des hydrosystèmes : en Amérique du Nord (Kaushal et al., 2010), en Europe (Orr et al., 2015 ; Hannah et Garner, 2015), et en Asie (Chen et al., 2016). En France, la température des fleuves augmente également et cette tendance devrait continuer avec le réchauffement climatique (Poirel et al., 2008 ; Moatar et Gailhard, 2006 ; Bustillo et al., 2014). En effet, en France métropolitaine, les températures moyennes de l'air ( $T_a$ ) devraient augmenter de 0,6 à 5,1 °C à l'horizon 2071-2100, par rapport la fin du 20ème siècle, en fonction du scénario d'émission de gaz à effet de serre (Ouzeau et al., 2014). Ce réchauffement pourrait avoir de lourdes conséquences pour certaines espèces aquatiques, et on recherche actuellement des mesures de compensation afin d'assurer la survie des espèces les plus sensibles.

Dans ce contexte, il est important de comprendre les processus qui déterminent la sensibilité thermique des hydrosystèmes au changement climatique. Cette sensibilité thermique a été quantifiée par de nombreux auteurs (Hilderbrand et al., 2014 ; Kelleher et al., 2012 ; Molinero et al., 2016 ; O'Driscoll et DeWalle, 2006) en se basant sur la pente de la régression linéaire  $T_w$ - $T_a$ . Cette méthode a l'avantage d'être assez simple et de caractériser le régime thermique avec un seul chiffre. La plupart des études analysant la sensibilité thermique à une échelle régionale sont réalisées sur des bassins dont le climat est hétérogènes, en raison d'un gradient d'élévation (Hilderbrand et al., 2014 ; Chang et Psaris, 2013, Chu et Jones, 2011, Jackson et al., 2017, Kelleher et al., 2012, Molinero et al., 2016, Moore, 2006) ou de latitude (Laizé et al., 2017 ; Garner et al., 2014a). Peu d'études se concentrent sur une zone climatiquement homogène où la variabilité de  $T_w$  est causée par d'autres facteurs que la variabilité de  $T_a$ .

Afin de comprendre et de prévoir la répartition spatiale des espèces aquatiques sous les conditions climatiques actuelles ou futures (Buisson et al., 2008 ; Tisseuil et al., 2012 ; Boisneau et al., 2008 ; Brown et al., 2005), et comme il n'est pas possible d'instrumenter tous les cours d'eau, il est nécessaire de modéliser la température des cours d'eau à l'échelle régionale. Les modèles statistiques sont basés sur des relations empiriques entre  $T_w$  et d'autres variables qui peuvent être obtenues facilement, comme  $T_a$ , les débits, ou des caractéristiques disponibles facilement à partir d'analyse SIG. Pour cette raison, ils sont assez faciles à mettre en œuvre et sont parfois en mesure de calculer  $T_w$  pour chaque tronçon d'un grand bassin versant (Jackson et al., 2017). Cependant, les modèles physiques sont plus pratiques pour étudier les processus impliqués parce que l'effet causal peut être isolé, tandis que les modèles empiriques ne lient que différentes variables à la réponse thermique, sans prouver l'effet causal (Moore, 2006).

Plusieurs modèles de température de cours d'eau à base physique ont été développés et appliqués sur de grands bassins ( $> 10\,000\text{ km}^2$ ) (Chen et al., 1998b ; Haag et Luce, 2008 ; Wu et al., 2012 ; Cheng et Wiley, 2016). Cependant, seulement quelques-uns d'entre eux ont été conçus pour modéliser  $T_w$  au pas de temps horaire et avec une haute efficacité de calcul. C'est la raison pour laquelle Aurélien Beaufort a développé le modèle T-NET au cours de sa thèse et l'a appliqué sur le bassin de la Loire ( $10^5\text{ km}^2$ ). Beaufort et al. (2016) ont obtenu une RMSE moyenne (racine carrée de l'erreur quadratique) de  $1.6\text{ °C}$  sur la température moyenne journalière de 128 stations (2008-2012). Cependant, certaines stations montrent une précision moindre, avec des RMSE supérieures à  $2\text{ °C}$  en été, surtout lorsqu'on examine la température maximale quotidienne ( $T_{\max}$ ).

Beaufort et al. (2016) ont suggéré que la saisonnalité des biais pour les petites et moyennes rivières pourrait être corrigée par l'amélioration de la caractérisation de l'ombrage porté par la végétation rivulaire. Ce facteur est intéressant parce que la plantation d'arbres est le moyen le plus facile pour l'homme de diminuer  $T_w$ , et de nombreuses études ont montré que l'ombrage peut réduire considérablement la température des cours d'eau petits à moyens (Moore et al., 2005 ; Garner et al., 2014b). Plusieurs modèles de  $T_w$  ont été développés afin d'étudier l'impact de l'ombrage (Chen et al., 1998a ; Cox et Bolte, 2007 ; Loinaz et al., 2013 ; Sun et al., 2015 ; Lee et al., 2012 ; Tung et al., 2007). Cependant, il y a encore du travail pour améliorer l'exactitude de cette caractérisation tout en restant à l'échelle régionale.

Les échanges nappe-rivière ont également reçu une attention croissante parce qu'ils ont un impact important sur la température des cours d'eau (Lalot et al., 2015 ; Moatar et Gailhard, 2006 ; Wawrzyniak et al., 2017 ; O'Driscoll et DeWalle, 2006). En effet, les températures des eaux souterraines étant relativement constantes tout au long de l'année, les flux de nappe augmentent  $T_w$  en hiver et la diminuent en été. L'homme peut augmenter les flux de nappe en augmentant la recharge des eaux souterraines (limiter l'étendue des surfaces imperméables, limiter le pompage). La caractérisation précise de l'impact thermique des flux de nappe a toujours été difficile (et surtout à l'échelle régionale), essentiellement parce que ces flux ne peuvent pas être mesurés facilement. Plusieurs modèles de  $T_w$  ont été développés en se concentrant sur leur caractérisation, mais ils ont été appliqués à des bassins de taille inférieure à  $1000\text{ km}^2$  (Loinaz et al., 2013 ; Essaid et Caldwell, 2017). Par conséquent, il y a encore un potentiel d'amélioration sur ce sujet.

## **1.2 Objectifs et plan**

Dans cette thèse, nous avons choisi de nous concentrer sur le bassin versant de la Maine, un sous-bassin de la Loire de  $22\,350\text{ km}^2$  qui est climatiquement homogène mais hétérogène en ce qui concerne plusieurs autres paramètres (lithologie, végétation rivulaire, obstacles à l'écoulement). Il s'agit donc de caractériser la variabilité de la température de l'eau à partir de 44 stations de suivis (été 2008 - été 2015) et de trouver les meilleurs descripteurs permettant d'expliquer cette variabilité.

L'application du modèle physique T-NET (Beaufort et al, 2016) sur ce bassin (plus petit que le bassin de la Loire) permettra de mieux comprendre les forces et les faiblesses du modèle, ainsi que les processus impliqués. Cela facilitera également la manipulation de jeux de données importants ou dont l'intégration nécessite un travail manuel. Il s'agira de mieux prendre en compte deux processus

qui ont un rôle important pour la régulation thermique sous changement climatique : l'ombrage porté par la végétation rivulaire et les apports d'eau souterraine.

Après cette introduction (chapitre 1), la thèse sera structurée comme suit :

Chapitre 2 : Le bassin versant de la Maine et ses trois sous-bassins (Loir, Sarthe, Mayenne) seront présentés, avec leurs propriétés hydrométéorologiques.

Chapitre 3 : Les données mesurées par l'AFB (Agence Française pour la Biodiversité), la DREAL (Direction régionale de l'environnement, de l'aménagement et du logement) des Pays de la Loire et la Fédération de Pêche d'Eure et Loir à 44 stations sur le bassin versant de la Maine seront présentées. La variabilité spatio-temporelle du régime thermique à ces stations sera analysée afin de comprendre quels tronçons de rivière sont les plus vulnérables aux changements climatiques. Afin d'avoir un outil facile à mettre en œuvre à l'échelle régionale, un modèle empirique capable de prédire  $T_w$  à l'échelle de temps hebdomadaire sera développé et testé.

Chapitre 4 : Le modèle T-NET (tel que publié par Beaufort et al., 2016) sera décrit. Ses résultats sur le bassin versant de la Maine seront analysés dans le but d'identifier les forces et les faiblesses de la version de T-NET qui était disponible au début de la thèse. Des analyses de sensibilité seront réalisées sur les paramètres hydrauliques afin de bien comprendre le comportement du modèle.

Dans les chapitres 5 et 6, nous tenterons d'améliorer la précision du T-NET afin de répondre à la question : quelle précision peut-on atteindre avec un modèle applicable à l'échelle régionale, sur ce bassin particulier ? Dans quelle mesure l'inclusion d'un processus caractérisé à une échelle fine peut-elle améliorer la précision du modèle ?

Chapitre 5 : Nous nous concentrerons sur l'impact de la végétation rivulaire sur le rayonnement solaire et le rayonnement infrarouge qui atteint la rivière. Premièrement, 3 modifications apportées au modèle T-NET concernant le rayonnement solaire seront analysées :

- La prise en compte d'un albédo variant avec l'élévation solaire.
- L'amélioration de la phénologie des arbres pour déterminer comment le feuillage bloque le rayonnement.
- L'utilisation d'un nouveau jeu de données de rayonnement solaire (HelioClim) à la place des données SAFRAN. Nous avons acquis les données HelioClim parce qu'elles fournissent les rayonnements directs et diffus séparément et parce qu'elles sont générées à l'aide des images satellitaires Météosat, à une meilleure résolution spatiale que SAFRAN.

Ensuite, une caractérisation précise de l'impact de la végétation rivulaire sur le rayonnement solaire direct et diffus à l'aide de données LiDAR sera comparée à une méthode de complexité moyenne et à la méthode simple utilisée dans la version standard de T-NET au chapitre 4 (et par Beaufort et al., 2016). Ce travail, qui correspond globalement à un article publié dans *Science of the Total Environment*, ne sera réalisé que sur la rivière Loir en raison de la disponibilité initiale des données LiDAR. Cette partie sera suivie par des résultats n'a pas pu être ajouté dans l'article. Ensuite, les profils thermiques longitudinaux du Loir, modélisés avec la méthode basée sur l'utilisation de données LiDAR seront comparés à deux profils mesurés dans l'infrarouge thermique par télédétection aéroportée, le 10 septembre 2014 et le 5 février 2015. Enfin, l'impact de la végétation rivulaire sur le rayonnement infrarouge reçu par la rivière sera implémenté dans le modèle et discuté.

Chapitre 6 : Ce chapitre porte sur l'impact des flux de nappe. Les échanges nappe-rivière modélisés à une résolution de 1 km<sup>2</sup> par le modèle hydrogéologique distribué Eaudyssée (Baratelli et al., 2016) seront injectés dans T-NET. Cette approche sera comparée à la méthode originale utilisant les flux de nappe du modèle EROS. L'objectif est d'analyser dans quelle mesure cette modification améliore la performance de T-NET, l'objectif secondaire étant de quantifier l'impact réel des flux de nappe sur la Tw du Loir, en été.

# Chapter 1: Introduction (English)

## 1.1 Context

Stream temperature ( $T_w$ ) is a major water quality parameter because it controls oxygen solubility (Moatar et al., 2001), chemical reactions (Haag and Westrich, 2002), and physiological processes (Angilletta, 2009). Hence, it affects behaviour and survival of fishes (Magnuson et al., 1979) and of the whole aquatic communities (Woodward et al., 2010; Floury et al., 2013; Daufresne et al., 2004). It therefore influences the spatial distribution of these ectothermic species (Isaak et al., 2017).

Changes in climate and in landuse alter energy exchanges, which reflect in rises in hydrosystems temperature during the last decades: in north America (Kaushal et al., 2010), in Europe (Orr et al., 2015; Hannah and Garner, 2015), and in Asia (Chen et al., 2016). In France, temperature is already increasing across rivers, a trend which is expected to continue further under projected climate change (Poirel et al., 2008; Moatar and Gailhard, 2006; Bustillo et al., 2014). Indeed, toward the 2071-2100 period, depending on the greenhouse gases emission scenario, mean air temperatures ( $T_a$ ) are forecasted to rise by 0.6 to 5.1°C in metropolitan France, compared to the end of the 20<sup>th</sup> century (Ouzeau et al., 2014). Such a warming could have severe consequences for a range of aquatic species, and adaption measures are currently being sought with a review to ensuring the continued survival of temperature sensitive fluvial organisms.

In this context, it is important to understand the processes determining the thermal sensitivity of hydrosystems to climate change. This sensitivity has been quantified by many authors (Hilderbrand et al., 2014; Kelleher et al., 2012; Molinero et al., 2016; O'Driscoll and DeWalle, 2006) by computing the slope of the  $T_w$ - $T_a$  linear regression. This method has the advantage to be quite simple and to characterise the thermal regime with only one number. Most studies analysing the thermal sensitivity conducted at the regional scale are achieved on climatically heterogeneous catchments, because of an elevation gradient (Hilderbrand et al., 2014; Chang and Psaris, 2013, Chu and Jones, 2011, Jackson et al., 2017, Kelleher et al., 2012, Molinero et al., 2016, Moore, 2006) or because of a latitudinal gradient (Laizé et al., 2017; Garner et al., 2014a). Few studies focus on a climatically homogenous area where  $T_w$  variability will be caused mainly by other factors than  $T_a$ .

In order to understand and forecast the spatial distribution of aquatic species under present or future climatic conditions (Buisson et al., 2008; Tisseuil et al., 2012; Boisneau et al., 2008; Brown et al., 2005), and since it is not possible to monitor all rivers, there is a need to model stream temperature at the regional scale. Statistical models are based on empirical relationships between  $T_w$  and other variables that can be obtained more easily, like  $T_a$ , discharge or landscape characteristics available from GIS analysis. For this reason, they are quite easy to implement and are sometime able to compute  $T_w$  for every reaches of a large catchment (Jackson et al., 2017). However, physical models are more practical to study the involved processes because the causal effect can be isolated, while empirical models only link different variables to the thermal response, without proving the causal effect (Moore, 2006).

Several physically based stream temperature models have been developed and applied on large catchments (>10 000 km<sup>2</sup>) (Chen et al., 1998b; Haag and Luce, 2008; Wu et al., 2012; Cheng and Wiley, 2016). However, only few of them were designed to model  $T_w$  at the hourly time step and with

a high computational efficiency. Hence, Aurélien Beaufort developed the T-NET model during his thesis and applied it on the Loire river basin ( $10^5$  km<sup>2</sup>). Beaufort et al. (2016) computed an average root mean square error on mean daily temperature at 1.6 °C on the basis of 128 water temperature stations (2008–2012). However, some stations show lesser accuracy, with RMSE above 2°C in summer, especially when looking at the maximum daily temperature ( $T_{max}$ ).

Beaufort et al. (2016) suggested that the seasonality of biases for small and medium rivers could be corrected by improving the characterisation of shading by riparian vegetation. This process is interesting because planting trees is the easiest way for human to decrease  $T_w$ , and many studies have shown that shade can greatly reduce water temperature of small and medium size rivers (Moore et al., 2005; Garner et al., 2014b). Several  $T_w$  models have been developed in order to study the shading effect (Chen et al., 1998a; Cox and Bolte, 2007; Loinaz et al., 2013; Sun et al., 2015; Lee et al., 2012; Tung et al., 2007). However, more work can be achieved to improve the accuracy of this characterisation while staying at the regional scale.

Stream-aquifer exchanges have also been given increasing research attention, because they have an important impact on stream temperature (Lalot et al., 2015; Moatar and Gailhard, 2006; Wawrzyniak et al., 2017; O’Driscoll and DeWalle, 2006). Indeed, groundwater temperatures being relatively constant throughout the year, groundwater fluxes to the river increase  $T_w$  in winter and decrease it in summer. Human can increase groundwater fluxes by increasing groundwater recharge (limit building of impervious surfaces, limit water pumping). The accurate characterisation of the groundwater thermal impact has always been challenging (and especially at the regional scale), especially because these fluxes cannot be measured easily. Several stream temperature models have been developed with a focus on their characterisation but they have been applied to catchments with sizes smaller than 1000 km<sup>2</sup> (Loinaz et al., 2013; Essaid and Caldwell, 2017). Hence, more research can be achieved on this topic.

## **1.2 Aims and plan**

In this thesis, we chose to focus on the Maine catchment, a 22 350 km<sup>2</sup> sub-catchment of the Loire basin which is climatically homogeneous but heterogeneous regarding several other factors (lithology, vegetation cover, obstacles to flow). The aim is thus to characterise  $T_w$  variability from 44  $T_w$  monitoring stations (summer 2008 - summer 2015) and to find the best descriptors to explain it.

The application of the physically based T-NET model (Beaufort et al, 2016) on this basin smaller than the Loire basin will allow a better understanding of the strengths and weaknesses of T-NET, as well as the processes involved. It will also facilitate the handling of dataset that are heavy or that need a manual work. The aim is to better take into account two processes that are important in the climate change mitigation: shading by riparian vegetation and groundwater fluxes.

After this introduction (chapter 1), the thesis will be structured as follows:

Chapter 2: The Maine catchment and its 3 sub-catchments (Loir, Sarthe, Mayenne) will be presented in chapter 2, with their hydrometeorological properties.

Chapter 3: The data measured by Agence Française pour la Biodiversité, DREAL (Direction régionale de l'environnement, de l'aménagement et du logement) des Pays de la Loire, and Fédération de

Pêche d'Eure et Loir at the 44 stations on the Maine catchment will be presented. The spatio-temporal variability of the thermal regime at these stations will be analysed, in order to understand when and where a monitored river reach is vulnerable to climate change. In order to have a tool that is very easy to implement at the regional scale, an empirical model able to predict water temperature at the weekly time scale will be developed and tested.

Chapter 4: The T-NET model (as published by Beaufort et al., 2016) will be described. We will analyse its results on the Maine catchment, in order to identify the strengths and weaknesses of the T-NET version available at the beginning of the thesis. A sensitivity analysis will be achieved on the hydraulic parameters, in order to fully understand the model's behaviour.

In chapter 5 and 6, we will attempt to improve T-NET accuracy, in order to answer the question: what accuracy can be reached with a model applicable at the regional scale, on this challenging basin? To what extent, the inclusion of a process characterised at a fine-scale can improve the model accuracy?

Chapter 5: We will focus on the impact of riparian vegetation on the solar and the downward longwave radiation. Firstly, 3 modifications brought to the T-NET model regarding the solar radiation will be analysed:

- The consideration that the albedo depends on the solar elevation.
- The improvement of the tree foliage phenology, i.e. how we determine when trees are in leaf and block sunrays.
- The use of a new radiation dataset (Helioclim) instead of SAFRAN global radiation data. We acquired the Helioclim data because they provide direct and diffuse radiation separately and because they are generated with the help of Meteosat satellites imagery at a better spatial resolution than SAFRAN.

Then, a precise characterisation of the impact of riparian vegetation on the direct and the diffuse solar radiation using LiDAR data will be compared to a method of medium complexity and to the simple method used in the standard version of T-NET in chapter 4 (and in Beaufort et al., 2016). This work, which corresponds to an article published in Science of the Total Environment, will be achieved only on the Loir River because of the availability of the LiDAR data there. This part is followed by results that could not be added in the article. Then, the thermal longitudinal profiles on the Loir modelled with the method using LiDAR data will be compared to two profile measured by thermal infrared airborne remote-sensing on the 10 September 2014 and the 5 February 2015.

Finally, the impact of riparian vegetation on the downward longwave radiation will be implemented and discussed.

Chapter 6: This chapter focuses on the impact of groundwater fluxes. Stream-aquifer exchanges modelled at a 1 km<sup>2</sup> resolution by the Eaudyssée distributed hydrogeological model (Baratelli et al., 2016) will be taken as input of T-NET. This approach will be compared to the original method using groundwater fluxes from the semi-distributed model EROS. The goal is to analyse to what extent this modification improves T-NET performance, with a secondary goal that is to quantify the actual impact of groundwater fluxes on water temperature of the Loir, in summer.



## Chapter 2: Study site of the Maine catchment

### 2.1 Résumé en français

Le bassin de la Maine est situé dans le centre-ouest de la France. Sa superficie est de 22350 km<sup>2</sup> et il se compose des sous-bassins de la Mayenne, de la Sarthe et du Loir (Figure 2.1). L'altitude varie entre 13 et 416 m. La Sarthe devient la Maine à la confluence avec la Mayenne, et s'écoule ensuite dans la Loire. Le bassin est hétérogène, puisqu'il s'étend sur deux hydro-éco régions (ligne rouge sur Figure 2.1). La partie ouest correspond au massif armoricain, composé de roches cristallines qui sont généralement imperméables, bien que de petits aquifères peuvent être présents. La partie Est est composée de roches sédimentaires qui font partie du Bassin Parisien. On y trouve 4 formations aquifères superposées. Les calcaires de Beauce situés tout à l'Est du bassin drainent les tronçons amonts des rivières Conie et Aigre, qui sont sèches la plupart du temps. Une couche de craie du Crétacé affleure plus à l'ouest, suivie d'une formation sableuse du Cénomanién (Crétacé supérieur), et enfin d'une couche de calcaire du Jurassique. L'agriculture occupe en moyenne 52% du territoire, avec une emprise plus importante sur le bassin du Loir. Les prélèvements en eau nécessaires pour l'agriculture sont importants dans la Beauce. Le taux de végétation rivulaire moyen calculé par Valette et al. (2012) sur une zone tampon de 10 m appliqué aux polygones de végétation de la BD TOPO suit un gradient Ouest-Est sur les ordres de Strahler 1 à 4 avec un taux de végétation important sur la partie amont du Loir. Les températures du mois de juillet moyennées sur 1980-2010 varient entre 17 et 20 °C et sont corrélées avec l'altitude (Figure 2.6). Les précipitations moyennes annuelles sont les plus importantes dans le nord du bassin de la Mayenne, à cause de la présence de reliefs (Figure 2.7). Les analyses réalisées dans cette thèse seront réalisées sur la période août 2008 - juillet 2015. La variabilité de la température de l'air, moyennée sur tout le bassin, est représentée à la Figure 2.8. Des vagues de chaleurs sont présentes aux étés 2010 et 2013. Les débits spécifiques mesurés aux 3 stations de jaugeage les plus en aval sur chaque sous-bassin suivent un gradient Est-Ouest, particulièrement en hiver. Celui-ci est dû au différentiel de précipitations, mais aussi de perméabilité. Le rapport entre le débit spécifique estival et le débit spécifique moyen suit le même gradient. Il n'y a pas de grands barrages sur le bassin de la Maine mais un grand nombre de seuils et d'étangs. La base de données ROE (Référentiel des Obstacles à l'Écoulement) référence 1616 obstacles avec leurs hauteurs de chute (médiane = 1 m). L'impact de ces seuils peut être calculé via différents indicateurs comme la densité sur 100 km ou le taux d'étagement, qui est le rapport entre les hauteurs de chute cumulées et la différence d'altitude entre deux points. Les deux indicateurs montrent un impact le plus important sur le Loir.

### 2.2 General description and elevation

The Maine catchment is a 22350 km<sup>2</sup> sub-catchment of the Loire basin, located in central-west France (Figure 2.1). The total river network (BD Carthage modified to be tree shaped) is 16 975 km long. It is composed of 3 sub-catchments: the Mayenne (5840 km<sup>2</sup>), the Sarthe (8020 km<sup>2</sup>) and the Loir (8250 km<sup>2</sup>) basins. The Sarthe has a major tributary, the Huisne River (catchment area of 2300 km<sup>2</sup>). The Loir and the Mayenne flow into the Sarthe, but the river name becomes the Maine at the confluence with the Mayenne. The Mayenne and the Sarthe are Strahler order 6 in their downstream parts, while the Loir is an order 5, due to the lowest network density on this sub-basin.

The 50 m resolution Digital Elevation Model from Institut national de l'information géographique et forestière (IGN) shows that elevation ranges from 13 to 416 m above sea level. Maximum is 416 m in the Mayenne and Sarthe basins and 286 m in the Loir basin. Median altitudes are similar between catchments (Mayenne: 117 m, Sarthe: 118 m, Loir: 130 m). Latitudinal range of the whole basin is 150 km.

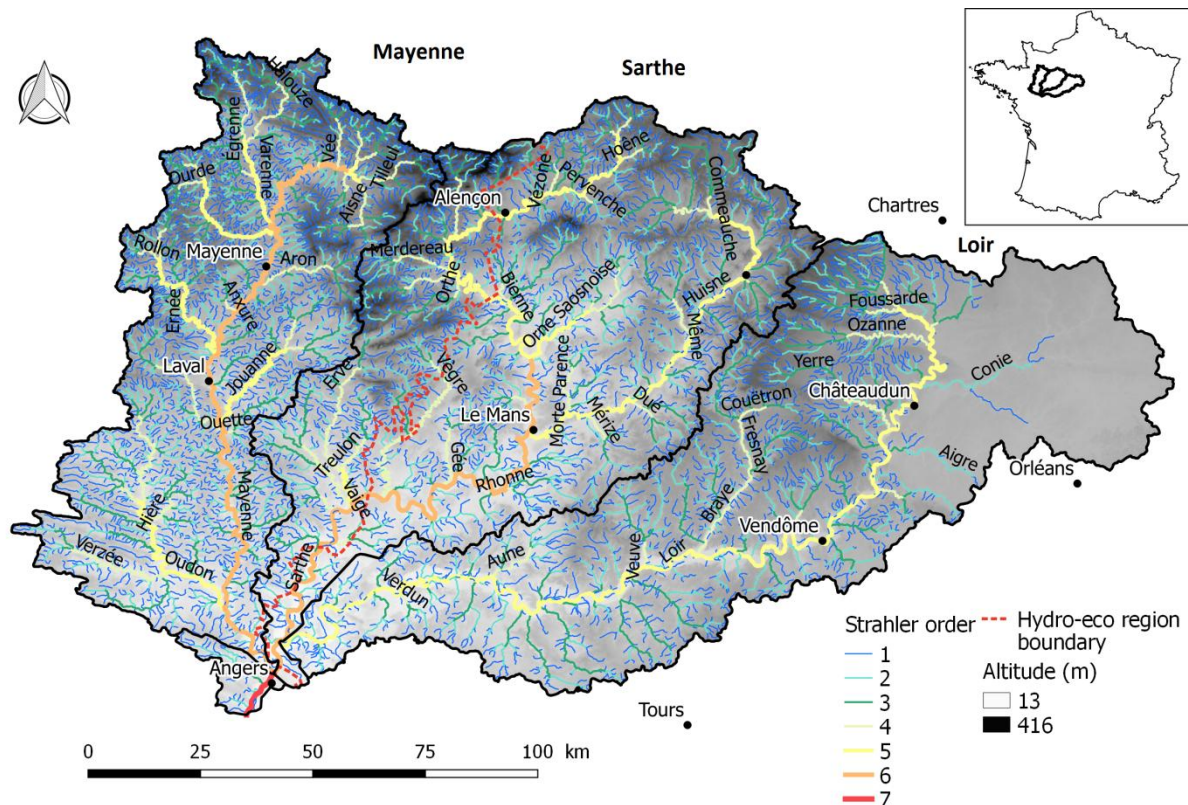


Figure 2.1: The Maine catchment with the 3 subcatchments, elevation, the hydro-eco region boundary, river classified by Strahler order and the main cities

### 2.3 Lithology and hydrogeology

The hydro-eco region boundary (Wasson et al., 2002) shown in red on Figure 2.1 splits the basin in two area of contrasted geology. On the west side is found the Armorican massif, composed of crystalline rocks (Figure 2.2). Although these rocks are basically impervious, two different kind of small aquifer of medium productivity can be found in this area. The first type is formed by the presence of an altered rock layer located above a fragmented rock layer. The altered layer has a high porosity but a low permeability, which means that water can be stored in this layer but cannot move easily. The underlying layer has a higher permeability, allowing groundwater fluxes to rivers (Mardhel et al., 2007), which heat them in winter and cool them in summer. The second type of aquifer is created by the presence of exogenous and more pervious rock that filled a graben-type basin (Chrétien et al., 2014). Some alluvial formations can also be found in the Armorican massif. All that explains why average contribution of groundwater to river discharge is close to zero for the Mayenne River (upstream of the confluence with the Oudon River), while it is about 20% for the Oudon itself (Mardhel et al., 2007).

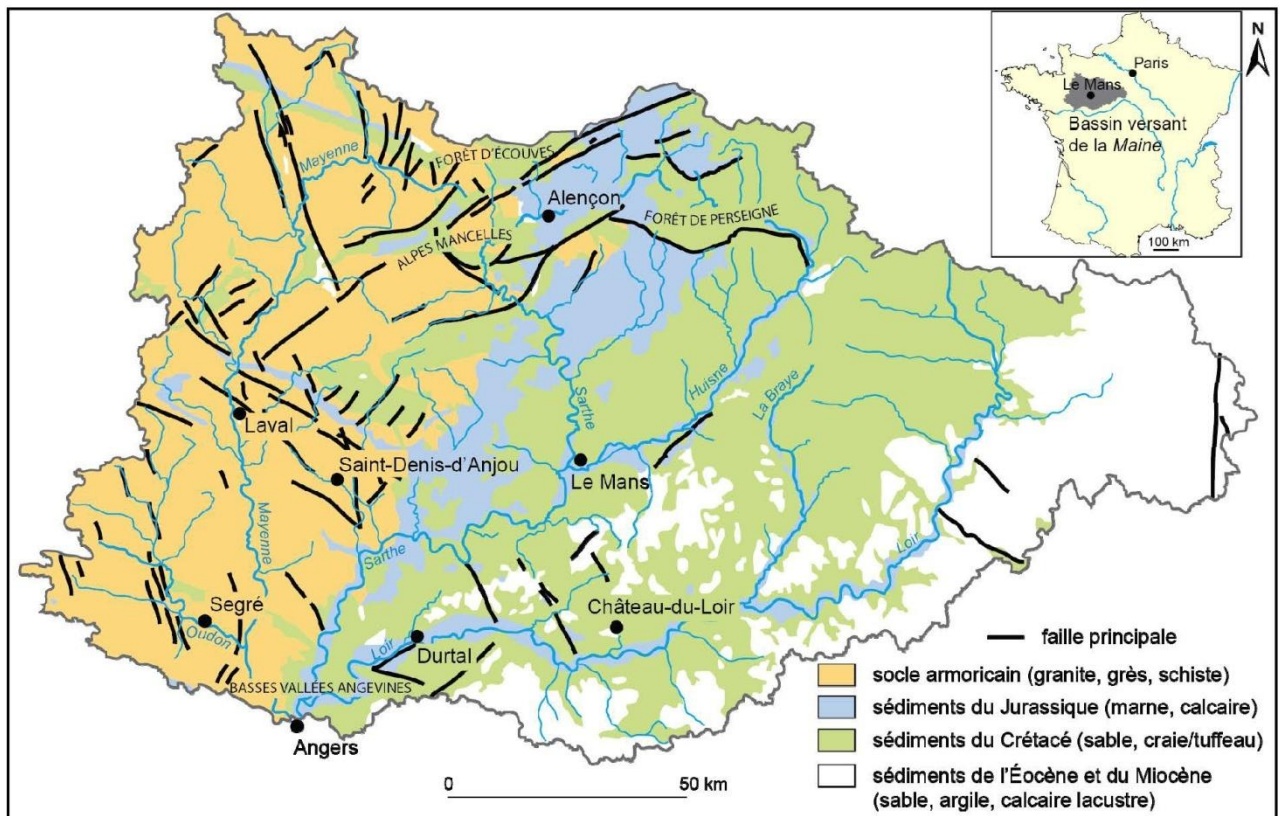


Figure 2.2: Geology of the Maine catchment. Source: Alhaskeer et al. (2014), data from BRGM (1980).

The area located east of the hydro-eco boundary is made of sedimentary rocks which are part of the Paris basin. Four large aquifers are present:

The Beauce limestone aquifer is one of the biggest aquifer in France. It extends on about 9000 km<sup>2</sup> in the Centre-Val de Loire and Ile-de-France regions (Martin, 1999). It is found in the eastern part of the Loir basin, where the upstream reaches of the Conie and the Aigre River sometime flow. These river reaches are actually dry most of the time and their discharge depend on the groundwater table level. This limestone is highly fractured and sometime karstic. The Beauce aquifer, located in a multi-layer system with a deep unsaturated zone, usually flows toward the south, with little flow toward the Loir River (Mardhel et al., 2007). Intensive water withdrawal is done in this area for agriculture.

Underneath the Beauce limestone is found a chalk layer from the Cretaceous, with high porosity but low permeability. The presence of cracks or alteration is needed to form an aquifer. This aquifer is drained by streams and there are exchanges with the Loir's alluvial groundwater (Mardhel et al., 2007). Like for the Beauce aquifer, piezometric levels are influenced by long-term climatology.

The Cenomanian sands formation (also called the Perche sands) outcrops at the east of the Sarthe River, in the Huisne catchment and in the valleys of the west part of the Loir, where many spring are found. The groundwater flows toward east, where it becomes rapidly confined. There is thus a transfer of water from the Sarthe basin to the Loir basin (Mardhel et al., 2007).

Finally, a Jurassic limestone outcrops just east of the hydro-eco region boundary (blue on Figure 2.2). Because it's a compact limestone, these aquifers are productive only where there are cracks, like it can be found close to the Armorican massif. The aquifer is well drained by rivers (Mardhel et al., 2007).

## 2.4 Landuse and riparian vegetation

According to landuse data retrieved by Alhaskeer (2012) on satellite imagery of 2003, 52% of the Maine basin landuse is dedicated to crops and temporary grasslands. Permanent grassland extends on 26% of the catchment, forest on 18% and the built environment on 3%. There are more crops in the Loir basin (66%) than in the others (44%), because of the high fertility of the Beauce region. Permanent grasslands are more present in the Mayenne basin (37% vs. 29% in Sarthe and 14% in Loir basins), while forest are more present in the Sarthe basin (22% vs. 15% in Mayenne and 17% in Loir). The ratio of coniferous forest related to deciduous forest follow the same trend (23% in Sarthe, 11% in Mayenne and 18% in Loir). This spatial heterogeneity was mapped with the CORINE Land Cover 2012 data, provided by the European Environment Agency (Figure 2.3).

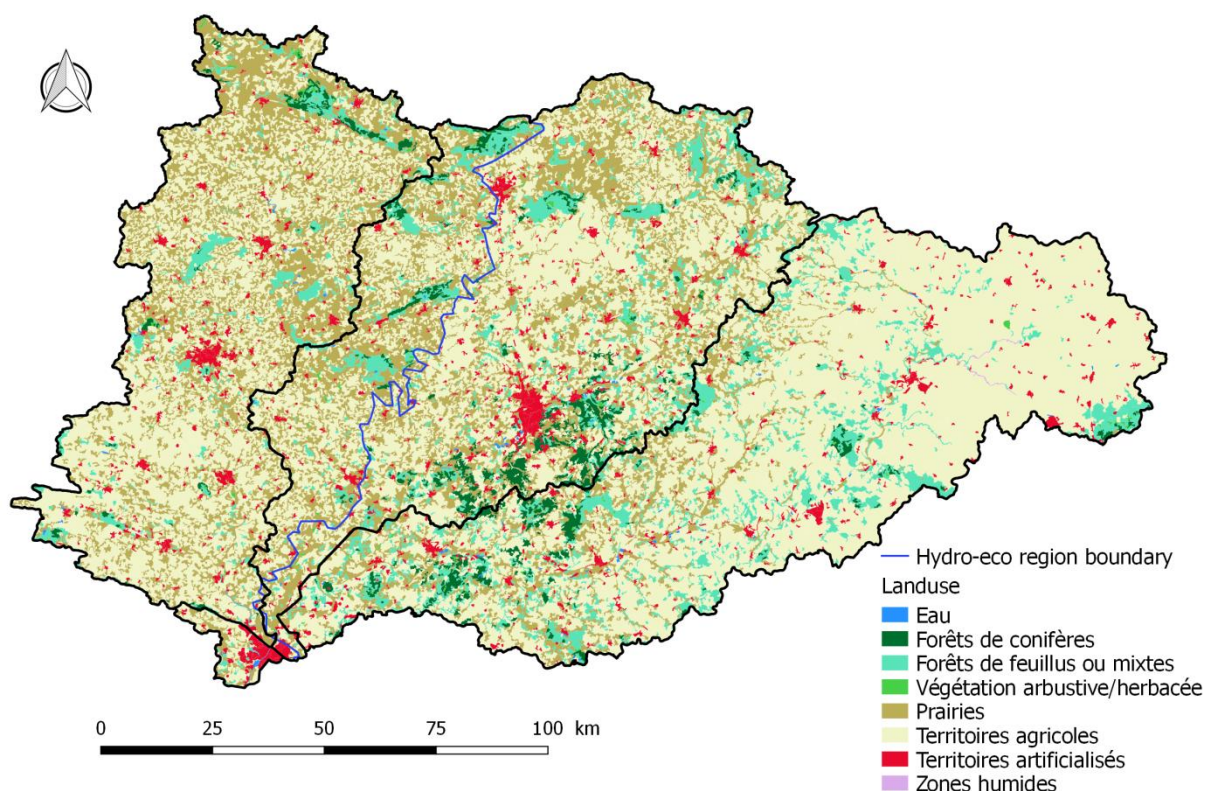


Figure 2.3: Landuse from Corine Land Cover 2012

To characterise the variability in riparian vegetation, we use vegetation cover data provided by Valette et al. (2012). They computed the percentage of vegetation polygons (Institut géographique national) in a buffer of 10 m around river reaches. Data was transferred from original river network to the T-NET river network by taking the value of the closest reach. Because of this, and because base GIS data has a limited resolution, absolute values have a limited accuracy (Beaufort, 2015). However, it can be used for relative comparisons. Spatial distribution on the T-NET network is shown on Figure 2.4. The mean vegetation cover is higher on the Loir basin than on the Sarthe and Mayenne basins. On average, there is a west-east gradient in vegetation cover, at least for Strahler order 1 to 4 (Figure 2.5).

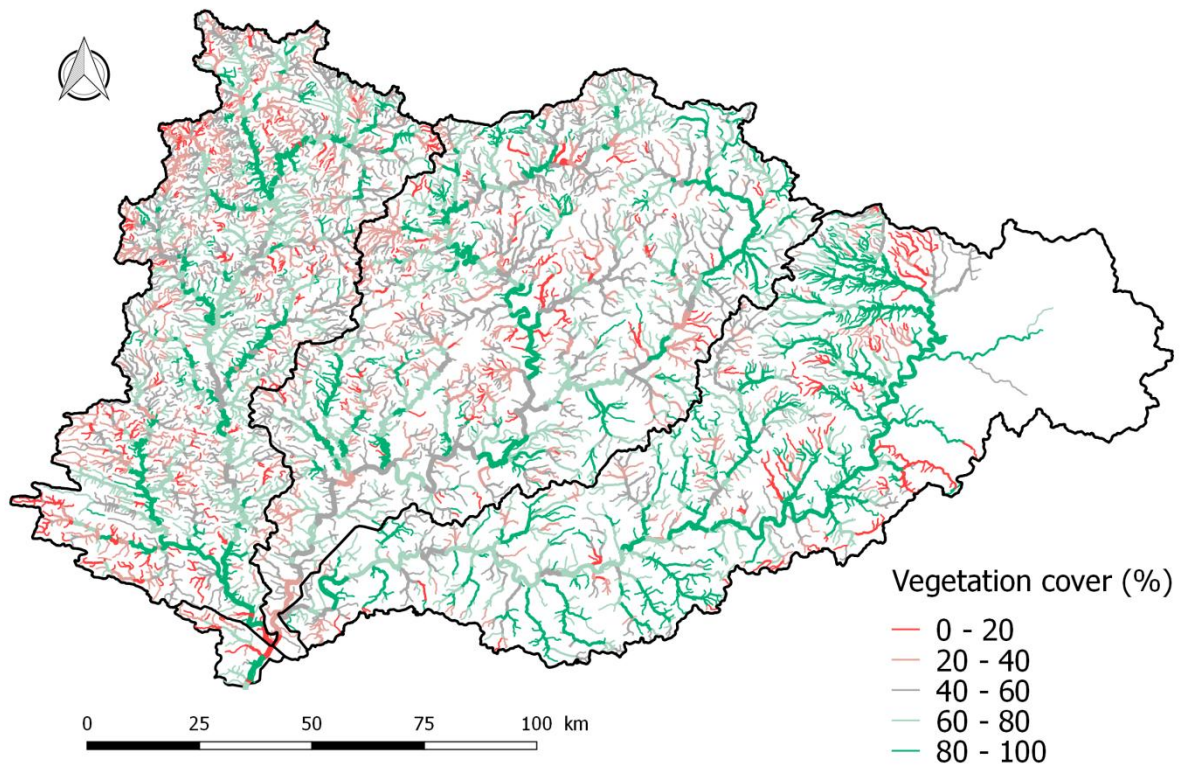


Figure 2.4: Vegetation cover data computed by Valette et al. (2012) in a 10m buffer around their own river network and extrapolated on our river network

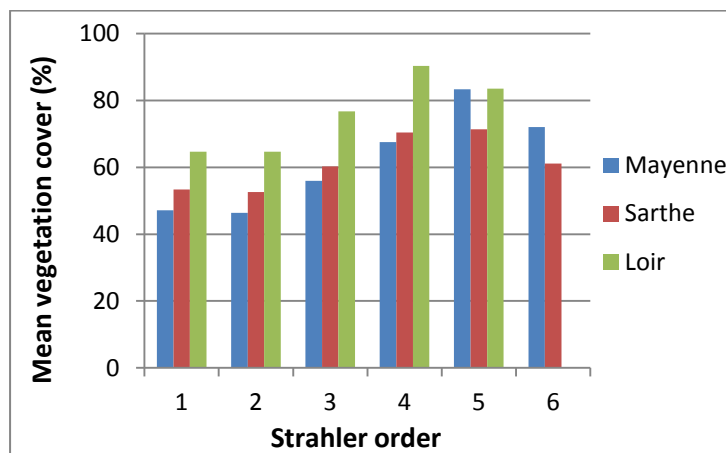


Figure 2.5: Mean vegetation cover for each sub-catchment and by Strahler order

## 2.5 Climatic conditions

Averaged climatic variables computed by Météo-France on 1981-2010 (Canellas et al., 2014) show that mean air temperatures ( $T_a$ ) in July ranges within 3°C, from 17 to 20°C (Figure 2.6). Spatial pattern show that these temperatures are correlated with altitudes (Figure 2.1). Mean values are 18.6, 18.8 and 19.2 °C on the Mayenne, Sarthe and Loir catchments respectively.

Precipitations are higher in the west part of the basin (Figure 2.7), because of the reliefs located north-west of the basin, and because south-west is a major wind direction. Mean precipitations are 831 mm on the Mayenne basin, 755 mm on the Sarthe basin, and 694 mm on the Loir basin.

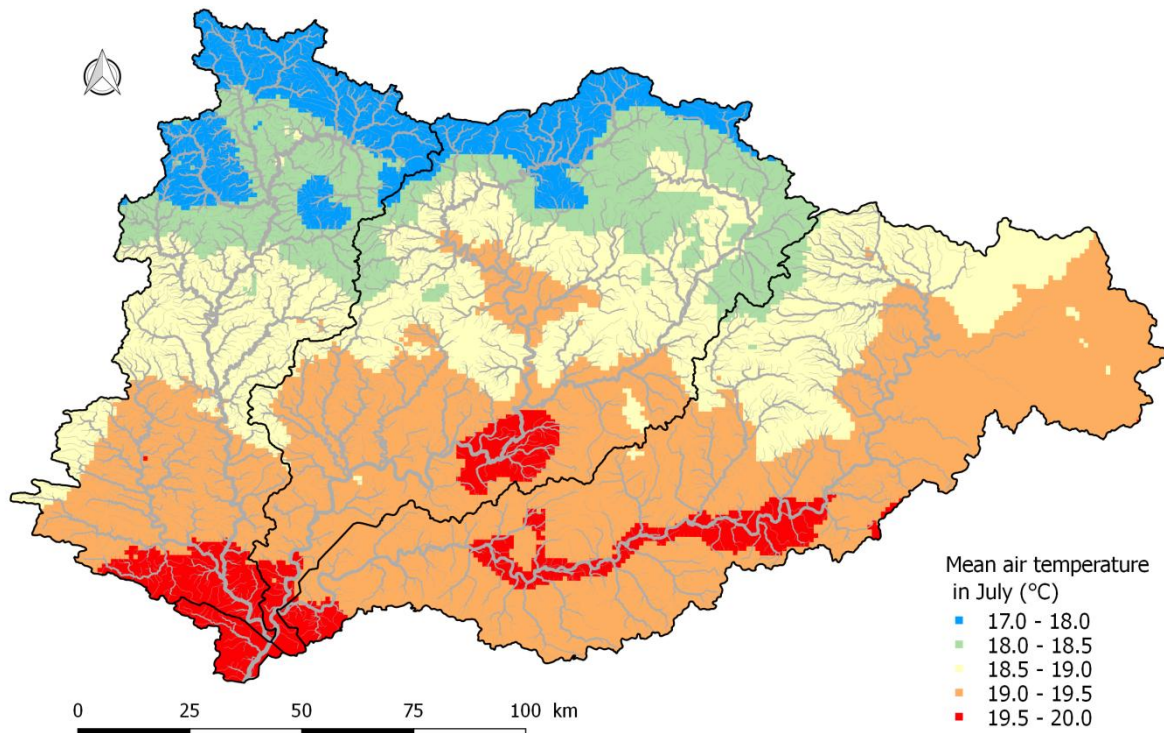


Figure 2.6: Mean air temperature in July on 1981-2010 (Aurely data from Météo-France)

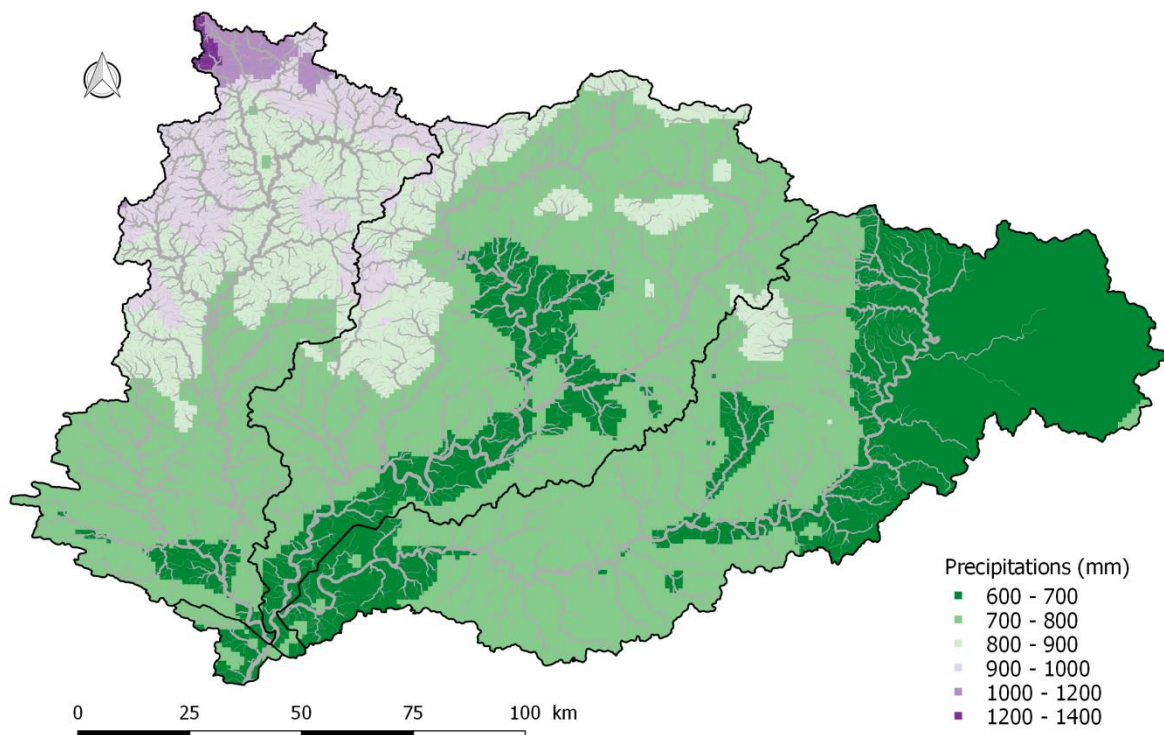


Figure 2.7: Mean yearly precipitations on 1981-2010 (Aurely data from Météo-France)

The period from August 2008 until July 2015 will be used for most of the analysis work. Hence, we need to know the interannual variability of  $T_a$  during this period. Figure 2.8 shows the monthly air temperature deviations around the 08/1985-07/2015 monthly averages on the Maine basin. It was computed from the SAFRAN dataset (Quintana-Seguí et al., 2008). Winters 2009 and 2010 are colder than averages while there is also a cold snap in February 2012. The spring of 2011 is hotter than

averages by more than 3°C. In summer, July 2013 is hotter than averages by more than 2°C. 2010 is also hot from mid-June to mid-July (+1.9 °C).

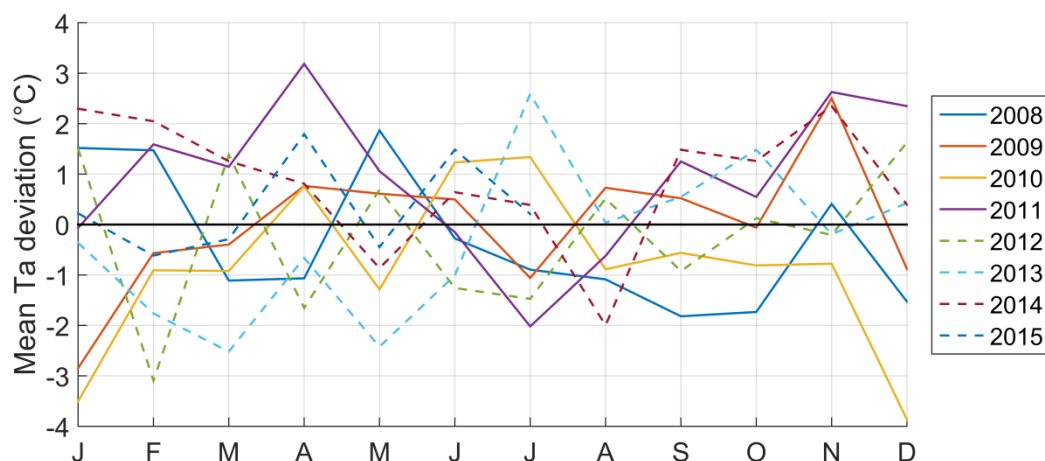


Figure 2.8: Monthly air temperature deviations around the 08/1985-07/2015 monthly averages on the Maine catchment (SAFRAN data from Météo-France)

## 2.6 Hydrological conditions

The averaged specific discharges observed at the three downstream-most gauging stations of each sub-basin (labelled on Figure 2.10) are shown on Figure 2.9. The hydrological regime is pluvial. Indeed, moderate elevations and proximity to the ocean make that little snow falls on the catchment. The specific discharges follow a gradient from East to West, especially in winter. It can be explained by the gradient of precipitations, but also by the gradient of permeability.

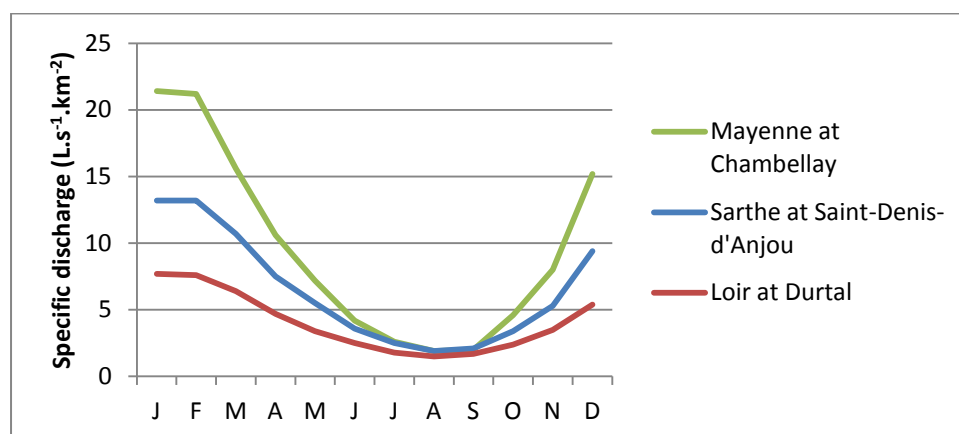


Figure 2.9: Interannual averages of specific discharge measured at the downstream most gauging stations of each sub-basin. Data are from the French hydrologic. Availability is 1965-2016 for the Mayenne, 1970-2016 for the Sarthe, 1960-2016 for the Loir.

The mean discharge ranges from  $6 \text{ m}^3 \cdot \text{s}^{-1}$  in summer to  $75 \text{ m}^3 \cdot \text{s}^{-1}$  in winter (Mayenne at Chambellay); 12 to  $80 \text{ m}^3 \cdot \text{s}^{-1}$  (Sarthe at Saint-Denis-d'Anjou), and 11 to  $45 \text{ m}^3 \cdot \text{s}^{-1}$  (Loir at Durtal). Time series of discharges measured at the 3 gauging stations are shown in appendix A. Figure 2.10 shows the ratio between the average specific discharge in August and the yearly average. This ratio is related to the equivalent ratio for the precipitations, but also to the ability of the catchment of each station to release groundwater in summer. A global West to East gradient is observed, according to the hydrogeology. The highest ratios (>60%) are observed on the Conie and Aigre rivers (Loir basin), as well as on the Moire, the Cloche, the Berthe and the Huisne rivers (Sarthe basin).

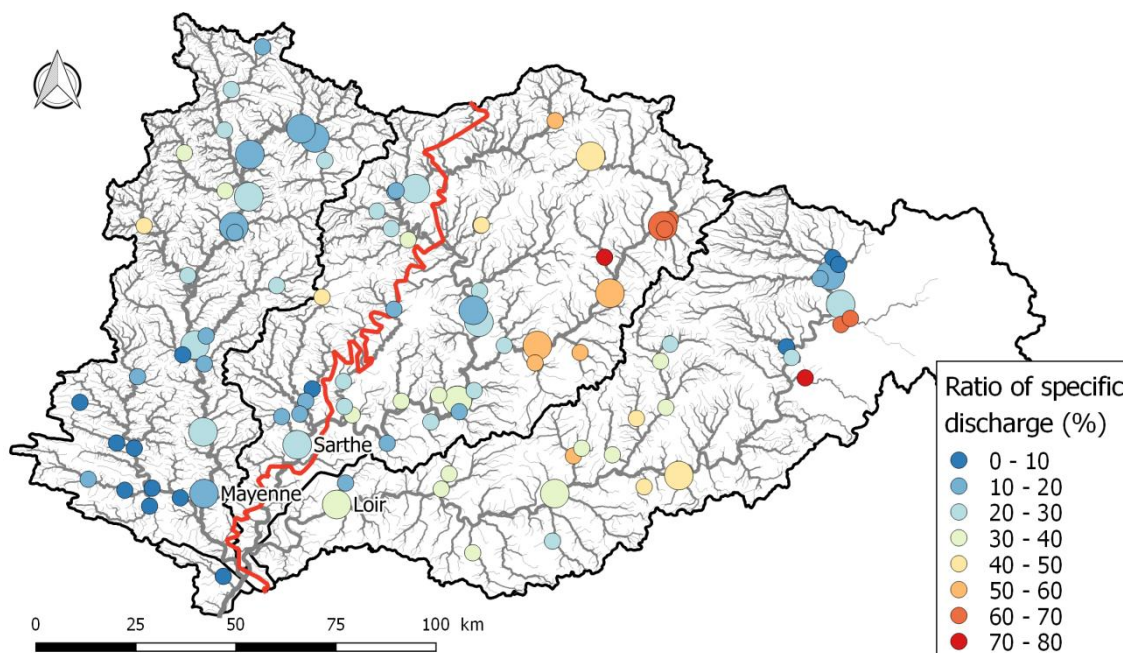


Figure 2.10: Ratio of mean specific discharge in August on annual average. Stations with bigger symbols are located on the main rivers

## 2.7 Obstacles to flow

There is no big dam built for electricity production on the Maine catchment, but a lot of small weir and artificial ponds ended by small dams. The ROE database (Référentiel des Obstacles à l'Écoulement) identifies 1616 obstacles, with height of fall ranging from 1 cm (bridge foundation for example) to 7.5 m. These highest height of fall usually correspond to the drop measured downstream of artificial pond located on the upstream network. The median height of fall is 1 m. Table 2.1 summarise the distribution of obstacles on the different entities of the Maine basin. The tiering rate is the ratio between the cumulated height of obstacles and the difference of altitude, both considered between the station of interest and a point located upstream. Here, the considered point is the source of the stream. The resulting tiering rates are shown for all reaches of the river network on Figure 2.11. All indicators show that the Loir River is the most impacted by obstacles. It is however restricted to the main channel, while this impact is more spread on the tributaries in the Sarthe basin. Impact is smaller on the Mayenne, especially in the upstream part.

Table 2.1: Repartition of obstacles on the different entities of the Maine basin

|               | Number | Density (number of obstacles/100 km) |
|---------------|--------|--------------------------------------|
| Mayenne basin | 379    | 5.3                                  |
| Sarthe basin  | 604    | 7.7                                  |
| Loir basin    | 631    | 13.7                                 |
| Mayenne river | 57     | 27.6                                 |
| Sarthe river  | 79     | 25.9                                 |
| Loir river    | 113    | 35.6                                 |

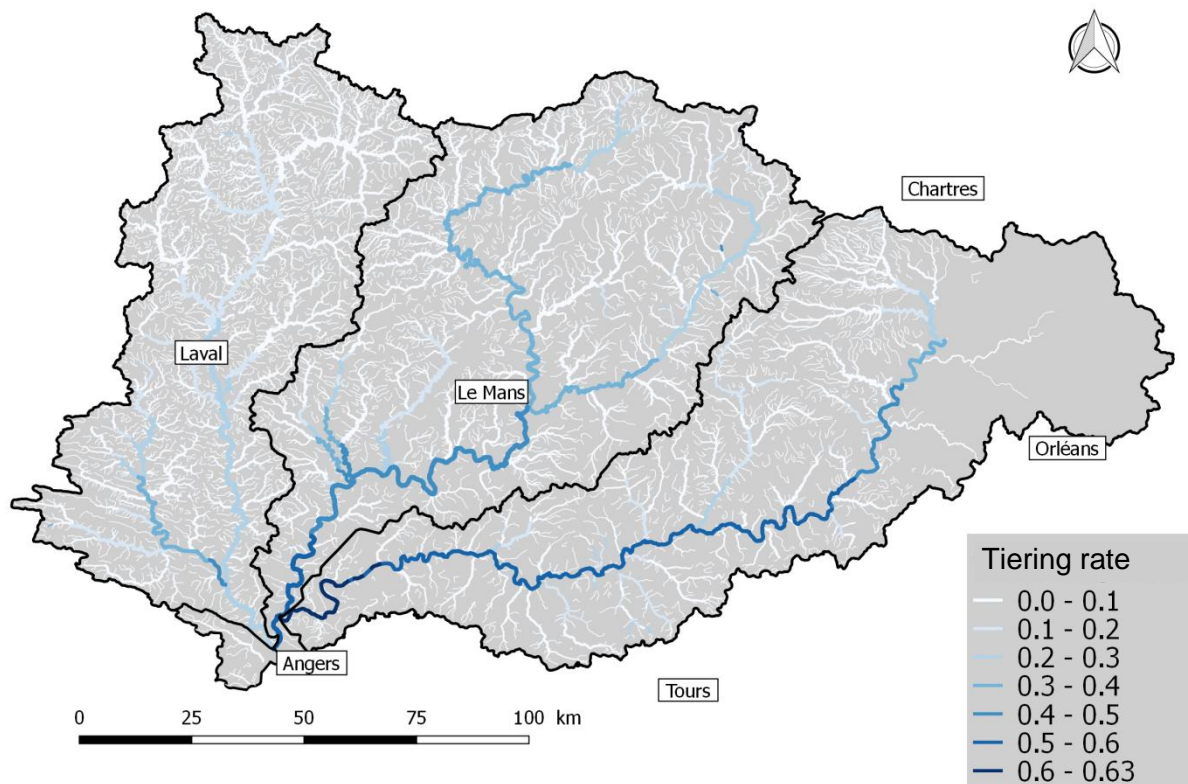


Figure 2.11: Tiering rate computed from each river reach all the way to the source of the corresponding river

## 2.8 Conclusion

Air temperatures are quite comparable among the 3 subcatchments, with mean values in July between 17 and 20 °C. Other characteristics usually differ among basins. The contrasted lithology leads to a west-east increasing gradient in permeability. The largest aquifers are found in the sedimentary basin, although some small aquifers can also be found in the Armorican massif. The east-west gradient in precipitations combines with the lithology gradient to result in an east-west gradient in specific river discharge, which is less effective in summer. The riparian vegetation cover also follows a west-east gradient on Strahler orders 1 to 4. Finally, there is also an east-west gradient regarding the presence of small weirs, with a maximal impact in the downstream part of the Loir. On this basis, we make the hypothesis that this variability may lead the spatial variability in stream temperature on the Maine catchment.



# Chapter 3: Spatio-temporal variability of stream temperature in the Maine catchment

## 3.1 Résumé en français

Dans ce chapitre, le régime thermique est analysé à 44 stations de mesure de la température de l'eau ( $T_w$ ) réparties sur le bassin de la Maine (Figure 3.1). Vingt-sept proviennent de l'Agence Française pour la Biodiversité, 12 proviennent de la DREAL Pays de la Loire, et 5 stations proviennent de la Fédération de Pêche d'Eure-et-Loir. La disponibilité des données est variable (Figure 3.3). Afin d'éviter de biaiser les résultats à cause de la variabilité climatique sur les différentes périodes de disponibilité des données, le régime thermique a tout d'abord été analysé uniquement sur 2010, qui est l'année avec le maximum de stations ayant des données sur l'année complète (24 stations). Cette année, le temps est particulièrement chaud de mi-juin à mi-juillet (+1.9 °C par rapport à la moyenne de cette période sur 1985-2015). Les métriques caractérisées sont :  $T_w$  annuelle moyenne,  $T_w$  moyenne en juillet et en janvier (magnitude), amplitude annuelle et amplitude journalière en juillet (taux de changement), le jour du maximum de la moyenne mobile sur 30 jours (timing), la proportion de temps durant laquelle  $T_w$  dépasse plusieurs seuils entre -5 à 25 °C (durée) ou l'intervalle [4,19 °C], au-delà duquel la truite ne se nourrit plus. Finalement, la sensibilité thermique correspond à la pente de la régression linéaire  $T_w$  en fonction de  $T_a$ , calculée sur des moyennes hebdomadaires. Elle permet de quantifier simplement la sensibilité d'un cours d'eau au réchauffement climatique. Ces métriques sont largement corrélées entre elles, excepté l'amplitude journalière en juillet et le jour de  $T_w$  maximale. L'analyse de ces métriques montre que leur variabilité est assez importante, malgré que l'on soit sur un bassin climatiquement homogène. A l'aide d'un algorithme de régression linéaire multiple qui sélectionne pas à pas les meilleurs facteurs explicatifs parmi 6 variables montrées au Table 3.7, on montre que la variance de l'amplitude journalière est la mieux expliquée par les logarithmes népériens de la profondeur d'eau et de l'ordre de Strahler, alors que la variance du jour de  $T_w$  maximale est la mieux expliquée par le rapport débit mensuel minimal sur débit mensuel maximal (en moyenne interannuelle), qui est censé caractériser les flux de nappe, ainsi que par l'ordre de Strahler. Les sensibilités thermiques calculées sur toute la période 08/2008-07/2015 varient entre 0.42 et 1.17 avec des  $R^2$  entre 0.87 et 0.97. Cela signifie que la  $T_w$  est parfois plus chaude que la température de l'air ( $T_a$ ) aux stations aval (sensibilités thermiques élevées), ce qui s'explique par l'accumulation d'énergie. La relation linéaire n'est pas adéquate pour deux stations ayant des nuages de points concave et convexe (Figure 3.9 c et d), qui s'expliquent probablement par la présence d'étang et de végétation rivulaire importante, respectivement. La sensibilité thermique calculée sur 2010 et 2013 est plus faible que sur les autres années, ce qui s'explique probablement parce que le niveau piézométrique est plus faible. L'algorithme de régression linéaire multiple pas à pas montre que les pentes et ordonnées à l'origine des régressions  $T_w$ - $T_a$  hebdomadaires calculées sur 2008-2015 sont le mieux expliquées par le logarithme de la distance à la source et par le rapport entre le débit mensuel minimal et le débit mensuel maximal (en moyenne interannuelle). D'après ces relations, un modèle empirique a été callé sur les  $T_w$  observées à 22 stations, afin de garder les 22 autres stations pour la validation. Ce modèle est résumé au Table 3.13. La RMSE obtenue sur les 22 stations est de 1.35 °C, le biais moyen est de -0.13 °C et l'écart-type des erreurs est de 1.34 °C. Le nuage de points des  $T_w$  modélisées en fonction des  $T_w$  observées (Figure 3.16) montre l'inadéquation

du modèle linéaire pour les 2 stations. L'avantage de ce modèle est qu'il peut être appliqué facilement dès lors que des mesures de débit et de température de l'air sont disponibles. Ce modèle empirique peut également être appliqué à chaque tronçon du réseau hydrographique du bassin de la Maine (Figure 3.19), en se basant sur les  $Q_{min}/Q_{max}$  simulés par le modèle EROS et répartis sur chaque tronçon par le modèle T-NET.

### 3.2 State of the art of stream temperature regime characterisation

The thermal regime of a river is the description of the seasonal variability of stream temperature ( $T_w$ ), usually computed on long term data. Its characterisation aims to facilitate analysis and modelling, to quantify a reference and/or a disturbed state, to classify thermal regimes, and possibly to focus on thermal conditions that matter. Indeed, the different development phases of fishes occur at different timing and do not have the same thermal requirement. For example, spawning of the brown trout (*Salmo trutta*), which is present in the Maine catchment, usually occurs in autumn and winter and the critical  $T_w$  for eggs survival is 0-13 °C, while the limits for adults feeding are closer to 4-19 °C (Elliott and Elliott, 2010).

The most obvious method to quantify a thermal regime is to compute metrics summarising time series of water temperature (Chu et al., 2010; Beaufort, 2015). They can be chosen according to the objectives and describe the magnitude, duration, frequency, occurrence and variation of thermal conditions (Arismendi et al., 2013). If many metrics are computed, they are usually correlated, leading to some redundancy that can be resolved by a principal component analysis (Daigle et al., 2017; Maheu, 2015). Moving average or Fourier series fitting can be used to smooth the thermal signal and extract metrics (Maheu et al., 2016; Poirel et al., 2008; Steele, 1982; Kothandaraman, 1971).

Several studies analysed the thermal regime at the regional scale. Many of them are carried out with a focus on cold water species threatened by climate change. Hence, they mainly rely on metrics summarising warmest  $T_w$ . However, several other metrics may be ecologically relevant. For example, diel  $T_w$  amplitude can have an impact on the biodiversity as well as on the nutrient processing (Vannote et al., 1980; Thomas et al., 1986).  $T_w$  in winter is a stress for many species and its increase influences local population dynamics and their potential northward expansion (Straile and Stenseth, 2007). Table 3.1 summarise the  $T_w$  metrics used in studies analysing the thermal regime at a regional scale.

Table 3.1: Summary of  $T_w$  metrics used by other authors

| Magnitude                |                               |  |
|--------------------------|-------------------------------|--|
| Mean daily $T_w$ (°C)    | Annual average                | Maheu et al. (2016); Chu et al., 2010); Laizé et al. (2017); Daigle et al. (2017); Grabowski et al. (2016) |
|                          | Average in July               | Woznicki et al. (2016); Wehrly et al. (2003); Steen et al. (2008)  |
|                          | Average in August             | Tague et al. (2007)  |
|                          | Average 15 July-15 August     | Isaak et al. (2010)  |
|                          | Highest 30-day moving average | Daigle et al. (2017)   |
|                          | Monthly averages              | Olden and Naiman (2010)  |
| Maximum daily $T_w$ (°C) | Annual average                | Chu et al., 2010)  |

|  |  |  |
|--|--|--|
|  | MWMT (maximum weekly maximum temperature) = highest after a 7-day moving average | Chang and Psaris (2013); Chu et al., 2010); Jackson et al. (2017); Isaak et al. (2010) |
|  | Highest without moving average   | Daigle et al. (2017)   |
| Minimum daily Tw (°C)  | 7-day moving average   | Grabowski et al. (2016)  |
| Annual amplitude (°C)  | By fit of a Fourier series   | Maheu et al. (2016)  |
| <b>Timing</b>  |  |  |
| Day of maximum/minimum (Julian day)                              |  | Maheu et al. (2016); Chu et al., 2010)   |
| <b>Frequency</b>   |  |  |
| Number of days with daily mean temperature between 4°C and 19°C. |  | Daigle et al. (2017)   |
| Number of days with maximum temperature exceeding 17.8 °C        |  | Grabowski et al. (2016)  |
| <b>Rate of change</b>  |  |  |
| Diel amplitude (°C)  | mean   | Chu et al., 2010)  |
|  | maximum  | Chu et al. (2010)  |
|  | in summer (July-August)  | Maheu et al. (2016)  |
| Average weekly July fluctuation                                  |  | Wehrly et al. (2003)   |
| Rate of change (spring/fall) (°C.day <sup>-1</sup> )             |  | Chu et al. (2010)  |
| Variance of mean daily Tw on the sampling period (°C)            |  | Braun et al. (2015)  |

Maheu et al. (2016) classified the thermal regime of 135 sites across the USA, with data availability ranging from 5 to 33 years. The mean annual Tw, the annual amplitude and the day of maximum/minimum Tw were extracted by fitting Fourier series. Diel variability was quantified by the mean daily range in July and August, the period with the highest variability. They obtained 6 classes by using hierarchical clustering on the annual cycle descriptors, because using daily variability descriptor led to unstable classification.

Chu et al., 2010) classified the thermal regime of 90 sites throughout the Great Lakes Basin (226 000 km<sup>2</sup>, Ontario) with existing and newly developed temperature metrics. Maximum weekly maximum temperature and spring rate of change were used to cluster the sites in 3 classes, which were found to be correlated to latitude. These two metrics were chosen because they provided the most stable classification.

Wehrly et al. (2003) classified the thermal regime of 171 measured sites and 499 modelled sites located in the Lower Peninsula of Michigan (104 000 km<sup>2</sup>, USA). It is one of the few study analysing Tw on a region with limited latitudinal (446 km) and altitudinal gradient (elevation ranges from 174 to 520 m). Classification was based on mean Tw and Tw fluctuation categories. They found that observed differences in patterns of stream fishes community are largely linked to these classes.

Thanks to Fourier series fitting, Steele (1982) characterised intermittent Tw measured between 1961 and 1972 at 60 sites in Pakistan. Regional patterns showed a negative correlation between the mean Tw and site altitude.

Besides the analysis of stream temperature (Tw), many studies also analyse the relationship between Tw and air temperature (Ta), taken as a surrogate of the main climatic drivers (Garner et al., 2014a). Indeed, Ta is easily measured on the field, is strongly correlated to solar radiation, and is the variable with the lowest uncertainty regarding climate projection (Bustillo et al., 2014). Availability of Ta time series allows to compute the thermal sensitivity (TS), which was defined by Kelleher et al. (2012) as the slope of the regression line between air and stream temperature. Thermal sensitivity is a key metric because it quantifies the potential Tw warming related to the expected increase of Ta. Regression can be linear or logistic and can be fitted on data averaged at different timescales (Stefan and Preud'homme, 1993; Pilgrim et al., 1998; Webb et al., 2003). Table 3.2 summarise the methods used by several authors to compute the thermal sensitivity. Kelleher et al. (2012) worked on Tw from 57 sites in the whole state of Pennsylvania (120 000 km<sup>2</sup>). They found that Tw-Ta fit (R<sup>2</sup>) was globally better for weekly logistic regressions than for daily linear regressions, because of the averaging of the daily noise in the thermal signal. They fitted a model aiming at predicting TS based on landscape and hydrologic descriptors.

Hilderbrand et al. (2014) used linear regressions on daily mean Tw to analyse thermal sensitivity and develop models for forested streams with 3rd order Strahler or smaller in Maryland (USA). Regressions were fitted for the whole state, for each of the 3 geographic regions and for each station. They found that model R<sup>2</sup> was positively correlated to the thermal sensitivity and that models accuracy was increased by using discharge as explanatory variable. TS was negatively correlated to channel gradient and amount of forest.

For a water quality modelling aim, Ducharne (2008) used data from 88 stream temperature stations in the Seine catchment (78600 km<sup>2</sup>) over 1993–1999 to fit a linear model relating Tw to Ta. She found that both TS and the lag used in the moving average of Ta providing the best R<sup>2</sup> between Tw and lagged Ta are correlated with Strahler order.

**Table 3.2: Methods previously used to compute the thermal sensitivity**

|                     |  |   |
|---------------------|--|---|
| Linear regression   | Daily                                      | Hilderbrand et al. (2014)<br>Chang and Psaris (2013); Arora et al. (2016); Kelleher et al. (2012); Pilgrim et al. (1998); Stefan and Preud'homme (1993) |
|                     | Weekly                                     | Kelleher et al. (2012); Pilgrim et al. (1998); Stefan and Preud'homme (1993); Krider et al. (2013)  |
|                     | Moving average on different number of days | Ducharne (2008)   |
|                     | Monthly                                    | Laizé et al. (2017); Arora et al. (2016); Pilgrim et al. (1998)   |
| Logistic regression | Daily                                      | Kelleher et al. (2012)  |
|                     | Weekly                                     | Kelleher et al. (2012); Mohseni et al. (1998)   |
|                     | Monthly                                    | Arora et al. (2016)   |

Empirical Tw models can be improved by including other explanatory variables using multiple linear regressions. These landscape descriptors can also be used to model TS directly instead of Tw. Table 3.3 summarise the landscape descriptors used in empirical models applied at the regional scale.

**Table 3.3: Overview of statistical models built with landscape descriptors at the regional scale (adapted from Goullet, 2017)**

| Study                    | Tested variables (X)  | Selection criteria   | Metrics used (Y)                                      | Significant Variables   | Model performance  |
|--------------------------|---|--|---|---|--|
| Wehrly et al. (1998)     | Area, 3 classes of landcover, 3 classes of sediment texture, %forest and potential groundwater in 2 kinds of buffer, cross-sectional area, depth, width, slope; specific flow | adjusted R <sup>2</sup> and standard error                       | July average weekly maximum Tw                        | Width, potential input of ground water, Ta max, % forest, slope, cross-sectional area | R <sup>2</sup> <sub>adj</sub> =0.60                          |
|                          |   |  | July average weekly minimum Tw                        | Width, Ta min, Ta max, %forest in a 4-km buffer                                       | R <sup>2</sup> <sub>adj</sub> =0.59                          |
| Hrachowitz et al. (2010) | Area, altitude, slope, %forest, shade, distance to coast  | Adjusted R <sup>2</sup> and BIC (Bayesian Information Criterion) | Monthly T <sub>max</sub>                              | Area, altitude (in winter), shade, distance to coast, slope (in summer)               | R <sup>2</sup> between 0.65 and 0.80, depending on the month |
|                          |   |  | Tw of the warmest week                                | %forest, distance from source,  | R <sup>2</sup> = 0.72  |
| Chang and Psaris (2013)  | BFI, dry season precipitation, Strahler order, distance to coast, latitude, area, altitude, slope, landuse  | Highest R <sup>2</sup> and lowest residuals                      | Highest maximum daily Tw after a 7-day moving average | BFI, Strahler order, %forest  | R <sup>2</sup> between 0.56 and 0.62 depending on the basin  |
|                          |   |  | Thermal sensitivity                                   | Distance to coast, BFI, area  | R <sup>2</sup> between 0.53 and 0.6 depending on the basin   |
| Jackson et al. (2017)    | Altitude, area, %forest, shade, width, orientation, slope, distance from source   | AICc (Akaike information criterion corrected)                    | Lowest minimum daily Tw after a 7-day moving average  | Altitude, %forest, slope  | AICc = 61.5  |
|                          |   |  | Daily means   |   | AICc = 63.2  |

|                     |   |             |   |   |                                  |
|---------------------|---|-------------|---|---|----------------------------------|
|                     |   |             | Highest maximum daily Tw after a 7-day moving average | Width, %forest                                  | AICc = 66.27                     |
| Isaak et al. (2010) | Area, drainage density, elevation, %glaciated, slope, %alluviated, solar radiation, MWMTa, mean Ta, discharge | Spatial AIC | Mean Tw 15 Jul-15 Aug                                 | Elevation, solar radiation, Air MWMT, discharge | R <sup>2</sup> = 93%             |
|                     |   |             | MWMT  | Elevation, solar radiation, Air_MWMT, discharge | R <sup>2</sup> = 87%<br>AIC = 51 |

Garner et al. (2014a) analysed the spatial patterns and the inter-annual variability of 1989-2006 monthly averaged Tw and Ta in England and Wales. They used a sensitivity index based on conditional probability to quantify the link between Tw and Ta regimes. This index was itself linked to basin properties, with the most important being the basin permeability and basin area.

Laizé et al. (2017) analysed the seasonal (3-month-averaged) Tw at 35 sites located on 21 rivers in UK, for the period 1984–2007. They built linear regressions between Tw and climate variables (air temperature, downward short-wave and long-wave radiation, wind speed, specific humidity and precipitation) to assess the influence of basin properties as modifiers of these relationships. They found that basin permeability was the most important factor in the climate–Tw association, followed by basin area and elevation.

In order to identify landscape factors affecting Tw measured at 74 stations in the Columbia River basin, Chang and Psaris (2013) analysed spatial patterns of both thermal sensitivity and maximum 7-day moving average of daily maximum Tw. They chose this specific metric because maximum stream temperature is associated with critical limits for the life cycle of salmonids, and seven day average of maximum daily stream temperature has been used by local management agencies. TS was computed by fitting a linear regression on daily maximum air temperature vs. 7-day average daily maximum stream temperature. They found that thermal sensitivity is controlled by distance to the coast, base flow and contributing area, while the maximum Tw is mainly controlled by base flow, forest land cover and stream order.

Isaak et al. (2010) analysed Tw of 512 stations located in a mountainous catchment of Idaho, USA (6900 km<sup>2</sup>). Tw metrics used are a mean Tw in summer (15 July- 15 August) and the maximum weekly maximum Tw. They fitted spatial statistical models, with four variables outputted for both Tw metrics: elevation, solar radiation, MWMT of air and discharge.

Most of these works analysed stream thermal regime on a wide area, and presence of latitudinal or elevation gradient caused a wide spatial variability of Ta, which hence lead Tw variability.

The goals of this chapter are (i) to describe the thermal regime of Tw monitoring stations for which the variation of Ta is not the main driver of the thermal spatial variability, (ii) to investigate the controls of the thermal sensitivity variability by regressing it to landscape/hydrologic descriptors, and (iii) to built an empirical model aimed at predicting mean weekly Tw for any point of the network as long as landscape and simple hydrologic descriptors are available.

### **3.3 Presentation of temperature monitoring stations**

There are 44 Tw hourly monitoring stations on the Maine basin (Figure 3.1). They will be identified by the names of the river followed by theirs distances from source (in kilometre). Two stations are duplicated because AFB and DREAL Pays de la Loire placed sensors at the same location, with concomitant measures (Mayenne 61) or without (Aune 20).

Twenty-seven stations were provided by Agence Française pour la biodiversité at an hourly time step. Unfortunately, there is an uncertainty regarding the exact time of data. Indeed, clock of data usually synchronised with computer clock when they were collected on the field. Time of switch regarding daylight saving time is thus unknown. For this reason, hourly data will not be much used in this work, but maximum, minimum, mean daily temperature as well as diel amplitudes will be considered.

Twelve stations were provided by DREAL Pays de la Loire at varying time steps that are supposed to reduce the data size without losing information. A shape-preserving piecewise cubic interpolation was applied to extract hourly data. Five stations in the East of the catchment come from Fédération Départementale de Pêche d'Eure-et-Loir. One of them was once found to be buried in the sediments resulting in very small variations. Corresponding signal was removed.

While data from DREAL were provided after a quality check, data from AFB had to be verified. For 4 stations (Aron 34, Huisne 55, Corbionne 21, Sarthe 5), unlikely data were detected by plotting daily mean Tw against daily mean Ta. For 6 other stations (Sarthe 62, Loir 283, Tusson 8, Loir 130, Loir 76, Maine 335), unlikely data were detected and removed by looking at the hourly thermal signal. Among data provided by Fédération de Pêche, the 2014 year was removed for Conie 27, because the sensor was slowly buried under sediments and showed small diel amplitudes.

The information regarding the depth of the sensors was difficult to acquire in a systematic way. Depth of sensors from DREAL Pays de la Loire are reported as heterogeneous because they were placed at locations that were also convenient to measure the stream discharge. In general, the location of sensors from Agence Française pour la biodiversité was preferred to be at the bottom of the stream, in a shadowed location and far from any confluence or aquatic vegetation.

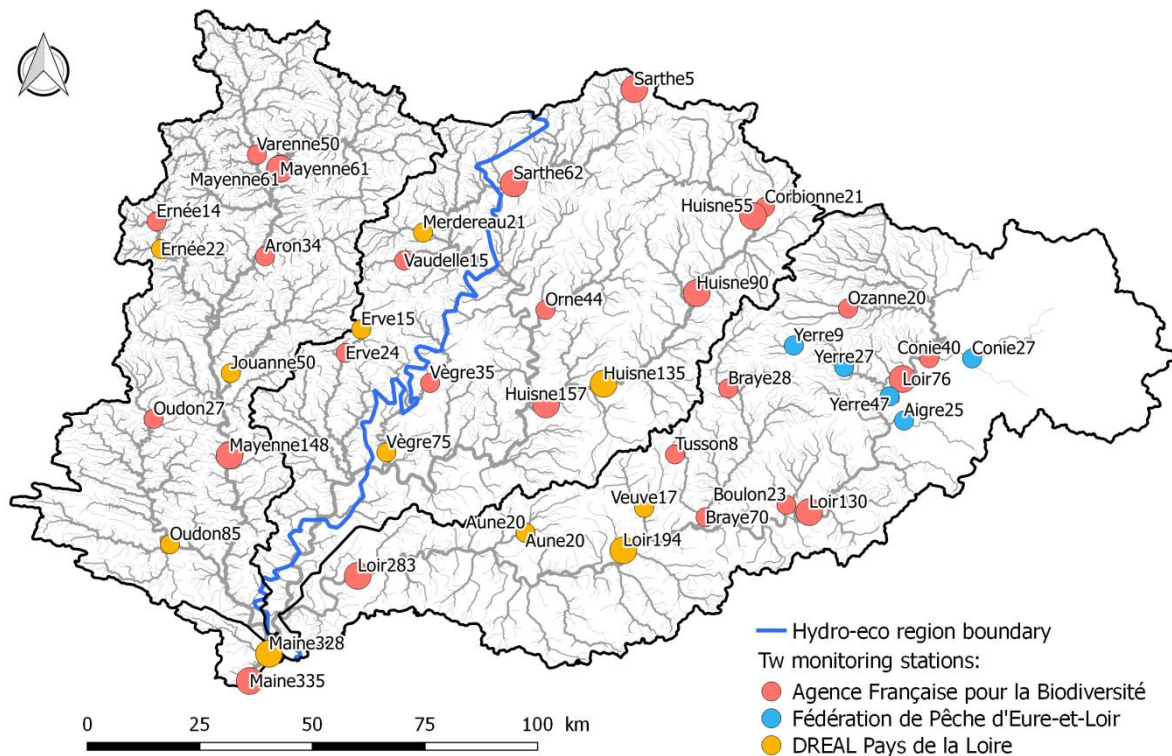


Figure 3.1: Spatial distribution of the 44 stream temperature monitoring stations and hydro-eco region boundary. Numbers are distance from source (km). Stations with bigger symbols are located on the main rivers

Table 3.4 summarises the spatial repartition of stations in the subcatchments and on the main rivers. The density of stations is the highest in the upstream part of the Loir catchment thanks to stations of Fédération de pêche. In particular, the Yerre River, a tributary of the Loir, has a good density of 3 sensors on 50 km of river. The time series of mean daily Tw for streams where there are several stations are shown in appendix E.

Table 3.4: Number of stations on each sub-catchment and on the main rivers

|           | Mayenne          | Sarthe | Huisne | Loir             |
|-----------|------------------|--------|--------|------------------|
| Catchment | 10 (1 duplicate) | 14     | 5      | 18 (1 duplicate) |
| River     | 3 (1 duplicate)  | 2      | 4      | 4                |

The distance from source ranges from 5 km on the Sarthe to 335 km on the Maine with a high density of station at less than 100 km from the source (Figure 3.2).

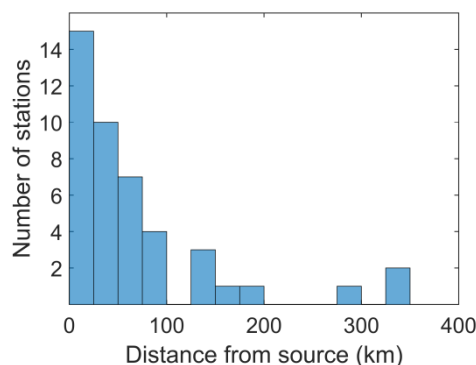


Figure 3.2: Histogram of distances from source of the 44 stations

The distribution of stations by Strahler orders is shown at Table 3.5. The east-west gradient in the station repartition is related to the gradient in the network density. Hence, Strahler orders increase faster on the west part of the catchment.

**Table 3.5: Distribution of Tw monitoring stations by Strahler order**

| Strahler order | Mayenne basin | Sarthe basin | Loir basin |
|----------------|---------------|--------------|------------|
| 2              |               |              | 3          |
| 3              |               | 4            | 4          |
| 4              | 3             | 4            | 4          |
| 5              | 4             | 6            | 4          |
| 6              | 3             |              |            |
| 7              |               | 2 (Maine)    |            |

Figure 3.3 shows the availability of data and Figure 3.4 shows the number of stations with available data for each day from 08/2008 to 07/2015. Although the number of stations with concomitant data peaks in 2009 and 2011, 2010 is the year with the highest number of stations with full year of data (Table 3.6). There are 27 stations with at least 3 years of continuous stations.

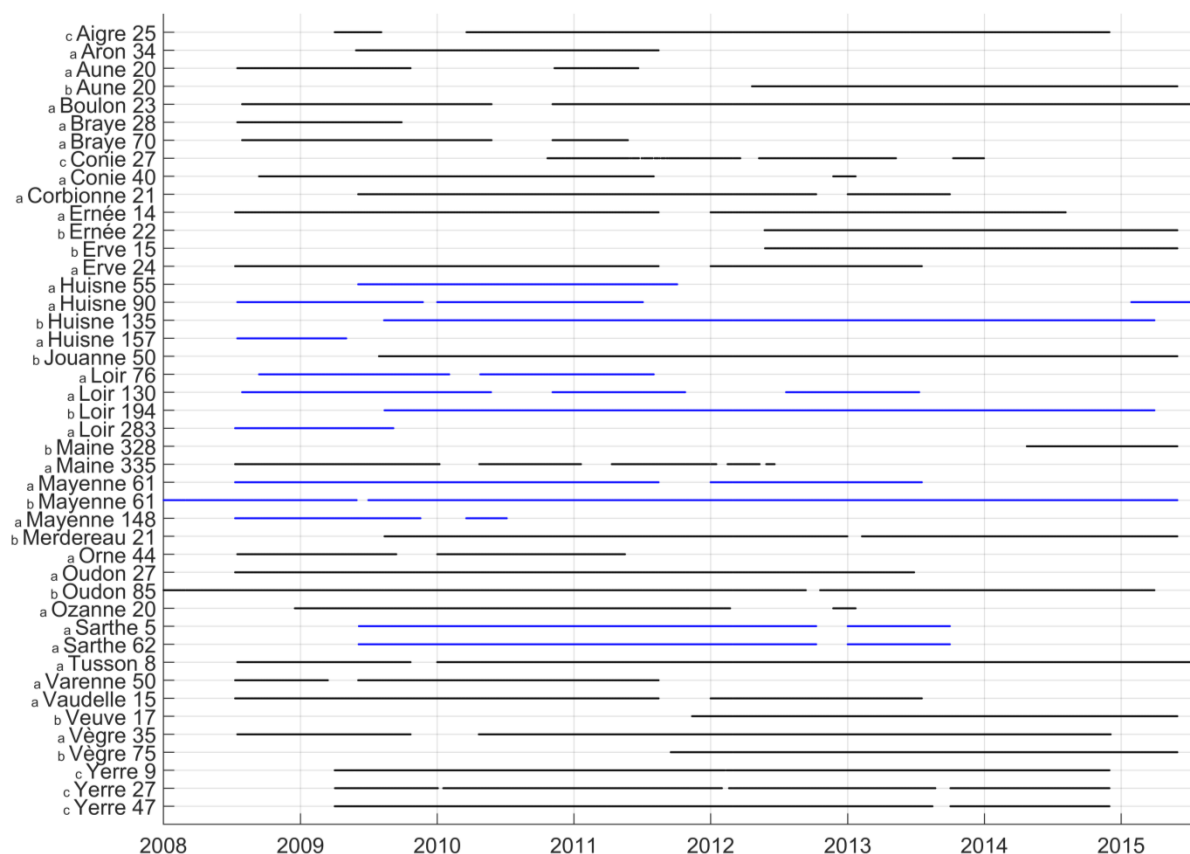


**Figure 3.3: Availability of data at the 44 Tw monitoring stations. Blue stations are located on the main rivers. Stations <sup>a</sup> are provided by Agence Française pour la biodiversité, <sup>b</sup> are provided by DREAL Pays de la Loire and <sup>c</sup> by Fédération Départementale de Pêche d'Eure-et-Loir. Numbers are distance from source (km).**

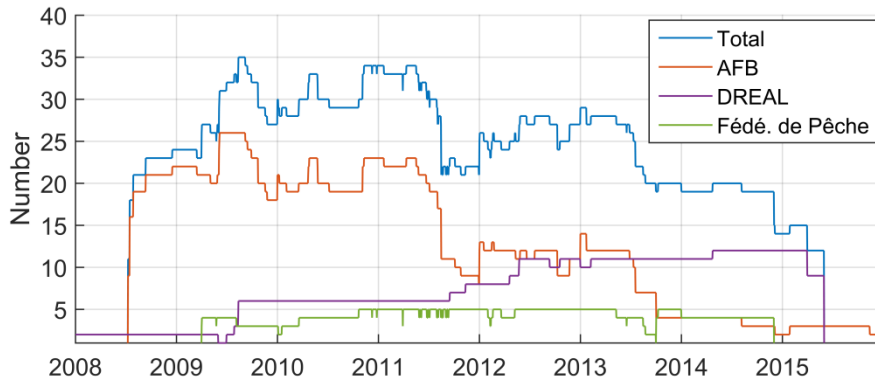


Figure 3.4: Number of stations with available data for each day on 2008 - 2015

Table 3.6: Number of stations with data available for each year

| Number of stations     | 2008 | 2009 | 2010 | 2011 | 2012 | 2013 | 2014 | 2015 |
|------------------------|------|------|------|------|------|------|------|------|
| with full year of data | 2    | 13   | 24   | 16   | 17   | 15   | 13   | 0    |
| with data              | 24   | 37   | 35   | 36   | 31   | 30   | 19   | 15   |

### 3.4 Method of spatio-temporal analysis of stream temperature

In order to characterise the thermal regime, we computed metrics of magnitude, rate of change, timing and duration, considering only the 2010 year. June and July 2010 are respectively 1.2 °C and 1.3 °C warmer than 1985-2015 monthly average (Figure 2.8), with a hot peak between the end of June and mid-July (+1.9 °C). August is 0.9 °C colder than average, while January and December are more than 3 °C colder than average.

Magnitude was characterised by the mean  $T_w$  on the whole year ( $T_wY$ ), in July ( $T_wJul$ ) and in January ( $T_wJan$ ). The rate of change was characterised by both the annual and the diel amplitude. The annual amplitude ( $aA$ ) is the difference between  $T_wJul$  and  $T_wJan$ . Mean diel amplitude ( $dAJul$ ) was computed in July because they are the highest in summer (Maheu et al., 2016). The timing was characterised by the Julian day of the maximum of the 30-day moving average of daily mean  $T_w$  ( $DayOfTwMax30J$ ), which is practical to smooth the thermal signal and is a good indicator of seasonal extreme conditions during the warmest period (Daigle et al., 2017). Duration was characterised by the percentage of time that  $T_w$  (at the hourly time step) exceed several temperature threshold from -5 to 25°C, as well as by the percentage of time that  $T_w$  is comprised between 4 and 19 °C, the limits for feeding of adult trout (Daigle et al., 2017; Elliott and Elliott, 2010) (%TimeTroutFeeding). Every metrics is depicted on Figure 3.5.

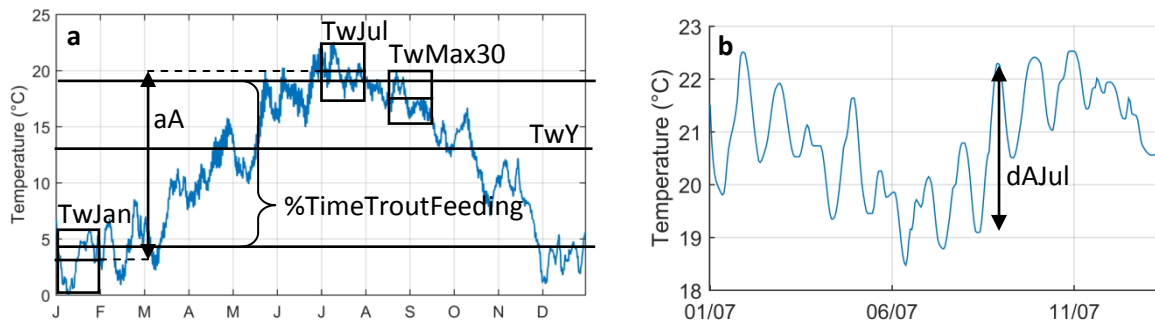


Figure 3.5: Representation of the different metrics on the Tw time series of Jouanne 50  
 (a) 2010 (b) between 01/07 and 12/07/2010.

Because the thermal sensitivity (TS) characterises the behaviour of a stream reach regarding Tw instead of its climatology, TS is not supposed to change with varying climatic conditions, unless the hydrosystem is modified (O'Driscoll and DeWalle, 2006; Stefan and Preud'homme, 1993). Since our Tw observed data are discontinuous, TS is an interesting metric if we want to consider all measured data and hence all stations. In order to compute averaged TS for every station, Tw-Ta linear regressions were fitted on weekly averages for each station with all data available between August 2008 and July 2015. Ta were taken from the SAFRAN reanalysis, provided at the 8 km resolution and at the hourly time step (Quintana-Seguí et al., 2008). Linear regressions were used because of their simplicity and because we did not observe so much an S-shaped behaviour in our data. Weekly averages were used because they usually provide better fit than daily averages (Pilgrim et al., 1998). Tw and Ta under 0 °C were not considered since subject to freezing and latent heat exchanges. The slope and intercept of regressions were used to classify the stations in 3 classes thanks to a hierarchical clustering method based on the standardized Euclidean distance. In order to look if there is any temporal variation in TS, Tw-Ta linear regressions were fitted on weekly averages for each station and year when data was present during more than 60% of the year, which makes a total of 166 stations-years.

Several landscape and hydrologic descriptors have been computed in order to analyse what are the controls of TS and two other metrics: dAJul and DayOfTwMax30J. As it will be demonstrated later, these 2 metrics are not correlated with TS and the other Tw metrics describing the magnitude of the mean annual cycle. The second goal is to fit a model explaining the variability of the slopes (TS) and the intercepts of the Tw-Ta regressions (44 stations) thanks to descriptors that are easily obtained from GIS analysis and from existing gauging stations. In order to test the model on data that were not used to build it, stations were classified by increasing TS and odd stations from this list were selected as the fit group, while the even stations formed the validation group. The descriptors include the distance from source, tiering rate, Strahler order, reach slope, altitude and  $Q_{\min}/Q_{\max}$ , the ratio between the minimum monthly mean discharge and the maximum monthly mean discharge, taken from a mean interannual cycle on 08/2008-07/2015 as simulated by the EROS model (Thiéry and Moutzopoulos, 1992; more details on the model and its output in section 4.4.2). This ratio is supposed to be proportional to the average groundwater fluxes, because a river draining an aquifer shows a discharge that is more constant than a river only fed by precipitations. Its spatial distribution (Figure 3.6) shows that the 3 stations with the highest ratio are located above the Beauce limestone aquifer while all stations located in the Armorican massif have low values as expected. Mean river depth modelled on 08/2008-07/2015 with the ESTIMKART empirical equations (Lamouroux et al.,

2010; more details in section 4.3.3) is also included as descriptor. Tw at a station results from energy exchanged upstream of the station. The conditions closer to the station have more impact than those located further, but the relation distance-impact is unclear (Isaak et al., 2010). Hence, tiering rate was firstly computed by considering different distances upstream of the stations: 25, 50, 75, 100 km and an unlimited distance (i.e. all the way to the source). These methods provide different results only on stations that are on the largest Strahler orders. Simple linear regressions on TS against each of these methods show that tiering rate computed on 75 km upstream provides the highest adjusted R<sup>2</sup> (0.7). This variable was hence selected as a potential explanatory variable.

Because many of these variables are correlated (Table 3.7), we used a stepwise linear regression algorithm to build the models with variables that have the most explanatory power. The criterion to add or remove a variable is the significance (p-value < 0.05 to add and >0.10 to remove) for an F-test of the change in the sum of squared error. Since the plot of TS against variables showed logarithmic behaviour, the logarithm of each variable was also proposed as explanatory variables.

**Table 3.7: Correlation coefficient between landscape and hydrologic descriptors**

|                      | Distance from source | Tiering rate | Strahler order | Slope | Altitude | Qmin/Qmax | Mean depth |
|----------------------|----------------------|--------------|----------------|-------|----------|-----------|------------|
| Distance from source | 1                    |              |                |       |          |           |            |
| Tiering rate         | 0.86                 | 1            |                |       |          |           |            |
| Strahler order       | 0.70                 | 0.65         | 1              |       |          |           |            |
| Slope                | -0.36                | -0.40        | -0.32          | 1     |          |           |            |
| Altitude             | -0.65                | -0.68        | -0.59          | 0.43  | 1        |           |            |
| Qmin/Qmax            | -0.06                | -0.11        | -0.40          | -0.26 | 0.00     | 1         |            |
| Mean depth           | 0.96                 | 0.83         | 0.78           | -0.44 | -0.67    | -0.02     | 1          |

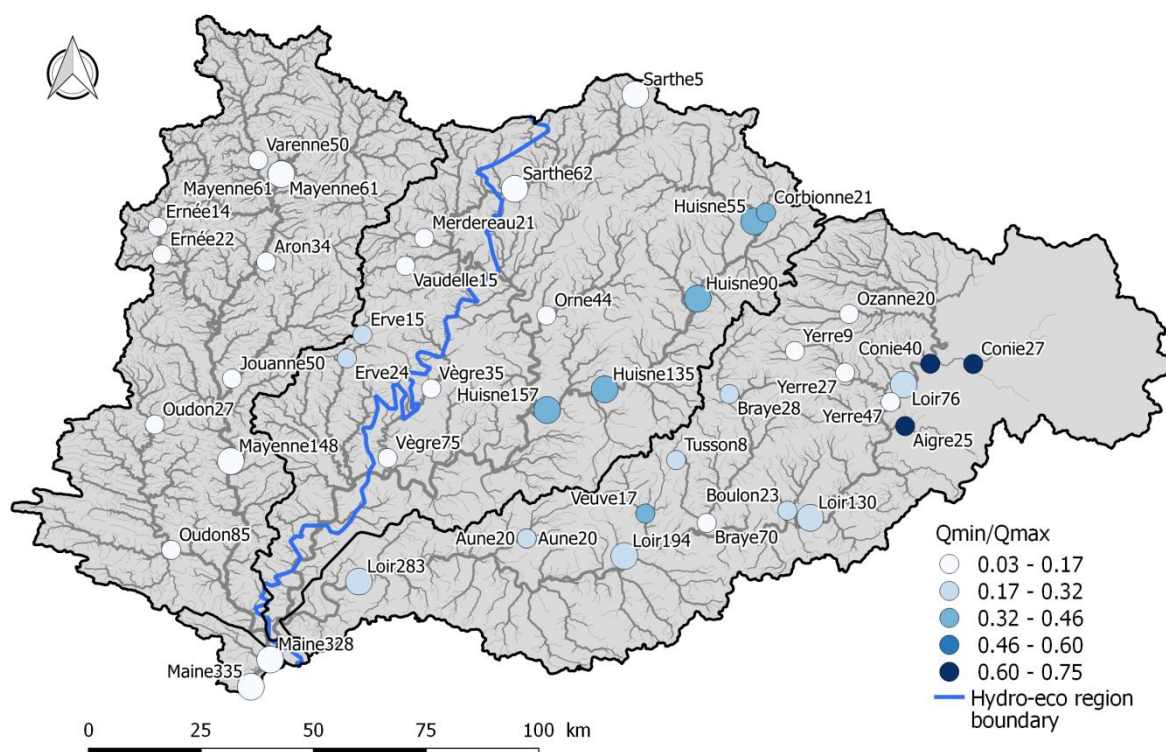


**Figure 3.6: Spatial distribution of the ratio between the minimum and maximum monthly mean discharge on 08/2008-07/2014**

### 3.5 Contrasted variability of stream thermal metrics compared to air temperature metrics

The different metrics computed for water and air temperatures are shown on Figure 3.7. The 44 stations are ordered by increasing  $Q_{\min}/Q_{\max}$ .

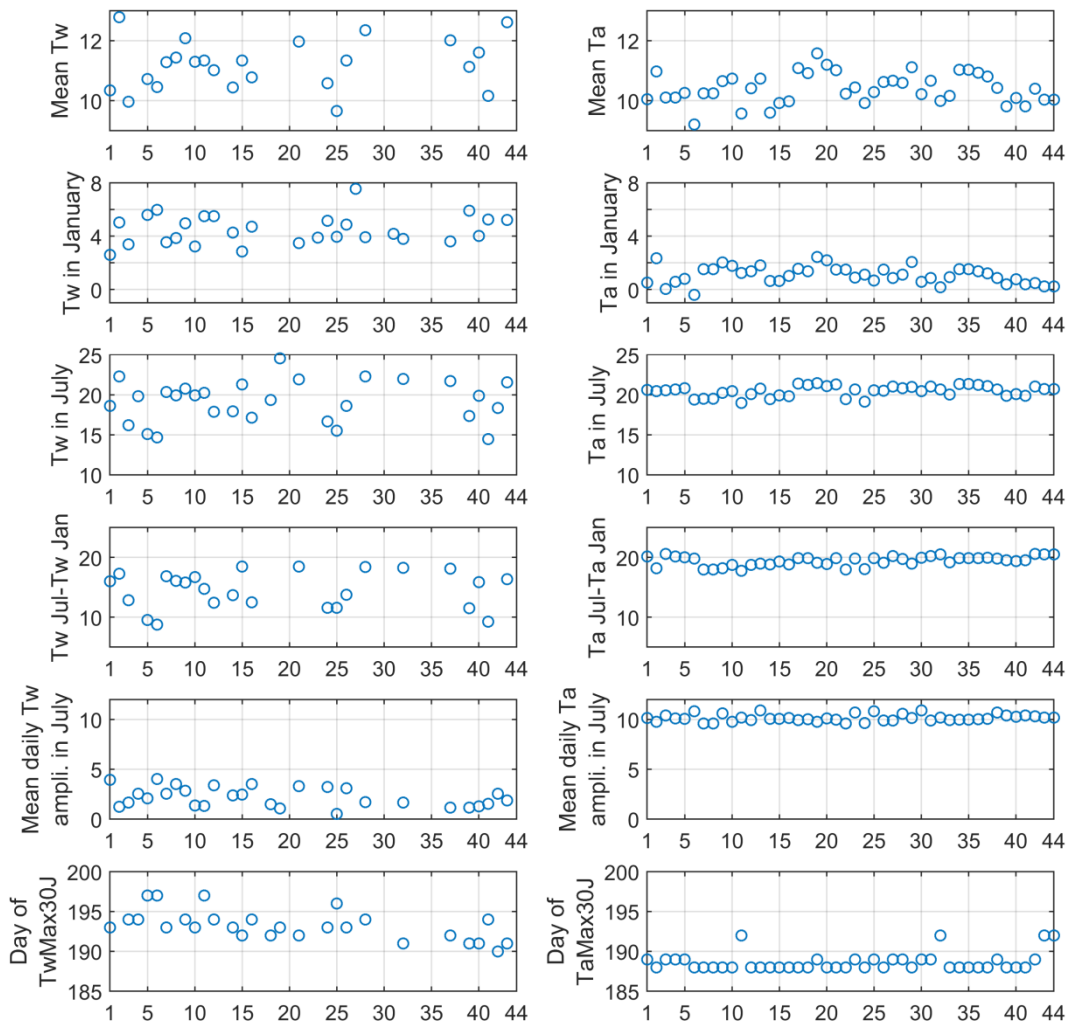


Figure 3.7: Criteria's for 2010 and the 44 stations ordered by increasing  $Q_{\min}/Q_{\max}$ , the ratio between the minimum and maximum monthly mean discharge on 08/2008-07/2014. Numbers can be found in appendix B.

Mean Tw ranges from 9.7 °C (Tusson 8) to 12.8 °C (Conie 40). Although these 2 stations are known to be both impacted by groundwater fluxes, Conie40 is located downstream of a pond that heat the water. Mean Ta is within a similar range, although average Tw at the 24 stations is 0.8°C warmer than Ta.

Tw in January ranges between 2.6 °C (Ozanne 20) and 7.6 °C (Boulon 23). Ozanne20 is the third most elevated station. Tw in January is always warmer than Ta. The difference between TwJan and TJan reaches 6.7 °C for Boulon 23 but the mean difference is 3.5 °C.

Tw in July ranges from 14.4 °C (Corbionne 21) to 24.6 °C (Maine 335, the downstream-most station). Variability of TwJul between stations (10.2 °C) is more important than TaJul (2.5 °C) and is twice bigger than TwJan (5.0 °C). TwJul is warmer than TaJul for 41% of the stations.

The annual amplitude of Tw has a wide variability since it ranges from 8.7 °C (Sarthe 5) to 18.5 °C (Sarthe 62, Orne 44, Loir 194). The annual amplitude of Ta varies within a smaller range of 2.8°C.

The diel amplitude in July ranges from 0.5 °C (Tusson 8) to 4 °C (Sarthe 5). Small and large diel amplitudes can thus be observed on stations located close to sources. The mean diel amplitude equates 2.3 °C for Tw and is much larger for Ta (10.2 °C). It is the best explained by the logarithm of the water depth (Table 3.8), which makes sense since amplitude is related to the ratio between thermal inertia ( $\approx$ depth  $\times$  width) and wetted width, where most energy exchanges occur. The natural logarithm of the Strahler order seems to improve a bit the multiple model although the single linear regression between dAJul and log(Strahler order) provides a non significant relation.

Finally, the day of the maximum daily Tw (after smoothing by a 30 days moving average) ranges from the 9 July (Aigre 25) to the 16 July (Sarthe 5, Varenne 50, Yerre 47). The  $Q_{\min}/Q_{\max}$  ratio is the best predictor of DayOfTwMax30J, showing that the groundwater fluxes delay the summer Tw peak (Table 3.8).

**Table 3.8: Linear regression models resulting of a stepwise selection**

| Y variable | X                  | Number of stations & period | Selected X variables                                    | Coeff.                  | p-values                      | R <sup>2</sup> <sub>adjusted</sub><br>RMSE |
|------------|--------------------|-----------------------------|---|-------------------------|-------------------------------|--|
| dAJul      | Global descriptors | 29<br>2010                  | intercept<br>log(depth)<br>log(Strahler order)          | -2.07<br>-2.17<br>1.98  | 0.16<br>9E-4<br>0.02          | 0.30<br>0.82 °C                            |
| DayOfTw30J | Global descriptors | 27<br>2010                  | intercept<br>$Q_{\min}/Q_{\max}$<br>log(Strahler order) | 198.2<br>-6.85<br>-2.65 | 1.24E-36<br>4.97E-5<br>7.9E-3 | 0.48<br>1.35 day                           |

The duration plot shows the percentage of the time that Tw is above the Y-axis temperature (Figure 3.8).

Table 3.9 summarise the values for the Armorican massif and the sedimentary basin.

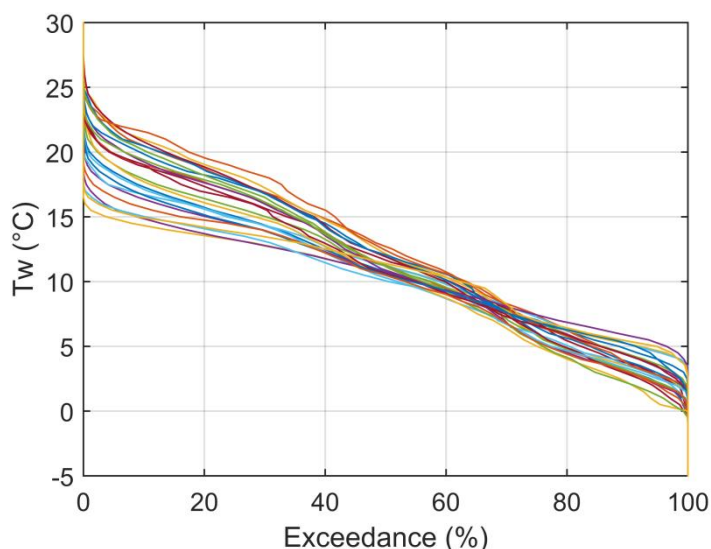


**Figure 3.8: Duration plot for the 24 stations with full data in 2010, built on hourly Tw**

Only few stations located far from sources experience negative Tw (between 0°C and -1°C): Sarthe 62, Orne 44, Huisne 135 and Jouanne 50 (the only one in the Armorican basin). Different behaviours are observed close to the freezing point. For example, Ozanne 20 is the station with the longest observation below 1 °C (6% of the time) but Tw at this station is never below 0°C. At 15°C, the

exceedance ranges from 4% (Corbionne 21) to 42% (Oudon 85). It is the only point where there is a large difference between hydro-eco region, with a minimum at 20.5% in the Armorican massif and 4% in the sedimentary basin. No station experience Tw above 25°C, except Orne44 (0.5% of the time). Exceedance variability is minimal at 8.3 °C, where it ranges from 62% to 70%. Duration comprised between 4 and 19°C, the limits for adult brown trout feeding, ranges between 65% (Huisne 157) and 99% (Loir 76), with little variability between hydro-eco regions.

**Table 3.9: Percentage of time that observed Tw (hourly data) exceed given threshold in 2010**

|                 | Armorican massif |        |      | Sedimentary basin |        |      |
|-----------------|------------------|--------|------|-------------------|--------|------|
|                 | Min              | Median | Max  | Min               | Median | Max  |
| 0 °C            | 99.8             | 100    | 100  | 99.2              | 100    | 100  |
| 5 °C            | 76.8             | 84.2   | 91.4 | 75.1              | 79.4   | 96.5 |
| 10 °C           | 52.0             | 55.7   | 63.3 | 50.5              | 58.8   | 62.7 |
| 15 °C           | 20.5             | 31.4   | 41.6 | 3.8               | 28.4   | 39.2 |
| 20 °C           | 0.1              | 4.4    | 17.4 | 0                 | 2.5    | 15.4 |
| 25 °C           | 0                | 0      | 0    | 0                 | 0      | 0.5  |
| Between 4-19 °C | 64.9             | 80.8   | 93.4 | 64.7              | 78.6   | 99.3 |

These metrics are positively or negatively correlated between them, except dAJul and DayOfTwMax30J (Table 3.10).

**Table 3.10: Correlation matrix for Tw metrics. TwY = mean annual Tw; TwJan = mean Tw in January; TwJul = mean Tw in July; aA = annual amplitude; dAJul = diel amplitude in July; DayOfTwMax30J = day of maximum Tw after 30 days moving average; %TimeTroutFeeding = the percentage of hourly Tw between 4 and 19 °C; TS = thermal sensitivity.**

|                   | TwY   | TwJan | TwJul | aA    | dAJul | Day of TwMax30J | %TimeTroutFeeding | TS |
|-------------------|-------|-------|-------|-------|-------|-----------------|-------------------|----|
| TwY               | 1     |       |       |       |       |                 |                   |    |
| TwJan             | 0.02  | 1     |       |       |       |                 |                   |    |
| TwJul             | 0.88  | -0.41 | 1     |       |       |                 |                   |    |
| aA                | 0.72  | -0.65 | 0.96  | 1     |       |                 |                   |    |
| dAJul             | -0.12 | 0.02  | -0.22 | -0.12 | 1     |                 |                   |    |
| DayOfTwMax30J     | 0.01  | -0.20 | -0.12 | -0.17 | 0.14  | 1               |                   |    |
| %TimeTroutFeeding | -0.67 | 0.67  | -0.90 | -0.96 | 0.15  | -0.01           | 1                 |    |
| TS                | 0.72  | -0.62 | 0.94  | 0.96  | -0.18 | 0.01            | -0.91             | 1  |

### 3.6 Air-water temperature relationship

#### 3.6.1 Global Tw-Ta regressions and performances

All the regressions fitted on the whole 08/2008-07/2015 period are significant at the 5% confidence level. Thermal sensitivity ranges from 0.42 (Boulon 23, Figure 3.9a) to 1.17 (Maine 328, Figure 3.9b). R<sup>2</sup> ranges from 0.87 to 0.97 but is below 0.9 for only 3 stations: Conie 27, Mayenne 148 and Yerre 47. Conie 27 (Figure 3.9c) shows a concave cloud of point suggesting the presence of a heating process in summer. At this station, the sensor is placed in a pond which is very likely to heat when solar radiation is strong. The opposite behaviour is observed for Yerre 47 (Figure 3.9d), which shows a convex cloud of point probably due to the shading effect of the riparian vegetation. This behaviour is not observed on Yerre 9 and Yerre 27. Mayenne 148 has an evenly scattered cloud of point (not shown). Maine 328 and Boulon 23 have the maximum and minimum TS but the same R<sup>2</sup>. Indeed, no significant correlation is found between TS and R<sup>2</sup> (p-value = 0.56).

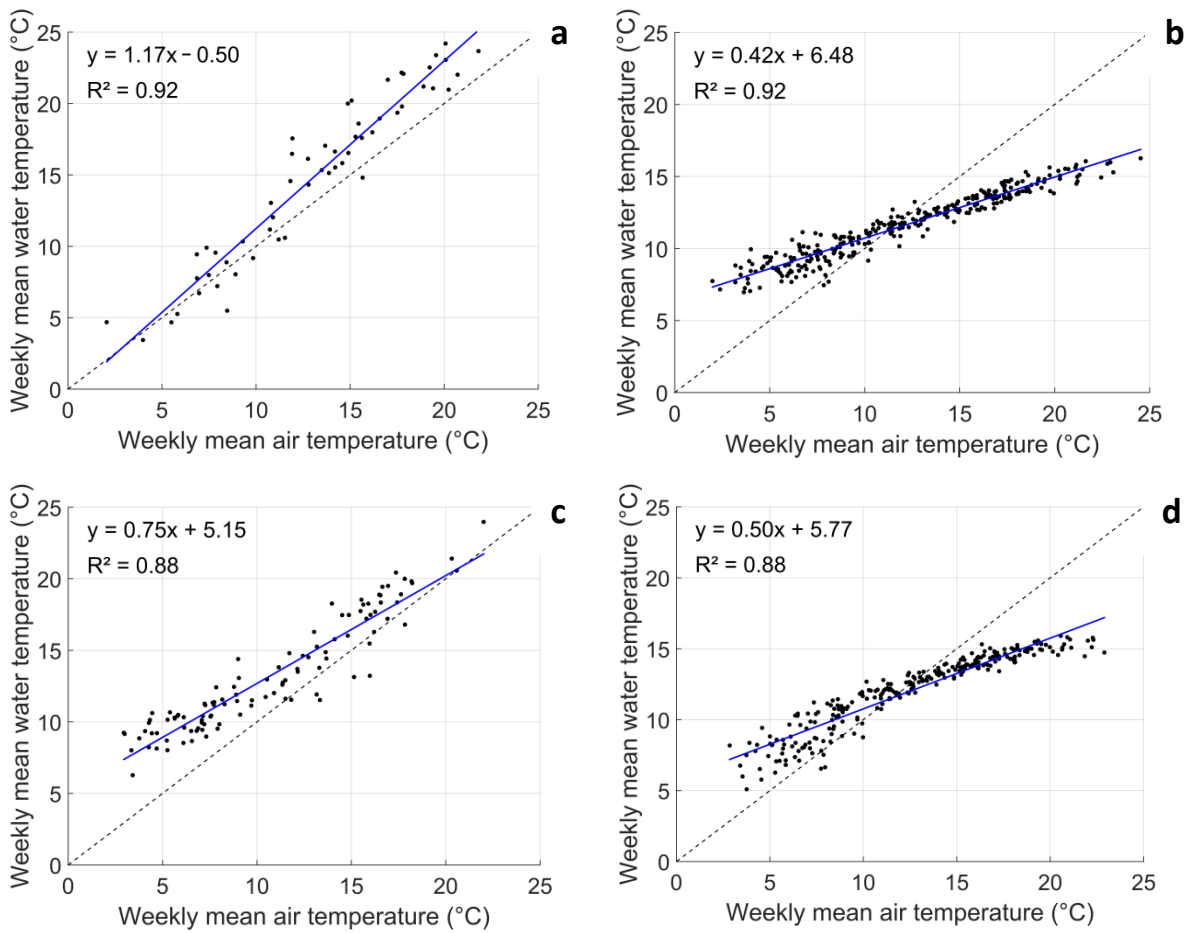


Figure 3.9: Tw-Ta weekly linear regression (a) Maine 328, with the highest TS (b) Boulon 23 with the lowest TS (c) Conie 27, (d) Yerre 47

Regression lines for all stations are shown on Figure 3.10, which confirms that there is a wide range of thermal sensitivity and that variability of Tw is more important in summer than in winter. Regressions lines are mainly arranged around a pivot point located around 8°C, although some stations are warmer (e.g. Aigre 25, Conie 27) or colder (e.g. Tusson 8) at this point. All scatterplots are shown in appendix F.

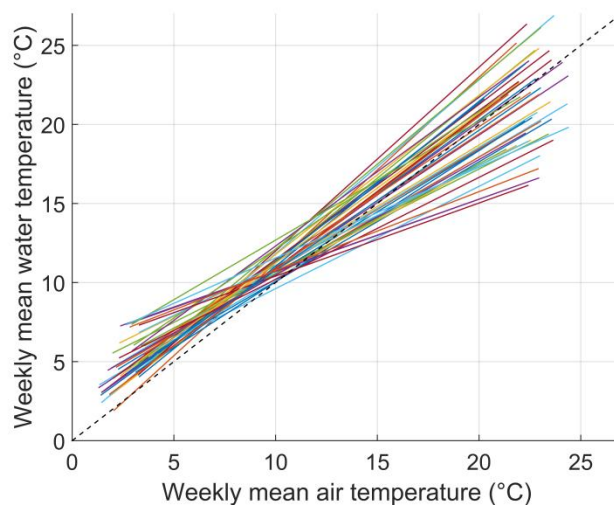


Figure 3.10: Linear regressions fitted on data available between August 2008 and July 2015 for the 44 stations

Figure 3.11 shows the spatial distribution of thermal sensitivities. Although TS lower than 0.55 are found only in the sedimentary basin, low TS between 0.55 and 0.67 are also found in the Armorican massif. A two sample t-test on TS of the Armorican massif and the sedimentary basin show that characteristics (means and variances) of both samples are not significantly different. The Yerre can be noticed by the variability of TS on its 3 stations that is not correlated to the distance from source.

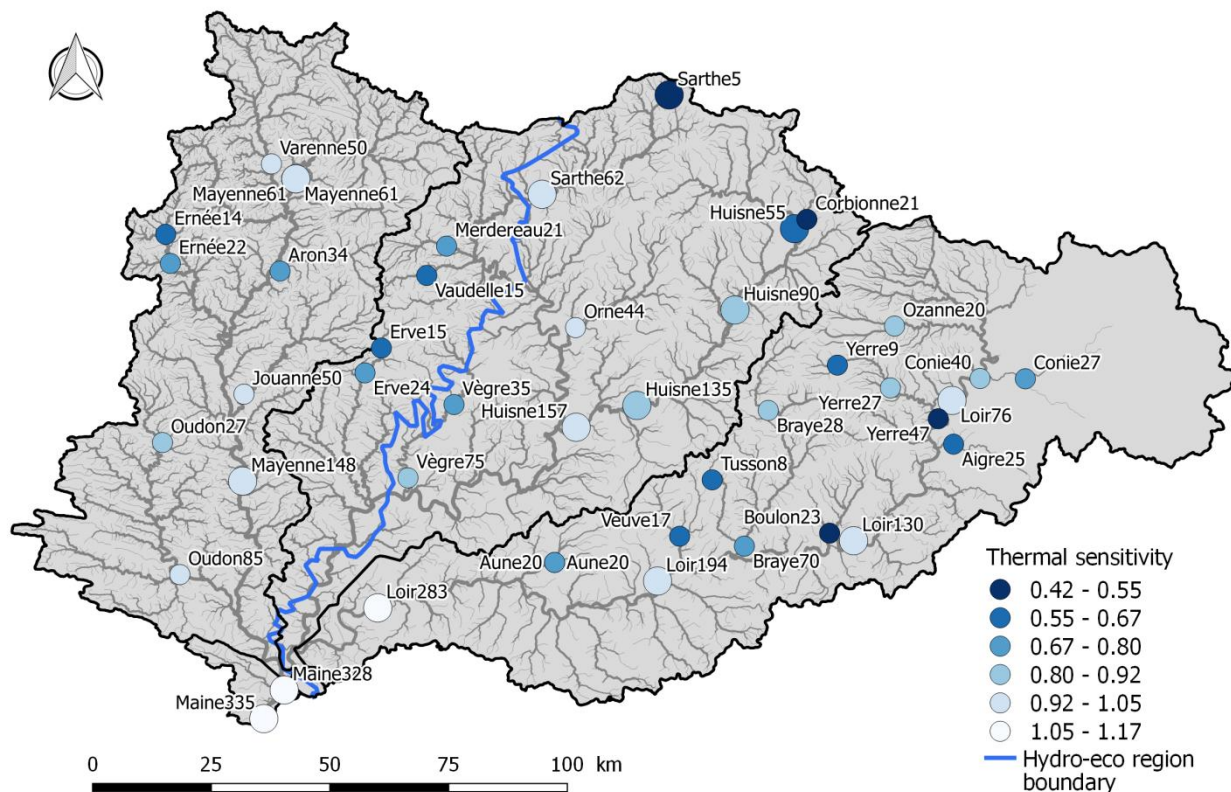


Figure 3.11: Spatial distribution of thermal sensitivities computed on weekly  $T_w$ - $T_a$  regressions

The slopes and intercepts of regressions are correlated, although not perfectly. The correlation coefficient equates -0.94. Figure 3.12 shows this relationship and its variability, with a regression line aiming at showing the general behaviour, as well as colours indicating the results of the hierarchical clustering method.

The variation of slope is theoretically related to the groundwater fluxes, because they heat in winter and cool in summer. On the other hand, for a given slope, the residual of the slope-intercept regression line is an indicator of a heating/cooling process happening the whole year. However, the ability of descriptors to explain the residuals of the slope-intercept regression is limited ( $R^2=36\%$ , Table 3.11). There is a significant but counter-intuitive positive influence of  $Q_{\min}/Q_{\max}$  (Table 3.11). Most part of this relation is due to the presence of 3 stations with both high residuals and high  $Q_{\min}/Q_{\max}$  (Aigre 25, Conie 27 and Conie 40). The tiering rate appears as improving the model but, taken alone, its relationship with the residuals is not significant ( $R^2 = 0.02$ ,  $p$ -value = 0.19).

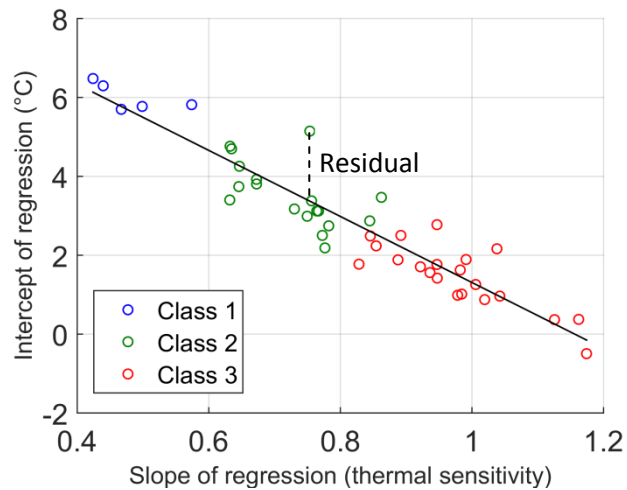


Figure 3.12: Relationship between intercept and slope of Tw-Ta weekly regressions

Table 3.11: Linear regression model resulting of a stepwise selection between the residuals of the slope-intercept and the descriptors

| Y variable                                  | X                  | Number of stations & period | Selected X variables               | Coeff. | p-values | R <sup>2</sup> <sub>adjusted</sub> RMSE |
|---|--------------------|-----------------------------|------------------------------------|--------|----------|---|
| Residuals of the slope-intercept regression | Global descriptors | 44<br>2008-2015             | Intercept                          | -0.50  | 2.4E-4   | 0.36                                    |
|   |                    |                             | Q <sub>min</sub> /Q <sub>max</sub> | 1.82   | 2.1E-5   | 0.46 °C                                 |
|   |                    |                             | Tiering rate                       | 0.53   | 0.037    |   |

The spatial distribution of the classification results is shown on Figure 3.13. The 5 stations with high groundwater influence are located in the sedimentary basin and at a maximal distance of 47 km from source. Distance from source of stations with mixed influence is comprised between 8 and 90 km, while this distance for stations with air influence starts at 20 km.

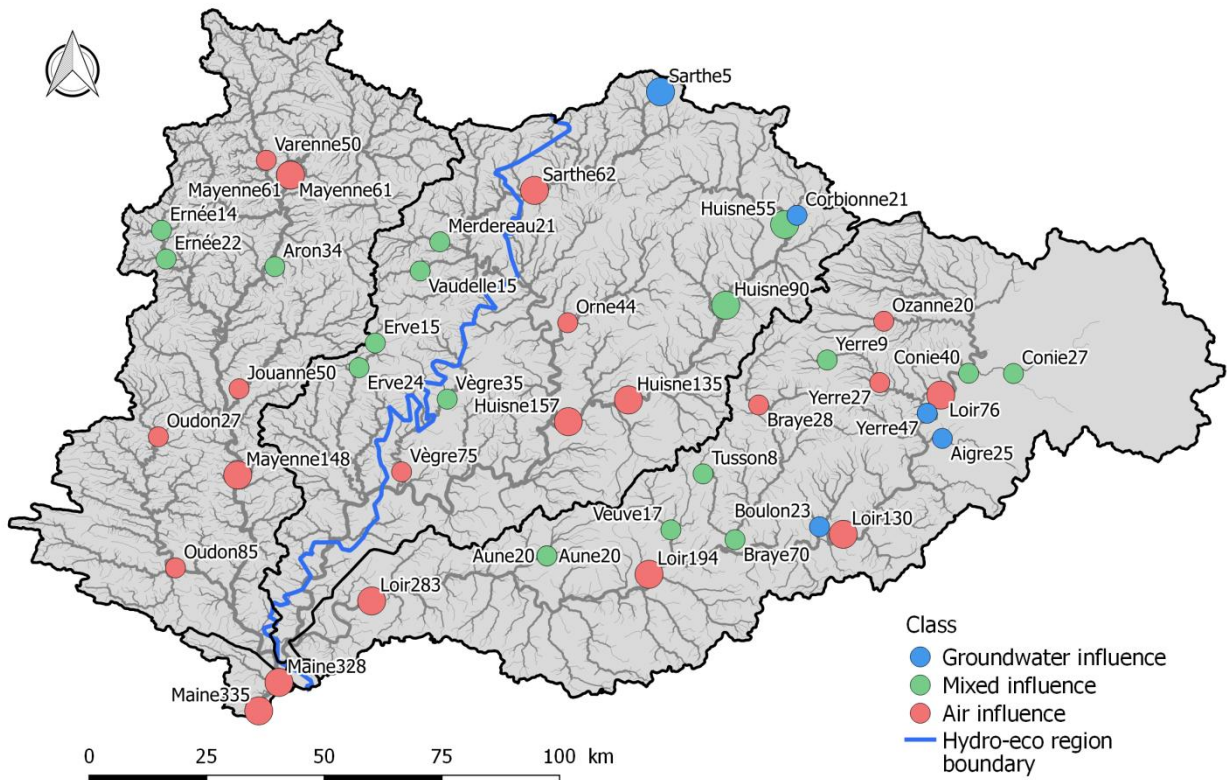


Figure 3.13: Spatial distribution of stations classified thanks to the hierarchical clustering method

### 3.6.2 Interannual variations of thermal sensitivity

Thermal sensitivities computed on each station-year are shown on Figure 3.14. They range from 0.28 to 1.25. All regressions are significant at the 5% level. TS is above 1 for 21 station-years. At these stations, water becomes warmer than air in summer by gaining and keeping energy due to its high specific heat. Considering the 95% confidence intervals for the TS estimates, only Maine 335, which is the most downstream station, has a TS significantly higher than 1 in 2009. Considering the 95% confidence intervals for the TS estimates, significant changes of TS appear between 2010 and 2011 only for Mayenne 61 and Oudon 85, both located in the Mayenne catchment. This trend is however observed at all stations (Figure 3.14). In order to test if the low TS values of 2010 are due to the high climatic amplitudes occurring that year (January and December are cold, while mid-June to mid-July is hot), TS were computed after removal of data of these periods. The impact is limited to +0.05 on average. Hence, low values of TS in 2010 and 2013 are likely due to relatively higher groundwater level (Chrétien et al., 2014). When TS are computed on hydrologic years (August to July), results are completely different, with significant changes for 5 stations (Erve 24, Sarthe 5, Veuve 17, Vègre 35 and Yerre 9).

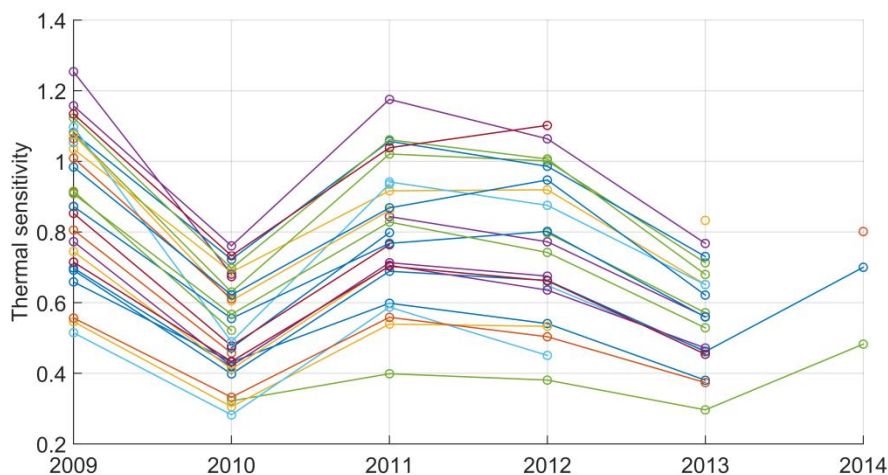


Figure 3.14: Temporal evolution of thermal sensitivity

### 3.7 Can we predict thermal metrics based on hydrology and basin properties?

The stepwise linear regression fitted on 22 stations show that there is a strong link between the thermal sensitivity and the natural logarithm of the distance from source (Table 3.12 and Figure 3.15). The ratio  $Q_{\min}/Q_{\max}$  has smaller explanatory power. In a single linear regression relating this ratio to TS,  $R^2$  is only 0.02 and p-value equates 0.18. The best controls of the slopes and the intercepts of the Tw-Ta regressions are the same, which is not surprising given the correlation between the 2 variables.

Table 3.12: Linear regression models resulting of the stepwise selection

| Y variable                          | X variable         | Number of stations & period | Selected X variables              | Coeff. | p-values | $R^2_{\text{adjusted}}$<br>RMSE |
|-------------------------------------|--------------------|-----------------------------|-----------------------------------|--------|----------|---------------------------------|
| Slope of the Tw-Ta regressions (TS) | Global descriptors | 22<br>2008-2015             | Intercept                         | 0.26   | 0.035    | 0.64<br>0.113 °C/°C             |
|                                     |                    |                             | $\log(\text{distanceFromSource})$ | 0.16   | 1.7E-5   |                                 |
|                                     |                    |                             | $Q_{\min}/Q_{\max}$               | -0.31  | 0.017    |                                 |
| Intercept of the Tw-Ta regressions  | Global descriptors | 22<br>2008-2015             | Intercept                         | 6.57   | 2.4E-6   | 0.69<br>0.97 °C                 |
|                                     |                    |                             | $\log(\text{distanceFromSource})$ | -1.22  | 7.5E-5   |                                 |
|                                     |                    |                             | $Q_{\min}/Q_{\max}$               | 4.66   | 2.0E-4   |                                 |

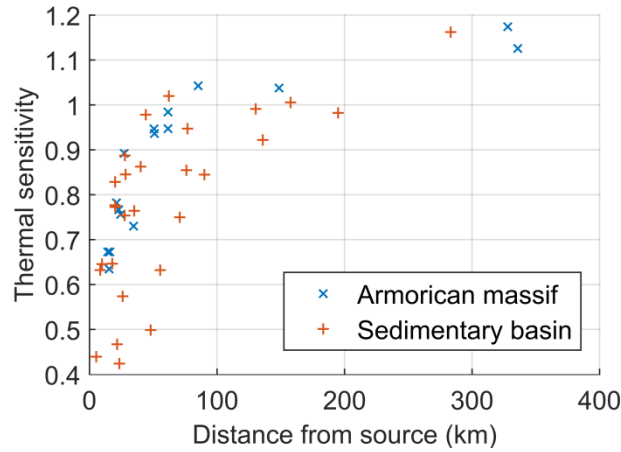


Figure 3.15: Thermal sensitivity as a function of distance from source

The final model is shown at Table 3.13:

Table 3.13: Empirical model at the weekly time scale fitted on the 22 stations (fit group among the 44 stations).

|  |                           |
|--|---------------------------|
| $T_w(\text{week}) = \text{interceptRegTwTa} + TS \times T_a(\text{week})$                                      |                           |
| $\text{interceptRegTwTa} = 6.57 - 1.22 \times \log(\text{distanceFromSource}) + 4.66 \times Q_{\min}/Q_{\max}$ | $R^2_{\text{adj}} = 0.69$ |
| $TS = 0.26 + 0.16 \times \log(\text{distanceFromSource}) - 0.31 \times Q_{\min}/Q_{\max}$                      | $R^2_{\text{adj}} = 0.65$ |

When this model is applied on the validation group, the  $R^2$  is 0.90, global RMSE is 1.35 °C, the mean bias is close to zero (-0.13 °C) and the standard deviation of errors (SDE) is 1.34 °C. The modelled weekly  $T_w$  vs. observed weekly  $T_w$  are shown on Figure 3.16. The minimal/maximal biases averaged on each station are -1.2 °C for Mayenne 148 and 0.74 °C for Aune 20 respectively. The minimal and maximal biases (without averages) on weekly  $T_w$  are found on Mayenne 148 (-7.4 °C) and Yerre47 (+7.3 °C), respectively due to the scattered cloud of point and the convex behaviour discussed above.

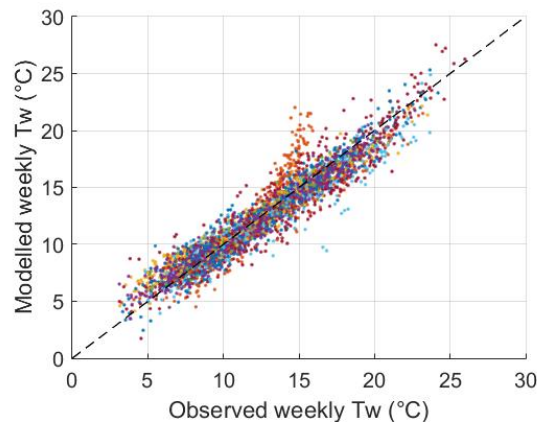


Figure 3.16: Modelled weekly  $T_w$  vs. observed weekly  $T_w$  (validation group of 22 stations, with a colour for each station)

The map of the biases on the validation stations is shown at Figure 3.17. Although it seems that the bias could be correlated with TS, the relationship is not significant ( $p$ -value = 0.34).

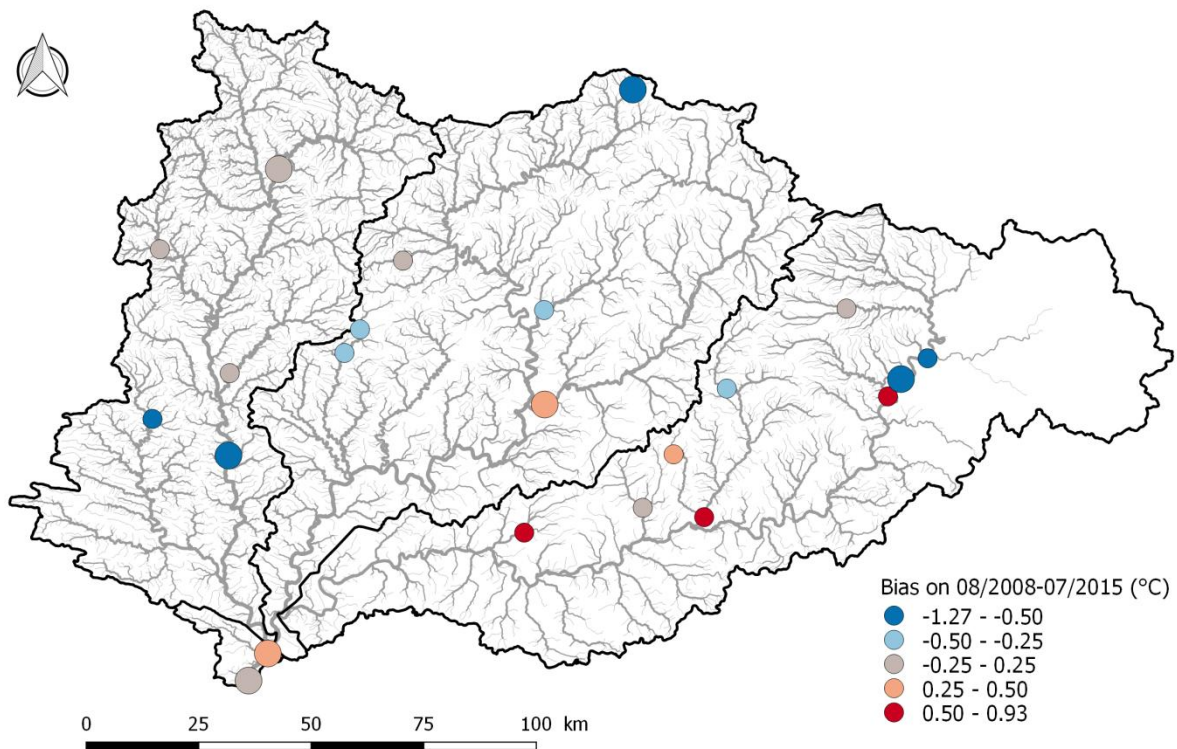


Figure 3.17: Biases of the statistical model on the validation stations, computed on data available on the 08/2008-07/2015 period

RMSE computed for each hydro-eco region are similar (1.31 °C in the Armorican massif and 1.36 in the sedimentary basin). RMSE computed separately for each class are 1.8, 1.03 and 1.47 °C for classes 1, 2 and 3 respectively. The modelled weekly Tw, averaged by group of stations and by hydrological years, are shown on Figure 3.18. As expected, the stations with air influence have the highest annual amplitude. The stations with high groundwater influence are the coldest in summer but are not the warmest in winter. That fact, as well as the highest RMSE for the class 1 (groundwater influence) may be explained by the smaller number of station in this class (3 stations in the fit group, 2 for validation) but also by the presence of Yerre 47 in the validation group. The results are not changed much when fit and validation are achieved on all stations, and a modification of the classes would probably be needed in order to better discriminate the annual cycles of modelled Tw (Figure 3.18).

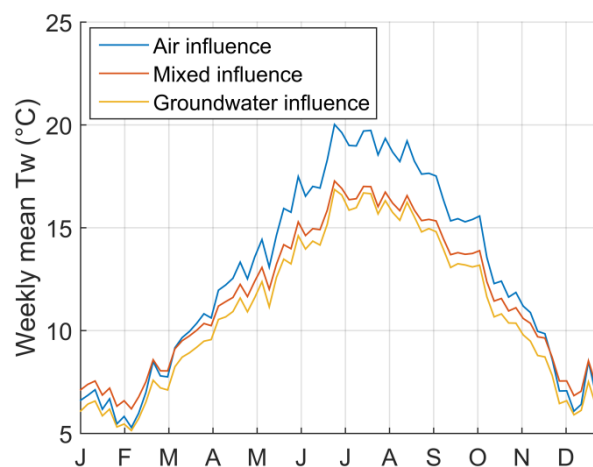


Figure 3.18: Annual cycle of modelled weekly mean, averaged on 07/2008-08/2015 and for each group of stations on the 22 validation stations

With the use of discharges simulated with the EROS model at the catchment scale and spread on each river reach according to their respective length, the  $Q_{\min}/Q_{\max}$  ratio can be computed and the empirical model can be applied on the whole river network of the Maine catchment. Figure 3.19 shows the results on the 13-31/08/2009 period (to match with the validation period used in the next chapters). Thermal sensitivities and intercepts outside of the observed range (0.42 to 1.17 for TS and -0.5 to 6.5 for the intercept) were discarded. Modelled Tw range from 12.6 to 24.4 °C. The second half of the Loir and Sarthe are warmer than the Mayenne, because distances from source at these points are higher. Colder streams are found in the north-west of the catchment according to the mean air temperature (see Figure 2.6).

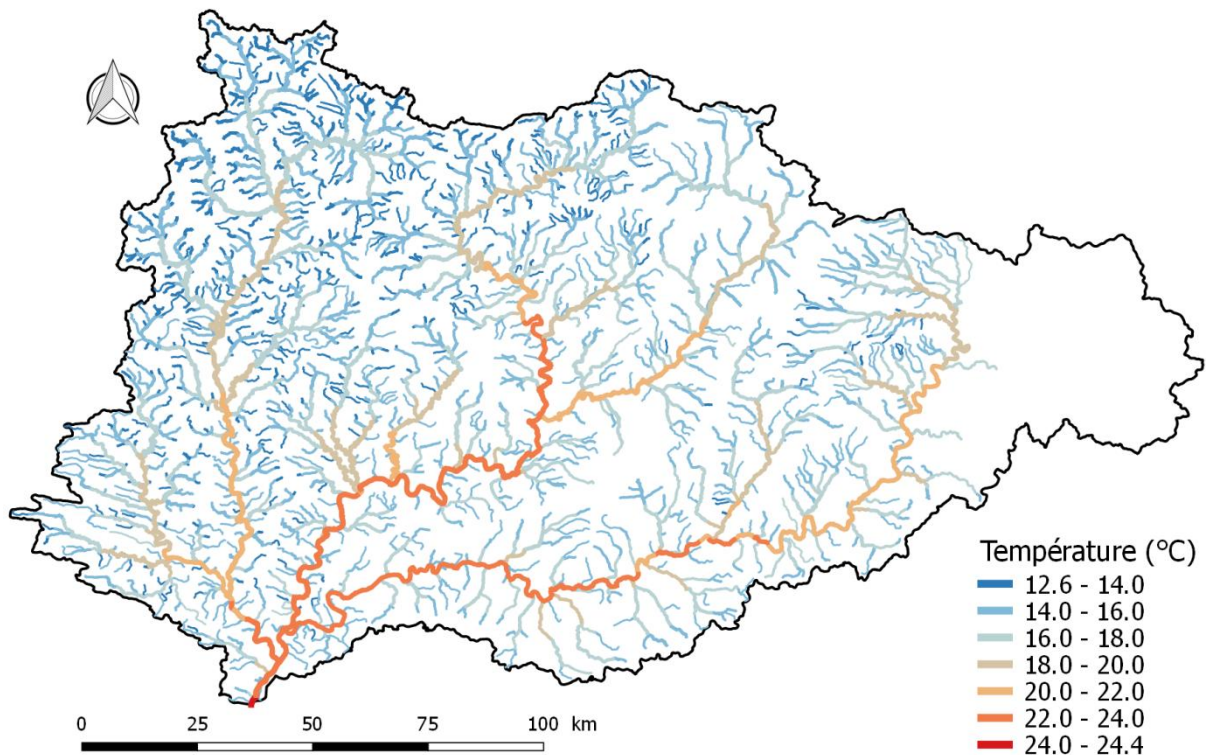


Figure 3.19: Mean temperature simulated with the empirical model on the 13-31/08/2009 period

In order to characterise the thermal behaviour with only one number, TS can also be computed on the whole river network (Figure 3.20). As expected, the most downstream reaches are the most sensitive. Because the river network is denser in the west part of the catchment, more reaches with low sensitivity are found there.

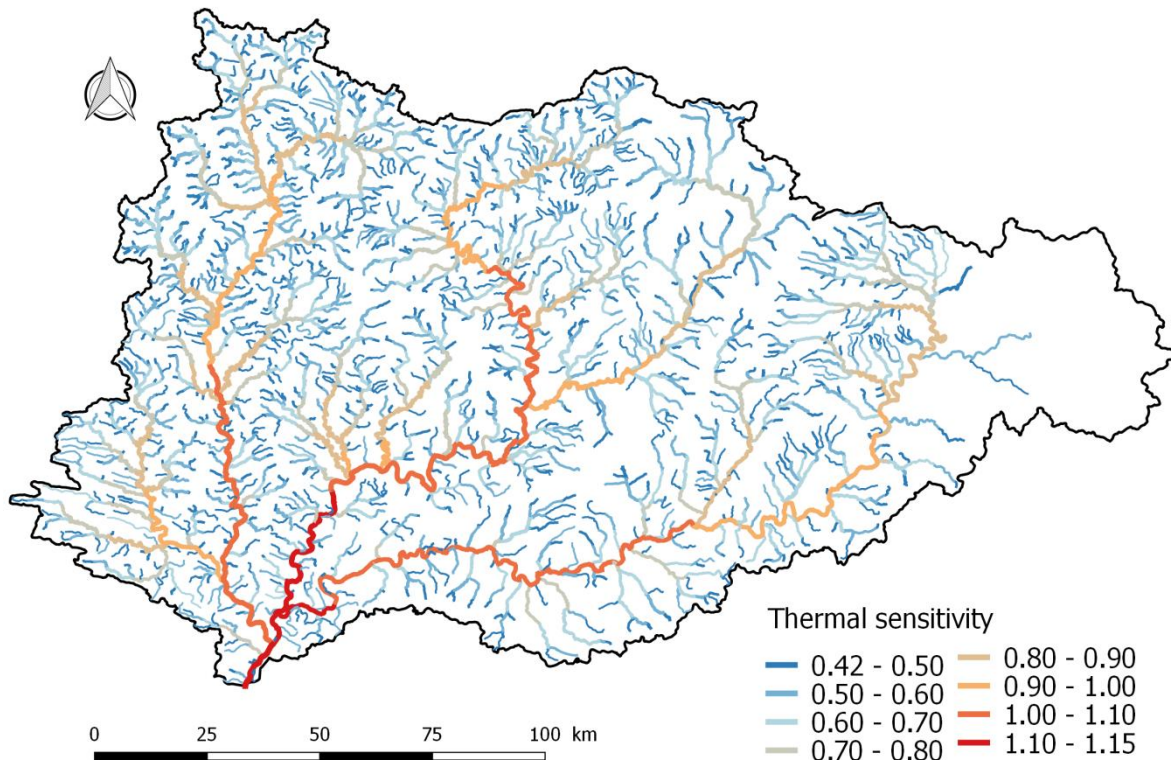


Figure 3.20: Thermal sensitivity computed on the whole river network

### 3.8 Discussion

The large variability in  $T_w$  metrics observed on the Maine catchment is similar to what is found in other studies. For example,  $T_w$ Jul reported by Wehrly et al. (2003) for lower Michigan (USA) range from 10 °C to 26 °C with the majority of sites between 16 °C and 24 °C (this study: 14.4 °C to 24.6 °C). Annual amplitude reported by Maheu et al. (2016) across the whole USA ranges from 3.4 °C to 32.2 °C (this study: 8.7 °C to 18.5 °C), while they report a daily amplitude in summer between 0.4 °C and 9.6 °C, with a mean value of 3.7 °C (this study 0.5 °C to 4 °C). They found  $T_w$  diel amplitude to be correlated with  $T_a$  diel amplitude, which may be expected to be higher in some area of USA than on the Maine basin. For 90 stream sites throughout the Great Lakes Basin (Ontario), Chu et al. (2010) reports diel amplitudes closer to our results, from 0.6 °C to 3.5 °C with a mean of 2 °C. The diel amplitude in July does not behaves exactly like the conceptual model found in Caissie (2006), which shows a maximum for wide and shallow river (Strahler order around 4), with a minimum near the source and when water depth is high (Figure 3.21a). Indeed, a wide variability of  $dA_{Jul}$  is observed for stations located close to stream sources, showing the differences in groundwater fluxes.

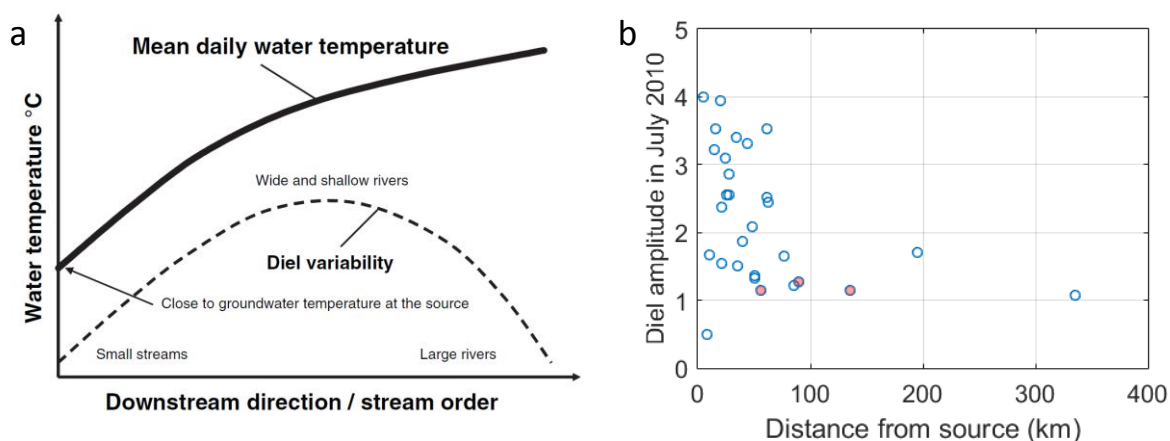


Figure 3.21: Diel amplitude as a function of distance from source (a) As described in Caissie (2006) (b) observed on the Maine catchment (Sarthe River stations are in red)

Thermal sensitivities reported by Hilderbrand et al. (2014) for rivers (Strahler order  $\leq 3$ ) in Maryland (USA) range from 0.13 to 0.79 (this study: 0.42 to 1.17). They observed substantial interannual variations in TS for some stations, with minimum values in 2008. They explained it by the lower-than-average summer  $T_a$  in 2008, although the relationship was not statistically significant. Kelleher et al. (2012) report TS between 0.02 and 0.93 for Pennsylvanian streams ( $1 \geq$  Strahler order  $\geq 7$ ), while Ducharne (2008) found maximum TS above 1 for Strahler orders 6 and 7 in the Seine catchment. The presence of TS above 1 may be explained by the accumulation of energy that is proportional to the travel time. A correlation between TS and  $R^2$  was found by Hilderbrand et al. (2014), while it was not observed in our data. It shows that low TS are not due to noise in the signal but to a well established process like the groundwater fluxes.

Our results show that the distance from source and  $Q_{\min}/Q_{\max}$  are the main drivers of the thermal sensitivity. The empirical model of Kelleher et al. (2012) and Chang and Psaris (2013) are very close to ours since they involve the Strahler order/contributing area respectively and the BFI (the long-term ratio of baseflow to average flow), with global  $R^2$  varying between 0.43 and 0.65 depending on the catchment (this study:  $R^2=0.65$ ). Ducharne (2008) demonstrated the dependence of slope and intercept of the  $T_w$ - $T_a$  regression with the Strahler order, while Garner et al. (2014a) also linked their climatic sensitivity index to basin permeability and basin area. On the opposite, Hilderbrand et al. (2014) did not find a significant relationship between TS and basin size, but with channel slope.

The accuracy of our model ( $R^2 = 0.90$ , RMSE = 1.35 °C and SDE = 1.34 °C) is usually better than simple  $T_w$ - $T_a$  models computed at the regional scale: Pilgrim et al. (1998) and Stefan and Preud'homme (1993) reported SDE of 2.6 °C and 2.1°C respectively for global regressions computed at the weekly timestep. The accuracy of our model is similar to those obtained with other empirical models relating  $T_w$  to  $T_a$  with landscape descriptors.

Ducharne (2008) reports a RMSE of 1.45 °C at the daily time scale. In her model, the slope and intercept of the regression are dependent on the Strahler order. Hilderbrand et al. (2014) reports a RMSE of 0.96 °C for a linear model at the daily time scale based on discharge and with a categorical variable related to one of the 3 regions used as only landscape descriptor. Finally, Isaak et al. (2010) report a  $R^2$  of 0.93 for the prediction of the mean summer  $T_w$  (15 July- 15 August) based on  $T_a$ , elevation, solar radiation, and discharge.

### 3.9 Conclusion

We showed that the different metrics of Tw measured on the Maine catchment have a wide range of variability, showing that even on a climatically homogeneous catchment there is a range of different thermal habitats. The variability in thermal sensitivity means that these river reaches will not respond the same manner to climate change. As demonstrated by our empirical models, TS is linked to the proximity of the river reaches to the river sources. Thermal habitats of fishes living in the headwaters like the brown trout are thus less threatened by climate change than habitats of fishes living more downstream, like the Spirlin (*Alburnoides bipunctatus*). TS is also related to the groundwater fluxes. It is why the decrease of TS in 2010 and 2013 are likely explained by decrease of the groundwater level. It is thus important that groundwater piezometric levels stay high enough to maximise these groundwater flows. The tiering rate, a landscape descriptor that was not used in previous studies and quantifying the presence of weirs, did not significantly explain the Tw metrics. Our statistical method did not provide evidence that presence of weirs has a warming effect in summer. The empirical model developed in this chapter can easily be used to compute mean weekly Tw for reaches without Tw monitoring stations. Because it was fitted on stations from two very different hydro-eco regions, this model may be applied on other catchments located close to our study area, as long as the climate is similar. Indeed, the linear regressions were appropriate on this basin (except for 2 stations) because temperature range is limited (4.4 % of mean weekly Tw are above 20°C). If climate is warmer, logistic regressions would be needed to model properly the Tw-Ta relationship.



## **Chapter 4: The T-NET model on the Maine catchment: standard configuration, sensitivity analysis and comparison with a hydraulic model**

### **4.1 Résumé en français**

T-NET est un modèle à base physique qui permet de calculer  $T_w$  sur tous les tronçons d'un réseau hydrographique (réseau CARTHAGE modifié). T-NET a été développé et appliqué à tout le bassin de la Loire (100 000 km<sup>2</sup>) par Beaufort (2015) avec 128 stations de validations, dont 25 étaient dans le bassin de la Maine. L'objectif de ce chapitre est d'analyser la performance du modèle T-NET (tel que publié par Beaufort et al., 2016) sur le bassin de la Maine, avec 19 stations supplémentaires, afin d'identifier ses points faibles et les méthodes potentielles pour les corriger.

T-NET prend en compte l'advection du signal thermique et effectue un mélange aux confluences. L'équation de la chaleur évaluée selon l'espace est résolue analytiquement après linéarisation grâce au concept de température d'équilibre, qui est la température à laquelle la somme des flux énergétiques est nulle. Les flux énergétiques pris en compte sont décrits au Table 4.1. Les données météorologiques sont fournies par la réanalyse SAFRAN sur des mailles carrées de 8 km et au pas de temps horaire. Les débits (issus du ruissellement et des flux souterrains) sont calculés au pas de temps journalier par le modèle semi-distribué EROS aux exutoires de 82 sous-bassins, qui correspondent aux stations de jaugeage. Les débits sont ensuite redistribués à l'échelle des tronçons T-NET en fonction de leurs longueurs respectives. Les largeurs et hauteurs d'eau sont calculées par un modèle empirique qui a été callé sur 78 tronçons de rivières françaises. Celui-ci dépend du module, du débit du jour et de la pente, qui a été calculé sur un MNT de l'IGN à 25 m de résolution. La vitesse de transfert est le rapport entre le débit et la section mouillée. En moyenne, les débits modélisés par EROS sont sous-estimés en hiver et surestimés en été et cela contrebalance légèrement l'imprécision du modèle Estimkart en été, qui malgré cela, sous-estime très probablement les largeurs et hauteurs d'eau.

L'application de T-NET sur le bassin de la Maine montre que les biais sont correctement contenus entre -1°C et +1°C en hiver, mais augmentent en été, avec des biais positifs pour les stations à petites sensibilité thermiques (proches de la source et/ou avec flux de nappes élevés) et des biais négatifs pour les sensibilités thermiques élevées. Cela suggère que l'impact des flux de nappe (débit ou température), ainsi que l'impact de l'ombrage, qui dépend de la largeur et donc de la distance à la source, sont mal caractérisés. D'autre part, les amplitudes journalières et les amplitudes des oscillations observées sur des pas de temps de 1-2 semaines sont surestimées toute l'année et de façon plus importante en été. Cela suggère que l'inertie thermique de la masse d'eau est sous-estimée.

Les résultats de T-NET sont comparés à ceux fournis par le modèle statistique présenté au chapitre 2, en août 2009. Bien que le modèle statistique fourni une gamme de température plus large, T-NET est le plus froid sur les ordres de Strahler de 1. Sur les ordres supérieurs, la différence entre les deux modèles semble suivre la même tendance que les biais de T-NET, puisque le modèle empirique est moins biaisé.

Des analyses de sensibilité sont ensuite effectuées sur les grandeurs hydrologiques. Les vitesses semblant généralement surestimées, une division des vitesses par 2 sans modifications des autres grandeurs (débit, largeur, hauteur) diminue l'impact de la  $T_w$  donnée à la source ( $T_w$  de nappe, approximée par la moyenne mobile de la température de l'air sur les 365 jours précédents).  $T_w$  est donc refroidi en hiver et réchauffé en été. Les largeurs modélisées par Estimkart semblent plutôt bonnes mais avec une tendance probable à la sous-estimation pour les largeurs  $> 30$  m. Un doublement des largeurs induit une division proportionnelle des vitesses et a globalement le même effet que la division par 2 des vitesses. Les hauteurs d'eau  $> 0.5$  m semblent sous-estimées par le modèle Estimkart. L'impact d'un doublement des hauteurs est faible sur les  $T_w$  moyennes mais important sur les amplitudes journalières, qui deviennent ainsi très peu biaisées. L'amplitude des variations du signal thermique sur 1-2 semaines est également diminuée. Une modification des débits impacte les résultats parce qu'elle implique des modifications des hauteurs, largeurs et donc de la vitesse. Finalement, une augmentation de  $2$  °C de la température de nappe augmente  $T_w$  jusqu'à  $0.9$  °C en moyenne sur les stations situées entre 5 et 20 km de la source, en janvier. L'impact est moins important sur les stations plus en aval, ainsi qu'en été, à cause de la diminution de la vitesse.

## 4.2 Context and objective

T-NET is a physically-based 1D model designed to compute depth and width-averaged water temperature along a hydrographic network (a GIS polyline), at the reach resolution and at the hourly time step. It uses the discharges provided by the semi-distributed model EROS (Thiéry and Moutzopoulos, 1992). Like all the physical models, it relies on a heat budget, but instead of relying on a numerical resolution of the advection-diffusion heat equation, it is based on the equilibrium temperature concept, which is defined as the water temperature at which the net rate of heat exchange at the interface of a water body is null (Bustillo et al., 2014). The use of the equilibrium temperature concept allows to linearise the heat equation and to resolve it analytically. T-NET takes into account the thermal signal advection and the mixing at confluences. The model was thus designed to be applied on well mixed streams and not on standing waters or large estuaries, where 2D (Cole and Wells, 2006; Becker et al., 2010; Ouellet et al., 2014) or 3D models (Maderich et al., 2008) are more appropriate. The advantage is that T-NET can model stream temperature at the regional scale ( $> 10\ 000$  km<sup>2</sup>).

Many other physically based models running on a network topology exist (Wu et al., 2012; Cheng and Wiley, 2016; Haag and Luce, 2008; Chen et al., 1998a; Loinaz et al., 2013; Allen et al., 2007; Cox and Bolte, 2007; Gallice et al., 2016; Sun et al., 2015). However, only a part of them run at the hourly time step, are accompanied by a hydrological model, and were designed to be applied on large catchments ( $> 10\ 000$  km<sup>2</sup>).

Among these models, Chen et al. (1998b) applied the SHADE-HSPF model on a  $1780$  km<sup>2</sup> basin in Oregon. SHADE-HSPF is a 1D model running at the hourly time step, where discharges are modelled by sub-catchments that have homogeneous characteristics in term of climate, landuse and soil characteristics. Three discharges are modelled: overland flow, interflow and groundwater flow. The model takes into account the impact of topographic and riparian vegetation on direct and diffuse radiation, which are mathematically partitioned from observed global radiation. It also takes into account the bed conduction of heat, a process that was shown to be important in low order streams.

The RMSE computed on hourly Tw measured at 27 stations during summers 1991 and 1992 range from 1.2 to 4.4 °C.

Haag and Luce (2008) applied the 1D LARSIM-WT model on a 14 000 km<sup>2</sup> watershed in south-west Germany, with a focus on 203 km of the lock-regulated part of the Neckar River and its major tributaries. This model is able to run on a river network although that was not achieved in this paper, because statistical models were more accurate to provide temperature of tributaries. Like the SHADE-HSPF model, it considers three kinds of discharge (direct runoff, interflow and groundwater). The impact of riparian vegetation on the global solar radiation can be taken into account but was considered as null in this paper because river width is about 100 m wide in the reaches of interest. This model uses a numerical resolution of the advection-dispersion equation. The RMSE computed on hourly Tw measured at 11 stations located on the main stream between the 1<sup>st</sup> January and the 1<sup>st</sup> September 2003 range from 0.6 to 1.1 °C.

Sun et al. (2015) applied the DHSVM-RBM model on an urban catchment (Washington State). Although this application catchment is small (31 km<sup>2</sup>), DHSVM-RBM can work from local to regional river systems. The vector-based stream temperature model RBM was developed by Yearsley (2009) and applied on large catchments in Pacific Northwest USA. Temperature is computed by following water parcels and storing the results at fixed positions. DHSVM is a grid-based hydrological model that takes into account runoff from urban impervious surfaces, as well as overland and subsurface flow in non-urban areas. DHSVM-RBM takes into account the impact of topographic and riparian shading. The RMSE were computed on hourly Tw measured at the outlet of the catchment from 2004 to 2012. They range from 0.36 °C (1<sup>st</sup> quartile of discharge) to 0.8 °C (4<sup>th</sup> quartile of discharge).

Among these models running on a network topology, T-NET is the only one based on the equilibrium temperature, a concept that has been successfully used to model Tw at the hourly time scale and the river reach scale (Hebert et al., 2011). Currently, the equilibrium temperature is computed thanks to a heat budget, but it may rely on simpler methods if one wants to apply T-NET on a catchment where meteorological data are not available (Mohseni et al., 1998; Caissie et al., 2005).

In his thesis, Beaufort (2015) analysed the global accuracy of T-NET on 128 Tw monitoring stations of the Loire basin (110 000 km<sup>2</sup>), whose 26 were in the Maine basin. The goal of this chapter is to analyse the accuracy of the T-NET model as published in Beaufort et al. (2016), in order to understand its weak points and the possible ways of improvement on the Maine catchment (22 350 km<sup>2</sup>), with a densified stations network (19 additional stations).

The first part of this chapter will describe the principle of the T-NET model. Results and performances will then be analysed on the whole annual cycle and then with a focus on summer. Results at this period will be compared to the ones provided by the statistical model built in chapter 20. Sensitivity analyses on input and hydraulic parameters will be achieved, in order to give insights on the possible ways to improve T-NET accuracy.

## 4.3 The standard version of the T-NET model

### 4.3.1 Heat fluxes

T-NET is a physically based model, meaning that it relies on a heat balance. The formulations of these fluxes as considered in the standard version of the model are summarised in Table 4.1.

**Table 4.1 : Formulations of heat fluxes taken into account at the atmospheric and the riverbed interfaces (Beaufort et al., 2016)**

| Heat flux ( $W \cdot m^{-2}$ )              | Formulations                                     | Parameters  | Assumptions  |
|---|--|---|--|
| Net solar radiation ( $H_{ns}$ )            | $H_{ns} = (1 - Alb) \cdot Rg \cdot (1 - SF)$     | $Alb$ : Surface water albedo<br>$Rg$ : Global radiation [ $W \cdot m^{-2}$ ]<br>$SF$ : Shading factor   | $Alb = 0.06$   |
| Longwave atmospheric radiation ( $H_{la}$ ) | Provided by the SAFRAN reanalysis                |   |  |
| Longwave emitted radiation ( $H_{lw}$ )     | $H_{lw} = \epsilon_w \sigma (T_w + 273.15)^4$    | $\epsilon_w$ : Water emissivity<br>$T_w$ : Water temperature [ $^{\circ}C$ ]  | $\epsilon_w = 0.97$<br>$\sigma = 5.67 \times 10^{-8} W \cdot m^{-2} \cdot K^{-4}$  |
| Convection ( $H_c$ )                        | $H_c = B \cdot f(w) \cdot (T_a - T_w)$           | $B$ : Bowen's coefficient<br>$f(w) = aw + b$ : wind function<br>$w$ : wind velocity at 2 m [ $m \cdot s^{-1}$ ]   | $a = 4 [W \cdot s \cdot m^{-3} \cdot mb^{-1}]$<br>$b = 7.4 [W \cdot m^{-2} \cdot mb^{-1}]$<br>$B = 0.62 mb \cdot K^{-1}$ |
| Evaporation ( $H_e$ )                       | $H_e = f(w) \cdot (e_s - e_a)$                   | $e_a$ : water vapour pressure in air [mb]<br>$e_s$ : saturation vapour pressure for $T_w$ [mb]  | Magnus-Tetens approx.:<br>$e_s = 6.11 \cdot \exp\left(\frac{17.27 \cdot T_w}{273.3 + T_w}\right)$                        |
| Streambed inputs ( $H_g$ )                  | $H_g = \rho_w C_{p_w} \frac{Q_G}{A} (T_g - T_w)$ | $T_g$ : Groundwater temperature [ $^{\circ}C$ ]<br>$\rho_w$ : Density of water [ $kg \cdot m^{-3}$ ]<br>$C_{p_w}$ : Specific heat capacity [ $J \cdot kg^{-1} \cdot K^{-1}$ ]<br>$Q_G$ : Groundwater flow [ $m^3 \cdot s^{-1}$ ]<br>$A$ : Exchange area between groundwater and river [ $m^2$ ] |  |

In the standard T-NET version, the shadow factor (SF) used in the net solar radiation computation (Table 4.1) is computed with:

$$SF = vc \times k \quad (\text{Eq. 4.1})$$

where  $vc$  is the vegetation cover (a number between 0 and 1) and  $k$  is a coefficient aiming to account for the influence of the reach width on shadow. It is fixed at 1 (maximum impact) for a Strahler order of 1 and at 0 (no impact of vegetation) for a Strahler order of 8. This coefficient is constant in time and vegetation is considered to be opaque all year long.

### 4.3.2 Principles and equations

T-NET is a 1D model operating on a river network (a GIS polyline). Indeed, we assume that  $T_w$  is homogeneous in the width and depth dimensions, which is true most of the time, except at the confluences (Caissie, 2006). Assuming that the thermal diffusion processes are negligible, the equation of heat is (Sinokrot and Stefan, 1993):

$$\frac{\partial T_w}{\partial t} + U \frac{\partial T_w}{\partial x} = \frac{\sum H_i(t)}{\rho_w C_{p_w} D} \quad (\text{Eq. 4.2})$$

with  $T_w$  the water temperature ( $^{\circ}C$ ),  $t$  the time (s),  $U$  the mean water velocity ( $m \cdot s^{-1}$ ),  $x$  the distance (m),  $H_i$  the heat fluxes that apply on the water body,  $\rho_w$  the density of water ( $kg \cdot m^{-3}$ ),  $C_{p_w}$  the specific heat of water ( $J \cdot kg^{-1} \cdot K^{-1}$ ), and  $D$  the river depth (m).

The model is run at the hourly time step and we will consider that there is no temperature variation with time within each hour (between the two computations), so that the first term of (Eq. 4.2 can be removed:

$$\frac{\partial T_w}{\partial x} = \frac{\sum H_i(t)}{\rho_w C p_w U D} \quad (\text{Eq. 4.3})$$

The model relies on the equilibrium temperature ( $T_e$ ) concept, which is defined as the water temperature at which the net rate of heat exchange would be zero (Edinger et al., 1968):

$$\sum_i H_i(T_e) = 0 \quad (\text{Eq. 4.4})$$

$T_e$  equates the root of the mathematical function  $\Sigma H$ , which depends on  $T_w$ . Because  $T_w$  cannot be isolated in this function, this root is found thanks to the Newton-Raphson method.

The difference between  $T_e$  and the actual  $T_w$  is proportional to the sum of the heat fluxes, weighted by  $K_e$ , the heat exchange coefficient ( $J.s^{-1}.m^{-2}.K^{-1}$ ), which determines the speed at which  $T_w$  approaches  $T_e$ :

$$\sum_i H_i = K_e(T_e - T_w) \quad (\text{Eq. 4.5})$$

Combining (Eq. 4.3 and (Eq. 4.5 gives:

$$\frac{\partial T_w}{\partial x} = \frac{K_e}{\rho_w C p_w U D} (T_e - T_w) \quad (\text{Eq. 4.6})$$

which is a first order linear differential equation and can be resolved analytically. The result is:

$$T_w(x + \Delta x) = T_e + [T_w(x) - T_e(x + \Delta x)]. \exp\left[\frac{-K_e}{\rho_w C p_w U D} \Delta x\right] \quad (\text{Eq. 4.7})$$

with  $\Delta x$  the distance travelled by the water during the computational time step  $\Delta t$  (1 hour).

$$\Delta x = U \Delta t \quad (\text{Eq. 4.8})$$

where

$$U = Q / A_s \quad (\text{Eq. 4.9})$$

with  $Q$  the discharge and  $A_s$  the cross-sectional area ( $m^2$ ).

If  $\Delta x$  is bigger than the reach length, it is limited to it, and only one computation will be done on the reach. Otherwise, several computations are done every hour.

As long as  $U$  is computed with (Eq. 4.9 and the river geometry is considered rectangular, (Eq. 4.7 can also be expressed as:

$$T_w(x + \Delta x) = T_e + [T_w(x) - T_e(x + \Delta x)]. \exp\left[\frac{-B K_e}{\rho_w C p_w Q} \Delta x\right] \quad (\text{Eq. 4.10})$$

where the influences of the wetted width ( $B$ ) and the discharge ( $Q$ ) replace those of the depth and velocity. It is interesting to note that, in a stationary regime, the characterisation of the depth is not needed as long as the discharge and the wetted width are provided. As soon as the regime is not stationary, the cross sectional area and hence the depth is needed to provide the timing information.

According to Edinger et al. (1968),  $K_e$  can be computed with:

$$K_e = -\sum_i \frac{\partial H_i}{\partial T_w} \quad (\text{Eq. 4.11})$$

That gives:

$$K_e(t) = 4\sigma(T_w(t) + 273.15)^3 + f(w) \left( 0.62 + 6.11 \cdot \frac{17.27 \times 237.3}{(237.3 + T_w(t))^2} \times \exp \left[ \frac{17.27 \times T_w(t)}{237.3 + T_w(t)} \right] \right) + \rho_w C_p \frac{Q_g(t)}{A} \quad (\text{Eq. 4.12})$$

Temperatures at the sources (Figure 4.2) are taken as the moving average of air temperature on the past 365 days. At a confluence,  $T_w$  of both tributaries are mixed according to their discharges:

$$T_{\text{downstream}} = \frac{T_{\text{trib1}} Q_{\text{trib1}} + T_{\text{trib2}} Q_{\text{trib2}}}{Q_{\text{trib1}} + Q_{\text{trib2}}} \quad (\text{Eq. 4.13})$$

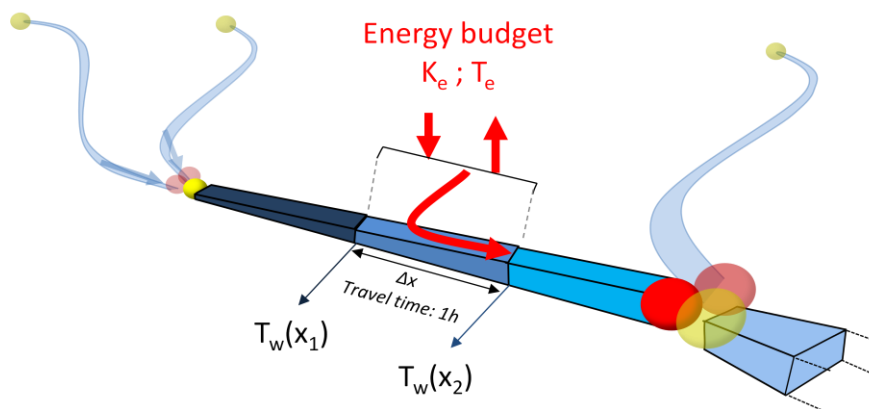


Figure 4.1: Principles of the T-NET model (Beaufort, 2015)

The Figure 4.2 summarises the evolution of modelled temperature starting from a source. The temperature is then pulled by the equilibrium temperature on reach 1 whose travel time is 3 hours. Mixing is achieved at the confluence, and temperature finally evolves on a reach 3 with a travel time of 1 hour.  $K_e$  and  $T_e$  are re-computed at each step.

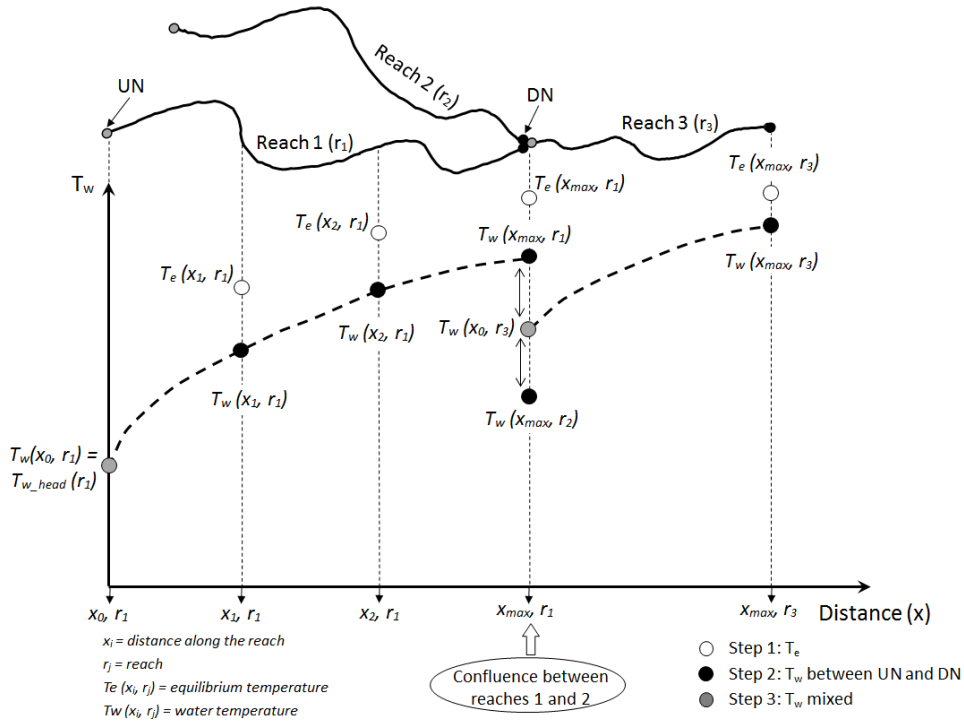


Figure 4.2:  $T_w$  computation scheme (Beaufort et al., 2016). Travel time in reach 1 is 3 hours, while it is 1 hour for reach 3. UN stands for upstream node, DN stands for downstream node.

### 4.3.3 River geometry

We consider that river have a rectangular cross-section:  $A_s = B \times D$ . Width (B) and depth (D) vary each day in relation with the discharge. They are both computed thanks to the Estimkart empirical equations (Lamouroux et al., 2010):

$$B(t) = a_d \bar{Q}^{b_d} \left[ \frac{Q(t)}{\bar{Q}} \right]^b$$

$$D(t) = c_d \bar{Q}^{f_d} \left[ \frac{Q(t)}{\bar{Q}} \right]^f$$

with  $\bar{Q}$  the mean annual discharge.  $a_d = \exp(2.122 - 0.076 * \sqrt{\text{SLO}})$ ;  $b_d = 0.475$ ;  $b = 0.125$ ;  $c_d = \exp(-0.966 - 0.058 * \sqrt{\text{SLO}})$ ;  $f_d = 0.298$ ;  $f = 0.302$ . SLO is the reach slope (%). These values were fitted on 78 French river reaches. The uncertainties (standard deviation) on each parameter (without considering error on the slope) are 1.05, 0.025, 0.05, 1.05, 0.028 and 0.03 respectively (Lamouroux et al., 2010).

### 4.4 Input datasets

Meteorology, discharge, and geomorphological data are needed as input of the model. They are summarised in Figure 4.3.

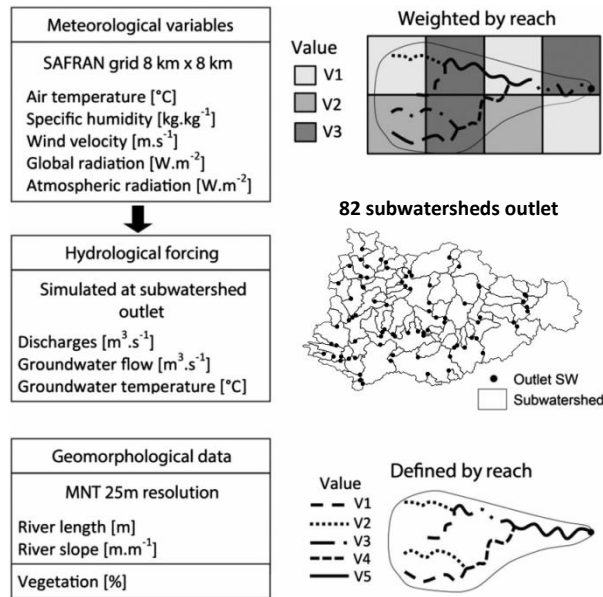


Figure 4.3: Summary of the use of the different input data (modified from Beaufort et al., 2016)

#### 4.4.1 Meteorological reanalysis

Air temperature ( $^{\circ}\text{C}$ ), specific humidity ( $\text{kg.kg}^{-1}$ ), wind velocity ( $\text{m.s}^{-1}$ ), global radiation ( $\text{W.m}^{-2}$ ) and atmospheric radiation ( $\text{W.m}^{-2}$ ) are provided by the SAFRAN reanalysis (Quintana-Seguí et al., 2008) at the hourly time step and a spatial resolution of 8 km. They are used in the formulations summarised in Table 4.1 and hence in the computation of  $T_e$  and  $K_e$ . If a river reach crosses several cells, a weighted average of data from each cell is achieved. SAFRAN computations are based on climatologically homogeneous area (612 in France). Resolution of 8 km is thus obtained by interpolation of the results. Precipitations are measured daily at 3675 stations in France. Air temperature, wind velocity and relative humidity computations are based on their respective observations achieved at 0, 6, 12, 18 UTC and at 1062, 465 and 819 stations respectively in France, while solar and longwave downward radiation computations are based on altitude fields of temperature, humidity, and cloudiness. Quintana-Seguí et al. (2008) validated these data against observed data of 08/2001-07/2002 from 5 stations spread in France (Sarrebouurg, Bordeaux, Puechabon (near Montpellier), Toulouse, Col de Porte (near Grenoble)), except for longwave radiation where data was available at only 2 stations (Toulouse, Col de Porte). The mean bias and RMSE are reported in Table 4.2. Bias of air temperature can reach  $-0.9^{\circ}\text{C}$  in some stations but is close to zero on average. Wind velocity is the less accurate variable, with correlations ranging from 0.58 to 0.86. Biases of relative humidity are in the  $\pm 4\%$  range. The global solar radiation is negatively biased, with a seasonal cycle that is not well reproduced (Quintana-Seguí et al., 2008).

Table 4.2: Biases and RMSE of the 5 variables provided by SAFRAN at the hourly time step on 08/2001-07/2002, averaged on the 5 validations stations (Sarrebouurg, Bordeaux, Puechabon, Toulouse, Col de Porte) (Quintana-Seguí et al., 2008)

|      | Ta ( $^{\circ}\text{C}$ ) | Wind velocity ( $\text{m.s}^{-1}$ ) | Relative humidity (%) | Global solar radiation ( $\text{W.m}^{-2}$ ) | Longwave radiation ( $\text{W.m}^{-2}$ ) |
|------|---------------------------|-------------------------------------|-----------------------|--|--|
| Bias | -0.1                      | -0.2                                | -1.8                  | -39  | -20                                      |
| RMSE | 1.7                       | 1.42                                | 11.2                  | 155  | 36                                       |
| Corr | 0.97                      | 0.71                                | 0.86                  | 0.91   | 0.72                                     |

#### 4.4.2 Discharge

Runoff and baseflow are computed by the EROS semi-distributed model on 82 sub-catchments. These sub-catchments were drawn according to the position of gauging stations, whose data were used to calibrate the model. Piezometric levels were not used in the calibration because few data was available. The principle of the EROS model is summarised on Figure 4.4. Discharge computed for each sub-basin are then redistributed at the reach scale according to the ratio between the total length of the network upstream the reach and the total length of the network inside this basin. For main rivers that cross several basins, discharge of upstream basins are added.

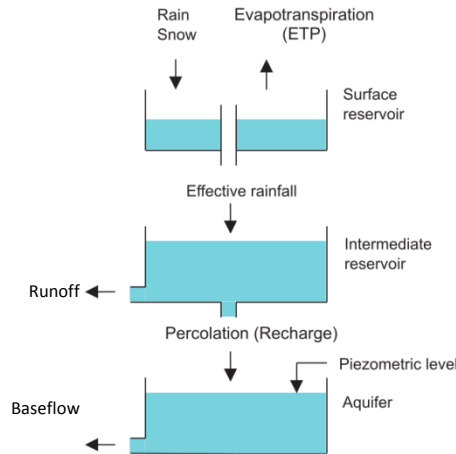


Figure 4.4: Principle of the EROS model (modified from Thiéry, 2005)

In order to characterise the goodness of modelling, the Nash–Sutcliffe coefficients (NSC) were computed for each sub-basin on available data between 08/1971 and 07/2015:

$$NSC = 1 - \frac{\sum_{t=1}^n (Q_{obs}^t - Q_{sim}^t)^2}{\sum_{t=1}^n (Q_{obs}^t - \overline{Q_{obs}})^2}$$

where obs denote observations, sim denotes simulation, t remind that Q depends on the day. Because the high flows have more impact than the low flows in the computation of the classical NSC, a similar index is computed using the natural logarithm of the discharges, which give more impact to the low flows:

$$NSC_{lowflow} = 1 - \frac{\sum_{t=1}^n (\ln(Q_{obs}^t) - \ln(Q_{sim}^t))^2}{\sum_{t=1}^n (\ln(Q_{obs}^t) - \overline{\ln(Q_{obs}^t)})^2}$$

The criterions are mapped on Figure 4.5. Two catchments have a NSC below 0.5. Mean discharges measured at the outlet of these basins are low (0.10 and 0.05 m<sup>3</sup>/s respectively). NSC at the Aigre River sub-basin is also low (0.51) with a higher mean observed discharge (1.47 m<sup>3</sup>/s). For these 3 catchments, modelled peak flows are much smaller than measures and the opposite happen for baseflows. These discrepancies may be explained by the high permeability in this region, as well as by the high water withdrawing operated for agriculture. Other basins have good NSC ranging from 0.71

to 0.95. Modelling accuracy is worst for low flows. Seven sub-basins have a  $NSC_{lowflow}$  below 0.5, 38 between 0.5 and 0.8 and 35 above 0.8, with a maximum of 0.92.

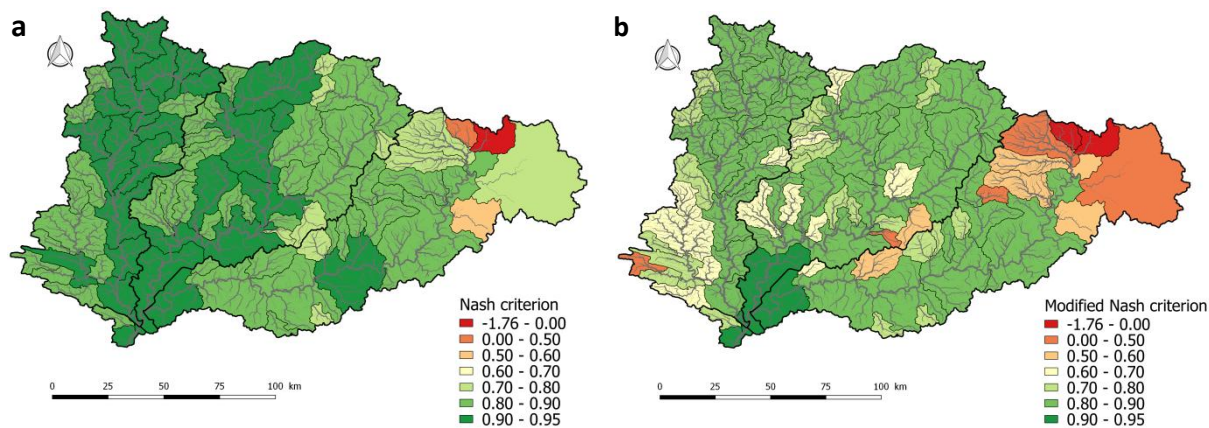


Figure 4.5: Nash-Sutcliffe coefficient computed on 1971-2015  
 (a) classic criterion (b) modified criterion focusing on low flows

The comparison of simulated and observed discharges for each season (Figure 4.6) shows that EROS usually overestimates discharges in summer (+51 % on average) and fall (+15%) and underestimates them in winter (-11%), except on the Conie River catchment, where mean discharge is overestimated the whole year. These overestimations may be due to the fact that water withdrawals are not taken into account in EROS.

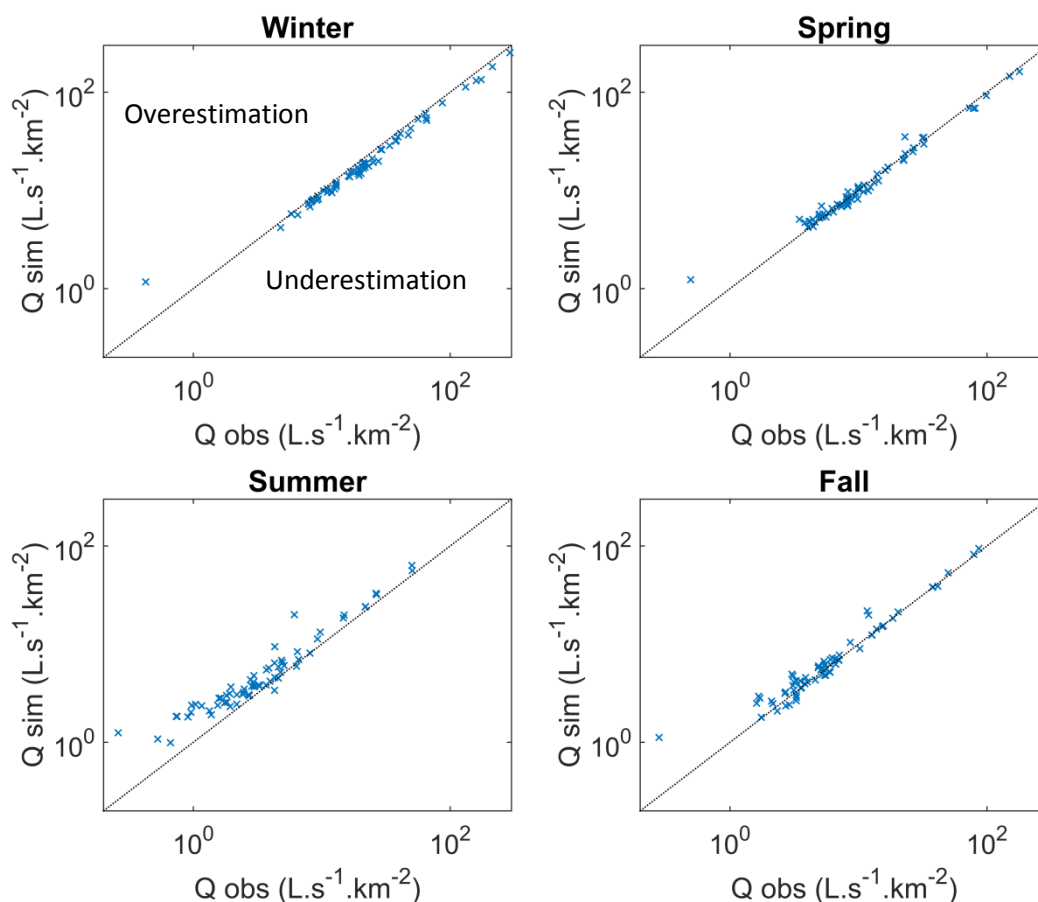


Figure 4.6: Simulated vs. observed discharges. Each cross is a sub-basin, averaged on the given season and on the 08/2008-07/2015 period.

Figure 4.7 shows how the biases on modelled discharges are reflected in the computations of wetted width, water depth, and water velocity (because the Estimkart equations rely on the discharge). The resulting errors on these parameters range from -10 % to +80% for wetted width, from -10% to +60% for river depth, and from -14% to +80% for water velocity, depending on the season. Width, depth and velocity are thus a bit underestimated in winter, while the opposite occurs in summer, in a larger extent. Geometry and velocity of the Conie is overestimated during the 4 seasons. The second outlier on the summer graph, with  $Q_{sim}/Q_{obs}$  at 3.2 is a small sub-basin crossed by the Loir River and located on the north-west of the Conie sub-basin.

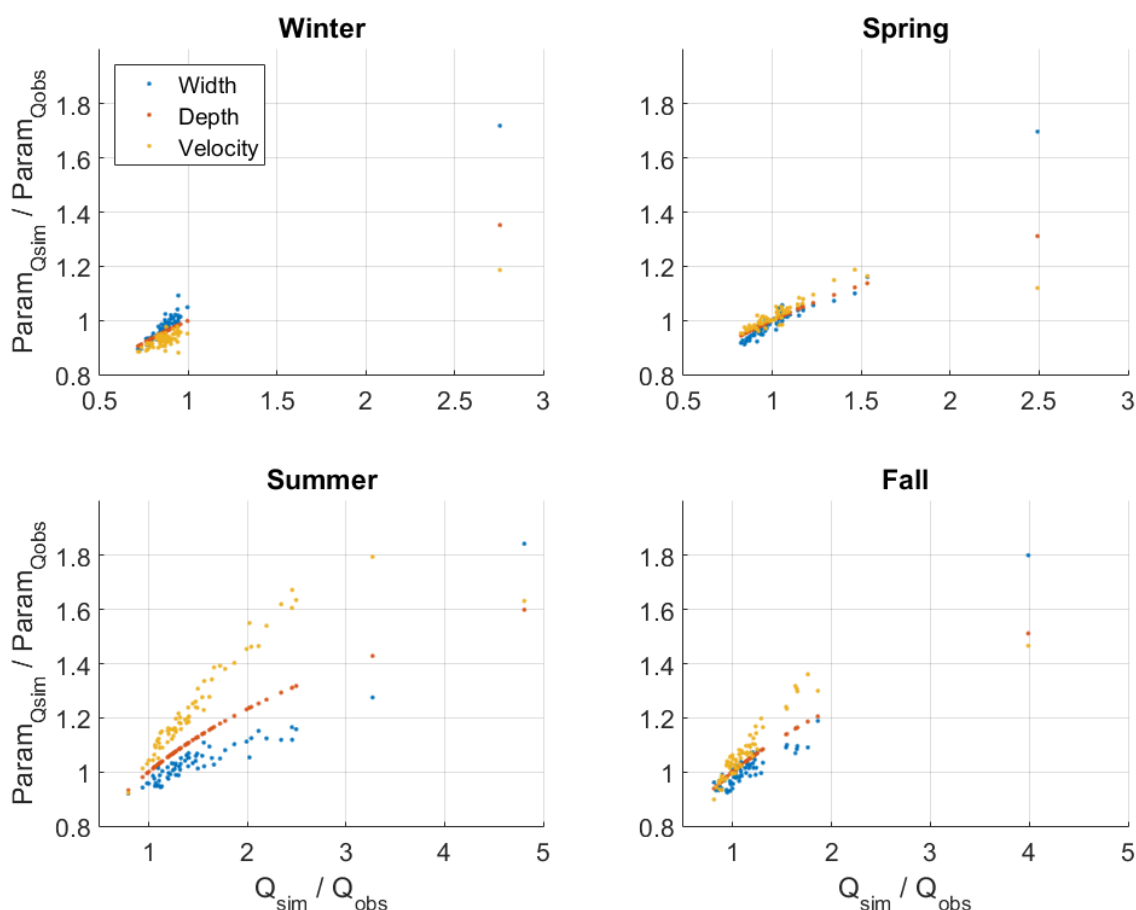


Figure 4.7: Errors on modelled hydraulic parameters computed from the Estimkart equations, as a function of biases of modelled discharge. Both X and Y scales are ratio, so that a value of 2 means that the value relying on simulated discharge is twice bigger than the value related to the observed discharge. Each point is a sub-basin, averaged on the given season and on the 08/2008-07/2015 period.

The average ratios between the runoff and the total (runoff + baseflow) river discharge are mapped in Figure 4.8. This variable was chosen instead of the formerly used  $Q_{min}/Q_{max}$  because it directly characterise the output of the model. Some large and strange differences between sub-basins are observed. High ratios (>0.8) are observed in the west part of the basin even though they are not really expected there (Armorican massif without geological fault; see Figure 2.2).

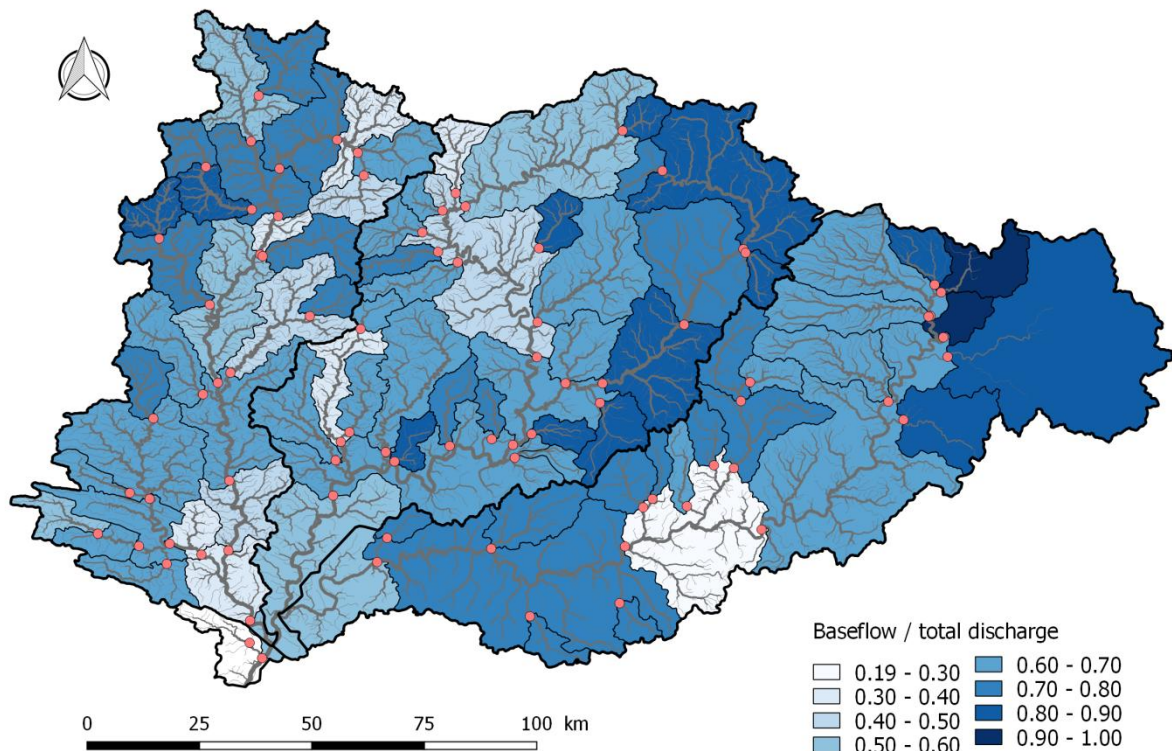


Figure 4.8: Ratio between the baseflow and the total flow modelled on each sub-basin by EROS (08/2008-07/2015 average)

#### 4.4.3 River network, topography and vegetation cover

The river network used by T-NET originally comes from BD CARTHAGE. It was cleaned to get a tree-shaped network without multiple river branches. On the Maine catchment, there are 9998 reaches with a median length of 1.36 km. Table 4.1 shows the distribution of the reach lengths. Some reach lengths are comprised between 10 and 18 km, although there are not visible on the figure.

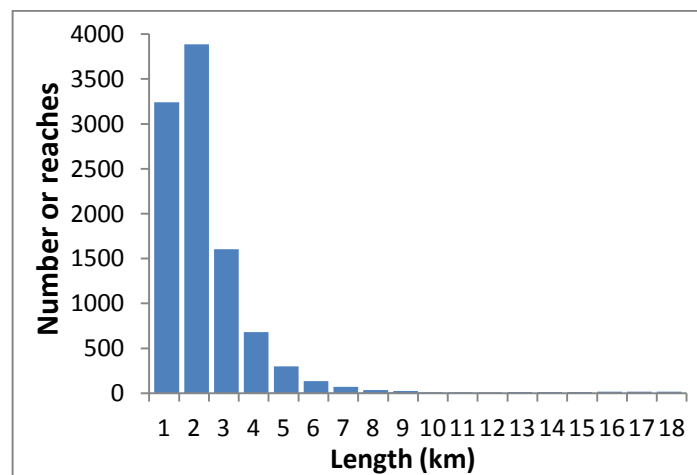


Figure 4.9: Histogram of the reach lengths on the Maine basin

Slopes of reaches, used to compute the width and depth, were computed by taking altitudes at the initial and end nodes of the GIS lines. Altitude comes from a 25 m resolution digital elevation model provided by Institut Géographique National. Riparian vegetation was taken from Valette et al. (2012) dataset, which corresponds to the percentage of vegetation polygons located in a buffer of 10 m around the river reaches (see section 2.4).

## 4.5 Results with the standard version

### 4.5.1 Mean accuracy on the 44 stations

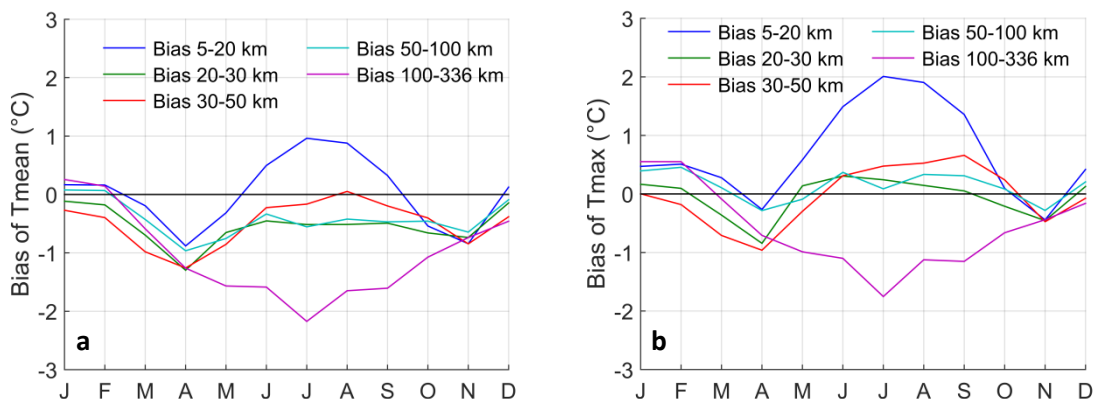
The bias ( $T_{sim}-T_{obs}$ ), standard deviation of errors (SDE) and RMSE of daily maximum, mean and minimum Tw (“Tmax”, “Tmean”, “Tmin”) were computed on the whole time series of available observed data between 08/2008 and 07/2015. Averaged on the 44 stations, the mean bias on Tmean is  $-0.54\text{ }^{\circ}\text{C}$ , the SDE is  $1.6\text{ }^{\circ}\text{C}$  and the RMSE is  $1.84\text{ }^{\circ}\text{C}$ . Bias of Tmax is close to zero, while bias of Tmin is worse than bias of Tmean (Table 4.3). Mean standard deviation of errors (SDE) is the highest for Tmax. Modelled diel amplitudes are on average  $1.1\text{ }^{\circ}\text{C}$  higher than observations.

**Table 4.3: Bias ( $T_{sim}-T_{obs}$ ), standard deviation of errors and root mean square error ( $^{\circ}\text{C}$ ) computed on maximum, mean and minimum daily Tw and diel amplitude**

|       | Bias ( $^{\circ}\text{C}$ ) | SDE ( $^{\circ}\text{C}$ ) | RMSE ( $^{\circ}\text{C}$ ) |
|-------|-----------------------------|----------------------------|-----------------------------|
| Tmin  | -1.09                       | 1.62                       | 2.03                        |
| Tmean | -0.54                       | 1.60                       | 1.84                        |
| Tmax  | 0.01                        | 1.80                       | 2.05                        |
| Ampli | 1.10                        | 1.16                       | 1.65                        |

### 4.5.2 Annual cycle of the bias

The biases of Tmean, Tmax and Tmin vary throughout the year, especially for the closest or furthest stations to sources (Figure 4.10 a, b, c). In winter, all biases are properly contained between  $-1$  and  $1\text{ }^{\circ}\text{C}$ . They become more negative in spring and autumn for all stations. In summer, biases of Tmean become more positive for stations close to sources, while they become more negative for stations far from source. Because modelled diel amplitudes are too high in summer (Figure 4.10 d), it is not surprising that Tmax biases are higher and Tmin biases are lower than Tmean biases. Little pattern is observed in the SDE of Tmean, both in temporal and spatial scales.



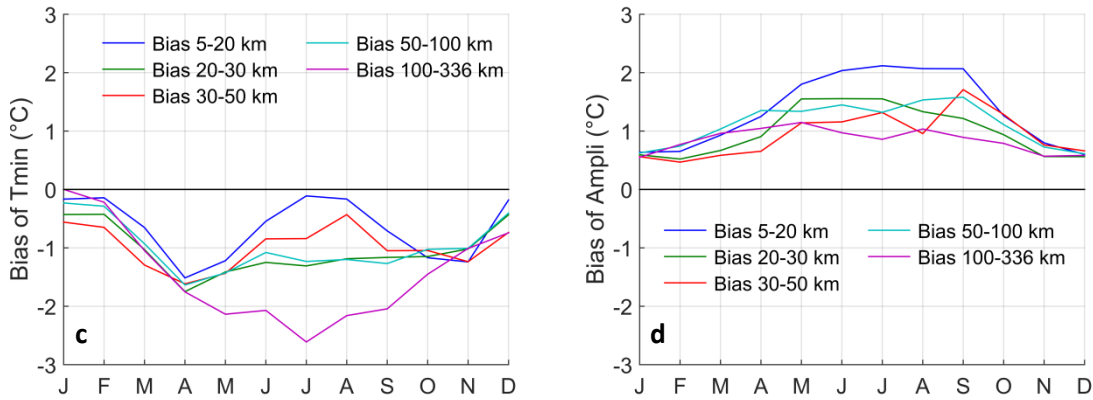


Figure 4.10: Temporal evolution of bias on the 44 stations, averaged by classes of distance from source (2008-2015 average). Classes of increasing distance from source have 7, 13, 5, 11 and 8 stations respectively. (a) Tmean (b) Tmax (c) Tmin (d) diel amplitudes

The T-NET underestimation is actually more important on the Loir River than on the other rivers, especially in summer (Figure 4.11).

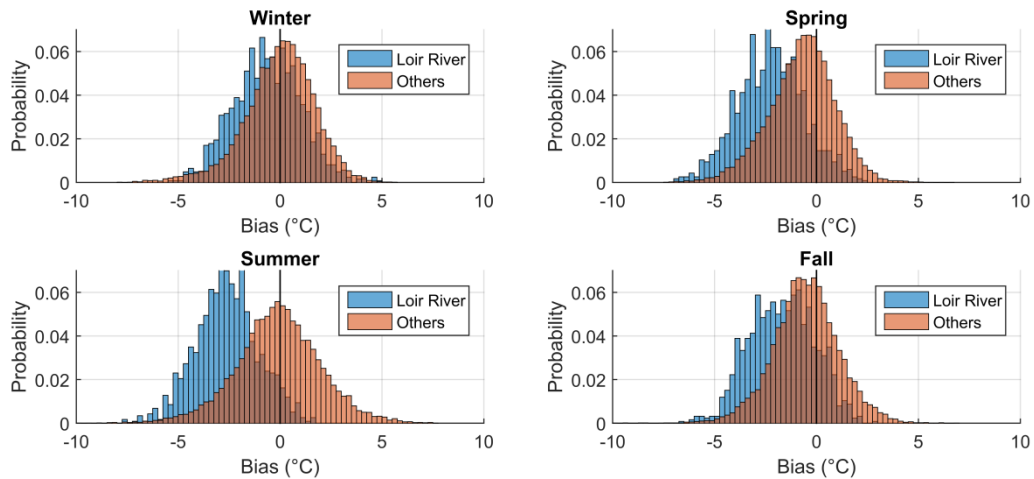


Figure 4.11: Histogram of biases computed on available observed mean daily temperature on the 2008-2015 period, displayed for each season and discriminated for the Loir River and the other rivers.

### 4.5.3 Accuracy in summer

The most underestimated stations in summer are actually on the Loir, Conie, Aigre, Maine, and Oudon (Figure 4.12).

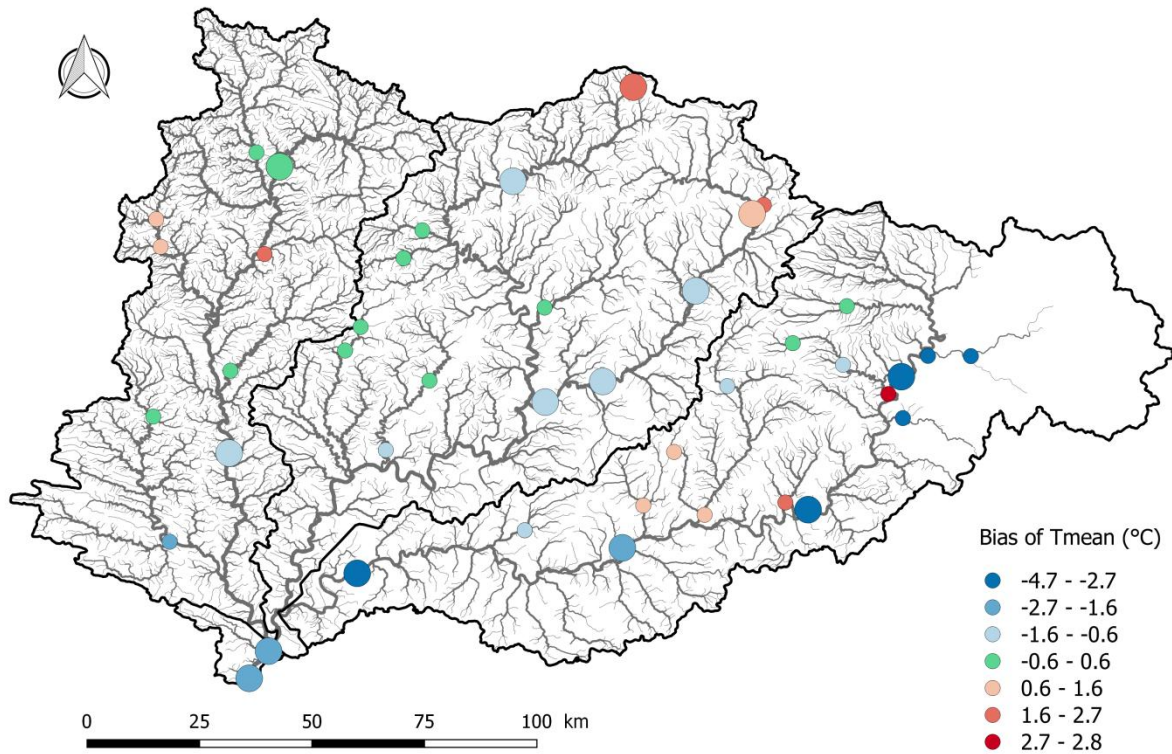


Figure 4.12: Bias of mean daily temperature on July-August of the 2008-2015 period

The biases of Tmean in summer are negatively correlated ( $p$ -value =  $6.49E-4$ ) to  $Q_{\min}/Q_{\max}$ , the ratio between the minimum monthly mean discharge and the maximum monthly mean discharge, taken from a mean interannual cycle (08/2008-07/2015) as simulated by the EROS model, and used as a proxy of groundwater fluxes. Tmean biases are also correlated to the thermal sensitivity (TS, the slope of the linear regression of weekly water temperature against weekly air temperature) (Figure 4.13a,  $p$ -value =  $4.83E-6$ ). Stations with low TS (i.e. with high groundwater fluxes or located near the sources) have modelled Tmean that is too warm, and conversely. Ten stations have a bias comprised between -1 and +1 °C. The positive biases may thus be explained by groundwater fluxes that are too low or by a groundwater temperature that is too high. The negative biases cannot totally be explained by too high groundwater fluxes, since a simulation with no groundwater fluxes still provides 12 stations with bias below -1 (vs. 16 stations in the standard configuration; Figure 4.13 b).

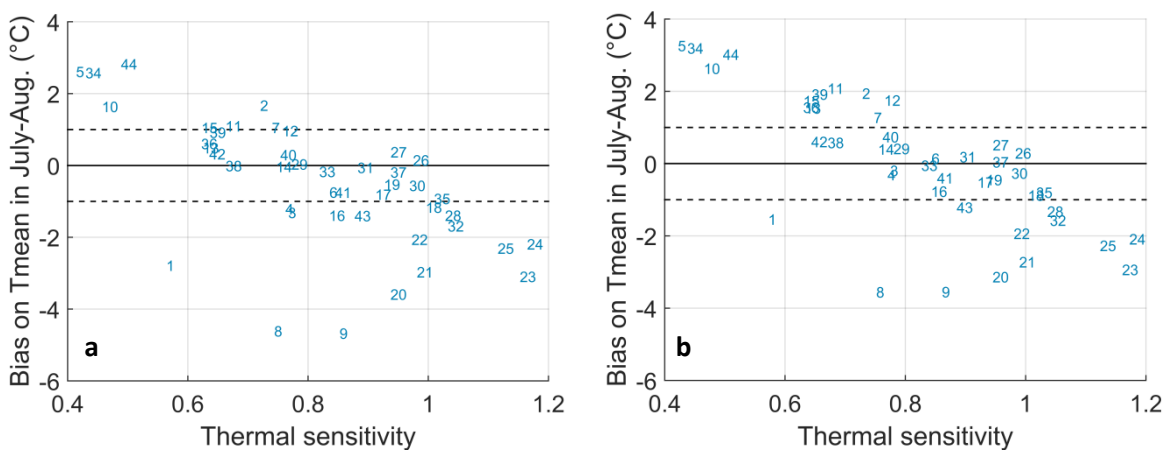


Figure 4.13: Bias (Tsim-Tobs) of mean daily temperature in July-August as a function of thermal sensitivity (2008-2015 average) (a) standard configuration (b) with no groundwater fluxes. Stations numbers are in appendix B.

As an example, annual cycles of modelled and observed Tmean are shown at Figure 4.14 for stations with the highest (Yerre 47), close to zero (Merdereau 21), and lowest (Conie 40) bias in July-August. Simulated mean daily temperatures are compared to observations for all stations and years in appendix G.

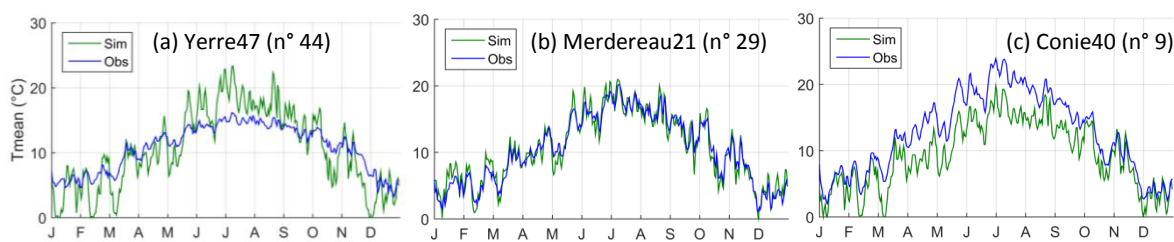


Figure 4.14: Simulated and observed mean daily temperature in 2010 (a) Yerre 47 (b) Merdereau 21 (c) Conie 40

The simulated longitudinal profiles of Tmean of the 4 main rivers averaged on the 13-31/08/2009 period are shown at Figure 4.15. This period contains the highest number of stations with concurrent observation on the 4 main rivers. Discharges are low on the Maine at this period (between 22 and 16 m<sup>3</sup>.s<sup>-1</sup>, while the mean yearly long-term discharge is 127 m<sup>3</sup>.s<sup>-1</sup>). Averaged on the Maine basin, mean Ta is 19.4 °C while mean maximum Ta is 25.3 °C (SAFRAN).

Figure 4.15 shows a fast Tw increasing trend in the upstream part of the 4 rivers, due to the evolution from the source (groundwater) temperature to the equilibrium temperature. The cooling impacts of many tributaries are seen. Decreases modelled on the Sarthe around river km 50, 70 and 85 are due to variations in vegetation cover. There are large differences between rivers that can reach up to 2.5 °C. In the downstream part, the Loir River is the coldest simulated while observations are relatively warm. The higher vegetation cover on the Loir may explain these low modelled Tw (Figure 2.4). Moreover, the Loir and Huisne rivers are Strahler order 5 on most of their courses; Mayenne is order 6 and Huisne becomes order 6 at river km 155. Since the simple shading characterisation used in the standard version of T-NET relies on the Strahler order (k=0.6 for order 5 and k=0.8 for order 6 in (Eq. 4.1), this may partly explain the differences of modelled Tw between rivers.

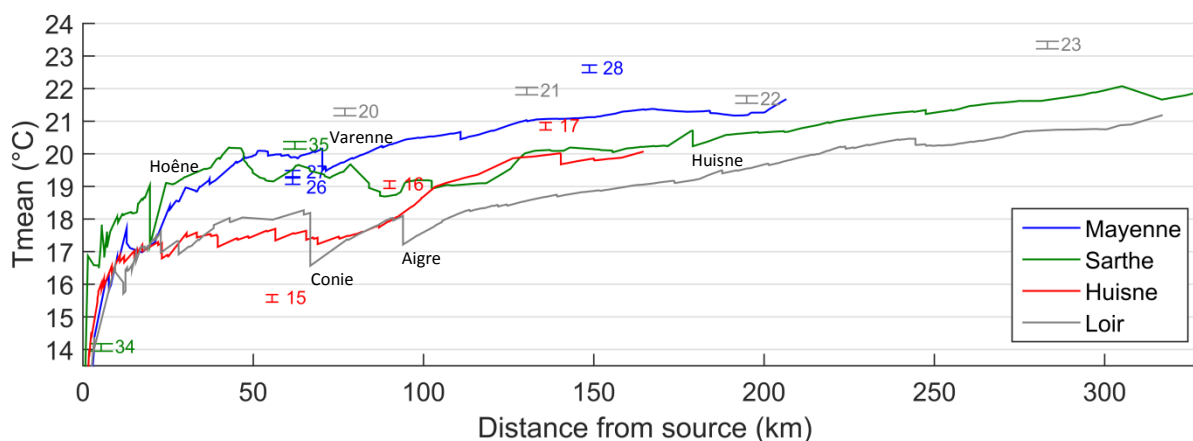


Figure 4.15: Longitudinal profile of simulated daily mean temperature on the 4 main rivers of the Maine catchment, averaged on the 13-31/08/2009 period

In July-august, biases of the diel amplitude are mainly positive, with only 8 stations between -1 and +1 °C and one station at -2.3 °C (Conie 27). The relationship is not significant with distance from source or thermal sensitivity but with  $Q_{min}/Q_{max}$  (p-value = 2.18E-6), although the relationship is pulled by 5 stations: Oudon 27 (n° 31) and Oudon 85 (n° 32) in the minimal values, and Aigre 25 (n° 1), Conie 27

(n° 8), and Conie 40 (n° 9) for the maximal values (Figure 4.16). This suggests that groundwater fluxes may be too low for most of the stations. More generally, thermal inertia (water depth) may also be too low.

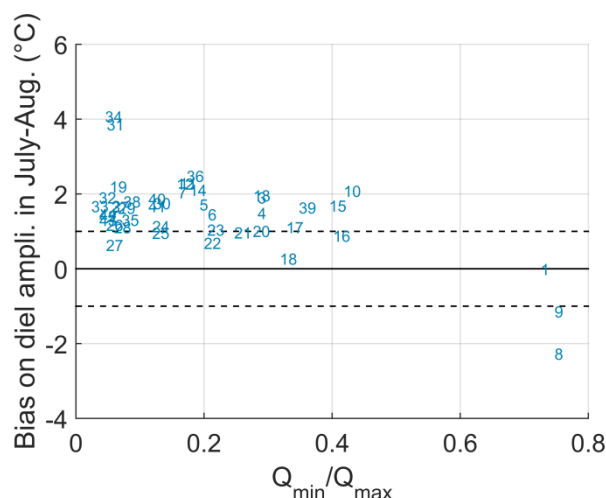


Figure 4.16: Bias of diel amplitudes ( $Ampli_{sim} - Ampli_{obs}$ ) as a function of the  $Q_{min}/Q_{max}$  ratio (2008-2015 average). Stations numbers are in appendix B.

As an example, modelled and observed hourly temperatures in August 2011 are shown at Figure 4.17 for stations with the highest (Sarthe 5), closest to zero (Aigre 25), and lowest (Conie 27) diel amplitude bias in July-August.

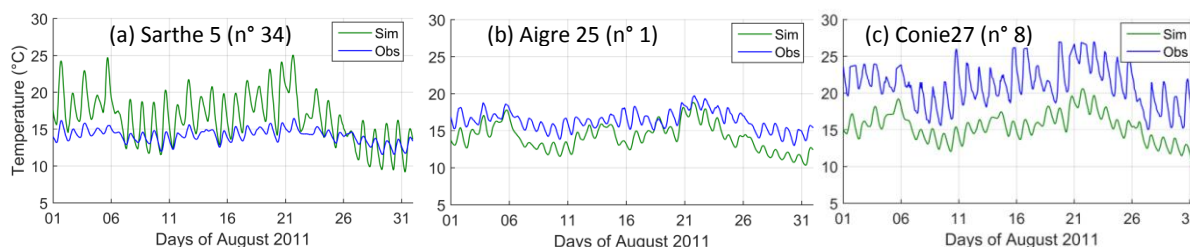


Figure 4.17: Simulated and observed  $T_w$  in 2011 (a) Sarthe 5 (b) Aigre 25 (c) Conie 27

In comparison with results shown in Beaufort et al. (2016) for the whole Loire catchment, results obtained on the Maine catchment with validation data currently available are more negatively biased. RMSE are below 2 °C for 73% of stations (81% in Beaufort et al., 2016).

#### 4.5.4 Comparison with the statistical model in August 2009

The spatial distribution of the  $T_{mean}$  simulated by T-NET on the 13-31/08/2009 period is shown on Figure 4.18. The map shows the increase of temperature in the downstream direction. The first orders are colder in the Mayenne catchment, according to the spatial distribution of air temperature (see Figure 2.6). In the downstream part, there are more warm tributaries in the Mayenne basin than in the Loir, which may be explained by the denser river network.

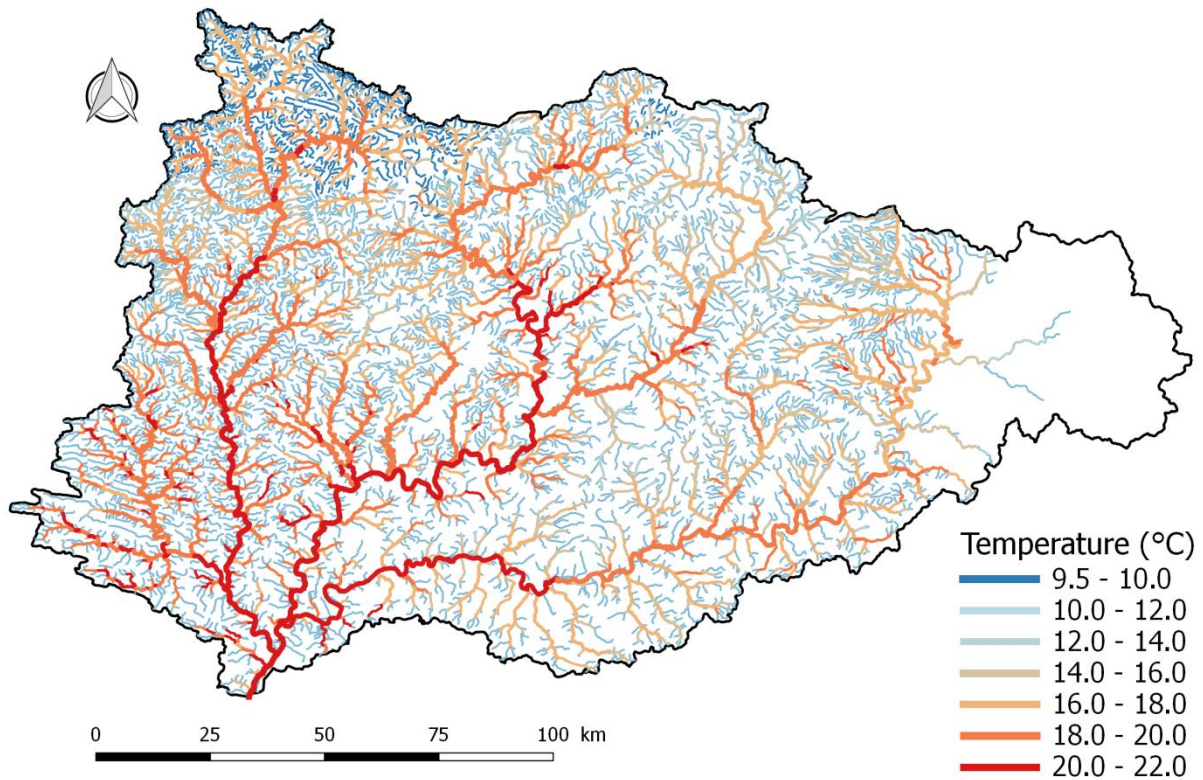


Figure 4.18: Mean temperature simulated with T-NET on the 13-31/08/2009 period

The range of  $T_w$  is smaller than the one obtained with the statistical model (see Figure 3.19). However, on the first orders,  $T_{w-T-NET}$  is often colder than  $T_{w-stat}$ , as shown by Figure 4.19 and summarised at Figure 4.20.  $T_w$  injected at the sources in T-NET are assumptions, and no station localised on a first Strahler order was used to fit the statistical model, so that accuracy of both models is unknown at the 1<sup>st</sup> Strahler order. On Strahler orders higher than 1, the differences  $T_{w-T-NET} - T_{w-stat}$  follow the pattern described at Figure 4.13, given that the statistical modelled is less biased. Figure 4.19 shows a clear East-West gradient in the difference between both models that is likely to follow the global gradient of the T-NET biases observed at Figure 4.12. On weekly averages, the mean RMSE computed with T-NET on the stations used to validate the empirical model is 2.02 °C, to be compared to 1.35 °C obtained with the empirical model. This is not surprising, since the mean bias of the empirical model is lower.

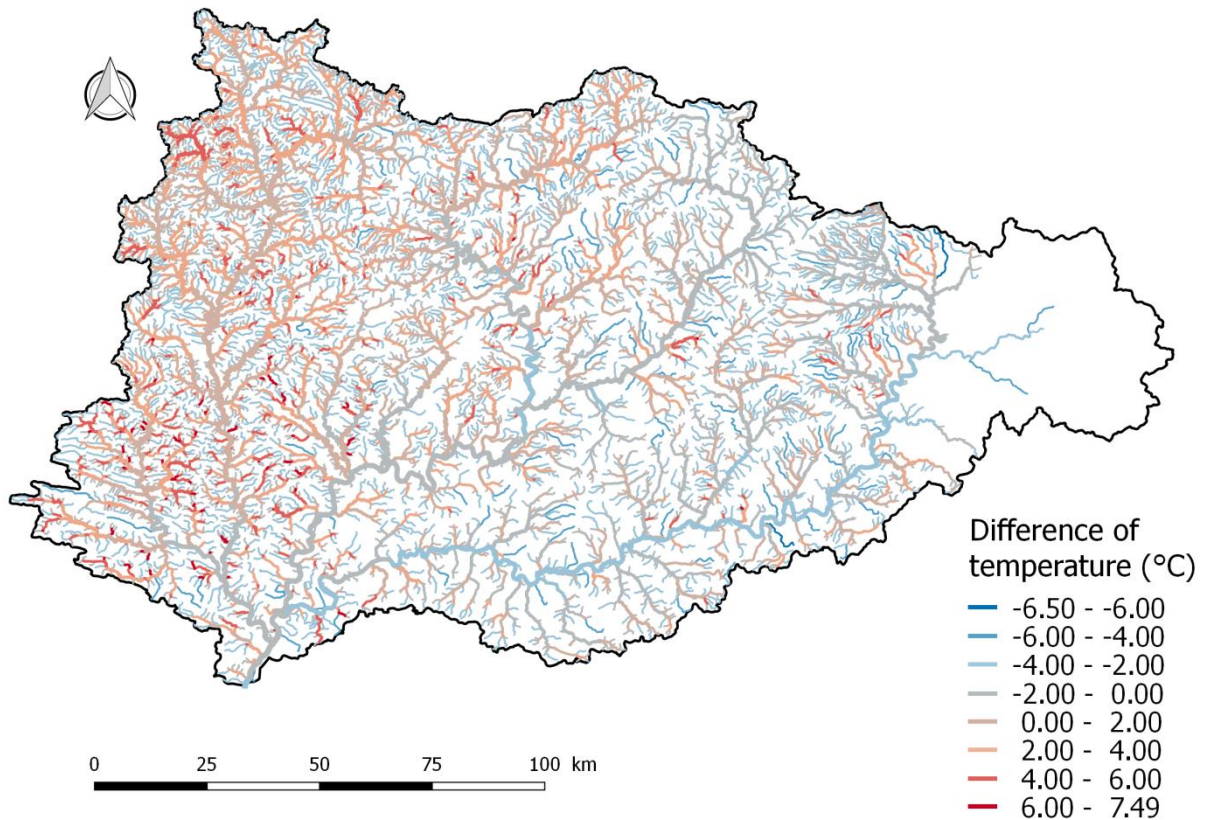


Figure 4.19: Map of the difference  $T_{w-T-NET} - T_{w-statistical\ model}$  (average on the 13-31/08/2009 period)

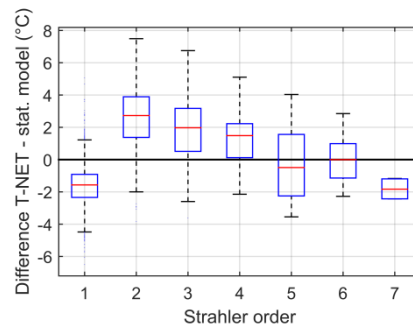


Figure 4.20: Difference  $T_{w-T-NET} - T_{w-statistical\ model}$  (average on the 13-31/08/2009 period).  
Boxplots over the 9998 reaches of the Maine catchment.

#### 4.6 Sensitivity analysis with the standard version

The sensitivity analyses achieved in this section involves the modification of the hydraulic geometry parameters. In T-NET, these parameters are computed at the daily time step and written in the hydrology files. Water depth and velocity used in (Eq. 4.7) are then directly taken from these files during the  $T_w$  computations, which are achieved at the hourly time step. On the other hand, travel times of each reaches are rounded to the closest integer values (in hour, with a minimum of 1 hour), because the model must synchronise the spatial steps to the hourly time step. The differences between the travel times computed in the hydrology files and the rounded travel times are illustrated at Figure 4.21 a. Averaged on the whole Loir river, the difference can reach up to 200% of the travel time when it is low, i.e. when discharge is high in winter. In summer, when discharge is low, the difference equates approximately 5%. These discrepancies are thus non-linear and decrease when water velocity is decreased, and inversely. Hence, if the travel time is doubled, the discrepancies decrease (Figure 4.21 b). In the next sensitivity analyses, all hydraulic parameters were re-computed

according to the rounded travel times, in order to discard the potential impacts of using both rounded and non-rounded parameters in the same computation.

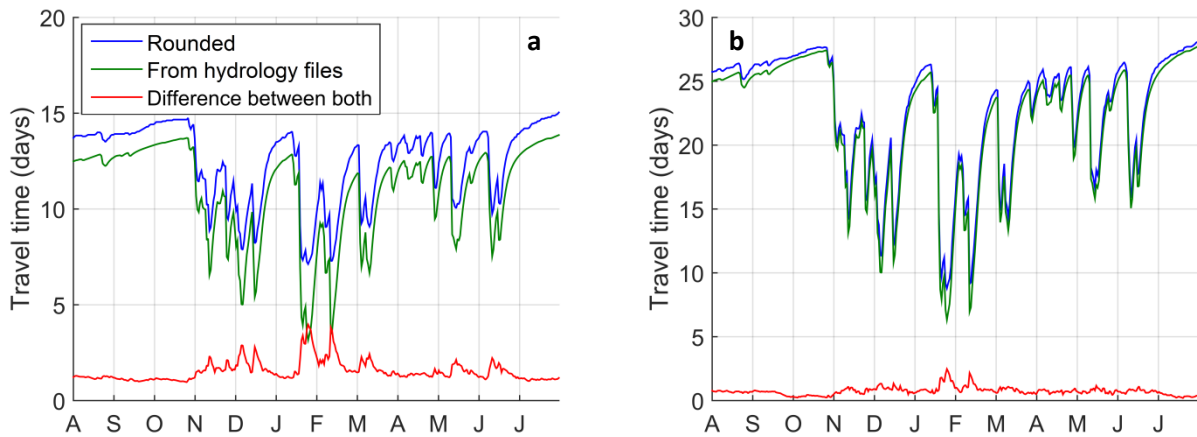


Figure 4.21: Time to travel the whole Loir River (317 km) on the 09-10 hydrological year (a) the standard configuration of T-NET (b) with doubled travel time

#### 4.6.1 Water velocity (isolated)

Water velocity is computed with (Eq. 4.9 ( $U = Q / A_s$ )).  $A_s$  is determined by the Estimkart empirical equations, which include the discharge and the slope as parameters (see section 4.3.3). Although the slope is higher in the upstream part of the catchment (Figure 4.22), water velocities increase in the downstream direction (Figure 4.23a), with substantial differences among rivers. On the 13-31 August 2009 period, the Huisne is the fastest to flow, and the Sarthe the slowest. Although we have no measure of water velocity or travel time for this exact period, these modelled velocities seem quite high. The corresponding travel times are shown on Figure 4.23 b.

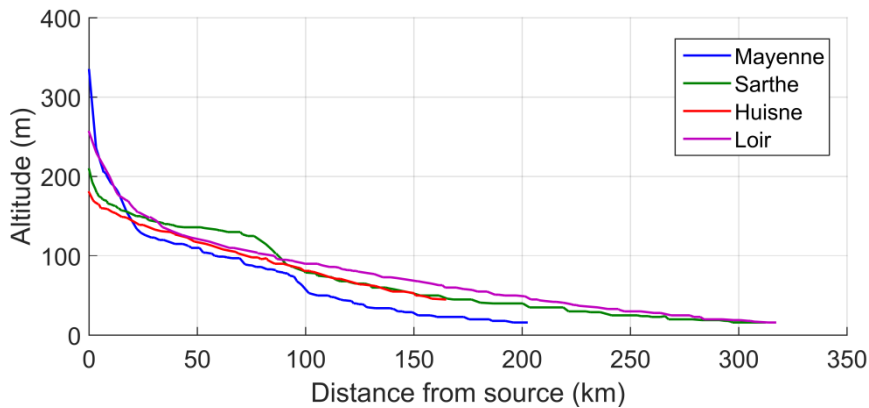


Figure 4.22: Longitudinal profile of altitudes for the four main rivers of the Maine catchment

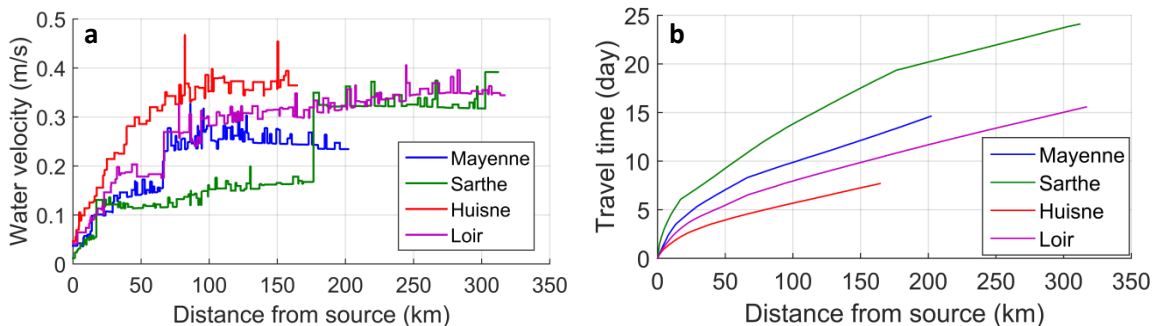
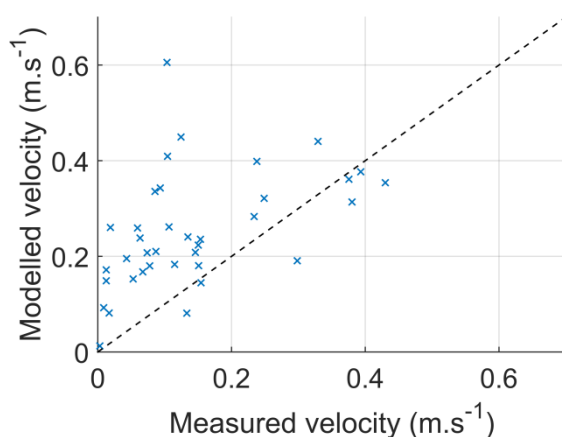


Figure 4.23: (a) water velocity and (b) travel time for the 4 main rivers of the Maine catchment, averaged between the 13 and the 31 August 2009

The water velocities modelled on the Maine catchment can be compared with 42 values obtained thanks to field measurements of hydraulic geometry and discharge achieved as part of the Carhyce framework (Gob et al., 2014). They were measured at 40 stations located on 32 different streams of the Maine catchment between 2009 and 2014, mostly in low discharge conditions. These measures correspond to averages of 15 cross-sectional measurements spanning on 15x the measured bankfull width. Depth is measured 7x on each cross-section. On Figure 4.24, these observations are compared to the corresponding modelled velocities, which are averaged at the reach scale, so that we must be careful in the comparison. Based on the hypothesis that Carhyce measurements were achieved on representative reaches, Figure 4.24 shows that modelled velocities are likely more often overestimated than underestimated.



**Figure 4.24: Water velocities computed from 42 Carhyce field measurements compared to the corresponding reach-averaged modelled velocities. Measurements were achieved on 40 stations located on 32 different streams of the Maine catchment between 2009 and 2014.**

The reduction of water velocity by a factor 2, without modification of depth, width and discharge tend to cool  $T_{mean}$  in winter and to warm it in summer (Figure 4.25 a continuous lines). This is expected for stations located close to source, since slower velocity implies longer time of equilibration with air temperature, hence decreasing the buffering influence of groundwater temperature given at the source. Also, as long as there is an upstream-downstream temperature gradient, which is usually present in summer, it is expected that this gradient is increased with lower velocity, and conversely. This can explain the influence of this analysis on the stations located far from sources. In winter, the impact is more important on stations close to source, as expected. In summer, the relationship with the distance from source is less evident clear. SDE of  $T_{mean}$  are not modified by more than 0.1°C. Impact on  $T_{max}$  and  $T_{min}$  is similar. Diel amplitudes are not modified by more than 0.2 °C. Diel amplitude are not modified significantly (Figure 4.25 b).

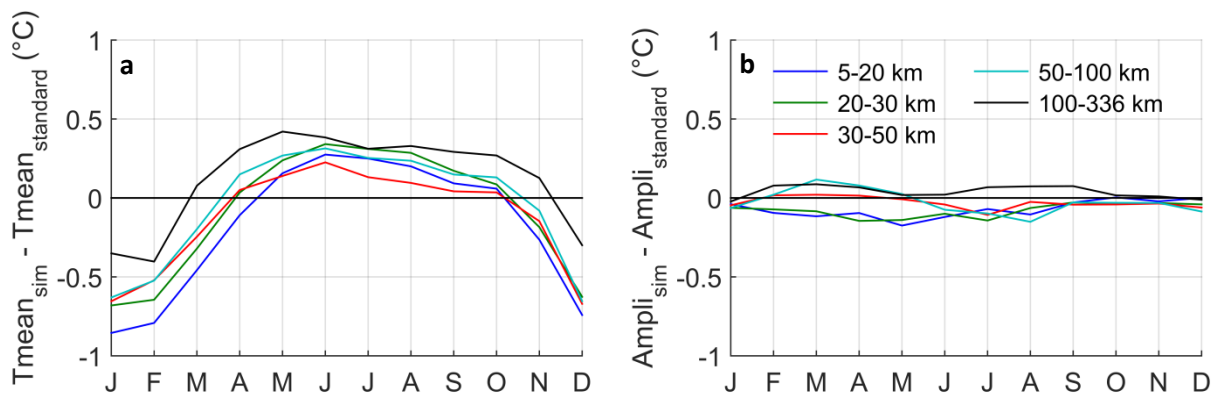


Figure 4.25: Difference of biases between a simulation where water is 2x slower and the standard simulation  
 (a) mean daily temperature (b) diel amplitude

### 4.6.2 Wetted width

The wetted widths modelled on the 4 main rivers on the 13-31/08/2009 period are shown on Figure 4.26. As expected, they are increasing in the downstream direction, since they are mainly related to the discharge. Influence of tributaries are seen (Varenne, Husine, Loir).

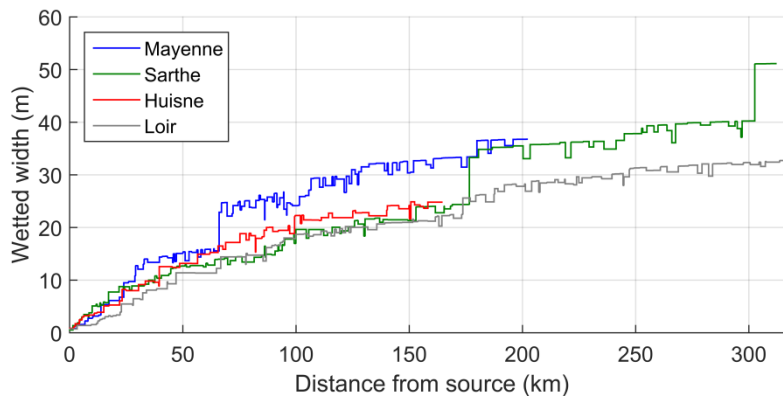


Figure 4.26: Longitudinal profile of wetted width on the 4 main rivers, averaged on the 13-31/08/2009 period

Analysis of Carhyce data show a good fit for widths smaller than 20 m. Above this value, there is a likelihood of underestimation, although the number of measurements is too small to confirm it.

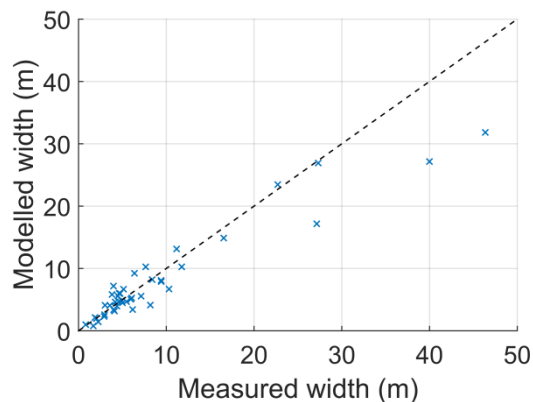


Figure 4.27: Wetted widths measured during 42 Carhyce field measurements compared to the corresponding reach-averaged modelled widths.

The impact of doubling the wetted widths is similar to the effect of doubling the travel times (section 4.6.1), although it is a bit more important on the Tmean (Figure 4.28). This can be explain because, in this version of the model, the width only influences the wetted cross-section used in the computation

of the water velocity, as well as the exchange area for the computation of groundwater fluxes. However, the latter term has a minor impact.

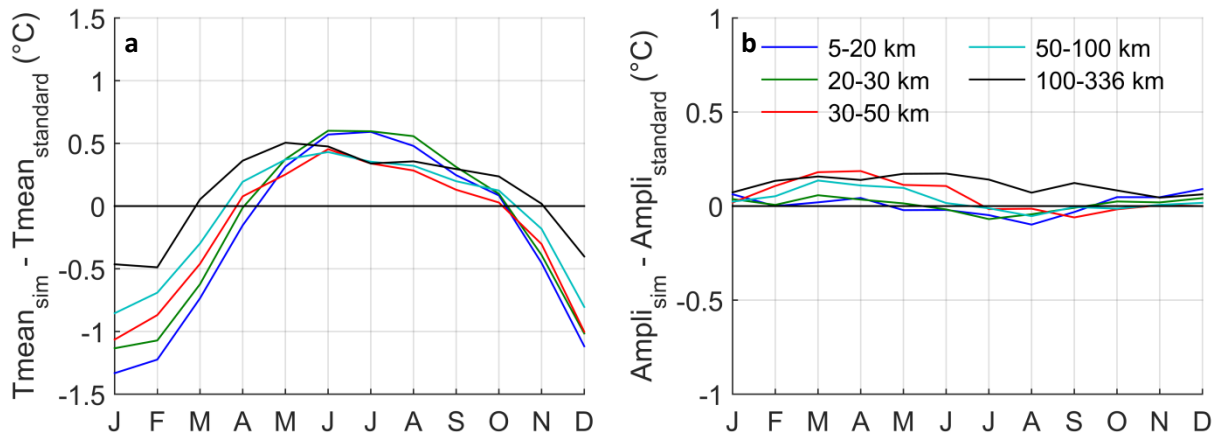


Figure 4.28: Difference of biases between a simulation with doubled wetted widths and the standard simulation (a) mean daily temperature (b) diel amplitude

### 4.6.3 Depth

The Figure 4.29 shows the mean water depths as modelled by the Estimkart empirical equations on the four main rivers and on the 13-31/08/2009 period. The maximum depth is 1 m.

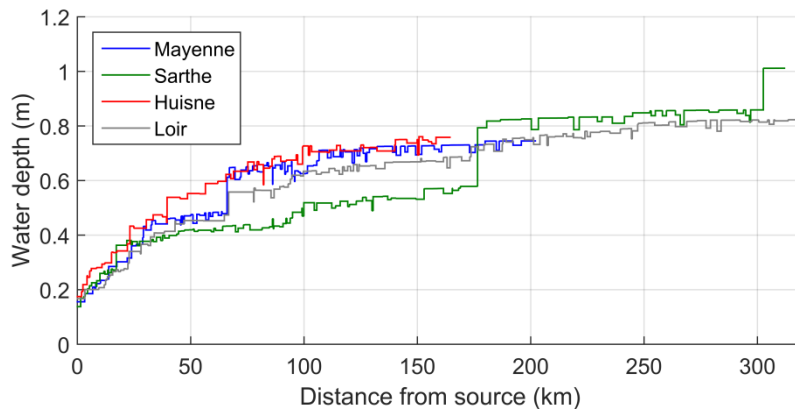


Figure 4.29: Longitudinal profile of water depth on the 4 main rivers on the 13-31/08/2009 period

There are several reasons to think that water depth as modelled by the Estimkart empirical equation are underestimated in T-NET. The first is the comparison of modelled reach-averaged values with Carhyce observations. Figure 4.30 shows that modelled depths are all underestimated when depth is higher than 50 cm.

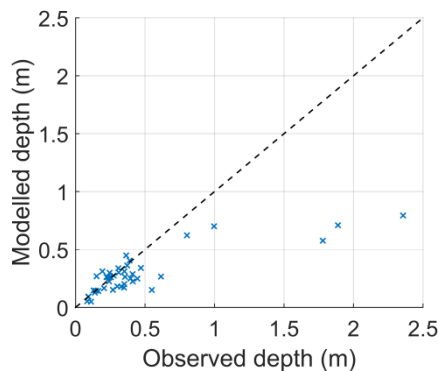


Figure 4.30: Water depths measured during 42 Carhyce field measurements compared to the corresponding reach-averaged modelled depth.

The second reason is the comparison with results of a hydraulic model applied on the Loir River, discussed at section **Erreur ! Source du renvoi introuvable.**

The resulting biases of  $T_{mean}$  are not changed a lot, with maximal differences between  $\pm 0.1$  °C when averaged by stations and going up to  $\pm 0.3$  °C for some months and stations (not shown). Mathematically, this can be explained because the doubling of depth implies that water velocity is divided by 2, which leads to a mathematical cancellation in (Eq. 4.7). Hence, the modification of the depth and thus the travel time only impacts the  $\Delta x$  term. The standard deviation of errors is decreased, especially at the downstream-most stations (Figure 4.31 a, continuous lines). It means that the amplitudes of the mean daily thermal signal are decreased and hence closer to reality. The diel amplitudes are significantly decreased, on a proportionate basis. The absolute impact (in °C) is thus more important when and where the diel amplitudes are basically high, i.e. in summer and where thermal inertia is low. Diel amplitudes are hence improved (Figure 4.31 b) for all stations, except for Aigre 25, Conie 27 and Conie 40, which already had biases close to or below zero in the standard configuration (Figure 4.32). Discharge of the two Conie stations is overestimated by 380% so that depth may be accurate in the standard simulation.

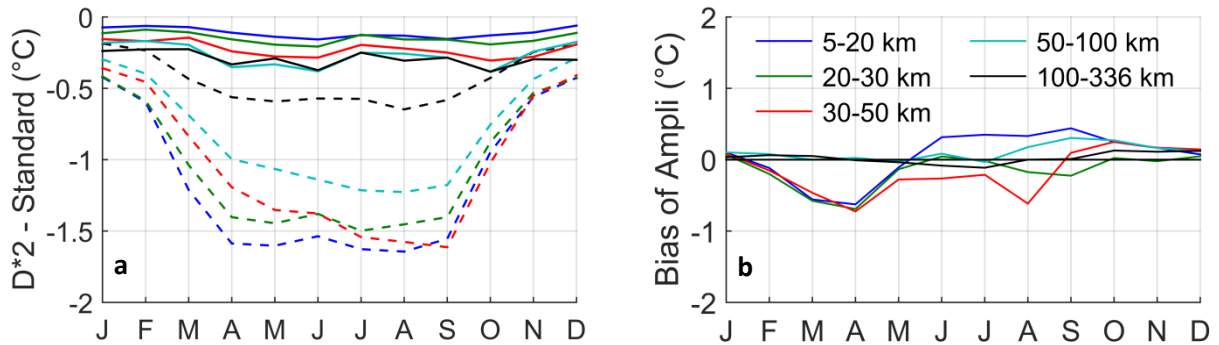


Figure 4.31: Impact of doubling the water depth. (a) Difference with the standard simulation. SDE of mean daily temperature (continuous) and bias of diel amplitude (dashed) (b) Bias of diel amplitude with  $D*2$

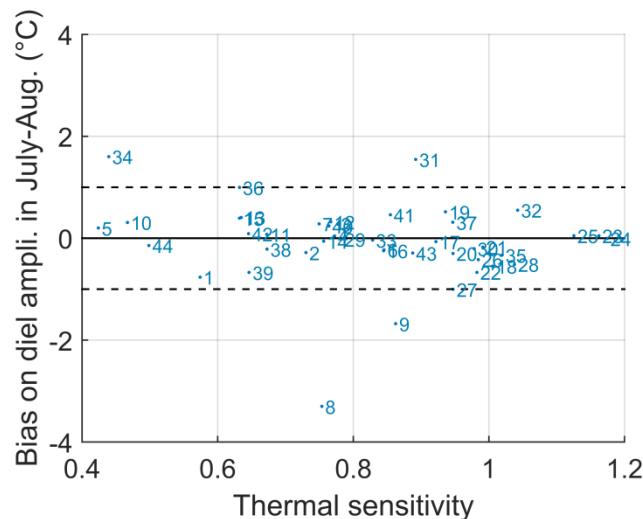


Figure 4.32: Bias of the diel amplitudes in July-August as a function of thermal sensitivity (2008-2015 average) with doubled river depth

#### 4.6.4 Discharge

As discussed in section 4.4.2, modelled discharge are mainly underestimated in winter and overestimated in summer. On the 13-31 August 2009 period, discharge of the 82 sub-catchments is overestimated by 70% on average.

When input discharges are divided by 2, wetted width, water depth, and hence cross-sectional area are also reduced by approximately 28%, 17% and 40% respectively (computed on the 13-31 August 2009 period), so that water velocity is decreased by 16%. The impact on the annual cycle of Tmean is similar to the results obtained when water is slowed (Figure 4.33a continuous line). SDE of Tmean are decreased by 0.1 °C on average. Diel amplitudes are increased (Figure 4.33b) and hence worsen by 0.24 °C on average, because of the decrease of thermal inertia (water depth). The impact of a discharge doubling is symmetrically inversed.

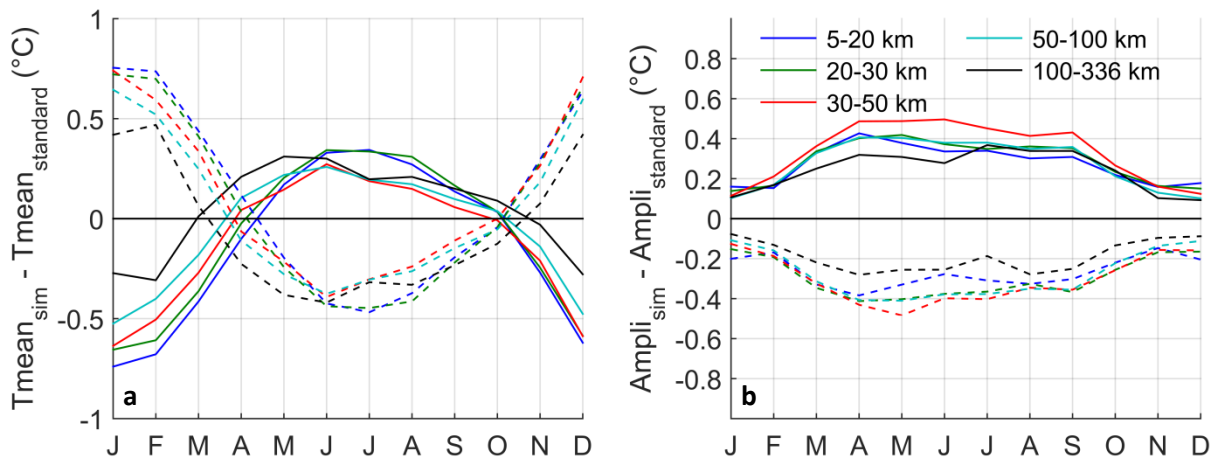


Figure 4.33: Difference of biases between a simulation where discharge is 2x smaller (continuous)/2x larger (dashed) and the standard simulation (a) mean daily temperature (b) diel amplitude

Figure 4.34 shows the impact on Tmean and diel amplitudes when discharge is doubled, for the station with the highest impact on diel amplitudes in summer (Aron 34).

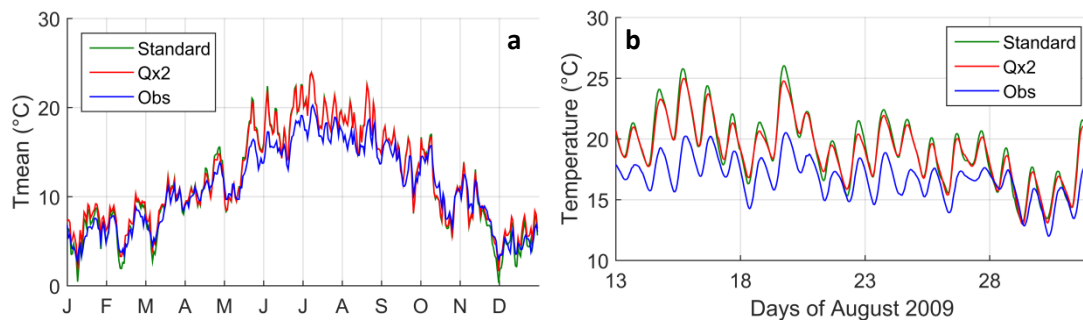


Figure 4.34: Water temperature at Aron 34 (a) daily means on 2010 (b) hourly values between 13 and 31 August 2009

#### 4.6.5 Groundwater temperature

In the standard version of the model, the headwater temperature is computed as the moving average of the air temperature on the past 365 days. This relation was shown by Karanth (1987) and Todd (1980). Beaufort (2015) showed that an averaged on 365 days provided the best results in comparison with averages on 90 and 180 days. Some authors add 1 °C to this value. For this reason, we want to analyse the impact of the groundwater temperature, which is used both as the headwater temperature and as the temperature of groundwater fluxes. As expected, the impact is the most

important on the stations located close to the sources (Figure 4.35), as well as in winter, because of the faster travel time. The travel time effect is thus more important than the fact that the baseflow/total flow ratio is higher in summer.

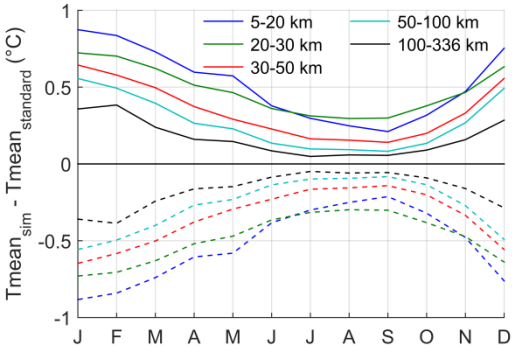


Figure 4.35: Difference of biases between a simulation where  $T_g = T_g + 2\text{ °C}$  (continuous)/  $T_g = T_g - 2\text{ °C}$  (dashed) and the standard simulation

When groundwater temperature is decreased by 2 °C, 5 stations keep a summer bias of Tmean above 1 °C (8 stations in the standard simulation). However, it also worsens stations with negative biases (Figure 4.36).

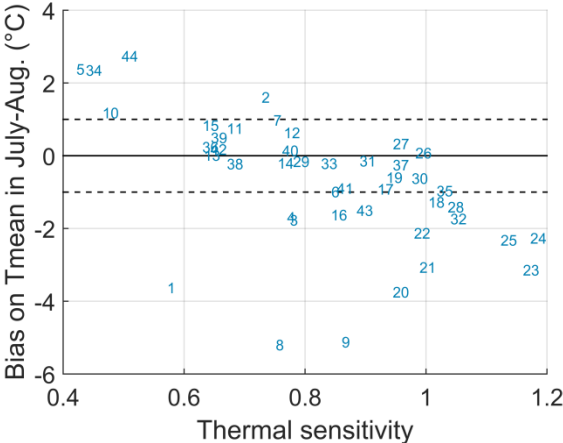


Figure 4.36: Bias ( $T_{sim} - T_{obs}$ ) of mean daily temperature in July-August as a function of thermal sensitivity (2008-2015 average) with groundwater temperature decreased by 2°C

The longitudinal profiles in late August 2009 (Figure 4.37) show that the impact of the source temperature variation is rapidly dampened (after the first reach) on the four main rivers. Then, groundwater temperature has more influence on the Loir and on the Huisne, because these rivers have more groundwater fluxes. The impact of groundwater temperature variation on diel amplitudes is very small (0.05 °C maximum).

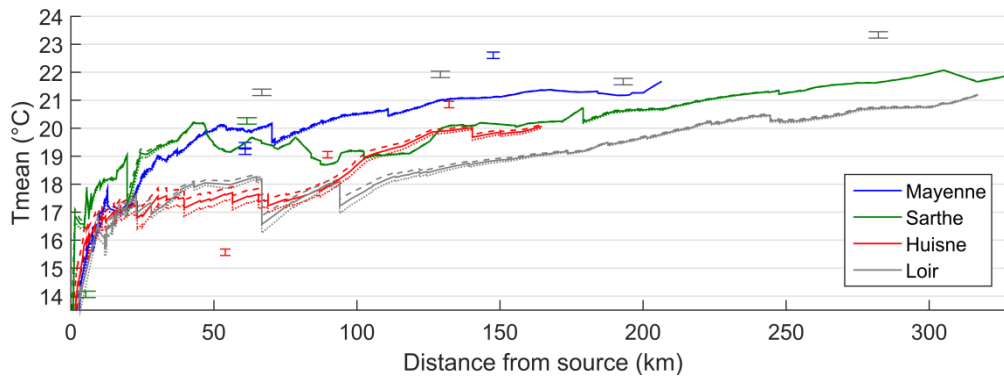


Figure 4.37: Longitudinal profile of stream temperature averaged on the 13-31 August 2009, with standard configuration (continuous),  $T_g + 2\text{ °C}$  (dashed),  $T_g - 2\text{ °C}$  (dotted).

## 4.7 Conclusion

Results presented in this chapter show that, on the Maine basin, biases of the 4 metrics ( $T_{\text{mean}}$ ,  $T_{\text{max}}$ ,  $T_{\text{min}}$ , diel amplitude) are in the  $[-1, +1\text{ °C}]$  interval in winter, but often depart from these values in summer.  $T_{\text{mean}}$  of stations with low (high) thermal sensitivity are too high (low) in summer, showing a potential lack of groundwater fluxes at the headwaters stations and/or a mischaracterisation of the shading process, which depends on the river width and hence on the distance from source as well. The average standard deviation of errors (SDE) of  $T_{\text{mean}}$  is at  $1.6\text{ °C}$ , which indicates that the modelled mean daily  $T_w$  signal varies too much compared to observations, whatever the season. It is also true at the hourly time step, since modelled diel amplitudes are higher than observed ones for most of the stations, especially in summer ( $+1.1\text{ °C}$  in average and  $+1.46\text{ °C}$  in July-August). This problem can be corrected by increasing the water depths, which are likely underestimated by the Estimkart empirical equations, especially as the discharge are, on the contrary, overestimated in summer on most sub-basins.



# Chapter 5: Thermal impact of riparian vegetation shading on solar and downward longwave radiation

## 5.1 Résumé en français

Sur les cours d'eau petits à moyens, l'ombrage porté par la végétation rivulaire peut réduire la température de façon conséquente, et particulièrement la température maximale journalière (Tmax). Il est donc important que les modèles caractérisent correctement cette influence.

Pour ce faire, trois modifications qui concernent la caractérisation du rayonnement solaire ont été préalablement apportées. La première est le remplacement d'un albédo fixé à 6% par l'utilisation d'un albédo variant en fonction de l'élévation solaire. Cette modification a très peu d'impact sur la Tw modélisée. La 2ème est la considération de la phénologie des arbres par la prise en compte d'une transmissivité variable au cours du temps. L'effet est un réchauffement toute l'année, avec un pic au printemps. Il varie entre +0.1 °C à l'automne sur les ordres de Strahler 7 à +0.9 °C en mars sur les ordres 2. La 3ème modification concerne l'utilisation du jeu de données de rayonnement solaire Helioclim à la place de SAFRAN. En effet, les données Helioclim ont une résolution plus fine (3 x 5 km approximativement) et sont calculées en utilisant les images satellitaires de Météosat, pour situer les nuages. De plus, un partitionnement entre le rayonnement direct et diffus est effectué. Les différences moyennes avec SAFRAN varient fortement dans le temps et se reflètent directement dans les Tw modélisées. En moyenne, la performance de T-NET n'est pas améliorée de façon significative, puisqu'elle est améliorée à certaines stations et est dégradée à d'autres.

La seconde partie de ce chapitre correspond globalement à un article publié dans *Science of the Total Environment* et cible sur l'impact de la végétation sur le rayonnement solaire direct et diffus et sur les températures maximales journalières. Des données LiDAR sont utilisées pour calculer l'impact de la végétation, tout au long de l'année et sur 270 km du Loir, une zone correspondant à la disponibilité des données LiDAR. Les données d'ombrage ainsi obtenues sont ensuite injectées dans le modèle T-NET afin de calculer les températures d'août 2007 à juillet 2014. Les Tmax modélisées sont validées grâce à 4 stations de mesure réparties sur le Loir et pour lesquelles les 4 séries de données sont disponibles en même temps seulement du 13 au 31/08/2009. En moyenne sur cette période, la végétation ainsi caractérisée refroidit les Tmax de 3.0 °C à l'amont à 1.3 °C à l'aval. La méthode *lidar* est comparée à 2 autres méthodes. La première est celle utilisée dans le chapitre 4 et par Beaufort et al. (2016). Elle utilise un facteur d'ombrage fixe dans le temps, proportionnel à un taux de végétation et à un facteur variant entre 0 et 1 en fonction de l'ordre de Strahler, afin de prendre en compte l'influence de la largeur sur le processus. Le taux de végétation est issu d'un jeu de donnée qui fournit le pourcentage de végétation telle que représentée dans la base de donnée BD TOPO de l'IGN, dans une zone tampon de 10 m autour d'un réseau hydrographique créé par Valette et al., (2012). Les données ont été reprojétées sur le réseau hydrographique T-NET, ce qui explique en partie la faible précision de ces données. La deuxième méthode calcule un ombrage au pas de temps horaire pour chaque tronçon, en fonction du taux de végétation, de sa hauteur (fixé à 15 m), de la largeur de la rivière, de la position du soleil et de l'orientation du tronçon. Comparé à ces 2 méthodes, la méthode *lidar* améliore le biais négatif calculé sur les Tmax de 0.62 °C en moyenne entre avril et septembre. Les différences entre les méthodes d'ombrage peuvent atteindre 2°C à l'amont de la station la plus en

amont. Les écarts-types sur les erreurs ne sont pas améliorés. Lorsque la méthode de complexité intermédiaire est utilisée avec des taux de végétation proches de la réalité, celle-ci fournit des résultats similaires à ceux donnés par la méthode *lidar*. L'amélioration de la qualité des données de taux de végétation est donc un point crucial pour améliorer la précision des modèles de température.

L'article est complété en analysant les performances de T-NET sur les températures journalières moyennes (Tmean) et minimales (Tmin), ainsi que sur les amplitudes journalières. Les biais sont améliorés sur Tmean et Tmin. Par contre, les amplitudes journalières étant déjà surestimées dans la version standard du modèle, leur précision est dégradée car elles sont augmentées avec la prise en compte de la variation diurne de l'ombrage. Parce que la méthode *lidar* n'a pu être utilisée que sur le cours d'eau principal (le Loir à partir du kilomètre 38), l'impact limité de la méthode d'ombrage utilisée sur les affluents est discuté.

Ensuite, la méthode *lidar* est appliquée au calcul de l'impact de la végétation sur le rayonnement infrarouge qui atteint la rivière. Parce que ce flux énergétique a une importance relative plus élevée durant la nuit, l'impact de la végétation est plus important sur les Tmin, qui sont réchauffées de 0.7 (station amont) à 0.4 °C (station aval), en été. Les amplitudes journalières sont réduites et les biais de toutes les métriques (Tmax, Tmean, Tmin et amplitude journalière) sont ainsi améliorés. En moyenne interannuelle, l'impact total de la végétation (solaire direct et diffus + infrarouge) est le plus important de avril à septembre et à l'amont du Loir. A l'aval du Loir, l'impact est rarement plus faible que -1 °C durant cette période alors que la largeur de la rivière est de 40-50 m.

Avec toutes les modifications apportées dans ce chapitre, les profils longitudinaux modélisés par T-NET au 10 septembre 2014 et au 5 février 2015 sont comparés avec des profils obtenus par imagerie thermique à ces dates. En été, la tendance modélisée par T-NET est similaire à celle du profil observé, dans les limites de la résolution spatiale du modèle et avec toutefois un écart moyen important. En hiver, T-NET reproduit correctement les tendances globales sur seulement un tiers du profil, à cause de la surestimation de l'impact des affluents.

## 5.2 Introduction

In the context of climate change, riparian shade has been given increasing research attention, because of its ability to regulate river temperature. Indeed, many studies have shown that shade can moderate water temperature of relatively small rivers (Moore et al., 2005; Garner et al., 2014b; Leach and Moore, 2010). Conversely, in larger rivers, Teti (2006) showed (using shade measurements acquired along an increasing-width stream) that riparian vegetation has a limited impact on rivers larger than 30 m. DeWalle (2008) quantified the maximal wetted width for which riparian vegetation can effectively reduce received solar radiation. However, no study has yet quantified the thermal impact of shading on rivers of intermediate width (>15 m and <30 m) or at the regional scale.

In order to improve the ability of T-NET to take into account the impact of riparian vegetation on the solar radiation, three modifications regarding solar radiation were brought to T-NET: the consideration of a variable albedo, a foliage transmissivity that vary with the seasons, and the use of the Helioclim radiation data instead of the SAFRAN global radiation data. These modifications will be presented in this chapter and their thermal effects will be analysed on the Maine stations. The second part of this chapter focuses on the Loir River because the methodology involves the use of LiDAR data

that were firstly only available on this stream. This part broadly corresponds to an article published in Science of the Total Environment. In this part, only the maximum daily temperature was considered for brevity. Analysis considering  $T_{mean}$ ,  $T_{min}$ ,  $T_{max}$  and diel amplitudes is included afterwards.

Then, the LiDAR data will be used to compute the impact of vegetation on the longwave downward radiation, which has been shown to be increased with presence of vegetation (Leach and Moore, 2010; Hannah et al., 2008), given that a part of the longwave radiation emitted from the sky is replaced by radiation emitted by vegetation. Among the stream temperature models that were applied at the regional scale, we only found the DHSVM-RBM model (Sun et al., 2015) to take into account the impact of vegetation on longwave radiation, with few details about its implementation.

Finally, the longitudinal profile of temperature modelled with this last version of T-NET will be compared to 2 thermal infrared profiles obtained in summer 2014 and winter 2015.

### 5.3 Modification 1: a variable albedo

#### 5.3.1 Equations

In the standard version of the model, the water albedo is fixed at 6%. In reality, the albedo is dependent on the angle between the sun and the reflecting surface. We will consider that water surface is horizontal and use the formulation of Anderson (1954):

$$\alpha_{dir} = 1 \quad \text{if } \Psi < 1.24^\circ$$

$$\alpha_{dir} = 1.18 * \Psi^{-0.77} \quad \text{otherwise}$$

where  $\Psi$  is the angle between the horizon and the sun in degrees.

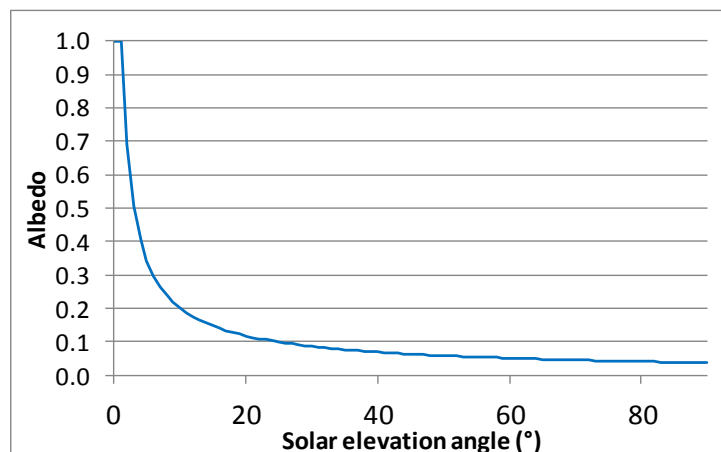


Figure 5.1: Variable albedo parameterisation as a function of solar elevation angle

The albedo can hence be very high when the sun is close to the horizon. Since received energy is also low at these moments, this new parameterisation should not have a big impact on  $T_w$ . The maximal possible elevation angle on the Maine catchment is  $66^\circ$  the 21<sup>st</sup> of June and the corresponding albedo is 0.05.

#### 5.3.2 $T_w$ results and performance with a variable albedo

This parameterisation provides results that are a little bit colder than the standard configuration (Figure 5.2). However, the average difference is only 0.06 °C. Performance is thus a little bit decreased

for stations located far from sources and a bit increased in summer for stations close to sources. The average RMSE is increased by 0.01 °C.

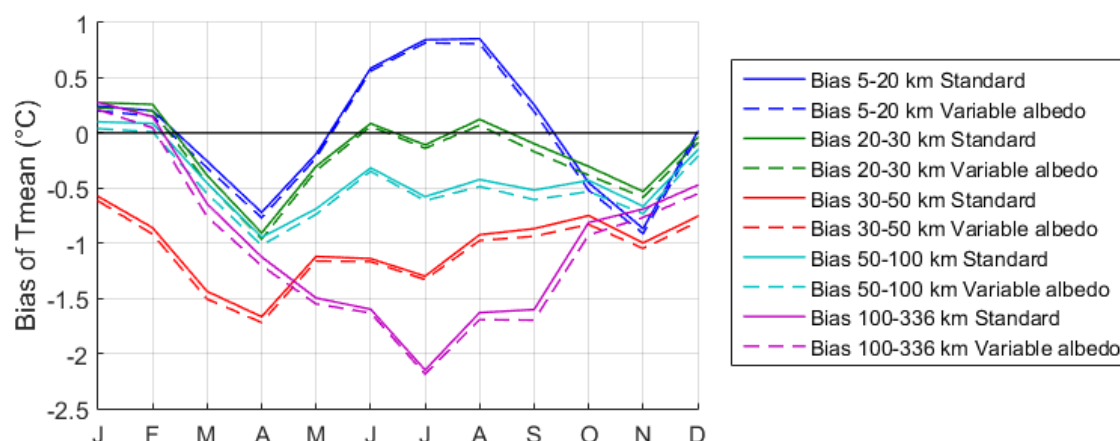


Figure 5.2: Bias of mean daily  $T_w$  averaged by classes of distance from source and on 2008-2015. Comparison between the fixed and the variable albedo parameterisations.

Diel amplitudes are a little bit higher from May to August and a little bit lower from September to April (Figure 5.3). Differences reach about 0.04 °C. Indeed, sun is low in the sky in winter, albedo is hence increased compared to the standard configuration, and net solar radiation is decreased, hence decreasing diel amplitude.

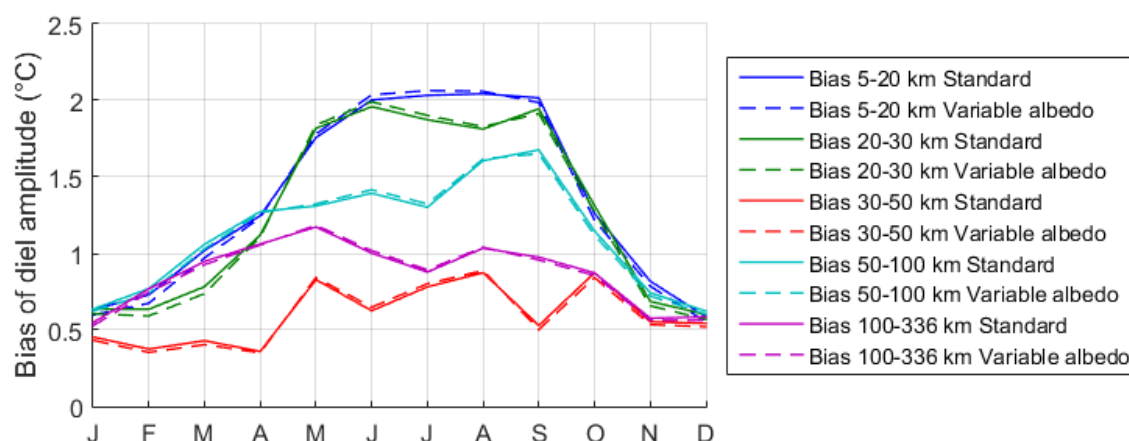


Figure 5.3: Bias of diel amplitudes averaged by classes of distance from source and on 2008-2015. Comparison between the fixed and the variable albedo parameterisations.

## 5.4 Modification 2: an improved phenology

### 5.4.1 Method for phenology characterisation

In the standard version of T-NET, the shadow factor (SF, Table 4.1) has a value that is constant in time. However, under our latitudes, trees leaves fall in autumn and blossom in spring, and that impact the shadowing effect of vegetation. In order to take that fact into account, SF will be weighted by  $(1-\tau)$ , where  $\tau$  is the transmissivity of vegetation to solar radiation.  $\tau$  was fixed at 50% in winter and 15% in summer. These values are averages of global solar radiation transmissivities given by Cantón et al. (1994), Sattin et al. (1997) and Konarska et al. (2014) for deciduous tree species. Transitions between winter and summer values are described with an ascending and descending logistic regression whose equation is:

$$\tau = \frac{\kappa}{1 + \exp(\pm\gamma \cdot DoY - \beta)} + \mu \quad (\text{Eq. 5.1})$$

Where *DoY* is the day of year and  $\kappa$ ,  $\beta$ ,  $\gamma$  and  $\mu$  are the parameters fitted by least squares adjustment to an average annual cycle of ground-based NDVI measured from oak trees during 2008-2012 (Soudani et al., 2012). These trees are located in the forest of Fontainebleau (60 km to the south of Paris and ~150 km away from the centre of the Loir catchment). Data from Lebourgeois et al. (2008) indicates that, for oak trees, there is little phenologic difference between Fontainebleau and the Loir catchment. However, remote sensing observations from Muller (1995) show that, in 1987 and in the region of Toulouse (South of France), leaf emergence of riparian trees occurs about 15 days earlier than for oaks. In order to take into account this difference between oak and riparian species, we hence considered an enlarged growing season compared to oak's phenology ( $\beta-15$  days in spring,  $\beta+15$  days in autumn). After fitting the four parameters on NDVI values,  $\kappa$  and  $\mu$ , representing the upper and lower values, are adjusted to fit the winter and summer values of transmissivity (50 and 15%).

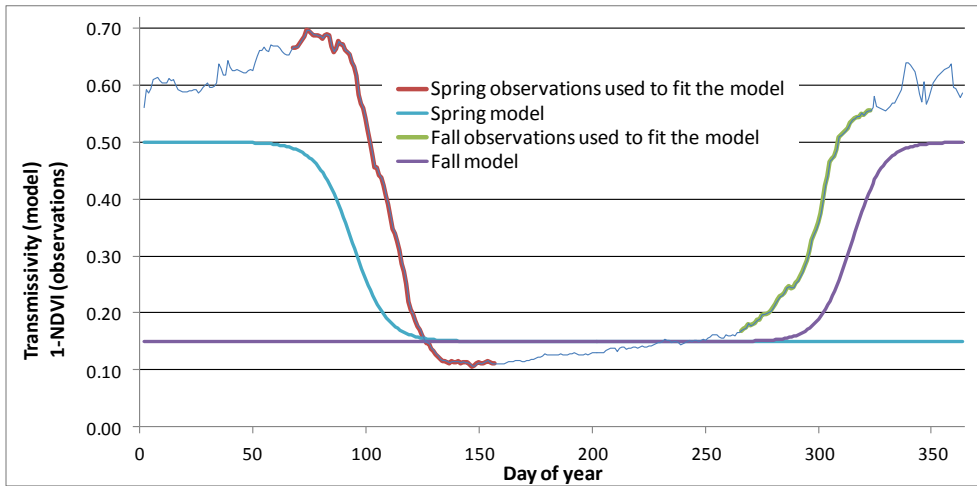


Figure 5.4: Transmissivity parameterisation on ground-based NDVI measured from oak trees during 2008-2012 (Soudani et al., 2012)

The solar radiation equation is now:

$$H_{ns} = R_{dir} (1 - \alpha_{dir}) ((1 - SF) + SF \tau) \quad (\text{Eq. 5.2})$$

Where  $(1-SF)$  represents the non-shaded area at the river reach surface and  $SF \cdot \tau$  represents the shaded area.

#### 5.4.2 Tw results and performance with a variable transmissivity

Compared to the standard simulation, the variable transmissivity leads to an increase of simulated temperature that is more important on small streams, where shading is more important (Figure 5.5 a). The maximal impact on Tmean (Tmax) occurs in March and ranges from 0.6 to 0.9 °C (0.6 to 1.4 °C). Indeed, the change in transmissivity between both configurations is high in winter (from 0 to 50%) but solar radiation is low. In spring, solar radiation increases before the leaf blooming, which explains the peak in March. In summer, change of transmissivity is smaller (from 0 to 15%) but solar radiation is stronger.

As a consequence, biases of Tmean are improved in summer for stations located far from sources but they are decreased for stations located close to sources (Figure 5.5 b, to be compared with Figure 4.10a). Averaged on all stations and at the monthly time scale, SDE of Tmean are not modified by more than 0.05 °C.

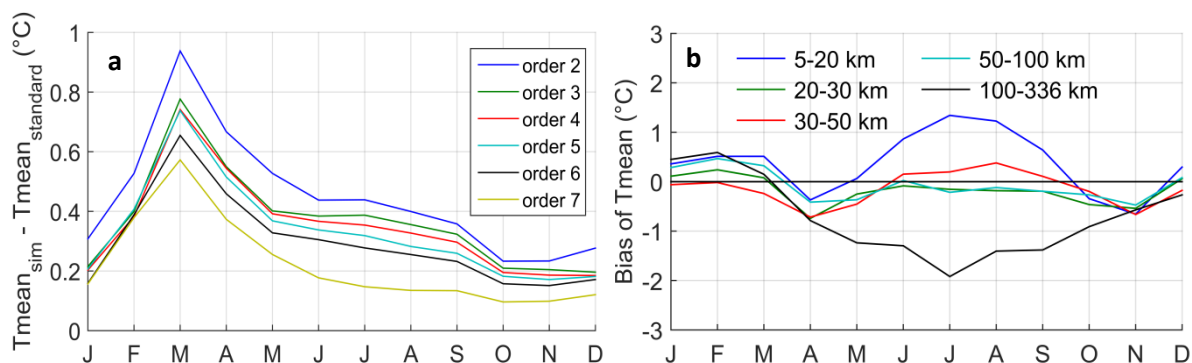


Figure 5.5: Daily mean Tw bias, averaged by Strahler order and on 2008-2015  
 (a) Bias<sub>Variable transmissivity</sub> - bias<sub>Standard</sub> (b) Absolute values

Since the transmissivity impacts the net solar radiation, the behaviour of Tmax and Tmin biases are respectively of higher and lower amplitude than Tmean's bias behaviour (Table 5.1). For the same reason, diel amplitudes are increased, with a maximum in March (+0.58 °C). Since these diel amplitudes were already too high in the standard version, performances are globally decreased (Table 5.1).

Table 5.1: Difference of criteria with the standard simulation. Green and red denote improvements and degradation by more than 0.1 °C

|       | Bias (°C) | SDE (°C) | RMSE (°C) |
|-------|-----------|----------|-----------|
| Tmin  | +0.24     | +0.00    | -0.11     |
| Tmean | +0.35     | +0.01    | -0.04     |
| Tmax  | +0.48     | +0.04    | +0.11     |
| Ampli | +0.24     | +0.05    | +0.20     |

In the end, Tmean accuracy of stations with basically low accuracy is improved in winter, spring and fall, but improvement is mixed for stations that basically have the best accuracies and for all stations in summer (Figure 5.6). Finally, the average RMSE on Tmean is improved by only 0.04 °C.

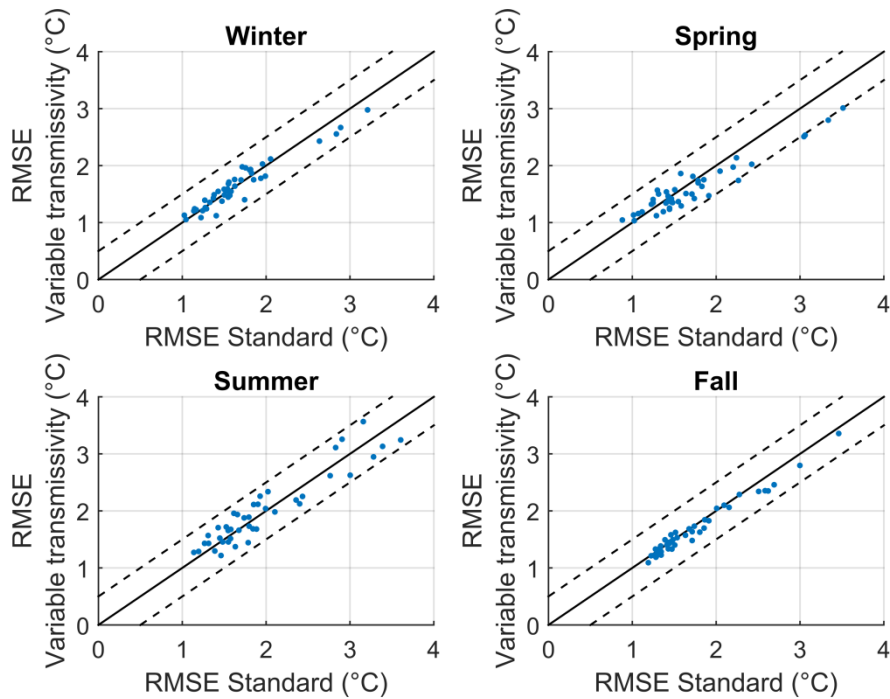


Figure 5.6: Comparison of RMSE computed on daily mean  $T_w$  between the standard configuration and the configuration with a variable transmissivity. Averages on available observed data on 2008-2015.

## 5.5 Modification 3: using Helioclim global solar radiation in place of SAFRAN

### 5.5.1 Comparison of Helioclim radiation dataset with SAFRAN radiation

We acquired Helioclim3-v5 dataset (Marchand et al., 2017), which provides direct and diffuse radiation separately, on a resolution of  $\sim 3 \times 5$  km and an hourly time step (Figure 5.7). The resolution is variable because Helioclim data are generated with the help of Meteosat satellite imagery, which indicate the position of clouds. It is supposed to make Helioclim data more accurate than SAFRAN, which are generated thanks to a radiative model.

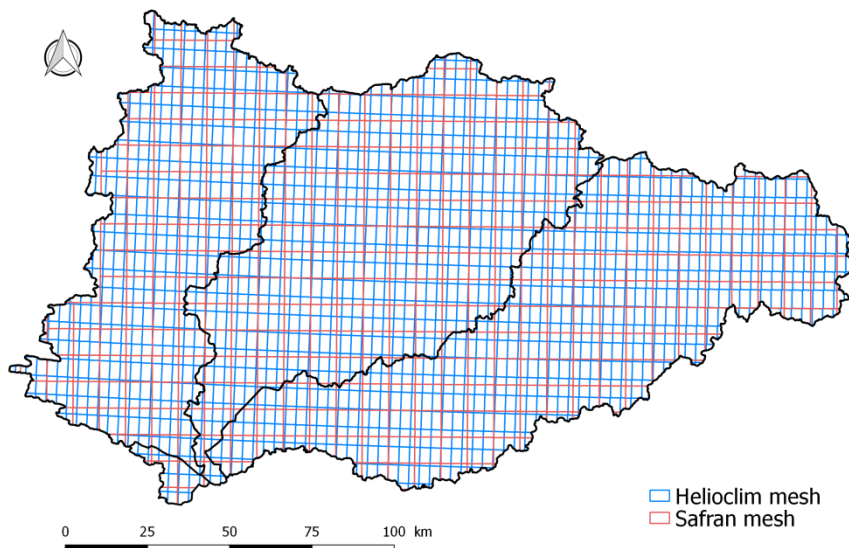


Figure 5.7: Comparison between SAFRAN and Helioclim mesh

On the full 08/2008-07/2015 period, cloudy days are more important and cloudier in SAFRAN than in Helioclim at all seasons (Figure 5.8). On the opposite, the sunniest days are usually sunnier in SAFRAN

than in Helioclim, especially in summer. However, distribution of SAFRAN radiation of sunny days seems to be less natural than for Helioclim, especially in winter, spring and autumn. The mean absolute difference in daily radiation between Helioclim and SAFRAN is 27.2 W/m<sup>2</sup>.

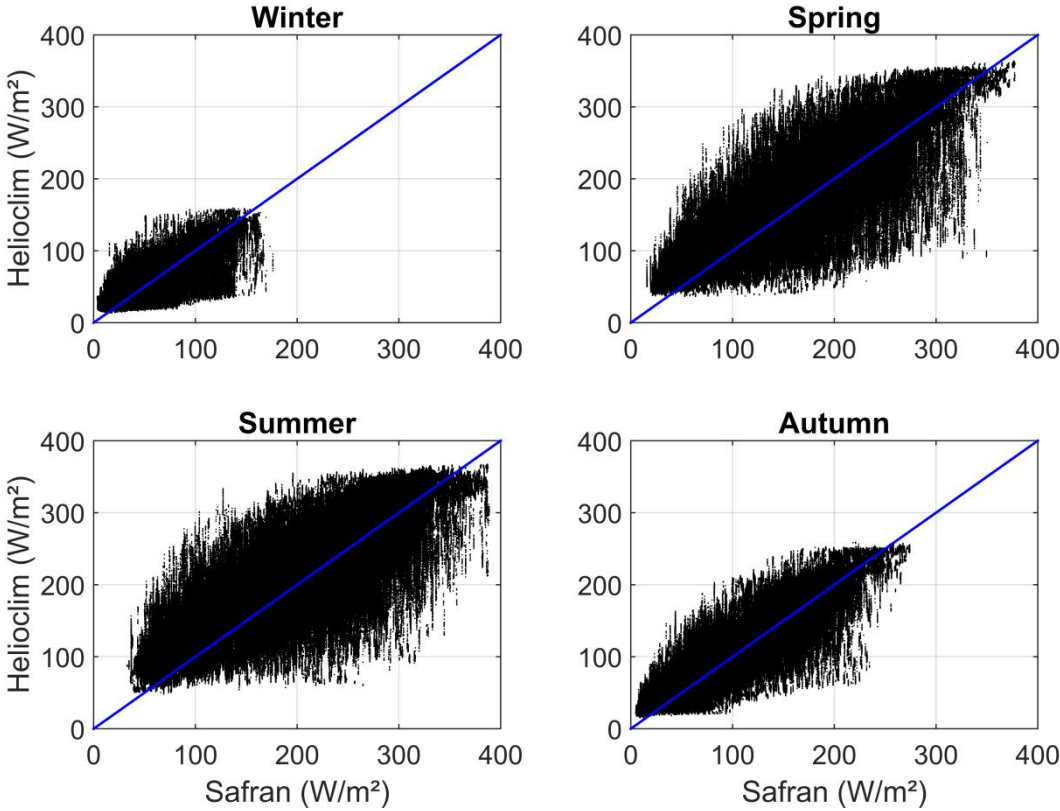


Figure 5.8: Comparison of Helioclim and SAFRAN daily (24h) mean global radiation distributions on 08/2008-07/2015. A SAFRAN equivalent was attributed to each Helioclim cell.

On average on the 08/2008-07/2015 period, the pattern of the Helioclim-Safran difference is similar to the precipitation pattern (Figure 5.9 a and Figure 2.7), showing the impact of the different cloud model used in both datasets. The standard deviation of differences is the lowest where the difference is positive, showing the consistency of at least one of the models in sunny conditions.

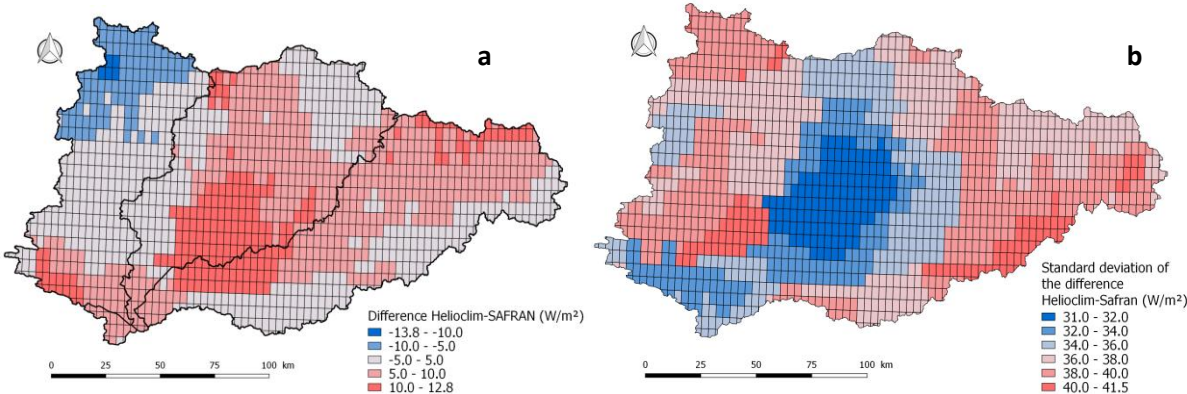


Figure 5.9: Spatial distribution of Helioclim - SAFRAN differences in global radiation over 08/2008-07/2015 (a) mean difference (b) standard deviation of the difference

However, the Helioclim-Safran difference is very variable in the time (Figure 5.10), with the highest differences in spring (Figure 5.10).

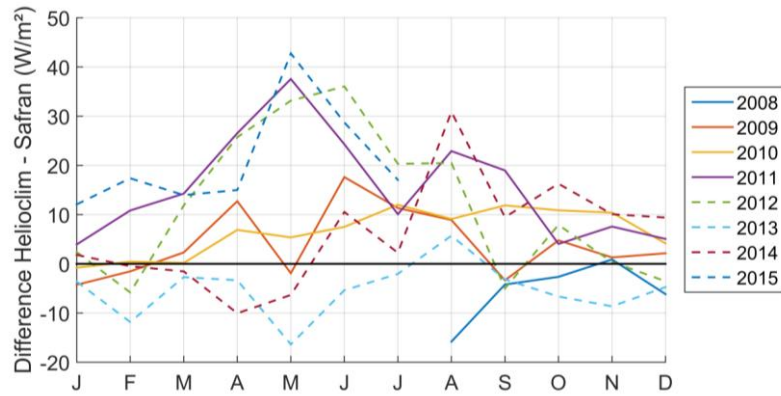


Figure 5.10: Monthly mean differences between Helioclim and Safran global radiation on the Maine basin ( $W.m^{-2}$ )

### 5.5.2 Results in simulated $T_w$

Averaged on the 44 stations, the difference  $T_{mean_{Helioclim}} - T_{mean_{Standard}}$  follows the differences in the forcing datasets (Figure 5.11). The difference ranges from  $-0.35\text{ }^{\circ}C$  (August 2008) to  $0.75\text{ }^{\circ}C$  (May 2011). In August 2009,  $T_{mean}$  is warmer by  $0.2\text{ }^{\circ}C$ .

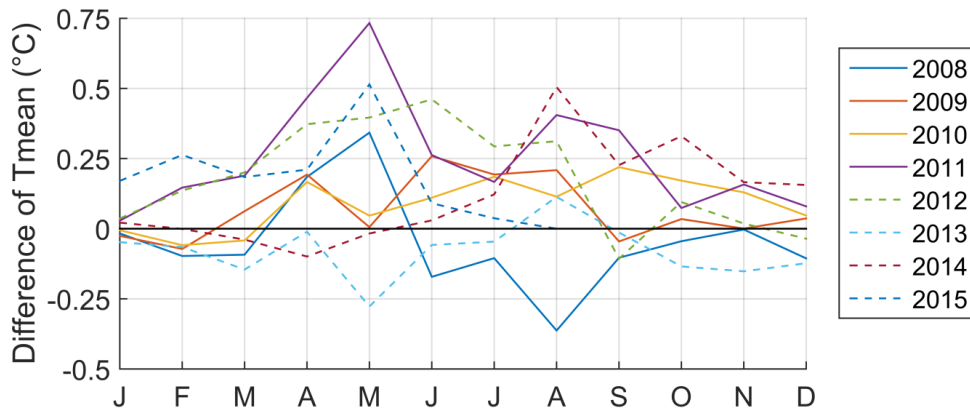


Figure 5.11:  $T_{mean_{Helioclim}} - T_{mean_{Standard}}$  for each year on 2008-2015, averaged on the 44 stations

The longitudinal profiles on the 13-31/08/2009 period show a maximal warming impact on the Loir River upstream of the Conie confluence, and an absence of impact in some parts of the Mayenne River. The biases are reduced for 8 stations and increased for 1 station.

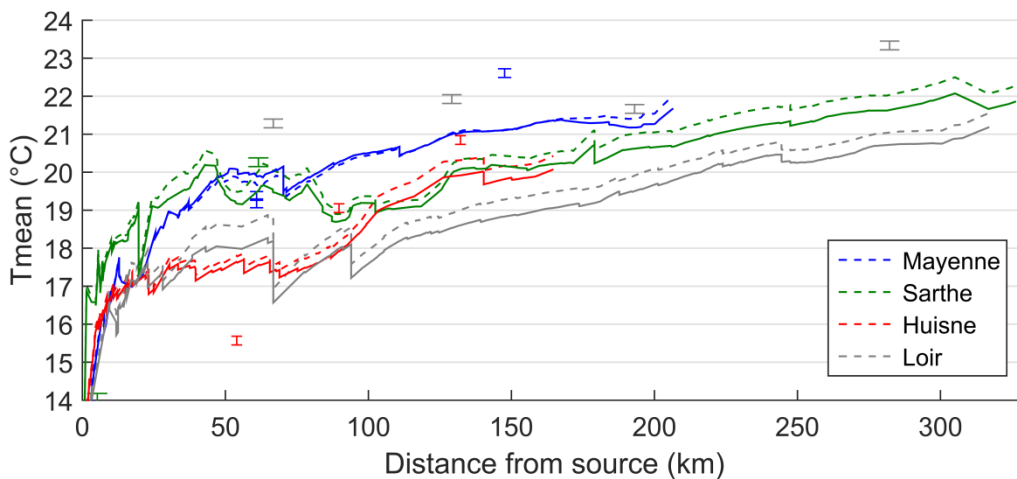


Figure 5.12: Longitudinal profile of simulated  $T_{mean}$  on the 4 main rivers of the Maine catchment, averaged on 13-31/08/2009. Standard simulation (continuous), simulation with Helioclim (dashed).

Performances averaged on the whole period and on the 44 stations are given in Table 5.2, to be compared with Table 4.3. Bias of Tmean is improved by 0.07 °C but SDE is increased by 0.07 °C. Diel amplitudes are increased by 0.05 °C and errors are more variable (SDE is increased by 0.1 °C).

**Table 5.2: Bias, standard deviation of errors and root mean square error (°C) computed on maximum, mean and minimum daily Tw and diel amplitude. Green and red denote improvements and degradation by more than 0.1 °C compared to the standard simulation.**

|       | Bias (°C) | SDE (°C) | RMSE (°C) |
|-------|-----------|----------|-----------|
| Tmin  | -1.05     | 1.63     | 2.01      |
| Tmean | -0.44     | 1.62     | 1.83      |
| Tmax  | 0.13      | 1.83     | 2.08      |
| Ampli | 1.18      | 1.17     | 1.72      |

Accuracy is modified mainly in spring and in summer, when solar radiation is the highest (Figure 5.13). Accuracy is improved for some stations and decreased for others. Result may be highly dependent on the availability of validation data throughout the 2008-2015 period, since the Helioclim-Safran difference vary with the considered year (Figure 5.10).

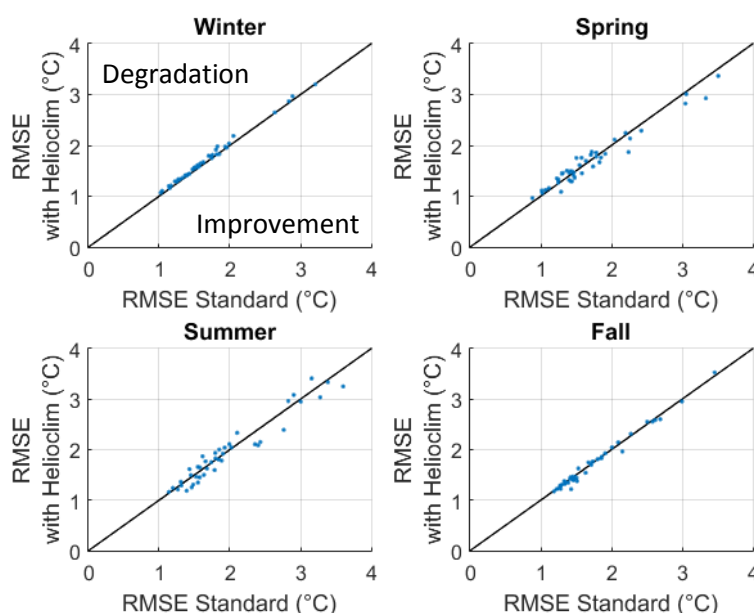


**Figure 5.13: Comparison of RMSE computed on mean daily Tw between the standard configuration and the configuration using Helioclim. Averages on available observed data on 2008-2015.**

## 5.6 Improving representation of riparian vegetation shading in a regional stream temperature model using LiDAR data

### 5.6.1 Introduction

Process-based river temperature models function by simulating the energy exchange processes heating or cooling a river, in particular through the input of solar radiation. This solar radiation is composed of direct (solar rays) and diffuse radiation (scattered by atmosphere), both of which are influenced in different ways by the presence of riparian vegetation. The impact of riparian vegetation on the direct radiation can be quantified by computing a shadow factor (SF), which is the proportion of a river being shaded at a given time. Several methods have been proposed to compute it at an hourly time step. Chen et al. (1998a) detailed a method to compute riparian shade from GIS polygons of riparian vegetation. Their method used stream azimuth and tree height (alongside solar position)

to determine whether a section of stream channel was in shade. However, this technique only accounted for the effect of vegetation located perpendicular to the stream centreline, and furthermore, did not denote the fraction of the channel cross-section that was shaded. As a result, Li et al. (2012) developed an enhanced version of the Chen et al. (1998a) methodology, allowing for the determination of the amount of channel cross-section covered by shade. This new method also enables the simulation of overhanging vegetation, but like its predecessor, only considers the effect of vegetation located perpendicular to the river reach. Approaches capable of simulating the effects of vegetation non-perpendicular to the reach include that of Cox and Bolte (2007), who devised a methodology capable of simulating shadow cast by vegetation located in 8 directions (steps of 45°) around each centreline node, and the Solar Analyst extension for ArcGIS (Fu and Rich, 1999), which can compute shadow factor at much finer spatial and temporal scales. Indeed, Johnson and Wilby (2015) applied this method to a small catchment in order to quantify the potential of planting trees, without using a physically-based river temperature model.

The impact of riparian vegetation on diffuse radiation can be quantified by computing a sky view factor (SVF). It is the ratio between the diffuse radiation actually reaching the water and the diffuse radiation that would reach this surface with no vegetation around. In a lowland area where topographic shade can be neglected, the tree view factor (TVF) can be defined as 1-SVF. Unlike SF, these view factors (VF) are constant in time since they do not depend on the sun's position. For short reaches, a precise calculation can be achieved through hemispheric photography. For larger areas, remote sensing products or vegetation polygons are needed. Most previous studies (Chen et al., 1998a, Cox and Bolte, 2007, Loinaz et al., 2013, Sun et al., 2015) simply use the angle between the horizon and the tree in the directions perpendicular to the river, from one fixed point of view (usually the centre of the river). Moore et al. (2014) introduced the computation of width-averaged sky view factors, with equations considering infinitely long rivers, with or without overhanging trees.

With an approach similar to the one used to compute direct radiation, the Solar Analyst extension for ArcGIS handles the computation of diffuse radiation by overlaying a viewshed and a discretised sky map. Two different methods can be used to quantify the amount of radiation coming from each cell of the open sky (uniform radiation or depending on the zenith angle). This method was modified and used by Sridhar et al. (2004) to include the shading effects of near stream vegetation.

In order to quantify the impact of riparian shading, existing regional-scale stream temperature models usually rely on theoretical values regarding vegetation characteristics (Sun et al., 2015; Loinaz et al., 2013), on simplified assumptions regarding shading process (Haag and Luce, 2008; Cheng and Wiley, 2016), or incorporate shading data from low-resolution DEMs (Cox and Bolte, 2007). Nowadays however, LiDAR can provide accurate data at a large scale. In order to develop a tool for riparian shade inventories using LiDAR data, Guzy et al. (2015) adapted the insolation module of the Heat Source model (Boyd and Kasper, 2003). They created polygons of homogenous potential canopy height and extracted the 75<sup>th</sup> percentile of the computed frequency distribution of canopy height provided by LiDAR. Greenberg et al. (2012) used LiDAR data and the r.sun module of GRASS GIS to compute clear-sky solar radiation for three summer days in order to understand the impact of a potential trees removal around a delta, without the use of a network based temperature model. Finally, Wawrzyniak et al. (2017) used LiDAR data to compute the impact of riparian forest in a

deterministic water temperature model of a 21 km-long reach, during 5 days in summer 2010 and 2011. There is thus a range of data sources and methods available to compute both SF and VF. However, there remains a lack of information comparing the various methodologies, especially with regards to shading routines in regional-scale models. Moreover, the use of LiDAR as a method for the computation of riparian shading is still in its infancy and has never been used to compute the impact of riparian vegetation in a large-scale stream temperature model, during a whole annual cycle.

The goal of this paper is therefore to test the influence of shadow and sky view factor computed from LiDAR data on the simulation of maximum daily water temperature ( $T_{max}$ ) with the T-NET model, a dynamic physically based model for simulating stream temperature at the regional scale using the equilibrium temperature concept. We compute SF and VF based on a LiDAR-derived raster and incorporate these data into the radiative balance of a T-NET model of the Loir River (France) (see Beaufort et al., 2016b). We then compare the  $T_{max}$  simulated with LiDAR data to two other methods used in the T-NET model for computing riparian shading at the regional scales. Model validation is achieved using data from 4 temperature monitoring stations that are spread over the Loir River.

## 5.6.2 Methods

### 5.6.2.1 Net solar radiation calculation

In order to improve T-NET's ability to model the impact of riparian vegetation on solar radiation, modifications were made to the original model detailed by Beaufort et al. (2016). Similar to the approach of LeBlanc et al. (1997), net solar radiation ( $H_{ns}$ ) is now computed as:

$$H_{ns} = R_{dir} (1 - \alpha_{dir}) ((1 - SF) + SF \tau) + R_{diff} (1 - \alpha_{diff}) ((1 - TVF) + TVF \tau) \quad (\text{Eq. 5.3})$$

Where  $R_{dir}$  and  $R_{diff}$  are the direct and diffuse solar radiation [ $\text{W}\cdot\text{m}^{-2}$ ] derived from the Helioclim3-v5 product,  $\alpha_{dir}$  and  $\alpha_{diff}$  are the water surface albedo associated with direct and diffuse radiation respectively,  $\tau$  is the transmissivity of riparian vegetation (i.e. the fraction of solar radiation that passes through the canopy),  $SF$  is the shadow factor and  $TVF$  is the tree view factor.  $\alpha_{diff}$  was held at a constant of 0.09, following the recommendation of Sellers (1965) and  $\alpha_{dir}$  was computed using the formulation of Anderson (1954):

$$\alpha_{dir} = 1 \quad \text{if } \Psi < 1.24^\circ \quad (\text{Eq. 5.4})$$

$$\alpha_{dir} = 1.18 * \Psi^{-0.77} \quad \text{otherwise}$$

where  $\Psi$  is the angle between the horizon and the sun in degrees.

$\tau$  was fixed at 50% in winter and 15% in summer. These values are the averages of global solar radiation transmissivities given by Cantón et al. (1994), Sattin et al. (1997) and Konarska et al. (2014) for deciduous tree species. Transitions between winter and summer values are described with an ascending and descending logistic regression whose equation is:

$$\tau = \frac{\kappa}{1 + \exp(\pm\gamma \cdot DoY - \beta)} + \mu \quad (\text{Eq. 5.5})$$

Where  $DoY$  is the day of year and  $\kappa$ ,  $\beta$ ,  $\gamma$  and  $\mu$  are the parameters fitted by least squares adjustment to an average annual cycle of ground-based NDVI measured from oak trees during 2008-2012 (Soudani et al., 2012). These trees are located in the forest of Fontainebleau (60 km to the south of Paris and ~150 km away from the centre of the Loir catchment). Data from Lebourgeois et al. (2008)

indicate that, for oak trees, there is little phenologic difference between Fontainebleau and the Loir catchment. However, remote sensing observations from Muller (1995) show that, in 1987 and in the region of Toulouse (South of France), leaf emergence of riparian trees occurs about 15 days earlier than for oaks. In order to take into account this difference between oak and riparian species, we hence considered an enlarged growing season compared to oak's phenology ( $\beta-15$  days in spring,  $\beta+15$  days in autumn). After fitting the four parameters on NDVI values,  $\kappa$  and  $\mu$ , representing the upper and lower values, are adjusted to fit the winter and summer values of transmissivity (50 and 15%, respectively).

### 5.6.2.2 Shadow factor and view factor calculations

In order to test the influence of different riparian shading algorithms on water temperatures simulated with T-NET, we used three approaches to compute both the shadow factor (SF) and the tree view factor (TVF).

In the first approach (hereafter referred to as the *constant* method), SF and TVF are held as coefficients that are constant in time but vary as a function of Strahler order based on the equation:

$$SF = TVF = vc \times k \quad (\text{Eq. 5.6})$$

where  $vc$  is vegetation cover (%) computed at the reach scale in a buffer of 10 m around the river, and  $k$  is a coefficient aiming to account for the influence of the reach width on shadow (where 1 (maximum impact) denotes a Strahler order of 1 and 0 (no impact) is associated with a Strahler order of 8). This approach is used in Beaufort et al. (2015, 2016).

In the second approach (hereafter referred to as the *variable* method), SF and TVF are derived from geometric calculations made at the reach scale, taking into account river width, tree height, vegetation cover, and position of the sun (for the shadow factor). To compute SF at an hourly time step, the model of Li et al. (2012) was implemented in its simplest version, i.e. considering rectangular trees, located at the edge of the bank, without overhang:

$$SF = \frac{H \times \cot \Psi \times \sin \delta}{W} \times vc \quad (\text{Eq. 5.7})$$

where  $H$  is tree height,  $W$  is river width,  $\Psi$  is the solar elevation angle,  $\delta$  is the angle between solar azimuth and the mean azimuth [ $0^\circ - 180^\circ$ ] of each T-NET reach (computed by considering the first and last vertices of each reach).

To compute VF, we used the second model described in Moore et al. (2014). It provides SVF for channels of infinite length, without taking into account overhanging trees. For a channel with vertical banks and fixed tree height, the width- and reach-averaged tree view factor is computed as:

$$TVF = \left[ 1 - \frac{0.5}{W} \left( \sqrt{H^2 + W^2} + \sqrt{H^2 + W^2} - 2H \right) \right] \times vc \quad (\text{Eq. 5.8})$$

The third approach (subsequently referred to as the *lidar* method) is a spatially-explicit method that computes SF and TVF from a LiDAR-derived digital surface model (DSM). It requires a) a high-resolution digital surface model ( $\sim 1$  m) describing the elevation of riparian vegetation, b) information

about the exact location of the river in order to define water and non-water pixels and c) polygons of river area, allowing the DSM pixels to be linked to a given T-NET reach.

To compute SF, we modified the r.sun module (Hofierka and Suri, 2002) of GRASS GIS (GRASS Development Team, 2015) to map per-pixel shade cast by the DSM. Using this algorithm, a water pixel is defined as being in shade if the elevation of the highest DSM pixel located along a 50 m track in the direction of the sun is greater than the solar elevation. Dividing the number of shaded pixels by the number of water pixels belonging to each river polygon thus provides a shadow factor for each T-NET reach. Because shading at a given hour vary slowly throughout the year, the computation was done every hour when the sun is above the horizon, every 15 days of a standard non-leap year, for every water pixel. A piecewise cubic interpolation is then applied to the SF of each hour separately in order to get a value for each day of the year.

To compute SVF from the DSM, we represented the sky as a hemisphere of radius R centred on a water pixel (as in Essery et al. (2008), Johnson and Watson (1984) and Tung et al. (2006); Figure 5.14). We used the r.horizon module of GRASS GIS to calculate the angle  $\theta$  between the horizon and the highest DSM pixel as seen from each water pixel at horizontal azimuth steps  $\phi$  of  $10^\circ$ . The whole hemisphere is thus made of  $n=36$  segments. The diffuse radiation emission is considered to be isotropic and the river surface to be horizontal. The SVF for each segment is computed from the sphere area formula:

$$\frac{R^2 \int_0^{\frac{\pi}{2}} \int_0^\phi \cos \theta \sin \theta d\phi d\theta}{R^2 \int_0^{\frac{\pi}{2}} \int_0^\phi \cos \theta \sin \theta d\phi d\theta} = \frac{1 + \cos 2\theta}{2} \quad (\text{Eq. 5.9})$$

It therefore follows that the SVF for the whole hemisphere is given by:

$$SVF = \frac{1}{2} + \frac{1}{n} \sum_{i=1}^n \cos 2\theta_i \quad (\text{Eq. 5.10})$$

An averaged TVF value ( $TVF=1-SVF$ ) is subsequently attributed to each T-NET reach as the mean TVF value for all DSM pixels located within the reach.

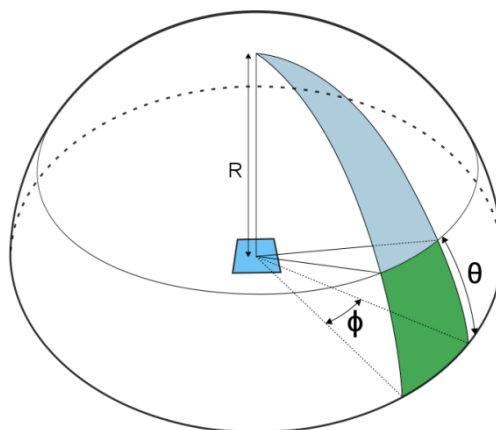


Figure 5.14: Calculation of a sky view factor from measures of  $\theta$ , the angle between the horizon and the highest vegetation seen from a water pixel and with an angular step  $\phi$  of  $10^\circ$ . R is the radius of the hemisphere

### 5.6.2.3 Study site and water temperature observations

The Loir River basin is an  $8283 \text{ km}^2$  sub-catchment of the Maine River watershed located in central France (Figure 5.15). The river network of the Loir basin is 4420 km long, of which the Loir River itself

is 316 km. The basin is generally low-lying, with altitudes ranging from 20 to 140 meters above sea level. As highlighted by the river network's variable drainage density (Figure 5.15), a calcareous aquifer with high permeability is present in the north-east of the catchment. It feeds the river network with groundwater exchanges in its upstream sections (Baratelli et al., 2016). Channel slope (computed from a 25 m resolution digital terrain model of the watershed) ranges from 0.01% to 5%, with a median value of 0.5%. The main tributaries of the Loir are the Conie, the Yerre and the Aigre, with catchments areas of 530, 300 and 280 km<sup>2</sup> respectively. The mean discharge of the Loir at its downstream-most gauging station (1961-2015) is 31.8 m<sup>3</sup>·s<sup>-1</sup> (specific discharge = 4.0 l·s<sup>-1</sup>·km<sup>-2</sup>). The flows of the Aigre (specific discharge = 5.4 l·s<sup>-1</sup>·km<sup>-2</sup>) and the Conie (specific discharge = 3.4 l·s<sup>-1</sup>·km<sup>-2</sup>) show little variation during the year, compared to the Loir. However, interannual fluctuations are much greater, driven by piezometric fluctuations of the Beauce aquifer.

Eighteen temperature loggers allowing for the model validation are located in the catchment. They acquired data at an hourly time step with varying periods of availability (extending from summer 2008 to summer 2014). The loggers were generally placed at a depth greater than 1 meter (according to the mean interannual water level), and steps were taken to ensure that they were installed within well-mixed sections of the channel to avoid potential stratification biases. Four of these stations are located within the main stem of the Loir (S1 to S4), where LiDAR data are available. The period of measurement is different for each station and is given in Figure 5.16. The annual cycle of mean daily temperature of the Loir River ranges from 2 to 24 °C at station 1 (between 08/2010 and 07/2011), while the annual amplitude of the Aigre and the Yerre are smaller because of the groundwater fluxes (5-21 °C and 4-16 °C on the same period, respectively). Temperature regime of the Conie River is strongly dependent on the groundwater level. Its variability can be similar to the Loir River (2009, 2010) or very limited (annual range of 8-14 °C in 2014).

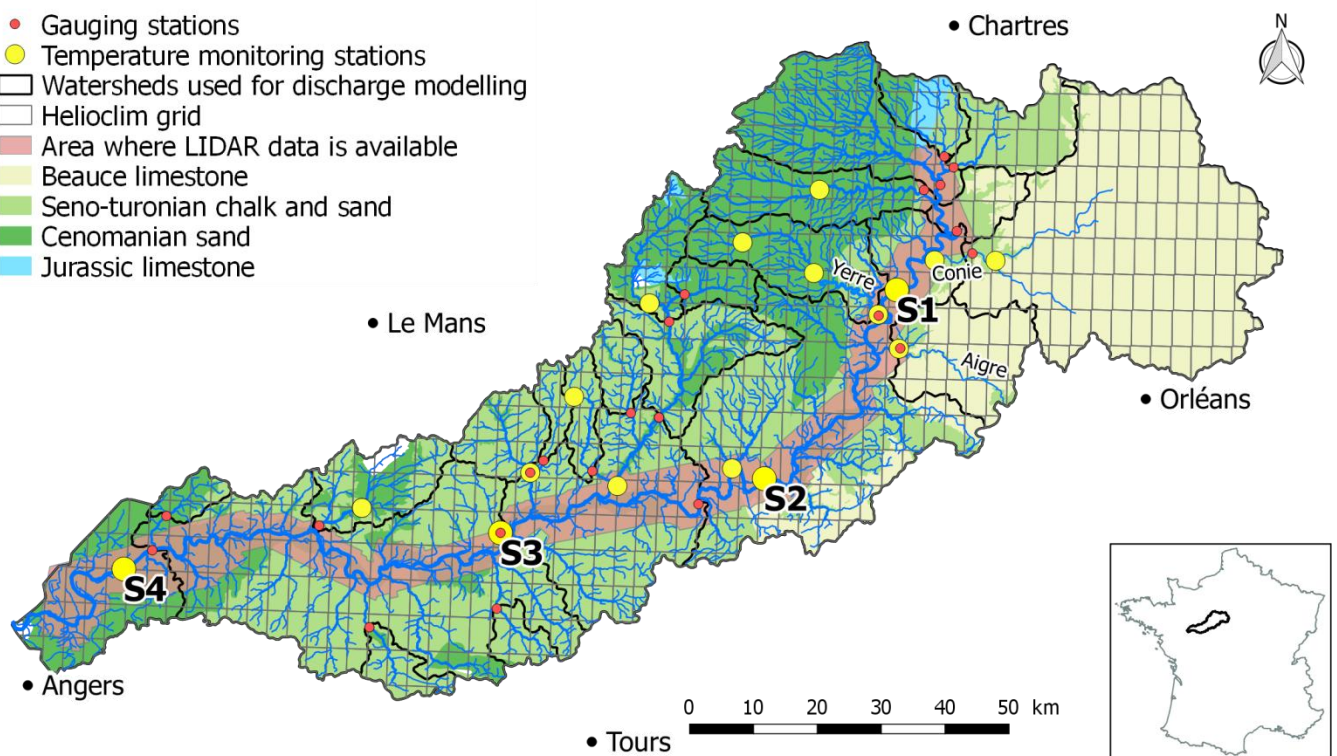


Figure 5.15: Map of the Loir catchment, with stream temperature monitoring stations, gauging stations, watersheds used for discharge modelling, LiDAR area, geologic formations, Helioclim grid.

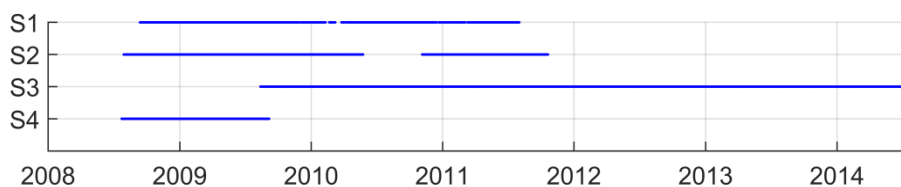


Figure 5.16: Period of availability of stream temperature observation at the four logger stations located on the Loir River

#### 5.6.2.4 T-NET model implementation and criteria of model performance

The Loir River basin was implemented in the T-NET model. It consists of 2206 reaches, of which the Loir River itself is covered by 161 reaches. Simulated discharge and groundwater inputs used to drive T-NET (derived from the EROS hydrological model) were found to agree reasonably well with observed data. Nash-Sutcliffe (Nash and Sutcliffe, 1970) model efficiency coefficient (NSE) calculated against hydrometric observations ranged from 0.59 to 0.95 (1974-2012 period) for 21 of the 23 sub-basins of the Loir catchment. The remaining two sub-basins ( $<0.10 \text{ m}^3 \cdot \text{s}^{-1}$ ; located in the upper portions of the watershed) yielded negative NSE values.

In order to compare the three shading methods detailed in section 5.6.2.2, we ran the T-NET model three times on seven hydrologic years (from August 2007 to July 2014).

For the *constant* method, vegetation cover (*vc*) was derived from a dataset available at the national scale (Valette et al., 2012), which is based on river and vegetation polygons from the BD TOPO® database, provided by Institut national de l'information géographique et forestière (IGN).

For the *variable* method, *vc* was also derived from this dataset. Tree height *H* was fixed at 15m and river width *W* was estimated using the ESTIMKART empirical model (Lamouroux et al., 2010).

For the *lidar* method, the digital surface model (DSM) required for the shading computation was derived from a LiDAR survey conducted by IGN on approximately 270 km of the Loir River (85% of the total river length) on 26 May 2012. That day, average discharge was  $25.5 \text{ m}^3 \cdot \text{s}^{-1}$  at the downstream-most gauging station (interannual average is  $31.8 \text{ m}^3 \cdot \text{s}^{-1}$ ). The DSM was generated by gridding the LiDAR first returns at a resolution of  $1 \text{ m}^2$ . LiDAR accuracy was assessed as  $\sim 60 \text{ cm}$  in the horizontal and  $\sim 20 \text{ cm}$  in the vertical components. Because water does not reflect the LiDAR pulses, no data was available for the water pixels (unless emergent aquatic vegetation was present), and we used this property to discriminate water vs. non-water pixels inside the river polygons of the BD TOPO database. Elevations for these water pixels as well as for other sporadic data gaps were computed by attributing values from a digital elevation model (DEM) to the no data pixels. This 1-m resolution DEM, built from LiDAR final returns, provides values above water by interpolation of altitudes between the river banks. Finally, polygons from BD TOPO were also used to attribute DSM pixels to each reach of the T-NET network. Because LiDAR data were not available on the tributaries and the headwaters of the Loir, the *constant* method was applied on these reaches. With this configuration, the *lidar* method takes less than 5 hours to run on a computer with 16 CPUs and 64 Gb of RAM. Finally, in order to compare the *lidar* method with a situation without riparian vegetation, a supplementary simulation was done with SF and TVF fixed at zero everywhere.

In order to characterise differences in vegetation cover between the DSM and that derived from the BD TOPO database (Valette et al., 2012), a DEM was also used to create a raster of vegetation height

by subtracting the DEM (ground) elevations from the DSM. A vegetation cover map was then extracted from the vegetation height raster, where vegetation cover was defined as all pixels with vegetation higher than 1 m. A LiDAR-derived river width was also extracted for analysis purposes by dividing the area of water pixel inside each polygon by the length of the T-NET reaches.

Three model performance metrics were used to quantify the accuracy of the different methods regarding the maximum daily temperature. The root-mean-square error (RMSE) was used as a global

performance metric:  $RMSE = \sqrt{\frac{\sum(T_{sim}-T_{obs})^2}{N}}$  (Eq. 5.11)

where N is the number of observations,  $T_{sim}$  is the simulated river temperature and  $T_{obs}$  is the observed river temperature. Bias (defined as the mean difference between simulated and measured temperatures) was used to quantify the mean over/underestimation of the model. Finally, the standard deviation of errors (SDE) quantifies the variability of daily biases in a given period. Because the temperature time series used for model validation were not concomitant (Figure 5.16), model performance was analysed using two methods. First, we compared model performance against all available validation data. This allows for comparison between the three shading methods detailed in section 2.3. Second, in order to compare spatial variability in the model's performance between the 4 temperature logger stations, we used temperature data from the period during which concurrent measures were available at all 4 stations (13<sup>th</sup> to the 31<sup>st</sup> August 2009).

### 5.6.3 Results

#### 5.6.3.1 Characterisation of riparian vegetation cover

Analysis of vegetation cover extracted from the LiDAR data inside a single buffer of 10 m around the 270 km of river shows that 58% of the riparian zone is vegetated. The median vegetation height in this area is 10.0 m and the third quartile of the height (considered by Guzy et al., 2015) is 14.9 m, while the standard deviation is 6.5 m. Longitudinal profiles of vegetation cover, median and 3<sup>rd</sup> quartile of height are given in Figure 5.17. There is a slight but significant decreasing downstream trend for these three variables (p-value = 0.014). In comparison with the LiDAR-derived vegetation cover, vegetation cover derived from the BD TOPO database is overestimated everywhere with the exception of some small reaches (Figure 5.17). The median overestimation is 35% upstream of river km 160 and 22% downstream. This overestimation rises to more than 39% for 20% of the reaches.

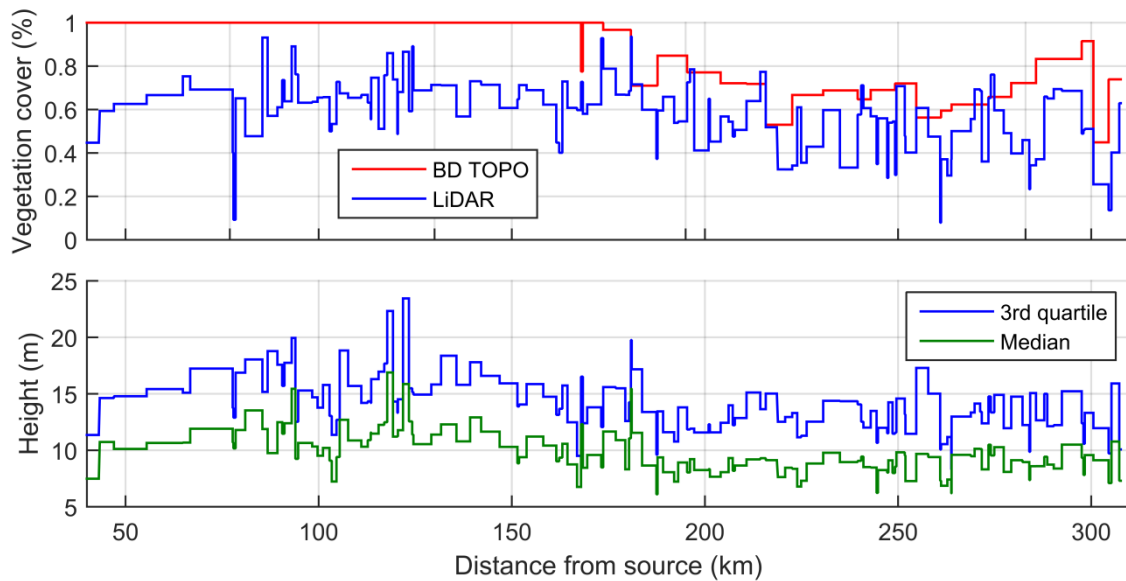


Figure 5.17: Characterisation of riparian vegetation for each T-NET reach (a) comparison of vegetation cover derived from the BD TOPO database (Valette et al., 2012) and LiDAR datasets (buffer of 10 m on both sides of the river polygons) (b) median and 3<sup>rd</sup> quartile vegetation heights from LiDAR data

### 5.6.3.2 Variation in riparian shading computed with the three methods

In the Loir catchment, direct and diffuse radiation comprise ~70% and ~30% respectively of the incoming solar radiation received at the river surface between 8 and 16h (period 2007-2014). This means that shadow factor has a greater impact on water temperature than view factor.

Figure 5.18 shows the longitudinal profile of SF on the Loir River for the three methods at midday on the summer solstice, when solar radiation is strongest. For the *constant* method, the reaches covered by LiDAR data have a uniform Strahler order of 5, so that the weighting coefficient  $k$  in this area is always equal to 0.4 (see section 2.3). The variation of SF is thus only dependent on the vegetation cover. The *variable* method varies strongly as a function of reach azimuth, even though the sun is at its highest elevation, while the *lidar* method shows smaller variations. The *lidar* method is thus less sensitive to reach azimuth, compared to the *variable* method.

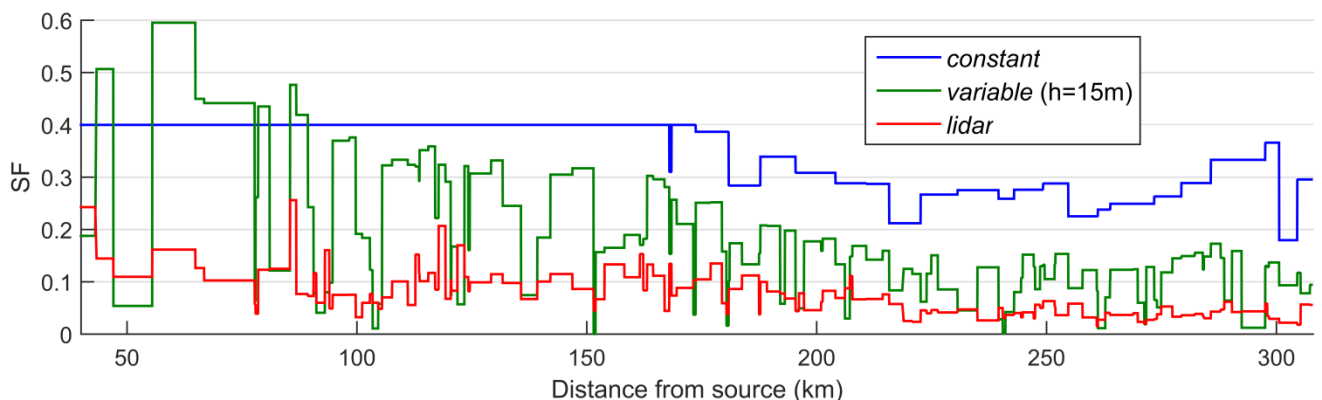


Figure 5.18: Longitudinal profile of shadow factor provided by the 3 methods on the Loir River at the summer solstice (21<sup>st</sup> June) at 12h UTC.

At noon, the Loir's SF computed with the *lidar* method lies between 0 and 0.3 in June (median=0.1; Figure 5.19a solid lines) and between 0.1 and 1 in December (median=0.5). There is thus more variability in winter than in summer, because reach azimuth has a much greater impact when the sun

is low in the sky. Seasonal variability in SF exhibits strong annual cyclicity, with SF minima centred on the summer solstice for every reach. Highest SF values are found on a reach located 85 km from the source, flowing East-West and bordered by persistent riparian forest cover (>20 m tall). Lowest SF values are found on a North-South oriented reach located 271 km from the source, explaining the weak annual cycle at noon (Figure 5.19a, pink solid line). Figure 5.19b shows the daily cycles at the summer solstice. The hour of minimum SF in a day is not always centred on noon because it depends on the reach orientation. SF obtained from the *variable* method is usually higher than that provided by the *lidar* method, except in winter and at noon for North-South oriented reaches (Figure 5.19a, dashed pink line). At the summer solstice, between 6 and 18h, the *variable* method yields higher SF than the *lidar* method 74% of the time, especially in the upstream parts of the watershed. Indeed, the *variable* method yields 184 occurrences of SF values equal to 1, while it only occurs 3 times with the *lidar* method.

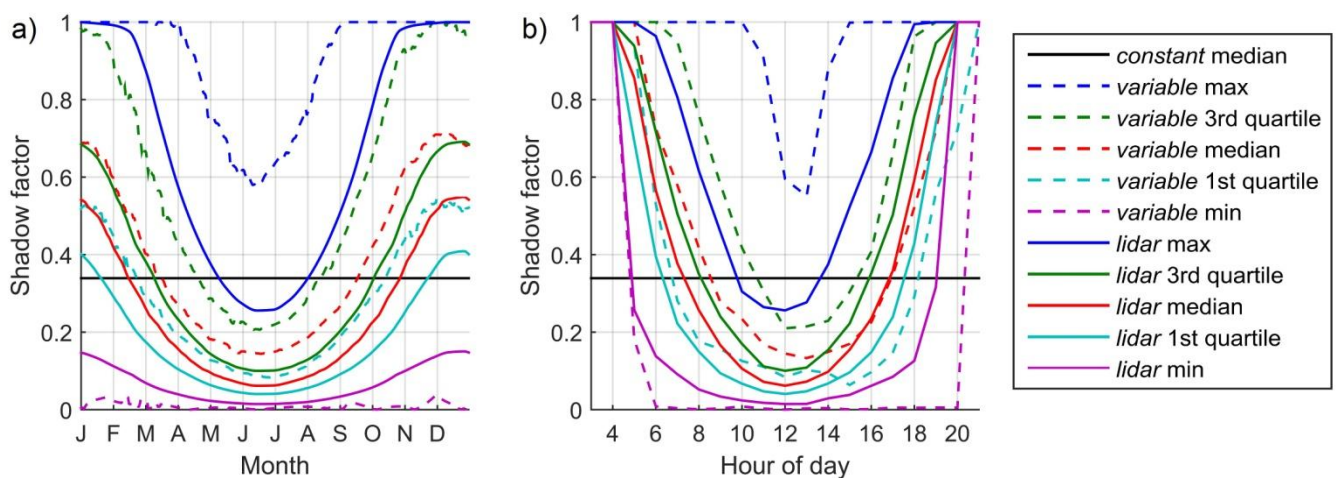


Figure 5.19: Percentiles of the SF distribution obtained with the three methods on the 135 T-NET reaches  
 (a) Annual cycles at noon (b) daily cycles at the summer solstice.

Figure 5.20 shows the longitudinal profile of TVF for the three methods. Mean values are 0.34, 0.38 and 0.26 for the *constant*, *variable* and *lidar* methods respectively. TVF computed with the *lidar* method comprises values between 0.47 and 0.11. Like for the SF, there is a significant ( $p < 0.01$ ) decreasing trend due to both the increasing width of the river and the decreasing vegetation cover. The *variable* method overestimates TVF, especially for the upstream portion of the river. Indeed, the inter-method variability in computed TVF values decreases as the influence of vegetation on TVF reduces with increasing river width.

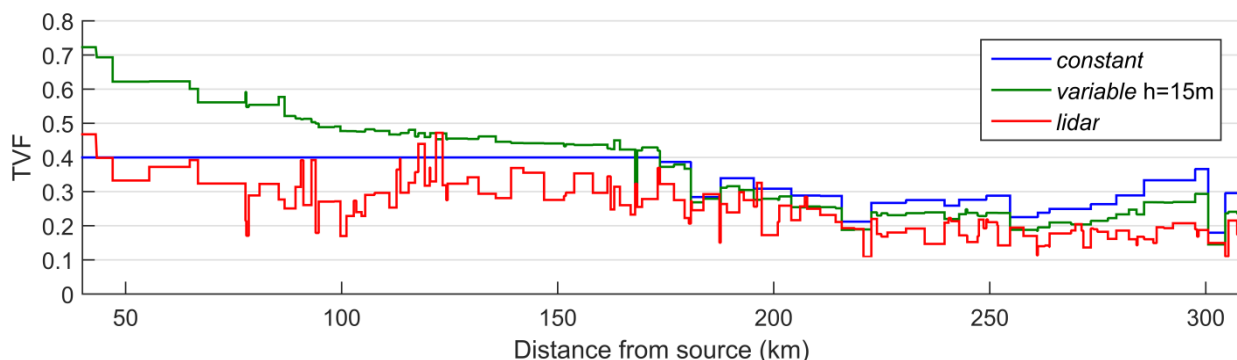


Figure 5.20: Longitudinal profile of tree view factor provided by the 3 methods on the Loir River.  
 Values from the *variable* method are averaged on 08/2007-07/2014

### 5.6.3.3 Impact of riparian shading method on annual and seasonal river temperature simulations

Results of this paper focus on the 4 temperature monitoring stations located on the Loir River, where LiDAR data are available. For the 14 other temperature monitoring stations located on the tributaries, the constant method provides a median annual RMSE on mean daily temperature at 1.69 °C (min=1.35 °C, max=2.89 °C). Seasonality in the accuracy is observed since median bias on mean daily temperature is -0.4 °C when computed for the full year but rises to 0.2 °C in summer. 67% of daily biases are comprised between  $\pm 2$  °C.

Biases, SDE and RMSE averaged on the four stations are shown in Table 5.3 for the April-September and the October-March periods. In the April-September period, the *lidar* method improves the mean bias by 0.62 °C in comparison with the *constant* method. The mean RMSE is improved by 0.22 °C although the mean SDE is increased by 0.10 °C. The three metrics show that the *constant* method provides better results than the *variable* method. During the October-March period, biases of the 3 methods are closer to zero. All criteria of the *constant* and the *lidar* methods are very similar because solar radiation is lower and vegetation transmissivity is high. However, the *variable* method is consistently colder than the other methods by  $\sim 0.3$  °C.

Table 5.3: Model performance criteria for maximum daily temperature, averaged for the 4 stations located on the Loir River from April to September and from October to March (°C)

|                                | April to September |      |      | October to March |      |      |
|--------------------------------|--------------------|------|------|------------------|------|------|
|                                | Bias               | SDE  | RMSE | Bias             | SDE  | RMSE |
| <i>Constant</i> method         | -1.44              | 1.61 | 2.17 | -0.31            | 2.04 | 2.07 |
| <i>Variable</i> method (h=15m) | -1.86              | 1.65 | 2.55 | -0.60            | 2.09 | 2.18 |
| <i>Lidar</i> method            | -0.82              | 1.75 | 1.95 | -0.33            | 2.05 | 2.08 |

Figure 5.21 shows the monthly biases ( $T_{sim}-T_{obs}$ ) of maximum daily temperature ( $T_{max}$ ) computed on available measured data (see Figure 5.16). At the four stations, the *lidar* method provides improved biases in comparison to both the *variable* and the *constant* method from April to September. Compared to the *variable* method, the maximum improvement occurs during the spring and autumn months (2 °C at S1; 1.5 °C at S2; 0.5 °C at S3; 0.7 °C at S4). Despite this improvement, the *lidar* method still underestimates river temperature by more than 1 °C during at least 2 months in summer at S1, S2 and S4. The *constant* method provides a consistently colder  $T_{max}$  than the *variable* (and *lidar*) methods at stations 3 and 4 from May to August, presumably because this method does not model the seasonal cycle of increasing and decreasing shadow length. Averaged annual cycles of SDE show little difference between methods and always stay above 1 °C (Figure 5.21). That means that simulated  $T_{max}$  is substantially more variable than observed data, whatever the method used.

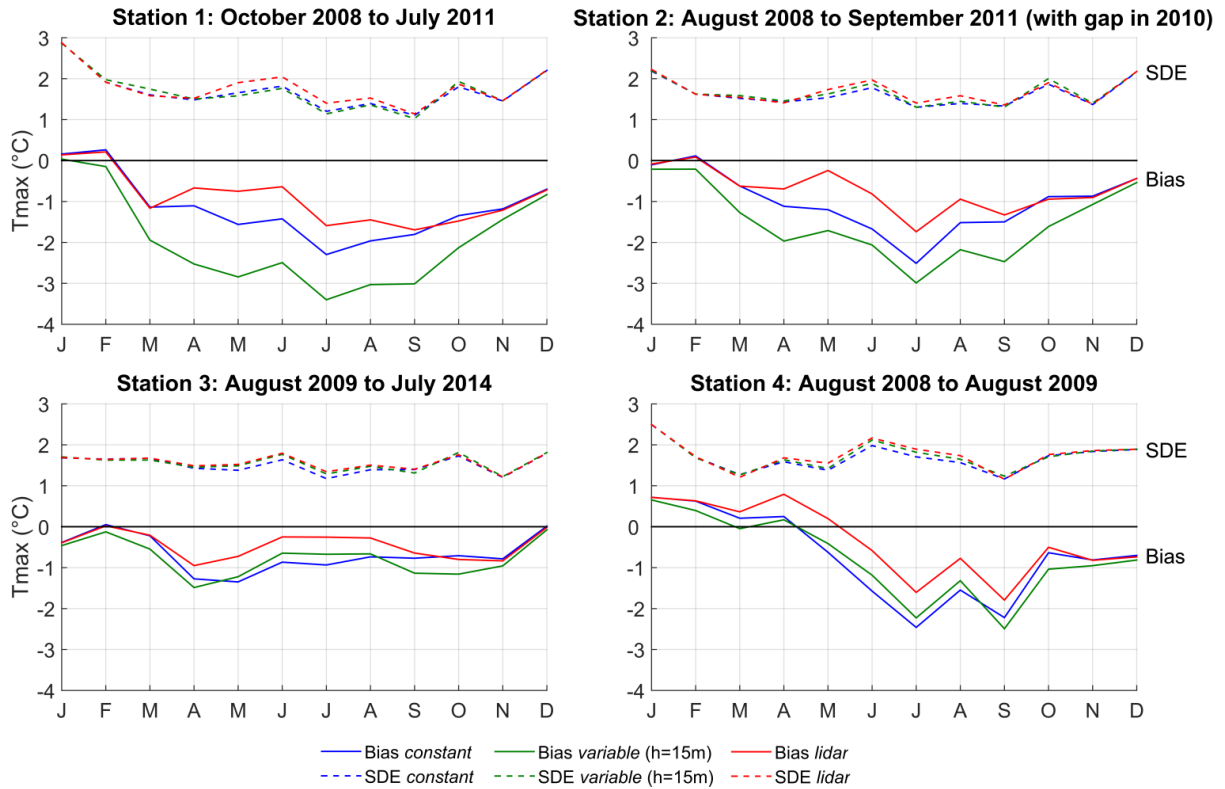


Figure 5.21: Monthly biases ( $T_{sim}-T_{obs}$ ) and standard deviation of errors of maximum daily temperature provided by the 3 methods at the 4 stations (averaged annual cycles computed on available observed data)

#### 5.6.3.4 Impact of riparian shading method on summer maximum daily temperature long profile

We analysed longitudinal profiles in summer by considering average maximum temperature between the 13<sup>th</sup> and the 31<sup>st</sup> August 2009. During this period, discharges were low ( $<7 \text{ m}^3 \cdot \text{s}^{-1}$  at the downstream-most gauging station) and the averaged maximum daily air temperature in the catchment was relatively high ( $25.9 \text{ }^\circ\text{C}$ ). The longitudinal profiles (Figure 5.22) exhibit discontinuities in the thermal signal that are driven by cool water inflows from the Conie and Aigre rivers, which drain the Beauce aquifer (Baratelli et al., 2016). Before entering the LiDAR-covered area (shown with a dashed vertical line), the *variable* method is colder than the *constant* method by more than  $2.5 \text{ }^\circ\text{C}$ . This difference decreases slowly in a downstream direction until it reverses and the *variable* method becomes warmer than the *constant*. Indeed, the three methods provide a persistent warming trend as a function of distance from source, but this trend is higher for the *variable* method ( $1.87 \text{ }^\circ\text{C}/100 \text{ km}$  compared to  $1.23 \text{ }^\circ\text{C}/100 \text{ km}$  and  $1.25 \text{ }^\circ\text{C}/100 \text{ km}$  for the *constant* and *lidar* methods respectively). This difference in longitudinal trend persists across all summers in the 2007-2014 simulation period. On average between the 13<sup>th</sup> and 31<sup>st</sup> August 2009, the *lidar* methods provide warmer  $T_{max}$  than the two other methods all along the Loir, with biases close to zero at stations 3 and 4. However,  $T_{max}$  is still underestimated by 1.6 and  $1.3 \text{ }^\circ\text{C}$  at stations 1 and 2. RMSE values are 1.99, 2.08, 1.43 and  $1.79 \text{ }^\circ\text{C}$  on S1 to S4 respectively. Figure 5.22 also shows the simulation considering the absence of riparian vegetation. The difference between this output and the *lidar* method reaches up to  $3.0 \text{ }^\circ\text{C}$  just upstream of the Conie confluence, where sensitivity analysis shows that the *lidar* method simulation

is no longer under the influence of the constant method applied upstream of the LiDAR area. This difference reaches a minimal value of 1.3 °C at the downstream-most point.

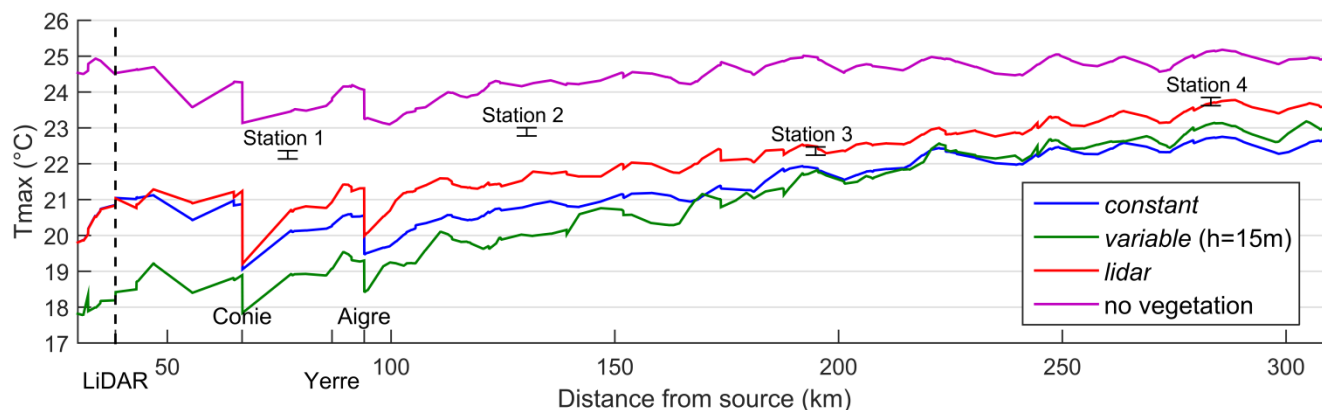


Figure 5.22: Longitudinal profile of maximum daily temperature (averaged between the 13 and the 31 August 2009) provided by the 3 methods and by a vegetation-free simulation. The vertical dashed line depicts the start of LiDAR cover. Conie, Yerre and Aigre are the main tributaries.

## 5.6.4 Discussion

### 5.6.4.1 Discrepancies in computed SF and TVF

The global overestimation of SF and TVF provided by the *variable* method compared to the *lidar* method can be explained by four key factors. First, the BD TOPO database that weights the results of the *variable* method clearly overestimates vegetation cover in relation to the LiDAR-derived values (discussed in section 5.6.3). Second, comparison of the wetted widths used in the *variable* method with LiDAR-derived river widths and with bankfull widths from BD TOPO (Figure 5.23) shows that the former are underestimated, especially upstream of ~150 km and downstream of ~250 km from the source. These width uncertainties drive an increase in SF (TVF) of 6% (4%) when averaged over the entire modelling period and 14% (9%) between 13<sup>th</sup> and 31<sup>st</sup> August 2009.

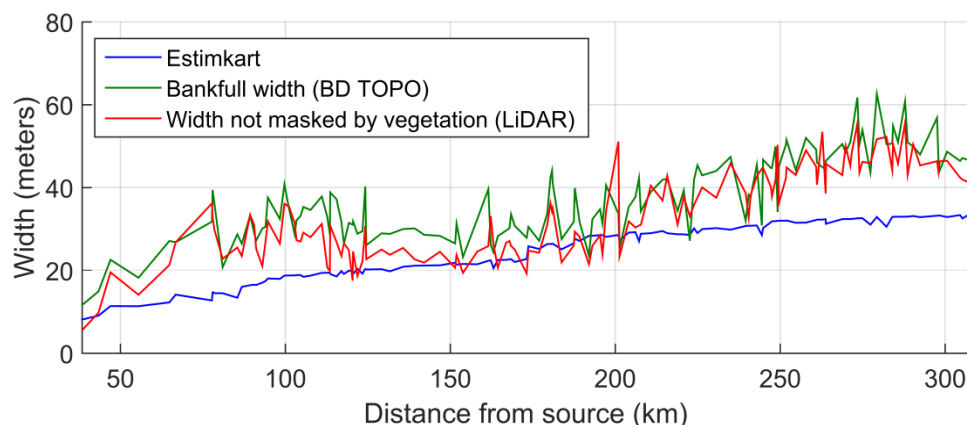


Figure 5.23: Width obtained with 3 methods on the 13-31/08/2009 period. BD TOPO width was obtained by the ratio between the polygons area and the length of the river lines inside these polygons.

Third, discrepancies may also arise from the fact that the *variable* method uses averaged stream azimuths while the *lidar* method intrinsically considers the position of vegetation in regard to the water surface. Indeed, reach azimuth impacts the timing of minimum SF (Li et al. 2012), the hourly amount of direct solar radiation and hence the maximum daily temperature (Garner et al., 2017). In order to quantify these discrepancies, we cut the Loir river GIS line in 50 m parts and compared

azimuths of these small reaches with the original T-NET reaches azimuths. The mean absolute difference is  $26^\circ$  and  $R^2$  is 0.66. Finally, the characterisation of vegetation cover and height at high resolution with the LiDAR data may not be reproducible in the *variable* method by taking an average of these data at the reach scale. Indeed, Greenberg et al. (2012) report that 28% of the change in insolation caused by removal of riparian vegetation characterised with LiDAR data could not be explained by considering averages at the reach scale. In our case, a multiple linear regression between LiDAR-derived TVF and LiDAR-derived tree height, vegetation cover and river width averaged at the reach scale provides  $R^2=0.83$ . Hence, 17% of the TVF variance cannot be explained by these three variables when averaged at the reach scale.

#### 5.6.4.2 Influence of shading routine on simulated river temperatures

In order to separate the influence of the *variable* method itself from the influence of the vegetation cover data used to drive it, we injected the vegetation cover computed from the LiDAR data (10 m buffers on each river bank for each reach) into the *variable* method. As a first step, tree height was kept at 15 m. The resulting longitudinal profile (13 to 31 August 2009 average) shows that, in this configuration, the *variable* method closely approximates the *lidar* method (Figure 5.24). The mean bias (computed against observed temperatures) between April and September is  $-1.19^\circ\text{C}$ , compared to  $-0.94^\circ\text{C}$  for the *lidar* method and to  $-1.86^\circ\text{C}$  for the *variable* method with the original vegetation cover. The median vegetation height computed from the LiDAR dataset was subsequently also injected into the *variable* method. In this case, mean bias is further reduced to  $-0.78^\circ\text{C}$ . Using the same approach with the *constant* method provides a profile that is warmer than the *lidar* method profile prior to river km 100 and colder after river km 200. Hence, a coefficient  $k=0.4$  seems to be appropriate for a river width of 25-30 m, during the month of August.

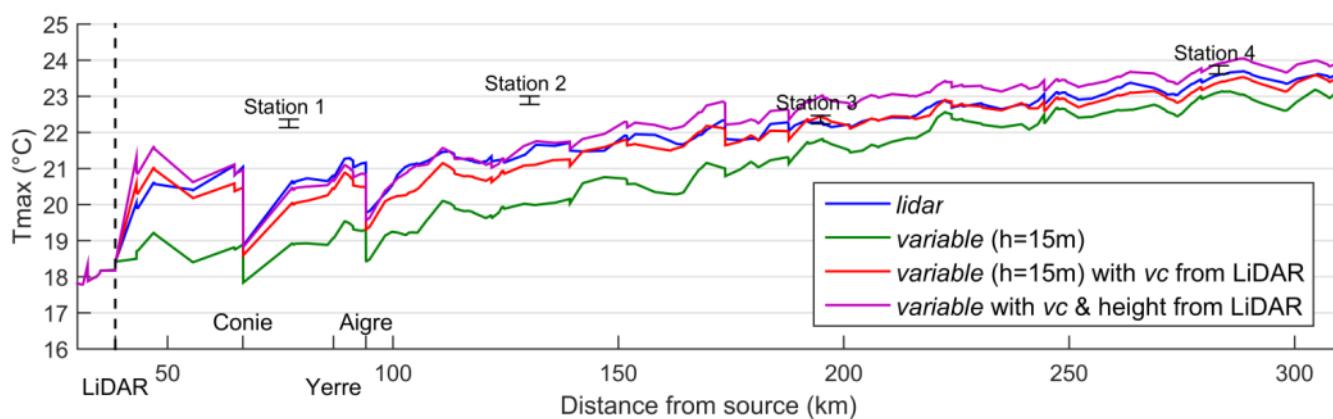


Figure 5.24: Longitudinal profile of maximum daily temperature (averaged between the 13 and the 31 August 2009) provided by injecting the *variable* method with vegetation cover (*vc*) and median height from LiDAR data. The vertical dashed line depicts the start of LiDAR cover. Conie, Yerre and Aigre are the main tributaries.

#### 5.6.4.3 Performance of T-NET model on the Loir River

Although the T-NET model of the Loir River (driven with the *lidar* method) provides relatively unbiased temperature at station 3, it still underestimates temperature at stations 1 and 2 and to a lesser extent at station 4 (Figure 5.21). Sensitivity analyses show that uncertainty about the impact of vegetation on tributaries (because of the application of the *constant* method in areas where LiDAR data do not exist) cannot fully explain the underestimation of modelled temperatures on the Loir.

Underestimation at station 1 is partly due to the underestimation of the Conie tributary. An impoundment located at the source of the river likely explains why the Conie is warmer than expected (Pedersen and Sand-Jensen, 2007; Dripps and Granger, 2013). Impoundments on several other tributaries may have the same effect and contribute to warming the Loir River and hence explain the negative biases at station 2. Station 4 is located just upstream of a small weir. There are more than 120 small weirs (height <3m) on the Loir River that may partially explain the temperature underestimation. Indeed, by increasing water depth, they increase travel time and thus sensitivity to air temperature. By decreasing water velocity, they can favour thermal stratification in summer (Torgersen et al., 2001) and since water is usually released by weir-overflow, warmer water may be selectively released. This process is not taken into account in T-NET because it only considers the longitudinal dimension. Other more complex hydrodynamic models (eg. Becker et al., 2010; Cole and Wells, 2006; Maderich et al., 2008; Deltares, 2014) would therefore be required to incorporate this process. The high temporal variability in modelled temperatures (compared to observed data) is likely due to modelled flow velocities that exceed real values. Unfortunately however, we have no observed values of travel time to compare with. Finally, it must be kept in mind that 1) computed model performances are dependent on the number of validation stations, which is limited to 4 in the current study and 2) that the T-NET model is driven with re-analysis data which are themselves subject to errors. In particular, the number of meteorological stations providing air temperature as input of the SAFRAN reanalysis in the Loir catchment is limited: approximately 10 stations are located upstream of S1 but only 2 stations located close to each other cover the rest of the basin (Quintana-Seguí et al., 2008). The density of stations is still lower for wind velocity and relative humidity but is higher for precipitations.

#### **5.6.4.4 Implications, shading methods limitations and perspectives**

Our results show that the *lidar* method has good potential for computation of SF and SVF at hourly timesteps on medium to large rivers and at large temporal and spatial scales. For small rivers (width < 10 m), whose precise location can be hard to determine using remote sensing due to obscuration by the tree canopy, the *variable* method may be more suitable, as long as it is fed with accurate vegetation cover data. Indeed, our results show that differences of modelled  $T_{max}$  can be large if the methods are used with inaccurate vegetation cover data. The quality of these input data is therefore highly important for improving stream temperature modelling. LiDAR covers of riparian zones are increasingly available, in particular because of their use for flood risk assessments. Furthermore, vegetation heights can also be obtained at the catchment scale by photogrammetric techniques (eg. Michez et al., 2017), while satellite and airborne high resolution imagery can provide accurate location of riparian vegetation (Tormos et al., 2014). These new techniques could potentially be valuable for improving future river temperature modelling efforts.

Our results show that in late August 2009, the Loir's vegetation decreases  $T_{max}$  up to 3 °C in the upstream part of the river and by 1.3 °C at the downstream-most reaches. This difference is caused by the increasing wetted width (from ~25 to ~50 m) but also by decreasing vegetation cover in the downstream direction. These quantifications of the thermal impact of riparian vegetation are likely minimum values for two reasons. First, the impact of overhanging trees was neglected (as in all methods used in this paper) (Li et al., 2012; DeWalle, 2008). Secondly, the summer transmissivity

value comes from publications studying single trees' transmissivity. However, because riparian buffers are often composed of several rows of trees, real world transmissivity values are likely to be lower, resulting in slightly cooler water temperatures (Duursma and Mäkelä, 2007; Dugdale et al., 2018). Beside this, further research is needed to validate the accuracy of shadows obtained with the *lidar* method against aerial imagery. As an example, Greenberg et al. (2012) reported an overall accuracy of 92%. Since their LiDAR data and ours were both acquired when trees were in leaf, a similar accuracy may be expected.

A wide range of values is reported in the literature regarding the cooling effect of vegetation (Moore et al., 2005), mainly for streams narrower than 10 m, for which the response of  $T_{max}$  to clear-cutting can range from 2 to 8°C (Gomi et al., 2006). For streams wider than 10 m, a modelling approach is usually used to quantify the impacts of vegetation on stream temperature. Our results are in agreement with Woltemade and Hawkins (2016), who modelled a cooling effect of vegetation of approximately 2 °C for a 14 m wide North-West/South-East oriented stream flowing in a mountainous catchment of California (low-flow conditions). A topographic shade of 17% was considered in the deforested scenario; their result would thus be higher in an environment without mountains, like the Loir catchment. Using LiDAR data, Wawrzyniak et al. (2017) modelled a cooling impact of 0.4 °C on  $T_{max}$  on a 22 km-long groundwater-fed river reach with a wetted width ranging from 50 to 120 m. The overall NNE-SSW orientation of this river is likely to decrease the impact of riparian vegetation, in comparison with the Loir, which is globally east-west orientated. Other studies show that the impact of vegetation decreases steadily as wetted width increases to about 30 m (Teti, 2006), 10 m (Davies-Colley and Quinn, 1998) and 17 to 43 m for East-West to North-South oriented streams (DeWalle, 2008). Our results suggest that the cooling effect can remain above 1 °C even for widths larger than 40 m.

Potential improvements to our *lidar* method include the incorporation of wetted widths related to the discharge. Although this is possible at small spatial and temporal scales by using a hydraulic model (Wawrzyniak et al., 2017), modelling wetted widths at regional scales can be very complex, especially without field measures of hydraulic geometry. Channel morphology from bathymetric LiDAR data may be one potential solution to this issue (eg. Hilldale and Raff, 2008; Bailly et al., 2010). Another potential improvement to our methodology relates to the use of Beer's law to model the extinction of solar rays through the tree canopy, as demonstrated by several investigations using coarse vegetation data (Sun et al., 2015; Tung et al., 2007; Sridhar et al., 2004; Lee et al., 2012). Transmission of light beneath the canopy of overhanging trees could also be modelled, but requires information or hypotheses regarding the shape of trees. When aerial imagery is available, more complex methods considering position of individual trees may be used in order to model the transmission of light beneath the canopy (Essery et al., 2008).

Finally, this paper focuses on the impact of vegetation on solar radiation and hence on maximum daily temperature (Johnson, 2004; Garner et al., 2017). Although the impact of vegetation on longwave radiation is limited on sunny days (Leach and Moore, 2010; DeWalle, 2008), view factors computed in this paper could be used to quantify the impact of vegetation on longwave fluxes at both regional scales and during a complete annual cycle. LiDAR data could also be used to model the impact of vegetation on water temperature resulting from decreased air temperature and wind

velocity engendered by the riparian canopy. Indeed, forest canopies can reduce daytime air temperature by 3 °C to more than 6 °C and wind velocity by 10-20 % in comparison with open areas (Moore et al., 2005).

### 5.7 Impact of vegetation uncertainty of tributaries on the Loir thermal profile

A limitation of the current study is that the LiDAR data was used only on the main stem of the Loir. In order to quantify the impact of the potential uncertainties regarding vegetation cover on the tributaries and on the first orders of the Loir (where LiDAR data are not present), we ran T-NET with both zero and full vegetation on these area (*variable* method with a vegetation height of 15 m) (Figure 5.25). Before entering the LiDAR area (shown with a vertical line), the difference related to the absence/presence of vegetation on the main stem of the Loir is up to 6.5°C. After entrance in the LiDAR area, temperatures converge after ~26 km. Confluences with the Conie, the Aigre and the Braye tributaries raise the range of this sensitivity analysis (green and red lines) to 3.2, 2.1 and 1.5°C respectively. Outside of these influences, this range is limited to 1°C, with occasional rises up to 1.3°C. This sensitivity analysis being made with extreme values (no/full vegetation cover), it shows that the shadow model applied on the tributaries has a limited impact on the  $T_{max}$  modelled on the Loir River, except for reaches located within 10 km downstream of a significant tributary.

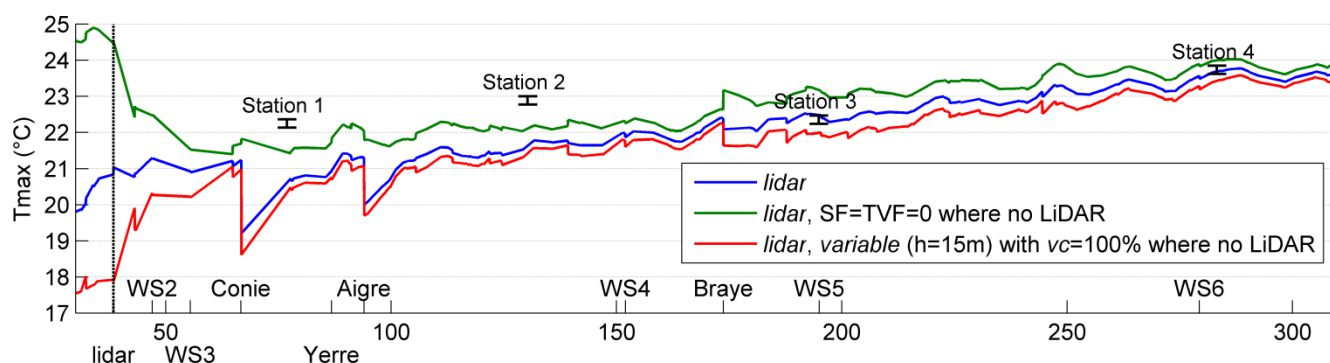


Figure 5.25: Longitudinal profile of the maximum daily temperature on the Loir River averaged from 13 to 31 August 2009. WS are the subwatersheds, numbers are the distances from source (km), and names are the main tributaries

### 5.8 Additional results on $T_{mean}$ , $T_{min}$ and diel amplitudes

On the 4 stations located on the Loir River, the simulated  $T_{min}$  are colder than observations by more than 2°C in summer (Table 5.4). Like for  $T_{max}$ , the *lidar* method improves the mean biases computed between April and September on  $T_{min}$ , although in a lesser extent. The improvement is of 0.28°C compared to the *constant* method. The *variable* method is the most negatively biased in both warm and cold periods. The standard deviations of errors are very similar for the three simulations.

Table 5.4: Model performance criteria for minimum daily temperature, averaged for the 4 stations located on the Loir River from April to September and from October to March (°C)

| Tmin                    | April to September |      |      | October to March |      |      |
|-------------------------|--------------------|------|------|------------------|------|------|
|                         | Bias               | SDE  | RMSE | Bias             | SDE  | RMSE |
| Constant method         | -2.75              | 1.45 | 3.12 | -1.30            | 1.73 | 2.17 |
| Variable method (h=15m) | -3.19              | 1.45 | 3.52 | -1.53            | 1.78 | 2.36 |
| Lidar method            | -2.47              | 1.49 | 2.91 | -1.31            | 1.74 | 2.19 |

As expected, biases of modelled  $T_{mean}$ , as well as the differences of accuracy between methods, are between those computed on  $T_{min}$  and  $T_{max}$ . Bias is improved by 0.47°C compared to the *constant* method.

**Table 5.5: Model performance criteria for mean daily temperature, averaged for the 4 stations located on the Loir River from April to September and from October to March (°C)**

| Tmean                          | April to September |      |      | October to March |      |      |
|--------------------------------|--------------------|------|------|------------------|------|------|
|                                | Bias               | SDE  | RMSE | Bias             | SDE  | RMSE |
| <i>Constant</i> method         | -2.07              | 1.47 | 2.55 | -0.82            | 1.82 | 2.00 |
| <i>Variable</i> method (h=15m) | -2.54              | 1.48 | 2.97 | -1.09            | 1.87 | 2.17 |
| <i>Lidar</i> method            | -1.66              | 1.55 | 2.28 | -0.84            | 1.83 | 2.02 |

The *constant* method provides the diel amplitudes that are the less biased on the April-September period (Table 5.6). Indeed, modelled amplitudes are basically too high. The *variable* and the *lidar* methods, by making SF variable, increase the diel amplitude, which depart further from observed values. Again, the different methods have a very low impact on diel amplitudes in the cold period from October to March.

**Table 5.6: Model performance criteria for diel amplitudes, averaged for the 4 stations located on the Loir River from April to September and from October to March (°C)**

| Diel amplitudes                | April to September |      |      | October to March |      |      |
|--------------------------------|--------------------|------|------|------------------|------|------|
|                                | Bias               | SDE  | RMSE | Bias             | SDE  | RMSE |
| <i>Constant</i> method         | 1.31               | 0.81 | 1.54 | 0.99             | 0.94 | 1.37 |
| <i>Variable</i> method (h=15m) | 1.32               | 0.87 | 1.59 | 0.93             | 0.96 | 1.35 |
| <i>Lidar</i> method            | 1.63               | 0.97 | 1.90 | 0.99             | 0.96 | 1.38 |

## 5.9 Improvement of the longwave downward radiation characterisation on the Loir River thanks to LiDAR data

As suggested in the discussion of section 5.6.4.4, the view factors computed thanks to the LiDAR data can be used to improve the characterisation of downward longwave radiation. Similarly to the approach used by Cox and Bolte (2007) and by Hebert et al. (2011), we will consider that the vegetation is at the atmospheric temperature :

$$LW = LW_{SAFRAN} \cdot (SVF + \tau \cdot TVF) + (TVF - \tau \cdot TVF) \cdot \epsilon_{veget} \cdot \sigma \cdot (T_{air} + 273.15)^4$$

where  $LW_{SAFRAN}$  is the longwave radiation provided by the SAFRAN reanalysis ( $W \cdot m^{-2}$ ), SVF is the sky view factor, TVF the tree view factor ( $=1-SVF$ ),  $\epsilon_{veget}$  is the emissivity of vegetation, fixed at 0.95 according to Cox and Bolte (2007),  $\sigma$  is the Stefan-Boltzmann constant ( $5.67 \times 10^{-8} W \cdot m^{-2} \cdot K^{-4}$ ). The term  $\tau \cdot TVF$  added and subtracted to each component represents the porosity in the tree foliage. The *variable* method is applied on the reaches without LiDAR data with a tree height of 15 m.

Results show that the impact of riparian vegetation on the longwave radiation is the most important from April to September and on Tmin (Figure 5.26 a). Indeed, the impact is proportional to the mean temperature of water and air and the relative influence is more important when solar radiation is null. As expected, the impact is also the most important on the upstream stations where river width is the smallest. Biases of Tmin are increased by 0.4 to 0.7 °C in summer, which bring them closer to zero. Diel amplitudes are also reduced by 0.2 to 0.5 °C (Figure 5.26 b).

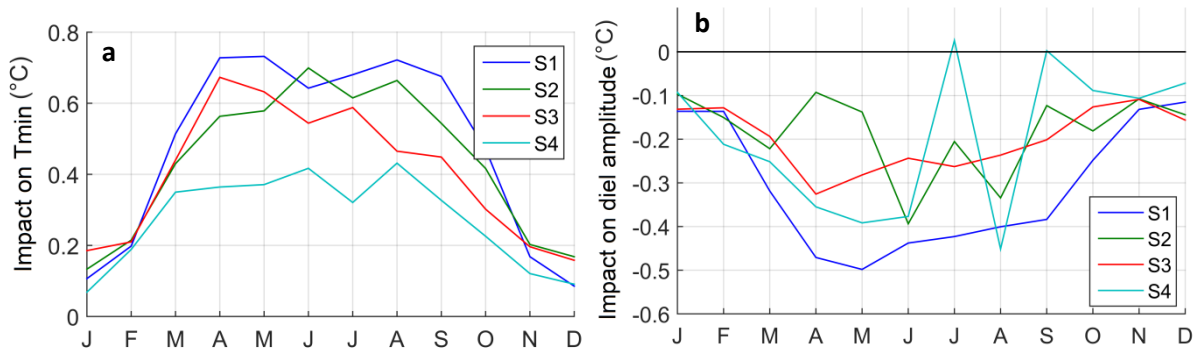


Figure 5.26: Mean annual cycle of the impact of riparian vegetation on the longwave downward radiation at the 4 Loir's monitoring stations (2008-2014) (a) minimum daily temperature (b) diel amplitude.

In average on the 13-31/08/2009 period, the thermal impact of riparian vegetation on downward longwave radiation ranges from +0.2 °C to +1 °C on Tmin (Figure 5.27 a, green line compared to red), with only a small trend of 0.17 °C/100 km in the downstream direction (computed from river km 100). The total impact of riparian vegetation (solar and longwave radiation considered) on Tmin ranges from -1.5 °C (river km 80) to -0.2 °C (river km 290). The total impact on Tmax is not much changed compared to the impact computed only on solar radiation (section 5.6.3.4): it evolves from -2.8 °C just upstream of the Conie confluence to -1.1 °C at the downstream-most reach (Figure 5.27 b).

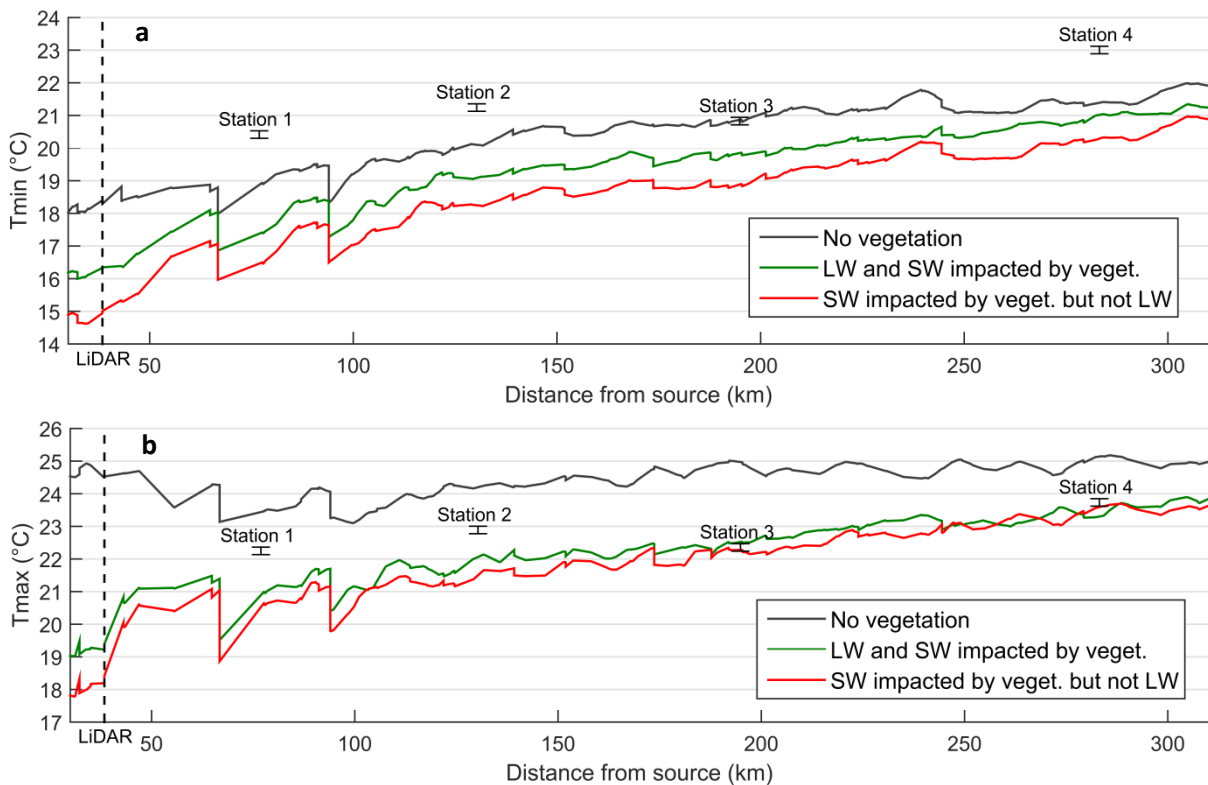


Figure 5.27: Longitudinal profile on the Loir and on average on the 13-31/08/2009 period with and without considering the impact of vegetation on the longwave downward radiation (a) on minimum daily temperature (b) on maximum daily temperature. SW = shortwave (solar) radiation; LW = longwave downward radiation.

The temporal evolution of the impact at the downstream-most reach is shown at Figure 5.28. This impact is proportional to the solar radiation but also to the difference between the surface air temperature and the air temperature at higher altitude, which, along with cloudiness, has an influence on the atmospheric downward radiation modelled in SAFRAN. This gradient is often higher

in spring, and that could explain the peaks observed in April 2010 and 2011. The influence of cloudiness on the atmospheric longwave radiation is likely to explain why the daily evolution of the total riparian impact is so noisy.

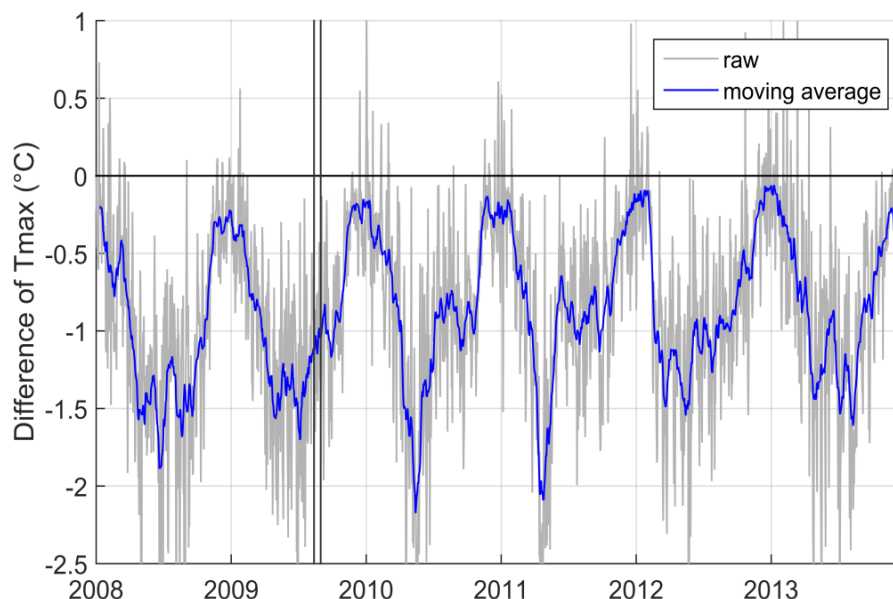


Figure 5.28: Temporal evolution of the total (solar and longwave radiation) impact of riparian vegetation at the downstream-most Loir's reach of the LiDAR area. Vertical lines delimit the 13-31/08/2009 period. Moving average is over 21 days.

In the end, accuracy of the 4 metrics (Tmax, Tmean, Tmin and diel amplitude) are improved by more than 0.1 °C compared to a simulation where riparian impact on longwave radiation is not taken into account, both in summer and winter (Table 5.7). Diel amplitudes are improved by 0.3 °C on average on the April-September period.

Table 5.7: Model performance criteria (raw and compared to a simulation where riparian vegetation impact on longwave downward radiation is null), averaged for the 4 stations located on the Loir River from April to September and from October to March (°C). Green denotes improvement by more than 0.1 °C. All methods rely on LiDAR data where available.

|            | April to September |       |       | October to March |       |       |
|------------|--------------------|-------|-------|------------------|-------|-------|
| Raw values | Bias               | SDE   | RMSE  | Bias             | SDE   | RMSE  |
| Tmin       | -2.04              | 1.45  | 2.53  | -1.16            | 1.64  | 2.02  |
| Tmean      | -1.38              | 1.51  | 2.06  | -0.79            | 1.70  | 1.89  |
| Tmax       | -0.75              | 1.77  | 1.93  | -0.37            | 1.91  | 1.96  |
| Ampli      | 1.29               | 1.04  | 1.68  | 0.79             | 0.89  | 1.21  |
| Change     |                    |       |       |                  |       |       |
| Tmin       | 0.57               | -0.08 | -0.51 | 0.24             | -0.11 | -0.23 |
| Tmean      | 0.43               | -0.07 | -0.35 | 0.16             | -0.11 | -0.17 |
| Tmax       | 0.27               | -0.10 | -0.21 | 0.08             | -0.12 | -0.13 |
| Ampli      | -0.30              | -0.10 | -0.29 | -0.15            | -0.08 | -0.16 |

## 5.10 Validation with the thermal infrared imagery in summer and winter

### 5.10.1 Thermal infrared imagery acquisition and treatment

Two thermal infrared (TIR) imageries were acquired by helicopter on 94 km of the Loir River during September 2014 and February 2015 (Lalot et al, in preparation). They will be compared to T-NET's output on the Loir River, obtained with the most advanced version of the model available in 2014-2015, i.e. with variable albedo and transmissivity, the use of Helioclim data, and the *lidar* method

applied on both solar and longwave radiation. Table 5.1 summarises the weather and hydrologic conditions at times of acquisition.

**Table 5.1: Conditions occurring when TIR imagery was acquired. Meteorological conditions come from the Météo-France weather station of Châteaudun. Discharge is given for the downstream most gauging station on the Loir (Durtal), where mean interannual discharge is 31.7 m<sup>3</sup>.s<sup>-1</sup>)**

|        | Time                          | Sky   | Daily mean air temp. (°C) | Daily mean wind velocity (m.s <sup>-1</sup> ) | Loir discharge at Durtal (close to S4) (m <sup>3</sup> .s <sup>-1</sup> ) |
|--------|-------------------------------|-------|---------------------------|---|---|
| Summer | 10/09/2014 15h28 to 16h37 UTC | clear | 16.2                      | 3.7   | 17.2  |
| Winter | 5/02/2015 10h41 to 11h55 UTC  | clear | 1.3 °C                    | 5.7   | 40.4  |

The resolution of images is ~1 m and the spectral range goes from 7.5 to 14 μm. Pixels located in a buffer of 2 m around the river centreline were extracted. The temperature was then averaged by 100 m long sections from the water courses (Lalot et al, in preparation).

Four (twelve) temperature data loggers (accuracy of ±0.1°C) were placed in the river in summer (winter), to measure in-situ water temperature. TIR images measure the skin water temperature. This temperature is obtained from the measurement of the spectral radiance, using Planck’s law and considering a water emissivity of 1. On average, the thermal imagery temperature underestimated by 2°C the in-situ Tw during the winter campaign and overestimated it by 0.8°C during the summer campaign. In winter, a constant value (2°C) was therefore added to the longitudinal temperature profile. In summer, no modifications to the longitudinal temperature profile were made, considering the low number of in-situ measurements.

### 5.10.2 Results of the comparison of the lidar method with TIR profile in summer and winter

In summer, the thermal profile modelled by T-NET is broadly colder than the TIR profile by 2 °C to 1.4 °C (Figure 5.29). It can be explain by both the TIR overestimation by ~0.8 °C, as well as by the tendency of T-NET to underestimate Tw in this area of the Loir. The cold impact of the Conie and Aigre are well found in both profiles. In situ measurements show that the cooling impact of the Conie may be underestimated on the TIR profile. Indeed, the cool water may flow beneath the warmer water. Two Tw variations located between the Conie and the Aigre confluences are not seen by T-NET, because its spatial resolution is too coarse. T-NET simulates properly the general warming trend observed on the TIR profile.

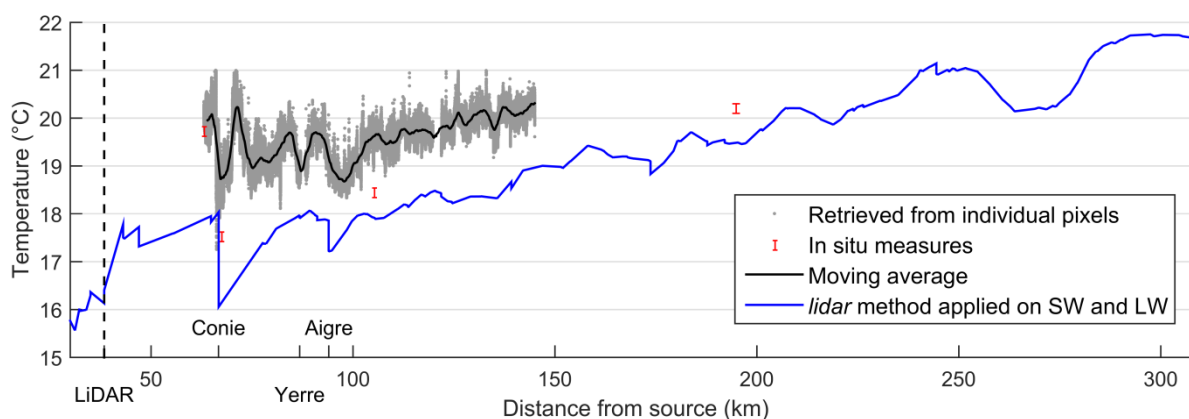


**Figure 5.29: Temperature modelled with the lidar method and observed on the thermal imagery the 10 September 2014 at 16h UTC**

In winter, the thermal profile modelled with T-NET is colder than in situ observations (Figure 5.30). T-NET overestimates the warming impact of both the Conie and the Aigre. As a consequence, the longitudinal  $T_w$  gradients are inverted between Conie and Aigre confluences. After river km 125, the TIR profile increase, maybe due to an influence of Vendôme town.

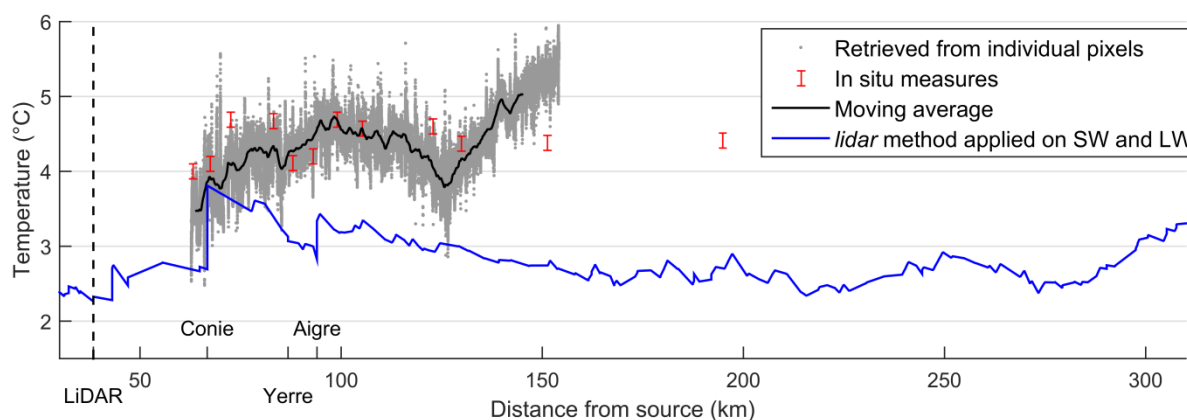


Figure 5.30: Temperature modelled with the *lidar* method and retrieved from thermal imagery and in-situ observations on the 5 February 2015 at 11h UTC

## 5.11 Conclusion

The main goal of this chapter was to understand the influence of using a LiDAR-derived digital surface model to quantify the impact of riparian vegetation on solar and then on longwave radiation, on 270 km of the Loir River. Three preliminary modifications were brought to the model. Making the albedo variable leads to very small changes on  $T_w$  signal ( $-0.06$  °C on average). The implementation of a vegetation transmissivity that follows the phenology provides a warming effect that is more important on the small orders, with a maximum in March ( $T_{max} +1.4$  °C). Hence, summer biases are improved for stations located far from sources (with high thermal sensitivity). Because diel amplitudes are increased, their accuracies are mainly decreased. Finally, using global solar radiation provided by Helioclim instead of SAFRAN does not improve accuracy as much as expected (warming of  $0.12$ °C on  $T_{max}$  and RMSE not changed).

When applied only on the solar radiation, we demonstrated that the use of LiDAR data improves the mean biases of simulated  $T_w$  ( $T_{max}$ ,  $T_{mean}$  and  $T_{min}$ ) in summer, compared to two other simpler methods for computing the effects of riparian shading at large scales. However, it did not improve the standard deviation of errors, which are more influenced by the hydraulic parameters.

The monthly-averaged difference in  $T_{max}$  computed by the various shading methods can reach up to 2 °C at the upstream-most station and 1 °C at the downstream-most station. However, this difference is mainly due to the overestimation of vegetation cover in the dataset used to compute shadow and view factors in the non-*lidar* methods. Indeed, injection of vegetation cover extracted from the LiDAR data into the shading method of medium complexity (*variable method*) decreased the largest difference at the upstream-most station to 0.8 °C, suggesting that this method is sufficient for the computation of SF and VF provided that it is supplied with accurate (high-resolution) data pertaining to vegetation cover. Improving the quality of riparian vegetation data should therefore be a priority for improving stream temperature modelling at the regional scale. The simplest method (*constant method*) may be appropriate to model mean daily temperature for a given period of the year, as long as vegetation cover is weighted with a coefficient depending on the river width.

The effect of vegetation on downward longwave radiation was then added. It is a warming effect which is more important on Tmin than Tmax and is proportional to stream temperature and probably also to the vertical thermal gradient of the atmosphere. Tw are thus increased while diel amplitudes are decreased. Including the total effect of vegetation on solar and longwave radiation with the *lidar* method provides thus the best results on the 4 Loir's stations. On an interannual average (2007-2014), this effect can be high in spring and fall and is rarely weaker than -1 °C between April and September on the downstream-most Loir's reach (Figure 5.31).

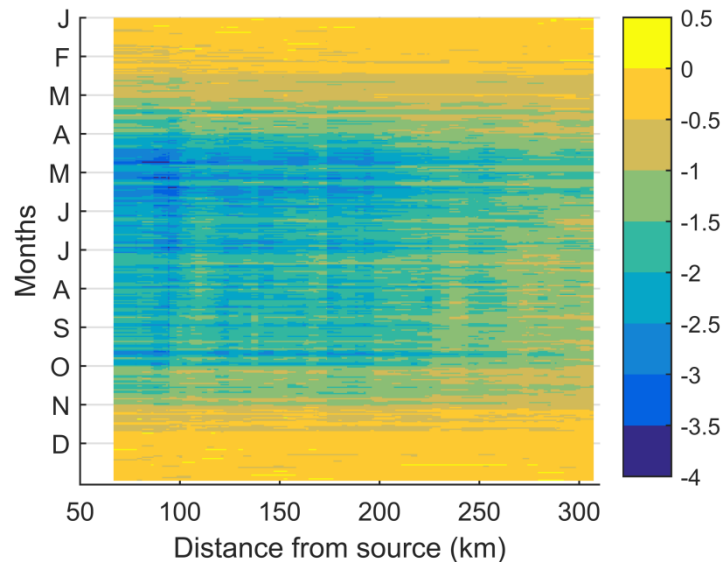


Figure 5.31: Total (solar and longwave radiation) impact of riparian vegetation on the Loir's maximum daily Tw using the *lidar* method (average on 08/2007-07/2014)

Finally, validation of the most advanced version of T-NET with fine scale thermal imagery confirmed its tendency of underestimation on the Loir. In summer, T-NET reproduces correctly the large-scale longitudinal trend. In winter, the impact of tributaries is overestimated and the longitudinal trend is well reproduced on one third of the profile.

The application and comparison of methods achieved in this chapter will improve understanding of the strengths and limitations of other existing stream temperature models. Enhancing the models' ability to simulate the impact of riparian vegetation is of key importance for the development of climate change adaptation measures and understanding the fundamental processes responsible for spatio-temporal variability of river temperature.

# Chapter 6: Impact of groundwater fluxes modelled with the hydrological-hydrogeological model Eaudyssée on the Loir catchment

## 6.1 Résumé en français

Les flux de nappe ont une importance majeure sur la Tw. En effet, l'eau de nappe se trouvant à une température relativement stable tout au long de l'année, son passage vers la rivière a tendance à tamponner Tw (refroidir en été et réchauffer en hiver). Les modèles de température prennent souvent en compte ce facteur mais avec des modélisations de flux effectuée à la résolution du sous-bassin (comme cela est fait dans la version standard de T-NET avec EROS). Dans ce chapitre, les flux de nappe modélisés au pas de temps journalier et sur des mailles de 1 km par le modèle Eaudyssée (Baratelli et al., 2016) sont injectés dans T-NET sur la période 08/2008-07/2013 et sur le bassin du Loir uniquement, car Eaudyssée a été appliqué sur les grands aquifères uniquement (Figure 6.1). Le modèle Eaudyssée a la particularité d'utiliser une hauteur de rivière variable et Baratelli et al. (2016) ont montré que cette prise en compte avait une influence importante sur la caractérisation des flux de nappe journaliers. En moyenne, l'exfiltration (nappe->rivière) prédomine sur la plus grande partie du bassin (Figure 6.2), alors qu'une infiltration moyenne est modélisée sur les premiers kilomètres de certains affluents et sur l'amont du Loir. Les flux modélisés par Eaudyssée sont beaucoup plus variables que ceux modélisés par EROS, et plus important, sauf pour 4 stations sur les 17 évaluées. Par conséquent, les Tw sont généralement augmentées en hiver et diminuées en été, avec des changements plus faibles au printemps et à l'automne (Figure 6.7). Comme cela s'applique à la fois à des stations surestimées et sous-estimées en été, il en résulte que la précision des températures moyennes journalières est significativement améliorée pour 5 stations et dégradée pour 6 stations, en été. Les amplitudes journalières sont généralement diminuées et donc améliorées. En moyenne sur la période 13-31/08/2009, l'impact des flux de nappes tels que modélisés par Eaudyssée, en comparaison avec une simulation sans flux de nappe, varie entre  $-0.52$  °C et  $-1.2$  °C pour la température moyenne sur la majorité du Loir, avec un pic à  $-2.8$  °C au km 22 (Figure 6.13). L'injection de flux de nappes modélisés à cette résolution et à l'échelle régionale dans un modèle de température est inédite et démontre l'importance d'une caractérisation précise de ces flux.

## 6.2 Context and objective

A part of the temperature models that were previously applied on a river network at the regional scale and at hourly or daily time step do not take into account groundwater fluxes in the thermal budget (Wu et al., 2012; Haag and Luce, 2008). Other models can take them into account at the sub-basin scale (Chen et al., 1998a; Du et al., 2017; Cheng and Wiley, 2016; Battin et al., 2007; Ficklin et al., 2012). However, none of them rely on a hydrogeological modelling at high resolution. At small catchment scale in Idaho (231 km<sup>2</sup>), Loinaz et al. (2013) applied the MIKE SHE/MIKE 11 model at a spatial resolution of 300 m. It has a hydrogeological module that resolves the Darcy equation in 3 dimensions. The transfer to the nearest rivers occurs when the piezometric level is above a specified elevation. Essaid and Caldwell (2017) also applied a coupled surface water/groundwater flow model

on a 640 km<sup>2</sup> catchment of Montana, with a spatial resolution of 200 m, in order to understand the impact of irrigation on stream temperature.

The goal of this chapter is to analyse to what extent the injection of groundwater fluxes modelled by the coupled hydrological/hydrogeological model Eaudyssée (Baratelli et al., 2016) at a resolution of 1 km improves T-NET accuracy. A secondary goal is to quantify the actual impact of groundwater fluxes on water temperature of the Loir, in summer. Data provided by Eaudyssée will be characterised, and results in water temperature will be compared with the simulation using EROS groundwater fluxes, as well as with a simulation with no groundwater flux.

### 6.3 Methods

The results of chapter 4 show that temperature is overestimated by more than 1°C in summer at 5 stations on the Maine catchment (2 stations of the Loir catchment: Boulon 23 and Yerre 47). This may be due to the underestimation of groundwater fluxes that cool the river in summer. The characterisation of these fluxes can be improved by injecting into T-NET the results of the Eaudyssée model. Eaudyssée was applied on 38000 km<sup>2</sup> of the Loire catchment, downstream of the confluence between the Loire and the Allier rivers, at the spatial resolution of 1 km and the temporal resolution of 1 day, on the 1996-2013 period (Baratelli et al, 2016). Groundwater fluxes were only output for streams draining more than 50 km<sup>2</sup> and located above the 3 main aquifers: the Beauce limestone aquifer, the Cretaceous chalk layer, and the Cenomanian sands (Figure 6.1). Hence, data are available on the Loir catchment and on a small part of the Huisne catchment. For this reason, this chapter will focus on the 2008-2013 period and on the Loir catchment, where all Tw monitoring stations except Tusson 8 can be linked to an Eaudyssée cell (17 stations).

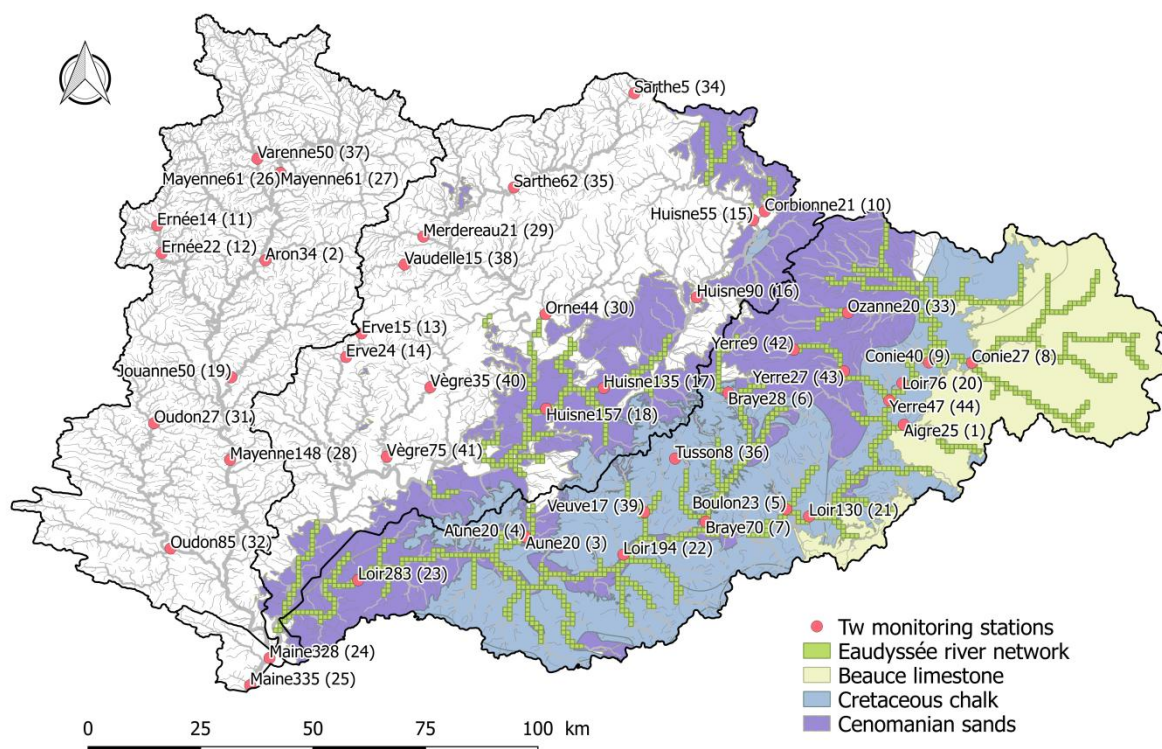


Figure 6.1: Eaudyssée river network on the Maine catchment

### 6.3.1 The Eaudyssée model and resulting data

Eaudyssée is a surface/subsurface model that computes both the hydrologic and the hydrogeologic transfers at the resolution of 1 km and a daily temporal resolution. It computes the variation of 6 parameters from precipitations and potential evapotranspiration input data: runoff, river flow, river depth, flow in the unsaturated zone and flow in the saturated zone. The 3 aquifers are modelled as 3 layers with horizontal flows, while flows are considered vertical in the aquitards (present below the 3 first layers). The river network was obtained from DEM analysis and was resampled at the 1 km resolution. The stream water level is variable and was obtained with a simplified Manning-Strickler equation. As input of this equation, the longitudinal slope is extracted from a 25 m resolution DEM. The river width was taken as a constant value from the SYRAH database (Valette et al., 2012), where width ranges from 1.5 to 58 m on the Loir River. The riverbed elevation was obtained by combining the DEM extraction and the application of the Manning-Strickler equation to a bankfull situation. The roughness coefficient was calibrated against observed discharge. The stream-aquifer exchange is proportional to the difference between the piezometric level and the stream water level, weighted by a conductance parameter which is linked to the horizontal hydraulic conductivity. Like EROS, Eaudyssée is forced by precipitation and potential evapotranspiration provided by SAFRAN reanalyses at the daily time scale and 8 km resolution. Observed time series of discharge as well as piezometric and river level are used to calibrate and validate the model. Water withdrawals are taken into account (Baratelli et al., 2016).

### 6.3.2 Eaudyssée stream-aquifer exchange data

The resulting average stream-aquifer exchanges on the 08/2008-07/2013 period are mapped at Figure 6.2. Exfiltration (aquifer to river) is observed on most part of the river network. Infiltration occurs mainly on the upstream part of the Loir and at the upstream reaches of some tributaries. Rivers flowing upon the Beauce limestone aquifer often have exchanges values close to zero because they are dry most of the time (Conie, Aigre). An extreme and outlier value of  $0.552 \text{ m}^3 \cdot \text{s}^{-1} \cdot \text{km}^{-1}$  occurs on the Loir, upstream of the confluence with the Conie.

The correlation of the mean exchanges provided at the cells located at the 17 monitoring stations with the corresponding thermal sensitivities equates 0.29, and 0.11 when correlated with the  $Q_{\min}/Q_{\max}$  ratio. When excluding the Conie 40 station, where the mean groundwater flux is very high ( $0.1 \text{ m}^3 \cdot \text{s}^{-1} \cdot \text{km}^{-1}$ ), the correlation coefficients reach 0.36 for the thermal sensitivity and -0.59 for  $Q_{\min}/Q_{\max}$ .

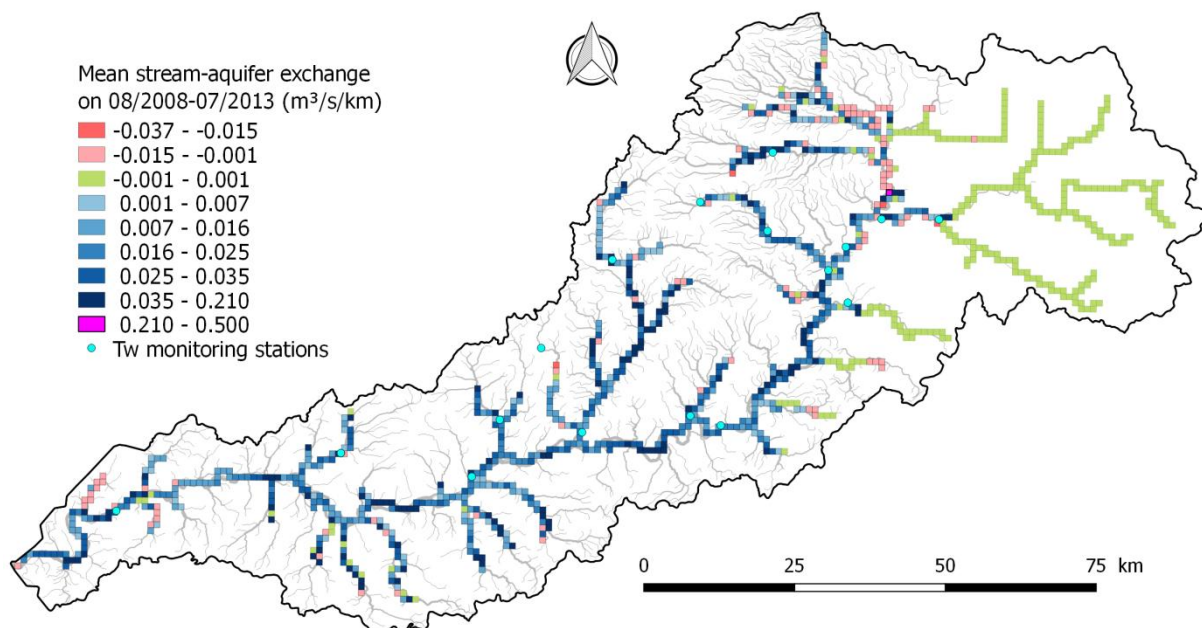


Figure 6.2: Mean stream-aquifer exchanges on 08/2008-07/2013. Values are negative when river is drained by the aquifer

The median of exchanges on the whole period is  $0.008 \text{ m}^3$  and 57% of the values are strictly positive (up to  $1.08 \text{ m}^3 \cdot \text{s}^{-1} \cdot \text{km}^{-1}$ ), 38% are null, and hence 5% are negative, whose 2% are at the minimum value of  $-0.1 \text{ m}^3 \cdot \text{s}^{-1} \cdot \text{km}^{-1}$ . This minimum value is due to the bounding of infiltration values that is applied when the groundwater level is well below the river (Baratelli et al., 2016). The distribution of exchanges is quite similar between seasons (Figure 6.3), although the probability of null exchange is higher in summer and fall because more cells are dry. The probability of infiltration is higher in winter since it is driven by the water level.

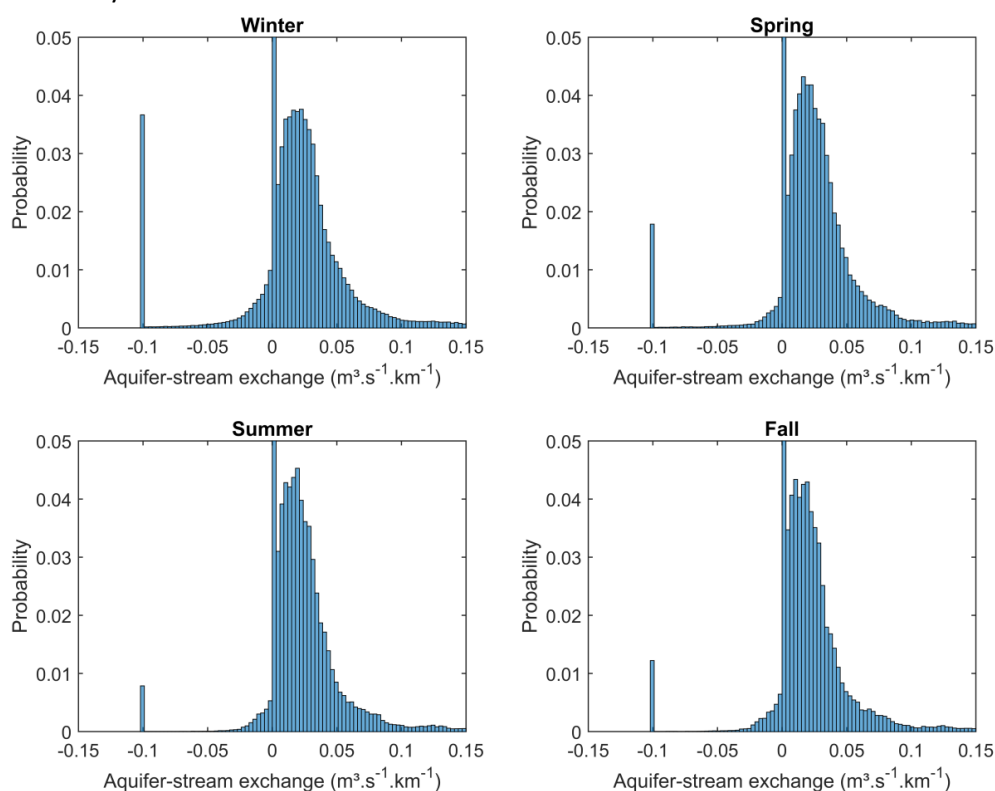


Figure 6.3: Histogram of the values on the Loir catchment and on the 08/2008-07/2013. Probability for the zero value are 0.36, 0.37, 0.42 and 0.44 in winter, spring, summer and fall respectively

Stream-aquifer exchanges can be very variable with the time, since they are related to water depth. Large fluctuations around zero occur when the river water level is close to the groundwater level. Indeed, when an hydrologic event occurs, the delay between the rise of the river depth and the groundwater level entertain a cycle of infiltration followed by exfiltration (Baratelli et al., 2016). In late August 2009, this process occurs for the Loir downstream-most station (Figure 6.4). High infiltration occurs at Conie 27, while exfiltration occurs at Conie 40. Flux is null for Aigre 25 and between 0 and  $0.05 \text{ m}^3 \cdot \text{s}^{-1} \cdot \text{km}^{-1}$  for the other cells.

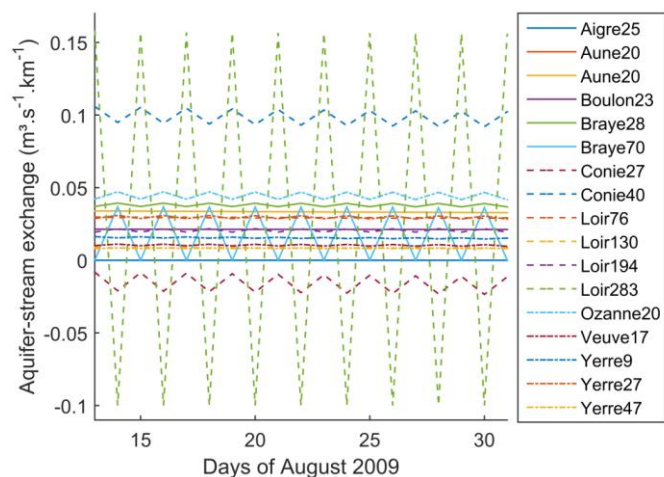
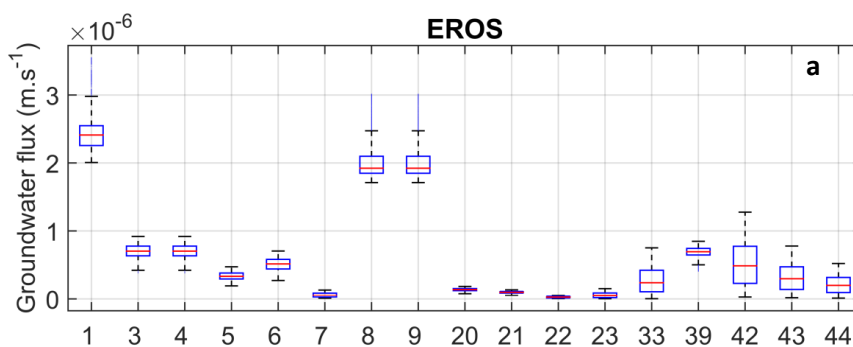


Figure 6.4: Stream-aquifer exchanges at the 17 Tw monitoring stations linked to an Eaudyssée mesh on the 13-31 August 2009 period.

In order to compare Eaudyssée groundwater fluxes with EROS, we will consider the fluxes computed on the T-NET reaches where Tw monitoring stations are localised. Because it is the variable that is output by T-NET, we will compare  $Q_G/A$  where  $Q_G$  is the groundwater flux ( $\text{m}^3 \cdot \text{s}^{-1}$ , always positive) and  $A$  is the cross sectional area ( $\text{m}^2$ , unchanged between simulations). On the full 08-13 period, the Eaudyssée groundwater fluxes are much more variable than EROS groundwater fluxes (Figure 6.5). Average values are also much higher (up to 30 times); except for Aigre 25, Conie 27 and 40 and Yerre 9 (n° 1, 8, 9, 42) where mean EROS fluxes are higher than in Eaudyssée (by maximum 2x and 16x for Yerre 9).



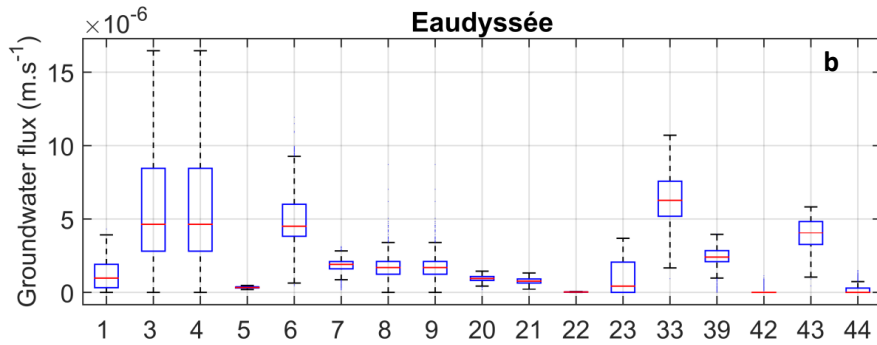


Figure 6.5: Groundwater fluxes variability on the 2008-2013 period and at the 17 stations linked to an Eaudyssée mesh. Variable plotted is  $Q_G/A$  where  $Q_G$  is the groundwater flux ( $m^3.s^{-1}$ ) and  $A$  is the cross sectional area ( $m^2$ ). (a) EROS (b) Eaudyssée.

Also on average on the 13-31 August 2009, Eaudyssée provides groundwater fluxes that are significantly higher and more variable than EROS (Figure 6.6).

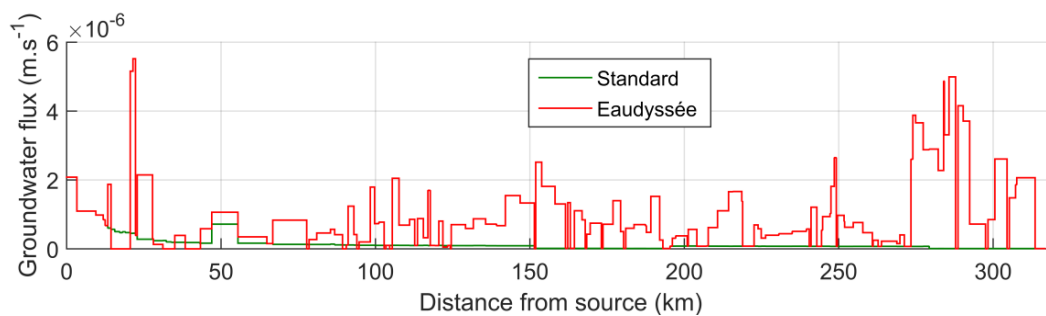


Figure 6.6: Longitudinal profile of the groundwater fluxes averaged on the Loir River and on the 13-31 August 2009. Variable plotted is  $Q_G/A$  where  $Q_G$  is the groundwater flux ( $m^3.s^{-1}$ ) and  $A$  is the cross sectional area ( $m^2$ )

### 6.3.3 Method to inject the Eaudyssée output into T-NET

Each T-NET reach belonging to the main rivers modelled in Eaudyssée was manually linked to an Eaudyssée mesh. When a T-NET reach is linked to several Eaudyssée cells, the sum of the fluxes is considered. Only the positive (exfiltration) fluxes are considered because the infiltration has no impact on the water temperature. Because Eaudyssée data are in  $m^3.s^{-1}.km^{-1}$ , data are weighted by the length of the T-NET reach (in km) in order to get the groundwater flow  $Q_G$  (see Table 4.1). When a T-NET reach is not linked with an Eaudyssée cell, the EROS groundwater fluxes are taken.

## 6.4 Results in water temperature

### 6.4.1 Annual cycle at Tw stations

The difference of monthly biases of mean daily  $T_w$  between the simulation using Eaudyssée and the standard simulation (using EROS) are shown at Figure 6.7. For a majority of stations (13), temperatures are increased in winter and decreased in summer. This is only due to the higher groundwater fluxes modelled by Eaudyssée, since the computation of groundwater temperature was not changed (equates the moving average of  $T_a$  on the last year). The maximal difference occurs at Braye 28, with  $+2.4\text{ °C}$  in winter and  $-2.8\text{ °C}$  in summer. Impact is not significant on Yerre 9. As expected given the analysis of groundwater flux differences, the behaviour is opposite for Aigre 25, Conie 27 and 40. Conie 27 and 40 are located on the same T-NET reach, where both ex- and infiltration occur; processes may thus compensate. Results on  $T_{max}$  and  $T_{min}$  are very similar. As a consequence of the changes, the biases on  $T_{mean}$  stay negative by more than  $-1\text{ °C}$  for 12 stations in

summer, and they become very variable in winter (Figure 6.8b to be compared to the original bias on Figure 6.8a).

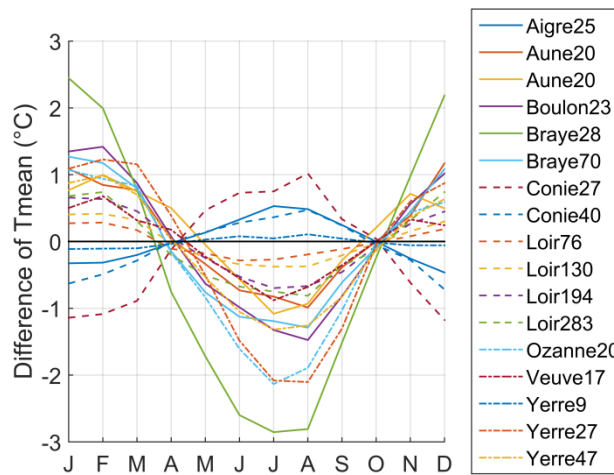


Figure 6.7:  $Bias_{Eaudyssée} - Bias_{Standard}$  on mean daily temperature on 08/2008-07/2013 for the 17 stations linked to an Eaudyssée cell

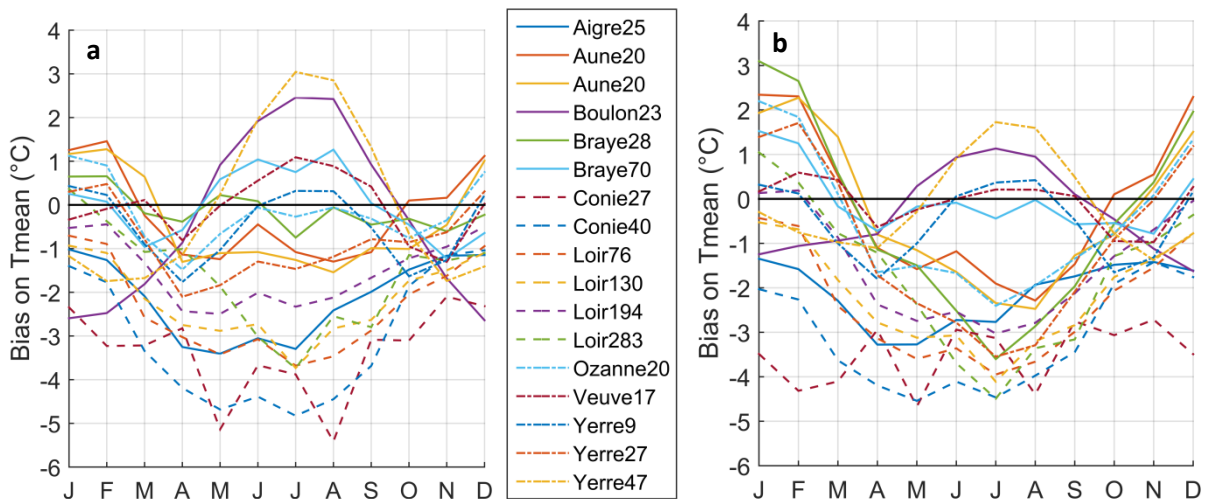


Figure 6.8: Mean daily biases on 08/2008-07/2013 for the 17 stations linked to an Eaudyssée cell (a)  $Bias_{Standard}$  (b)  $Bias_{Eaudyssée}$

RMSE on Tmean are improved by more than 0.5 °C for Yerre 47 (n°44) and Boulon 23 (n°5) at the four seasons and for Braye 70 (n°7), Veuve 17 (n°39) and Conie 27 (n°8) in summer (Figure 6.9). They are worsened by more than 0.5 °C in both winter and summer for 3 stations (Aune 20 (n°3), Braye 28 (n°6) and Ozanne 20 (n°33)). Two examples of improvement/degradation of the annual cycle of mean daily temperature in 2010 are shown at Figure 6.10. These two examples are on the Yerre River, where it has been shown that thermal sensitivities are heterogeneous (see Figure 3.11).

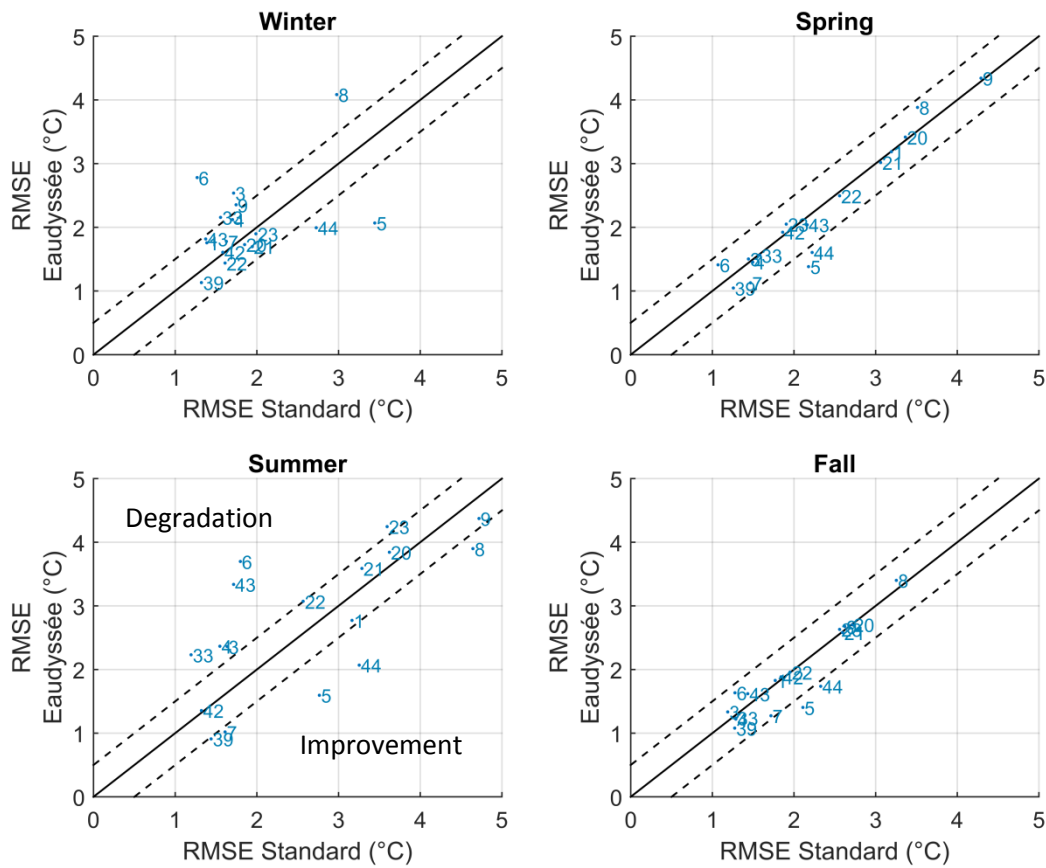


Figure 6.9: Comparison of RMSE computed on mean daily Tw between the standard configuration and the configuration using Eaudyssée. Averages on available observed data on 2008-2013.

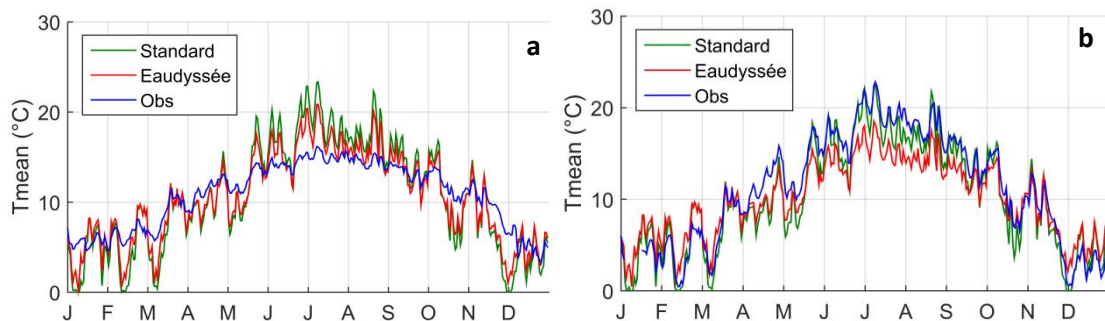


Figure 6.10: Mean daily temperature modelled and measured in 2010 at (a) Yerre 47 (n°44), where accuracy is improved (b) Yerre 27 (n°43), where accuracy is decreased

For stations where groundwater fluxes are increased by Eaudyssée, diel amplitudes are decreased, with the maximal impact being usually in spring (Figure 6.11). There is a sharp decrease up to  $-0.9\text{ °C}$  in September at Ozanne 20, which comes from high differences in 2009 and 2010. Diel amplitude accuracy is thus improved for most of the stations, since they are usually overestimated in the standard simulation. Amplitude accuracy of Conie 27 is also increased because it is underestimated in the standard simulation.

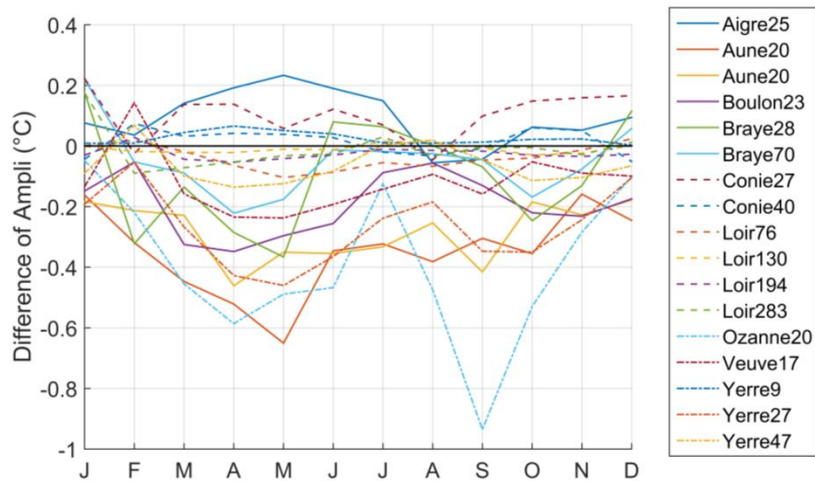


Figure 6.11:  $\text{Bias}_{\text{Eaudyssée}} - \text{Bias}_{\text{Standard}}$  of diel amplitude on 08/2008-07/2013 for the 17 stations linked to an Eaudyssée cell

### 6.4.2 Thermal impact in August 2009

On average on the 13-31 August 2009 period, the Loir and its main tributaries located upstream of river km 40 and downstream of river km 140 are colder by more than 0.5 °C, compared to the simulation forced with EROS (Figure 6.12). Temperature of the Yerre River is also decreased. Only the left tributaries located above the Beauce limestone are warmer, because of a decrease of groundwater fluxes.

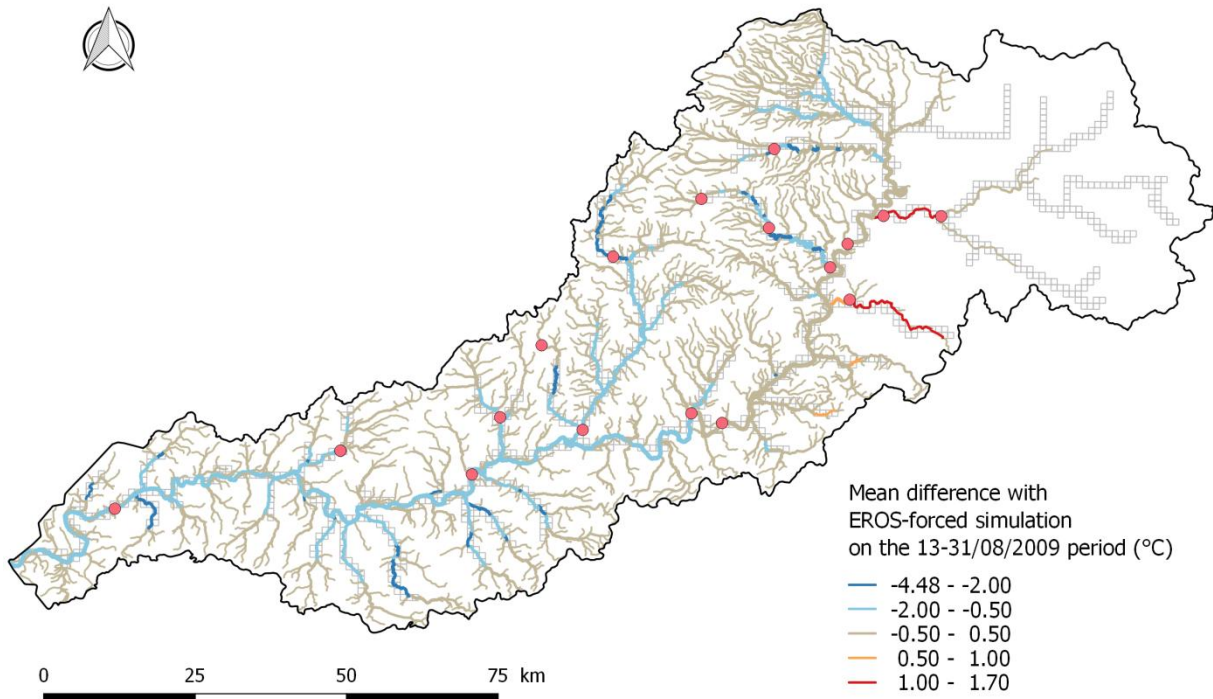


Figure 6.12:  $T_{\text{mean}_{\text{Eaudyssée}}} - T_{\text{mean}_{\text{EROS}}}$ , on average on the 13/31/08/2009 period

The longitudinal profile of  $T_{\text{mean}}$  on the Loir shows a growing difference in the downstream direction after the confluence with the Aigre, and a maximal difference of 2.1 °C at river km 22. The cooling impact of the Conie tributary is reduced. Biases are thus increased compared to the standard simulation.

The cooling impact of groundwater fluxes as modelled by Eaudyssée, in comparison with a simulation without groundwater flux ranges from  $-0.52\text{ °C}$  to  $-1.2\text{ °C}$  for  $T_{\text{mean}}$  on most of the longitudinal profile, with a peak at  $-2.8$  at river km 22 (Figure 6.13). Results are similar for  $T_{\text{max}}$  ( $-0.49$  to  $-1.27\text{ °C}$  with a peak at  $-2.7\text{ °C}$ ).

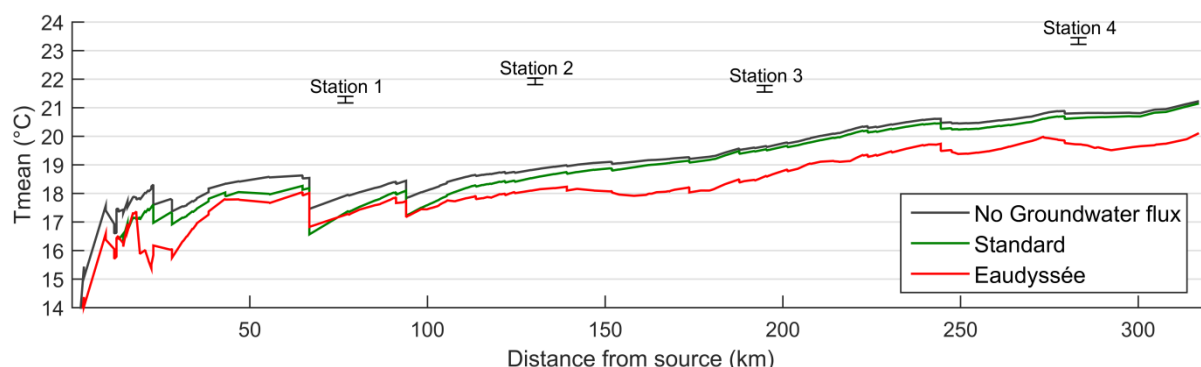


Figure 6.13: Longitudinal profile of mean daily temperature on the Loir River, averaged on the 13-31/08/2009 period

The Figure 6.14 shows that the thermal impact of groundwater fluxes on the 13-31/08/2009 period downstream of the Loir is representative of the other summer conditions. The daily variability is higher than during other summers, probably because the water levels in the stream and in the aquifer are very close. Figure 6.14 also shows that, on average, the thermal impact is a bit more important in winter than in summer.

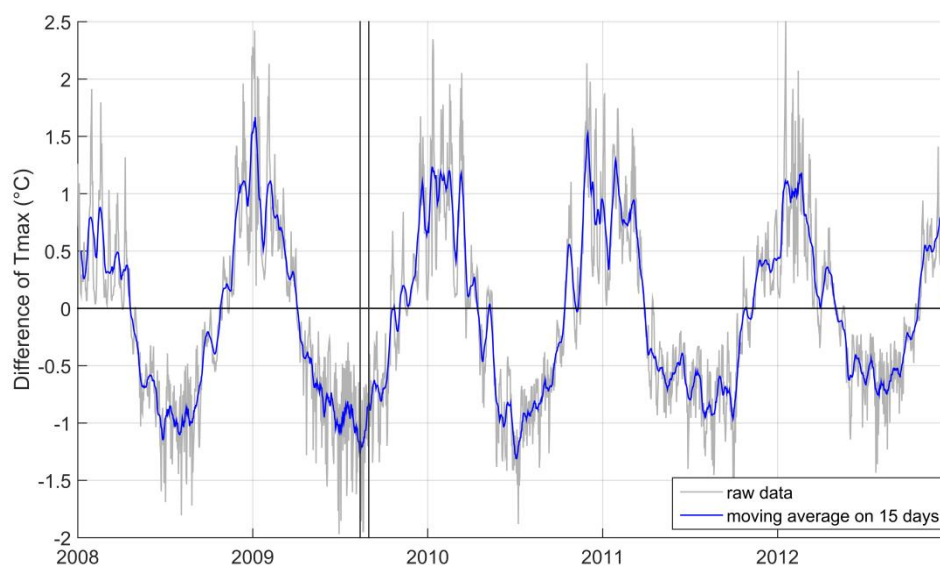


Figure 6.14: Temporal evolution of the thermal impact of groundwater fluxes on maximum daily  $T_w$  as modelled by Eaudyssée at the downstream-most Loir's reach of the LiDAR area (for consistency with Figure 5.28), in comparison with a simulation with no groundwater flux.

### 6.4.3 Average accuracy

Averaged on the full year, the use of Eaudyssée input data has a small effect on temperature accuracies because the winter impacts counterbalance the summer impacts. The maximum degradation is  $-0.14\text{ °C}$  on  $T_{\text{max}}$  biases (Table 6.1). The mean bias of diel amplitudes is improved by a small  $0.1\text{ °C}$ .

Table 6.1: Performance criteria on available data on the 08/2008-07/2013 period (a) values for the Eaudyssée simulation (b) Criteria<sub>Eaudyssée</sub> - criteria<sub>Standard</sub> (green/red = improvement/degradation by more than 0.1 °C)

| (a)   | Bias (°C) | SDE (°C) | RMSE (°C) | (b)   | Bias (°C) | SDE (°C) | RMSE (°C) |
|-------|-----------|----------|-----------|-------|-----------|----------|-----------|
| Tmin  | -1.58     | 1.83     | 2.53      | Tmin  | -0.04     | +0.12    | +0.13     |
| Tmean | -1.23     | 1.77     | 2.32      | Tmean | -0.09     | +0.06    | +0.10     |
| Tmax  | -0.91     | 1.87     | 2.34      | Tmax  | -0.14     | -0.01    | +0.02     |
| Ampli | 0.67      | 1.11     | 1.38      | Ampli | -0.10     | -0.04    | -0.09     |

## 6.5 Conclusion

The groundwater fluxes modelled by Eaudyssée at the spatial resolution of 1 km were injected in T-NET on the main river of the Loir catchment. To our knowledge, a combination of groundwater fluxes modelled at this resolution with a stream temperature model has never been achieved at the regional scale. Fifty-seven percent of the stream-aquifer exchanges values modelled by Eaudyssée characterise an exfiltration process (flux from groundwater to the river) and hence have an impact on the river temperature. These fluxes are more variable than those modelled by EROS because they are computed according to the difference between the river water level and the groundwater level, where water does not have the same mobility. Fluxes modelled with Eaudyssée are also usually more important, except for 2 stations for which EROS groundwater fluxes were already high. Hence, resulting temperature are colder in summer and warmer in winter for most stations, compared to the standard simulation. RMSE are improved and worsened for approximately the half of the stations. On a yearly average, the accuracy change on temperatures is small because winter effects tend to offset the summer effects. The diel amplitudes are a bit decreased and the bias is thus improved by 0.1°C. Finally, if the Eaudyssée modelling is considered as close to reality, the cooling effect of groundwater on the 13-31/08/2009 period ranges from -0.52 °C to -1.2 °C on most of the Loir river, with a peak at -2.8 °C in its upstream part. Averaged on 2007-2013, the effect globally ranges from -1 (summer) to +1°C (winter; Figure 6.15).

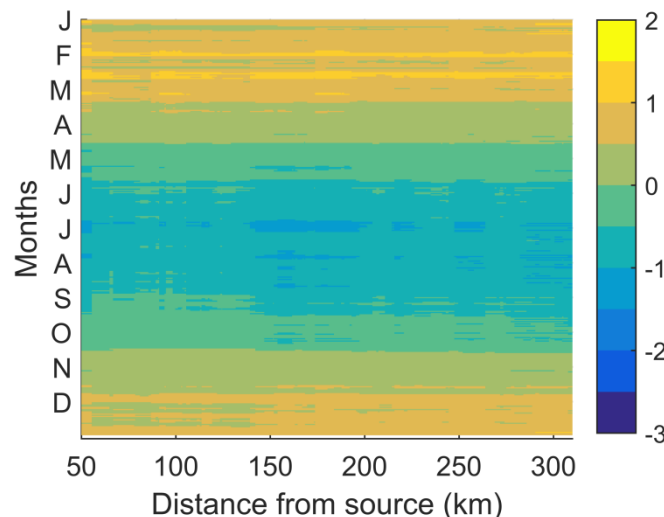


Figure 6.15: Thermal impact of groundwater fluxes as modelled by Eaudyssée on the Loir's maximum daily  $T_w$  (average on 08/2007-07/2013)



# Chapter 7: Conclusion and perspectives (English)

## 7.1 Aims

The goals of this thesis were (i) to analyse the variability of stream temperature ( $T_w$ ) at the regional scale on the climatically homogeneous Maine catchment (22 350 km<sup>2</sup>), thanks to temperature observations measured at 44 monitoring stations localised on Strahler order 2 to 7; (ii) develop an empirical model based on landscape and hydrologic descriptors and able to predict weekly water temperature; (iii) understand the weaknesses of the T-NET model when applied on this catchment and suggest potential methods to resolve them; (iv) try to solve them by injecting fine-scale input data of two important processes that are of particular importance in the context of climate change because they can cool the rivers: riparian shading and groundwater fluxes.

## 7.2 Characterisation of thermal regimes

The spatial variability of  $T_w$  metrics at the regional scale has already been analysed in several studies (Wehrly et al., 2003; Maheu et al., 2016; Chu et al., 2010), but the catchments sizes were much larger and climatically heterogeneous. In this thesis, the spatial heterogeneity in thermal regimes was analysed by computing several metrics on 2010, a year with a hot period in summer and with good data availability. Results show that the spatial variability of  $T_w$  is much greater than for air temperature ( $T_a$ ). As an example, the range of the mean  $T_w$  in July (January) across 29 stations with available data equates 10.2 °C (5 °C), while it is only 2.5 °C (2.8 °C) for  $T_a$ . In summer,  $T_w$  usually increases in the downstream direction while the diel amplitude decreases with the increasing depth (Table 7.1).

**Table 7.1: Two thermal metrics summarised by sub-catchment and by Strahler order (2010)**

| Mean $T_w$ in July/mean diel amplitude in July (°C)/number of stations |             |             |            |
|--|-------------|-------------|------------|
| Strahler order   | Mayenne     | Sarthe      | Loir       |
| 2  |             |             | 18.6/1.2/2 |
| 3  |             | 15.4/3.0/3  | 18.1/2.3/3 |
| 4  | 18.5/3.2/3  | 18.6/2.3/4  | 16.9/3.0/2 |
| 5  | 20.8/1.3/3  | 20.45/1.9/5 | 22.2/1.7/2 |
| 6  | 20.16/3.0/2 |             |            |
| 7  |             | 24.6/1.1/1  |            |

Among the 8 variables analysed, 2 are not correlated with others: the diel  $T_w$  amplitude in July (range: 0.5 to 4 °C), and the Julian day of maximum  $T_w$  after smoothing by a 30 days moving average (ranges from 9 July to the 16 July). The other metrics are correlated because they are influenced by the amplitude of the annual cycle. They can be summarised by the thermal sensitivity (TS, the slope of the weekly  $T_w$  vs.  $T_a$  linear regression). TS has a wide range of variability (0.42 to 1.17), which shows how the resilience and resistance of hydrosystems to climate change can be spatially variable. Water temperature is controlled by complex processes that are linked to climatic and hydrologic processes, buffered by the basins properties (Hannah and Garner, 2015).

## 7.3 Empirical model

A statistical model was built in order to predict water temperature where there is no  $T_w$  monitoring station. It was built in two steps. Firstly,  $T_w$ - $T_a$  weekly linear regressions were fitted for each station.

Then we sought the best descriptors explaining the intercept and the slope of these regressions. They were found to be the distance from source and the ratio of the minimum monthly discharge on the maximum monthly discharge. The first descriptor is linked to the time during which water is in contact with air, and the second is a proxy of the groundwater fluxes. After validation on stations that were not used for the fit, the model provides a  $R^2$  of 0.90, a RMSE of 1.35 °C and a mean bias of -0.13 °C. This accuracy is quite good compared to other models developed at the same temporal scale (Pilgrim et al., 1998; Stefan and Preud'homme, 1993). As long as modelled discharge and  $T_a$  data are available, this model can easily be applied on all reaches of a river network located inside or outside of the Maine catchment, as long as the climatic and hydrologic conditions are similar.

If thermal preferences of specific aquatic species are known, the results of this empirical model can be used as input of aquatic habitats models to map the spatial repartition of specific species at the regional scale. The opposite approach can be followed if species repartition data are available, in order to analyse the impact of temperature on these species (Isaak et al., 2017; Buisson et al., 2008).

The model may be applied to forecast the effect of climate change, in a limited manner however for summer conditions. Indeed, although warm summer months were taken into account for the model fit, they represent only some points in the scatter plot, so that forecast for weather conditions warmer than ~23 °C (the high end of the scatter plot) may be more biased, because it involves extrapolation beyond the range of observed conditions (Arismendi et al., 2014). Moreover, the potential warming of the groundwater on a long term perspective is not taken into account in the statistical models (Kurylyk et al., 2015).

In the future, a similar study could be achieved on catchments with different climates or hydrologic conditions, in the Loire basin (data from Beaufort, 2015), or at the national scale. At this occasion, more complex methods used in spatial statistical models (Ver Hoef et al., 2006; Isaak et al., 2014) and other basin/network properties could be tested (e.g. riparian vegetation if accurate dataset is available, or other indicators quantifying the weir density, like those suggested by Van Looy et al., 2014).

## **7.4 The T-NET model**

### **7.4.1 Performance of T-NET on the Maine catchment**

In comparison with statistical models, physically based models are more suitable to forecast the impact of climate change, because they are not fitted on past thermal conditions. Unlike most physically based models, T-NET was designed to be applied at the regional scale. It models  $T_w$  at the hourly time step and at the reach resolution. It is used in an eutrophication model (Minaudo et al., 2017), which opens perspectives regarding its use in the characterisation of climate change and anthropogenic impact.

In his thesis, Beaufort (2015) computed an average RMSE of 1.6 °C on the mean daily  $T_w$  ( $T_{mean}$ ) of 128 monitoring stations of the Loire basin (2008–2012). However, performance was lower at some stations, with a RMSE above 2 °C in summer. Based on the 26 stations that were available on the Maine basin during his thesis, the mean RMSE is 1.80 °C. With supplementary data at 18 stations and

on 2013-2015, the RMSE is not much changed (1.84 °C), but the relationship between the summer (July-August) biases and the thermal sensitivity is still more significant (p-value: 4.8E-6).

In winter, the T-NET model (as published in Beaufort et al., 2016) has a good accuracy (RMSE of  $T_{\text{mean}} = 1.6$  °C). In summer,  $T_w$  modelled at stations with low thermal sensitivity (i.e. close to source and/or with high groundwater fluxes) are usually overestimated (compared to measurements), showing a potential lack of groundwater fluxes and/or a mischaracterisation of riparian shade. On the opposite, stations with high thermal sensitivity are usually underestimated, probably because of a mischaracterisation of riparian shade and/or of the travel time. During the whole year, both the diel amplitudes and the variations of the thermal signal on longer periods (1-2 weeks) are too high compared to observations, except at a minority of stations.

#### **7.4.2 Fine scale characterisation on the Loir River and catchment**

In an attempt to improve T-NET accuracy, we developed a method to characterise the riparian shading on direct and diffuse solar radiation and on longwave downward radiation at a metric resolution. The phenology of tree leaves and the variation of albedo with the sun elevation were also included to better fit the reality. This method was applied only on the Loir River because of the availability of the LiDAR data. It helped to improve the biases on the 4 stations located on the Loir River, but it was not enough to reach the [-1 °C, 1 °C] interval for the  $T_{\text{mean}}$  on the 4 stations. The characterisation of shading on solar radiation at the hourly time step with the *lidar* method increases the diel amplitude and hence decreases their accuracy since they are basically overestimated. On another hand, considering the impact of riparian vegetation on the longwave radiation increases the temperature (especially on the minimum daily  $T_w$ ,  $T_{\text{min}}$ ) and reduces the diel amplitude, so that considering the total impact of vegetation with the *lidar* method provides the best results on the 4 Loir's stations. The RMSE of  $T_{\text{mean}}$  equates 2 °C and the bias of the diel amplitudes is +1.7 °C.

The *variable* method (which uses reach-averaged characteristics) has been shown to provide results close to those provided by the *lidar* method, as long as vegetation cover data are accurate. It is thus of primary importance to improve the quality of the vegetation cover datasets. Regarding the importance of the vegetation height characterisation, we have shown that the application of the *variable* method with a fixed tree height (15 m, the 3<sup>rd</sup> quartile of vegetation height provided by the LiDAR data) provides good results on the Loir and on the 13-31/08/2009 period. However, Beaufort (2015) showed that the impact of a height variation is the strongest between 10 and 15 m so that more research is needed to know how mean riparian vegetation height vary on other rivers. The *constant* method is suitable to be applied only for a limited period of the year, since it does not characterise the variation of the shade lengths through the annual cycle. We have also demonstrated that an accurate characterisation of the river width is important for shading characterisation. The comparison of shading methods achieved here will allow improving other models' accuracy and hence our understanding of the shading effect on other catchments.

The consideration of groundwater fluxes modelled by Eaudyssée (Baratelli et al., 2016) at the spatial resolution of 1 km and on the Loir catchment (area limited by the availability of data) leads to an increase of groundwater fluxes for ~75% of the stations considered.  $T_w$  at these stations are hence decreased in summer and increased in winter (up to  $\pm 2.5$  °C in January/August for Conie 27). The

impact is opposite for 4 stations where groundwater fluxes modelled by EROS were higher than fluxes modelled by Eaudyssée. In the end, summer RMSE are improved by more than 0.5 °C at 6 stations and degraded at 5 stations, while the effect is smaller on the remaining stations. The extent of the Tw changes at some stations shows that an accurate characterisation of the groundwater fluxes is of primary importance to improve Tw modelling. The combined use of Eaudyssée and T-NET, which are both able to run at the regional scale, is a big step toward this improvement.

The method to compute the groundwater temperature has not been modified in this thesis. A potential decrease of groundwater temperature would improve T-NET's accuracy at stations with low TS, but it would also decrease accuracy at stations with higher TS, in a lesser extent.

The fine-scale characterisation of both the riparian shading (on solar and longwave radiation) and the groundwater fluxes allows quantifying their respective effects on the Loir's temperature, by comparing them to simulations where the effects are fixed as null. The vegetation characterised with the *lidar* method provides a cooling effect on the maximum daily Tw (Tmax) ranging from -2.8°C (upstream) to -1.1°C (downstream) in late August 2009. At the same period, the cooling impact of groundwater fluxes as modelled by Eaudyssée on Tmax ranges from -0.5 °C (upstream) to -1.3 °C (downstream) on most of the longitudinal profile, with a local maximum at -2.8 °C in the upstream area. The impact of vegetation is thus approximately 2 times more important than the impact of groundwater fluxes.

### 7.4.3 T-NET performances on the Maine catchment with all modifications (applied where applicable)

In order to understand the combined impact of all modifications brought in this thesis, these were applied together on 2008-2013 (groundwater fluxes provided by Eaudyssée where available and by EROS otherwise, and with the impact of riparian vegetation on solar and downward longwave radiation characterised with the *lidar* method where available and with the *variable* method otherwise with tree height fixed at 10 m). The resulting mean Tw are shown in appendix G. The average RMSE computed on April-September on Tmean is improved by 0.24 °C compared to the standard simulation (Table 7.2). The Tmean are increased, but diel amplitudes are increased as well, so that accuracy on Tmin is improved while accuracy on Tmax is decreased.

**Table 7.2: Accuracy criteria of a simulation including all modifications brought in the thesis, and compared with the standard configuration. All values are in °C.**

|  | April to September |       |       | October to March |       |       |
|--|--------------------|-------|-------|------------------|-------|-------|
| Raw values                             | Bias               | SDE   | RMSE  | Bias             | SDE   | RMSE  |
| Tmin                                   | -1.22              | 1.37  | 1.96  | -0.35            | 1.48  | 1.71  |
| Tmean                                  | -0.35              | 1.43  | 1.76  | 0.09             | 1.45  | 1.65  |
| Tmax                                   | 0.54               | 1.79  | 2.23  | 0.52             | 1.52  | 1.80  |
| Ampli                                  | 1.76               | 1.32  | 2.27  | 0.87             | 0.80  | 1.20  |
| <b>Change with standard simulation</b> |                    |       |       |                  |       |       |
| Tmin                                   | 0.20               | -0.09 | -0.25 | 0.45             | -0.06 | -0.12 |
| Tmean                                  | 0.33               | -0.06 | -0.24 | 0.51             | -0.05 | -0.03 |
| Tmax                                   | 0.50               | 0.00  | -0.12 | 0.56             | -0.04 | 0.08  |
| Ampli                                  | 0.31               | 0.02  | 0.20  | 0.11             | -0.04 | 0.04  |

The correlation of the biases on Tmean (July-August) with the thermal sensitivity is still observed (Figure 7.1a, to be compared with Figure 7.1b). Accuracy at stations with the lowest biases was improved but it was also decreased at several stations. Among the 8 stations that are overestimated by more than 1 °C, 4 are located in the Eaudyssée area (5, 39, 42, 44). A potential underestimation of

the groundwater fluxes cannot be discarded, since accuracy of the Eaudyssée outputs (in term of groundwater fluxes) can hardly be quantified. An overestimation of the groundwater temperature could also explain these biases. Among the 4 other stations that are not in the Eaudyssée area (2, 13, 34, 36), 2 are located in the sedimentary basin and 2 are in the Armorican massif. As suggested in chapter 2 and 3, groundwater fluxes can also occur in the Armorican massif even if the aquifer productivity are lower. The Tw overestimations are less likely due to an underestimation of the vegetation cover since 7 stations among the 8 that are overestimated by more than 1 °C have a vegetation cover above 50%. Another potential cause, which has not been analysed in this thesis, is that T-NET does not take into account the bed conduction. This process has usually the same net effect (heating/cooling) as groundwater fluxes (Webb and Zhang, 2004) and is more important in shallow streams because of the higher diel amplitude (Chen et al., 1998a). It is dependent on the water depth, water turbidity and the water-bed temperature gradient. As an example, it has been reported to account for 24% of the total heat losses of a UK shallow stream in summer and autumn (Evans et al., 1998). This process has been implemented in several models that could be inspirational (e.g. Chen et al., 1998a; Haag and Luce, 2008).

The underestimations (Figure 7.1a) are likely explained by overestimated vegetation cover: 11 stations among the 12 that are underestimated by more than -1 °C (excluding the Loir' stations for which LiDAR data were used) have a vegetation cover above 70%.

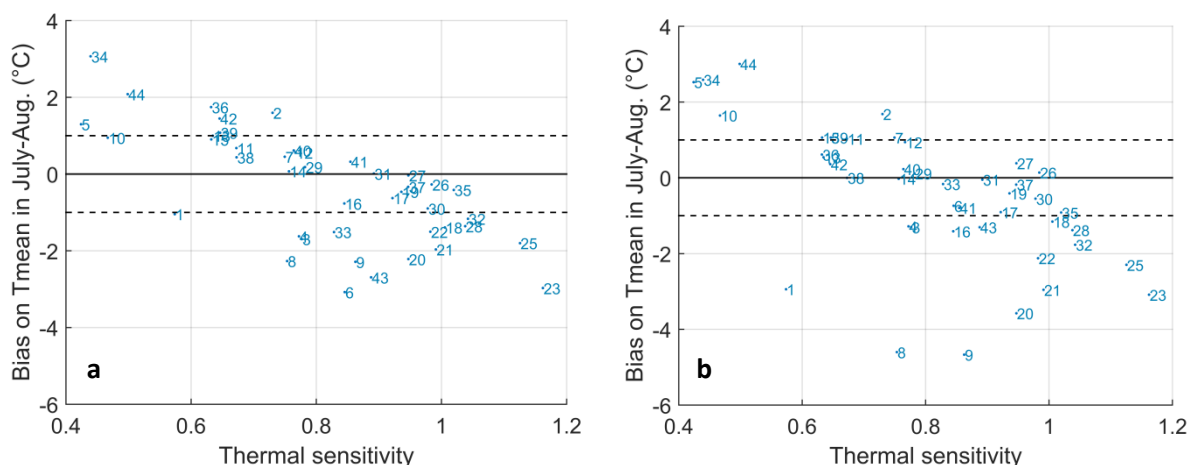


**Figure 7.1: Bias ( $T_{sim} - T_{obs}$ ) of mean daily temperature in July-August as a function of thermal sensitivity (2008-2013 average) (a) simulation including all modifications brought in the thesis (b) Standard simulation (configuration of Beaufort et al., 2016). Stations numbers are in appendix B.**

On average on the 13-31/08/2009 period, the longitudinal profiles obtained with the final simulation (which includes all modifications; Figure 7.2) are closer than the standard simulation to each observed Tw (except for station n°34).

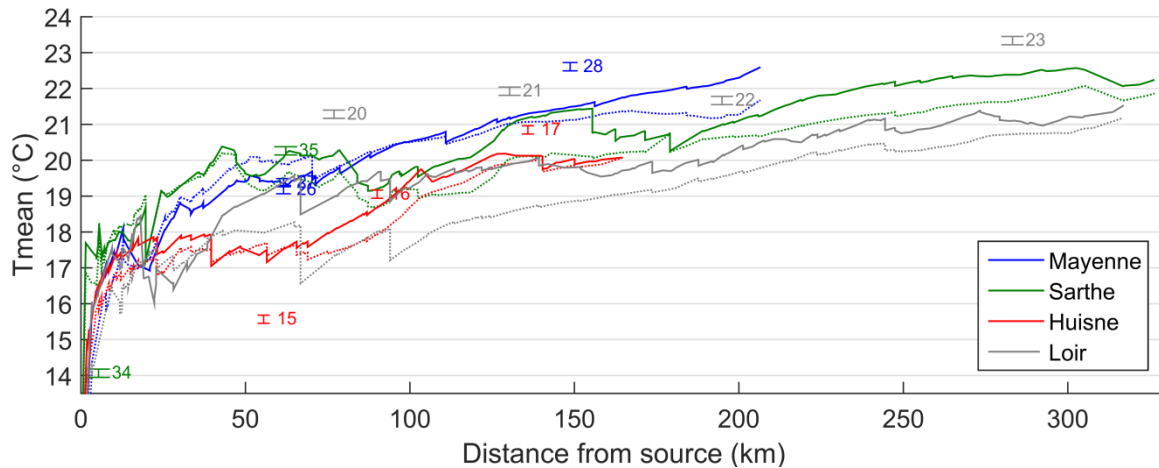


Figure 7.2: Longitudinal profile of daily mean temperature on the 4 main rivers of the Maine catchment, averaged on the 13-31/08/2009 period, simulated by the most complete version of T-NET (continuous) and by the standard version of T-NET (dotted)

The Conie (stations n° 8 and 9) remains the tributary with the most important impact on the summer Tw of the 4 main rivers in the Maine catchment. The underestimation of the Conie Tw is likely due to two causes. The first is that discharge on Conie's sub-basin is overestimated by EROS by more than 150% in winter and by more than 350% in summer, which leads to a flow that is too fast and thus too cold in summer. For the same reason, the modelled water depth is higher than on other streams, which explains why the diel amplitudes are underestimated, conversely to what is observed on the other stations. Taking into account the high water withdrawals that occur in this area would probably allow increasing the accuracy of discharge on this catchment. The second reason is that the influence of ponds is not taken into account in T-NET.

#### 7.4.4 Perspectives for the T-NET model development

The overestimation of both the diel amplitudes and the variations at the weekly time scale can be corrected by improving the accuracy of the water depths. At the same time, a better characterisation of wetted widths and slopes, and hence of water velocities can slightly improve the negative biases occurring in summer. This global improvement of hydraulic geometry can be achieved by a new fit of the Estimkart empirical equations' parameters, or by using the Manning-Strickler equation with calibrated coefficients. The Carhyce framework can provide some measurements, although their number is currently limited (~40 observations on the Maine catchment). The acquisition of rating curves at the 81 gauging stations would allow providing observed time series of water depth needed to calibrate the Estimkart equation or the Manning coefficients. Topographical measurements retrieved for hydraulic modelling regarding flood risk assessment could also be used in T-NET with the Manning equation. Recent techniques like the bathymetric LiDAR could also provide high resolution data about the river geometry, but it seems that there are still some technical challenges to resolve before it can be applied to stream temperature modelling, especially at the regional scale (Hilldale and Raff, 2008; Bailly et al., 2010). On most streams of the Maine catchment, the characterisation of constant-in-time widths could be sufficient because of their small variability. The bankfull widths can be extracted from BD TOPO for streams larger than 6 m.

Improving the vegetation cover data is likely to improve T-NET accuracy at negatively biased stations. Today, very high spatial resolution imagery can be retrieved at the regional scale and treated to inform the riparian vegetation cover accurately (Tormos et al., 2014). However, it involves the availability of a river network whose planimetric location is accurate, especially for the first orders reaches. The Topage river network project will increase this accuracy and should be available in 2019.

As highlighted by Michez et al. (2017), the combination of LiDAR and photogrammetry could allow obtaining the vegetation height data at relatively small cost where LiDAR data is not yet available (i.e. on the small streams). From these data, empirical relationships with variables like land cover could be built in order to characterise the riparian vegetation characteristics where both LiDAR and photogrammetric data are not available.

The groundwater fluxes characterisation is likely to have reached its most advanced level in this work. The only potential development is to apply a hydrogeological model also on the Armorican massif. However, this would be an extensive work that is beyond the scope of a water temperature modelling work. As discussed above, taking into account the bed conduction process may decrease the positive biases at low TS stations. A decrease of the groundwater temperature will also improve results for these stations. However, it must be accompanied with a successful modification to warm the negatively-biased stations, unless global performance will decrease. Some field measurements of  $T_w$  at source would be beneficial to know if the method currently used is appropriate to the contrasted hydrogeological context of the Maine basin.

Taking into account the influence of headwater impoundments is likely too improve T-NET performance at some stations that are currently underestimated (e.g. Conie). It would be quite innovative because no regional model takes them into account (to our knowledge). Today, it is still challenging because it is difficult to quantify the hydrological linkage between ponds and the flowing river. A good spatial accuracy of the river network is also needed to work on this topic. When the Topage river network will be available, it should be possible to take into account the impoundment area in the shading characterisation and in the computation of water velocity.

We have hypothesised that the presence of weirs could also explain some modelled biases. The *Référentiel des Obstacles à l'Écoulement (ROE)* database can provide the location of weirs as well as their corresponding height. An attempt to take them into account was actually achieved during this thesis, by considering the supplementary water volume stored behind the weirs. However, this approach is strongly dependent on the accuracy of the water depth, which was not good enough. As soon as the characterisation of river depth is improved, the thermal effect of weirs could be taken into account by modelling the thermal stratification, only when and where it is needed. Indeed, as discussed by Bormans and Webster (1997), thermal stratification need to be modelled only when  $T_w$  is increasing and when water velocity is small enough. The temperature of the upper layer could then be taken for the downstream propagation.

As soon as the biases on the daily mean  $T_w$  and on the diel amplitudes are improved, the model may be forced with air temperature and discharge resulting from climate change scenarios (Hardenbicker et al., 2016; Soto, 2017; Beaufort, 2015). Combined to models of fish habitats, the results will allow

understanding the future shrinking of cold-water fishes habitats (Isaak et al., 2015; Battin et al., 2007; Tung et al., 2006).

## Chapter 7: Conclusion et perspectives (français)

### 7.1 Objectifs

Les objectifs de cette thèse étaient : (i) analyser la variabilité de la température des rivières ( $T_w$ ) à l'échelle régionale sur le bassin de la Maine (22 350 km<sup>2</sup>), où le climat est relativement homogène, grâce à des observations de température mesurée à 44 stations situées sur des ordres de Strahler de 2 à 7 ; (ii) développer un modèle empirique basé sur différents descripteurs et capable de prédire la température de l'eau hebdomadaire ; (iii) comprendre les points forts et les faiblesses du modèle à base physique T-NET lorsqu'il est appliqué sur ce bassin versant et proposer des méthodes pour les résoudre ; (iv) tenter de les résoudre par l'injection de données d'entrée à haute résolution qui concerne deux processus importants dans le contexte du changement climatique car ils peuvent refroidir les rivières : l'ombrage porté par la végétation rivulaire et les flux de nappe.

### 7.2 Caractérisation des régimes thermiques

La variabilité spatiale de métriques de  $T_w$  à l'échelle régionale a été analysée par plusieurs études (Wehrly et al., 2003 ; Maheu et al., 2016 ; Chu et al., 2010), mais les bassins étudiés étaient beaucoup plus grands et plus hétérogènes d'un point de vue climatique. Dans cette thèse, l'hétérogénéité spatiale des régimes thermiques a été analysée via plusieurs métriques sur les données de 2010, une année avec une période chaude en été et avec une bonne disponibilité des données. Les résultats montrent que la variabilité spatiale est beaucoup plus élevée pour  $T_w$  que pour la température de l'air ( $T_a$ ). Par exemple, la moyenne de  $T_w$  en juillet (janvier) à l'échelle de 29 stations disposant de données varie sur 10.2 °C (5 °C), alors qu'elle varie seulement sur 2,5 °C (2.8 °C) pour les  $T_a$ . En été,  $T_w$  augmente généralement de l'amont vers l'aval, tandis que les amplitudes journalières diminuent avec l'augmentation de la profondeur (Table 7.1).

Tableau 7.1 : Deux métriques de  $T_w$  résumées par sous-bassin et par ordre de Strahler (2010)

| Tw moyenne en juillet/amplitude journalière moyenne en juillet (°C)/nombre de stations |             |             |            |
|--|-------------|-------------|------------|
| Ordre de Strahler  | Mayenne     | Sarthe      | Loir       |
| 2  |             |             | 18.6/1.2/2 |
| 3  |             | 15.4/3.0/3  | 18.1/2.3/3 |
| 4  | 18.5/3.2/3  | 18.6/2.3/4  | 16.9/3.0/2 |
| 5  | 20.8/1.3/3  | 20.45/1.9/5 | 22.2/1.7/2 |
| 6  | 20.16/3.0/2 |             |            |
| 7  |             | 24.6/1.1/1  |            |

Parmi les 8 variables analysées, deux ne sont pas corrélées avec les autres : l'amplitude journalière en juillet (varie entre 0.5 et 4 °C), et le jour de  $T_w$  maximale après lissage par moyenne mobile sur 30 jours (varie du 9 au 16 juillet). Les autres métriques sont corrélées parce qu'elles sont influencées par l'amplitude du cycle annuel. Elles peuvent être résumées par la sensibilité thermique (TS), qui correspond à la pente de la régression  $T_w$  vs  $T_a$  en moyenne hebdomadaire). TS varie sur une large gamme (0.42 à 1.17). Cette forte variabilité montre comment la résilience et la résistance des hydrosystèmes au changement climatique peut varier dans l'espace. La température de l'eau est contrôlée par des processus complexes qui sont liés à la dynamique climatique et hydrologique et qui sont modérés par les propriétés des bassins-versants (Hannah et Garner, 2015).

## 7.3 Modélisation statistique

Un modèle statistique a été conçu afin de pouvoir prédire la température des cours d'eau qui ne sont pas suivis. Il a été conçu en deux étapes. Tout d'abord, des régressions linéaires  $T_w$ - $T_a$  ont été effectuées pour chaque station. Ensuite, nous avons cherché les meilleurs descripteurs expliquant l'ordonnée à l'origine et la pente de ces régressions. Il s'agit de la distance à la source ainsi que du rapport entre le débit mensuel minimal et le débit mensuel maximal (en moyenne interannuelle). Le premier descripteur est lié au temps durant lequel  $T_w$  s'équilibre avec  $T_a$ , et le second est un proxy des flux de nappe. Après validation sur les stations qui n'ont pas été utilisées pour son calage, le modèle fournit un  $R^2$  de 0.90, une RMSE de 1,35 °C et un biais moyen de -0.13 °C. Cette précision est relativement bonne par rapport à d'autres modèles développés à la même échelle temporelle (Pilgrim et al., 1998 ; Stefan et Preud'homme, 1993). A partir du moment où des données de débit et de  $T_a$  sont disponibles, ce modèle peut facilement être appliqué sur tous les tronçons d'un réseau hydrographique situé à l'intérieur ou à l'extérieur du bassin versant de la Maine, tant que le climat et les conditions hydrologiques sont similaires.

Si les préférences thermiques d'espèces aquatiques spécifiques sont connues, les résultats de ce modèle peuvent être utilisés comme données d'entrée de modèles d'habitats afin de cartographier la répartition spatiale de ces espèces à l'échelle régionale. L'approche inverse peut être appliquée si des données de répartition d'espèces sont disponibles, afin d'analyser l'impact de la température sur ces espèces (Isaak et al., 2017 ; Buisson et al., 2008).

Le modèle pourrait être appliqué à la prévision de l'effet du changement climatique, de manière limitée cependant pour les conditions estivales. En effet, bien que des mois d'étés chauds aient été pris en compte pour l'ajustement du modèle, ils ne représentent que quelques points dans l'ajustement des régressions, de sorte que la prévision pour des conditions météorologiques plus chaudes que ~23 °C (le haut du nuage de points) peut être davantage biaisée, car elle implique une extrapolation au-delà de la gamme de conditions observées (Arismendi et al., 2014). De plus, le réchauffement potentiel des eaux souterraines sur le long terme n'est pas pris en compte dans les modèles statistiques (Kurylyk et al., 2015).

A l'avenir, une étude similaire pourrait être menée sur des bassins avec des climats et/ou des conditions hydrologiques différentes, dans le bassin de la Loire (données de Beaufort, 2015), ou à l'échelle nationale. À cette occasion, des méthodes plus complexes pourraient être testées, comme celles utilisées dans les modèles statistiques spatiaux (Ver Hoef et al., 2006 ; Isaak et al., 2014). D'autres descripteurs pourraient également être testés (par exemple, la végétation rivulaire si des données précises sont disponibles, ou des indicateurs quantifiant l'impact des seuils, comme ceux suggérés par Van Looy et al., 2014).

## 7.4 Le modèle T-NET

### 7.4.1 Performances de T-NET sur le bassin de la Maine

En comparaison avec les modèles statistiques, les modèles à base physique sont plus adaptés à la prévision de l'impact du changement climatique, parce qu'ils ne sont pas calés sur des observations (passées) de  $T_w$ . Contrairement à un grand nombre de modèles physiques, T-NET a été conçu pour

pouvoir être appliqué à l'échelle régionale. Il modélise  $T_w$  au pas de temps horaire et à la résolution du tronçon de rivière. Il est utilisé dans un modèle d'eutrophisation (Minaudo et al., 2017), ce qui ouvre des perspectives quant à son utilisation dans la caractérisation du changement climatique et de l'impact anthropique.

Dans sa thèse, Beaufort (2015) a obtenu une RMSE moyenne de 1.6 °C sur la  $T_w$  moyenne journalière ( $T_{mean}$ ) de 128 stations réparties sur le bassin de la Loire (2008-2012). Cependant, la précision était moindre à certaines stations, avec une RMSE au-dessus de 2 °C en été. Calculé sur les 26 stations qui étaient disponibles sur le bassin de la Maine au cours de sa thèse, la RMSE moyenne est de 1,80 °C. Avec les données supplémentaires aux 18 stations et sur la période 2013-2015, la RMSE est similaire (1,84 °C), mais la relation entre les biais estivaux (juillet-août) et la sensibilité thermique est encore plus significative (p-valeur : 4,8E-6).

En hiver, le modèle T-NET (tel que publié par Beaufort et al., 2016) a une bonne précision (RMSE sur  $T_{mean}$  = 1,6 °C). En été, la  $T_w$  modélisée aux stations ayant une faible sensibilité thermique (près de la source et/ou avec des flux de nappe importants) est généralement surestimée, ce qui montre une sous-estimation potentielle des flux de nappe et/ou une mauvaise caractérisation de l'ombrage porté par la végétation. Au contraire, la  $T_w$  modélisée aux stations ayant une sensibilité thermique élevée est généralement sous-estimée, probablement en raison d'une mauvaise caractérisation des vitesses de transfert ou de l'ombrage. Durant toute l'année, les amplitudes journalières, ainsi que l'amplitude des variations du signal thermique sur des périodes plus longues (1 à 2 semaines) sont surestimées par le modèle, sauf à une minorité de stations.

#### **7.4.2 Caractérisation à résolution fine sur la rivière Loir et son bassin**

Dans une tentative d'améliorer les performances de T-NET, nous avons développé une méthode pour caractériser l'impact de la végétation sur le rayonnement solaire direct et diffus et sur le rayonnement infrarouge qui atteint la rivière, à la résolution métrique. La phénologie des arbres et la variation de l'albédo avec l'élévation du soleil ont également été incluses afin de mieux correspondre à la réalité. Cette méthode a été appliquée uniquement sur le Loir en raison de la disponibilité des données LiDAR. Cela a contribué à améliorer les biais sur les 4 stations situées sur le Loir, mais cela n'a pas été suffisant pour atteindre l'intervalle [-1 °C, 1 °C] ( $T_{mean}$  sur les 4 stations). La caractérisation de l'ombrage sur le rayonnement solaire au pas de temps horaire avec la méthode *lidar* augmente les amplitudes journalières. Leur exactitude est donc moindre, puisqu'elles sont déjà surestimées dans la version standard du modèle. D'autre part, la prise en compte de l'impact de la végétation sur le rayonnement infrarouge augmente  $T_w$  (en particulier les minimums journaliers,  $T_{min}$ ) et réduit l'amplitude journalière, de sorte que la prise en compte de l'impact total de la végétation avec la méthode *lidar* donne les meilleurs résultats sur les 4 stations du Loir. La RMSE sur les  $T_{mean}$  est de 2 °C et les biais sur les amplitudes journalières est de +1.7 °C.

La méthode *variable* (qui est basée sur des caractéristiques moyennes à l'échelle du tronçon) fournit des résultats proches de ceux fournis par la méthode *lidar*, à partir du moment où les données de taux de végétation rivulaire sont exactes. Il est donc de première importance d'améliorer la qualité de ces jeux de données. Concernant l'importance de la caractérisation de la hauteur de végétation, nous avons montré que l'application de la méthode *variable* avec une hauteur fixe (15 m, le 3ème quartile

de la hauteur de la végétation fournie par les données LiDAR) donne de bons résultats sur le Loir et sur la période 13-31/08/2009. Cependant, Beaufort (2015) a montré que l'influence de la hauteur de végétation est la plus forte entre 10 et 15 m, de sorte qu'il reste à déterminer comment la hauteur de végétation varie sur d'autres rivières. La méthode *constante* est adaptée seulement pour être appliquée à une période limitée de l'année, puisqu'elle ne permet pas de caractériser la variation des longueurs d'ombrage au cours de l'année. Nous avons également montré qu'une bonne caractérisation de la largeur des rivières est importante pour la caractérisation de l'ombrage. La comparaison de ces méthodes permettra d'améliorer la précision d'autres modèles, et donc notre compréhension de l'effet de l'ombrage sur d'autres bassins versants.

La prise en compte des flux de nappe modélisés par le modèle Eaudyssée (Baratelli et al., 2016) à la résolution spatiale de 1 km et sur le bassin du Loir (zone limitée par la disponibilité des données) conduit à une augmentation des flux de nappe à environ 75% des stations considérées. A ces stations, les Tw sont ainsi diminuées en été et augmentées en hiver (jusqu'à  $\pm 2,5$  °C en janvier/août pour Conie 27). L'impact est inversé pour les 4 stations où les flux de nappe modélisés par EROS sont plus élevés que les flux modélisés par Eaudyssée. En fin de compte, les RMSE estivales sont améliorées de plus de 0,5 °C à 6 stations et dégradées à 5 stations, avec un effet moindre sur les autres stations. L'ampleur des changements de Tw à certaines stations montre que la précision de la caractérisation des flux de nappe est d'une importance primordiale pour améliorer les modèles de Tw. L'utilisation combinée des modèles Eaudyssée et T-NET, qui ont tous les deux été conçus pour être appliqués à l'échelle régionale, est un grand pas vers cette amélioration.

La méthode de calcul de la température des nappes n'a pas été modifiée dans ce travail. Une diminution de cette température permettrait d'améliorer la précision de T-NET aux stations à faibles TS mais cela diminuerait également la précision aux stations aux TS plus élevées, dans une moindre mesure.

La caractérisation à haute résolution de l'ombrage (rayonnement solaire et infrarouge) et des flux de nappe permet de quantifier leurs effets respectifs sur la Tw du Loir, en les comparant à des simulations où les impacts sont fixés à zéro. La végétation caractérisée par le LiDAR refroidit la Tw maximale journalière (Tmax) de -2.8°C (en amont) à -1.1°C (en aval) à la fin août 2009. À la même période, l'impact des flux de nappe tels que modélisés par Eaudyssée sur les Tmax évolue de -0.5 °C (en amont) à -1.3 °C (en aval) sur le profil longitudinal, avec un maximum local à -2.8 °C dans le secteur amont. L'impact de la végétation est donc environ 2 fois plus important que celui des flux de nappe.

### **7.4.3 Performances de T-NET sur le bassin versant de la Maine avec toutes les modifications (appliquées où cela est possible)**

Afin de comprendre l'impact combiné de toutes les modifications apportées dans cette thèse, celles-ci ont été appliquées ensemble sur la période 2008-2013 (flux de nappe Eaudyssée là où ils sont disponibles et flux EROS sinon, méthode *lidar* sur le Loir et méthode *variable* avec une hauteur de végétation de 10 m sinon). Les températures moyennes journalières obtenues sont représentées en annexe G. La RMSE moyenne sur les Tmean sur avril-septembre est améliorée de 0,24 °C par rapport à la simulation standard (Table 7.2). Les Tmean sont augmentées, mais les amplitudes journalières le

sont également, de sorte que la précision sur les Tmin est améliorée, alors que celle sur les Tmax est dégradée.

**Tableau 7.2 : Performance d'une simulation incluant toutes les modifications effectuées durant la thèse, comparée à la version standard. Toutes les valeurs sont en °C.**

| Raw values                             | April to September |       |       | October to March |       |       |
|--|--------------------|-------|-------|------------------|-------|-------|
|  | Bias               | SDE   | RMSE  | Bias             | SDE   | RMSE  |
| Tmin                                   | -1.22              | 1.37  | 1.96  | -0.35            | 1.48  | 1.71  |
| Tmean                                  | -0.35              | 1.43  | 1.76  | 0.09             | 1.45  | 1.65  |
| Tmax                                   | 0.54               | 1.79  | 2.23  | 0.52             | 1.52  | 1.80  |
| Ampli                                  | 1.76               | 1.32  | 2.27  | 0.87             | 0.80  | 1.20  |
| <b>Change with standard simulation</b> |                    |       |       |                  |       |       |
| Tmin                                   | 0.20               | -0.09 | -0.25 | 0.45             | -0.06 | -0.12 |
| Tmean                                  | 0.33               | -0.06 | -0.24 | 0.51             | -0.05 | -0.03 |
| Tmax                                   | 0.50               | 0.00  | -0.12 | 0.56             | -0.04 | 0.08  |
| Ampli                                  | 0.31               | 0.02  | 0.20  | 0.11             | -0.04 | 0.04  |

La corrélation des biais sur les Tmean (juillet-août) avec la sensibilité thermique est toujours observée (Figure 7.1a, à comparer avec Figure 7.1b). La précision aux stations ayant les biais les plus faibles a été améliorée, mais elle a aussi diminué à d'autres stations. Parmi les 8 stations qui sont surestimées de plus de 1 °C, 4 sont localisées sur le maillage Eaudyssée (5, 39, 42, 44). Une sous-estimation potentielle des flux de nappe ne peut être écartée, étant donné que la précision des résultats fournis par Eaudyssée (en termes de flux) est difficilement quantifiable. Une surestimation de la température de la nappe pourrait aussi expliquer ces biais. Parmi les 4 autres stations qui ne sont pas sur le maillage Eaudyssée (2, 13, 34, 36), 2 sont dans le bassin sédimentaire et 2 dans le massif Armoricaïn. Comme suggéré aux chapitres 2 et 3, des flux de nappes non négligeables peuvent également avoir lieu dans le massif Armoricaïn, même si les aquifères sont moins productifs que dans le bassin sédimentaire. Les surestimations ne sont probablement pas liées à une sous-estimation du taux de végétation rivulaire, puisque 7 stations parmi les 8 qui sont surestimées de plus de 1 °C ont un taux de végétation de plus de 50%. Une autre explication possible, qui n'a pas été analysée dans cette thèse, est que T-NET ne prend pas en compte la conduction de la chaleur depuis la masse d'eau vers le substrat sous-jacent. Ce processus a généralement un effet net qui va dans le même sens que celui des flux de nappe (Webb et Zhang, 2004) et est plus important dans les cours d'eau peu profonds en raison des amplitudes journalières plus marquées (Chen et al., 1998a). Il dépend de la profondeur d'eau, de la turbidité, et du gradient de température entre l'eau et le substrat. Par exemple, une étude a quantifié ce processus à 24% des pertes totales de chaleur en été et en automne pour une rivière peu profonde en Angleterre (Evans et al., 1998). Ce processus a été implémenté dans plusieurs modèles qui pourraient être source d'inspiration (Chen et al., 1998a ; Haag et Luce, 2008). Les sous-estimations (Figure 7.1) s'expliquent probablement par des taux de végétation surestimés : 11 stations parmi les 12 qui sont sous-estimées de plus de -1 °C (sans prendre en compte les stations du Loir pour lesquelles les données LiDAR ont été utilisées) ont un taux de végétation de plus de 70%.

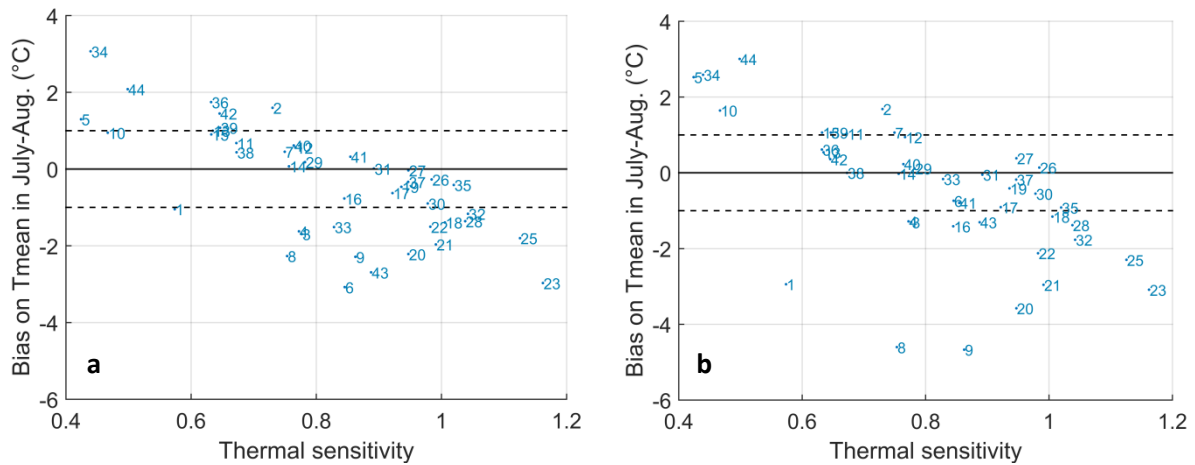


Figure 7.1 : Biais ( $T_{sim}-T_{obs}$ ) de la température moyenne journalière en juillet-août en fonction de la sensibilité thermique (2008-2013) (a) simulation incluant toutes les modifications apportées dans cette thèse (b) version standard du modèle (Beaufort et al., 2016). Les références aux numéros de stations sont en annexe B.

En moyenne sur la période 13-31/08/2009, les profils longitudinaux obtenus avec la version finale de T-NET (qui inclut toutes les modifications; Figure 7.2) sont plus proches que la simulation standard de toutes les températures observées (sauf à la station n°34).

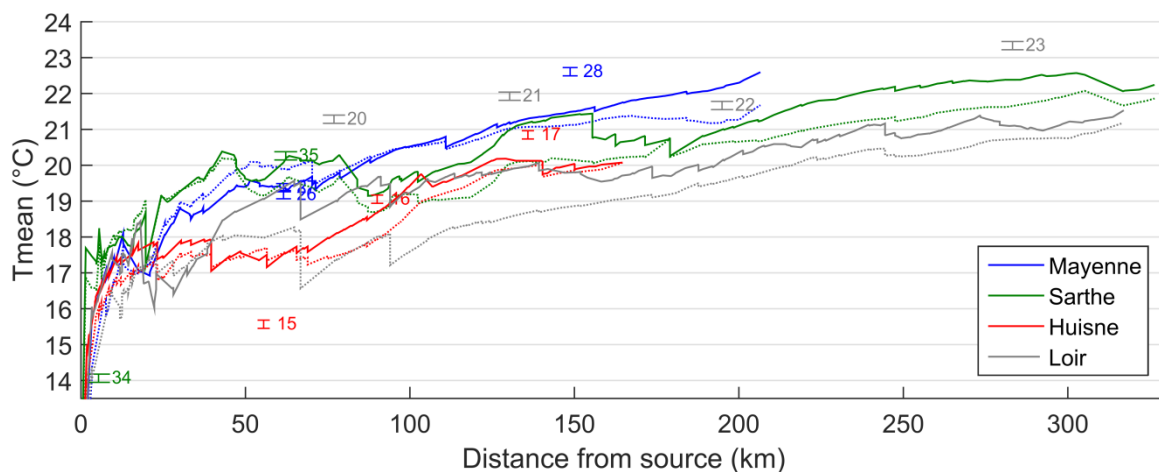


Figure 7.2: Profils longitudinaux des températures moyennes journalières sur les 4 rivières principales du bassin de la Maine, moyennés sur la période 13-31/08/2009, simulés avec la version la plus complète de T-NET (lignes continues) et avec la version standard (pointillés)

La Conie (stations n° 8 et 9) reste l'affluent ayant l'impact le plus important sur les  $T_w$  estivales des 4 rivières principales du bassin de la Maine. La sous-estimation de la  $T_w$  de la Conie est probablement due à deux causes. La première est que, sur le sous-bassin de la Conie, EROS surestime le débit de plus de 150% en hiver et de plus de 350% en été, ce qui conduit à un écoulement trop rapide et trop froid l'été. Pour la même raison, les hauteurs d'eau modélisées sont plus importantes que sur les autres rivières, ce qui explique pourquoi les amplitudes journalières sont sous-estimées, à l'inverse de ce qui est observé sur les autres stations. La prise en compte des prélèvements d'eau, qui sont significatifs dans cette région, pourrait permettre d'améliorer la caractérisation des débits sur ce sous-bassin. La deuxième raison est que l'influence des étangs n'est pas prise en compte dans T-NET.

#### 7.4.4 Perspectives pour le développement de T-NET

La surestimation globale des amplitudes journalières et des amplitudes du signal thermique sur des échelles de temps de 1 à 2 semaines peut être corrigée par une amélioration de la précision des

hauteurs d'eau. En même temps, une meilleure caractérisation des largeurs et des pentes, et donc des vitesses d'écoulement permettrait d'améliorer légèrement les biais négatifs estivaux. Cette amélioration globale de la géométrie hydraulique peut être réalisée par un nouvel ajustement des équations empiriques Estimkart, ou en utilisant l'équation de Manning-Strickler avec des coefficients calibrés. Le réseau Carhyce peut fournir des mesures de terrain, bien que leur nombre est actuellement limité (~40 observations sur le bassin de la Maine). L'acquisition de courbes de tarage aux 81 stations de jaugeage permettrait de fournir des séries temporelles de hauteurs d'eau nécessaires pour calibrer les équations Estimkart ou le coefficient de Manning. Des mesures topographiques acquises pour l'évaluation des risques d'inondation pourraient également être utilisées dans T-NET avec l'équation de Manning. Des techniques récentes comme le LiDAR bathymétrique pourraient aussi fournir des données de géométrie hydraulique à haute résolution, mais il semble qu'il y a encore quelques problèmes techniques à résoudre avant de pouvoir l'appliquer à la modélisation de Tw, en particulier à l'échelle régionale (Hilldale et Raff, 2008 ; Bailly et al., 2010). Sur la plupart des cours d'eau du bassin de la Maine, une caractérisation des largeurs constante dans le temps pourrait être suffisante en raison de leur faible variabilité. Les largeurs à plein bord peuvent être extraites à partir de la BD TOPO pour les cours d'eau de plus de 6 m de large.

L'amélioration des données de taux de végétation est susceptible d'améliorer les performances de T-NET aux stations négativement biaisées. Aujourd'hui, l'imagerie à très haute résolution spatiale peut fournir ces informations de façon précise et à l'échelle régionale (Tormos et al., 2014). Cependant, cela nécessite de disposer d'un réseau hydrographique dont la localisation est précise, en particulier pour les plus petits cours d'eau. Le projet Topage permettra d'augmenter cette précision et devrait être disponible d'ici 2019.

Comme l'ont souligné Michez et al. (2017), la combinaison de la technologie LiDAR avec la photogrammétrie pourrait permettre l'obtention des hauteurs de végétation à des coûts relativement faibles, pour les zones où les données LiDAR ne sont pas encore disponibles (c'est à dire sur les petits cours d'eau). À partir de ces données, des relations empiriques avec des variables comme l'occupation du sol pourraient être établies dans le but de caractériser les propriétés de la végétation là où les données LiDAR et la photogrammétrie ne sont pas disponibles.

La caractérisation des flux de nappes a probablement atteint le niveau le plus avancé possible. Un développement intéressant resterait d'appliquer un modèle hydrogéologique aussi sur le massif Armoricaïn. Cela représenterait cependant un travail considérable qui va au delà d'une étude sur la modélisation de Tw. Comme évoqué plus haut, la prise en compte des processus de conduction entre le cours d'eau et le substrat pourraient permettre de corriger les biais positifs aux stations à faible TS. Une diminution de la température des nappes améliorera la performance à ces mêmes stations. Cependant, cela doit être accompagné d'une modification pour réchauffer les stations négativement biaisées car sinon les performances globales diminueront. Des mesures de Tw aux sources des cours d'eau pourraient être utiles pour savoir si la méthode de calcul actuellement utilisée est adaptée au contexte hydrogéologique contrasté du bassin de la Maine.

La prise en compte de l'influence des étangs améliorera probablement les performances à certaines stations qui sont actuellement sous-estimées, comme sur la Conie. Cela serait tout à fait innovant car, à notre connaissance, aucun modèle adapté à l'échelle régionale ne prend actuellement cet aspect en

compte. Pour le moment, cela resterait un défi car il est difficile de quantifier les liens hydrologiques entre les plans d'eau et les cours d'eau. Un réseau hydrographique correctement positionné est aussi nécessaire pour progresser sur cette thématique. Dès que le réseau Topage sera disponible, il pourrait être possible de prendre en compte les superficies des plans d'eau dans le calcul de l'ombrage et dans le calcul des vitesses d'écoulement.

Nous avons émis l'hypothèse que la présence de seuils pourrait également expliquer en partie certains biais négatifs. Le Référentiel des Obstacles à l'Écoulement (ROE) fournit la localisation des seuils, ainsi que leur hauteur. Une tentative de prise en compte a été effectuée au cours de cette thèse, en considérant les volumes d'eau supplémentaires stockés derrière les seuils. Cependant, cette approche dépend fortement de la précision des hauteurs d'eau modélisées, qui n'est actuellement pas assez bonne. Dès que la caractérisation des hauteurs d'eau aura été améliorée, l'impact des seuils sur  $T_w$  pourrait être pris en compte en modélisant la stratification thermique, uniquement lorsque cela est nécessaire. En effet, comme l'indiquent Bormans et Webster (1997), la stratification thermique doit être modélisée uniquement lorsque  $T_w$  augmente et lorsque les vitesses d'écoulement sont faibles. La température de la couche supérieure pourrait alors être considérée dans la propagation vers l'aval.

Lorsque les biais sur les températures moyennes et sur les amplitudes journalières seront diminués, T-NET pourra être forcé avec des températures de l'air et des débits provenant de scénarios sous changement climatique (Hardenbicker et al., 2016 ; Soto, 2017 ; Beaufort, 2015). Combiné à des modèles d'habitats, les résultats permettront de comprendre et de prévoir le rétrécissement des habitats des espèces sensibles (Isaak et al., 2015 ; Battin et al., 2007 ; Tung et al., 2006).

## Bibliography

Alhaskeer Z. (2012, December) Cartographic analysis of the structure of landscapes of valleys : evaluation of landscape dynamics in valleys of Maine Watershed using remote sensing and GIS (Theses); Université du Maine. Retrieved from <https://tel.archives-ouvertes.fr/tel-00793094>

Alhaskeer Z., Corbonnois J., Messner F., Laurent F. (2014) Élaboration d'une typologie des formes de vallées. Application au bassin de la Maine (plateaux du Nord-Ouest de la France). *Physio-Géo. Géographie physique et environnement*, (Volume 8), 215–230.

Allen D., Dietrich W., Baker P., Ligon F., Orr B., others. (2007) Development of a mechanistically based, basin-scale stream temperature model: applications to cumulative effects modeling. *Proceedings of the redwood region forest science symposium: What does the future hold*, 11–24; Forest Service, USDA: Albany, CA.

Anderson E. R. (1954) Energy budget studies, Part of Water Loss Investigations—Lake Hefner Studies. US Geological Survey. Professional Paper, 269.

Angilletta M. J. (2009) *Thermal adaptation: a theoretical and empirical synthesis*; Oxford University Press.

Arismendi I., Johnson S. L., Dunham J. B., Haggerty R. (2013) Descriptors of natural thermal regimes in streams and their responsiveness to change in the Pacific Northwest of North America. *Freshwater Biology*, 58 (5), 880–894.

Arismendi I., Safeeq M., Dunham J. B., Johnson S. L. (2014) Can air temperature be used to project influences of climate change on stream temperature? *Environmental Research Letters*, 9 (8), 084015.

Arora R., Tockner K., Venohr M. (2016) Changing river temperatures in northern Germany: trends and drivers of change. *Hydrological Processes*, 30 (17), 3084–3096.

Bailly J.-S., Le Coarer Y., Languille P., Stigermark C.-J., Allouis T. (2010) Geostatistical estimations of bathymetric LiDAR errors on rivers. *Earth Surface Processes and Landforms*, 35 (10), 1199–1210.

Baratelli F., Flipo N., Moatar F. (2016) Estimation of stream-aquifer exchanges at regional scale using a distributed model: Sensitivity to in-stream water level fluctuations, riverbed elevation and roughness. *Journal of Hydrology*, 542, 686–703.

Battin J., Wiley M. W., Ruckelshaus M. H., Palmer R. N., Korb E., Bartz K. K., Imaki H. (2007) Projected impacts of climate change on salmon habitat restoration. *Proceedings of the National Academy of Sciences*, 104 (16), 6720–6725.

Beaufort A. (2015) *Modélisation physique de la température des cours d'eau à l'échelle régionale : Application au bassin versant de la Loire*.

Beaufort A., Curie F., Moatar F., Ducharne A., Melin E., Thiery D. (2016) T-NET, a dynamic model for simulating daily stream temperature at the regional scale based on a network topology. *Hydrological Processes*, 30 (13), 2196–2210.

Beaufort A., Moatar F., Curie F., Ducharne A., Bustillo V., Thiéry D. (2015) River Temperature Modelling by Strahler Order at the Regional Scale in the Loire River Basin, France. *River Research and Applications*, 32(4), 597-609.

Becker A., Kirchesch V., Baumert H. Z., Fischer H., Schöl A. (2010) Modelling the effects of thermal stratification on the oxygen budget of an impounded river. *River Research and Applications*, 26 (5), 572–588.

Boisneau C., Moatar F., Bodin M., Boisneau P. (2008) Does global warming impact on migration patterns and recruitment of Allis shad (*Alosa alosa* L.) young of the year in the Loire River, France? *Hydrobiologia*, 602 (1), 179–186.

- Bormans M., Webster I. T. (1997) A mixing criterion for turbid rivers. *Environmental Modelling & Software*, 12 (4), 329–333.
- Braun D. C., Reynolds J. D., Patterson D. A. (2015) Using watershed characteristics to inform cost-effective stream temperature monitoring. *Aquatic Ecology*, 49 (3), 373–388.
- BRGM. (1980) Carte géologique de la France à 1/1000000; BRGM, Orléans.
- Brown L. E., Hannah D. M., Milner A. M. (2005) Spatial and temporal water column and streambed temperature dynamics within an alpine catchment: implications for benthic communities. *Hydrological Processes*, 19 (8), 1585–1610.
- Buisson L., Blanc L., Grenouillet G. (2008) Modelling stream fish species distribution in a river network: the relative effects of temperature versus physical factors. *Ecology of Freshwater Fish*, 17 (2), 244–257.
- Bustillo V., Moatar F., Ducharne A., Thiéry D., Poirel A. (2014) A multimodel comparison for assessing water temperatures under changing climate conditions via the equilibrium temperature concept: case study of the Middle Loire River, France. *Hydrological Processes*, 28 (3), 1507–1524.
- Caissie D. (2006) The thermal regime of rivers: a review. *Freshwater Biology*, 51 (8), 1389–1406.
- Caissie D., Satish M. G., El-Jabi N. (2005) Predicting river water temperatures using the equilibrium temperature concept with application on Miramichi River catchments (New Brunswick, Canada). *Hydrological Processes*, 19 (11), 2137–2159.
- Canellas C., Gibelin A.-L., Lassègues P., Kerdoncuff M., Dandin P., Simon P. (2014) The 1981-2010 Aurelhy gridded climate normals. Retrieved from <http://hdl.handle.net/2042/53750>
- Cantón M. A., Cortegoso J. L., Rosa C. de. (1994) Solar permeability of urban trees in cities of western Argentina. *Energy and Buildings*, 20 (3), 219–230.
- Chang H., Psaris M. (2013) Local landscape predictors of maximum stream temperature and thermal sensitivity in the Columbia River Basin, USA. *Science of The Total Environment*, 461–462, 587–600.
- Chen D., Hu M., Guo Y., Dahlgren R. A. (2016) Changes in river water temperature between 1980 and 2012 in Yongan watershed, eastern China: Magnitude, drivers and models. *Journal of Hydrology*, 533, 191–199.
- Chen Y. D., Carsel R. F., McCutcheon S. C., Nutter W. L. (1998a) Stream Temperature Simulation of Forested Riparian Areas: I. Watershed-Scale Model Development. *Journal of Environmental Engineering*, 124 (4), 304–315.
- Chen Y. D., McCutcheon S. C., Norton D. J., Nutter W. L. (1998b) Stream Temperature Simulation of Forested Riparian Areas: II. Model Application. *Journal of Environmental Engineering*, 124 (4), 316–328.
- Cheng S.-T., Wiley M. J. (2016) A Reduced Parameter Stream Temperature Model (RPSTM) for basin-wide simulations. *Environmental Modelling & Software*, 82, 295–307.
- Chrétien P., Lucassou F., Rouxel E., Gautron C., Plouhinec H. (2014) Synthèse hydrogéologique des Pays de la Loire. Rapport final. BRGM/64044-FR.
- Chu C., Jones N. E. (2011) Spatial variability of thermal regimes and other environmental determinants of stream fish communities in the Great Lakes Basin, Ontario, Canada. *River Research and Applications*, 27 (5), 646–662.
- Chu C., Jones N. E., Allin L. (2010) Linking the thermal regimes of streams in the Great Lakes Basin, Ontario, to landscape and climate variables. *River Research and Applications*, 26 (3), 221–241.
- Cole T., Wells S. (2006) CE-QUAL-W2: A Two-dimensional, Laterally Averaged, Hydrodynamic and Water Quality Model, Version 3.5. Civil and Environmental Engineering Faculty Publications and Presentations. Retrieved from [http://pdxscholar.library.pdx.edu/cengin\\_fac/130](http://pdxscholar.library.pdx.edu/cengin_fac/130)

- Cowan W. L. (1956) Estimating hydraulic roughness coefficients. *Agricultural Engineering*, 37 (7), 473–475.
- Cox M. M., Bolte J. P. (2007) A spatially explicit network-based model for estimating stream temperature distribution. *Environmental Modelling & Software Special section: Environmental Risk and Emergency Management*, 22 (4), 502–514.
- Daigle A., Caudron A., Vigier L., Pella H. (2017) Optimization methodology for a river temperature monitoring network for the characterization of fish thermal habitat. *Hydrological Sciences Journal*, 62 (3), 483–497.
- Daufresne M., Roger M. C., Capra H., Lamouroux N. (2004) Long-term changes within the invertebrate and fish communities of the Upper Rhône River: effects of climatic factors. *Global Change Biology*, 10 (1), 124–140.
- Davies-Colley R. J., Quinn J. M. (1998) Stream lighting in five regions of North Island, New Zealand: Control by channel size and riparian vegetation. *New Zealand Journal of Marine and Freshwater Research*, 32 (4), 591–605.
- Deltares. (2014) *Delft3D-FLOW: Simulation of Multidimensional Hydrodynamic Flows and Transport Phenomena, including Sediments, User Manual*. Deltares Systems, Delft, The Netherlands, 684 pp.
- DeWalle D. R. (2008) Guidelines for Riparian Vegetative Shade Restoration Based Upon a Theoretical Shaded-Stream Model. *JAWRA Journal of the American Water Resources Association*, 44 (6), 1373–1387.
- Dripps W., Granger S. R. (2013) The impact of artificially impounded, residential headwater lakes on downstream water temperature. *Environmental Earth Sciences*, 68 (8), 2399–2407.
- Du X., Shrestha N. K., Ficklin D. L., Wang J. (2017) Incorporation of the equilibrium temperature approach in a Soil and Water Assessment Tool hydroclimatological stream temperature model. *Hydrol. Earth Syst. Sci. Discuss.*, 2017, 1–17.
- Ducharne A. (2008) Importance of stream temperature to climate change impact on water quality. *Hydrol. Earth Syst. Sci.*, 12 (3), 797–810.
- Dugdale S. J., Malcolm I. A., Kantola K., Hannah D. M. (2018) Stream temperature under contrasting riparian forest cover: Understanding thermal dynamics and heat exchange processes. *Science of The Total Environment*, 610, 1375–1389.
- Duursma R. A., Mäkelä A. (2007) Summary models for light interception and light-use efficiency of non-homogeneous canopies. *Tree Physiology*, 27 (6), 859–870.
- Edinger J. E., Duttweiler D. W., Geyer J. C. (1968) The Response of Water Temperatures to Meteorological Conditions. *Water Resources Research*, 4 (5), 1137–1143.
- Elliott J. M., Elliott J. A. (2010) Temperature requirements of Atlantic salmon *Salmo salar*, brown trout *Salmo trutta* and Arctic charr *Salvelinus alpinus*: predicting the effects of climate change. *Journal of Fish Biology*, 77 (8), 1793–1817.
- Essaid H. I., Caldwell R. R. (2017) Evaluating the impact of irrigation on surface water – groundwater interaction and stream temperature in an agricultural watershed. *Science of The Total Environment*, 599–600, 581–596.
- Essery R., Bunting P., Rowlands A., Rutter N., Hardy J., Melloh R., Link T., et al. (2008) Radiative Transfer Modeling of a Coniferous Canopy Characterized by Airborne Remote Sensing. *Journal of Hydrometeorology*, 9 (2), 228–241.
- Evans E. C., McGregor G. R., Petts G. E. (1998) River energy budgets with special reference to river bed processes. *Hydrological Processes*, 12 (4), 575–595.

- Ficklin D. L., Luo Y., Stewart I. T., Maurer E. P. (2012) Development and application of a hydroclimatological stream temperature model within the Soil and Water Assessment Tool. *Water Resources Research*, 48 (1), W01511.
- Floury M., Usseglio-Polatera P., Ferreol M., Delattre C., Souchon Y. (2013) Global climate change in large European rivers: long-term effects on macroinvertebrate communities and potential local confounding factors. *Global Change Biology*, 19 (4), 1085–1099.
- Fu P., Rich P. M. (1999) Design and implementation of the Solar Analyst: an ArcView extension for modeling solar radiation at landscape scales. *Proceedings of the Nineteenth Annual ESRI User Conference*, 1–31.
- Gallice A., Bavay M., Brauchli T., Comola F., Lehning M., Huwald H. (2016) StreamFlow 1.0: an extension to the spatially distributed snow model Alpine3D for hydrological modelling and deterministic stream temperature prediction. *Geosci. Model Dev.*, 9 (12), 4491–4519.
- Garner G., Hannah D. M., Sadler J. P., Orr H. G. (2014a) River temperature regimes of England and Wales: spatial patterns, inter-annual variability and climatic sensitivity. *Hydrological Processes*, 28 (22), 5583–5598.
- Garner G., Malcolm I. A., Sadler J. P., Hannah D. M. (2014b) What causes cooling water temperature gradients in a forested stream reach? *Hydrology and Earth System Sciences*, 18 (12), 5361–5376.
- Garner G., Malcolm I. A., Sadler J. P., Hannah D. M. (2017) The role of riparian vegetation density, channel orientation and water velocity in determining river temperature dynamics. *Journal of Hydrology*, 553, 471–485.
- Gob F., Bilodeau C., Thommeret N., Belliard J., Albert M.-B., Tamisier V., Baudoin J.-M., et al. (2014) Un outil de caractérisation hydromorphologique des cours d'eau pour l'application de la DCE en France (CARHYCE). *Géomorphologie: relief, processus, environnement*, 20 (1), 57–72.
- Gomi T., Moore R. D., Dhakal A. S. (2006) Headwater stream temperature response to clear-cut harvesting with different riparian treatments, coastal British Columbia, Canada. *Water Resources Research*, 42 (8), W08437.
- Goullet J. (2017) Vers une modélisation empirique de métriques de température de l'eau en été, à l'aide des caractéristiques spatiales des bassins versants. Unpublished report, Université de Tours.
- Grabowski Z. J., Watson E., Chang H. (2016) Using spatially explicit indicators to investigate watershed characteristics and stream temperature relationships. *Science of The Total Environment*, 551–552, 376–386.
- GRASS Development Team. (2015) Geographic Resources Analysis Support System (GRASS GIS) Software, Version 7.1; Open Source Geospatial Foundation. Retrieved from <http://grass.osgeo.org>
- Greenberg J. A., Hestir E. L., Riano D., Scheer G. J., Ustin S. L. (2012) Using LiDAR Data Analysis to Estimate Changes in Insolation Under Large-Scale Riparian Deforestation. *JAWRA Journal of the American Water Resources Association*, 48 (5), 939–948.
- Guzy M., Richardson K., Lambrinos J. G. (2015) A tool for assisting municipalities in developing riparian shade inventories. *Urban Forestry & Urban Greening*, 14 (2), 345–353.
- Haag I., Luce A. (2008) The integrated water balance and water temperature model LARSIM-WT. *Hydrological Processes*, 22 (7), 1046–1056.
- Haag I., Westrich B. (2002) Processes governing river water quality identified by principal component analysis. *Hydrological Processes*, 16 (16), 3113–3130.
- Hannah D., Garner G. (2015) River water temperature in the United Kingdom: Changes over the 20th century and possible changes over the 21st century. *Progress in Physical Geography*, 39, 68–92.

- Hannah D. M., Malcolm I. A., Soulsby C., Youngson A. F. (2008) A comparison of forest and moorland stream microclimate, heat exchanges and thermal dynamics. *Hydrological Processes*, 22 (7), 919–940.
- Hardenbicker P., Viergutz C., Becker A., Kirchesch V., Nilson E., Fischer H. (2016) Water temperature increases in the river Rhine in response to climate change. *Regional Environmental Change*. Retrieved from <http://link.springer.com/10.1007/s10113-016-1006-3>
- Hebert C., Caissie D., Satish M. G., El-Jabi N. (2011) Study of stream temperature dynamics and corresponding heat fluxes within Miramichi River catchments (New Brunswick, Canada). *Hydrological Processes*, 25 (15), 2439–2455.
- Hilderbrand R. H., Kashiwagi M. T., Prochaska A. P. (2014) Regional and Local Scale Modeling of Stream Temperatures and Spatio-Temporal Variation in Thermal Sensitivities. *Environmental Management*, 54 (1), 14–22.
- Hilldale R. C., Raff D. (2008) Assessing the ability of airborne LiDAR to map river bathymetry. *Earth Surface Processes and Landforms*, 33 (5), 773–783.
- Hofierka J., Suri M. (2002) The solar radiation model for Open source GIS: implementation and applications. *Proceedings of the Open source GIS-GRASS users conference*, 1–19.
- Hrachowitz M., Soulsby C., Imholt C., Malcolm I. A., Tetzlaff D. (2010) Thermal regimes in a large upland salmon river: a simple model to identify the influence of landscape controls and climate change on maximum temperatures. *Hydrological Processes*, 24 (23), 3374–3391.
- Isaak D. J., Luce C. H., Rieman B. E., Nagel D. E., Peterson E. E., Horan D. L., Parkes S., et al. (2010) Effects of climate change and wildfire on stream temperatures and salmonid thermal habitat in a mountain river network. *Ecological Applications*, 20 (5), 1350–1371.
- Isaak D. J., Peterson E. E., Ver Hoef J. M., Wenger S. J., Falke J. A., Torgersen C. E., Sowder C., et al. (2014) Applications of spatial statistical network models to stream data. *Wiley Interdisciplinary Reviews: Water*, 1 (3), 277–294.
- Isaak D. J., Wenger S. J., Young M. K. (2017) Big biology meets microclimatology: defining thermal niches of ectotherms at landscape scales for conservation planning. *Ecological Applications*, 27 (3), 977–990.
- Isaak D. J., Young M. K., Nagel D. E., Horan D. L., Groce M. C. (2015) The cold-water climate shield: delineating refugia for preserving salmonid fishes through the 21st century. *Global Change Biology*, 21 (7), 2540–2553.
- Jackson F. I., Hannah D. M., Fryer R. j., Millar C. p., Malcolm I. a. (2017) Development of spatial regression models for predicting summer river temperatures from landscape characteristics: Implications for land and fisheries management. *Hydrological Processes*, 31 (6), 1225–1238.
- Johnson G. T., Watson I. D. (1984) The Determination of View-Factors in Urban Canyons. *Journal of Climate and Applied Meteorology*, 23 (2), 329–335.
- Johnson M. F., Wilby R. L. (2015) Seeing the landscape for the trees: Metrics to guide riparian shade management in river catchments. *Water Resources Research*, 51 (5), 3754–3769.
- Johnson S. L. (2004) Factors influencing stream temperatures in small streams: substrate effects and a shading experiment. *Canadian Journal of Fisheries and Aquatic Sciences*, 61 (6), 913–923.
- Karant K. R. (1987) *Ground water assessment: development and management*; Tata McGraw-Hill Education.
- Kaushal S. S., Likens G. E., Jaworski N. A., Pace M. L., Sides A. M., Seekell D., Belt K. T., et al. (2010) Rising stream and river temperatures in the United States. *Frontiers in Ecology and the Environment*, 8 (9), 461–466.

- Kelleher C., Wagener T., Gooseff M., McGlynn B., McGuire K., Marshall L. (2012) Investigating controls on the thermal sensitivity of Pennsylvania streams. *Hydrological Processes*, 26 (5), 771–785.
- Konarska J., Lindberg F., Larsson A., Thorsson S., Holmer B. (2014) Transmissivity of solar radiation through crowns of single urban trees - application for outdoor thermal comfort modelling. *Theoretical and Applied Climatology*, 117 (3–4), 363–376.
- Kothandaraman V. (1971) Analysis of water temperature variations in large river. *Journal of the Sanitary Engineering Division*, 97 (1), 19–31.
- Krider L. A., Magner J. A., Perry J., Vondracek B., Ferrington L. C. (2013) Air-Water Temperature Relationships in the Trout Streams of Southeastern Minnesota's Carbonate-Sandstone Landscape. *JAWRA Journal of the American Water Resources Association*, 49 (4), 896–907.
- Kurylyk B. L., MacQuarrie K. T. B., Caissie D., McKenzie J. M. (2015) Shallow groundwater thermal sensitivity to climate change and land cover disturbances: derivation of analytical expressions and implications for stream temperature modeling. *Hydrol. Earth Syst. Sci.*, 19 (5), 2469–2489.
- Laizé C. L. R., Bruna Meredith C., Dunbar M. J., Hannah D. M. (2017) Climate and basin drivers of seasonal river water temperature dynamics. *Hydrol. Earth Syst. Sci.*, 21 (6), 3231–3247.
- Lalot E., Curie F., Wawrzyniak V., Baratelli F., Schomburgk S., Flipo N., Piegay H., et al. (2015) Quantification of the contribution of the Beauce groundwater aquifer to the discharge of the Loire River using thermal infrared satellite imaging. *Hydrol. Earth Syst. Sci.*, 19 (11), 4479–4492.
- Lamouroux N., Pella H., Vanderbecq A., Sauquet E., Lejot J. (2010) Estimkart 2.0: Une plate-forme de modèles écohydrologiques pour contribuer à la gestion des cours d'eau à l'échelle des bassins français. Version provisoire. Version provisoire. Cemagref, Agence de l'Eau Rhône-Méditerranée-Corse, Onema, Lyon (45 pp.).
- Leach J., Moore R. (2010) Above-stream microclimate and stream surface energy exchanges in a wildfire-disturbed riparian zone. *Hydrological Processes*, 24 (17), 2369–2381.
- LeBlanc R. T., Brown R. D., FitzGibbon J. E. (1997) Modeling the Effects of Land Use Change on the Water Temperature in Unregulated Urban Streams. *Journal of Environmental Management*, 49 (4), 445–469.
- Lebourgeois F., Pierrat J.-C., Perez V., Piedallu C., Cecchini S., Ulrich E. (2008) Phenological timing in French temperate forests - A study on stands in the Renecofor network. Retrieved from <http://hdl.handle.net/2042/19767>
- Lee T. Y., Huang J. C., Kao S. J., Liao L. Y., Tzeng C. S., Yang C. H., Kalita P. K., et al. (2012) Modeling the effects of riparian planting strategies on stream temperature: Increasing suitable habitat for endangered Formosan Landlocked Salmon in Shei-Pa National Park, Taiwan. *Hydrological Processes*, 26 (24), 3635–3644.
- Li G., Jackson C. R., Kraseski K. A. (2012) Modeled riparian stream shading: Agreement with field measurements and sensitivity to riparian conditions. *Journal of Hydrology*, 428, 142–151.
- Loinaz M. C., Davidsen H. K., Butts M., Bauer-Gottwein P. (2013) Integrated flow and temperature modeling at the catchment scale. *Journal of Hydrology*, 495, 238–251.
- Maderich V., Heling R., Bezhenar R., Brovchenko I., Jenner H., Koshebutskyy V., Kuschan A., et al. (2008) Development and application of 3D numerical model THREETOX to the prediction of cooling water transport and mixing in the inland and coastal waters. *Hydrological Processes*, 22 (7), 1000–1013.
- Magnuson J. J., Crowder L. B., Medvick P. A. (1979) Temperature as an Ecological Resource. *American Zoologist*, 19 (1), 331–343.

- Maheu A. (2015, November) Développement d'outils de caractérisation et de modélisation du régime thermique des rivières naturelles et régulées. (phd); Université du Québec, Institut national de la recherche scientifique, Québec. Retrieved from <http://espace.inrs.ca/4398/>
- Maheu A., Poff N. L., St-Hilaire A. (2016) A Classification of Stream Water Temperature Regimes in the Conterminous USA. *River Research and Applications*, 32 (5), 896–906.
- Marchand M., Al-Azri N., Ombe-Ndeffotsing A., Wey E., Wald L. (2017) Evaluating meso-scale change in performance of several databases of hourly surface irradiation in South-eastern Arabic Pensinsula. *Advances in Science and Research*, 14, 7.
- Mardhel V., Pinault J., Stollsteiner P., Allier D. (2007) Etude des risques d'inondation par remontées de nappes sur le bassin de la Maine. Rapport final BRGM RP-55562-FR.
- Martin J. C. (1999) Piézométrie de la nappe de Beauce. Bilan du réseau piézométrique. Etat corrigé de hautes eaux 1986. Rap. BRGM R 40379.
- Michez A., Piégay H., Lejeune P., Claessens H. (2017) Multi-temporal monitoring of a regional riparian buffer network (>12,000 km) with LiDAR and photogrammetric point clouds. *Journal of Environmental Management*, 202 (Part 2), 424–436.
- Minaudo C., Curie F., Jullian Y., Gassama N., Moatar F. (2017) QUAL-NET, a high temporal resolution eutrophication model in large hydrographic networks. *Biogeosciences Discuss.*, 2017, 1–33.
- Moatar F., Gailhard J. (2006) Water temperature behaviour in the River Loire since 1976 and 1881. *Comptes Rendus Geoscience*, 338 (5), 319–328.
- Moatar F., Miquel J., Poirel A. (2001) A quality-control method for physical and chemical monitoring data. Application to dissolved oxygen levels in the river Loire (France). *Journal of Hydrology*, 252 (1–4), 25–36.
- Mohseni O., Stefan H. G., Erickson T. R. (1998) A nonlinear regression model for weekly stream temperatures. *Water Resources Research*, 34 (10), 2685–2692.
- Molinero J., Larrañaga A., Pérez J., Martínez A., Pozo J. (2016) Stream temperature in the Basque Mountains during winter: thermal regimes and sensitivity to air warming. *Climatic Change*, 134 (4), 593–604.
- Moore R. D. (2006) Stream Temperature Patterns in British Columbia, Canada, Based on Routine Spot Measurements. *Canadian Water Resources Journal / Revue canadienne des ressources hydriques*, 31 (1), 41–56.
- Moore R. D., Leach J. A., Knudson J. M. (2014) Geometric calculation of view factors for stream surface radiation modelling in the presence of riparian forest. *Hydrological Processes*, 28 (6), 2975–2986.
- Moore R. D., Spittlehouse D. L., Story A. (2005) Riparian Microclimate and Stream Temperature Response to Forest Harvesting: A Review. *JAWRA Journal of the American Water Resources Association*, 41 (4), 813–834.
- Muller E. (1995) Phénologie forestière révélée par l'analyse d'images thematic mapper. *Comptes rendus de l'Académie des sciences. Série 3, Sciences de la vie*, 318 (9), 993–1003.
- Nash J. E., Sutcliffe J. V. (1970) River flow forecasting through conceptual models part I — A discussion of principles. *Journal of Hydrology*, 10 (3), 282–290.
- O'Driscoll M. A., DeWalle D. R. (2006) Stream–air temperature relations to classify stream–ground water interactions in a karst setting, central Pennsylvania, USA. *Journal of Hydrology*, 329 (1–2), 140–153.

- Olden J. D., Naiman R. J. (2010) Incorporating thermal regimes into environmental flows assessments: modifying dam operations to restore freshwater ecosystem integrity. *Freshwater Biology*, 55 (1), 86–107.
- Orr H. G., Simpson G. L., Clers S. des, Watts G., Hughes M., Hannaford J., Dunbar M. J., et al. (2015) Detecting changing river temperatures in England and Wales. *Hydrological Processes*, 29 (5), 752–766.
- Ouellet V., Secretan Y., St-Hilaire A., Morin J. (2014) Daily Averaged 2d Water Temperature Model for the St. Lawrence River. *River Research and Applications*, 30 (6), 733–744.
- Ouzeau G., Déqué M., Jouini M., Planton S., Vautard R. (2014) Le climat de la France au XXIe siècle. Rapport de la Direction générale de l'énergie et du climat.
- Pedersen N. L., Sand-Jensen K. (2007) Temperature in lowland Danish streams: contemporary patterns, empirical models and future scenarios. *Hydrological Processes*, 21 (3), 348–358.
- Pilgrim J. M., Fang X., Stefan H. G. (1998) Stream Temperature Correlations with Air Temperatures in Minnesota: Implications for Climate Warming. *JAWRA Journal of the American Water Resources Association*, 34 (5), 1109–1121.
- Poirel A., Lauters F., Desaint B. (2008) 1977-2006 : Trente années de mesures des températures de l'eau dans le Bassin du Rhône. *Hydroécologie Appliquée*, 16, 191–213.
- Quintana-Seguí P., Le Moigne P., Durand Y., Martin E., Habets F., Baillon M., Canellas C., et al. (2008) Analysis of near-surface atmospheric variables: Validation of the SAFRAN analysis over France. *Journal of applied meteorology and climatology*, 47 (1), 92–107.
- Sattin M., Milne R., Deans J. D., Jarvis P. G. (1997) Radiation interception measurement in poplar: sample size and comparison between tube solarimeters and quantum sensors. *Agricultural and Forest Meteorology*, 85 (3–4), 209–216.
- Sellers W. D. (1965) *Physical climatology*; University of Chicago Press.
- Sinokrot B. A., Stefan H. G. (1993) Stream temperature dynamics: Measurements and modeling. *Water Resources Research*, 29 (7), 2299–2312.
- Soto B. (2017) Climate-induced changes in river water temperature in North Iberian Peninsula. *Theoretical and Applied Climatology*, 1–12.
- Soudani K., Hmimina G., Delpierre N., Pontauiller J.-Y., Aubinet M., Bonal D., Caquet B., et al. (2012) Ground-based Network of NDVI measurements for tracking temporal dynamics of canopy structure and vegetation phenology in different biomes. *Remote Sensing of Environment*, 123, 234–245.
- Sridhar V., Sansone A. L., LaMarche J., Dubin T., Lettenmaier D. P. (2004) *Prediction of stream temperature in forested watersheds*; Wiley Online Library.
- Steele T. D. (1982) A characterization of stream temperatures in Pakistan using harmonic analysis. *Hydrological Sciences Journal*, 27 (4), 451–467.
- Steen P. J., Zorn T. G., Seelbach P. W., Schaeffer J. S. (2008) Classification Tree Models for Predicting Distributions of Michigan Stream Fish from Landscape Variables. *Transactions of the American Fisheries Society*, 137 (4), 976–996.
- Stefan H. G., Preud'homme E. B. (1993) Stream Temperature Estimation from Air Temperature. *JAWRA Journal of the American Water Resources Association*, 29 (1), 27–45.
- Straile D., Stenseth N. C. (2007) The North Atlantic Oscillation and ecology: links between historical time-series, and lessons regarding future climate warming. *Climate Research*, 34 (3), 259–262.
- Sun N., Yearsley J., Voisin N., Lettenmaier D. P. (2015) A spatially distributed model for the assessment of land use impacts on stream temperature in small urban watersheds. *Hydrological Processes*, 29 (10), 2331–2345.

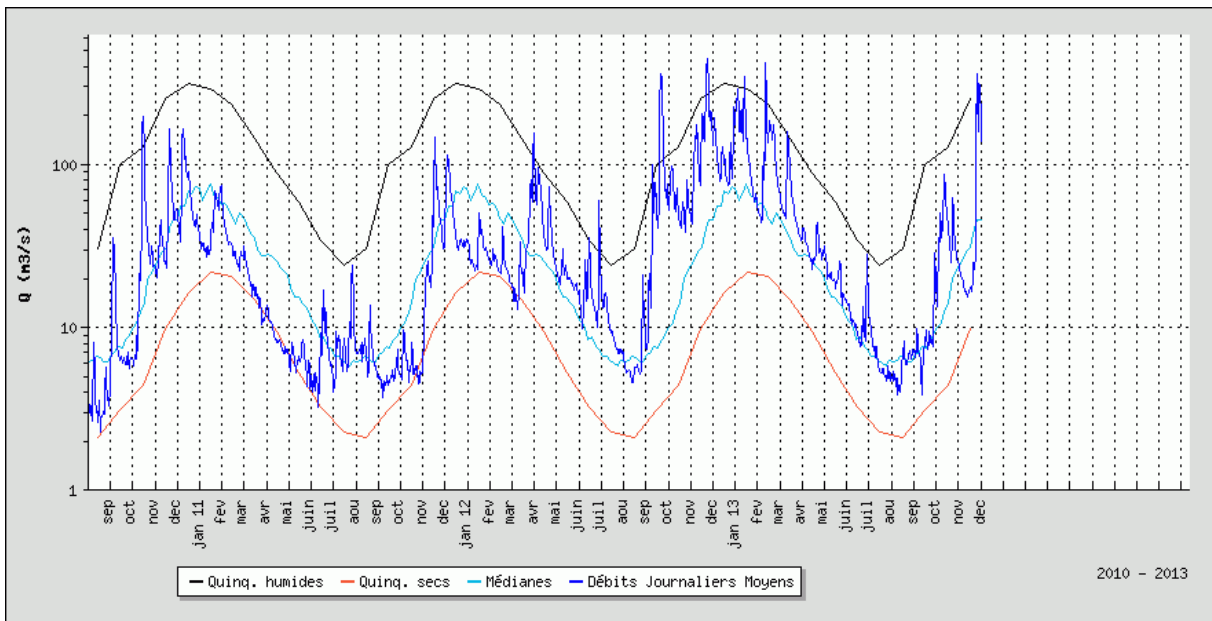
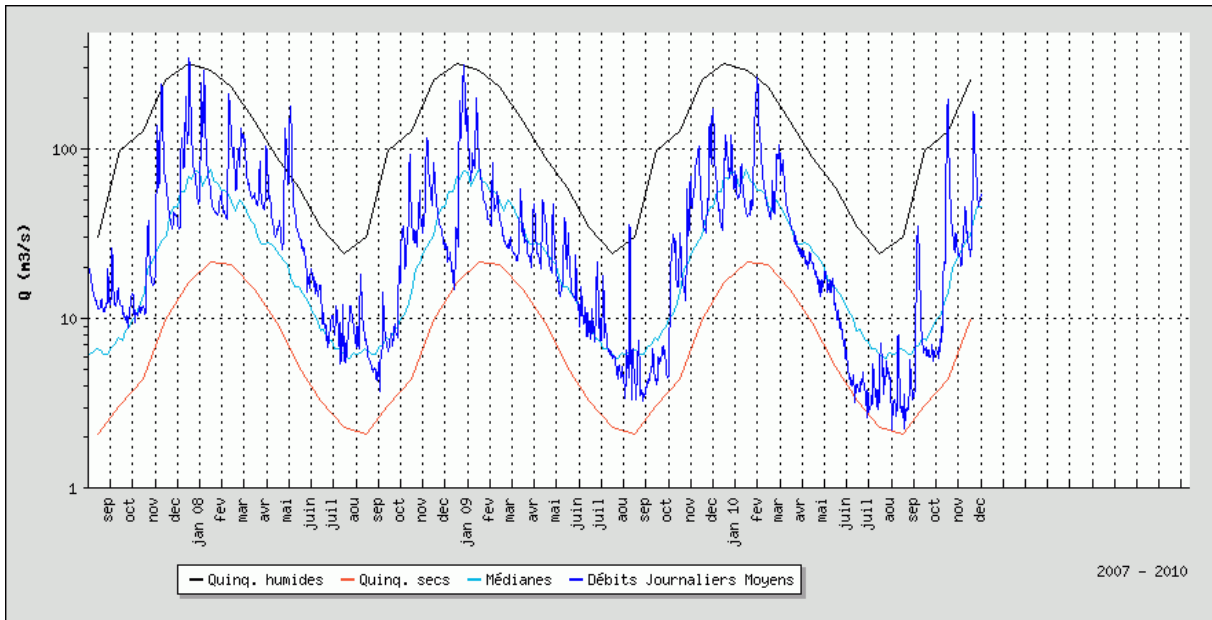
- Tague C., Farrell M., Grant G., Lewis S., Rey S. (2007) Hydrogeologic controls on summer stream temperatures in the McKenzie River basin, Oregon. *Hydrological Processes*, 21 (24), 3288–3300.
- Teti P. (2006) Stream shade as a function of channel width and riparian vegetation in the BC southern interior. *Streamline Watershed Manag. Bull.* (9), 10–15.
- Thiéry D. (2005) Code ÉROS v. 4.0: Description succincte du fonctionnement et des paramètres. Note technique NT EAU, 4.
- Thiéry D., Moutzopoulos C. (1992) Un modèle hydrologique spatialisé pour la simulation de très grands bassins: le modèle EROS formé de grappes de modèles globaux élémentaires. VIIIèmes journées hydrologiques de l'ORSTOM: Régionalisation en hydrologie, application au développement, 285–295; ORSTOM Editions.
- Thomas R. E., Gharrett J. A., Carls M. G., Rice S. D., Moles A., Korn S. (1986) Effects of Fluctuating Temperature on Mortality, Stress, and Energy Reserves of Juvenile Coho Salmon. *Transactions of the American Fisheries Society*, 115 (1), 52–59.
- Tisseuil C., Vrac M., Grenouillet G., Wade A. J., Gevrey M., Oberdorff T., Grodwohl J.-B., et al. (2012) Strengthening the link between climate, hydrological and species distribution modeling to assess the impacts of climate change on freshwater biodiversity. *Science of The Total Environment*, 424, 193–201.
- Todd D. K. (1980) *Groundwater Hydrology*, John Wiley, Hoboken, N. J..
- Torgersen C. E., Faux R. N., McIntosh B. A., Poage N. J., Norton D. J. (2001) Airborne thermal remote sensing for water temperature assessment in rivers and streams. *Remote Sensing of Environment*, 76 (3), 386–398.
- Tormos T., Van Looy K., Villeneuve B., Kosuth P., Souchon Y. (2014) High resolution land cover data improve understanding of mechanistic linkages with stream integrity. *Freshwater Biology*, 59 (8), 1721–1734.
- Tung C.-P., Lee T.-Y., Yang Y.-C. (2006) Modelling climate-change impacts on stream temperature of Formosan landlocked salmon habitat. *Hydrological Processes*, 20 (7), 1629–1649.
- Tung C.-P., Yang Y.-C. E., Lee T.-Y., Li M.-H. (2007) Modification of a stream temperature model with Beer's law and application to GaoShan Creek in Taiwan. *Ecological Modelling*, 200 (1–2), 217–224.
- Valette L., Piffady J., Chandesris A., Souchon Y. (2012) SYRAH-CE: description des données et modélisation du risque d'altération de l'hydromorphologie des cours d'eau pour l'Etat des lieux DCE. Rapport final, Pôle Hydroécologie des cours d'eau Onema-Irstea Lyon, MALY-LHQ, Lyon.
- Van Looy K., Tormos T., Souchon Y. (2014) Disentangling dam impacts in river networks. *Ecological Indicators*, 37 (Part A), 10–20.
- Vannote R. L., Minshall G. W., Cummins K. W., Sedell J. R., Cushing C. E. (1980) The River Continuum Concept. *Canadian Journal of Fisheries and Aquatic Sciences*, 37 (1), 130–137.
- Ver Hoef J. M., Peterson E., Theobald D. (2006) Spatial statistical models that use flow and stream distance. *Environmental and Ecological Statistics*, 13 (4), 449–464.
- Wasson J., Chandesris A., Pella H., Blanc L. (2002) Les hydro-écorégions de France métropolitaine: approche régionale de la typologie des eaux courantes et éléments pour la définition des peuplements de référence d'invertébrés. Convention MEDD-Cemagref, 06.
- Wawrzyniak V., Allemand P., Bailly S., Lejot J., Piégay H. (2017) Coupling LiDAR and thermal imagery to model the effects of riparian vegetation shade and groundwater inputs on summer river temperature. *Science of The Total Environment*, 592 (Supplement C), 616–626.
- Webb B. W., Clack P. D., Walling D. E. (2003) Water–air temperature relationships in a Devon river system and the role of flow. *Hydrological Processes*, 17 (15), 3069–3084.

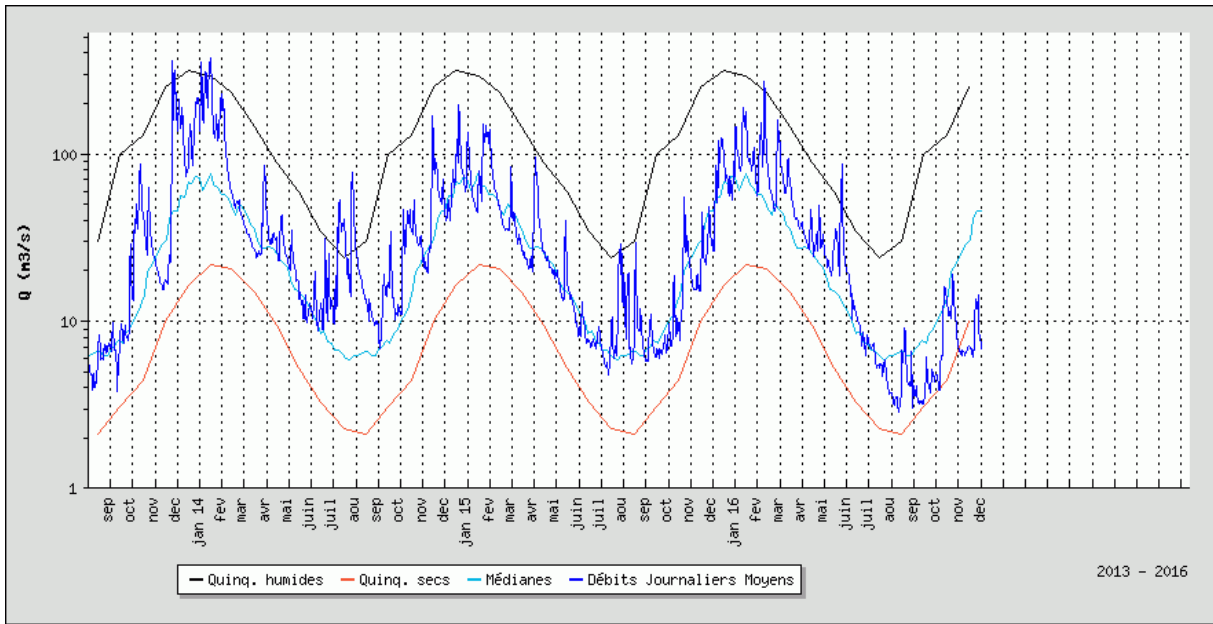
- Webb B., Zhang Y. (2004) Intra-annual variability in the non-advective heat energy budget of Devon streams and rivers. *Hydrological Processes*, 18 (11), 2117–2146.
- Wehrly K. E., Wiley M. J., Seelbach P. W. (1998) Landscape-based models that predict July thermal characteristics of lower Michigan rivers; Michigan Department of Natural Resources, Fisheries Division.
- Wehrly K. E., Wiley M. J., Seelbach P. W. (2003) Classifying Regional Variation in Thermal Regime Based on Stream Fish Community Patterns. *Transactions of the American Fisheries Society*, 132 (1), 18–38.
- Woltemade C. J., Hawkins T. W. (2016) Stream Temperature Impacts Because of Changes in Air Temperature, Land Cover and Stream Discharge: Navarro River Watershed, California, USA. *River Research and Applications*, 32 (10), 2020–2031.
- Woodward G., Perkins D. M., Brown L. E. (2010) Climate change and freshwater ecosystems: impacts across multiple levels of organization. *Philosophical Transactions of the Royal Society of London B: Biological Sciences*, 365 (1549), 2093–2106.
- Woznicki S. A., Nejadhashemi A. P., Tang Y., Wang L. (2016) Large-scale climate change vulnerability assessment of stream health. *Ecological Indicators*, 69, 578–594.
- Wu H., Kimball J. S., Elsner M. M., Mantua N., Adler R. F., Stanford J. (2012) Projected climate change impacts on the hydrology and temperature of Pacific Northwest rivers. *Water Resources Research*, 48 (11), W11530.
- Yearsley J. R. (2009) A semi-Lagrangian water temperature model for advection-dominated river systems. *Water Resources Research*, 45 (12), W12405.

# Appendices

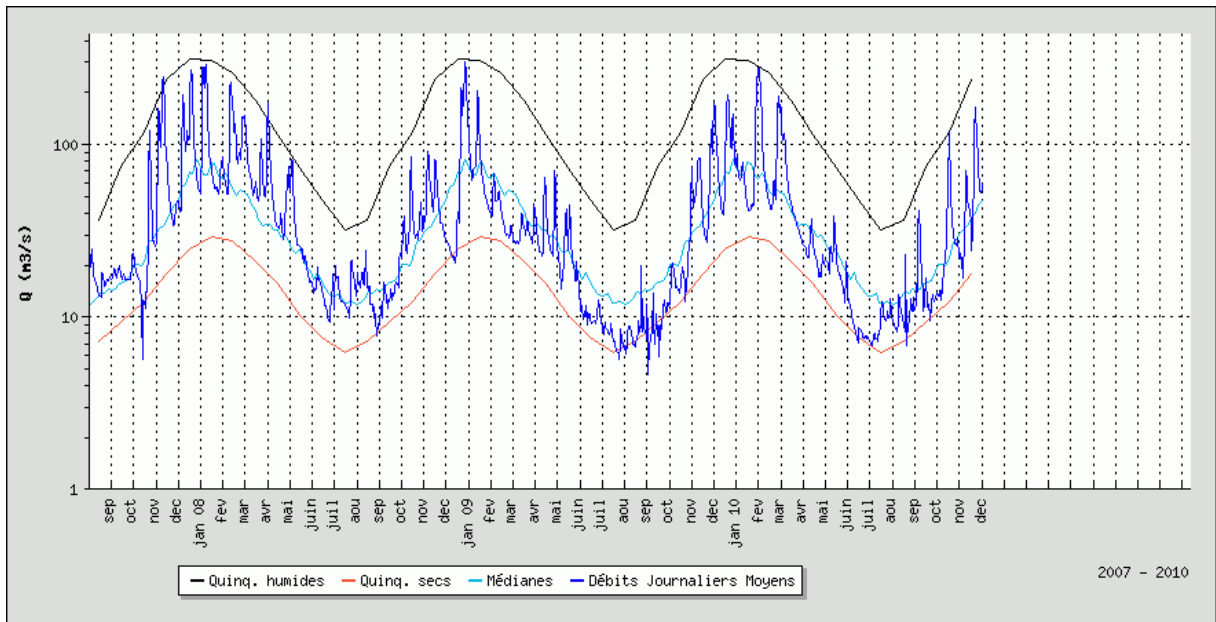
## Appendix A: Time series of observed discharges at the 3 downstream most gauging stations of each subcatchment

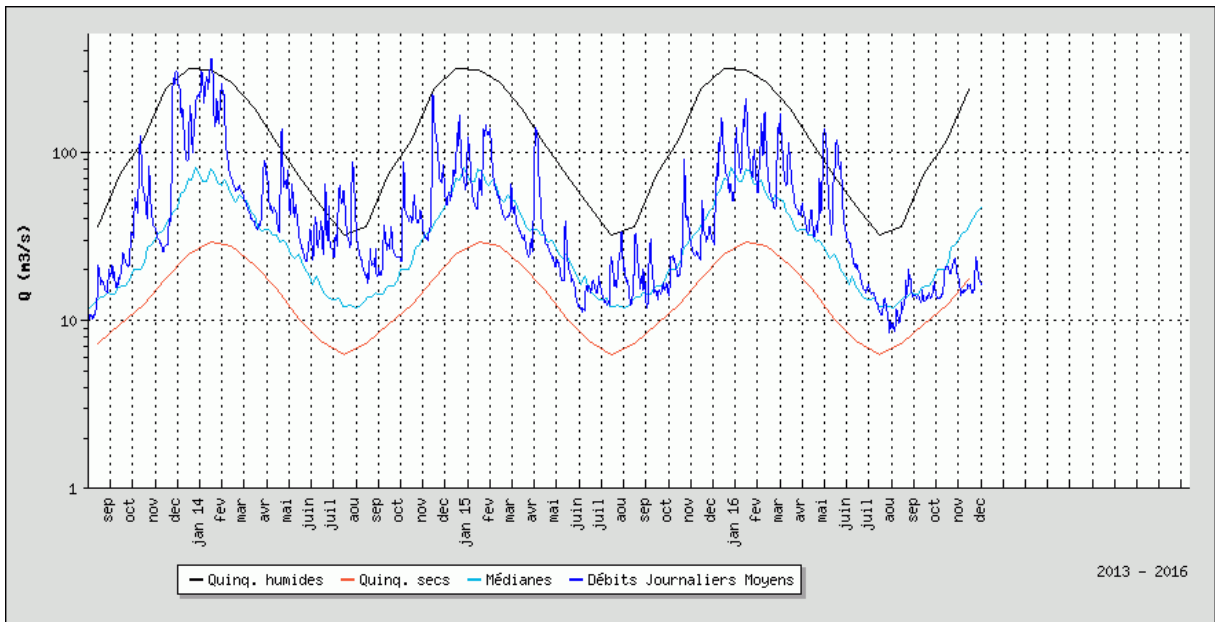
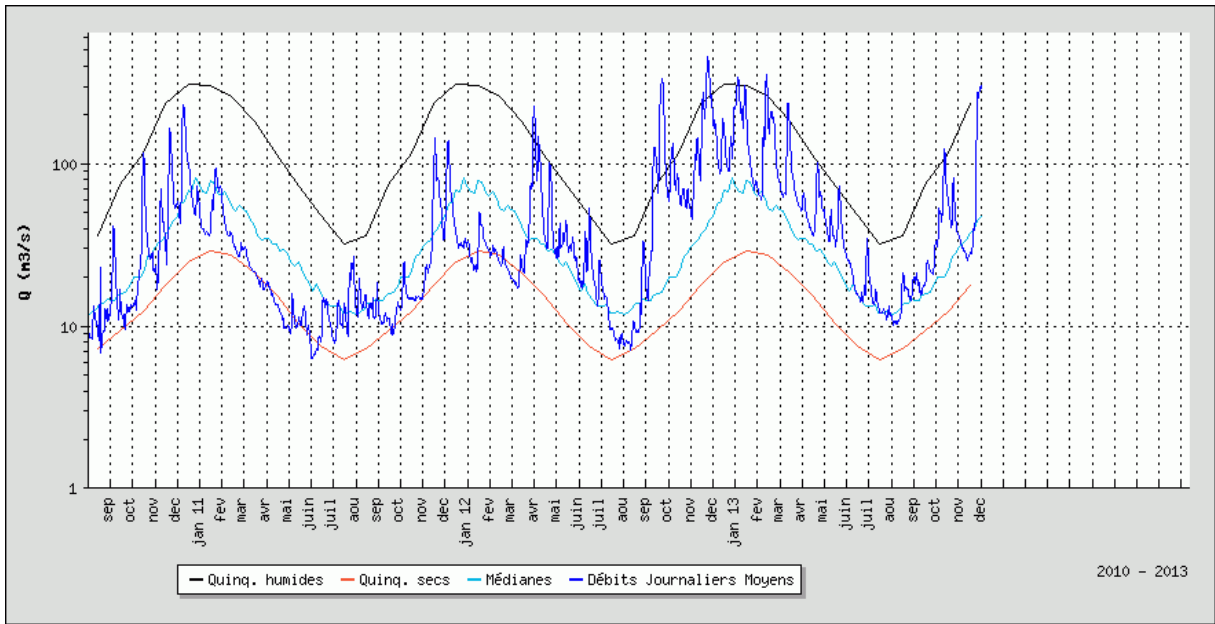
### The Mayenne River at Chambellay



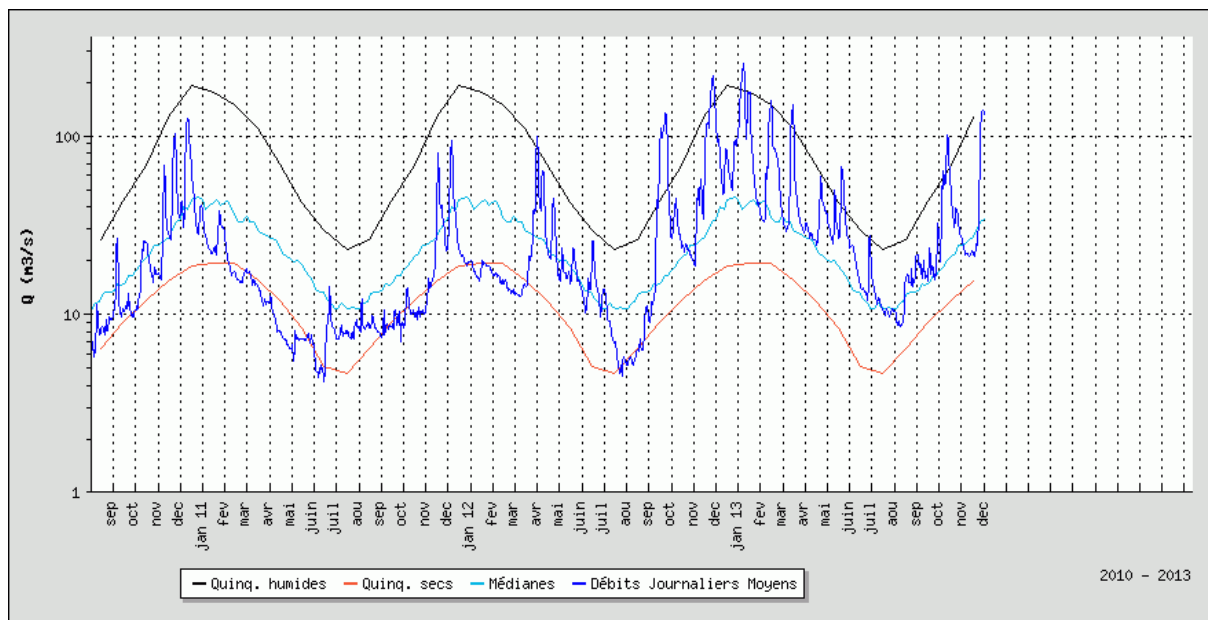
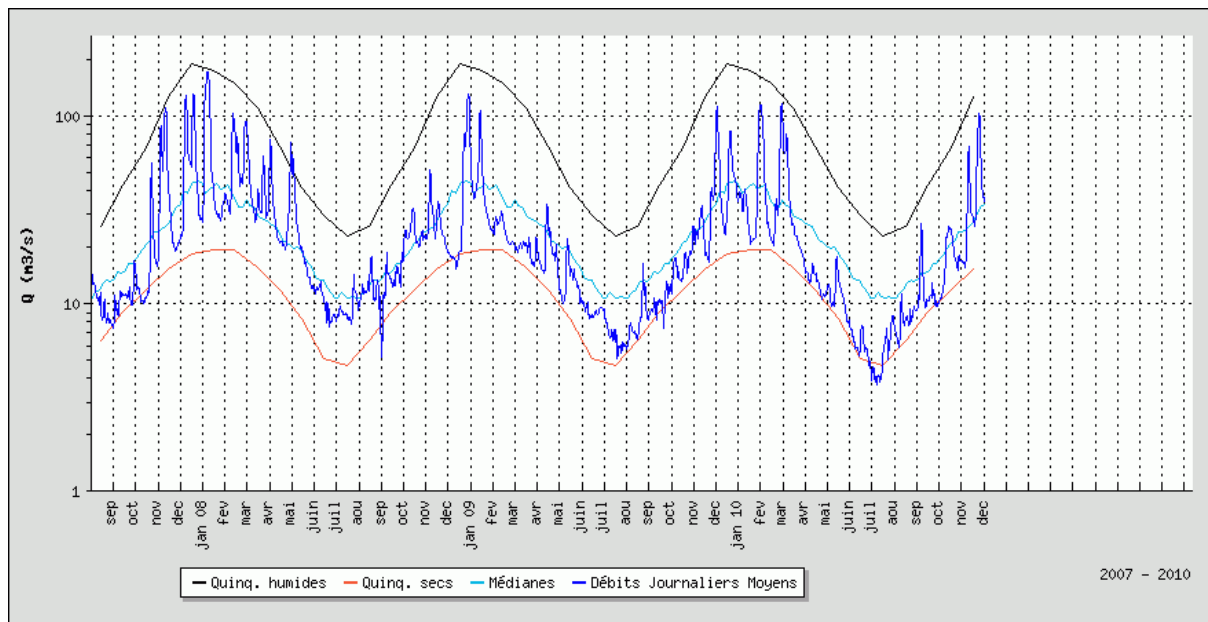


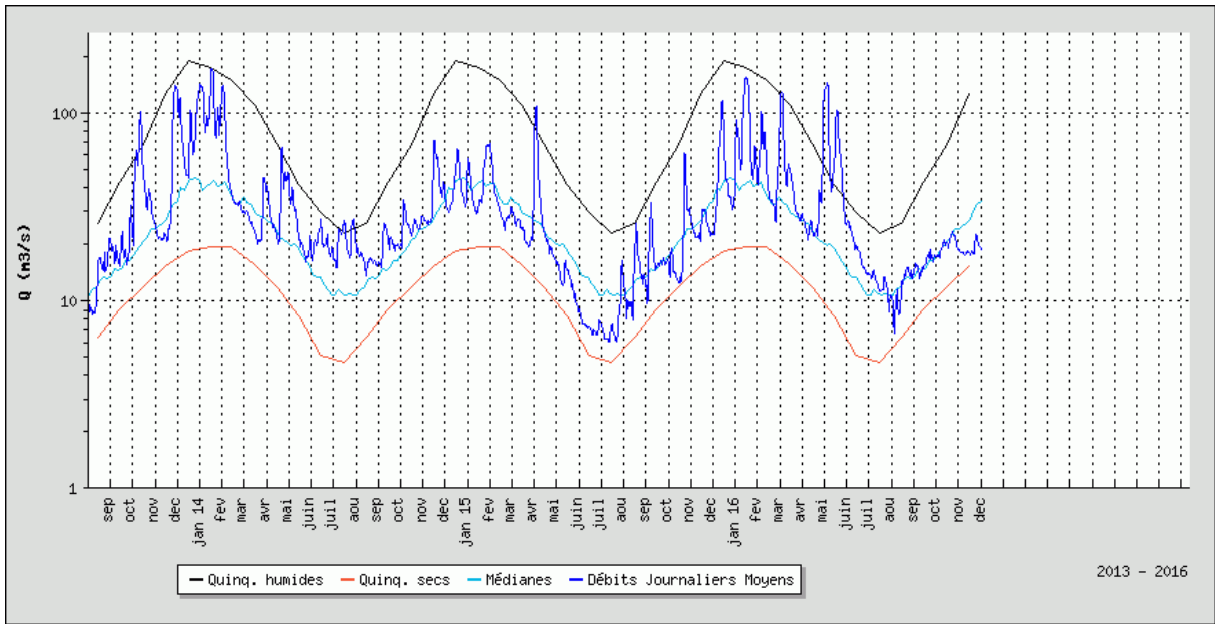
### The Sarthe River at Saint-Denis-d'Anjou



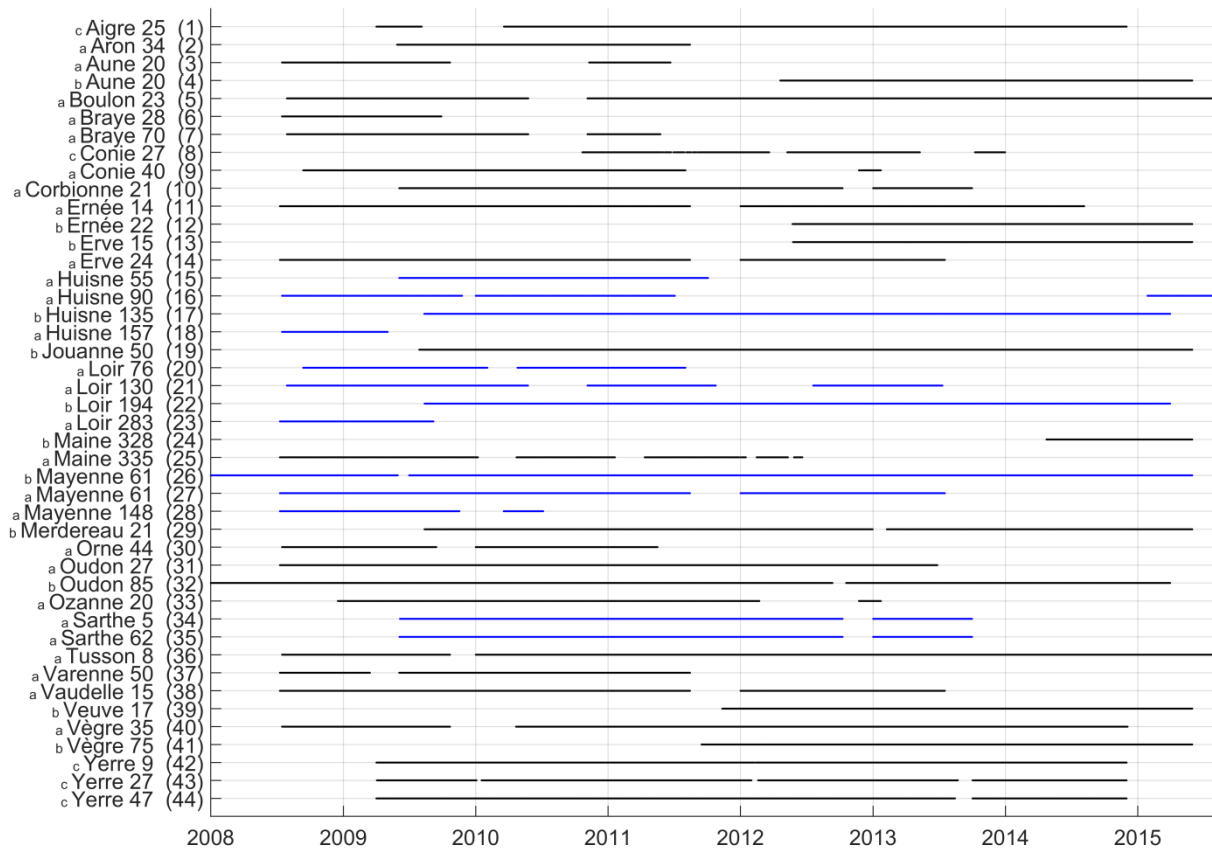


# The Loir River at Durtal





## Appendix B: Availability of measured temperature and stations numbers



Blue stations are located on the main rivers. Stations <sup>a</sup> are provided by Agence Française pour la biodiversité, <sup>b</sup> are provided by DREAL Pays de la Loire and <sup>c</sup> by Fédération Départementale de Pêche d'Eure-et-Loir.

## Appendix C: Water and air temperature metrics in 2010

| N° | Station      | mean Tw (°C) | mean Tw in January (°C) | mean Tw in July (°C) | TwJuly - TwJan (°C) | Mean diel Tw amplitude in July (°C) | Julian day of TwMax30J | %Time for trout | Thermal sensitivity (-) |
|----|--------------|--------------|-------------------------|----------------------|---------------------|-------------------------------------|------------------------|-----------------|-------------------------|
| 1  | Aigre 25     |              |                         | 18.38                |                     | 2.55                                | 190                    |                 | 0.57                    |
| 2  | Aron 34      | 11.01        | 5.49                    | 17.92                | 12.42               | 3.41                                | 194                    | 0.94            | 0.74                    |
| 3  | Aune 20      |              |                         |                      |                     |                                     | 329                    |                 | 0.77                    |
| 4  | Aune 20      |              |                         |                      |                     |                                     |                        |                 | 0.78                    |
| 5  | Boulon 23    |              | 7.56                    |                      |                     |                                     | 131                    |                 | 0.42                    |
| 6  | Braye 28     |              |                         |                      |                     |                                     |                        |                 | 0.85                    |
| 7  | Braye 70     |              | 3.87                    |                      |                     |                                     | 131                    |                 | 0.75                    |
| 8  | Conie 27     |              |                         |                      |                     |                                     | 312                    |                 | 0.75                    |
| 9  | Conie 40     | 12.62        | 5.21                    | 21.57                | 16.36               | 1.86                                | 191                    | 0.73            | 0.86                    |
| 10 | Corbionne 21 | 10.16        | 5.25                    | 14.45                | 9.20                | 1.54                                | 194                    | 0.99            | 0.48                    |
| 11 | Ernée 14     | 10.58        | 5.14                    | 16.68                | 11.54               | 3.23                                | 193                    | 0.92            | 0.67                    |
| 12 | Ernée 22     |              |                         |                      |                     |                                     |                        |                 | 0.77                    |
| 13 | Erve 15      |              |                         |                      |                     |                                     |                        |                 | 0.63                    |
| 14 | Erve 24      | 11.34        | 4.87                    | 18.60                | 13.74               | 3.09                                | 193                    | 0.89            | 0.76                    |
| 15 | Huisne 55    | 11.13        | 5.92                    | 17.37                | 11.45               | 1.15                                | 191                    | 0.98            | 0.65                    |
| 16 | Huisne 90    | 11.60        | 4.01                    | 19.89                | 15.88               | 1.28                                | 191                    | 0.79            | 0.84                    |
| 17 | Huisne 135   | 12.01        | 3.60                    | 21.72                | 18.12               | 1.15                                | 192                    | 0.67            | 0.92                    |
| 18 | Huisne 157   |              |                         |                      |                     |                                     |                        |                 | 1.01                    |
| 19 | Jouanne 50   | 11.29        | 3.22                    | 19.94                | 16.73               | 1.36                                | 193                    | 0.74            | 0.94                    |
| 20 | Loir 76      |              | 3.78                    | 21.99                | 18.21               | 1.65                                | 191                    |                 | 0.96                    |
| 21 | Loir 130     |              | 4.17                    |                      |                     |                                     | 130                    |                 | 0.96                    |
| 22 | Loir 194     | 12.34        | 3.92                    | 22.33                | 18.41               | 1.71                                | 194                    | 0.67            | 0.98                    |
| 23 | Loir 283     |              |                         |                      |                     |                                     |                        |                 | 1.16                    |
| 24 | Maine 328    |              |                         |                      |                     |                                     |                        |                 | 1.17                    |
| 25 | Maine 335    |              |                         | 24.58                |                     | 1.07                                | 193                    |                 | 1.13                    |
| 26 | Mayenne 61   | 11.28        | 3.53                    | 20.39                | 16.86               | 2.52                                | 193                    | 0.73            | 0.98                    |
| 27 | Mayenne 61   | 11.43        | 3.86                    | 19.93                | 16.07               | 3.53                                | 204                    | 0.72            | 0.95                    |
| 28 | Mayenne 148  |              |                         |                      |                     |                                     | 172                    |                 | 1.04                    |
| 29 | Merdereau 21 | 10.43        | 4.26                    | 17.92                | 13.66               | 2.37                                | 193                    | 0.85            | 0.78                    |
| 30 | Orne 44      | 11.97        | 3.48                    | 21.95                | 18.47               | 3.31                                | 192                    | 0.64            | 0.98                    |
| 31 | Oudon 27     | 12.08        | 4.98                    | 20.77                | 15.80               | 2.86                                | 194                    | 0.74            | 0.89                    |
| 32 | Oudon 85     | 12.79        | 5.04                    | 22.32                | 17.28               | 1.22                                | 201                    | 0.65            | 1.04                    |
| 33 | Ozanne 20    | 10.34        | 2.60                    | 18.61                | 16.01               | 3.95                                | 193                    | 0.76            | 0.83                    |
| 34 | Sarthe 5     | 10.45        | 5.97                    | 14.70                | 8.73                | 4.01                                | 197                    | 1.00            | 0.45                    |
| 35 | Sarthe 62    | 11.34        | 2.85                    | 21.33                | 18.48               | 2.45                                | 192                    | 0.64            | 1.02                    |
| 36 | Tusson 8     | 9.66         | 3.94                    | 15.53                | 11.59               | 0.50                                | 196                    | 0.85            | 0.63                    |
| 37 | Varenne 50   | 11.33        | 5.51                    | 20.24                | 14.73               | 1.33                                | 197                    | 0.82            | 0.95                    |
| 38 | Vaudelle 15  | 10.77        | 4.71                    | 17.16                | 12.45               | 3.53                                | 194                    | 0.94            | 0.67                    |
| 39 | Veuve 17     |              |                         |                      |                     |                                     |                        |                 | 0.65                    |
| 40 | Vègre 35     |              |                         | 19.37                |                     | 1.50                                | 192                    |                 | 0.76                    |
| 41 | Vègre 75     |              |                         |                      |                     |                                     |                        |                 | 0.85                    |
| 42 | Yerre 9      | 9.97         | 3.37                    | 16.19                | 12.82               | 1.67                                | 194                    | 0.83            | 0.65                    |
| 43 | Yerre 27     |              |                         | 19.86                |                     | 2.56                                | 194                    |                 | 0.89                    |
| 44 | Yerre 47     | 10.72        | 5.58                    | 15.13                | 9.55                | 2.08                                | 197                    | 0.98            | 0.50                    |

| <b>N°</b> | <b>Station</b> | <b>mean Ta (°C)</b> | <b>mean Ta in January (°C)</b> | <b>mean Ta in July (°C)</b> | <b>TaJuly - TaJan (°C)</b> | <b>Mean diel Ta amplitude in July (°C)</b> | <b>Julian day of TwMax30J</b> |
|-----------|----------------|---------------------|--------------------------------|-----------------------------|----------------------------|--|-------------------------------|
| 1         | Aigre 25       | 10.4                | 0.5                            | 21.1                        | 20.6                       | 10.3                                       | 189                           |
| 2         | Aron 34        | 10.4                | 1.4                            | 20.1                        | 18.8                       | 9.9  | 188                           |
| 3         | Aune 20        | 11.0                | 1.5                            | 21.3                        | 19.8                       | 10.0                                       | 188                           |
| 4         | Aune 20        | 11.0                | 1.5                            | 21.3                        | 19.8                       | 10.0                                       | 188                           |
| 5         | Boulon 23      | 10.7                | 0.8                            | 21.0                        | 20.2                       | 9.9  | 189                           |
| 6         | Braye 28       | 10.2                | 0.6                            | 20.5                        | 19.9                       | 10.9                                       | 189                           |
| 7         | Braye 70       | 10.4                | 0.9                            | 20.7                        | 19.8                       | 10.7                                       | 189                           |
| 8         | Conie 27       | 10.0                | 0.2                            | 20.7                        | 20.5                       | 10.2                                       | 192                           |
| 9         | Conie 40       | 10.0                | 0.2                            | 20.7                        | 20.5                       | 10.2                                       | 192                           |
| 10        | Corbionne 21   | 9.8                 | 0.4                            | 19.9                        | 19.5                       | 10.4                                       | 188                           |
| 11        | Ernée 14       | 9.9                 | 1.1                            | 19.1                        | 18.0                       | 9.7  | 188                           |
| 12        | Ernée 22       | 10.2                | 1.5                            | 19.5                        | 18.0                       | 9.6  | 188                           |
| 13        | Erve 15        | 10.2                | 0.9                            | 20.1                        | 19.1                       | 10.0                                       | 188                           |
| 14        | Erve 24        | 10.6                | 1.5                            | 20.5                        | 19.1                       | 9.9  | 188                           |
| 15        | Huisne 55      | 9.8                 | 0.4                            | 19.9                        | 19.5                       | 10.4                                       | 188                           |
| 16        | Huisne 90      | 10.1                | 0.8                            | 20.1                        | 19.4                       | 10.3                                       | 188                           |
| 17        | Huisne 135     | 10.8                | 1.2                            | 21.1                        | 19.9                       | 10.1                                       | 188                           |
| 18        | Huisne 157     | 10.9                | 1.4                            | 21.2                        | 19.9                       | 10.0                                       | 188                           |
| 19        | Jouanne 50     | 10.7                | 1.8                            | 20.5                        | 18.7                       | 9.8  | 188                           |
| 20        | Loir 76        | 10.0                | 0.2                            | 20.7                        | 20.5                       | 10.2                                       | 192                           |
| 21        | Loir 130       | 10.7                | 0.8                            | 21.0                        | 20.2                       | 9.9  | 189                           |
| 22        | Loir 194       | 10.6                | 1.1                            | 20.8                        | 19.7                       | 10.6                                       | 189                           |
| 23        | Loir 283       | 11.1                | 2.1                            | 21.0                        | 18.9                       | 10.2                                       | 188                           |
| 24        | Maine 328      | 11.2                | 2.2                            | 21.1                        | 18.9                       | 10.1                                       | 188                           |
| 25        | Maine 335      | 11.6                | 2.4                            | 21.5                        | 19.1                       | 9.8  | 189                           |
| 26        | Mayenne 61     | 10.2                | 1.5                            | 19.5                        | 18.0                       | 9.6  | 188                           |
| 27        | Mayenne 61     | 10.2                | 1.5                            | 19.5                        | 18.0                       | 9.6  | 188                           |
| 28        | Mayenne 148    | 10.7                | 1.8                            | 20.8                        | 19.0                       | 10.9                                       | 188                           |
| 29        | Merdereau 21   | 9.6                 | 0.6                            | 19.4                        | 18.8                       | 10.1                                       | 188                           |
| 30        | Orne 44        | 11.0                | 1.5                            | 21.3                        | 19.8                       | 10.0                                       | 188                           |
| 31        | Oudon 27       | 10.7                | 2.0                            | 20.2                        | 18.2                       | 10.6                                       | 188                           |
| 32        | Oudon 85       | 11.0                | 2.4                            | 20.5                        | 18.1                       | 9.8  | 188                           |
| 33        | Ozanne 20      | 10.0                | 0.5                            | 20.6                        | 20.1                       | 10.1                                       | 189                           |
| 34        | Sarthe 5       | 9.2                 | -0.4                           | 19.4                        | 19.8                       | 10.8                                       | 188                           |
| 35        | Sarthe 62      | 9.9                 | 0.6                            | 20.0                        | 19.3                       | 10.1                                       | 188                           |
| 36        | Tusson 8       | 10.3                | 0.7                            | 20.6                        | 19.9                       | 10.8                                       | 189                           |
| 37        | Varenne 50     | 9.6                 | 1.2                            | 19.0                        | 17.7                       | 10.2                                       | 192                           |
| 38        | Vaudelle 15    | 10.0                | 1.0                            | 19.8                        | 18.8                       | 10.1                                       | 188                           |
| 39        | Veuve 17       | 10.4                | 0.9                            | 20.7                        | 19.8                       | 10.7                                       | 189                           |
| 40        | Vègre 35       | 10.9                | 1.4                            | 21.2                        | 19.9                       | 10.0                                       | 188                           |
| 41        | Vègre 75       | 11.1                | 1.6                            | 21.4                        | 19.8                       | 9.9  | 188                           |
| 42        | Yerre 9        | 10.1                | 0.0                            | 20.6                        | 20.5                       | 10.4                                       | 189                           |
| 43        | Yerre 27       | 10.1                | 0.6                            | 20.7                        | 20.1                       | 10.1                                       | 189                           |
| 44        | Yerre 47       | 10.3                | 0.8                            | 20.8                        | 20.0                       | 10.1                                       | 189                           |

## Appendix D: Station characteristics (interannual average where appropriate)

| N° | Station      | Bassin  | Strahler<br>order | Pente (‰) | Altitude<br>(m) | Tiering rate on<br>75 km (%) | Qmin/Qmax | Thermal<br>sensitivity | Intercept | Residual | Class       |
|----|--------------|---------|-------------------|-----------|-----------------|------------------------------|-----------|------------------------|-----------|----------|-------------|
| 1  | Aigre 25     | Loir    | 3                 | 1.1       | 99              | 5.3                          | 0.73      | 0.57                   | 5.82      | 0.94     | Groundwater |
| 2  | Aron 34      | Mayenne | 4                 | 6.4       | 83              | 9.8                          | 0.06      | 0.73                   | 3.17      | -0.39    | Mixed       |
| 3  | Aune 20      | Loir    | 4                 | 1.4       | 41              | 19.1                         | 0.29      | 0.78                   | 2.19      | -0.99    | Mixed       |
| 4  | Aune 20      | Loir    | 4                 | 1.4       | 45              | 19.1                         | 0.29      | 0.77                   | 2.50      | -0.71    | Mixed       |
| 5  | Boulon 23    | Loir    | 4                 | 0.1       | 73              | 7.4                          | 0.19      | 0.42                   | 6.48      | 0.35     | Groundwater |
| 6  | Braye 28     | Loir    | 3                 | 1.9       | 109             | 13.1                         | 0.21      | 0.85                   | 2.49      | -0.11    | Air         |
| 7  | Braye 70     | Loir    | 4                 | 0.6       | 58              | 24.2                         | 0.16      | 0.75                   | 2.99      | -0.42    | Mixed       |
| 8  | Conie 27     | Loir    | 2                 | 0.3       | 113             | 0.0                          | 0.75      | 0.75                   | 5.15      | 1.78     | Mixed       |
| 9  | Conie 40     | Loir    | 2                 | 0.3       | 110             | 0.0                          | 0.75      | 0.86                   | 3.46      | 1.00     | Mixed       |
| 10 | Corbionne 21 | Sarthe  | 3                 | 3.1       | 120             | 6.6                          | 0.42      | 0.47                   | 5.70      | -0.07    | Groundwater |
| 11 | Ernée 14     | Mayenne | 4                 | 2.9       | 129             | 3.7                          | 0.16      | 0.67                   | 3.92      | -0.13    | Mixed       |
| 12 | Ernée 22     | Mayenne | 5                 | 1.0       | 111             | 9.4                          | 0.16      | 0.77                   | 3.12      | -0.14    | Mixed       |
| 13 | Erve 15      | Sarthe  | 3                 | 0.1       | 123             | 6.5                          | 0.28      | 0.63                   | 4.70      | 0.33     | Mixed       |
| 14 | Erve 24      | Sarthe  | 4                 | 3.8       | 81              | 18.7                         | 0.18      | 0.76                   | 3.38      | 0.03     | Mixed       |
| 15 | Huisne 55    | Sarthe  | 5                 | 0.8       | 113             | 19.4                         | 0.40      | 0.63                   | 4.76      | 0.37     | Mixed       |
| 16 | Huisne 90    | Sarthe  | 5                 | 0.8       | 88              | 29.8                         | 0.40      | 0.84                   | 2.87      | 0.27     | Mixed       |
| 17 | Huisne 135   | Sarthe  | 5                 | 0.9       | 56              | 46.5                         | 0.33      | 0.92                   | 1.71      | -0.26    | Air         |
| 18 | Huisne 157   | Sarthe  | 5                 | 1.1       | 46              | 60.1                         | 0.32      | 1.01                   | 1.26      | 0.00     | Air         |
| 19 | Jouanne 50   | Mayenne | 5                 | 0.4       | 47              | 20.7                         | 0.05      | 0.94                   | 1.56      | -0.28    | Air         |
| 20 | Loir 76      | Loir    | 5                 | 0.5       | 104             | 37.3                         | 0.28      | 0.95                   | 2.78      | 1.03     | Air         |
| 21 | Loir 130     | Loir    | 5                 | 0.4       | 77              | 99.1                         | 0.25      | 0.99                   | 1.89      | 0.51     | Air         |
| 22 | Loir 194     | Loir    | 5                 | 0.1       | 46              | 75.5                         | 0.20      | 0.98                   | 1.63      | 0.17     | Air         |
| 23 | Loir 283     | Loir    | 5                 | 1.7       | 20              | 87.6                         | 0.21      | 1.16                   | 0.38      | 0.43     | Air         |
| 24 | Maine 328    | Maine   | 7                 | 0.1       | 15              | 87.3                         | 0.12      | 1.17                   | -0.50     | -0.34    | Air         |
| 25 | Maine 335    | Maine   | 7                 | 0.1       | 16              | 80.0                         | 0.12      | 1.13                   | 0.37      | 0.11     | Air         |
| 26 | Mayenne 61   | Mayenne | 6                 | 2.3       | 100             | 9.3                          | 0.05      | 0.98                   | 1.01      | -0.43    | Air         |
| 27 | Mayenne 61   | Mayenne | 6                 | 2.3       | 100             | 9.3                          | 0.05      | 0.95                   | 1.42      | -0.33    | Air         |
| 28 | Mayenne 148  | Mayenne | 6                 | 0.1       | 30              | 74.2                         | 0.06      | 1.04                   | 2.16      | 1.17     | Air         |
| 29 | Merdereau 21 | Sarthe  | 4                 | 5.4       | 114             | 0.0                          | 0.07      | 0.78                   | 2.75      | -0.39    | Mixed       |
| 30 | Orne 44      | Sarthe  | 5                 | 0.1       | 55              | 7.5                          | 0.12      | 0.98                   | 0.99      | -0.51    | Air         |
| 31 | Oudon 27     | Mayenne | 4                 | 2.4       | 56              | 22.1                         | 0.05      | 0.89                   | 2.50      | 0.29     | Air         |
| 32 | Oudon 85     | Mayenne | 5                 | 0.4       | 21              | 77.0                         | 0.04      | 1.04                   | 0.97      | 0.01     | Air         |
| 33 | Ozanne 20    | Loir    | 4                 | 1.6       | 150             | 1.1                          | 0.03      | 0.83                   | 1.77      | -0.98    | Air         |
| 34 | Sarthe 5     | Sarthe  | 3                 | 3.0       | 179             | 13.7                         | 0.05      | 0.44                   | 6.29      | 0.29     | Groundwater |
| 35 | Sarthe 62    | Sarthe  | 5                 | 0.9       | 132             | 31.9                         | 0.07      | 1.02                   | 0.88      | -0.27    | Air         |
| 36 | Tusson 8     | Loir    | 2                 | 3.8       | 119             | 0.9                          | 0.17      | 0.63                   | 3.40      | -0.99    | Mixed       |
| 37 | Varenne 50   | Mayenne | 5                 | 1.0       | 103             | 15.6                         | 0.06      | 0.95                   | 1.77      | 0.02     | Air         |
| 38 | Vaudelle 15  | Sarthe  | 3                 | 7.6       | 130             | 0.0                          | 0.08      | 0.67                   | 3.80      | -0.25    | Mixed       |
| 39 | Veuve 17     | Loir    | 3                 | 1.6       | 61              | 11.2                         | 0.35      | 0.65                   | 4.25      | -0.02    | Mixed       |
| 40 | Vègre 35     | Sarthe  | 4                 | 0.5       | 73              | 15.9                         | 0.12      | 0.76                   | 3.12      | -0.16    | Mixed       |
| 41 | Vègre 75     | Sarthe  | 4                 | 0.6       | 33              | 25.3                         | 0.12      | 0.85                   | 2.24      | -0.29    | Air         |
| 42 | Yerre 9      | Loir    | 3                 | 1.9       | 182             | 1.8                          | 0.04      | 0.65                   | 3.74      | -0.54    | Mixed       |
| 43 | Yerre 27     | Loir    | 3                 | 1.4       | 143             | 6.6                          | 0.04      | 0.89                   | 1.88      | -0.37    | Air         |
| 44 | Yerre 47     | Loir    | 4                 | 2.3       | 98              | 7.6                          | 0.04      | 0.50                   | 5.77      | 0.27     | Groundwater |

## Appendix E: Time series of measured mean daily Tw

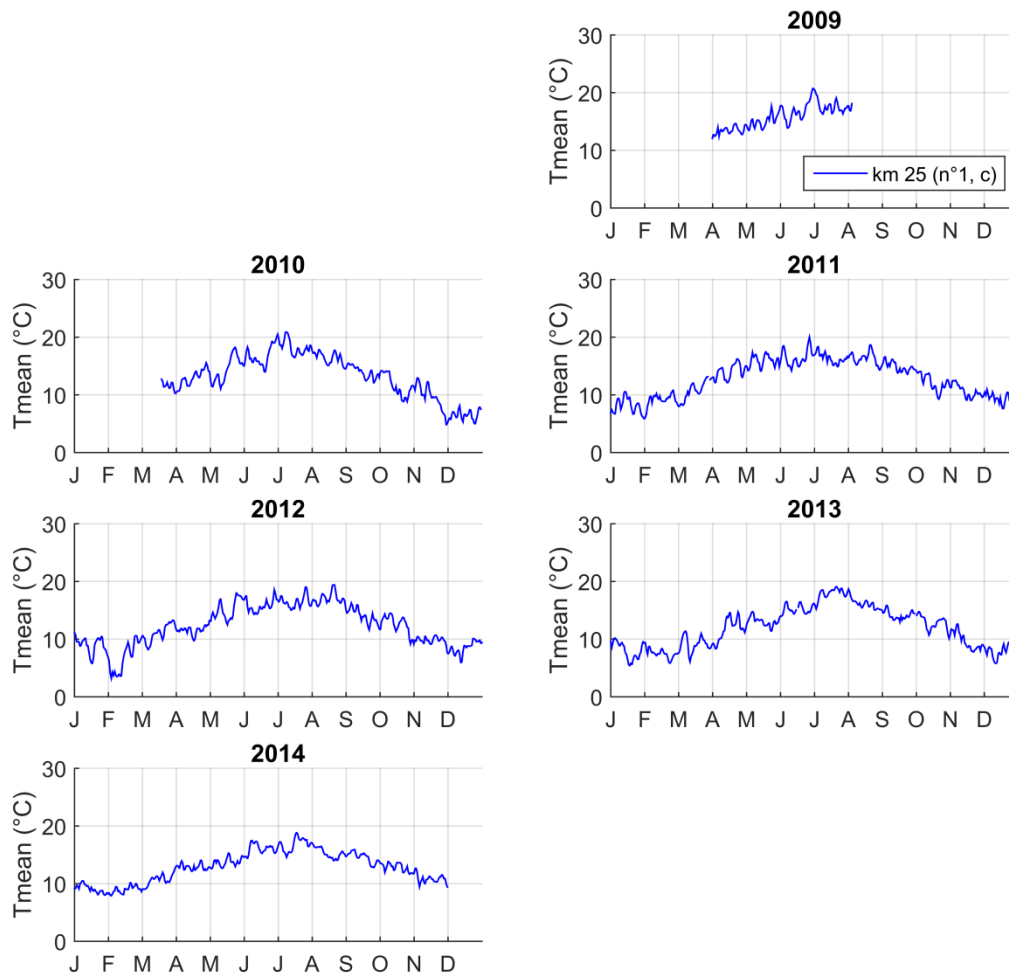
Data are provided by:

a : Agence Française pour la biodiversité,

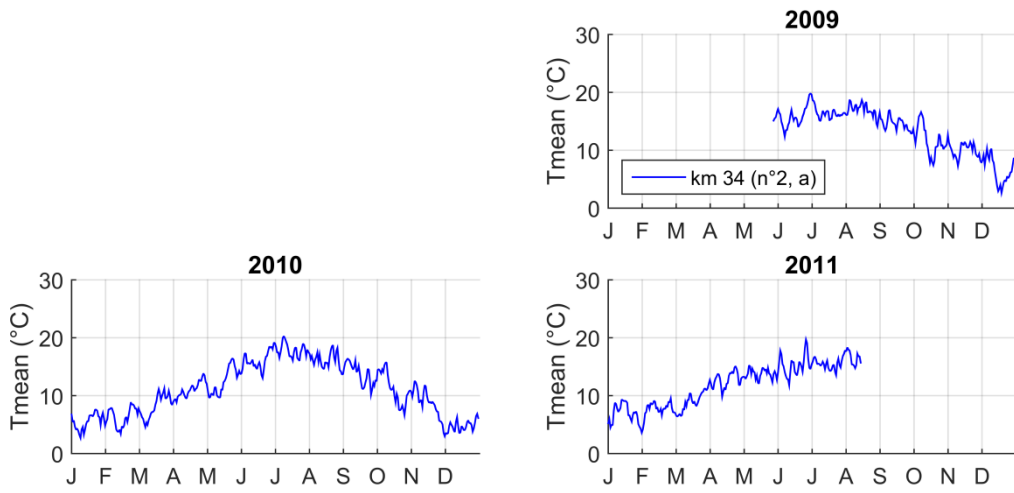
b : DREAL Pays de la Loire

c : Fédération Départementale de Pêche d'Eure-et-Loir.

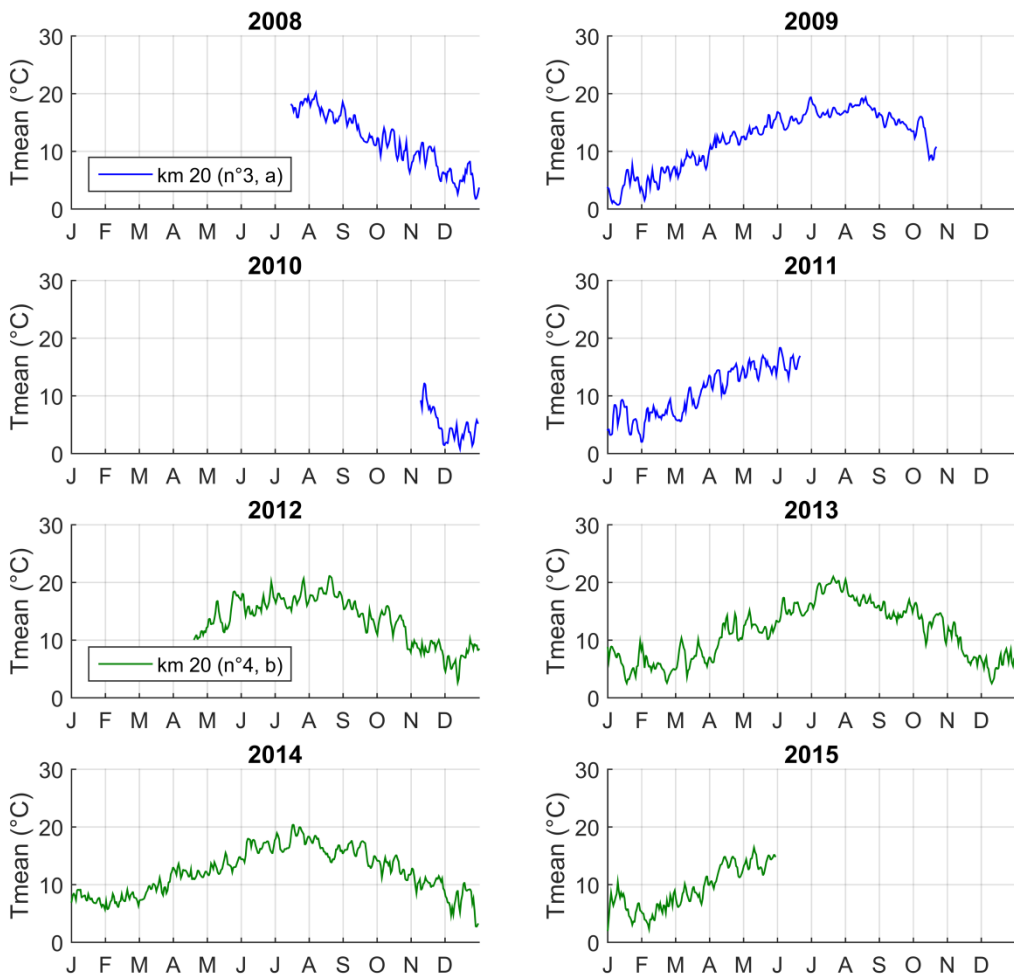
### Aigre



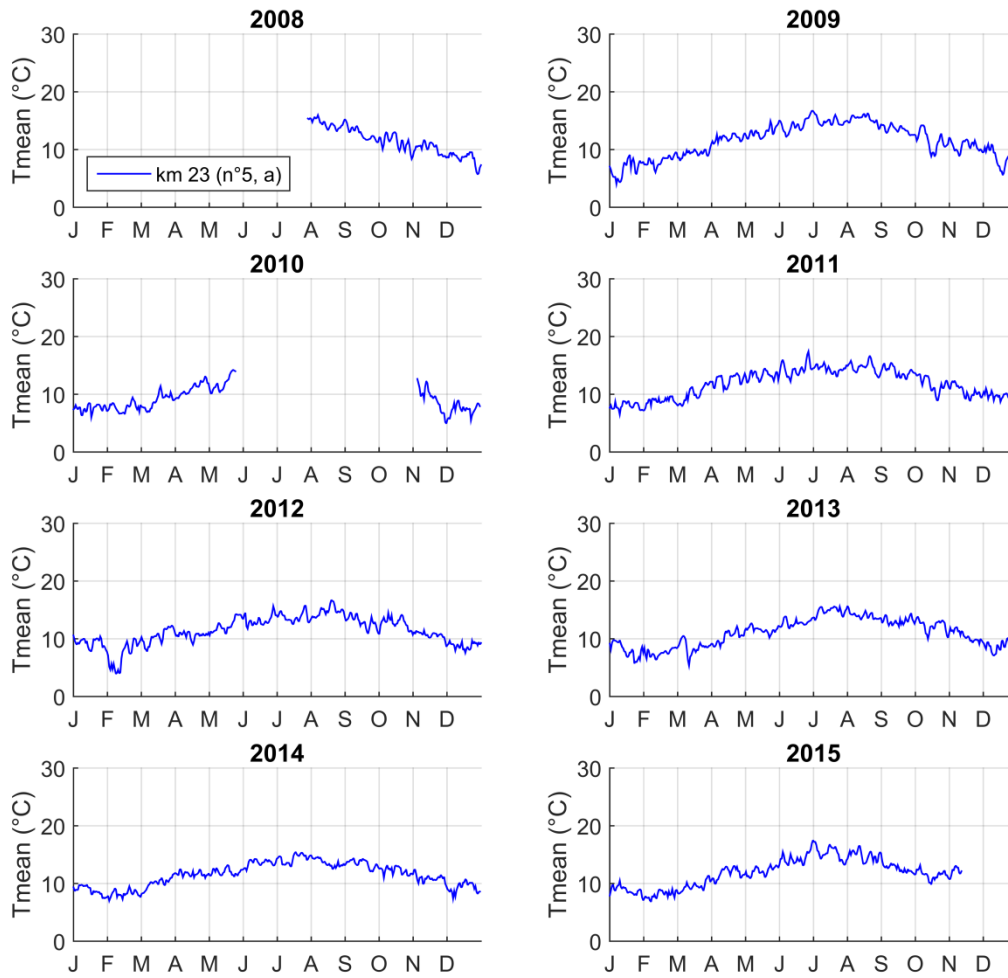
### Aron



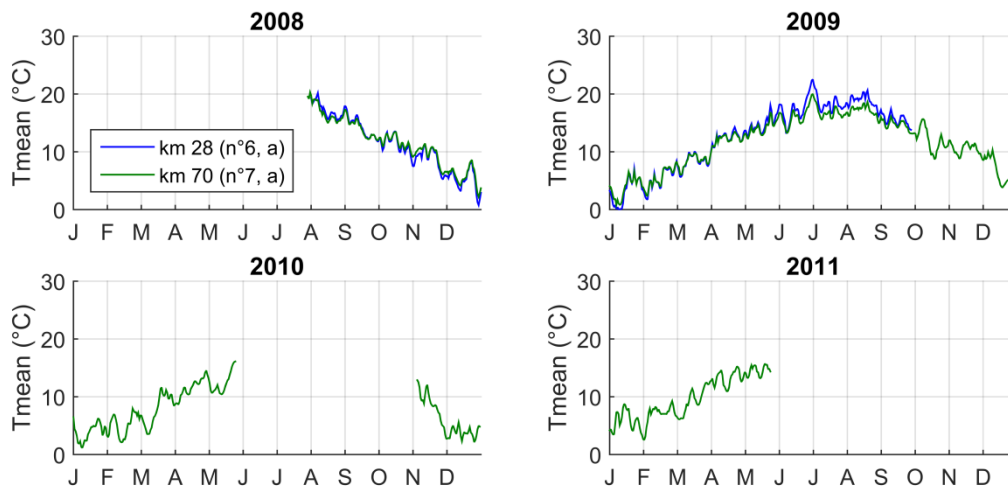
### Aune



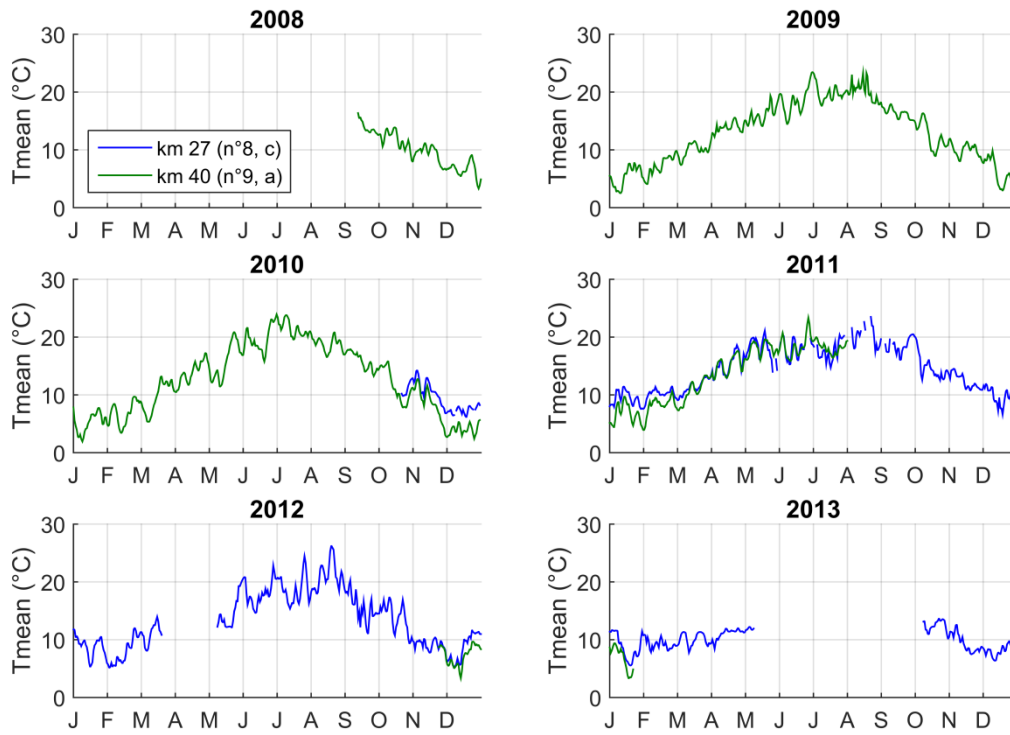
## Boulon



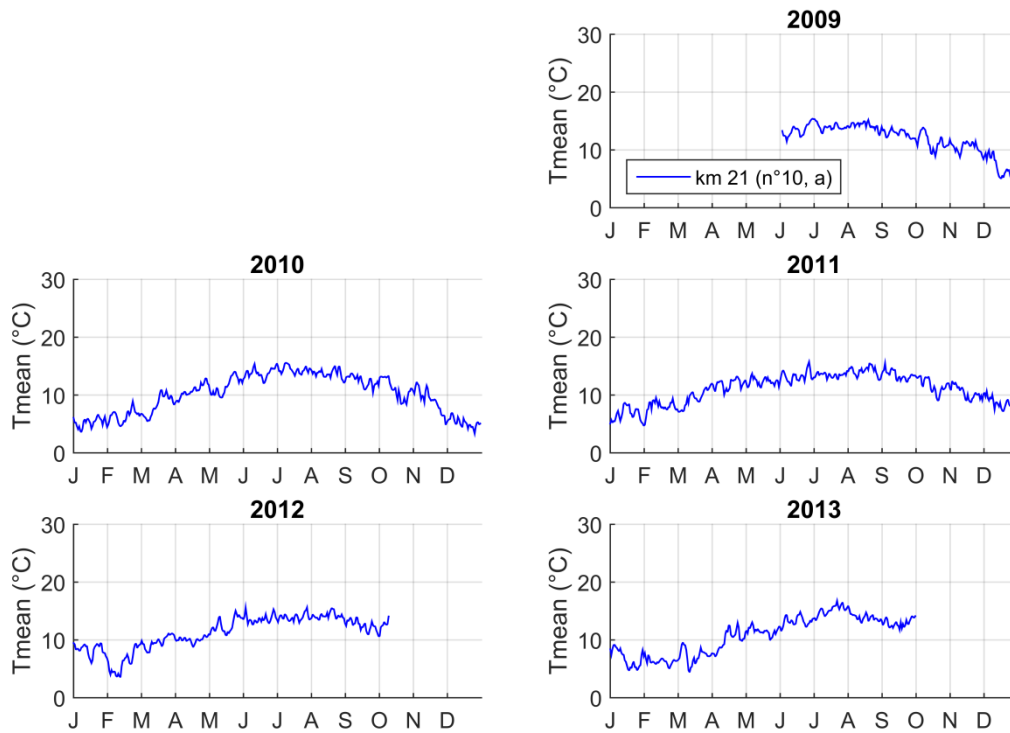
## Braye



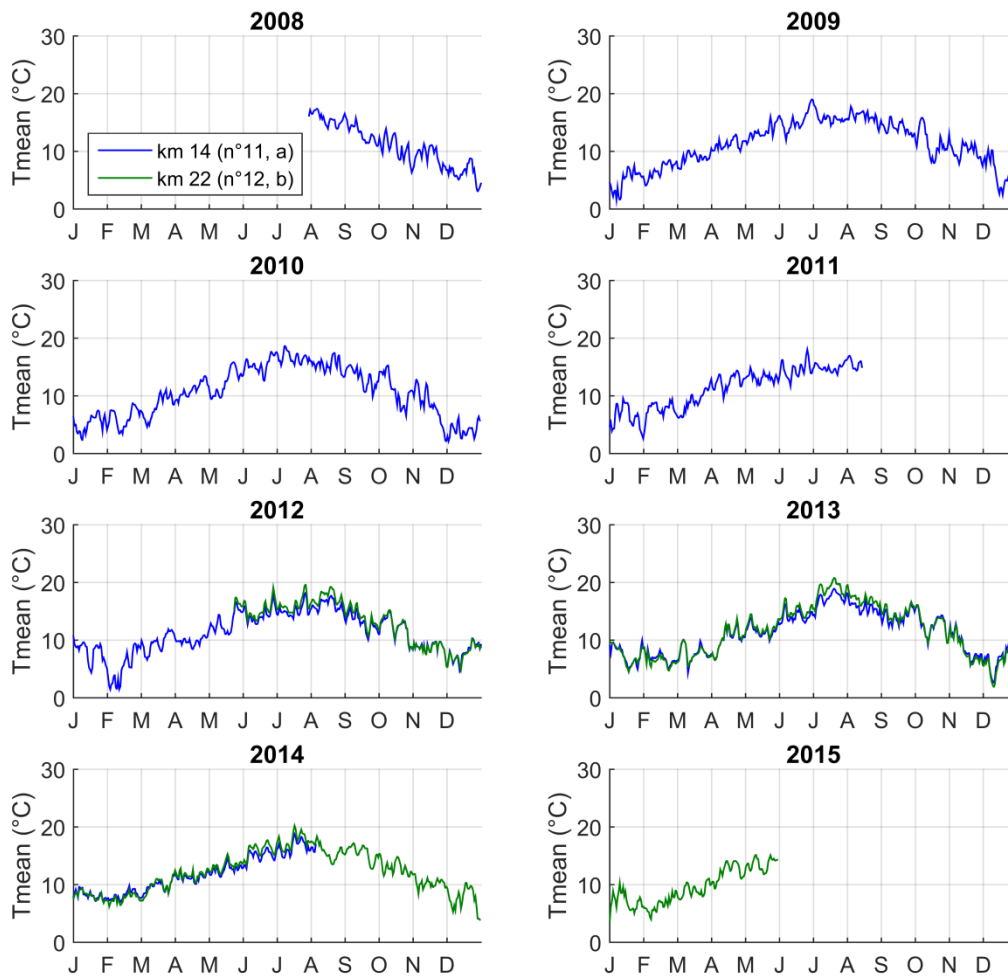
### Conie



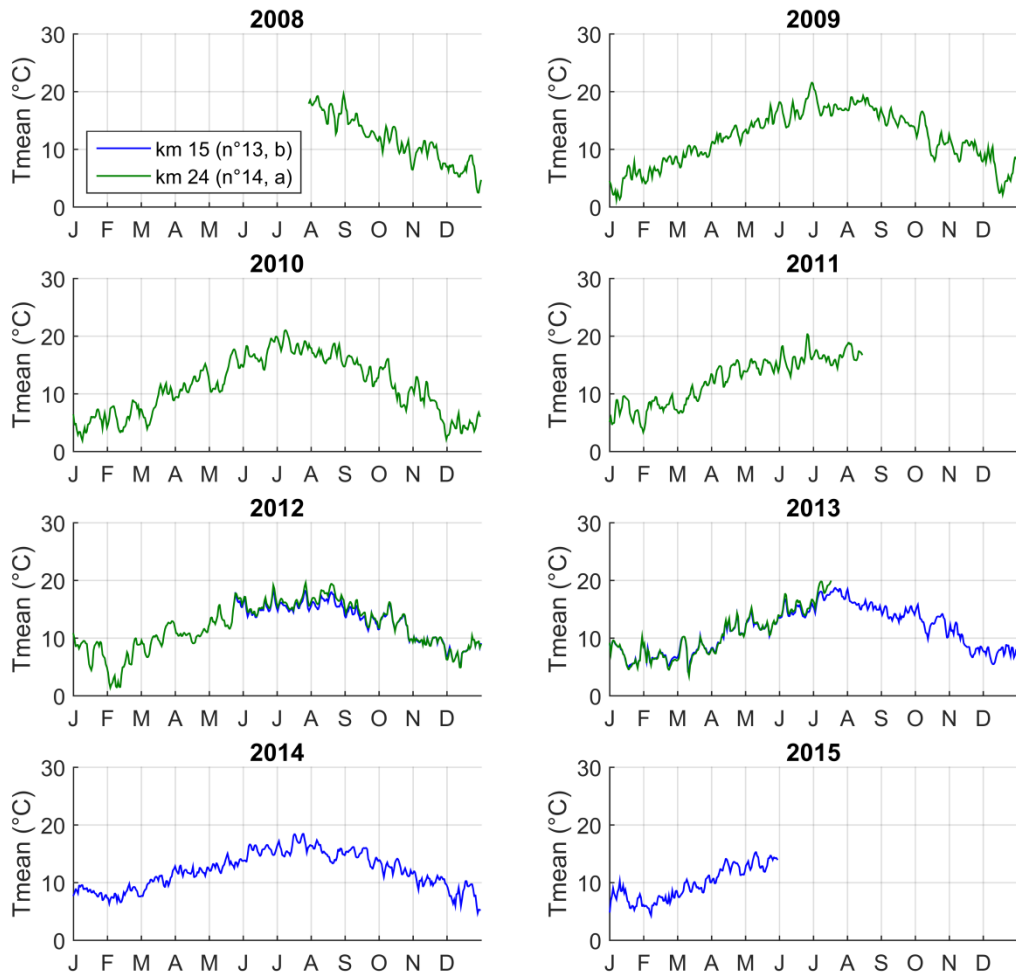
### Corbionne



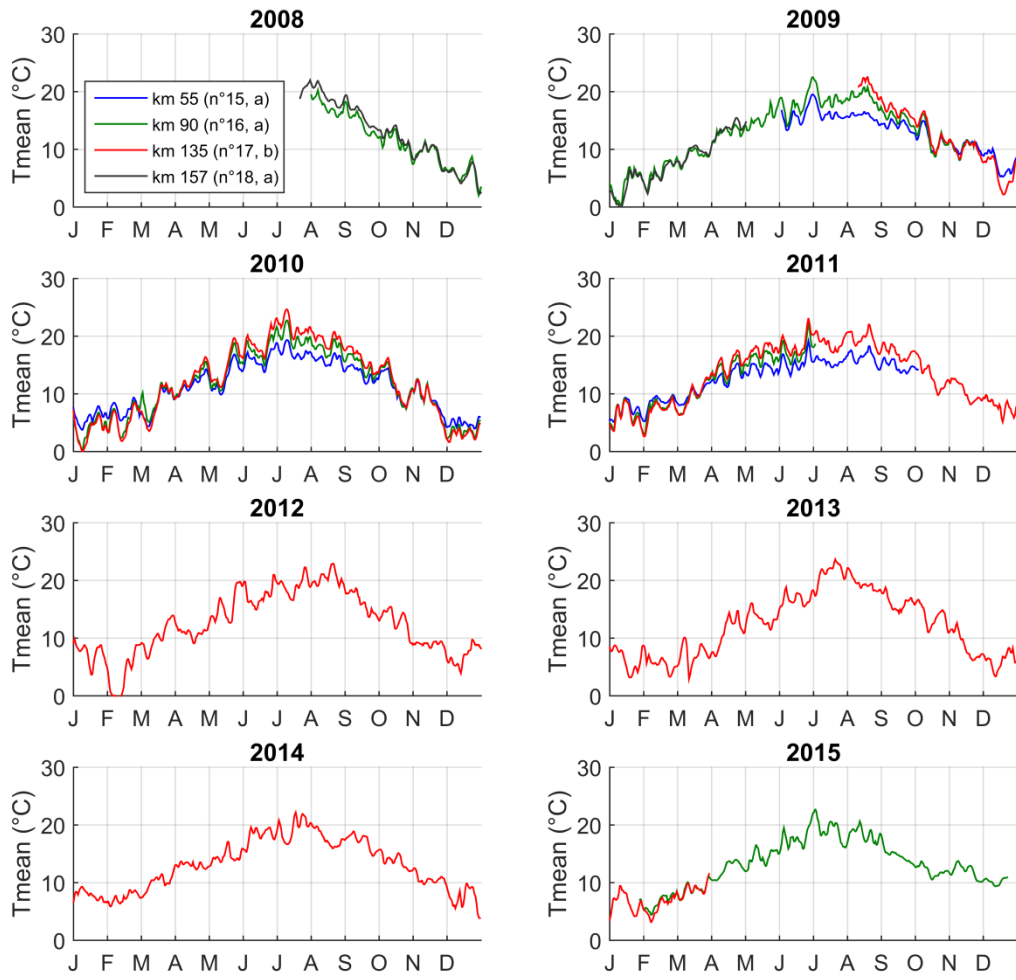
## Ernée



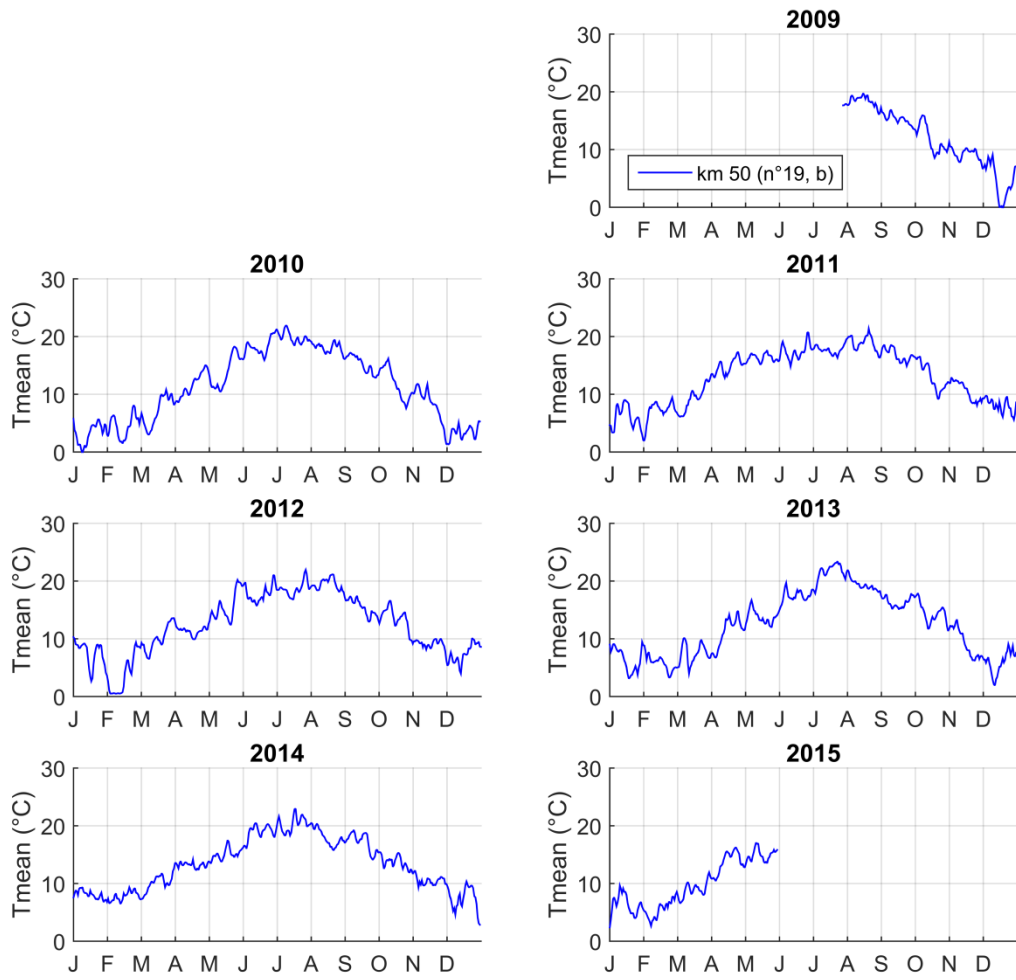
# Erve



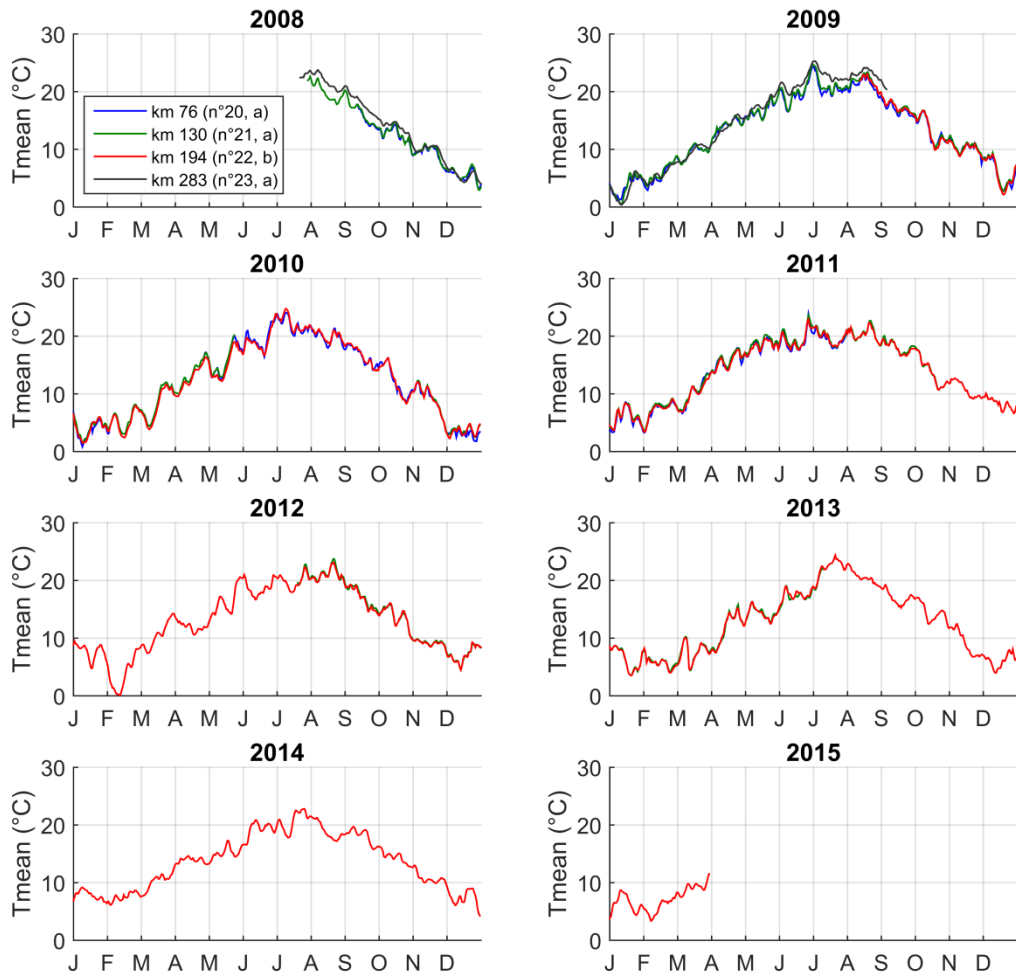
# Huisne



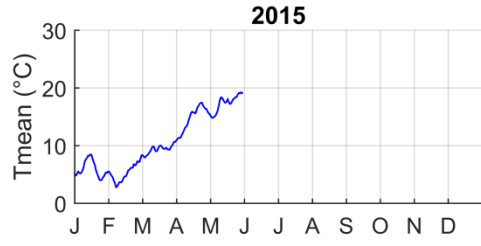
Jouanne



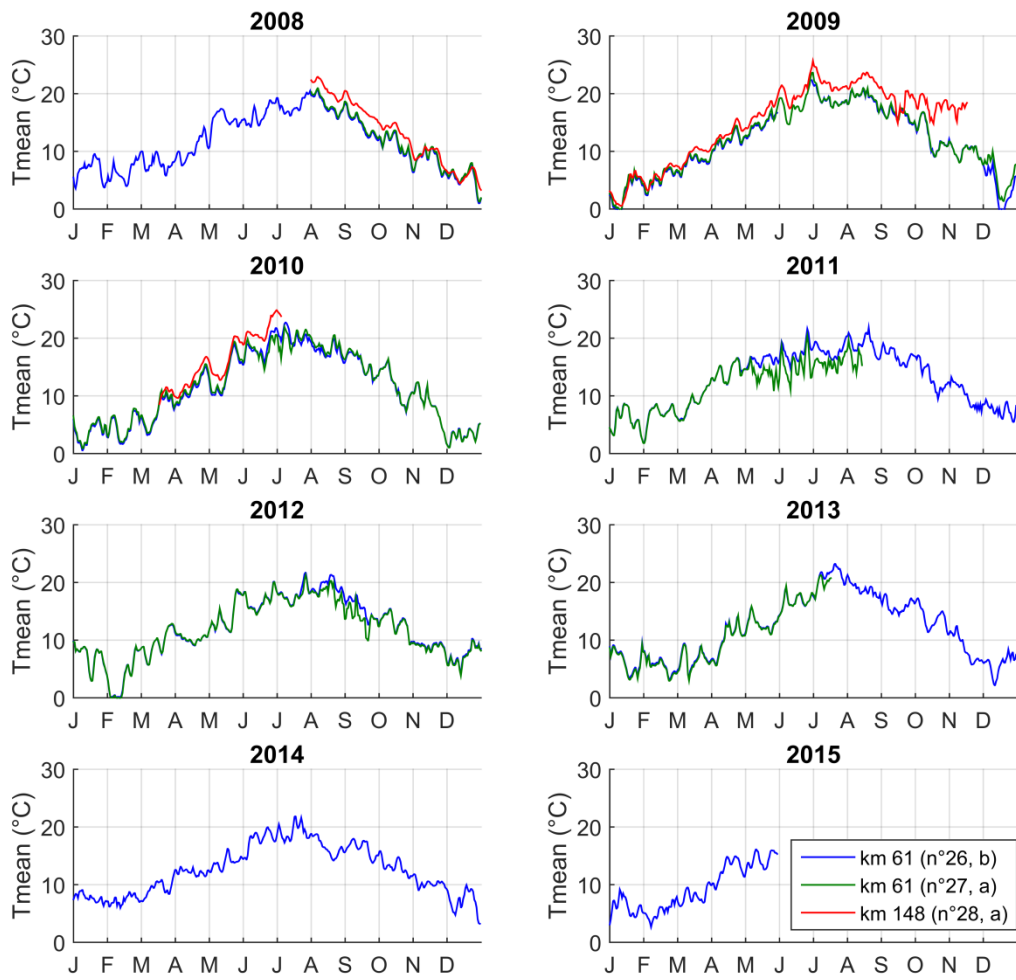
Loir



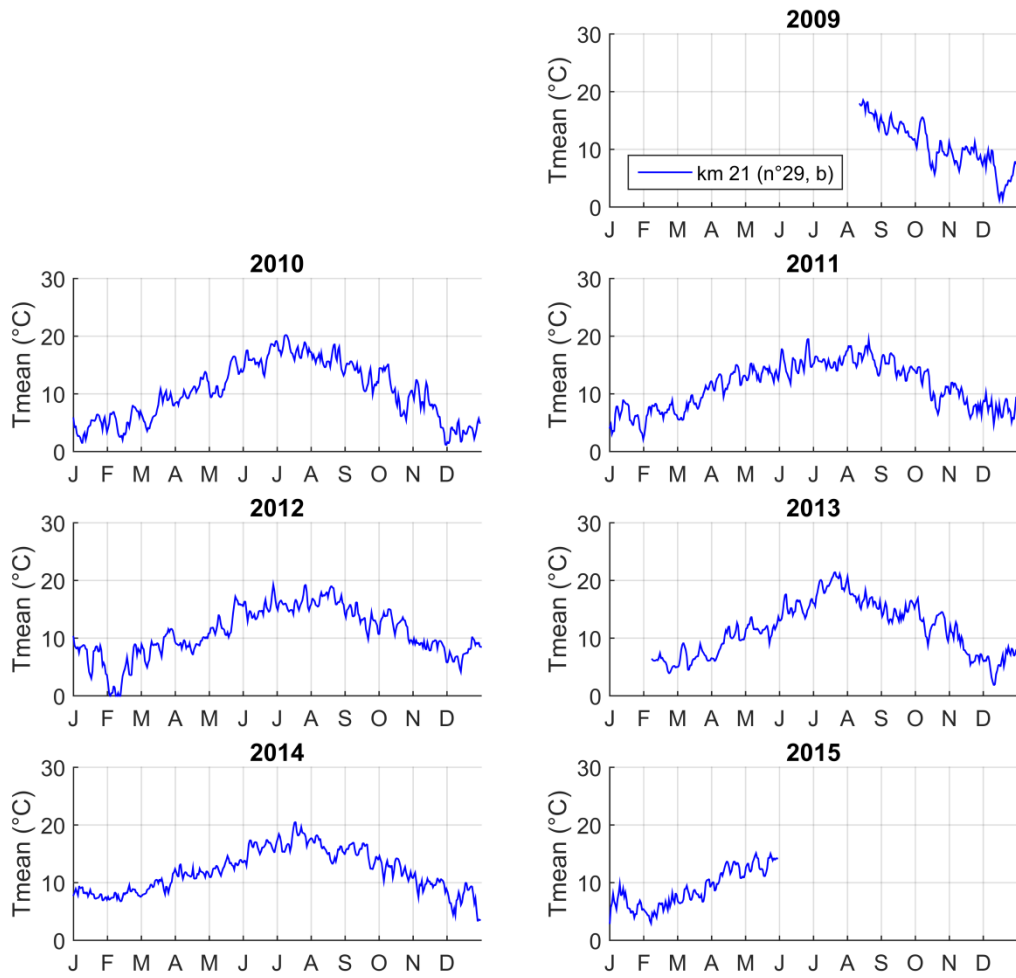
# Maine



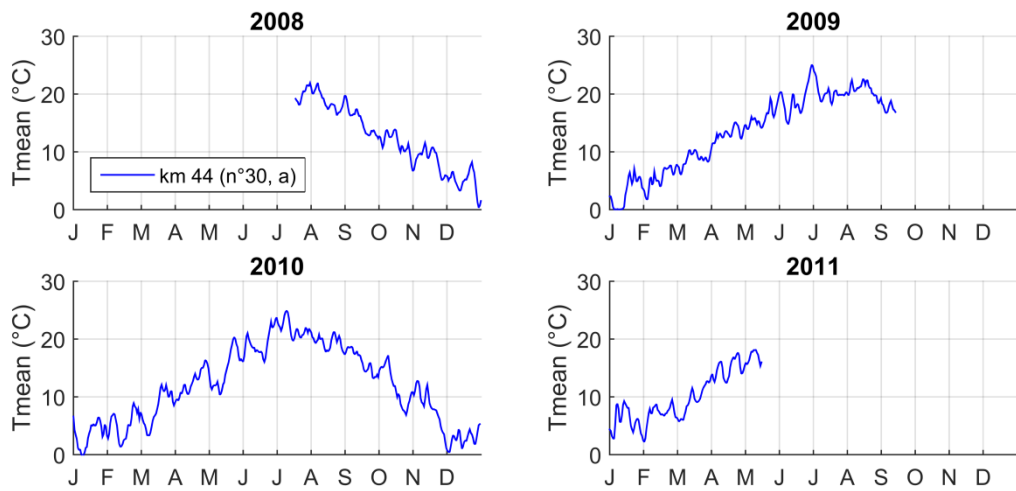
# Mayenne



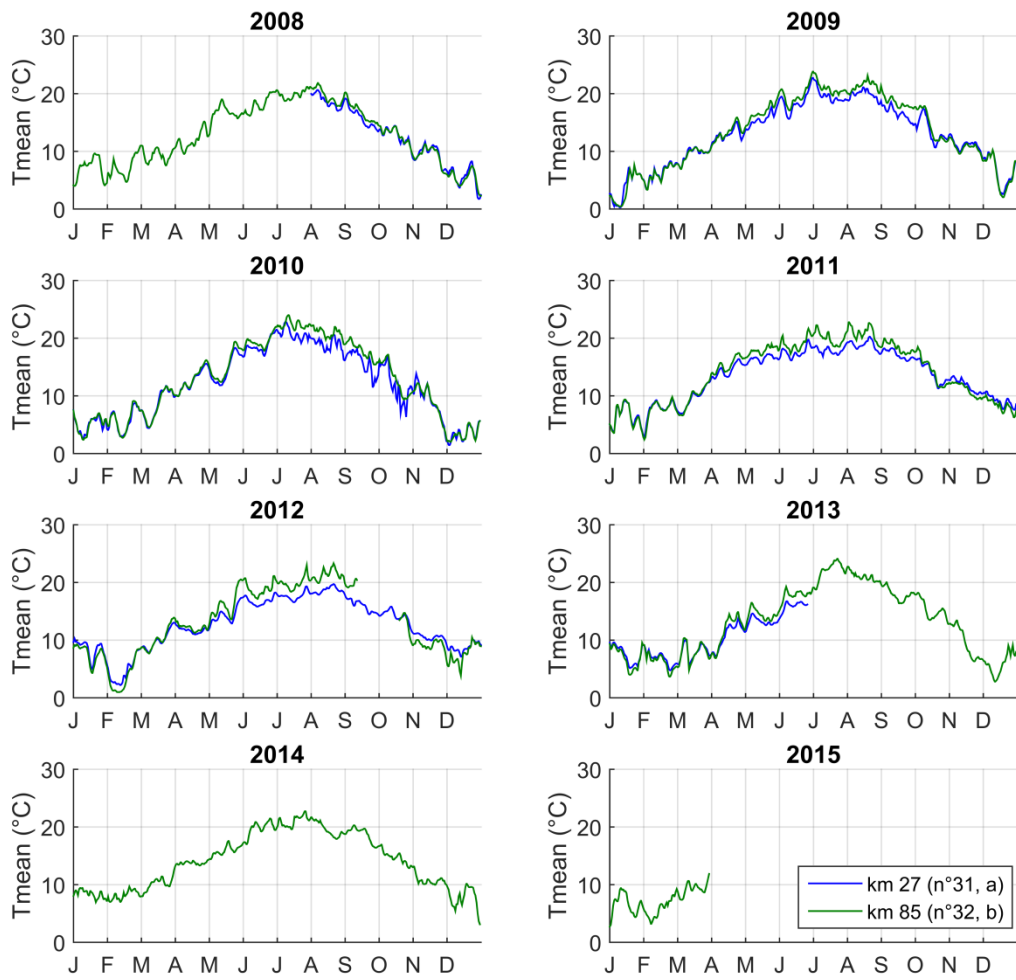
## Merdereau



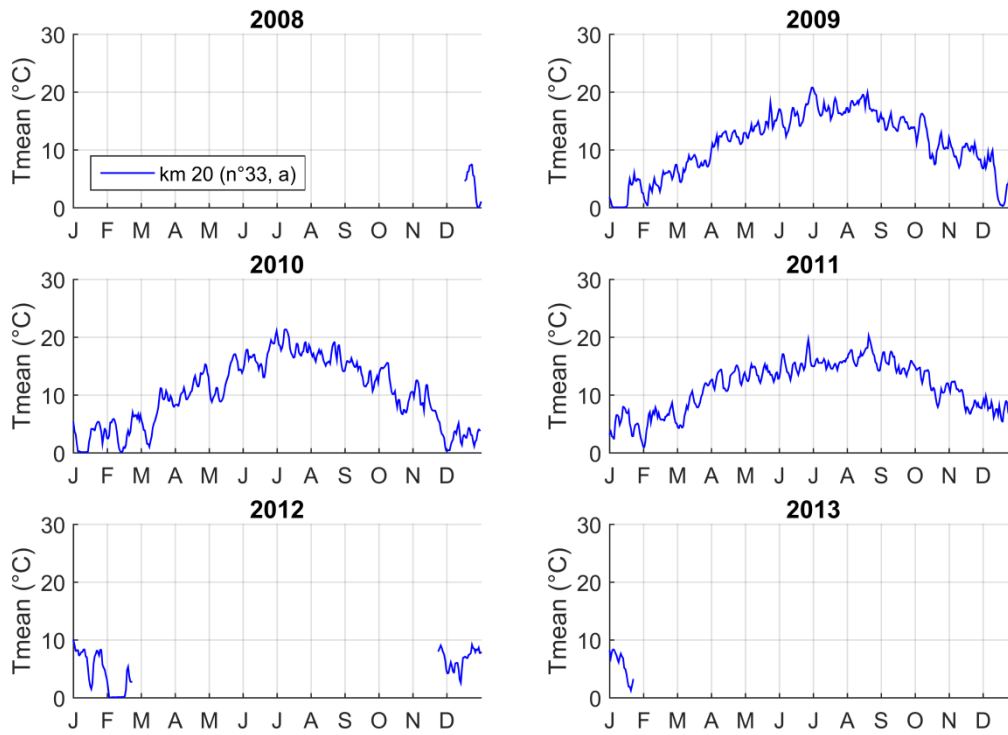
## Orne



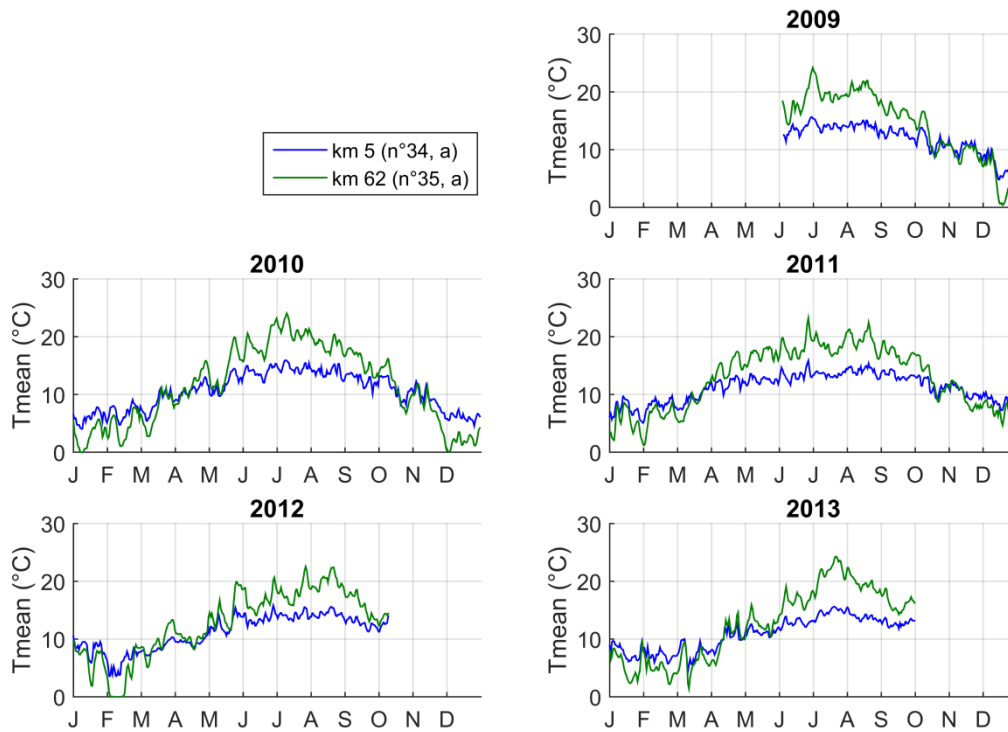
# Oudon



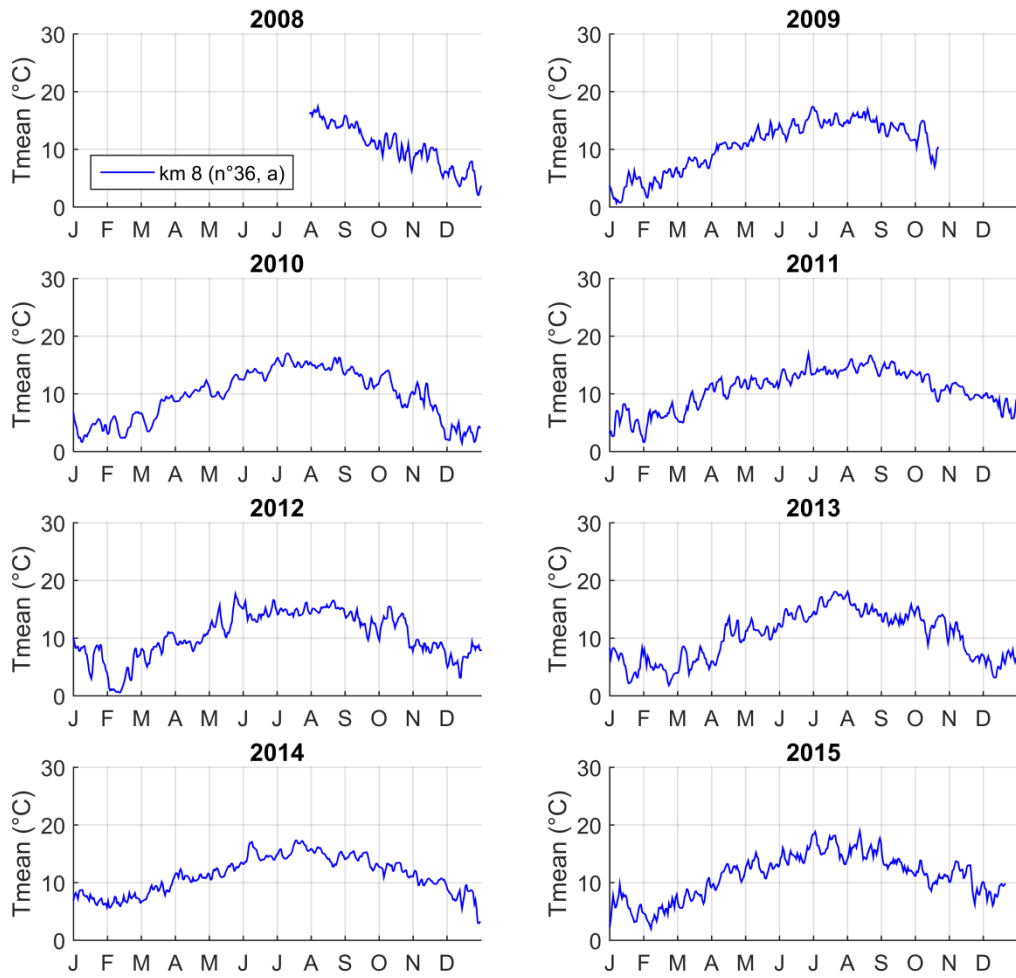
### Ozanne



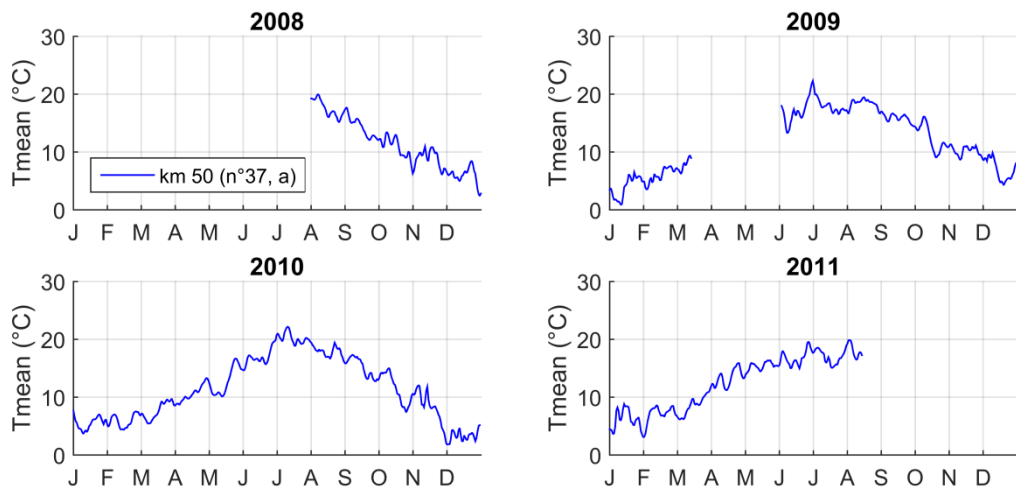
### Sarthe



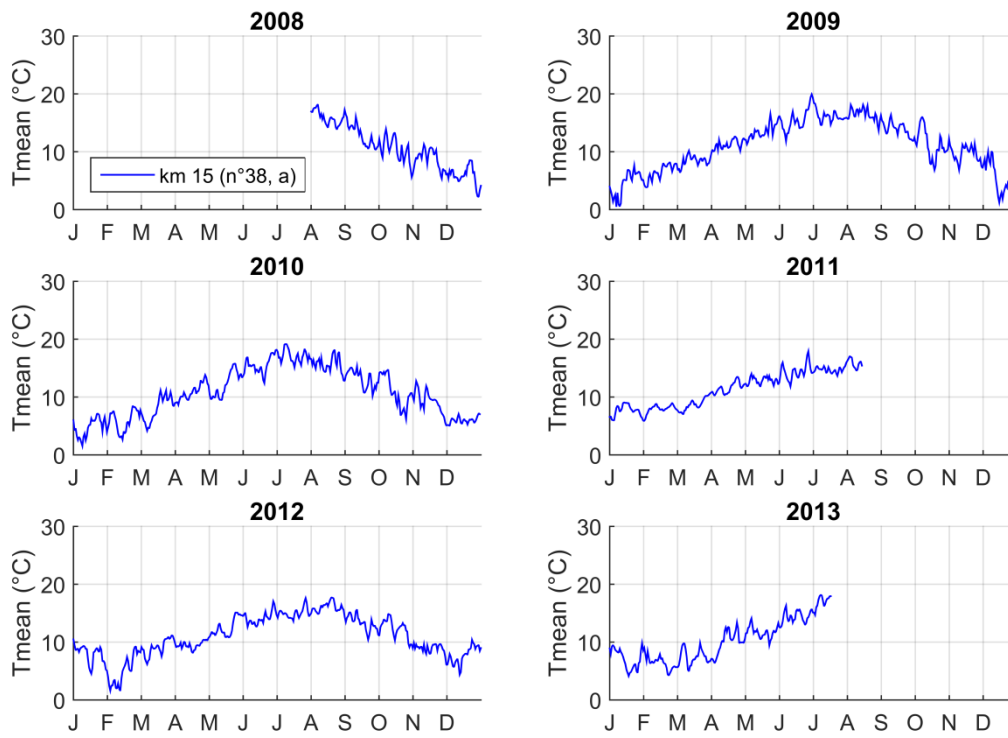
## Tusson



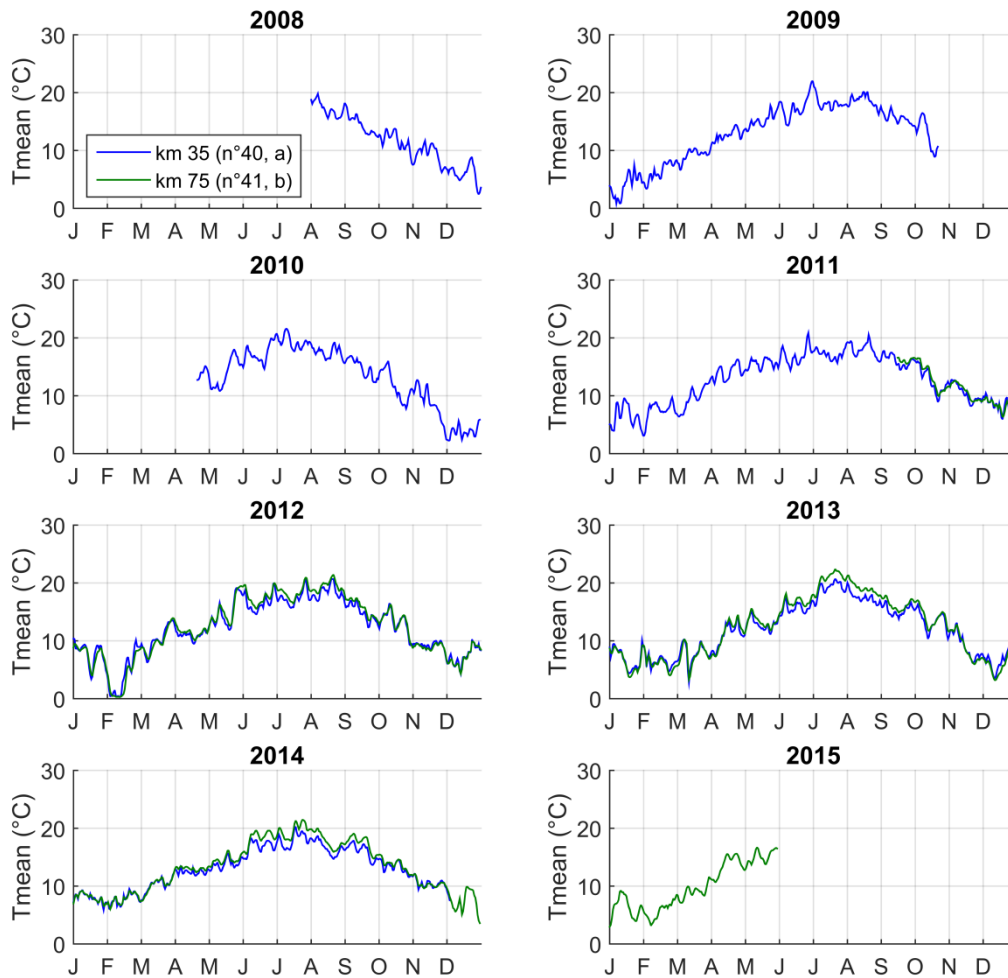
## Varenne



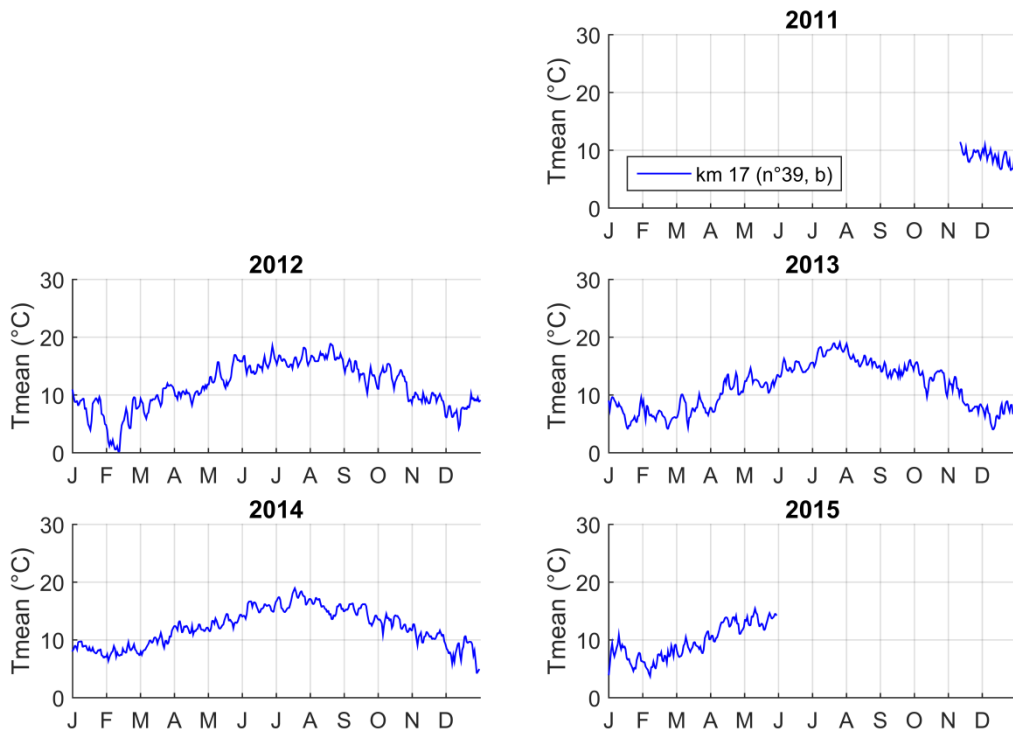
### Vaudelle



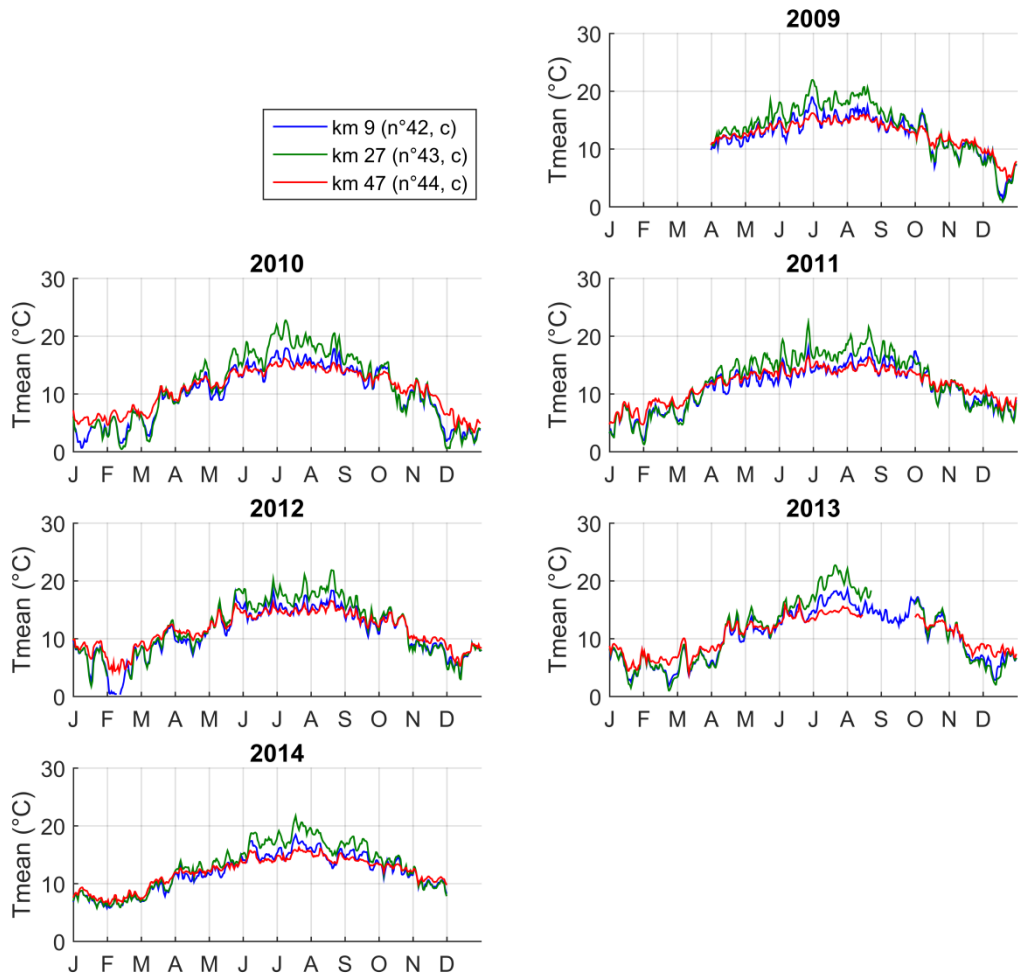
### Vègre



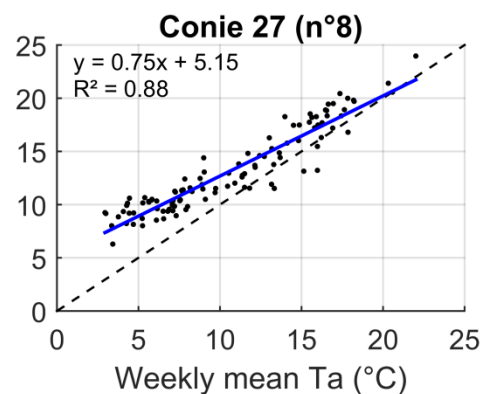
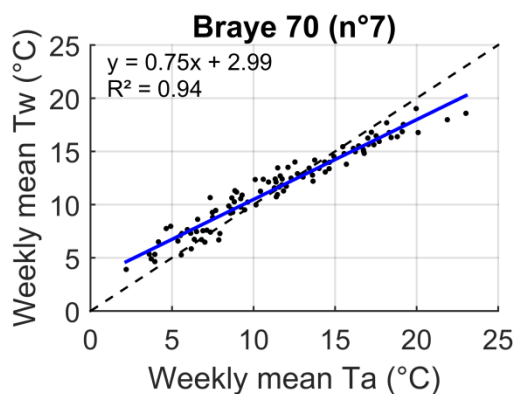
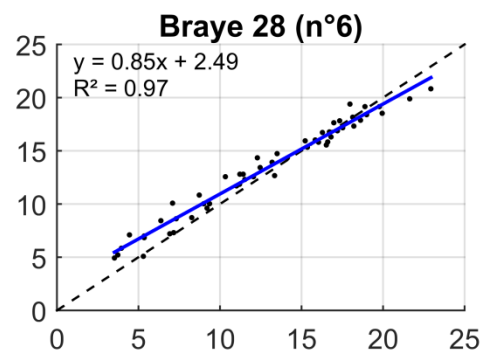
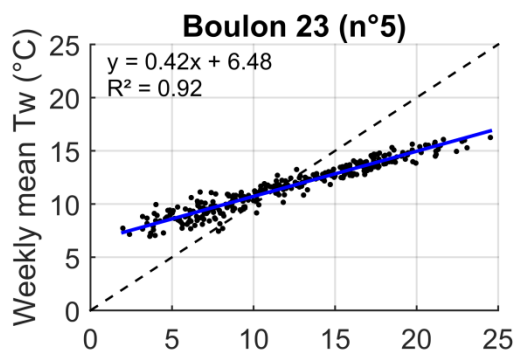
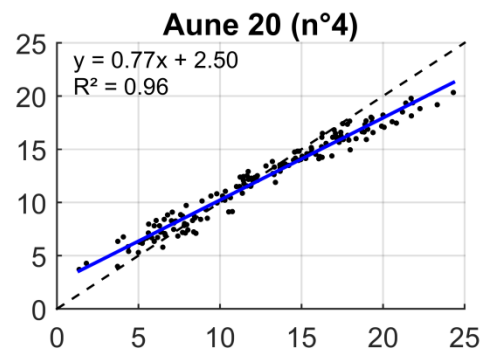
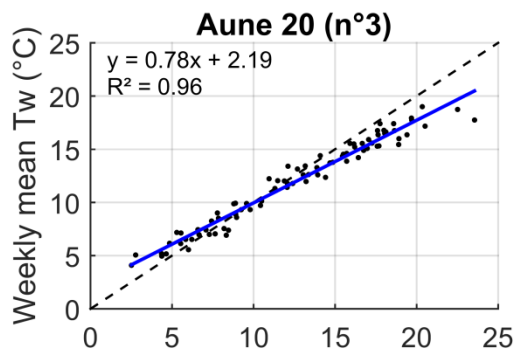
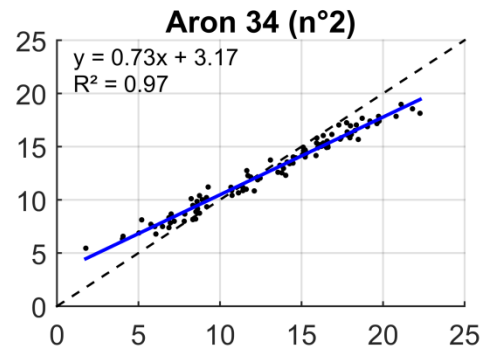
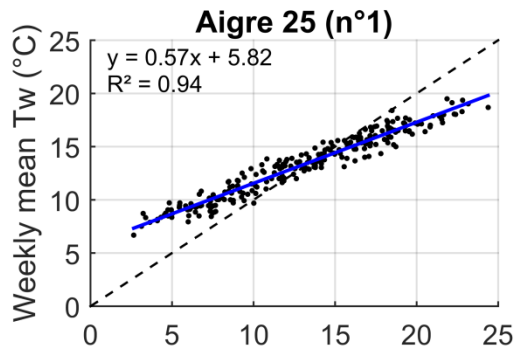
## Veuve

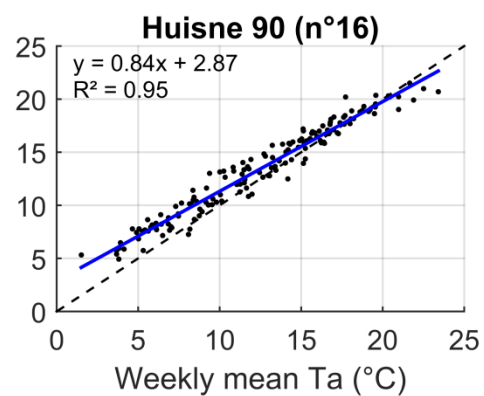
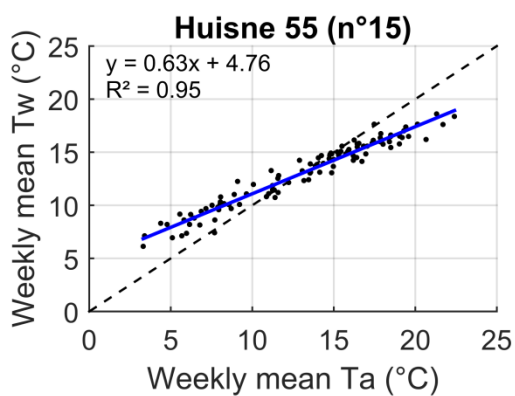
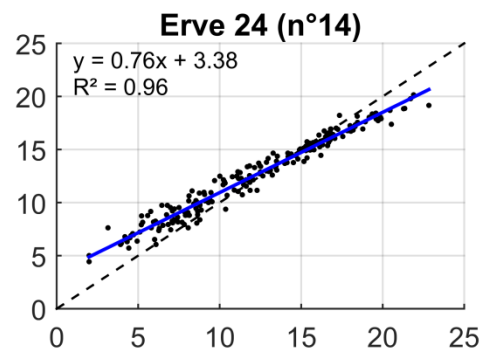
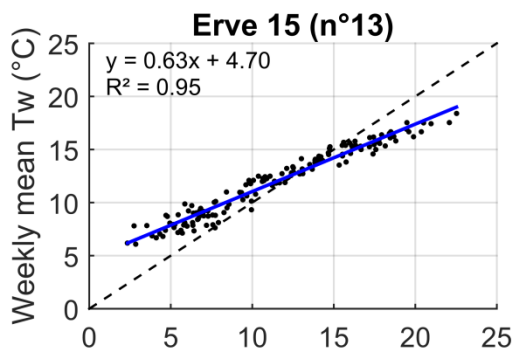
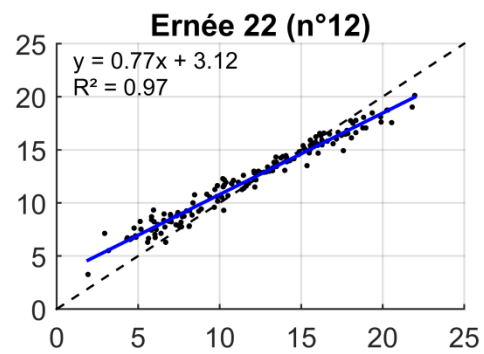
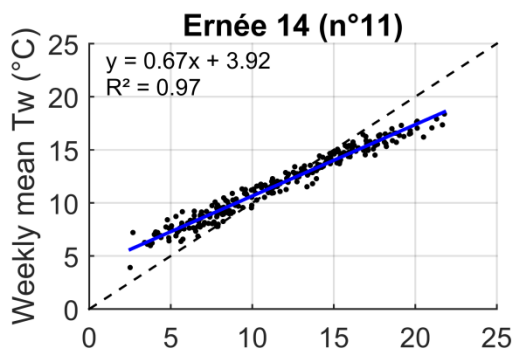
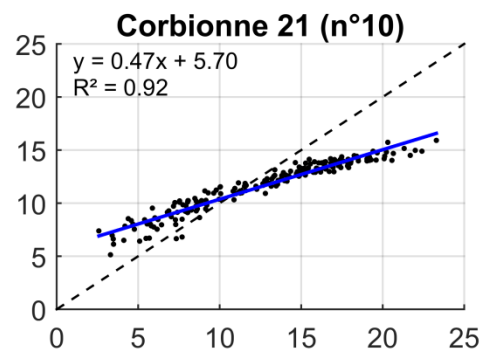
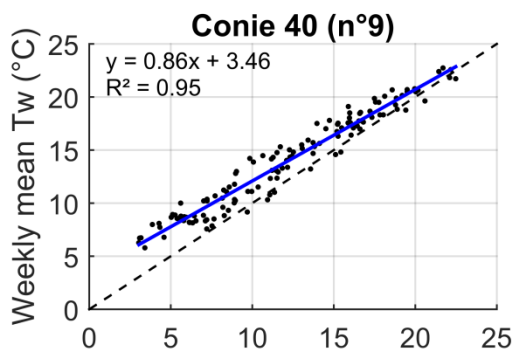


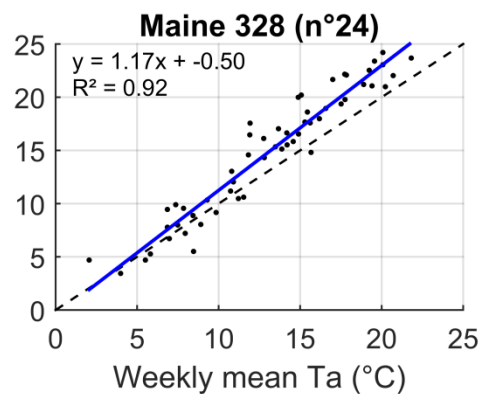
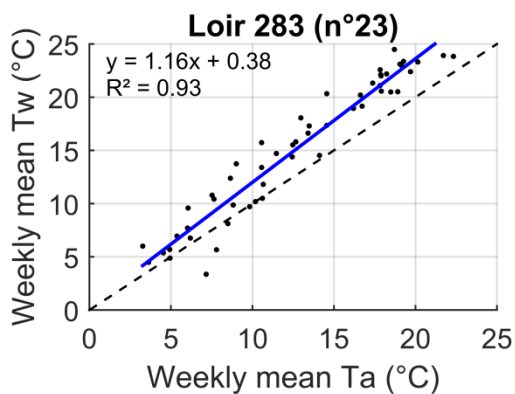
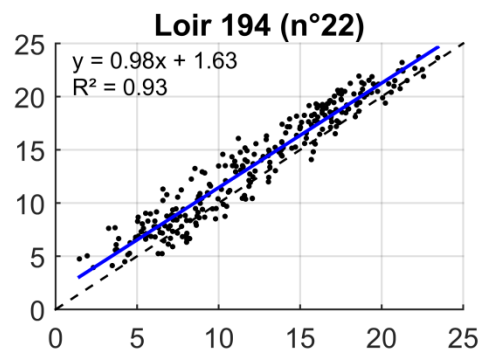
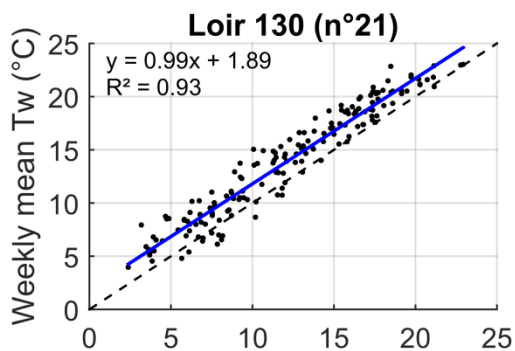
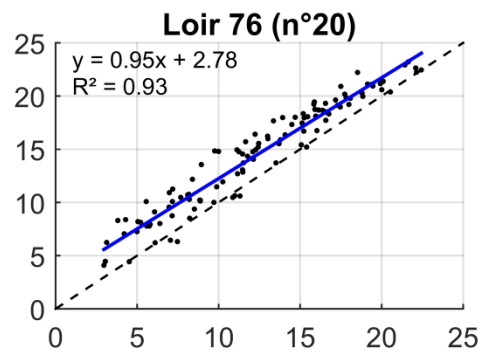
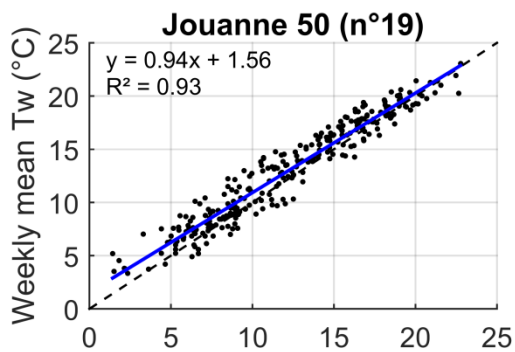
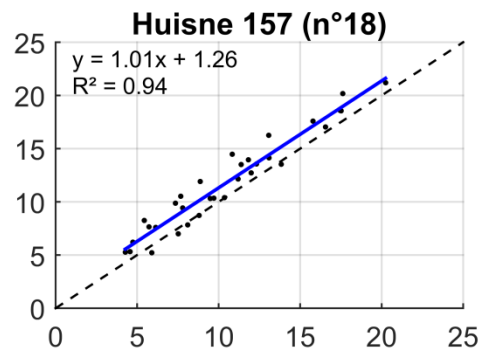
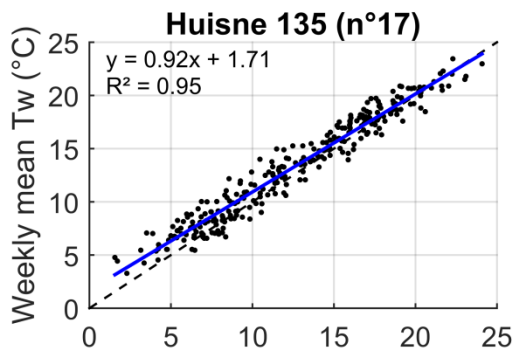
## Yerre

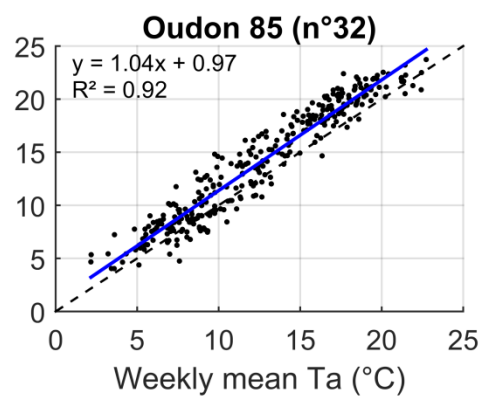
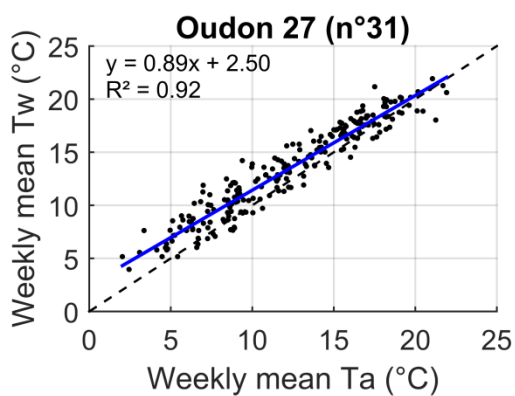
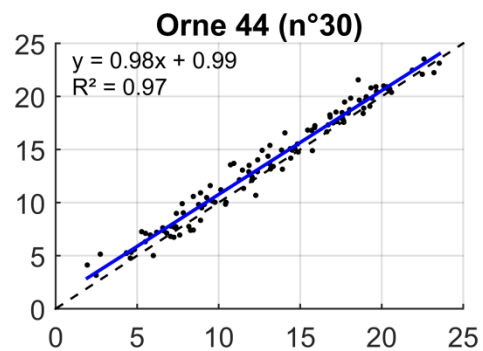
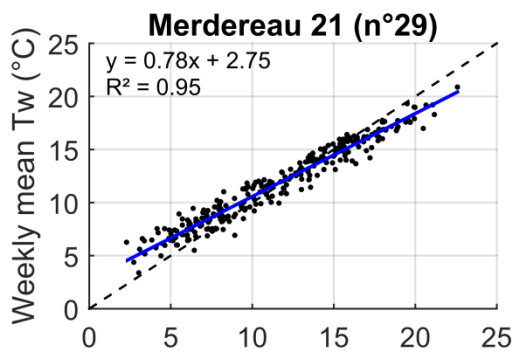
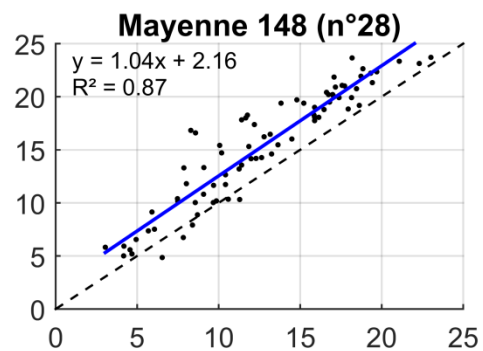
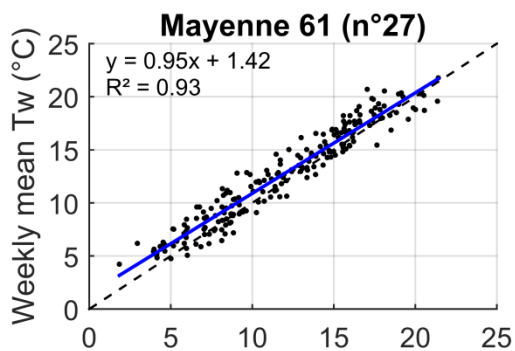
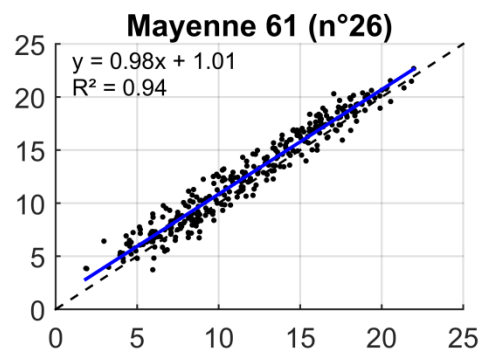
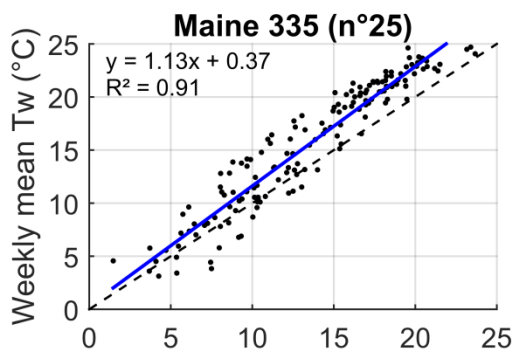


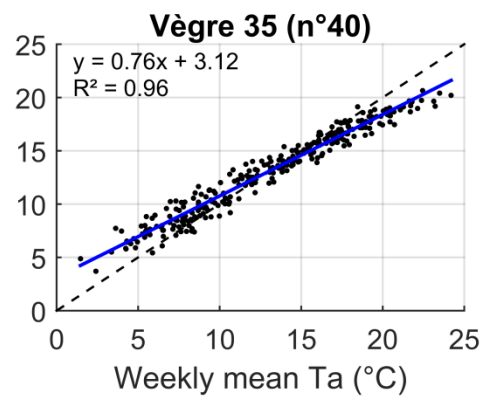
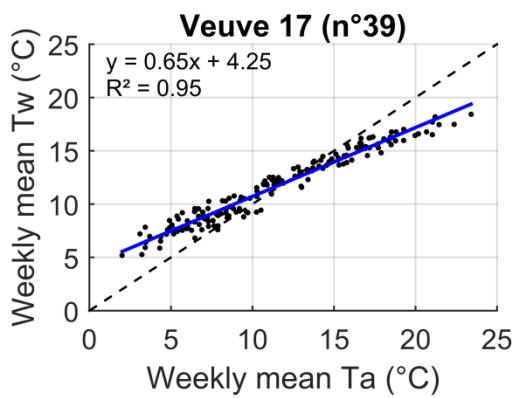
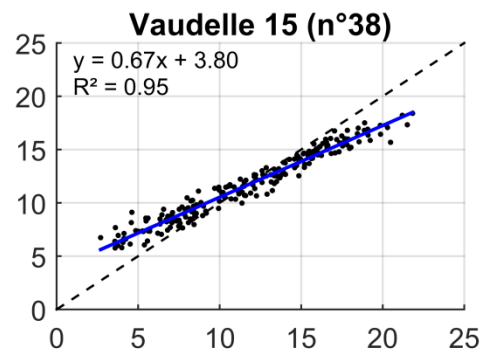
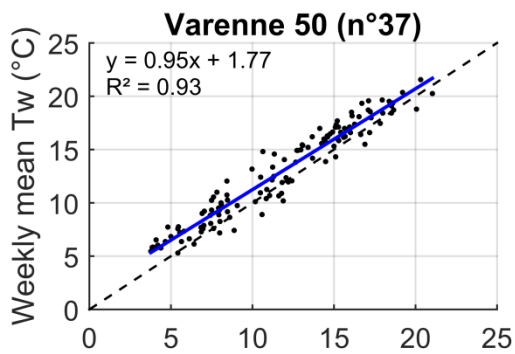
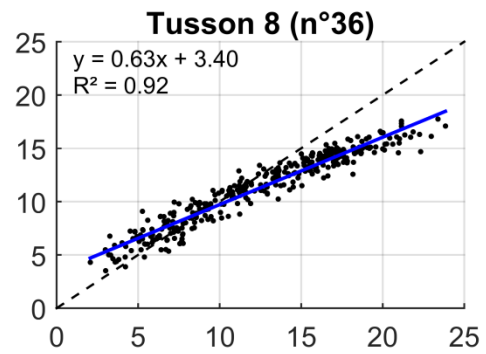
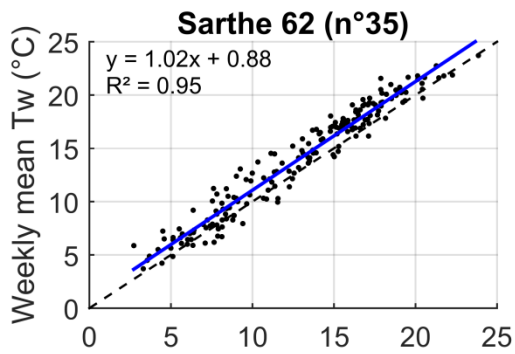
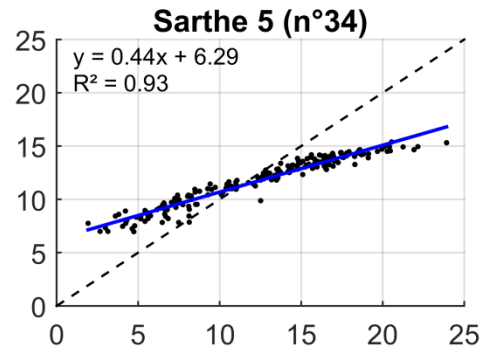
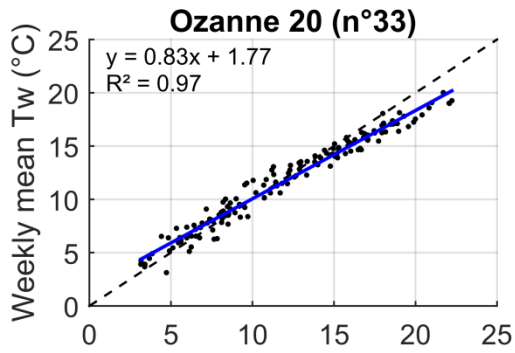
**Appendix F: Scatterplots of mean weekly water temperature as a function of mean weekly air temperature, using data available on the 08/2008-07/2015 period**

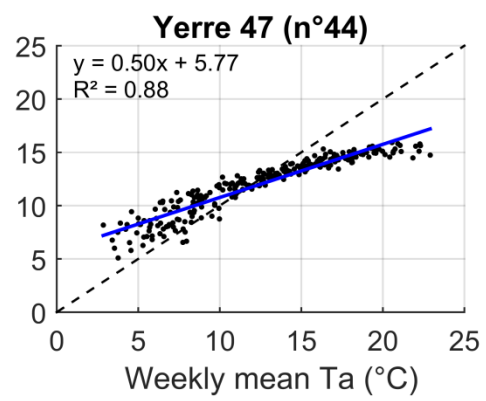
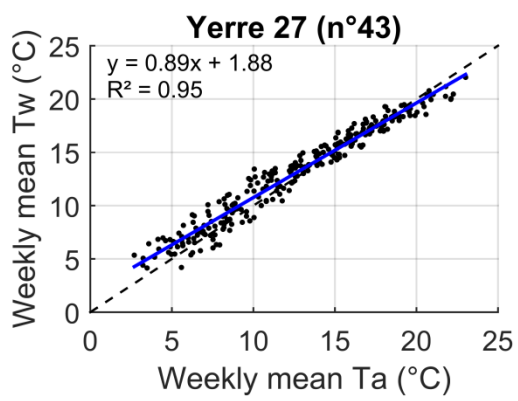
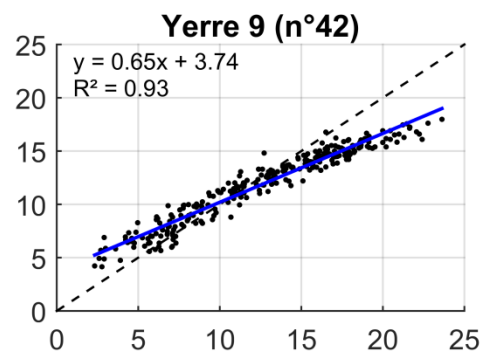
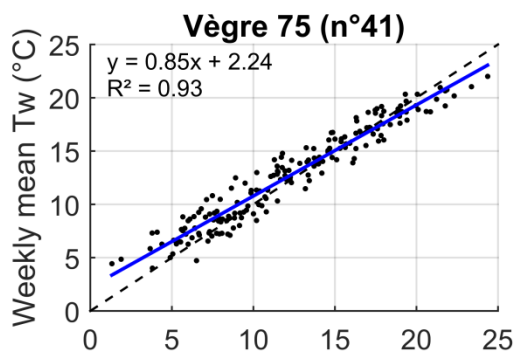




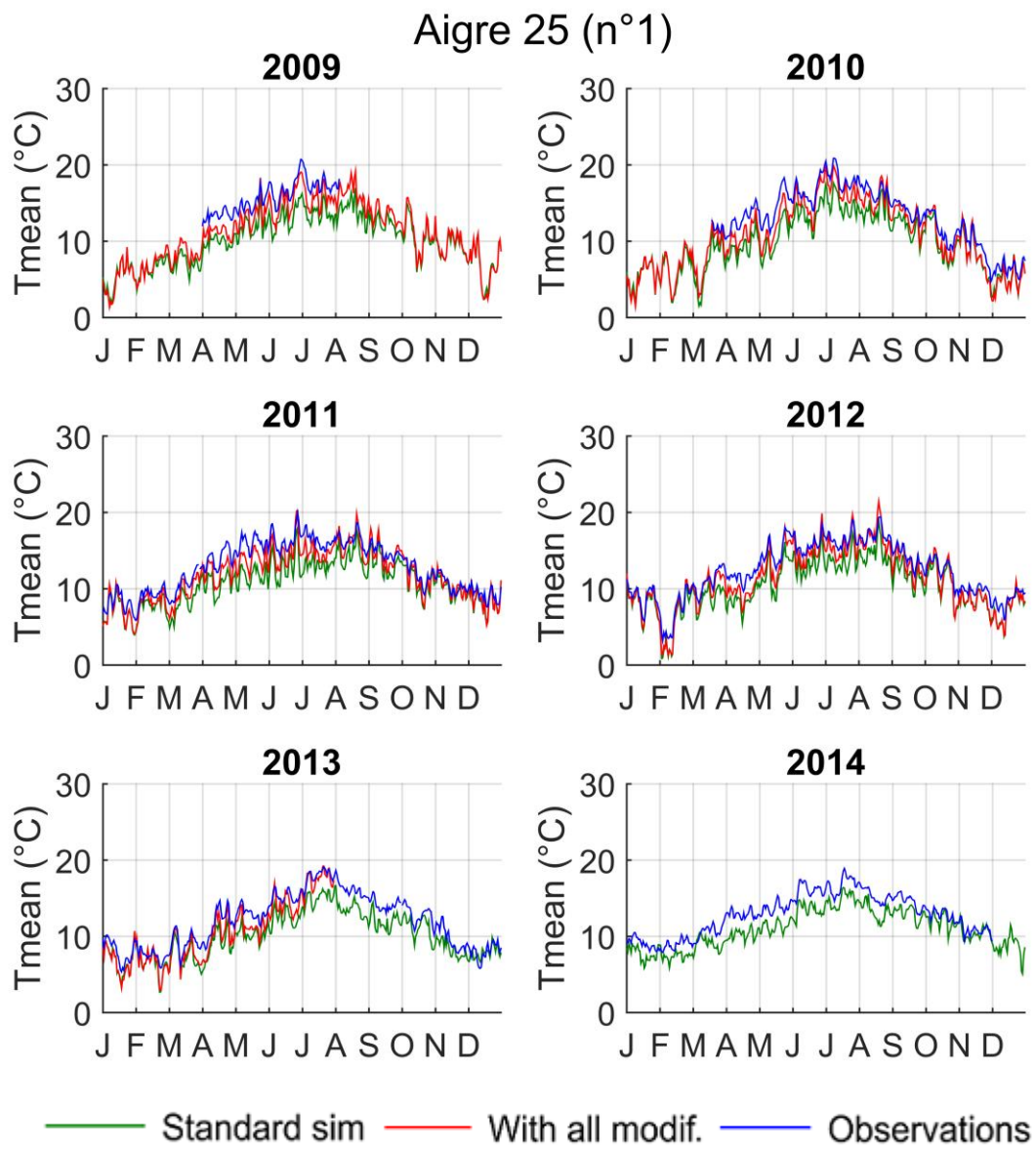




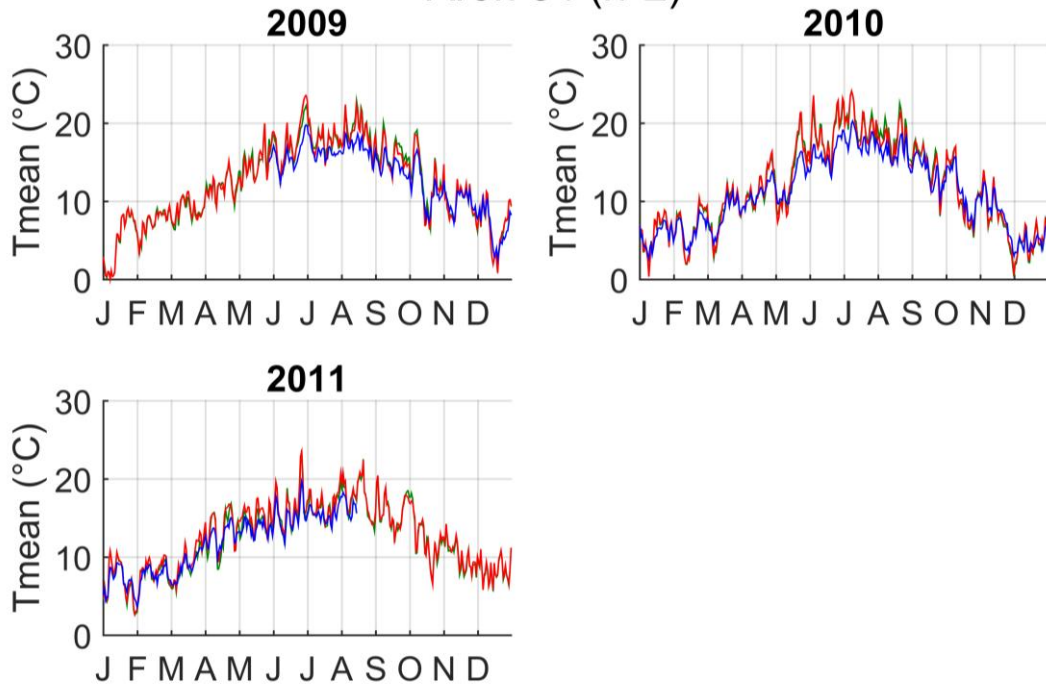




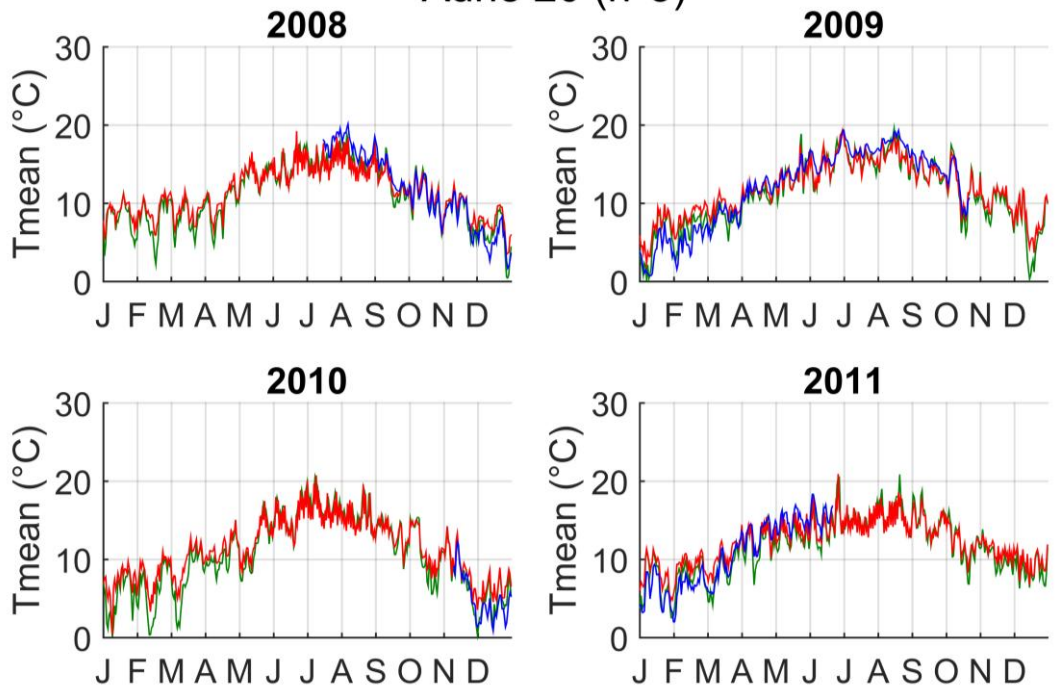
**Appendix G: Mean daily temperature modelled with the standard and the final version of T-NET, compared to observed values**



### Aron 34 (n°2)

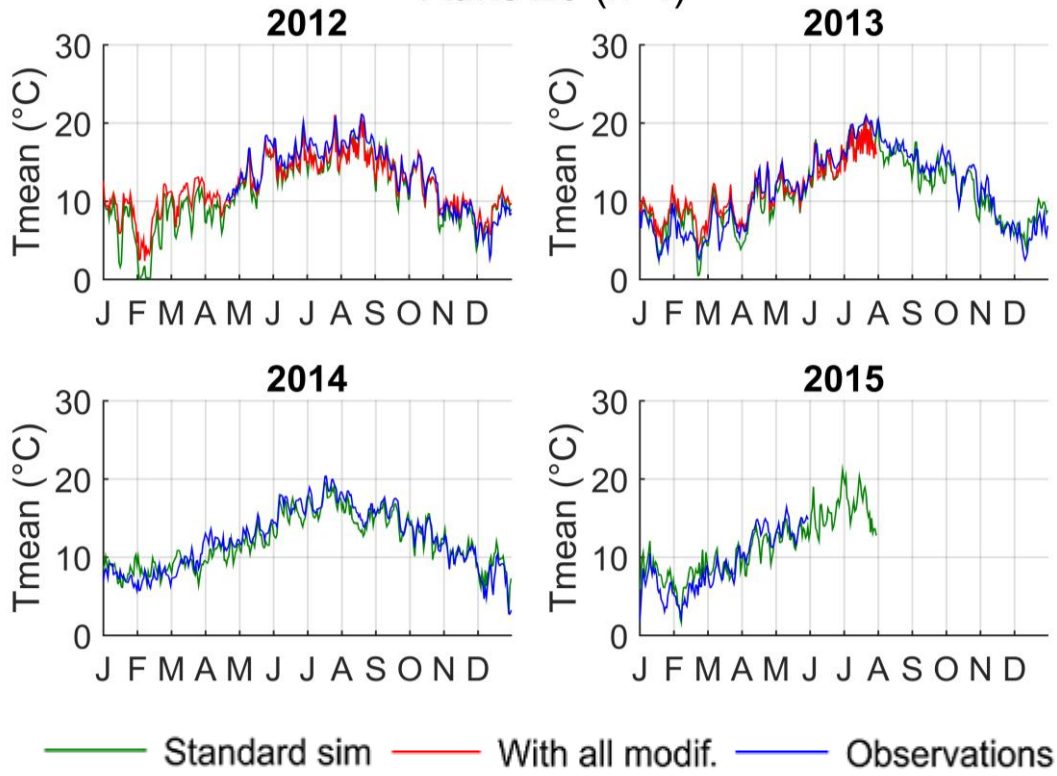


### Aune 20 (n°3)

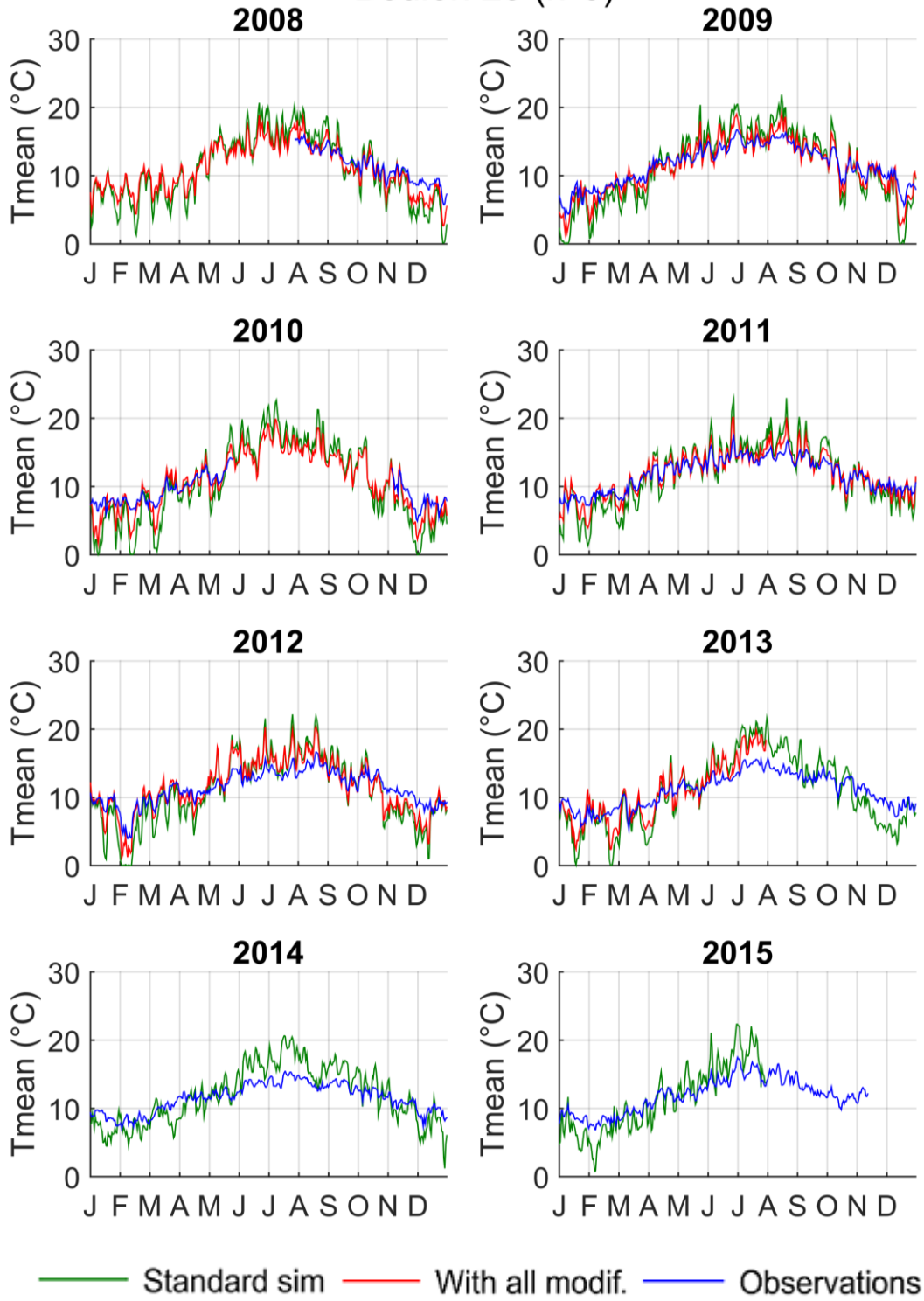


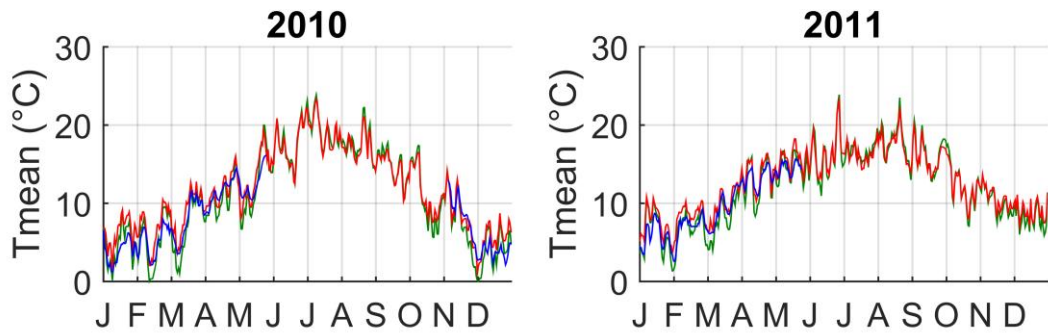
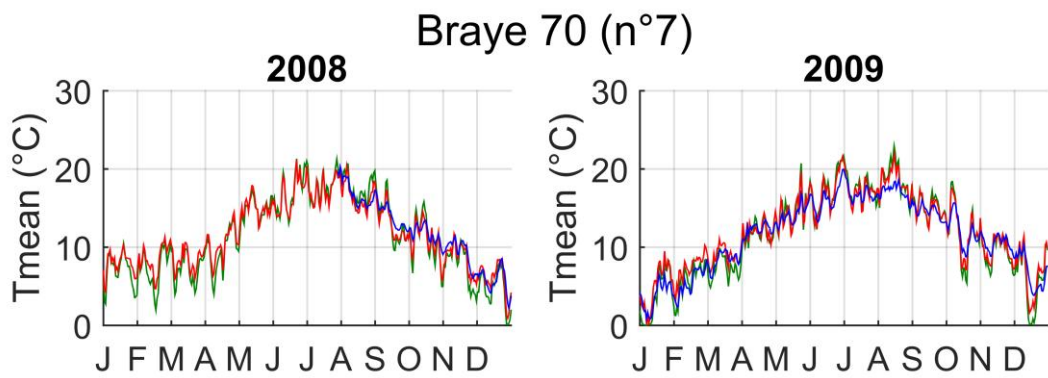
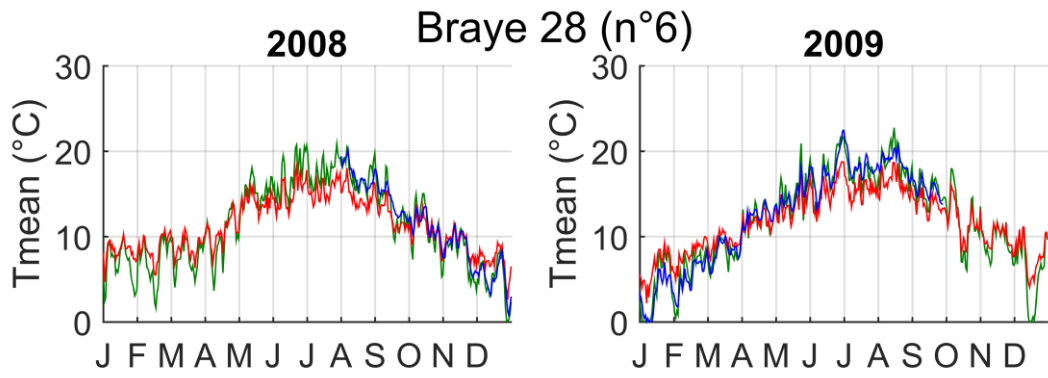
— Standard sim — With all modif. — Observations

Aune 20 (n°4)



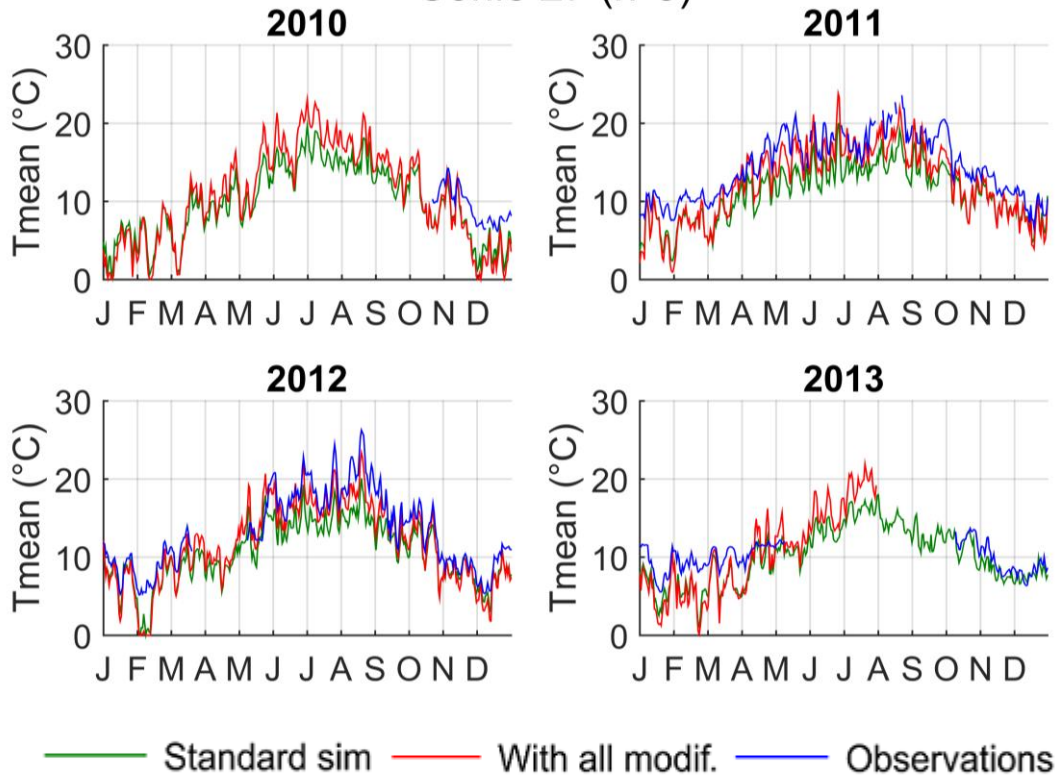
# Boulon 23 (n°5)



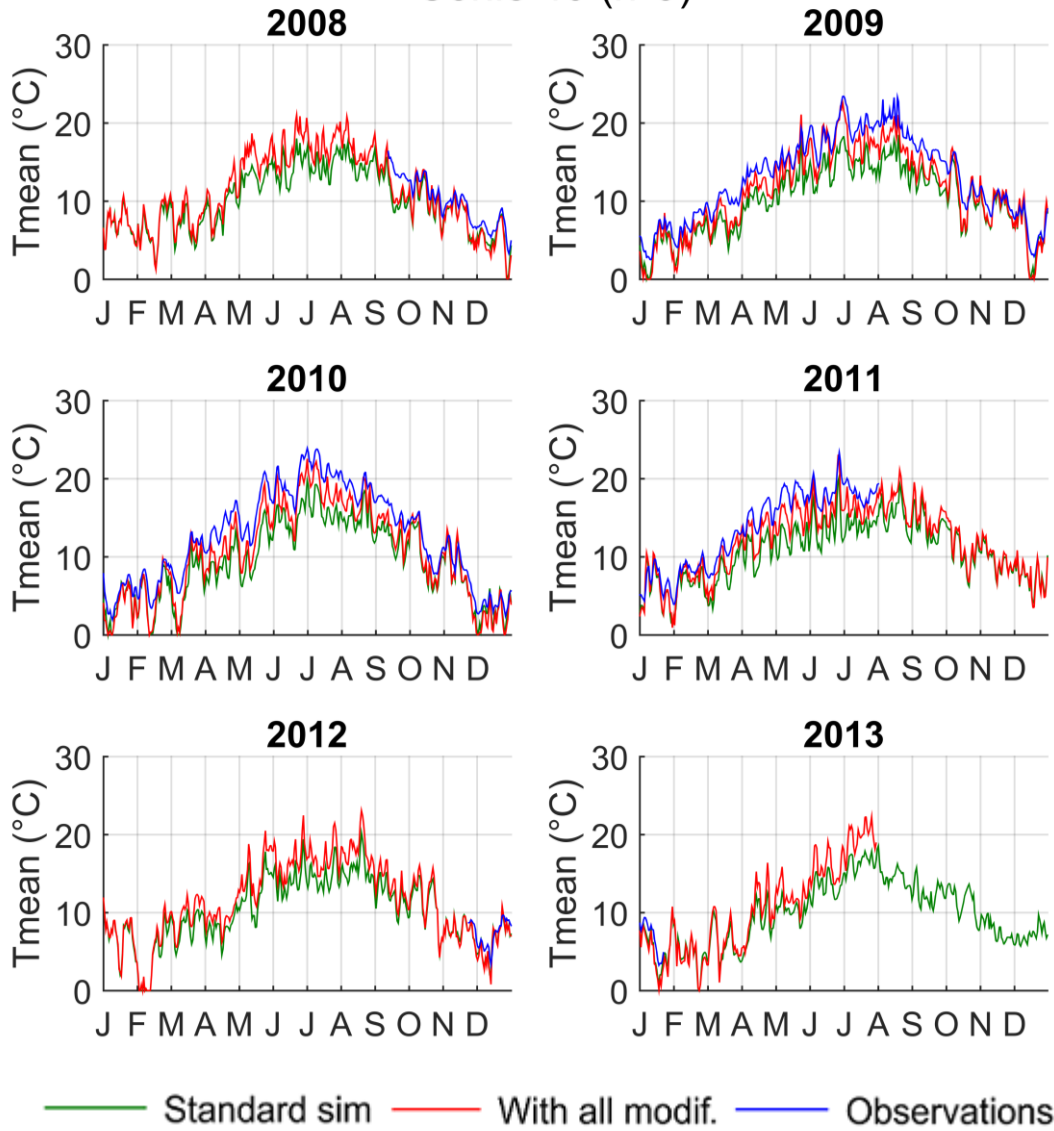


— Standard sim   
 — With all modif.   
 — Observations

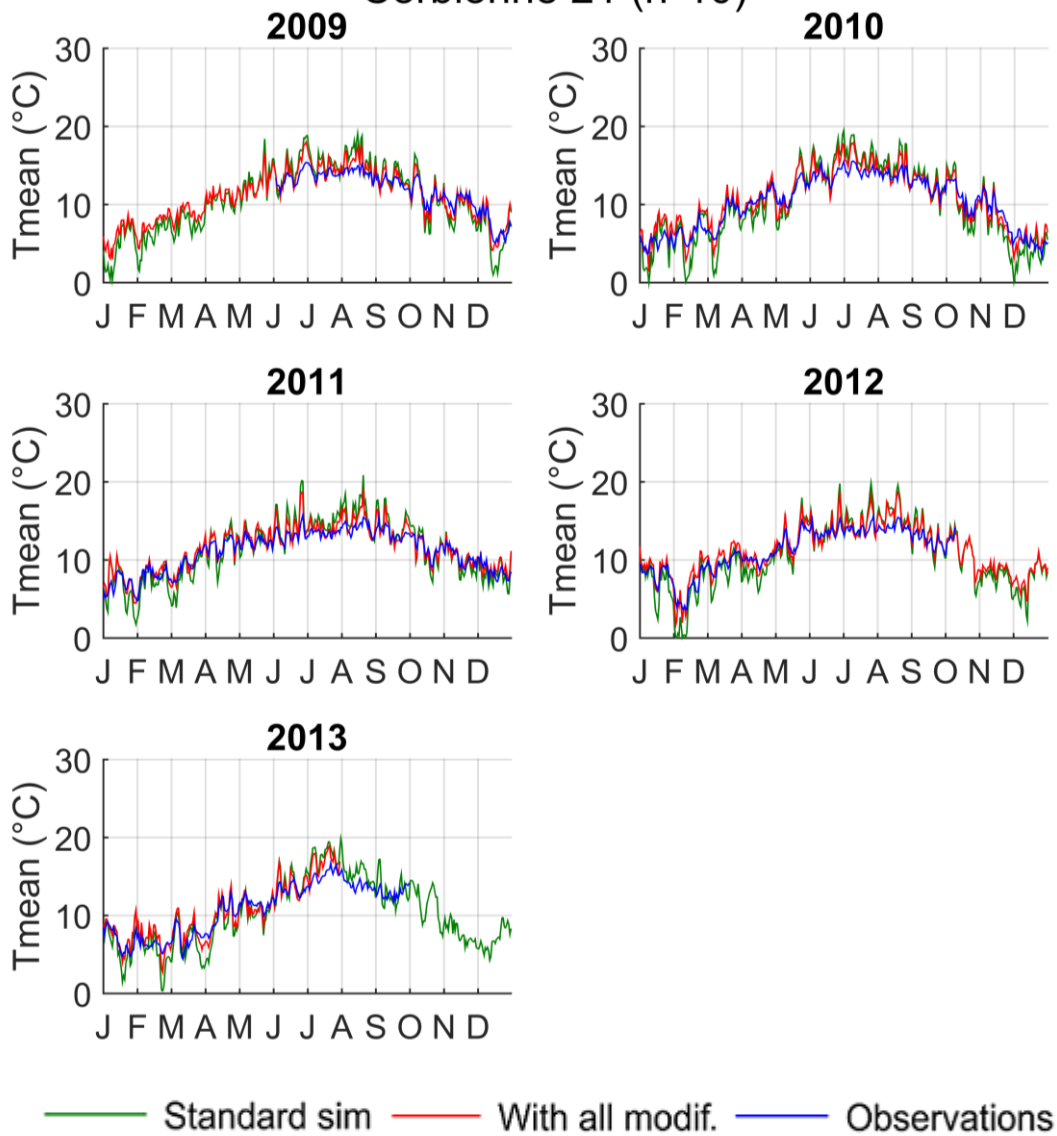
### Conie 27 (n°8)



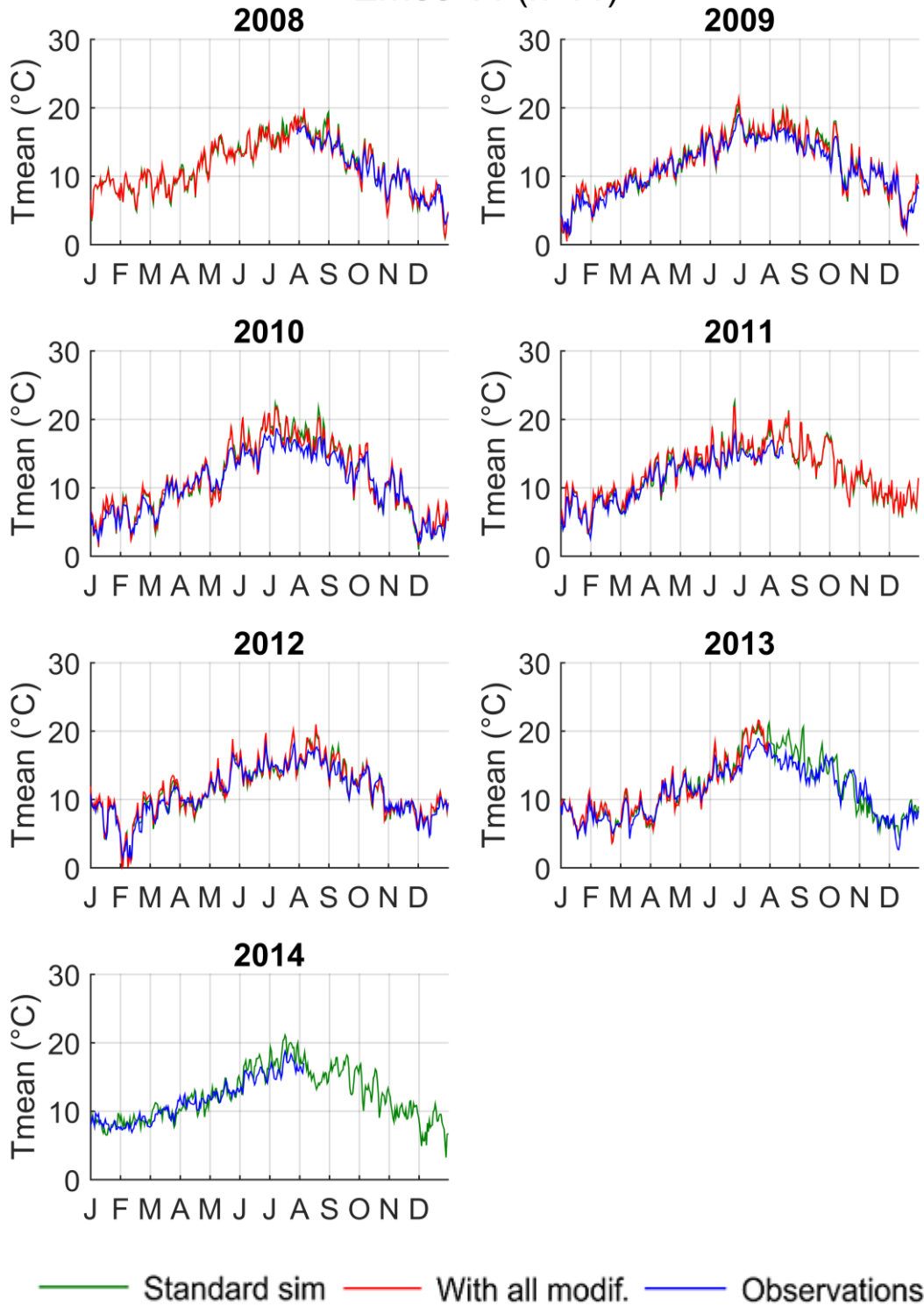
### Conie 40 (n°9)



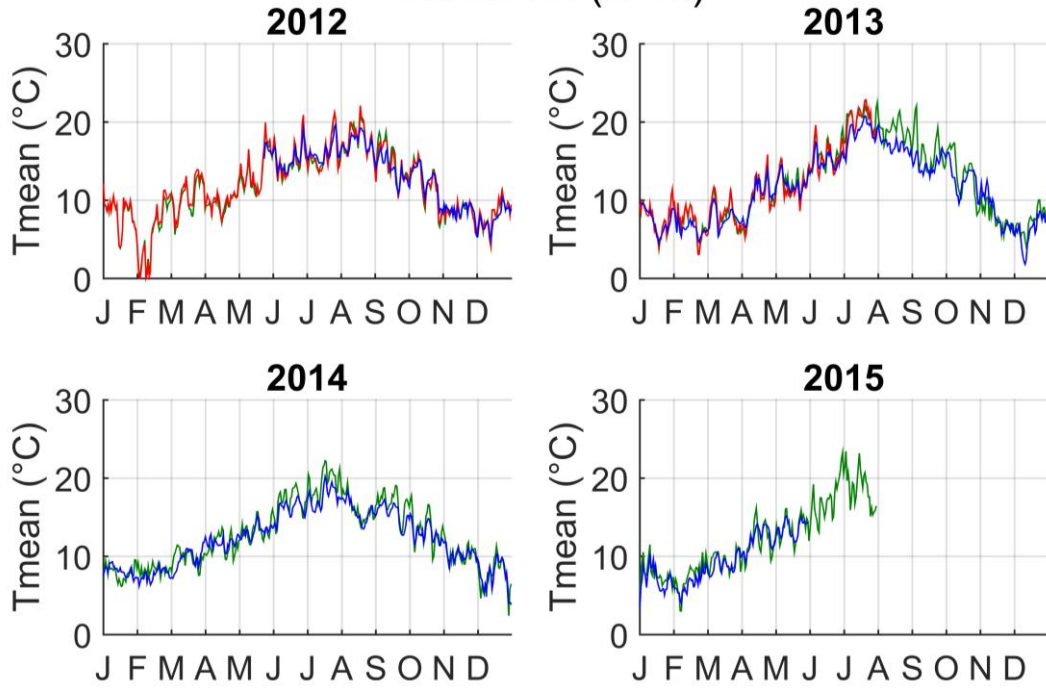
# Corbionne 21 (n°10)



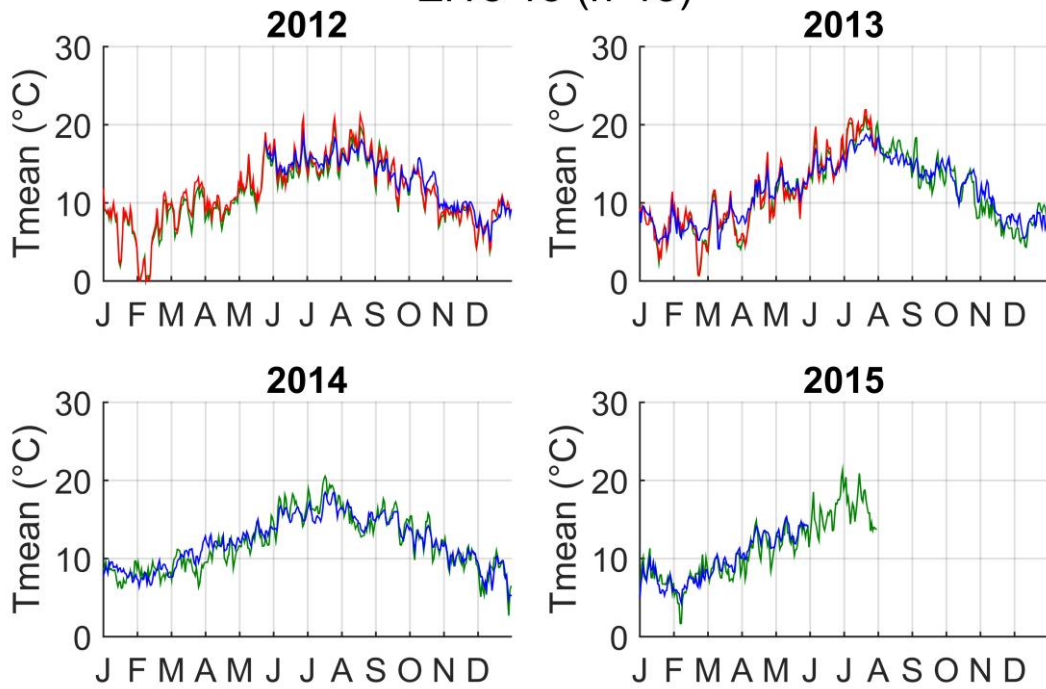
# Ernée 14 (n°11)



### Ernée 22 (n°12)

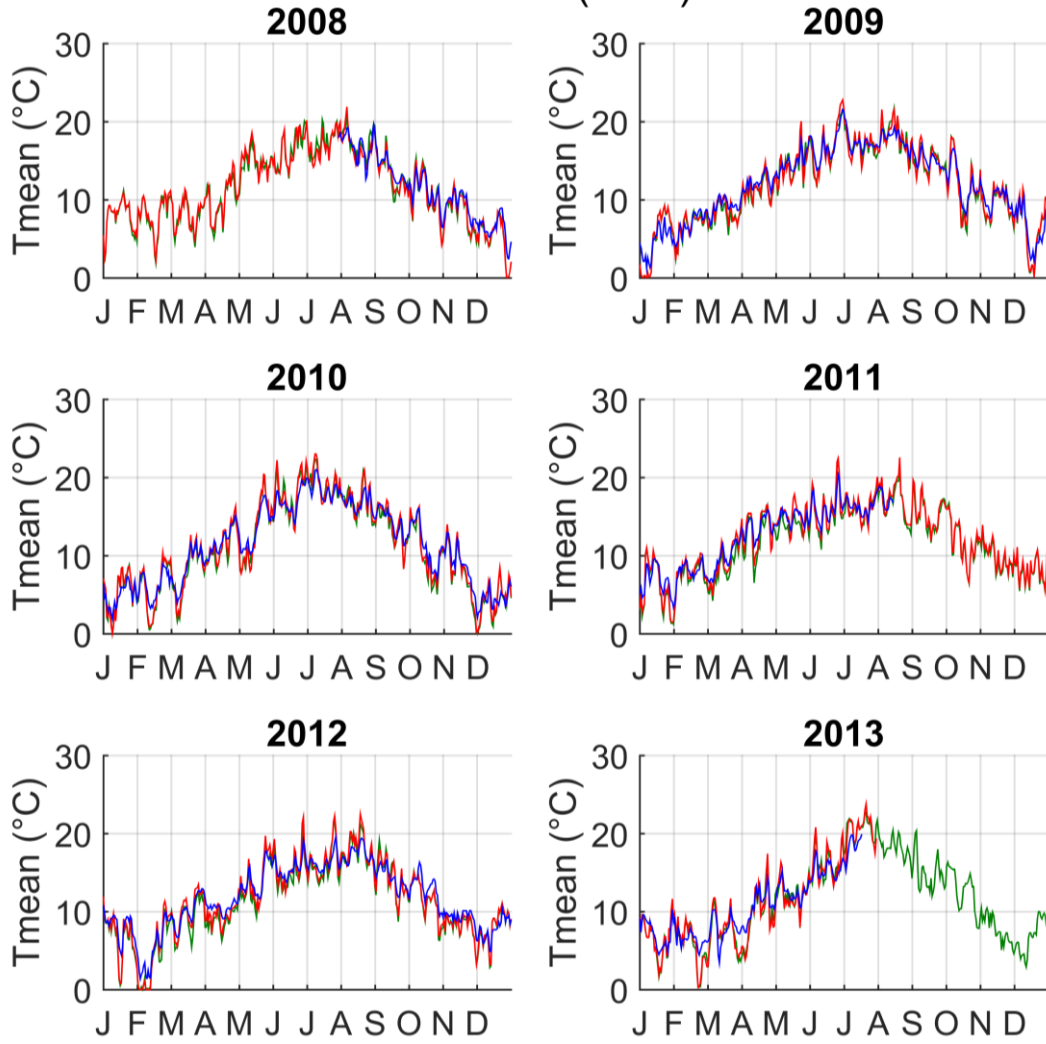


### Erve 15 (n°13)

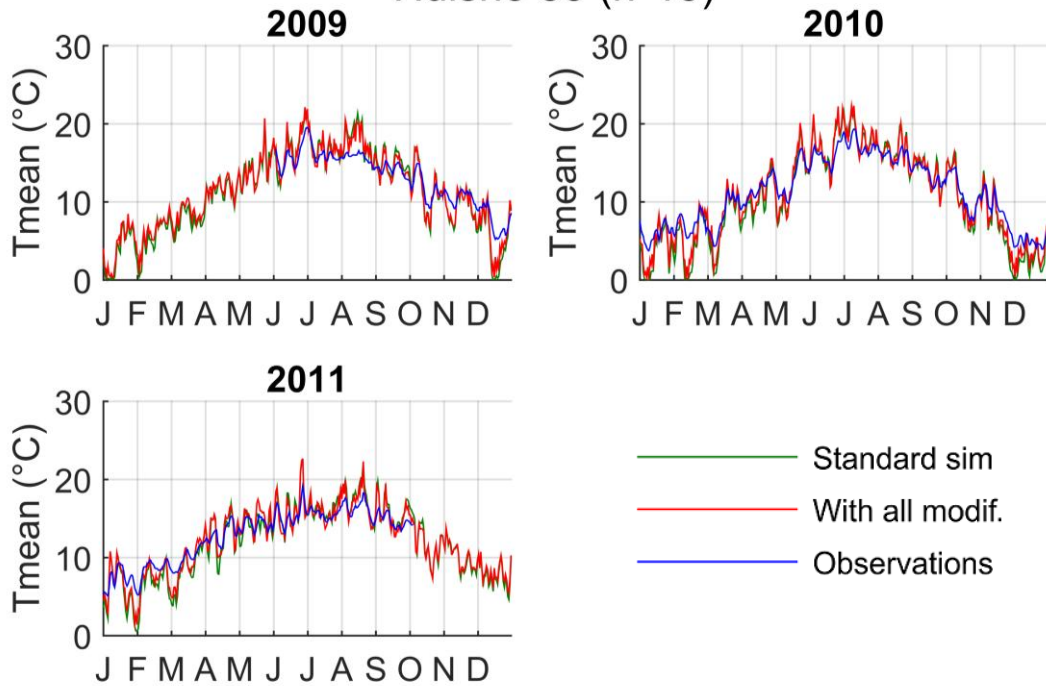


— Standard sim — With all modif. — Observations

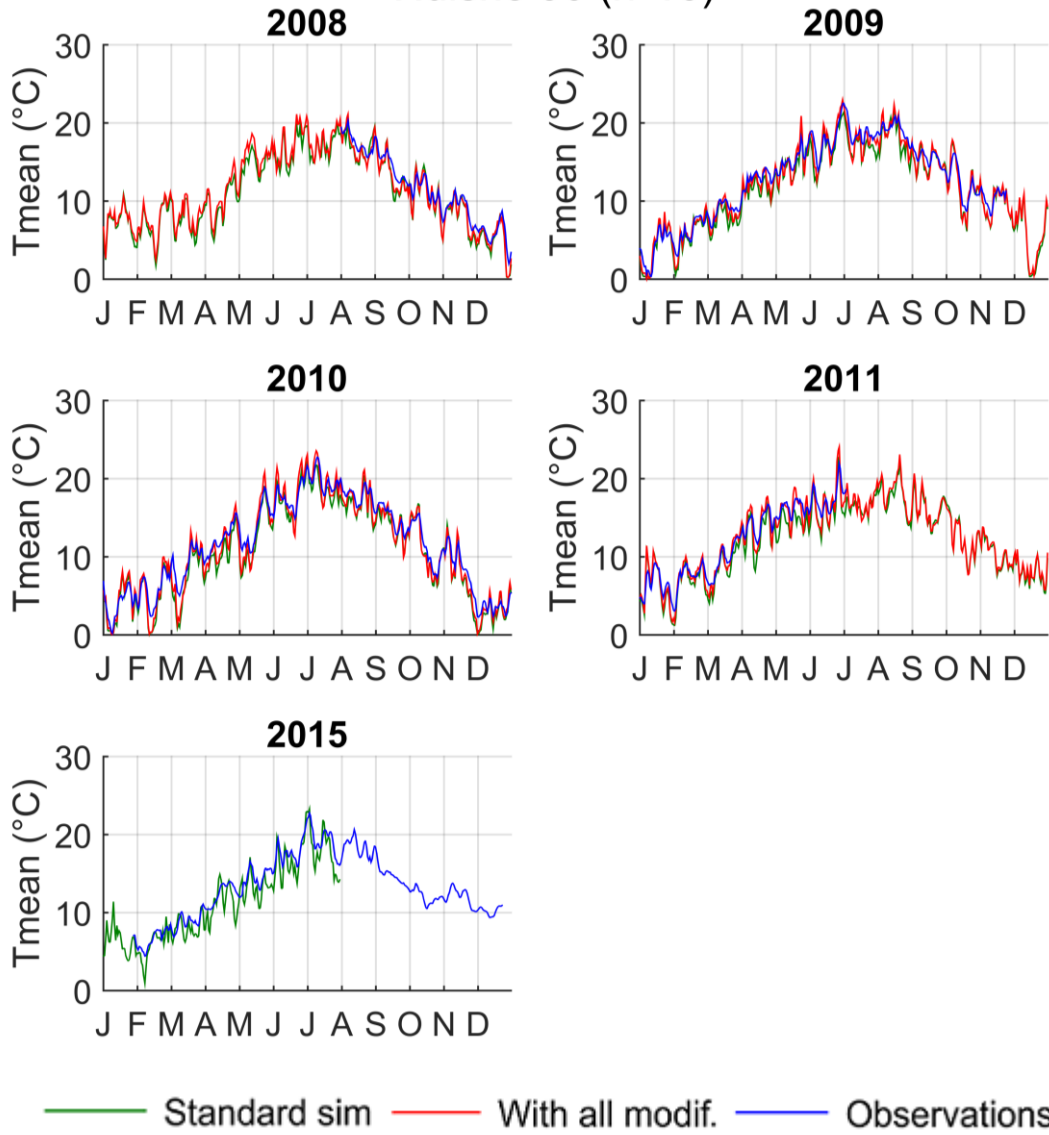
### Erve 24 (n°14)



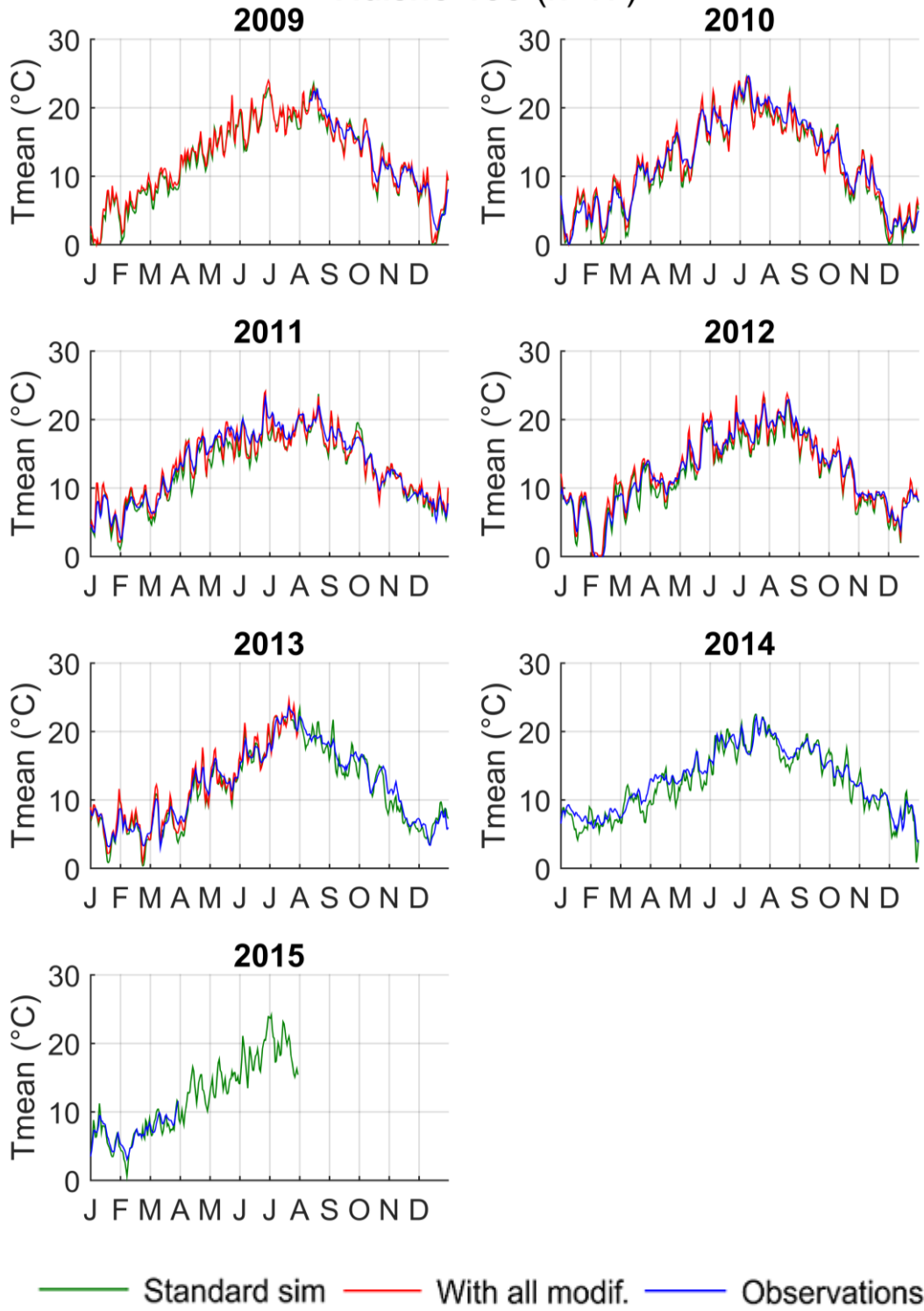
### Huisne 55 (n°15)

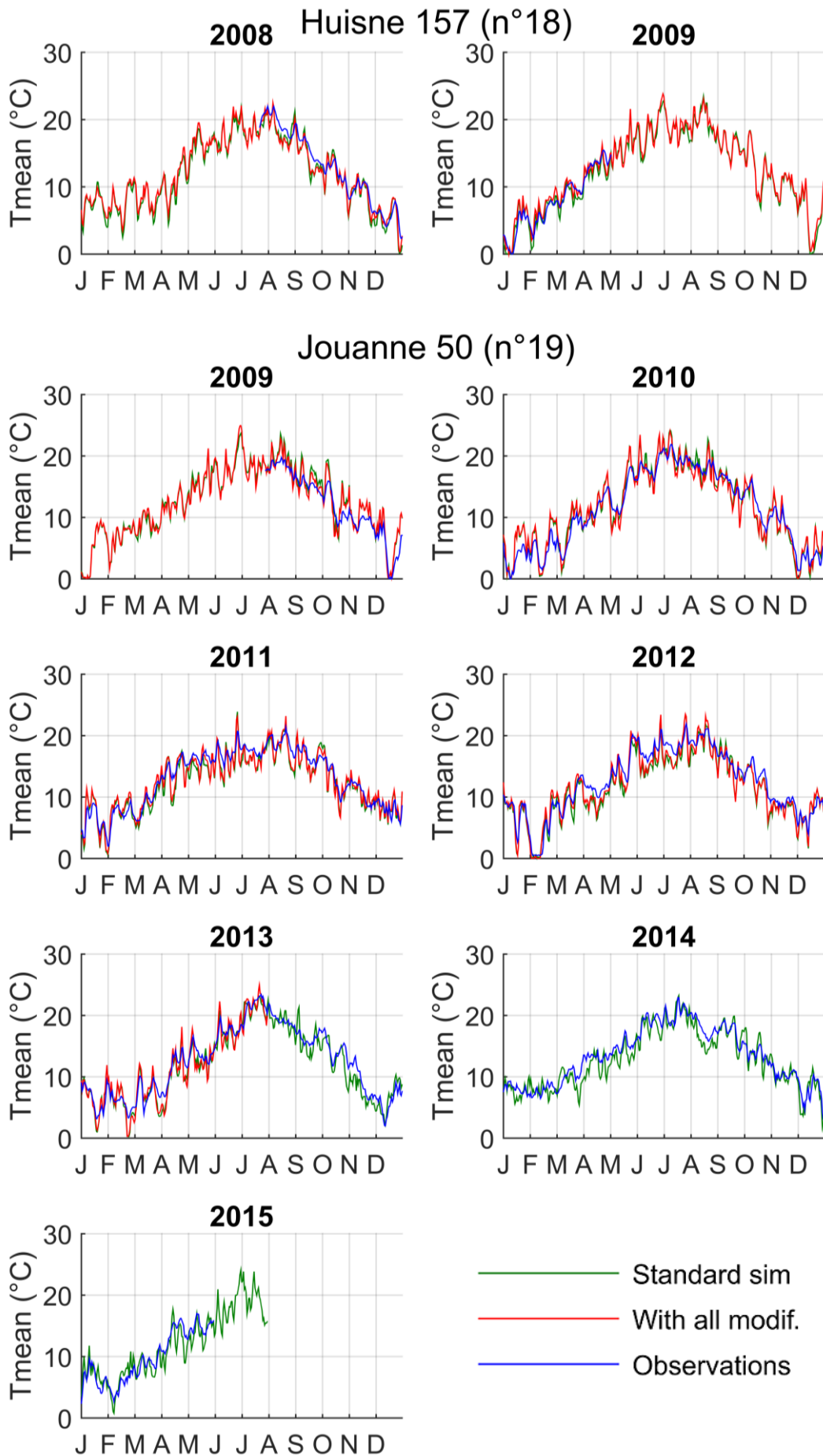


# Huisne 90 (n°16)

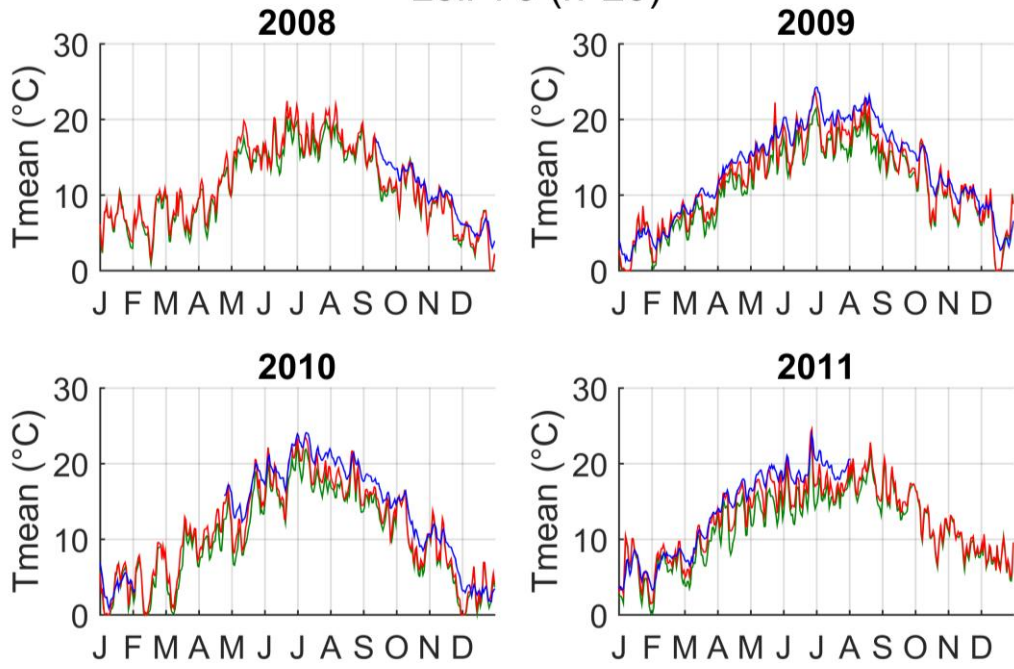


# Huisne 135 (n°17)

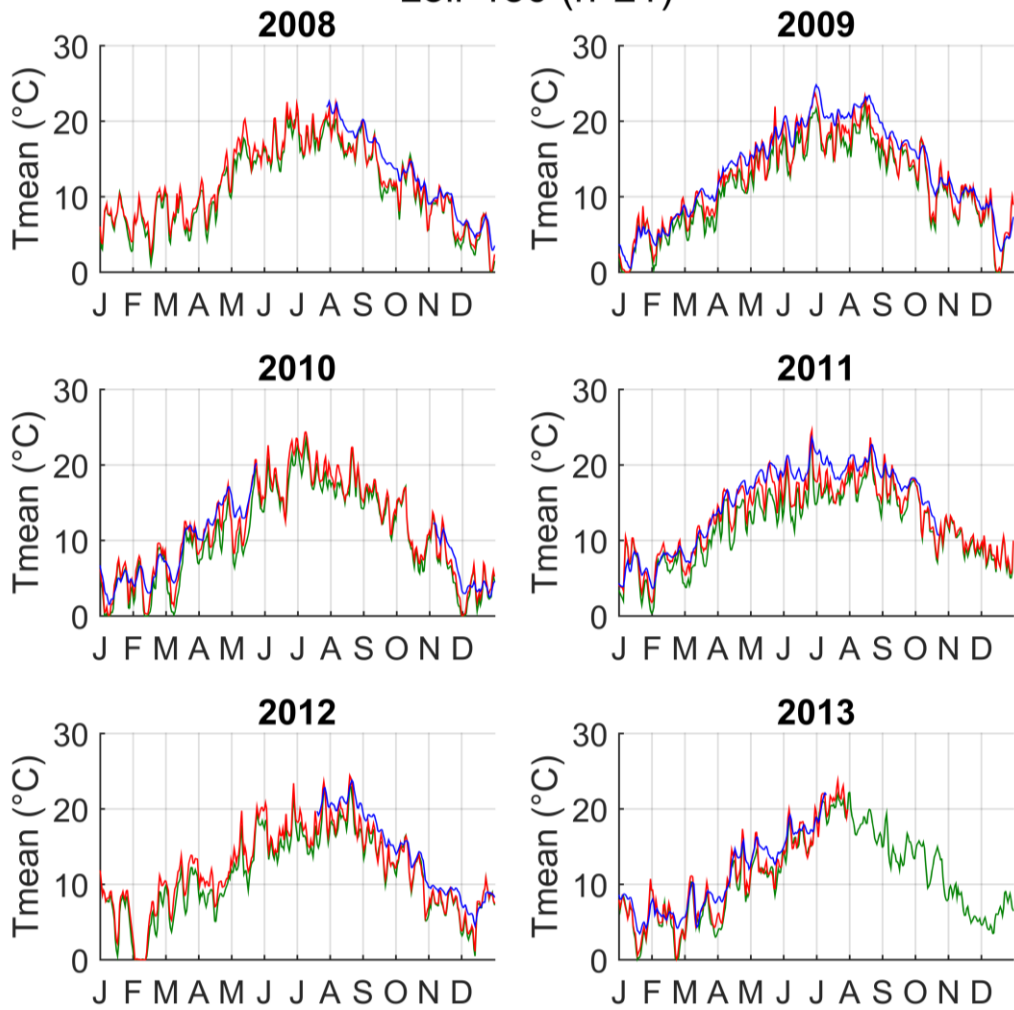




### Loir 76 (n°20)

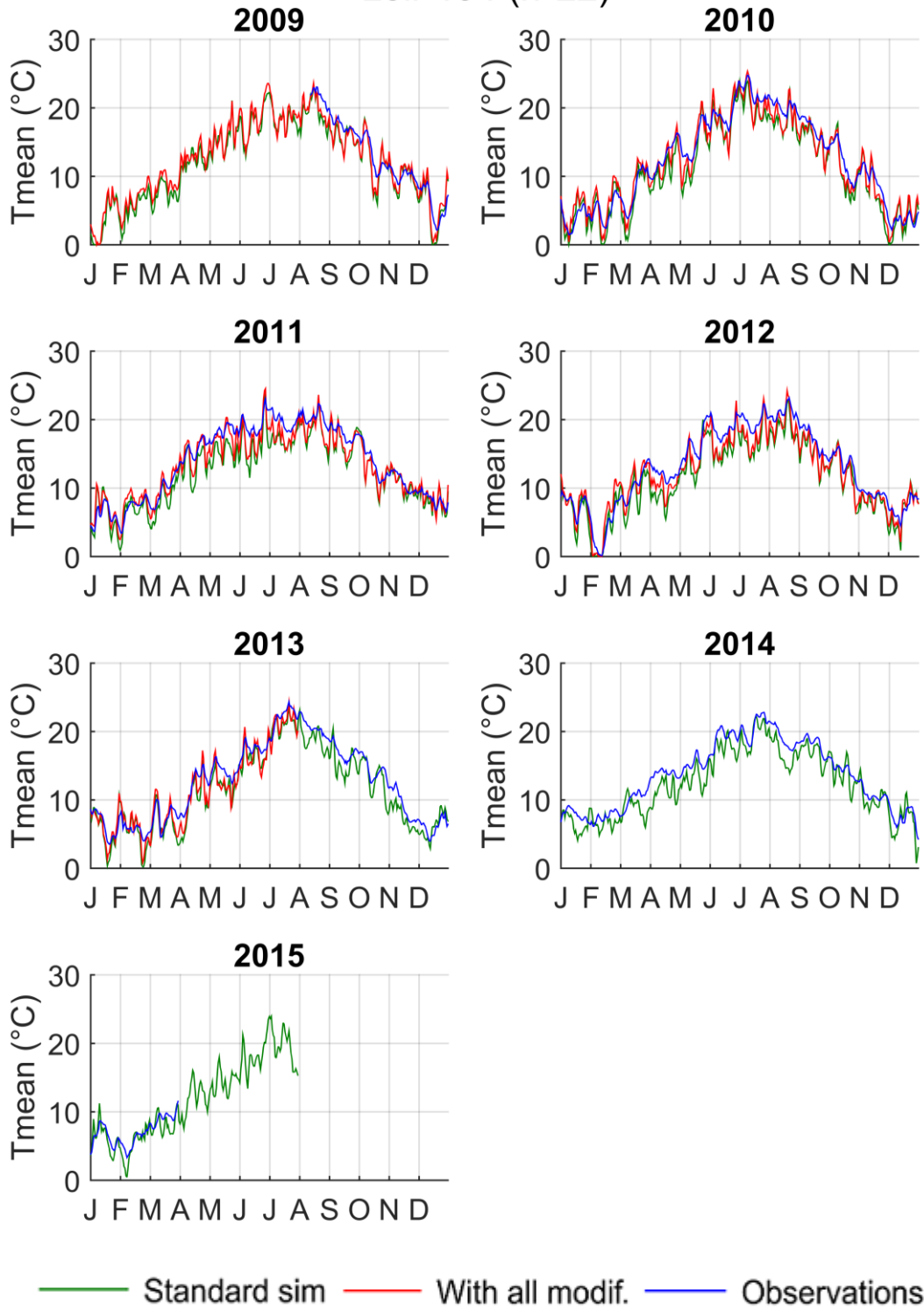


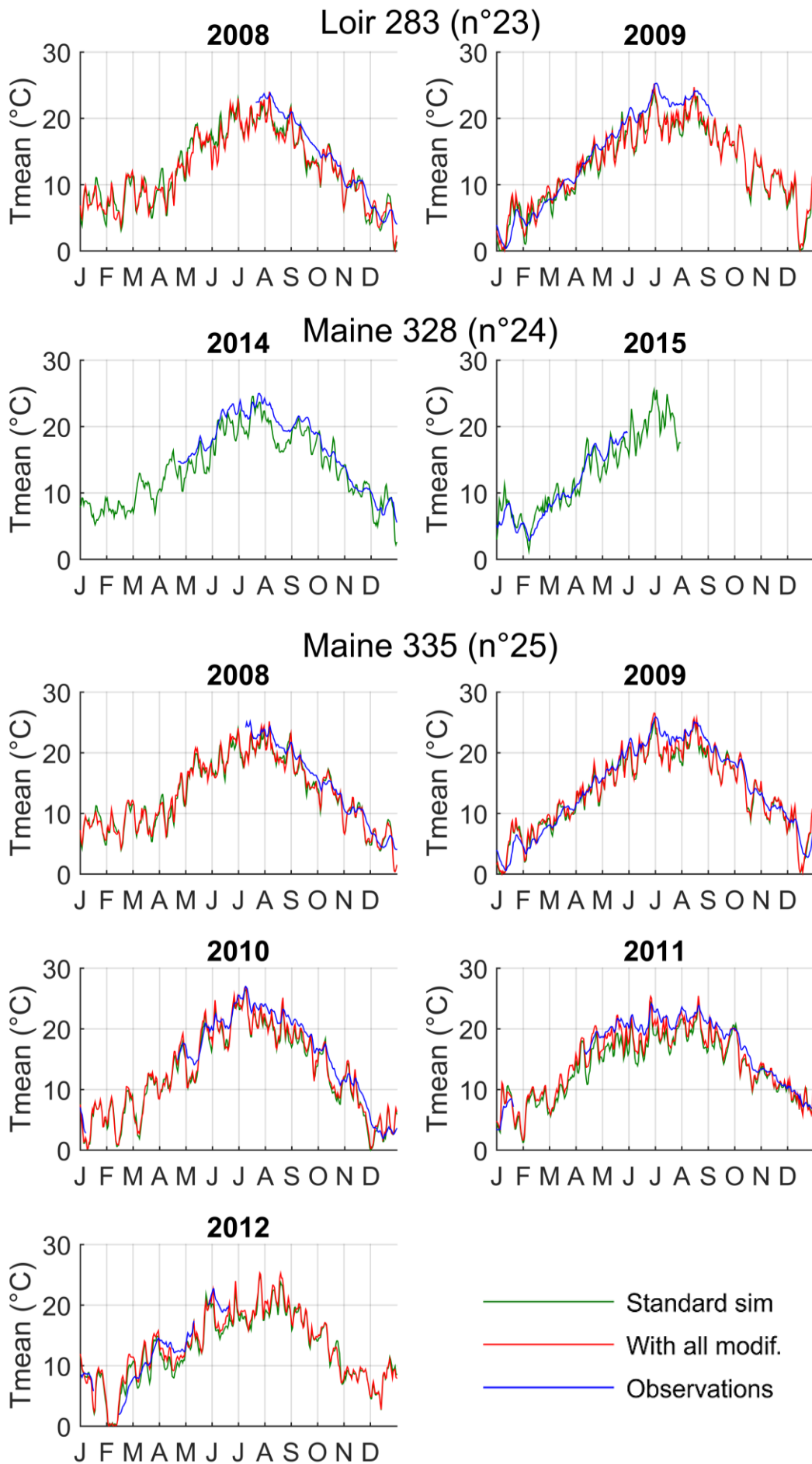
### Loir 130 (n°21)



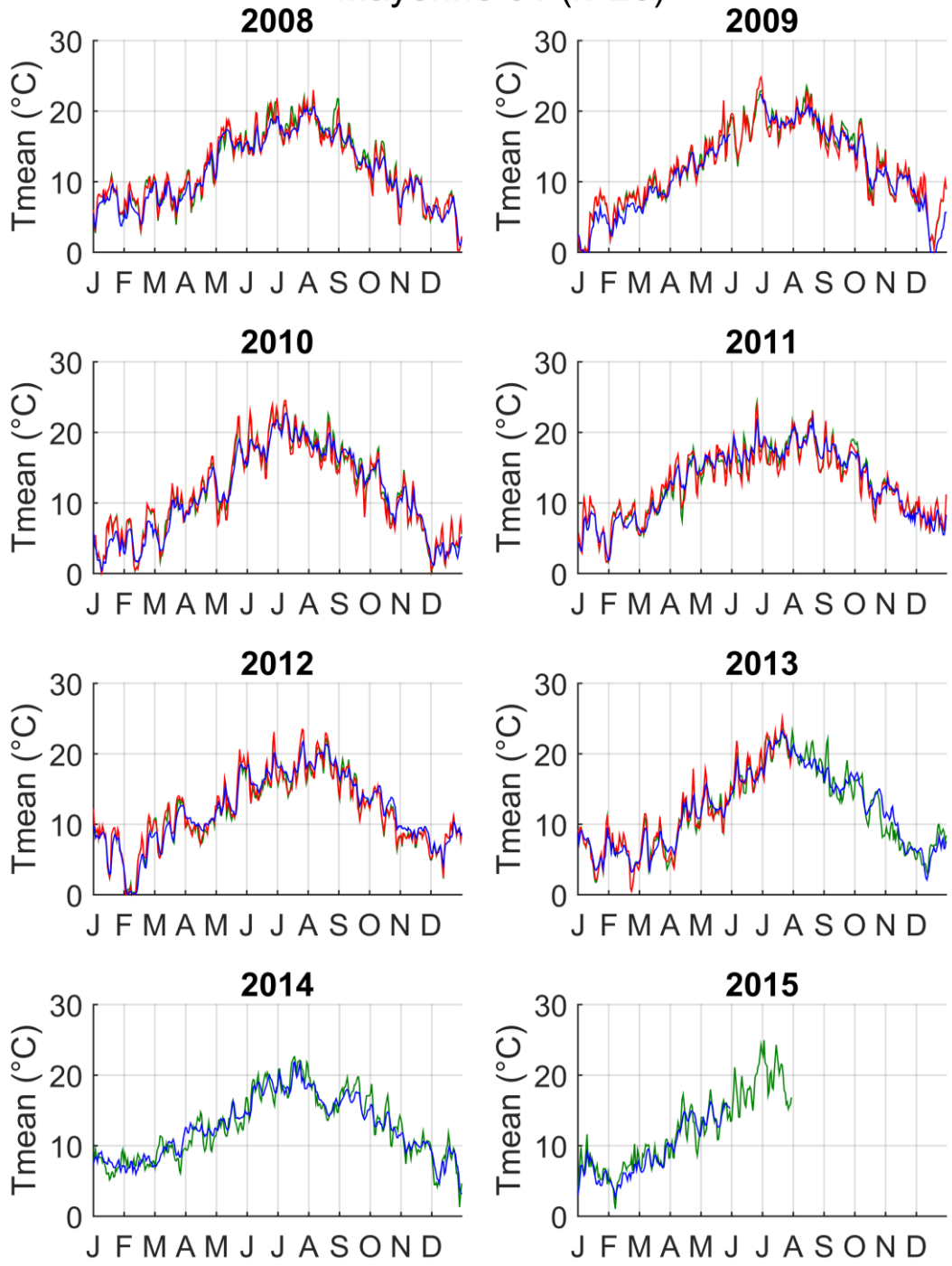
— Standard sim — With all modif. — Observations

# Loir 194 (n°22)



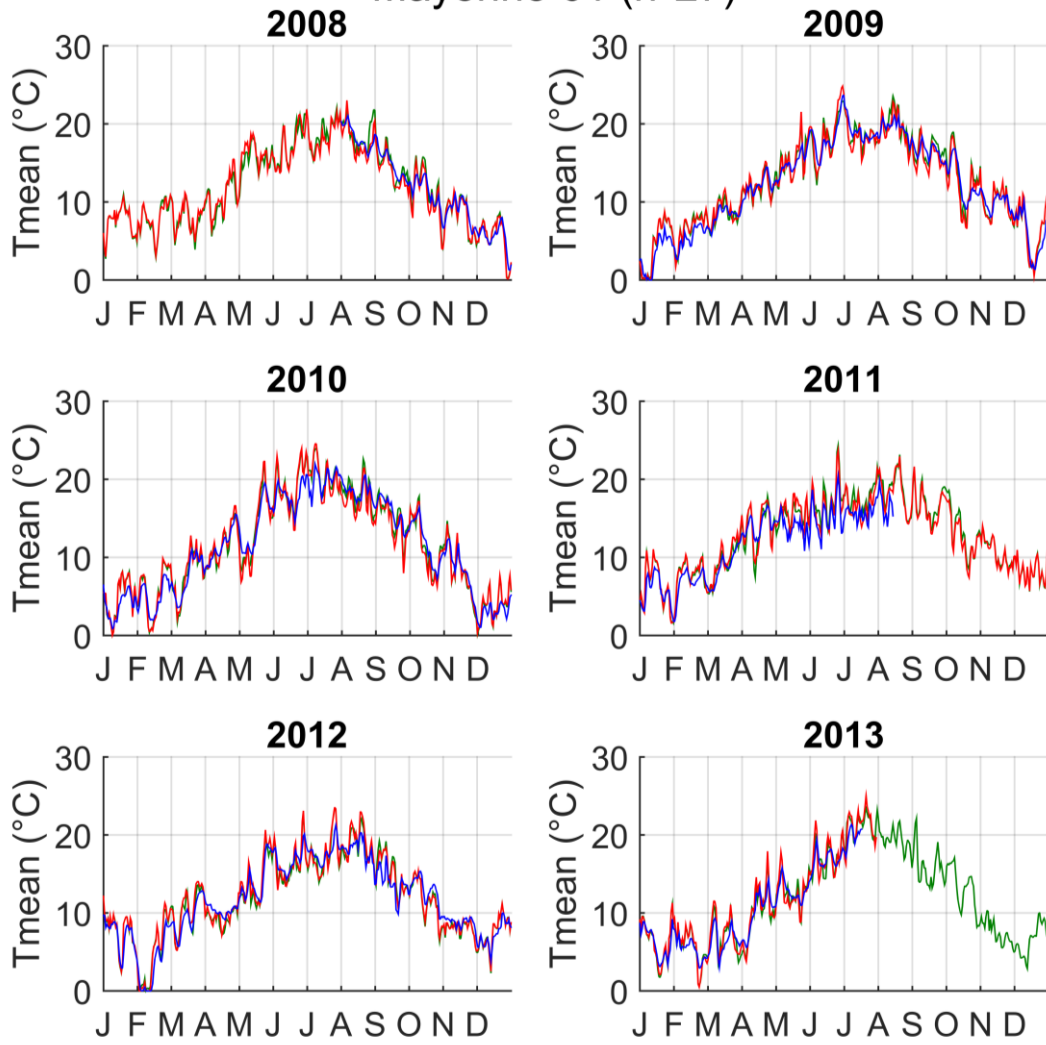


Mayenne 61 (n°26)

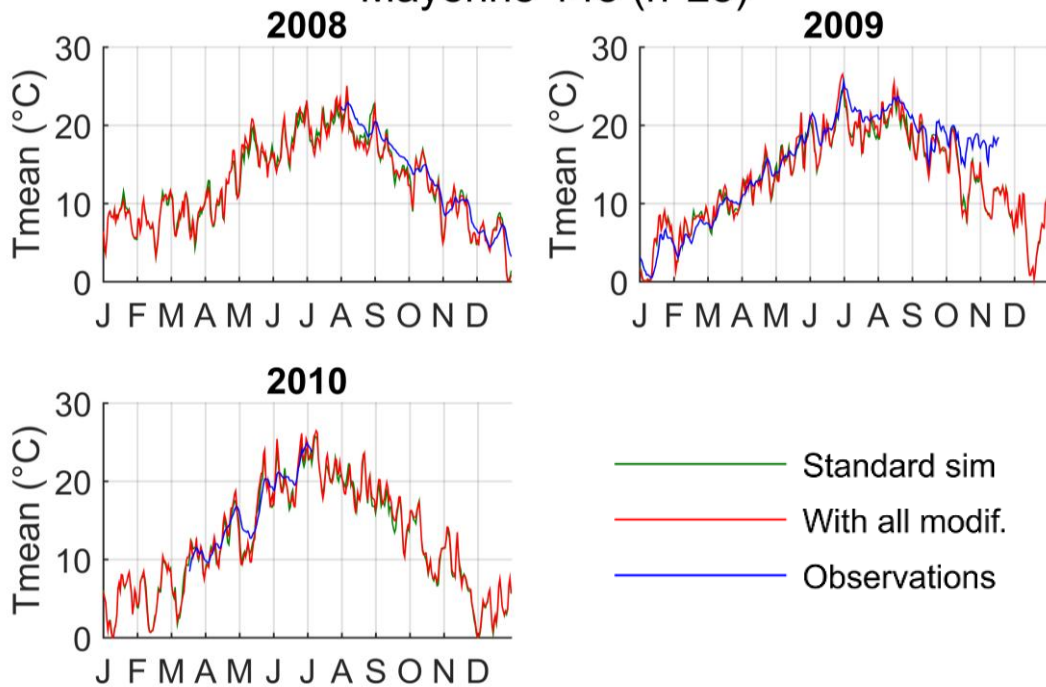


— Standard sim — With all modif. — Observations

### Mayenne 61 (n°27)

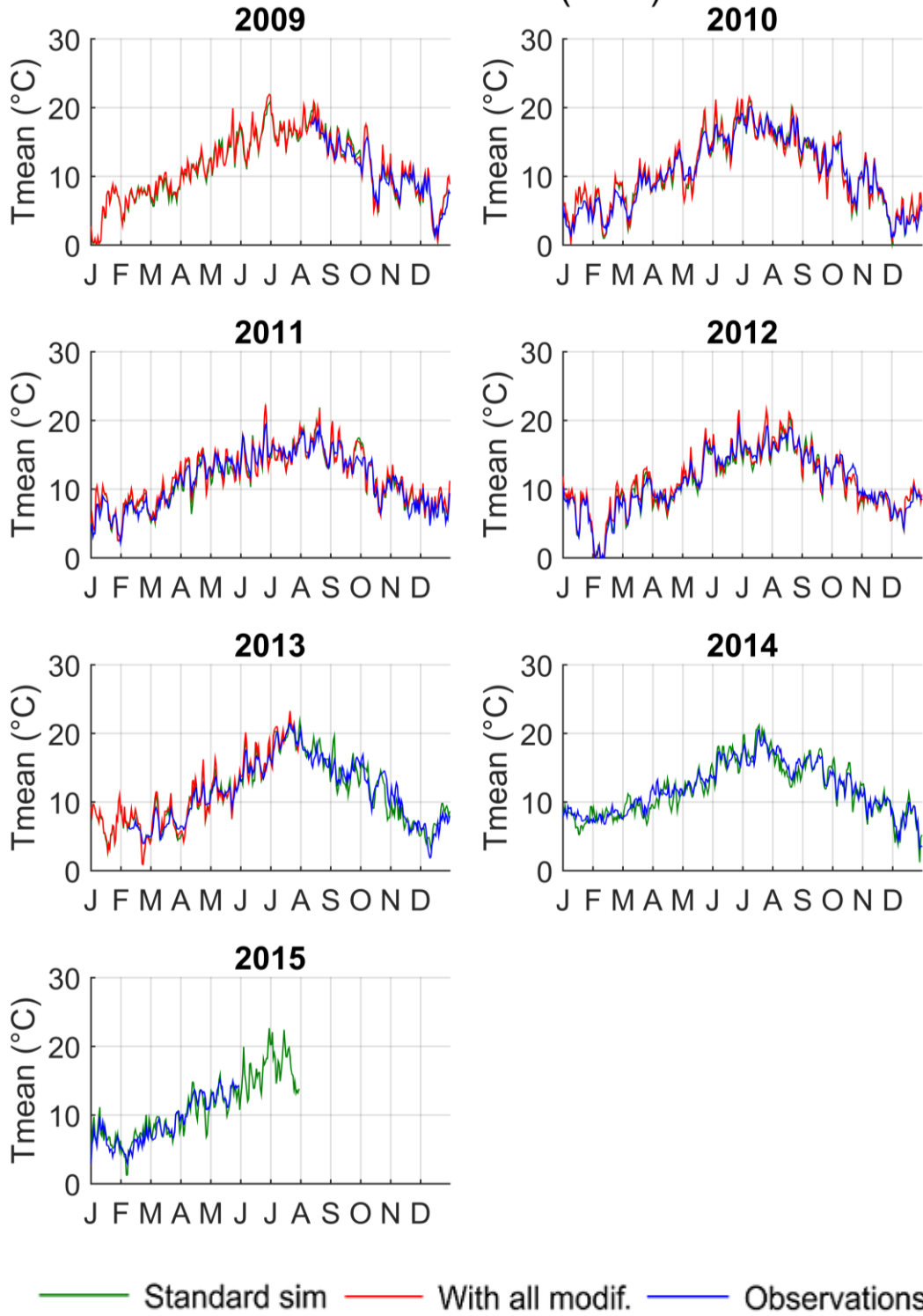


### Mayenne 148 (n°28)

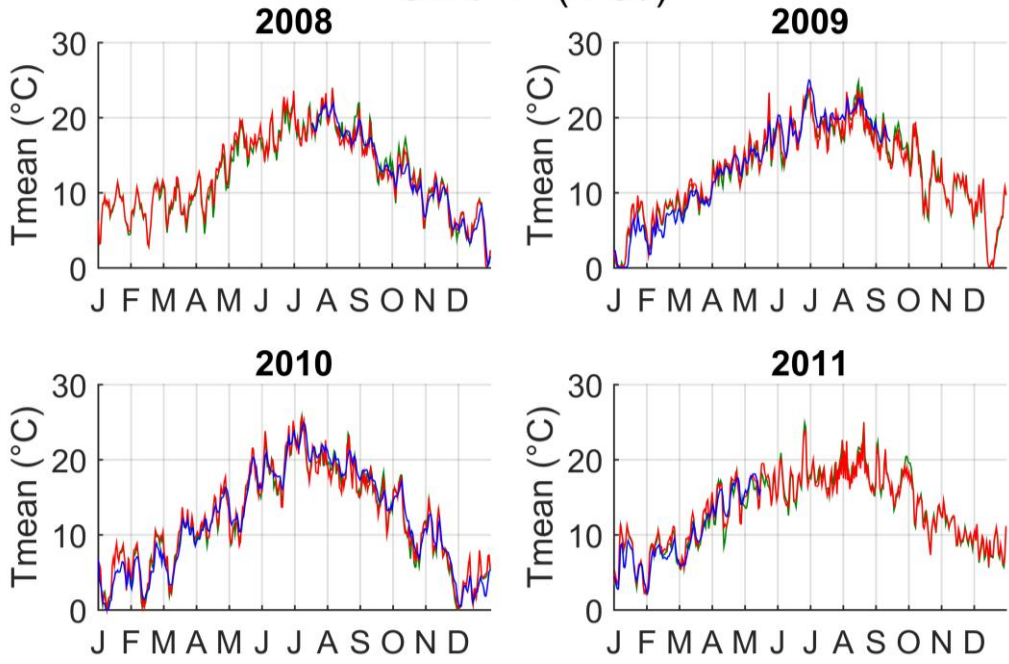


- Standard sim
- With all modif.
- Observations

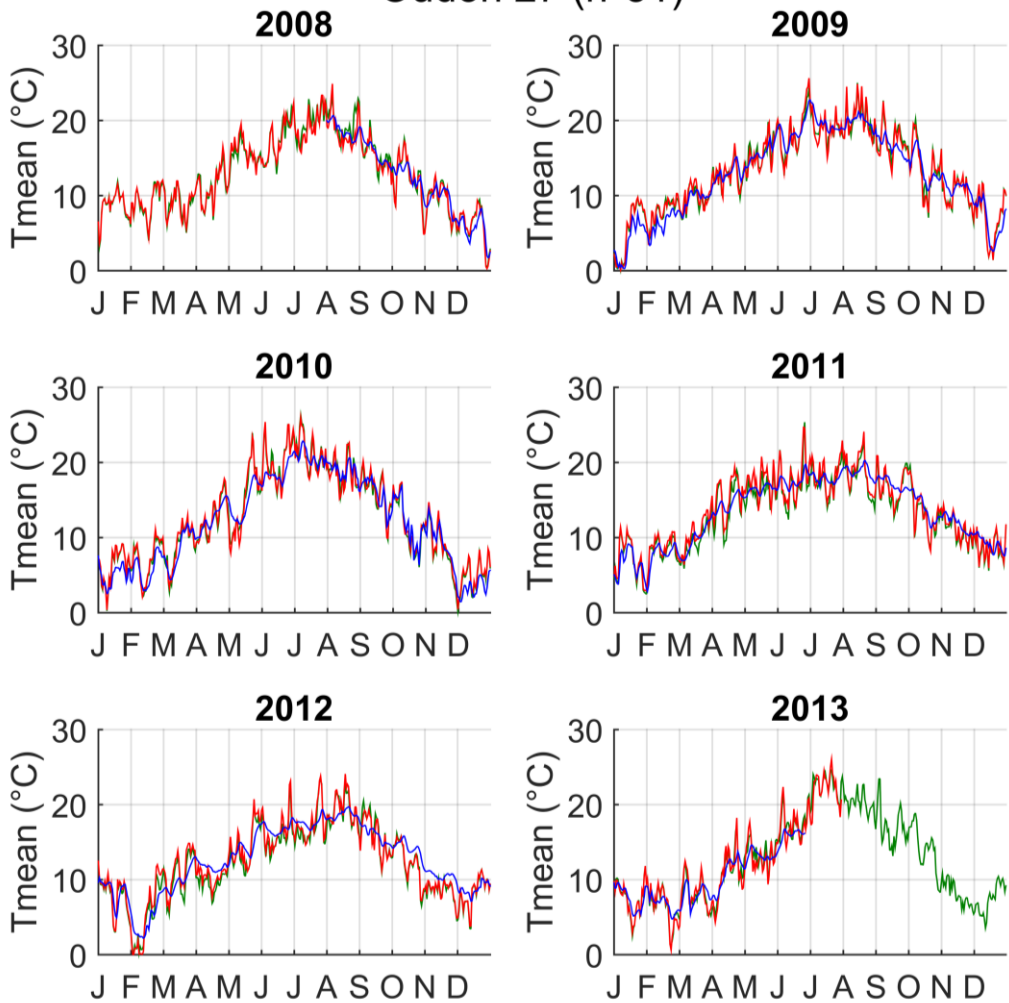
# Merdereau 21 (n°29)



Orne 44 (n°30)

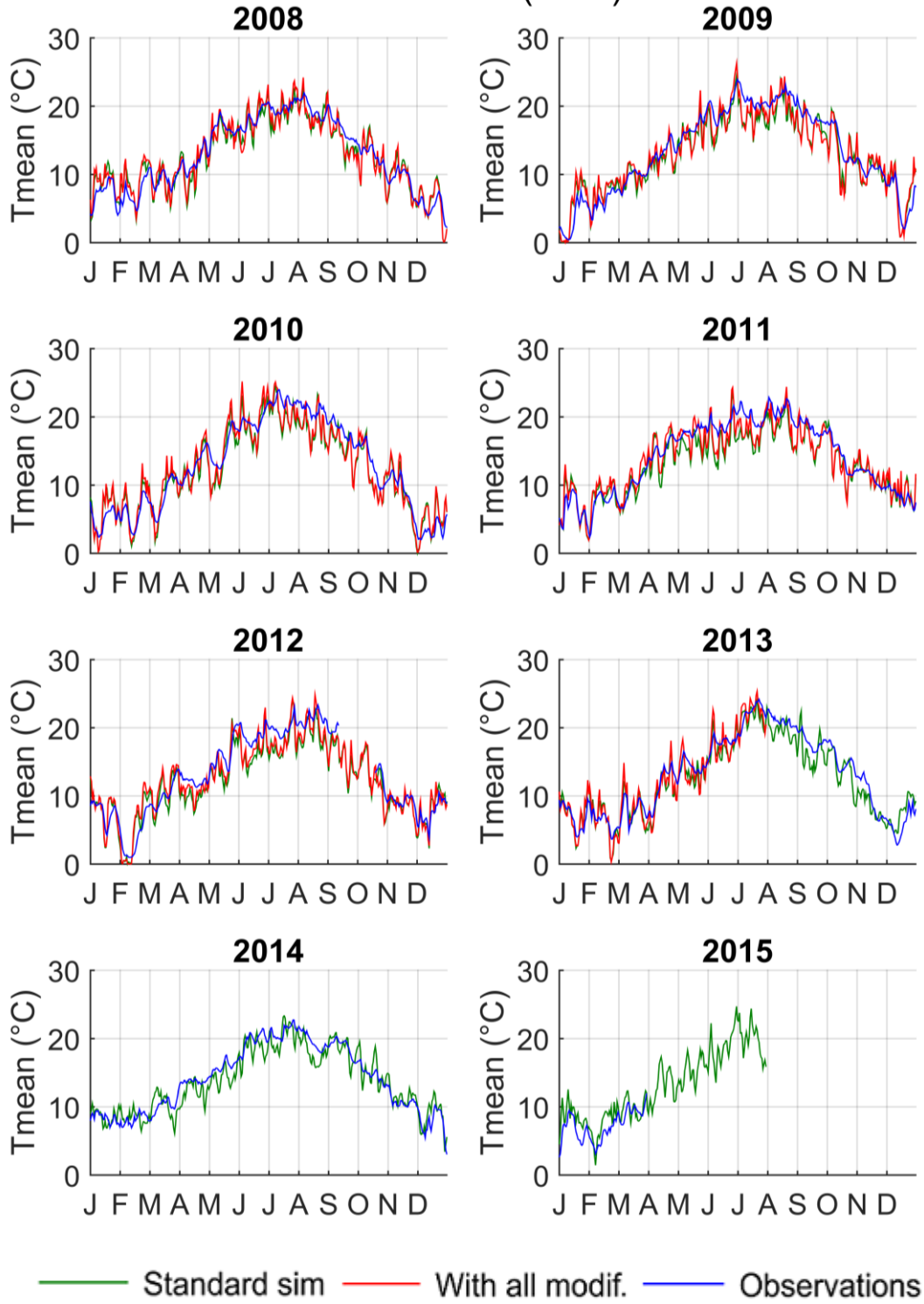


Oudon 27 (n°31)

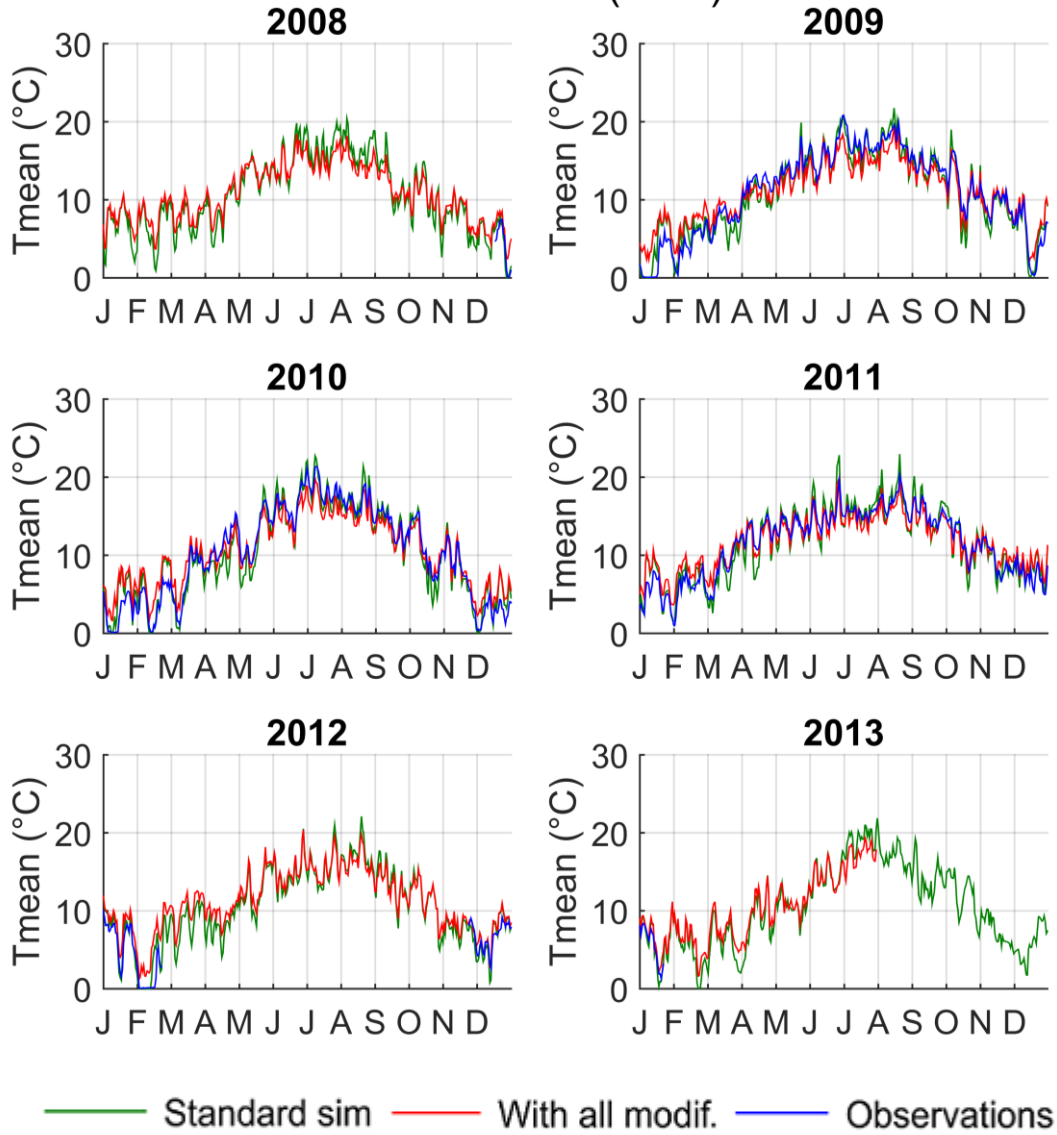


— Standard sim — With all modif. — Observations

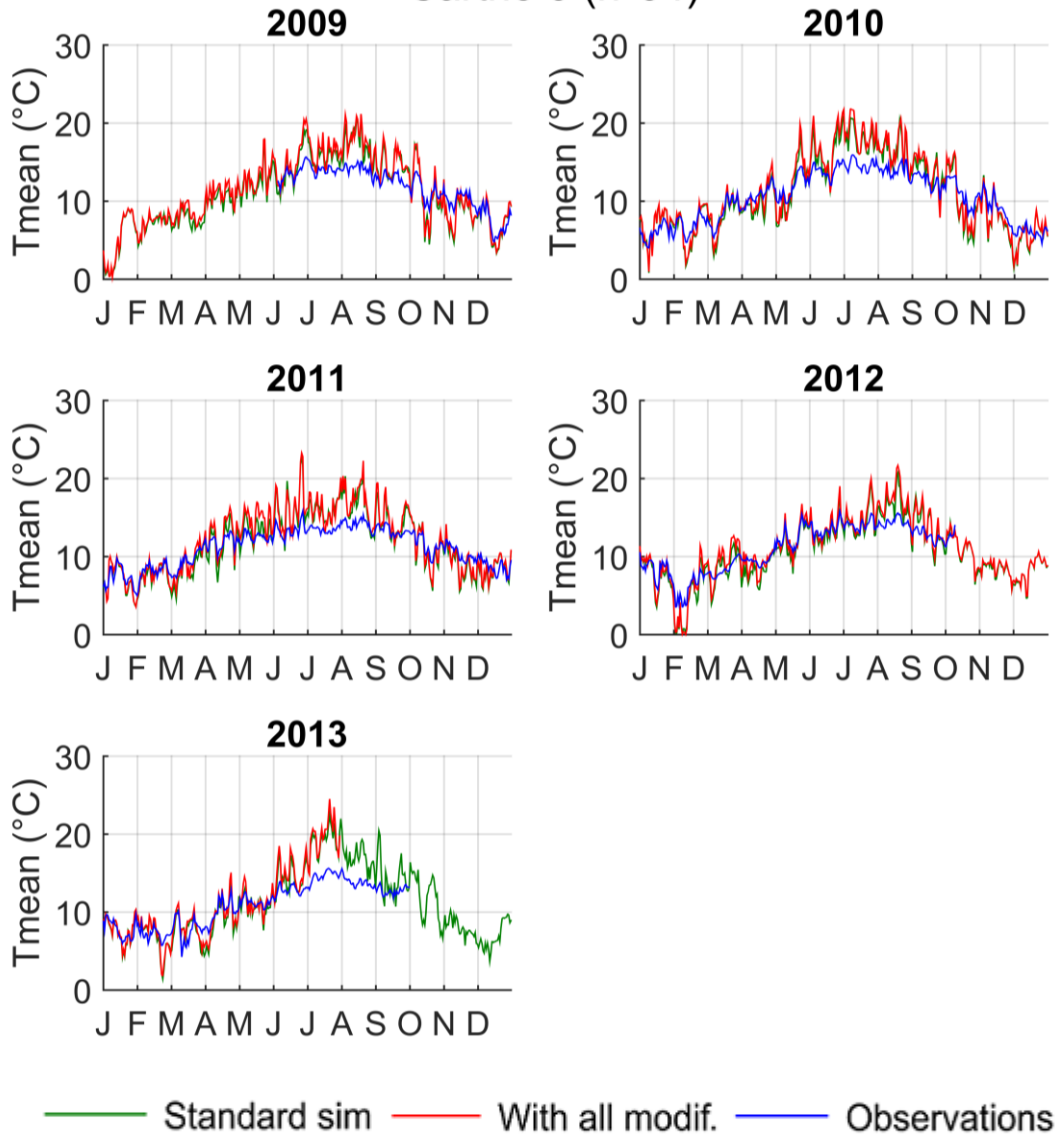
Oudon 85 (n°32)



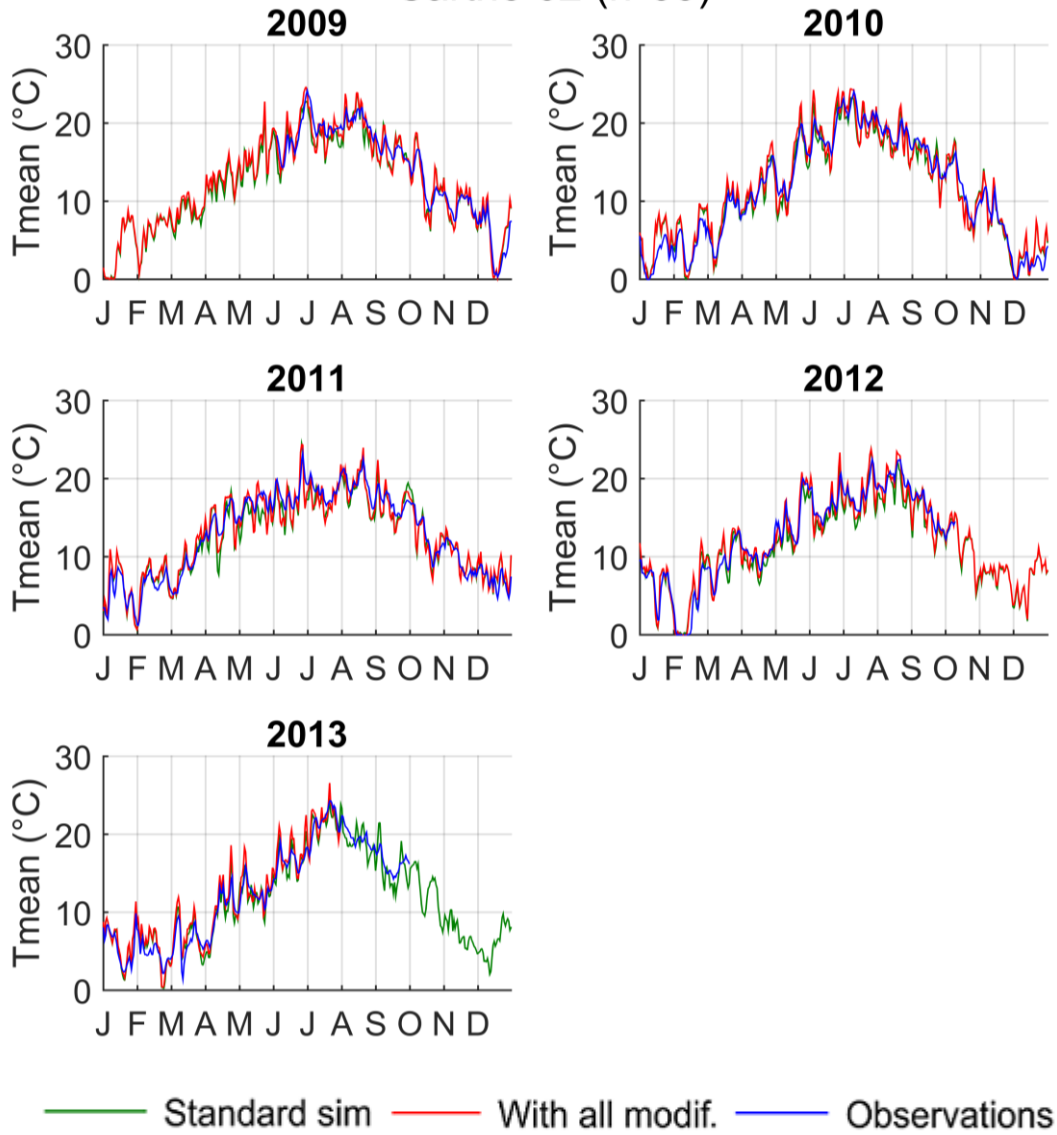
# Ozanne 20 (n°33)



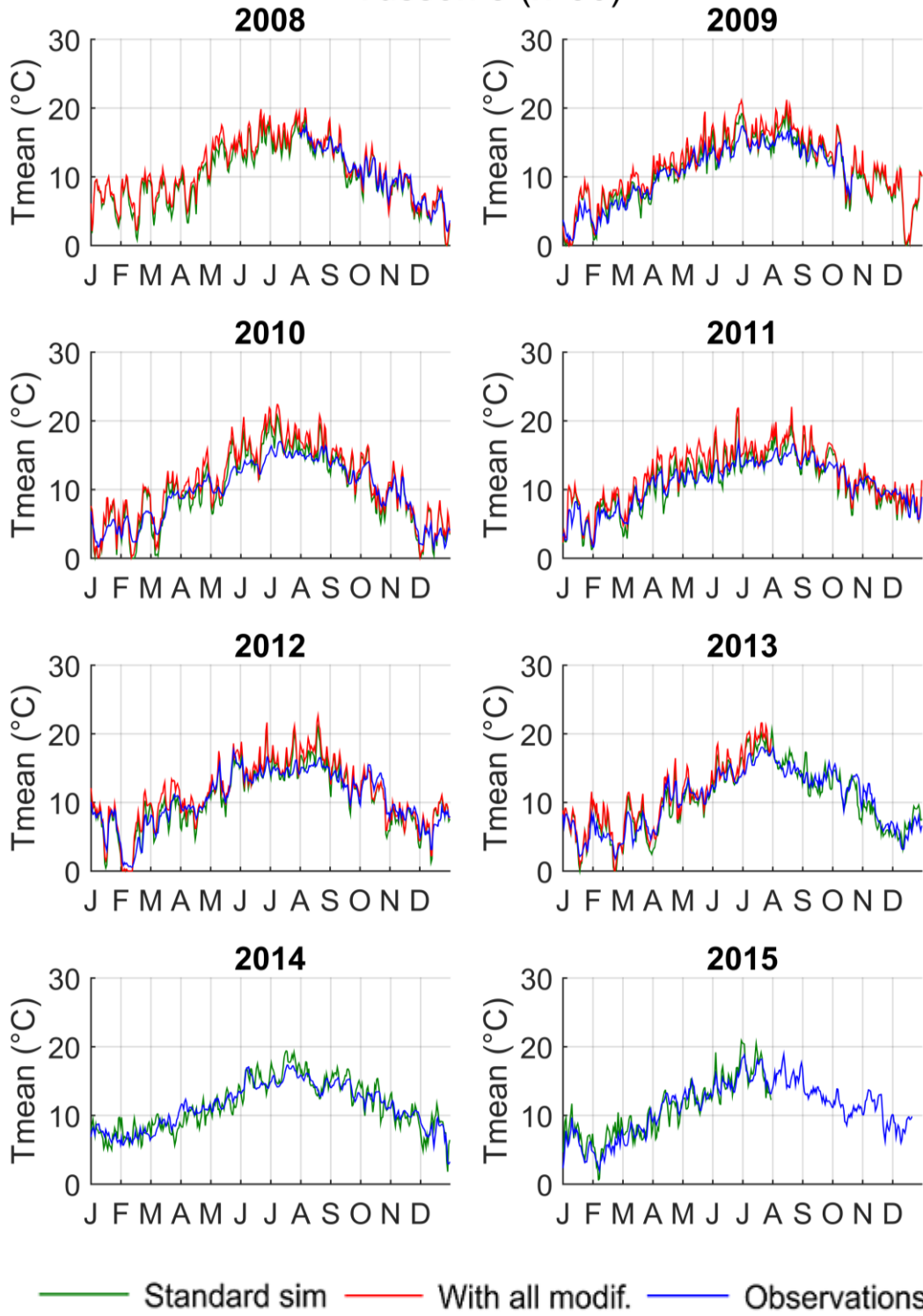
### Sarthe 5 (n°34)



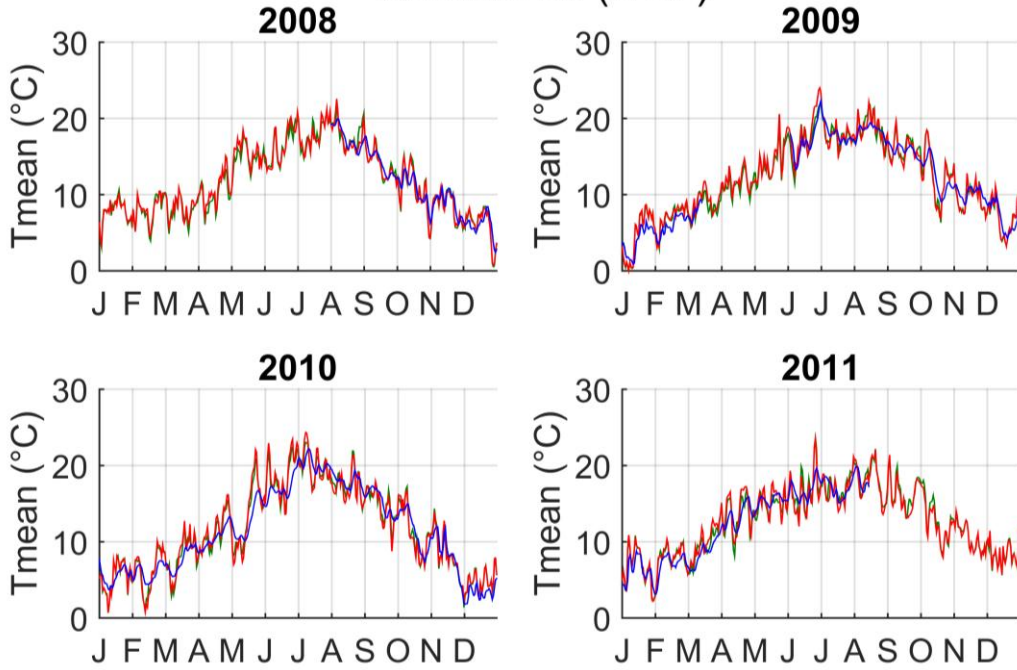
### Sarthe 62 (n°35)



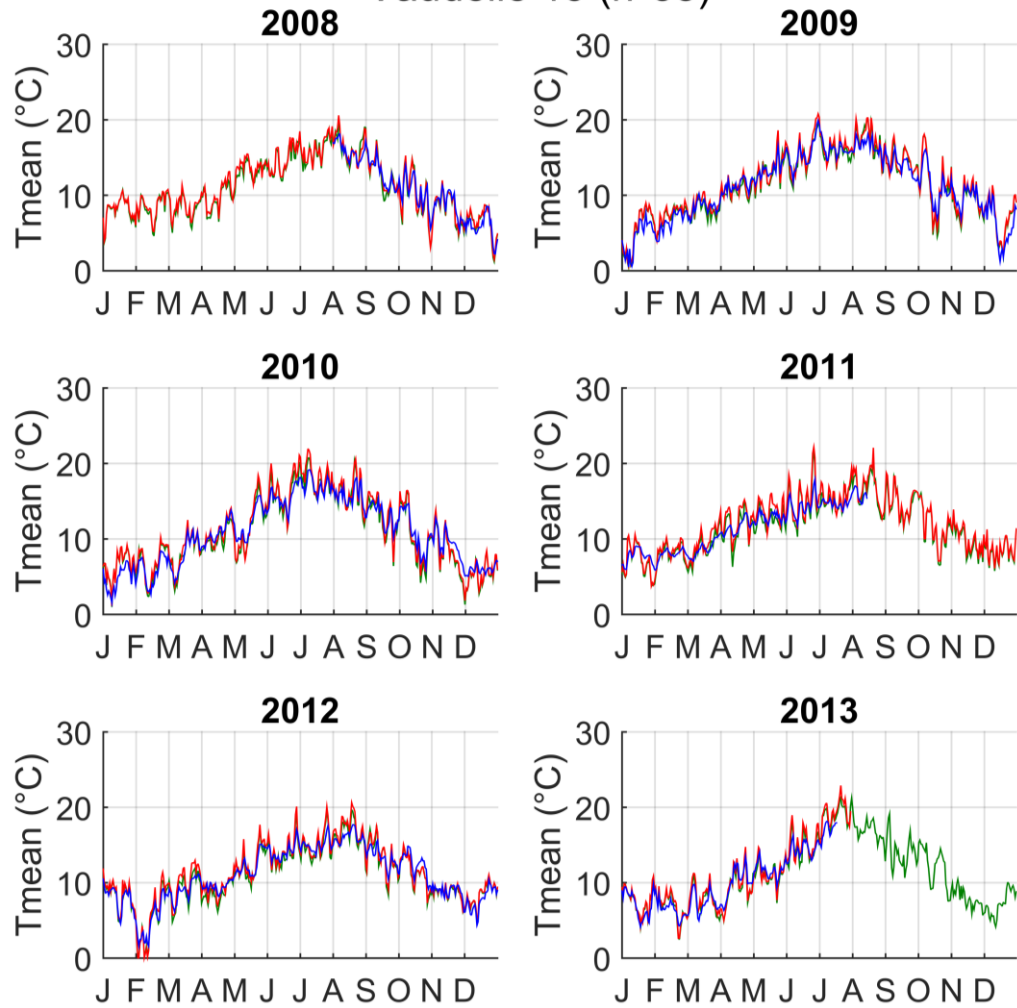
# Tusson 8 (n°36)



Varenne 50 (n°37)

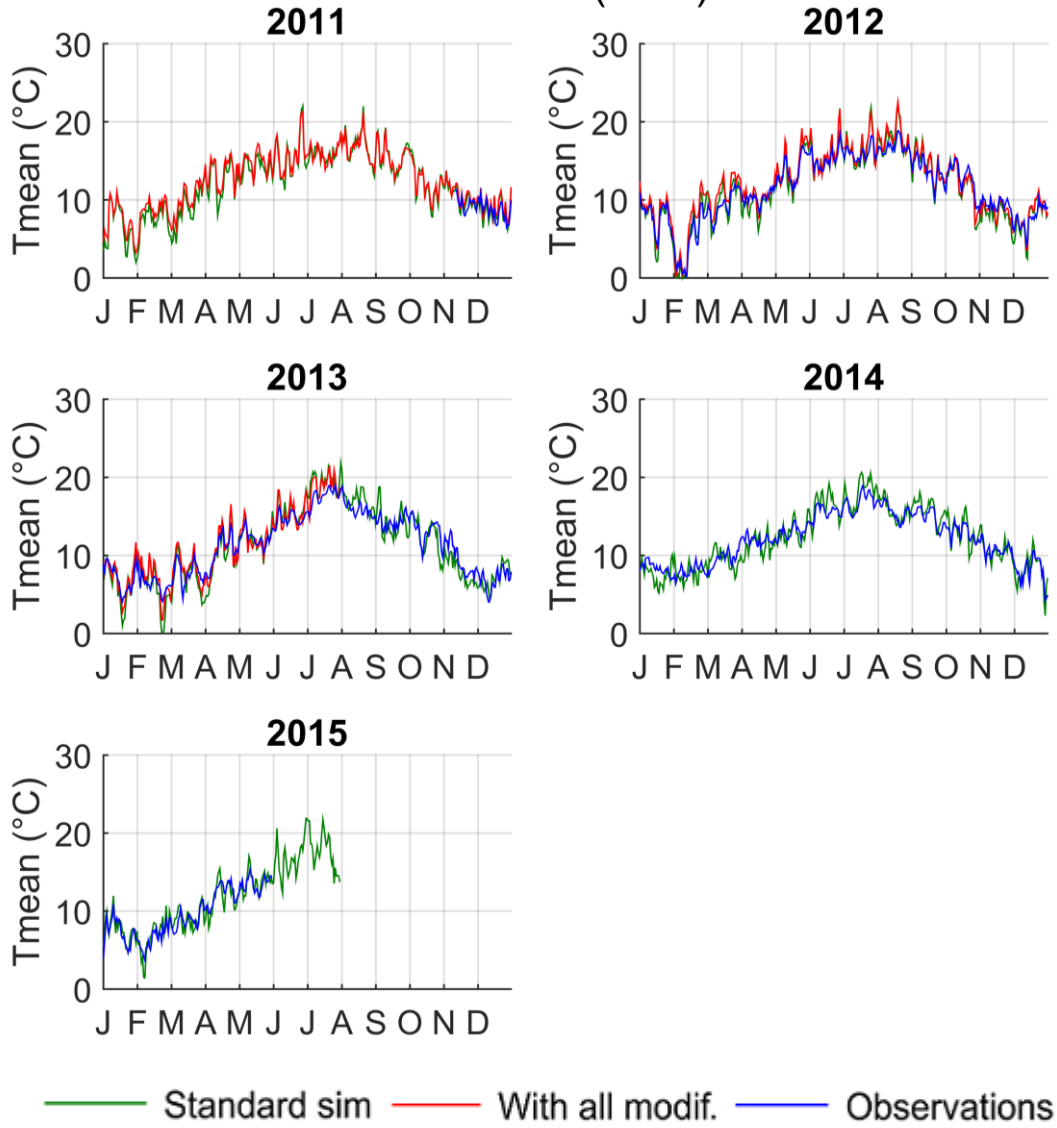


Vaudelle 15 (n°38)

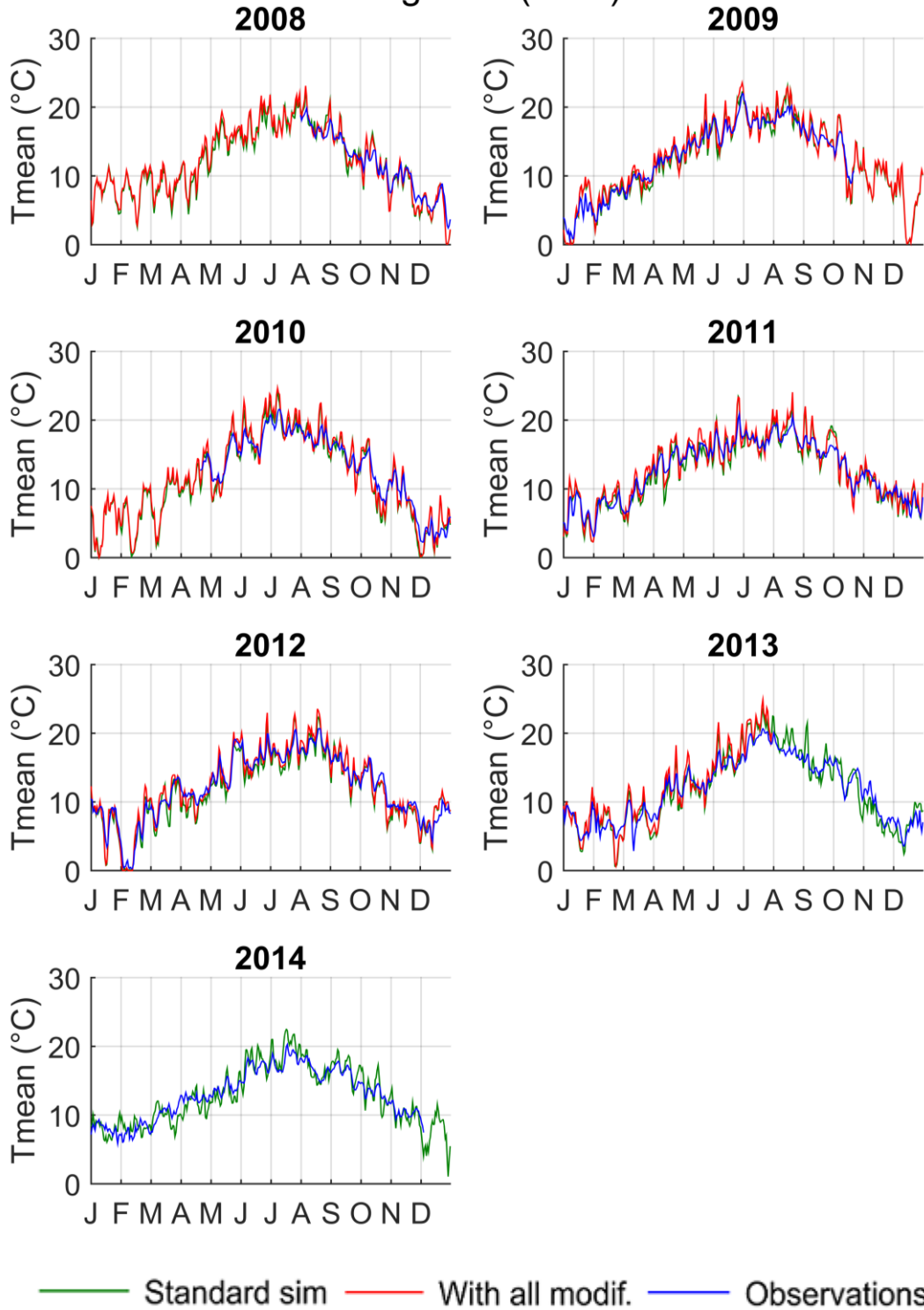


— Standard sim — With all modif. — Observations

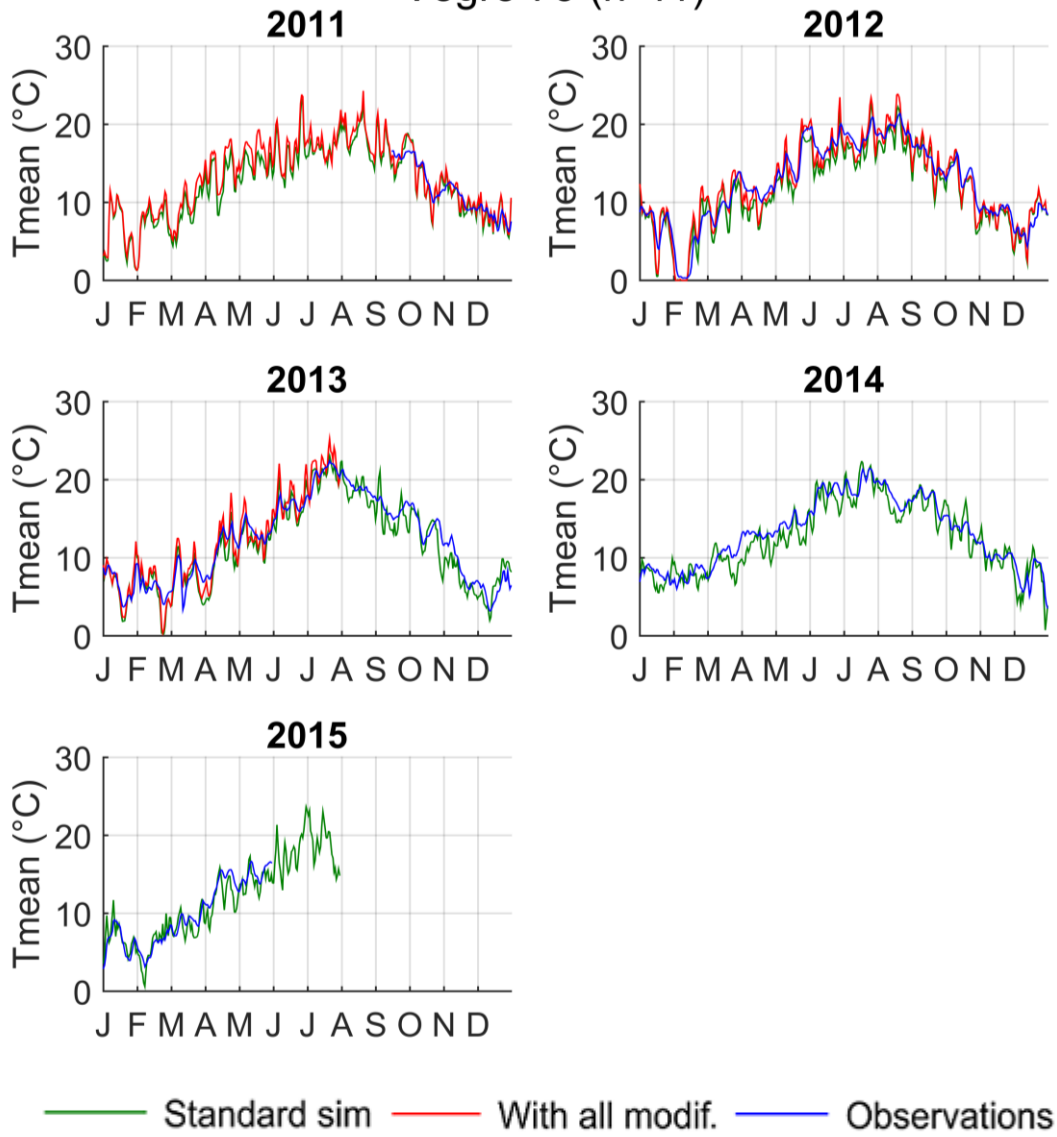
# Veuve 17 (n°39)



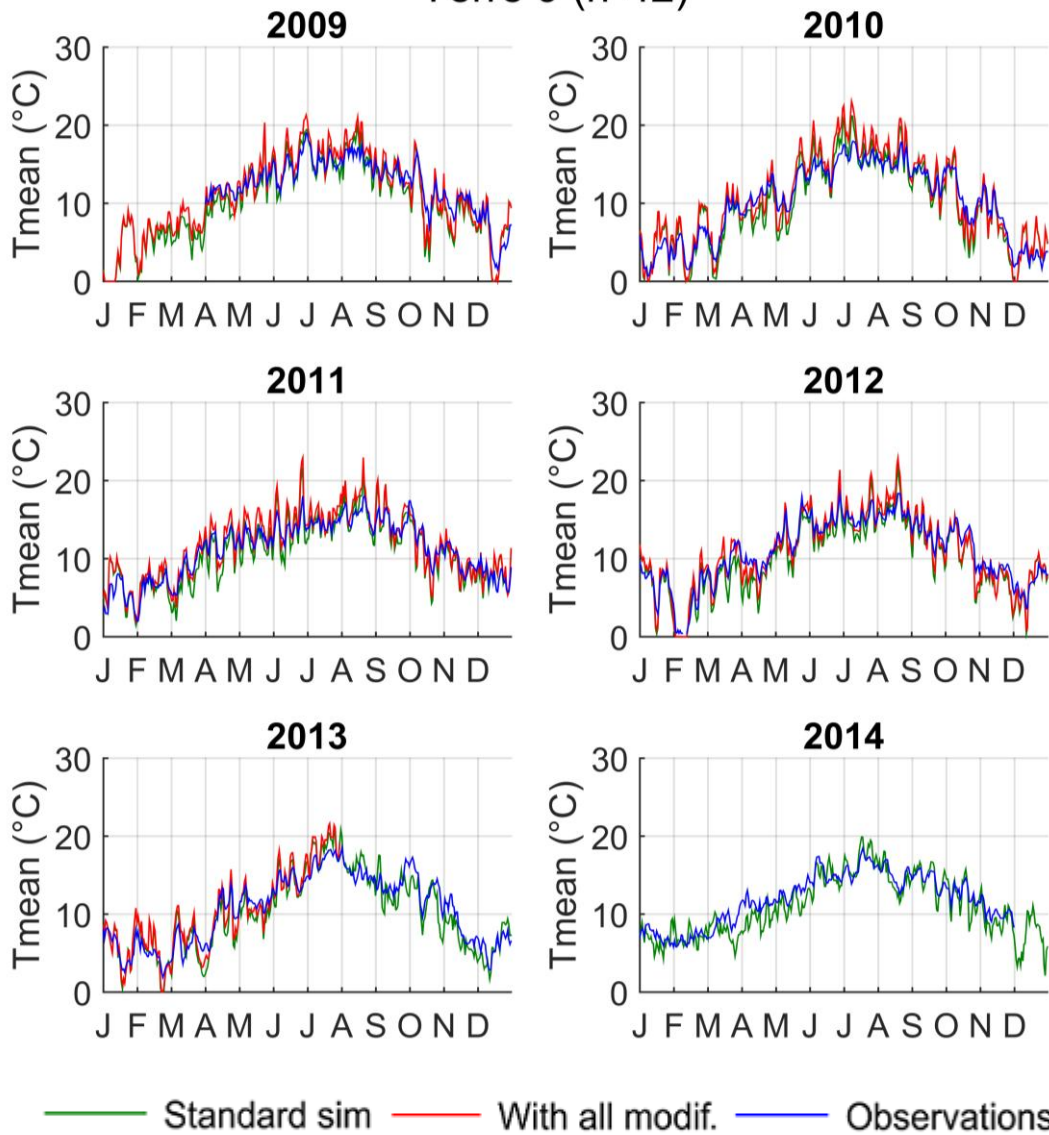
# Vègre 35 (n°40)



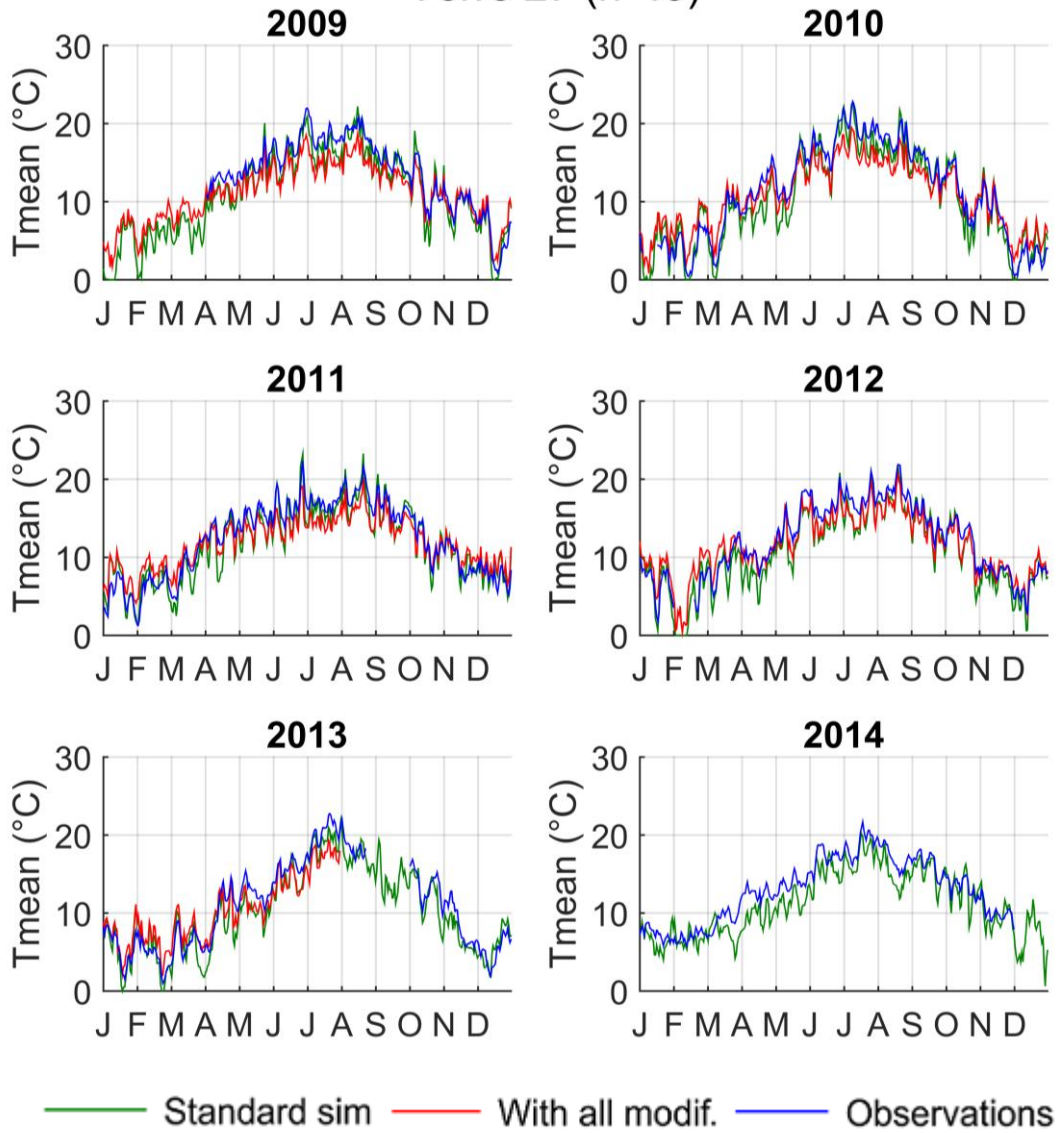
# Vègre 75 (n°41)



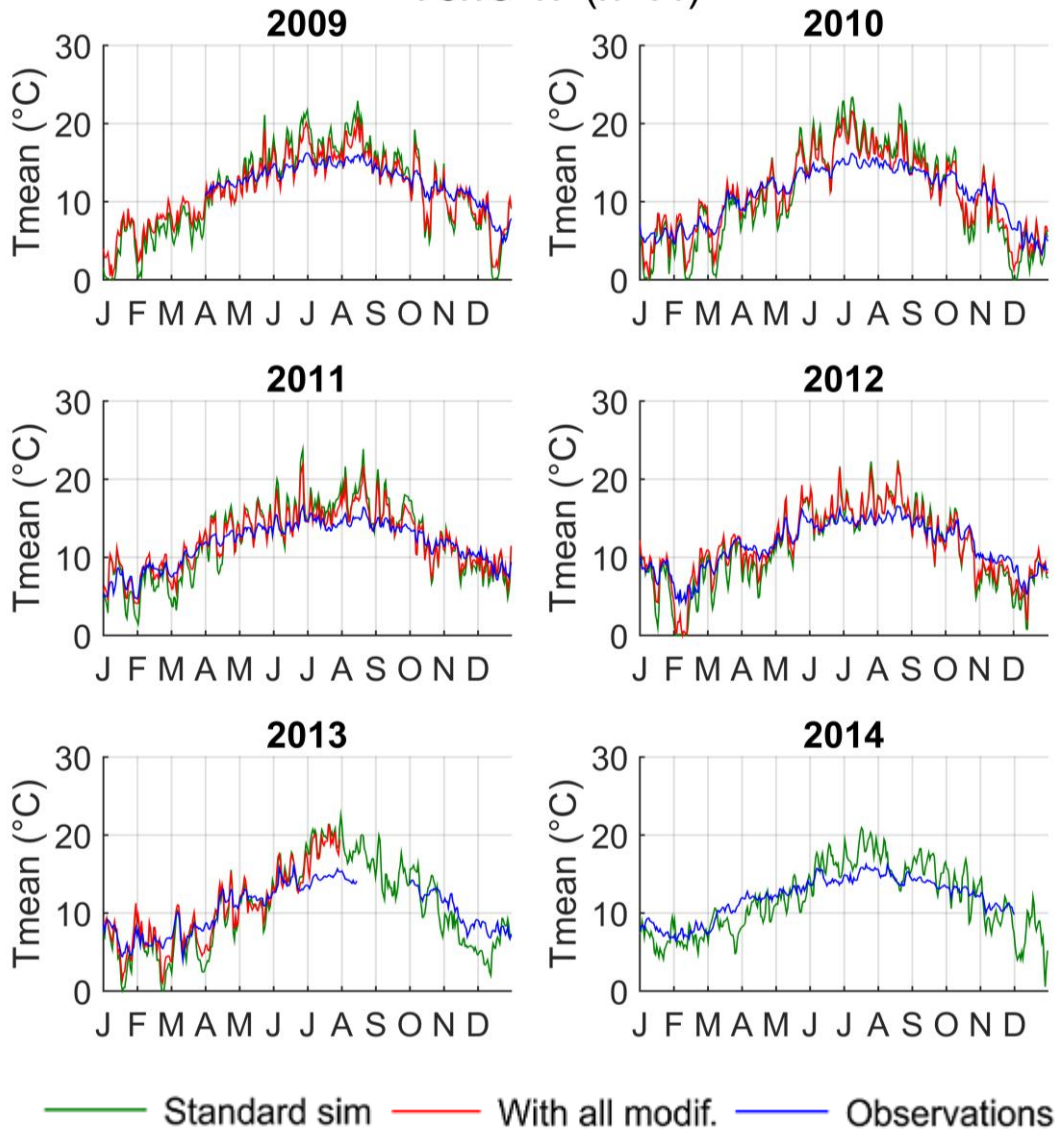
# Yerre 9 (n°42)



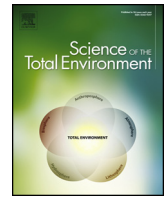
# Yerre 27 (n°43)



# Yerre 47 (n°44)



**Appendix H: Article published in *Sciences of the Total Environment*:  
Improving representation of riparian vegetation shading in a regional stream  
temperature model using LiDAR data**



# Improving representation of riparian vegetation shading in a regional stream temperature model using LiDAR data

Pierre Loicq<sup>a,\*</sup>, Florentina Moatar<sup>a</sup>, Yann Jullian<sup>b</sup>, Stephen J. Dugdale<sup>c</sup>, David M. Hannah<sup>c</sup>

<sup>a</sup> EA 6293 GÉHCO Géo-Hydrosystèmes Continentaux, Université François-Rabelais de Tours, Parc de Grandmont, 37200 Tours, France

<sup>b</sup> CaSciModOT, UFR Sciences et Techniques, Université François Rabelais, Parc de Grandmont, 37200 Tours, France

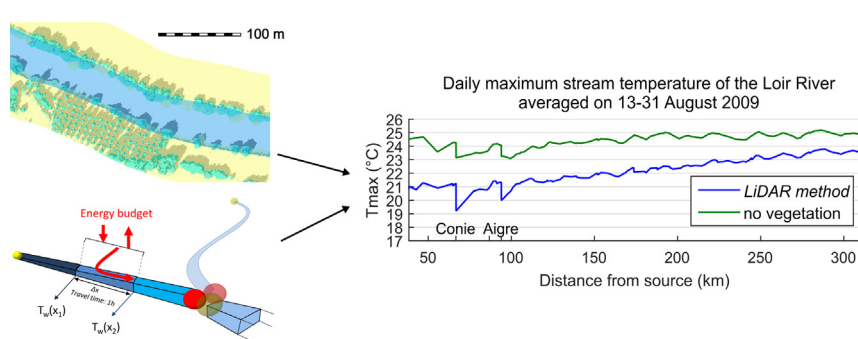
<sup>c</sup> School of Geography, Earth and Environmental Sciences, University of Birmingham, Edgbaston, Birmingham B15 2TT, United Kingdom



## HIGHLIGHTS

- Riparian shading was characterised on a 270 km stream using LiDAR data.
- Shading data were injected in a regional stream temperature model.
- Vegetation's cooling effect ranges from  $-3.0$  °C (upstream) to  $-1.3$  °C (downstream).
- Model accuracy is improved compared to simpler shade characterisation methods.
- Riparian vegetation data's quality is a key factor for stream temperature modelling.

## GRAPHICAL ABSTRACT



## ARTICLE INFO

### Article history:

Received 19 October 2017

Received in revised form 7 December 2017

Accepted 12 December 2017

Available online xxxx

Editor: Ouyang Wei

### Keywords:

River temperature modelling

Regional scale

Riparian shading

LiDAR

Loir River

## ABSTRACT

Modelling river temperature at the catchment scale is needed to understand how aquatic communities may adapt to current and projected climate change. In small and medium rivers, riparian vegetation can greatly reduce maximum water temperature by providing shade. It is thus important that river temperature models are able to correctly characterise the impact of this riparian shading. In this study, we describe the use of a spatially-explicit method using LiDAR-derived data for computing the riparian shading on direct and diffuse solar radiation. The resulting data are used in the T-NET one-dimensional stream temperature model to simulate water temperature from August 2007 to July 2014 for 270 km of the Loir River, an indirect tributary of the Loire River (France). Validation is achieved with 4 temperature monitoring stations spread along the Loir River. The vegetation characterised with the LiDAR approach provides a cooling effect on maximum daily temperature ( $T_{max}$ ) ranging from  $3.0$  °C (upstream) to  $1.3$  °C (downstream) in late August 2009. Compared to two other riparian shading routines that are less computationally-intensive, the use of our LiDAR-based methodology improves the bias of  $T_{max}$  simulated by the T-NET model by  $0.62$  °C on average between April and September. However, difference between the shading routines reaches up to  $2$  °C (monthly average) at the upstream-most station. Standard deviation of errors on  $T_{max}$  is not improved. Computing the impact of riparian vegetation at the hourly timescale using reach-averaged parameters provides results close to the LiDAR-based approach, as long as it is supplied with accurate vegetation cover data. Improving the quality of riparian vegetation data should therefore be a priority to increase the accuracy of stream temperature modelling at the regional scale.

© 2017 Elsevier B.V. All rights reserved.

\* Corresponding author.

E-mail address: [pierre.loicq@univ-tours.fr](mailto:pierre.loicq@univ-tours.fr) (P. Loicq).

## 1. Introduction

Temperature is a major water quality parameter because it controls not only oxygen solubility (Moatar et al., 2001) but also chemical and metabolic reactions (Haag and Westrich, 2002). Hence, it affects fish behaviour and survival (Magnuson et al., 1979). River water temperature modelling is thus important for understanding the distribution of aquatic species at regional scales, under present or future climatic conditions (Buisson et al., 2008; Tisseuil et al., 2012; Boisneau et al., 2008; Brown et al., 2005). River temperature is already increasing across French water courses, a trend which is expected to continue further under projected climate change (Moatar and Gailhard, 2006; Bustillo et al., 2014; Hannah and Garner, 2015). Such a warming could have severe consequences for a range of aquatic species, and adaptation measures are currently being sought with a view to ensuring the continued survival of temperature sensitive fluvial organisms. In this context, riparian shade and groundwater exchanges have been given increasing research attention, because of their ability to regulate river temperature (Lalot et al., 2015; Leach and Moore, 2010). Indeed, many studies have shown that shade can moderate water temperature of relatively small rivers (Moore et al., 2005; Garner et al., 2014). Conversely, in larger rivers, Teti (2006) showed (using shade measurements acquired along an increasing-width stream) that riparian vegetation has a limited impact on rivers larger than 30 m. DeWalle (2008) quantified the maximal wetted width for which riparian vegetation can effectively reduce received solar radiation. However, no study has yet quantified the impact of shading on temperature on rivers of intermediate width (>15 m and <30 m) or at the regional scale.

Process-based river temperature models function by simulating the energy exchange processes heating or cooling a river, in particular through the input of solar radiation. This solar radiation is composed of direct (solar rays) and diffuse radiation (scattered by atmosphere), both of which are influenced in different ways by the presence of riparian vegetation. The impact of riparian vegetation on the direct radiation can be quantified by computing a shadow factor (SF), which is the proportion of a river being shaded at a given time. Several methods have been proposed to compute it at an hourly time step. Chen et al. (1998) detailed a method to compute riparian shade from GIS polygons of riparian vegetation. Their method used stream azimuth and tree height (alongside solar position) to determine whether a section of stream channel was in shade. However, this technique only accounted for the effect of vegetation located perpendicular to the stream centreline, and furthermore, did not denote the fraction of the channel cross-section that was shaded. As a result, Li et al. (2012) developed an enhanced version of the Chen et al. (1998) methodology, allowing for the determination of the amount of channel cross-section covered by shade. This new method also enables the simulation of overhanging vegetation, but like its predecessor, only considers the effect of vegetation located perpendicular to the river reach. Approaches capable of simulating the effects of vegetation non-perpendicular to the reach include that of Cox and Bolte (2007), who devised a methodology capable of simulating shadow cast by vegetation located in 8 directions (steps of 45°) around each centreline node, and the Solar Analyst extension for ArcGIS (Fu and Rich, 1999), which can compute shadow factor at much finer spatial and temporal scales. Indeed, Johnson and Wilby (2015) applied this method to a small catchment in order to quantify the potential of planting trees, without using a physically-based river temperature model.

The impact of riparian vegetation on diffuse radiation can be quantified by computing a sky view factor (SVF). It is the ratio between the diffuse radiation actually reaching the water and the diffuse radiation that would reach this surface with no vegetation around. In a lowland area where topographic shade can be neglected, the tree view factor (TVF) can be defined as 1-SVF. Unlike SF, these view factors (VF) are constant in time since they do not depend on the sun's position. For short reaches, a precise calculation can be achieved through hemispheric photography. For larger areas, remote sensing products or vegetation polygons are

needed. Most previous studies (Chen et al., 1998; Cox and Bolte, 2007; Loiaz et al., 2013; Sun et al., 2015) simply use the angle between the horizon and the tree in the directions perpendicular to the river, from one fixed point of view (usually the centre of the river). Moore et al. (2014) introduced the computation of width-averaged sky view factors, with equations considering infinitely long rivers, with or without overhanging trees.

With an approach similar to the one used to compute direct radiation, the Solar Analyst extension for ArcGIS handles the computation of diffuse radiation by overlaying a viewshed and a discretised sky map. Two different methods can be used to quantify the amount of radiation coming from each cell of the open sky (uniform radiation or depending on the zenith angle). This method was modified and used by Sridhar et al. (2004) to include the shading effects of near stream vegetation.

In order to quantify the impact of riparian shading, existing regional-scale stream temperature models usually rely on theoretical values regarding vegetation characteristics (Sun et al., 2015; Loiaz et al., 2013), on simplified assumptions regarding shading process (Haag and Luce, 2008; Cheng and Wiley, 2016), or incorporate shading data from low-resolution DEMs (Cox and Bolte, 2007). Nowadays however, LiDAR can provide accurate data at a large scale. In order to develop a tool for riparian shade inventories using LiDAR data, Guzy et al. (2015) adapted the insolation module of the Heat Source model (Boyd and Kasper, 2003). They created polygons of homogenous potential canopy height and extracted the 75th percentile of the computed frequency distribution of canopy height provided by LiDAR. Greenberg et al. (2012) used LiDAR data and the r.sun module of GRASS GIS to compute clear-sky solar radiation for three summer days in order to understand the impact of a potential trees removal around a delta, without the use of a network based temperature model. Finally, Wawrzyniak et al. (2017) used LiDAR data to compute the impact of riparian forest in a deterministic water temperature model of a 21 km-long reach, during 5 days in summer 2010 and 2011. There is thus a range of data sources and methods available to compute both SF and VF. However, there remains a lack of information comparing the various methodologies, especially with regards to shading routines in regional-scale models. Moreover, the use of LiDAR as a method for the computation of riparian shading is still in its infancy and has never been used to compute the impact of riparian vegetation in a large-scale stream temperature model, during a whole annual cycle.

The goal of this paper is therefore to test the influence of shadow and sky view factor computed from LiDAR data on the simulation of maximum daily water temperature ( $T_{max}$ ) with the T-NET model, a dynamic physically based model for simulating stream temperature at the regional scale using the equilibrium temperature concept. We compute SF and VF based on a LiDAR-derived raster and incorporate these data into the radiative balance of a T-NET model of the Loir River (France) (see Beaufort et al., 2016). We then compare the  $T_{max}$  simulated with LiDAR data to two other methods used in the T-NET model for computing riparian shading at the regional scales. Model validation is achieved using data from 4 temperature monitoring stations that are spread over the Loir River.

## 2. Methods

### 2.1. Principles of the T-NET model

T-NET is a 1D physically-based model designed to compute water temperature along the longitudinal dimension of a hydrographic network (a GIS polyline). Reaches of this network are limited by two confluences, or by a source and a confluence (for first order reaches). T-NET was designed and applied at the regional scale (110 000 km<sup>2</sup>) by Beaufort et al. (2016). T-NET runs at an hourly time step and is based on the equilibrium temperature concept, which is defined as the water temperature at which the net rate of heat exchange at the interface of a water body is null (Bustillo et al., 2014). The model considers six fluxes [ $W \cdot m^{-2}$ ]: net solar radiation, atmospheric longwave radiation,

longwave radiation emitted from the water surface, evaporative heat flux, convective heat flux, and groundwater heat inflow. To compute these terms, the model uses the following parameters as gridded input data: air temperature [ $^{\circ}\text{C}$ ], specific humidity [ $\text{kg}\cdot\text{kg}^{-1}$ ], wind velocity [ $\text{m}\cdot\text{s}^{-1}$ ], atmospheric longwave radiation [ $\text{W}\cdot\text{m}^{-2}$ ] and direct and diffuse solar radiation [ $\text{W}\cdot\text{m}^{-2}$ ]. Parameters are allocated to each river reach as a function of the ratio between the length of the reach within a grid cell and the total reach length. All meteorological parameters except solar radiation are derived from the SAFRAN atmospheric reanalysis dataset (Vidal et al., 2010). These data are produced by Météo-France from both observations and modelling at an hourly time step and a spatial resolution of 8 km. Direct and diffuse solar radiation are derived from the Helioclim3-v5 dataset (Marchand et al., 2017), generated with the help of Meteosat satellite imagery at an hourly time step and a resolution of  $\sim 3 \times 5$  km. Inputs pertaining to river discharge and groundwater contributions to river flow are also required by the model. These are computed at a daily time step with the semi-distributed hydrological model EROS (Thiéry and Moutzopoulos, 1992). Both parameters are modelled at the outlets of sub-basins for which river discharge observations are available for calibration. They are then scaled to the reaches inside each sub-basin using the partial area concept. T-NET simulates longitudinal variability in water temperature between the upstream and downstream nodes of each reach, with a spatial resolution depending on the travel time (Fig. 1). Water velocity is given by the ratio between discharge and channel cross-section, which is computed using the ESTIMKART empirical model developed by Lamouroux et al. (2010). At the confluence of two reaches, the output temperature is defined as the sum of the product of the two confluences' temperature and discharge divided by the sum of the discharge of the two confluences. T-NET was thus designed to be applied on well mixed streams and not on standing waters or large estuaries, where 2D (Cole and Wells, 2006; Becker et al., 2010; Ouellet et al., 2014) or 3D models (Maderich et al., 2008) are more suitable.

## 2.2. Net solar radiation calculation

In order to improve T-NET's ability to model the impact of riparian vegetation on solar radiation, modifications were made to the original model detailed by Beaufort et al. (2016). Similar to the approach of LeBlanc et al. (1997), net solar radiation ( $H_{ns}$ ) is now computed as:

$$H_{ns} = R_{dir}(1 - \alpha_{dir})((1 - SF) + SF\tau) + R_{diff}(1 - \alpha_{diff})((1 - TVF) + TVF\tau) \quad (1)$$

where  $R_{dir}$  and  $R_{diff}$  are the direct and diffuse solar radiation [ $\text{W}\cdot\text{m}^{-2}$ ] derived from the Helioclim3-v5 product,  $\alpha_{dir}$  and  $\alpha_{diff}$  are the water surface albedo associated with direct and diffuse radiation respectively,  $\tau$  is the transmissivity of riparian vegetation (i.e. the fraction of solar radiation that passes through the canopy),  $SF$  is the shadow factor and  $TVF$  is the tree view factor.  $\alpha_{diff}$  was held at a constant of 0.09, following the

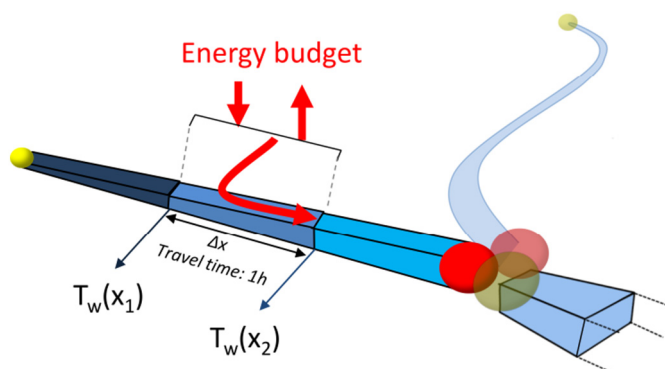


Fig. 1. Principles of the T-NET model.

recommendation of Sellers (1965) and  $\alpha_{dir}$  was computed using the formulation of Anderson (1954):

$$\alpha_{dir} = 1 \quad \text{if } \Psi < 1.24^{\circ} \\ \alpha_{dir} = 1.18 \cdot \Psi^{-0.77} \quad \text{otherwise} \quad (2)$$

where  $\Psi$  is the angle between the horizon and the sun in degrees.

$\tau$  was fixed at 50% in winter and 15% in summer. These values are the averages of global solar radiation transmissivities given by Cantón et al. (1994), Sattin et al. (1997) and Konarska et al. (2014) for deciduous tree species. Transitions between winter and summer values are described with an ascending and descending logistic regression whose equation is:

$$\tau = \frac{\kappa}{1 + \exp(\pm\gamma \cdot DoY - \beta)} + \mu \quad (3)$$

where  $DoY$  is the day of year and  $\kappa$ ,  $\beta$ ,  $\gamma$  and  $\mu$  are the parameters fitted by least squares adjustment to an averaged annual cycle of ground-based NDVI measured from oak trees during 2008–2012 (Soudani et al., 2012). These trees are located in the forest of Fontainebleau (60 km to the south of Paris and  $\sim 150$  km away from the centre of the Loir catchment). Data from Lebourgeois et al. (2008) indicate that, for oak trees, there is little phenologic difference between Fontainebleau and the Loir catchment. However, remote sensing observations from Muller (1995) show that, in 1987 and in the region of Toulouse (South of France), leaf emergence of riparian trees occurs about 15 days earlier than for oaks. In order to take into account this difference between oak and riparian species, we hence considered an enlarged growing season compared to oak's phenology ( $\beta - 15$  days in spring,  $\beta + 15$  days in autumn). After fitting the four parameters on NDVI values,  $\kappa$  and  $\mu$ , representing the upper and lower values, are adjusted to fit the winter and summer values of transmissivity (50 and 15%, respectively).

## 2.3. Shadow factor and view factor calculations

In order to test the influence of different riparian shading algorithms on water temperatures simulated with T-NET, we used three approaches to compute both the shadow factor (SF) and the tree view factor (TVF).

In the first approach (hereafter referred to as the *constant* method), SF and TVF are held as coefficients that are constant in time but vary as a function of Strahler order based on the equation:

$$SF = TVF = vc \times k \quad (4)$$

where  $vc$  is vegetation cover (%) computed at the reach scale in a buffer of 10 m around the river, and  $k$  is a coefficient aiming to account for the influence of the reach width on shadow (where 1 (maximum impact) denotes a Strahler order of 1 and 0 (no impact) is associated with a Strahler order of 8). This approach is used in Beaufort et al. (2015, 2016).

In the second approach (hereafter referred to as the *variable* method), SF and TVF are derived from geometric calculations made at the reach scale, taking into account river width, tree height, vegetation cover, and position of the sun (for the shadow factor).

To compute SF at an hourly time step, the model of Li et al. (2012) was implemented in its simplest version, i.e. considering rectangular trees, located at the edge of the bank, without overhang:

$$SF = \frac{H \times \cot\Psi \times \sin\delta}{W} \times vc \quad (5)$$

where  $H$  is tree height,  $W$  is river width,  $\Psi$  is the solar elevation angle,  $\delta$  is the angle between solar azimuth and the mean azimuth [ $0^{\circ} - 180^{\circ}$ ] of each T-NET reach (computed by considering the first and last vertices of each reach).

To compute VF, we used the second model described in Moore et al. (2014). It provides SVF for channels of infinite length, without taking

into account overhanging trees. For a channel with vertical banks and fixed tree height, the width- and reach-averaged tree view factor is computed as:

$$TVF = \left[ 1 - \frac{0.5}{W} \left( \sqrt{H^2 + W^2} + \sqrt{H^2 + W^2 - 2H} \right) \right] \times vc \quad (6)$$

The third approach (subsequently referred to as the *lidar* method) is a spatially-explicit method that computes SF and TVF from a LiDAR-derived digital surface model (DSM). It requires a) a high-resolution digital surface model (~1 m) describing the elevation of riparian vegetation, b) information about the exact location of the river in order to define water and non-water pixels and c) polygons of river area, allowing the DSM pixels to be linked to a given T-NET reach.

To compute SF, we modified the r.sun module (Hofierka and Suri, 2002) of GRASS GIS (GRASS Development Team, 2015) to map per-pixel shade cast by the DSM. Using this algorithm, a water pixel is defined as being in shade if the elevation of the highest DSM pixel located along a 50 m track in the direction of the sun is greater than the solar elevation. Dividing the number of shaded pixels by the number of water pixels belonging to each river polygon thus provides a shadow factor for each T-NET reach. Because shading at a given hour vary slowly throughout the year, the computation was done every hour when the sun is above the horizon, every 15 days of a standard non-leap year, for every water pixel. A piecewise cubic interpolation is then applied to the SF of each hour separately in order to get a value for each day of the year.

To compute SVF from the DSM, we represented the sky as a hemisphere of radius R centred on a water pixel (as in Essery et al., 2008, Johnson and Watson, 1984 and Tung et al., 2006; Fig. 2). We used the r.horizon module of GRASS GIS to calculate the angle  $\theta$  between the horizon and the highest DSM pixel as seen from each water pixel at horizontal azimuth steps  $\phi$  of  $10^\circ$ . The whole hemisphere is thus made of  $n = 36$  segments. The diffuse radiation emission is considered to be isotropic and the river surface to be horizontal. The SVF for each segment is computed from the sphere area formula:

$$\frac{R^2 \int_0^{\frac{\pi}{2}} \int_0^{\phi} \cos\theta \sin\theta d\phi d\theta}{R^2 \int_0^{\frac{\pi}{2}} \int_0^{\phi} \cos\theta \sin\theta d\phi d\theta} = \frac{1 + \cos 2\theta}{2} \quad (7)$$

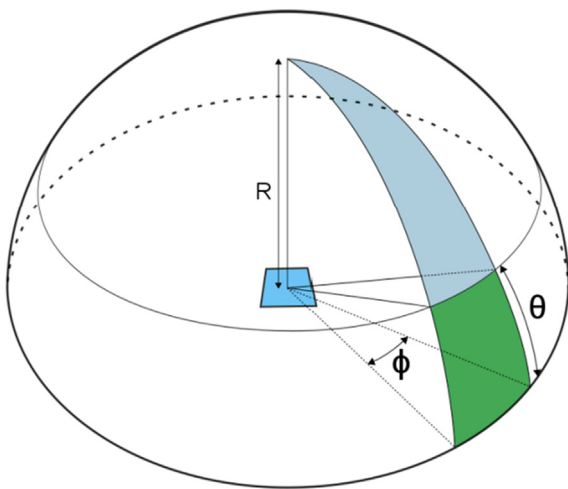


Fig. 2. Calculation of a sky view factor from measures of  $\theta$ , the angle between the horizon and the highest vegetation seen from a water pixel and with an angular step  $\phi$  of  $10^\circ$ . R is the radius of the hemisphere.

It therefore follows that the SVF for the whole hemisphere is given by:

$$SVF = \frac{1}{2} + \frac{1}{n} \sum_{i=1}^n \cos 2\theta_i \quad (8)$$

An averaged TVF value ( $TVF = 1 - SVF$ ) is subsequently attributed to each T-NET reach as the mean TVF value for all DSM pixels located within the reach.

#### 2.4. Study site and water temperature observations

The Loir River basin is an 8283 km<sup>2</sup> sub-catchment of the Maine River watershed located in central France (Fig. 3). The river network of the Loir basin is 4420 km long, of which the Loir River itself is 316 km. The basin is generally low-lying, with altitudes ranging from 20 to 140 m above sea level. As highlighted by the river network's variable drainage density (Fig. 3), a calcareous aquifer with high permeability is present in the north-east of the catchment. It feeds the river network with groundwater exchanges in its upstream sections (Baratelli et al., 2016). Channel slope (computed from a 25 m resolution digital terrain model of the watershed) ranges from 0.01% to 5%, with a median value of 0.5%. The main tributaries of the Loir are the Conie, the Yerre and the Aigre, with catchments areas of 530, 300 and 280 km<sup>2</sup> respectively. The mean discharge of the Loir at its downstream-most gauging station (1961–2015) is 31.8 m<sup>3</sup>·s<sup>-1</sup> (specific discharge = 4.0 l·s<sup>-1</sup>·km<sup>-2</sup>). The flows of the Aigre (specific discharge = 5.4 l·s<sup>-1</sup>·km<sup>-2</sup>) and the Conie (specific discharge = 3.4 l·s<sup>-1</sup>·km<sup>-2</sup>) show little variation during the year, compared to the Loir. However, interannual fluctuations are much greater, driven by piezometric fluctuations of the Beauce aquifer.

Eighteen temperature loggers allowing for the model validation are located in the catchment. They acquired data at an hourly time step with varying periods of availability (extending from summer 2008 to summer 2014). The loggers were generally placed at a depth > 1 m (according to the mean interannual water level), and steps were taken to ensure that they were installed within well-mixed sections of the channel to avoid potential stratification biases. Four of these stations are located within the main stem of the Loir (S1 to S4), where LiDAR data are available. The period of measurement is different for each station and is given in Fig. 4. The annual cycle of mean daily temperature of the Loir River ranges from 2 to 24 °C at station 1 (between 08/2010 and 07/2011), while the annual amplitude of the Aigre and the Yerre are smaller because of the groundwater fluxes (5–21 °C and 4–16 °C on the same period, respectively). Temperature regime of the Conie River is strongly dependent on the groundwater level. Its variability can be similar to the Loir River (2009, 2010) or very limited (annual range of 8–14 °C in 2014).

#### 2.5. T-NET model implementation and criteria of model performance

The Loir River basin was implemented in the T-NET model. It consists of 2206 reaches, of which the Loir River itself is covered by 161 reaches. Simulated discharge and groundwater inputs used to drive T-NET (derived from the EROS hydrological model) were found to agree reasonably well with observed data. Nash-Sutcliffe (Nash and Sutcliffe, 1970) model efficiency coefficient (NSE) calculated against hydrometric observations ranged from 0.59 to 0.95 (1974–2012 period) for 21 of the 23 sub-basins of the Loir catchment. The remaining two sub-basins (<0.10 m<sup>3</sup>·s<sup>-1</sup>; located in the upper portions of the watershed) yielded negative NSE values.

In order to compare the three shading methods detailed in Section 2.3, we ran the T-NET model three times on seven hydrologic years (from August 2007 to July 2014).

For the *constant* method, vegetation cover (*vc*) was derived from a dataset available at the national scale (Valette et al., 2012), which is

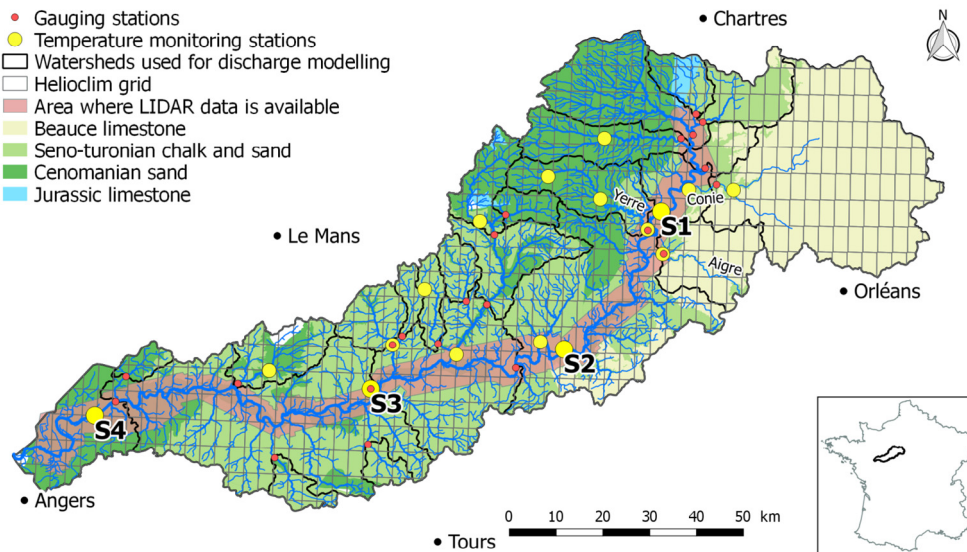


Fig. 3. Map of the Loir catchment, with stream temperature monitoring stations, gauging stations, watersheds used for discharge modelling, LiDAR area, geologic formations, Helioclim grid.

based on river and vegetation polygons from the BD TOPO® database, provided by Institut national de l'information géographique et forestière (IGN).

For the *variable* method, *vc* was also derived from this dataset. Tree height *H* was fixed at 15 m and river width *W* was estimated using the ESTIMKART empirical model (Lamouroux et al., 2010).

For the *lidar* method, the digital surface model (DSM) required for the shading computation was derived from a LiDAR survey conducted by IGN on approximately 270 km of the Loir River (85% of the total river length) on 26 May 2012. That day, average discharge was  $25.5 \text{ m}^3 \cdot \text{s}^{-1}$  at the downstream-most gauging station (interannual average is  $31.8 \text{ m}^3 \cdot \text{s}^{-1}$ ). The DSM was generated by gridding the LiDAR first returns at a resolution of  $1 \text{ m}^2$ . LiDAR accuracy was assessed as  $\sim 60 \text{ cm}$  in the horizontal and  $\sim 20 \text{ cm}$  in the vertical components. Because water does not reflect the LiDAR pulses, no data was available for the water pixels (unless emergent aquatic vegetation was present), and we used this property to discriminate water vs. non-water pixels inside the river polygons of the BD TOPO database. Elevations for these water pixels as well as for other sporadic data gaps were computed by attributing values from a digital elevation model (DEM) to the no data pixels. This 1-m resolution DEM, built from LiDAR final returns, provides values above water by interpolation of altitudes between the river banks. Finally, polygons from BD TOPO were also used to attribute DSM pixels to each reach of the T-NET network. Because LiDAR data were not available on the tributaries and the headwaters of the Loir, the *constant* method was applied on these reaches. With this configuration, the *lidar* method takes  $< 5 \text{ h}$  to run on a computer with 16 CPUs and 64 Gb of RAM. Finally, in order to compare the *lidar* method with a situation without riparian vegetation, a supplementary simulation was done with SF and TVF fixed at zero everywhere.

In order to characterise differences in vegetation cover between the DSM and that derived from the BD TOPO database (Valette et al., 2012), a DEM was also used to create a raster of vegetation height by subtracting the DEM (ground) elevations from the DSM. A vegetation

cover map was then extracted from the vegetation height raster, where vegetation cover was defined as all pixels with vegetation higher than 1 m. A LiDAR-derived river width was also extracted for analysis purposes by dividing the area of water pixel inside each polygon by the length of the T-NET reaches.

Three model performance metrics were used to quantify the accuracy of the different methods regarding the maximum daily temperature. The root-mean-square error (RMSE) was used as a global performance metric:

$$RMSE = \sqrt{\frac{\sum (T_{sim} - T_{obs})^2}{N}} \quad (9)$$

where *N* is the number of observations,  $T_{sim}$  is the simulated river temperature and  $T_{obs}$  is the observed river temperature. Bias (defined as the mean difference between simulated and measured temperatures) was used to quantify the mean over/underestimation of the model. Finally, the standard deviation of errors (SDE) quantifies the variability of daily biases in a given period. Because the temperature time series used for model validation were not concomitant (Fig. 4), model performance was analysed using two methods. First, we compared model performance against all available validation data. This allows for comparison between the three shading methods detailed in Section 2.3. Second, in order to compare spatial variability in the model's performance between the 4 temperature logger stations, we used temperature data from the period during which concurrent measures were available at all 4 stations (13th to the 31st August 2009).

### 3. Results

#### 3.1. Characterisation of riparian vegetation cover

Analysis of vegetation cover extracted from the LiDAR data inside a single buffer of 10 m around the 270 km of river shows that 58% of the

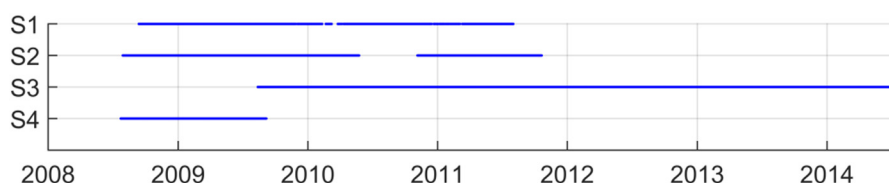


Fig. 4. Period of availability of stream temperature observations at the four logger stations located on the Loir River.

riparian zone is vegetated. The median vegetation height in this area is 10.0 m and the third quartile of the height (considered by Guzy et al., 2015) is 14.9 m, while the standard deviation is 6.5 m. Longitudinal profiles of vegetation cover, median and 3rd quartile of height are given in Fig. 5. There is a slight but significant decreasing downstream trend for these three variables ( $p$ -value = 0.014). In comparison with the LiDAR-derived vegetation cover, vegetation cover derived from the BD TOPO database is overestimated everywhere with the exception of some small reaches (Fig. 5). The median overestimation is 35% upstream of river km 160 and 22% downstream. This overestimation rises to >39% for 20% of the reaches.

### 3.2. Variation in riparian shading computed with the three methods

In the Loir catchment, direct and diffuse radiation comprise ~70% and ~30% respectively of the incoming solar radiation received at the river surface between 8 and 16 h (period 2007–2014). This means that shadow factor has a greater impact on water temperature than view factor.

Fig. 6 shows the longitudinal profile of SF on the Loir River for the three methods at midday on the summer solstice, when solar radiation is strongest. For the *constant* method, the reaches covered by LiDAR data have a uniform Strahler order of 5, so that the weighting coefficient  $k$  in this area is always equal to 0.4 (see Section 2.3). The variation of SF is thus only dependent on the vegetation cover. The *variable* method varies strongly as a function of reach azimuth, even though the sun is at its highest elevation, while the *lidar* method shows smaller variations. The *lidar* method is thus less sensitive to reach azimuth, compared to the *variable* method.

At noon, the Loir's SF computed with the *lidar* method lies between 0 and 0.3 in June (median = 0.1; Fig. 7a solid lines) and between 0.1 and 1 in December (median = 0.5). There is thus more variability in winter than in summer, because reach azimuth has a much greater impact when the sun is low in the sky. Seasonal variability in SF exhibits strong annual cyclicality, with SF minima centred on the summer solstice for every reach. Highest SF values are found on a reach located 85 km from the source, flowing East-West and bordered by persistent riparian forest cover (>20 m tall). Lowest SF values are found on a North-South oriented reach located 271 km from the source, explaining the weak annual cycle at noon (Fig. 7a, pink solid line). Fig. 7b shows the daily cycles at the summer solstice. The hour of minimum SF in a day is not always centred on noon because it depends on the reach orientation. SF obtained from the *variable* method is usually higher than that provided by the *lidar* method, except in winter and at noon for North-South oriented reaches (Fig. 7a, dashed pink line). At the summer solstice, between 6

and 18 h, the *variable* method yields higher SF than the *lidar* method 74% of the time, especially in the upstream parts of the watershed. Indeed, the *variable* method yields 184 occurrences of SF values equal to 1, while it only occurs 3 times with the *lidar* method.

Fig. 8 shows the longitudinal profile of TVF for the three methods. Mean values are 0.34, 0.38 and 0.26 for the *constant*, *variable* and *lidar* methods respectively. TVF computed with the *lidar* method comprises values between 0.47 and 0.11. Like for the SF, there is a significant ( $p < 0.01$ ) decreasing trend due to both the increasing width of the river and the decreasing vegetation cover. The *variable* method overestimates TVF, especially for the upstream portion of the river. Indeed, the inter-method variability in computed TVF values decreases as the influence of vegetation on TVF reduces with increasing river width.

### 3.3. Impact of riparian shading method on annual and seasonal river temperature simulations

Results of this paper focus on the 4 temperature monitoring stations located on the Loir River, where LiDAR data are available. For the 14 other temperature monitoring stations located on the tributaries, the constant method provides a median annual RMSE on mean daily temperature at 1.69 °C (min = 1.35 °C, max = 2.89 °C). Seasonality in the accuracy is observed since median bias on mean daily temperature is -0.4 °C when computed for the full year but rises to 0.2 °C in summer. 67% of daily biases are comprised between ± 2 °C.

Biases, SDE and RMSE averaged on the four stations are shown in Table 1 for the April–September and the October–March periods. In the April–September period, the *lidar* method improves the mean bias by 0.62 °C in comparison with the *constant* method. The mean RMSE is improved by 0.22 °C although the mean SDE is increased by 0.10 °C. The three metrics show that the *constant* method provides better results than the *variable* method. During the October–March period, biases of the 3 methods are closer to zero. All criteria of the *constant* and the *lidar* methods are very similar because solar radiation is lower and vegetation transmissivity is high. However, the *variable* method is consistently colder than the other methods by ~0.3 °C.

Fig. 9 shows the monthly biases ( $T_{sim} - T_{obs}$ ) of maximum daily temperature ( $T_{max}$ ) computed on available measured data (see Fig. 4). At the four stations, the *lidar* method provides improved biases in comparison to both the *variable* and the *constant* method from April to September. Compared to the *variable* method, the maximum improvement occurs during the spring and autumn months (2 °C at S1; 1.5 °C at S2; 0.5 °C at S3; 0.7 °C at S4). Despite this improvement, the *lidar* method still underestimates river temperature by >1 °C during at least 2 months

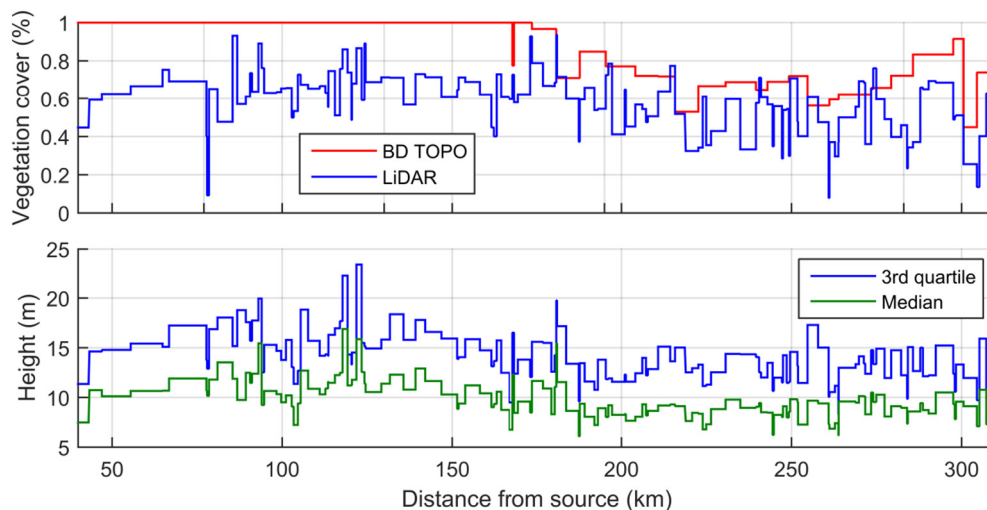


Fig. 5. Characterisation of riparian vegetation for each T-NET reach (a) comparison of vegetation cover derived from the BD TOPO database (Valette et al., 2012) and LiDAR datasets (buffer of 10 m on both sides of the river polygons) (b) median and 3rd quartile vegetation heights from LiDAR data.

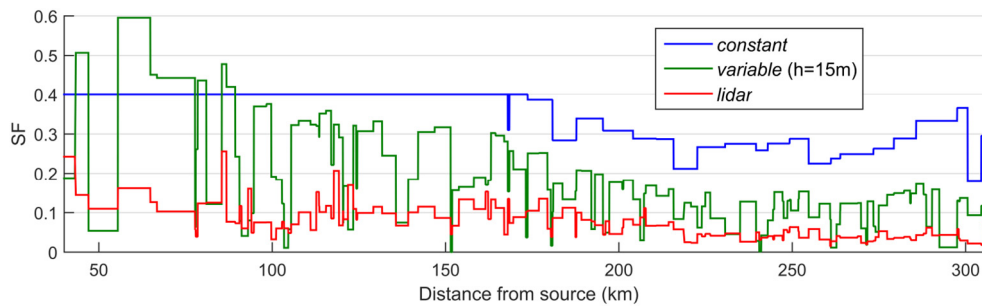


Fig. 6. Longitudinal profile of shadow factor provided by the 3 methods on the Loir River at the summer solstice (21st June) at 12 h UTC.

in summer at S1, S2 and S4. The *constant* method provides a consistently colder  $T_{max}$  than the *variable* (and *lidar*) methods at stations 3 and 4 from May to August, presumably because this method does not model the seasonal cycle of increasing and decreasing shadow length.

Averaged annual cycles of SDE show little difference between methods and always stay above 1 °C (Fig. 9). That means that simulated  $T_{max}$  is substantially more variable than observed data, whatever the method used.

### 3.4. Impact of riparian shading method on summer maximum daily temperature long profile

We analysed longitudinal profiles in summer by considering average maximum temperature between the 13th and the 31st August 2009. During this period, discharges were low ( $<7 \text{ m}^3 \cdot \text{s}^{-1}$  at the downstream-most gauging station) and the averaged maximum daily air temperature in the catchment was relatively high (25.9 °C). The longitudinal profiles (Fig. 10) exhibit discontinuities in the thermal signal that are driven by cool water inflows from the Conie and Aigre rivers, which drain the Beauce aquifer (Baratelli et al., 2016). Before entering the LiDAR-covered area (shown with a dashed vertical line), the *variable* method is colder than the *constant* method by  $>2.5$  °C. This difference decreases slowly in a streamwise direction until it reverses and the *variable* method becomes warmer than the *constant*. Indeed, the three methods provide a persistent warming trend as a function of distance from source, but this trend is higher for the *variable* method (1.87 °C/100 km compared to 1.23 °C/100 km and 1.25 °C/100 km for the *constant* and *lidar* methods respectively). This difference in longitudinal trend persists across all summers in the 2007–2014 simulation period. On average between the 13th and 31st August 2009, the *lidar* methods provide warmer  $T_{max}$  than the two other methods all along the Loir, with biases close to zero at stations 3 and 4. However,  $T_{max}$  is still underestimated by 1.6 and 1.3 °C at stations 1 and 2. RMSE values are 1.99, 2.08, 1.43 and 1.79 °C on S1 to S4 respectively. Fig. 10 also shows the simulation considering the absence of riparian vegetation. The difference between this output and the *lidar* method reaches up to 3.0 °C just upstream of the Conie

confluence, where sensitivity analysis shows that the *lidar* method simulation is no longer under the influence of the constant method applied upstream of the LiDAR area. This difference reaches a minimal value of 1.3 °C at the downstream-most point.

## 4. Discussion

### 4.1. Discrepancies in computed SF and TVF

The global overestimation of SF and TVF provided by the *variable* method compared to the *lidar* method can be explained by four key factors. First, the BD TOPO database that weights the results of the *variable* method clearly overestimates vegetation cover in relation to the LiDAR-derived values (discussed in Section 3.1). Second, comparison of the wetted widths used in the *variable* method with LiDAR-derived river widths shows that the former are underestimated, especially upstream of ~150 km and downstream of ~250 km from the source. These width uncertainties drive an increase in SF (TVF) of 6% (4%) when averaged over the entire modelling period and 14% (9%) between 13th and 31st August 2009. Third, discrepancies may also arise from the fact that the *variable* method uses averaged stream azimuths while the *lidar* method intrinsically considers the position of vegetation in regard to the water surface. Indeed, reach azimuth impacts the timing of minimum SF (Li et al., 2012), the hourly amount of direct solar radiation and hence the maximum daily temperature (Garner et al., 2017). In order to quantify these discrepancies, we cut the Loir river GIS line in 50 m parts and compared azimuths of these small reaches with the original T-NET reaches azimuths. The mean absolute difference is 26° and  $R^2$  is 0.66. Finally, the characterisation of vegetation cover and height at high resolution with the LiDAR data may not be reproducible in the *variable* method by taking an average of these data at the reach scale. Indeed, Greenberg et al. (2012) report that 28% of the change in insolation caused by removal of riparian vegetation characterised with LiDAR data could not be explained by considering averages at the reach scale. In our case, a multiple linear regression between LiDAR-derived TVF and LiDAR-derived tree height, vegetation cover and river width averaged at the reach scale

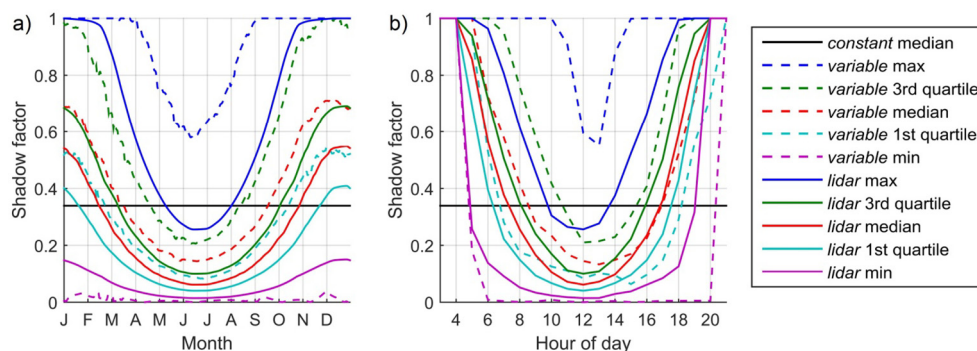


Fig. 7. Percentiles of the SF distribution obtained with the three methods on the 135 T-NET reaches (a) Annual cycles at noon (b) daily cycles at the summer solstice. (For interpretation of the references to color in this figure, the reader is referred to the web version of this article.)

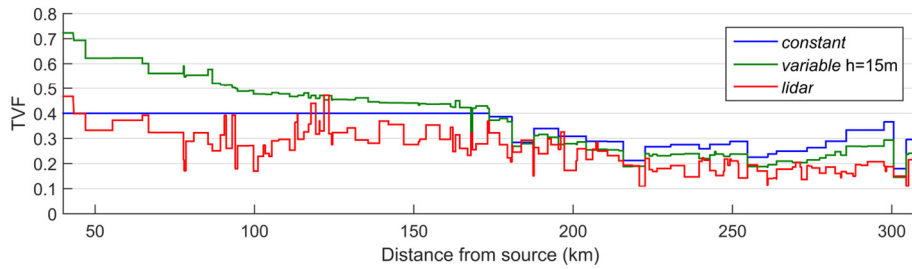


Fig. 8. Longitudinal profile of tree view factor provided by the 3 methods on the Loir River. Values from the *variable* method are averaged on 08/2007–07/2014.

provides  $R^2 = 0.83$ . Hence, 17% of the TVF variance cannot be explained by these three variables when averaged at the reach scale.

4.2. Influence of shading routine on simulated river temperatures

In order to separate the influence of the *variable* method itself from the influence of the vegetation cover data used to drive it, we injected the vegetation cover computed from the LiDAR data (10 m buffers on each river bank for each reach) into the *variable* method. As a first step, tree height was kept at 15 m. The resulting longitudinal profile (13 to 31 August 2009 average) shows that, in this configuration, the *variable* method closely approximates the *lidar* method (Fig. 11). The mean bias (computed against observed temperatures) between April and September is  $-1.19\text{ }^\circ\text{C}$ , compared to  $-0.94\text{ }^\circ\text{C}$  for the *lidar* method and to  $-1.86\text{ }^\circ\text{C}$  for the *variable* method with the original vegetation cover. The median vegetation height computed from the LiDAR dataset was subsequently also injected into the *variable* method. In this case, mean bias is further reduced to  $-0.78\text{ }^\circ\text{C}$ . Using the same approach with the *constant* method provides a profile that is warmer than the *lidar* method profile prior to river km 100 and colder after river km 200. Hence, a coefficient  $k = 0.4$  seems to be appropriate for a river width of 25–30 m, during the month of August.

4.3. Performance of T-NET model on the Loir River

Although the T-NET model of the Loir River (driven with the *lidar* method) provides relatively unbiased temperature at station 3, it still underestimates temperature at stations 1 and 2 and to a lesser extent at station 4 (Fig. 9). Sensitivity analyses show that uncertainty about the impact of vegetation on tributaries (because of the application of the *constant* method in areas where LiDAR data do not exist) cannot fully explain the underestimation of modelled temperatures on the Loir. Underestimation at station 1 is partly due to the underestimation of the Conie tributary. An impoundment located at the source of the river likely explains why the Conie is warmer than expected (Pedersen and Sand-Jensen, 2007; Dripps and Granger, 2013). Impoundments on several other tributaries may have the same effect and contribute to warming the Loir River and hence explain the negative biases at station 2. Station 4 is located just upstream of a small weir. There are >120 small weirs (height < 3 m) on the Loir River that may partially explain the temperature underestimation. Indeed, by increasing water depth, they increase travel time and thus sensitivity to air temperature. By decreasing water velocity, they can favour thermal stratification in summer (Torgersen et al., 2001) and since water is usually released by weir-overflow,

warmer water may be selectively released. This process is not taken into account in T-NET because it only considers the longitudinal dimension. Other more complex hydrodynamic models (e.g. Becker et al., 2010; Cole and Wells, 2006; Maderich et al., 2008; Deltares, 2014) would therefore be required to incorporate this process. The high temporal variability in modelled temperatures (compared to observed data) is likely due to modelled flow velocities that exceed real values. Unfortunately however, we have no observed values of travel time to compare with. Finally, it must be kept in mind that 1) computed model performances are dependent on the number of validation stations, which is limited to 4 in the current study and 2) that the T-NET model is driven with re-analysis data which are themselves subject to errors. In particular, the number of meteorological stations providing air temperature as input of the SAFRAN reanalysis in the Loir catchment is limited: approximately 10 stations are located upstream of S1 but only 2 stations located close to each other cover the rest of the basin (Quintana-Seguí et al., 2008). The density of stations is still lower for wind velocity and relative humidity but is higher for precipitations.

4.4. Implications, shading methods limitations and perspectives

Our results show that the *lidar* method has good potential for computation of SF and SVF at hourly timesteps on medium to large rivers and at large temporal and spatial scales. For small rivers (width < 10 m), whose precise location can be hard to determine using remote sensing due to obscuration by the tree canopy, the *variable* method may be more suitable, as long as it is fed with accurate vegetation cover data. Indeed, our results show that differences of modelled  $T_{max}$  can be large if the methods are used with inaccurate vegetation cover data. The quality of these input data is therefore highly important for improving stream temperature modelling. LiDAR covers of riparian zones are increasingly available, in particular because of their use for flood risk assessments. Furthermore, vegetation heights can also be obtained at the catchment scale by photogrammetric techniques (e.g. Michez et al., 2017), while satellite and airborne high resolution imagery can provide accurate location of riparian vegetation (Tormos et al., 2014). These new techniques could potentially be valuable for improving future river temperature modelling efforts.

Our results show that in late August 2009, the Loir's vegetation decreases  $T_{max}$  up to  $3\text{ }^\circ\text{C}$  in the upstream part of the river and by  $1.3\text{ }^\circ\text{C}$  at the downstream-most reaches. This difference is caused by the increasing wetted width (from ~25 to ~50 m) but also by decreasing vegetation cover in the streamwise direction. These quantifications of the thermal impact of riparian vegetation are likely minimum values for two reasons. First, the impact of overhanging trees was neglected (as in all methods used in this paper) (Li et al., 2012; DeWalle, 2008). Secondly, the summer transmissivity value comes from publications studying single trees' transmissivity. However, because riparian buffers are often composed of several rows of trees, real world transmissivity values are likely to be lower, resulting in slightly cooler water temperatures (Duursma and Mäkelä, 2007; Dugdale et al., 2018). Beside this, further research is needed to validate the accuracy of shadows obtained with the *lidar* method against aerial imagery. As an example, Greenberg et al. (2012) reported an overall accuracy of 92%. Since their LiDAR data

Table 1 Model performance criteria for maximum daily temperature, averaged for the 4 stations located on the Loir River from April to September and from October to March ( $^\circ\text{C}$ ).

|                            | April to September |      |      | October to March |      |      |
|----------------------------|--------------------|------|------|------------------|------|------|
|                            | Bias               | SDE  | RMSE | Bias             | SDE  | RMSE |
| Constant method            | -1.44              | 1.61 | 2.17 | -0.31            | 2.04 | 2.07 |
| Variable method (h = 15 m) | -1.86              | 1.65 | 2.55 | -0.60            | 2.09 | 2.18 |
| Lidar method               | -0.82              | 1.75 | 1.95 | -0.33            | 2.05 | 2.08 |

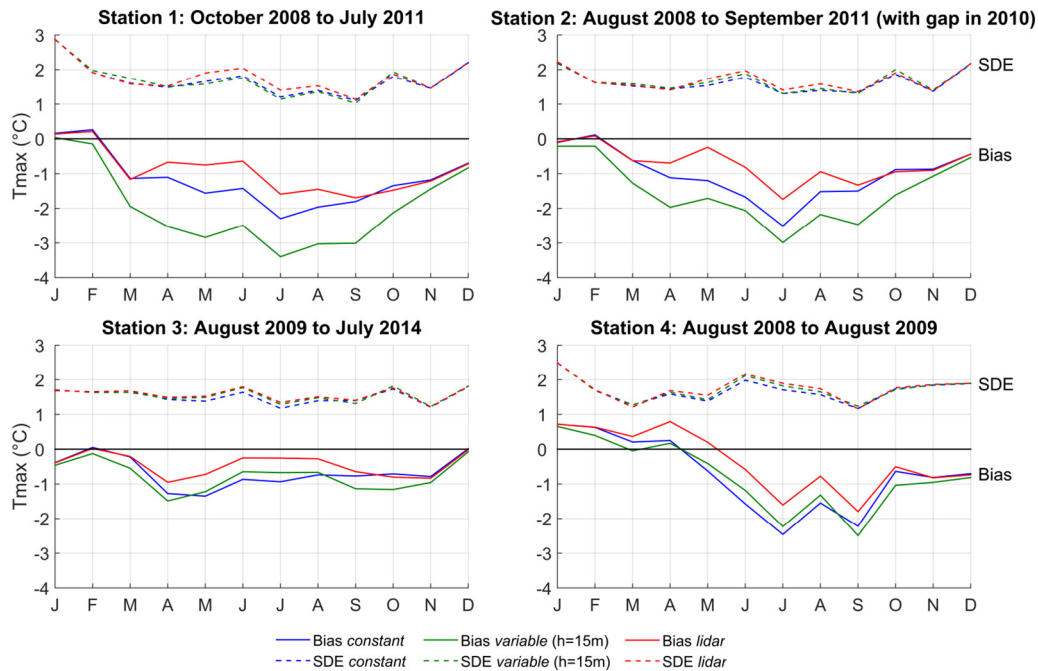


**Fig. 9.** Monthly biases ( $T_{sim}-T_{obs}$ ) and standard deviation of errors of maximum daily temperature provided by the 3 methods at the 4 stations (averaged annual cycles computed on available observed data).

and ours were both acquired when trees were in leaf, a similar accuracy may be expected.

A wide range of values is reported in the literature regarding the cooling effect of vegetation (Moore et al., 2005), mainly for streams narrower than 10 m, for which the response of  $T_{max}$  to clear-cutting can range from 2 to 8 °C (Gomi et al., 2006). For streams wider than 10 m, a modelling approach is usually used to quantify the impacts of vegetation on stream temperature. Our results are in agreement with Woltemade and Hawkins (2016), who modelled a cooling effect of vegetation of approximately 2 °C for a 14 m wide North-West/South-East oriented stream flowing in a mountainous catchment of California (low-flow conditions). A topographic shade of 17% was considered in the deforested scenario; their result would thus be higher in an environment without mountains, like the Loir catchment. Using LiDAR data, Wawrzyniak et al. (2017) modelled a cooling impact of 0.4 °C on  $T_{max}$  on a 22 km-long groundwater-fed river reach with a wetted width ranging from 50 to 120 m. The overall NNE-SSW orientation of this river is likely to decrease the impact of riparian vegetation, in comparison with the Loir, which is globally east-west orientated. Other studies show that the impact of vegetation decreases steadily as wetted width increases to about 30 m (Teti, 2006), 10 m (Davies-Colley and Quinn, 1998) and 17 to 43 m for East-West to North-South oriented streams

(DeWalle, 2008). Our results suggest that the cooling effect can remain above 1 °C even for widths larger than 40 m.

Potential improvements to our lidar method include the incorporation of wetted widths related to the discharge. Although this is possible at small spatial and temporal scales by using a hydraulic model (Wawrzyniak et al., 2017), modelling wetted widths at regional scales can be very complex, especially without field measures of hydraulic geometry. Channel morphology from bathymetric LiDAR data may be one potential solution to this issue (e.g. Hilldale and Raff, 2008; Bailly et al., 2010). Another potential improvement to our methodology relates to the use of Beer's law to model the extinction of solar rays through the tree canopy, as demonstrated by several investigations using coarse vegetation data (Sun et al., 2015; Tung et al., 2007; Sridhar et al., 2004; Lee et al., 2012). Transmission of light beneath the canopy of overhanging trees could also be modelled, but requires information or hypotheses regarding the shape of trees. When aerial imagery is available, more complex methods considering position of individual trees may be used in order to model the transmission of light beneath the canopy (Essery et al., 2008).

Finally, this paper focuses on the impact of vegetation on solar radiation and hence on maximum daily temperature (Johnson, 2004; Garner et al., 2017). Although the impact of vegetation on longwave radiation

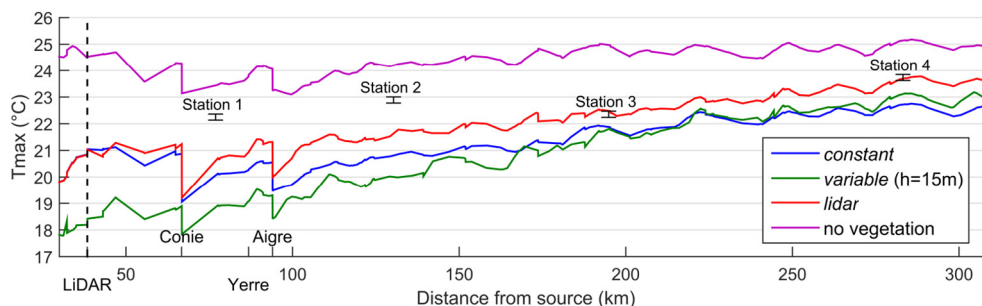


**Fig. 10.** Longitudinal profile of maximum daily temperature (averaged between the 13 and the 31 August 2009) provided by the 3 methods and by a vegetation-free simulation. The vertical dashed line depicts the start of LiDAR cover. Cohie, Yerre and Aigre are the main tributaries.

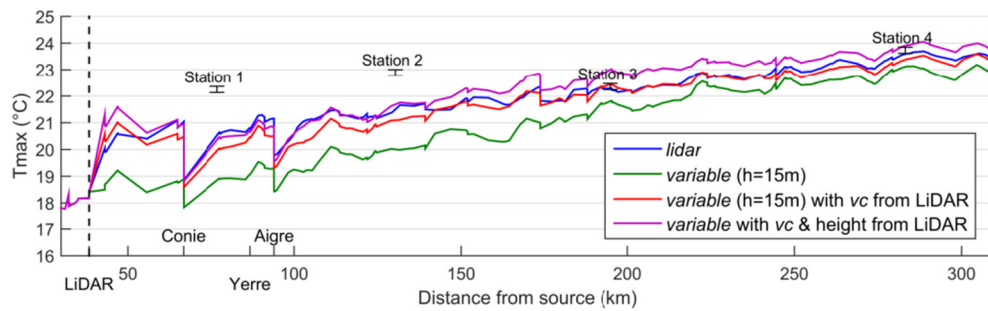


**Fig. 11.** Longitudinal profile of maximum daily temperature (averaged between the 13 and the 31 August 2009) provided by injecting the *variable* method with vegetation cover (vc) and median height from LiDAR data. The vertical dashed line depicts the start of LiDAR cover. Conie, Yerre and Aigre are the main tributaries.

is limited on sunny days (Leach and Moore, 2010; DeWalle, 2008), view factors computed in this paper could be used to quantify the impact of vegetation on longwave fluxes at both regional scales and during a complete annual cycle. LiDAR data could also be used to model the impact of vegetation on water temperature resulting from decreased air temperature and wind velocity engendered by the riparian canopy. Indeed, forest canopies can reduce daytime air temperature by 3 °C to >6 °C and wind velocity by 10–20% in comparison with open areas (Moore et al., 2005).

## 5. Conclusion

The main goal of this study was to understand the influence of using a LiDAR-derived digital surface model to quantify the impact of riparian vegetation on 270 km of the Loire River. We demonstrated that the use of LiDAR data improves the mean biases of simulated maximum daily temperatures ( $T_{max}$ ) in summer, compared to two other simpler methods for computing the effects of riparian shading at large scales. However, it did not improve the standard deviation of errors on  $T_{max}$ , which is likely more influenced by the presence of weirs and impoundments.

The monthly-averaged difference in  $T_{max}$  computed by the various shading methods can reach up to 2 °C at the upstream-most station and 1 °C at the downstream-most station. However, this difference is mainly due to the overestimation of vegetation cover in the dataset used to compute shadow and view factors in the non-*lidar* methods. Indeed, injection of vegetation cover extracted from the LiDAR data into the shading method of medium complexity (*variable method*) decreased the largest difference at the upstream-most station to 0.8 °C, suggesting that this method is sufficient for the computation of SF and VF provided that it is supplied with accurate (high-resolution) data pertaining to vegetation cover. Improving the quality of riparian vegetation data should therefore be a priority for improving stream temperature modelling at the regional scale. The simplest method (*constant method*) may be appropriate to model mean daily temperature for a given period of the year, as long as vegetation cover is weighted with a coefficient depending on the river width.

We hope that the application and comparison of methods demonstrated in this paper will improve understanding of the strengths and limitations of other existing stream temperature models. Enhancing the ability of models to simulate the impact of riparian vegetation is of key importance for the development of climate change adaptation measures and understanding the fundamental processes responsible for spatio-temporal variability of river temperature.

## Acknowledgements

This work forms part of a PhD thesis project supported by Agence française pour la biodiversité. Thanks are due to Météo-France for the SAFRAN database, to Transvalor for the Helioclim data, to D. Thiéry for the hydrological modelling, to A. Chandresris for the vegetation database, to K. Soudani for the NDVI data, to Direction régionale de l'environnement, de l'aménagement et du logement Pays de la Loire

and to Fédération Départementale de Pêche d'Eure et Loir for the temperature data. This paper was improved thanks to the comments of two anonymous reviewers. We also thank the CaSciModOT federation (Calcul Scientifique et Modélisation Orléans Tours) as well as Yves Lansac and Enrick Olive (GREMAN UMR 7347) for providing the computing resources.

## References

- Anderson, E.R., 1954. Energy budget studies, Part of Water Loss Investigations—Lake Hefner Studies. US Geol. Surv. Prof. Pap. 269.
- Bailly, J.-S., Le Coarer, Y., Languille, P., Stigermark, C.-J., Allouis, T., 2010. Geostatistical estimations of bathymetric LiDAR errors on rivers. *Earth Surf. Process. Landf.* 35 (10), 1199–1210.
- Baratelli, F., Flipo, N., Moatar, F., 2016. Estimation of stream-aquifer exchanges at regional scale using a distributed model: sensitivity to in-stream water level fluctuations, riverbed elevation and roughness. *J. Hydrol.* 542, 686–703.
- Beaufort, A., Moatar, F., Curie, F., Ducharme, A., Bustillo, V., Thiéry, D., 2015. River temperature modelling by Strahler order at the regional scale in the Loire River basin, France. *River Res. Appl.* 597–609.
- Beaufort, A., Curie, F., Moatar, F., Ducharme, A., Melin, E., Thiéry, D., 2016. T-NET, a dynamic model for simulating daily stream temperature at the regional scale based on a network topology. *Hydrol. Process.* 2196–2210.
- Becker, A., Kirchesch, V., Baumert, H.Z., Fischer, H., Schöl, A., 2010. Modelling the effects of thermal stratification on the oxygen budget of an impounded river. *River Res. Appl.* 26 (5), 572–588.
- Boisneau, C., Moatar, F., Bodin, M., Boisneau, P., 2008. Does global warming impact on migration patterns and recruitment of Allis shad (Alosa Alosa L.) young of the year in the Loire River, France? *Hydrobiologia* 602 (1), 179–186.
- Boyd, M., Kasper, B., 2003. Analytical methods for dynamic open channel heat and mass transfer: methodology for heat source model Version 7.0 Portland, OR USA.
- Brown, L.E., Hannah, D.M., Milner, A.M., 2005. Spatial and temporal water column and streambed temperature dynamics within an alpine catchment: implications for benthic communities. *Hydrol. Process.* 19 (8), 1585–1610.
- Buisson, L., Blanc, L., Grenouillet, G., 2008. Modelling stream fish species distribution in a river network: the relative effects of temperature versus physical factors. *Ecol. Freshw. Fish* 17 (2), 244–257.
- Bustillo, V., Moatar, F., Ducharme, A., Thiéry, D., Poirel, A., 2014. A multimodel comparison for assessing water temperatures under changing climate conditions via the equilibrium temperature concept: case study of the middle Loire River, France. *Hydrol. Process.* 28 (3), 1507–1524.
- Cantón, M.A., Cortegoso, J.L., de Rosa, C., 1994. Solar permeability of urban trees in cities of western Argentina. *Energ. Buildings* 20 (3), 219–230.
- Chen, Y.D., Carsel, R.F., McCutcheon, S.C., Nutter, W.L., 1998. Stream temperature simulation of forested riparian areas: I. Watershed-scale model development. *J. Environ. Eng.* 124 (4), 304–315.
- Cheng, S.-T., Wiley, M.J., 2016. A Reduced Parameter Stream Temperature Model (RPSTM) for basin-wide simulations. *Environ. Model. Softw.* 82, 295–307.
- Cole, T., Wells, S., 2006. CE-QUAL-W2: a two-dimensional, laterally averaged, hydrodynamic and water quality model, version 3.5. Civil and Environmental Engineering Faculty Publications and Presentations Retrieved from [http://pdxscholar.library.pdx.edu/cengin\\_fac/130](http://pdxscholar.library.pdx.edu/cengin_fac/130).
- Cox, M.M., Bolte, J.P., 2007. A spatially explicit network-based model for estimating stream temperature distribution. *Environ. Model. Softw.* 22 (4), 502–514.
- Davies-Colley, R.J., Quinn, J.M., 1998. Stream lighting in five regions of North Island, New Zealand: control by channel size and riparian vegetation. *N. Z. J. Mar. Freshw. Res.* 32 (4), 591–605.
- Deltares, 2014. Delft3D-FLOW: simulation of multidimensional hydrodynamic flows and transport phenomena, including sediments, User Manual. Deltares Systems, Delft, The Netherlands (684 pp.).
- DeWalle, D.R., 2008. Guidelines for riparian vegetative shade restoration based upon a theoretical shaded-stream model. *J. Am. Water Resour. Assoc.* 44 (6), 1373–1387.
- Dripps, W., Granger, S.R., 2013. The impact of artificially impounded, residential headwater lakes on downstream water temperature. *Environ. Earth Sci.* 68 (8), 2399–2407.

- Dugdale, S.J., Malcolm, I.A., Kantola, K., Hannah, D.M., 2018. Stream temperature under contrasting riparian forest cover: understanding thermal dynamics and heat exchange processes. *Sci. Total Environ.* 610, 1375–1389.
- Duursma, R.A., Mäkelä, A., 2007. Summary models for light interception and light-use efficiency of non-homogeneous canopies. *Tree Physiol.* 27 (6), 859–870.
- Essery, R., Bunting, P., Rowlands, A., Rutter, N., Hardy, J., Melloh, R., Link, T., et al., 2008. Radiative transfer modeling of a coniferous canopy characterized by airborne remote sensing. *J. Hydrometeorol.* 9 (2), 228–241.
- Fu, P., Rich, P.M., 1999. Design and implementation of the solar analyst: an ArcView extension for modeling solar radiation at landscape scales. Proceedings of the Nineteenth Annual ESRI User Conference, pp. 1–31.
- Garner, G., Malcolm, I.A., Sadler, J.P., Hannah, D.M., 2014. What causes cooling water temperature gradients in a forested stream reach? *Hydrol. Earth Syst. Sci.* 18 (12), 5361–5376.
- Garner, G., Malcolm, I.A., Sadler, J.P., Hannah, D.M., 2017. The role of riparian vegetation density, channel orientation and water velocity in determining river temperature dynamics. *J. Hydrol.* 553:471–485 retrieved from <http://www.sciencedirect.com/science/article/pii/S0022169417301695>.
- Gomi, T., Moore, R.D., Dhakal, A.S., 2006. Headwater stream temperature response to clear-cut harvesting with different riparian treatments, coastal British Columbia, Canada. *Water Resour. Res.* 42 (8), W08437.
- GRASS Development Team, 2015. Geographic Resources Analysis Support System (GRASS GIS) Software, Version 7.1; Open Source Geospatial Foundation. retrieved from <http://grass.osgeo.org>.
- Greenberg, J.A., Hestir, E.L., Riano, D., Scheer, G.J., Ustin, S.L., 2012. Using LiDAR data analysis to estimate changes in insolation under large-scale riparian deforestation. *J. Am. Water Resour. Assoc.* 48 (5), 939–948.
- Guzy, M., Richardson, K., Lambinos, J.G., 2015. A tool for assisting municipalities in developing riparian shade inventories. *Urban For. Urban Green.* 14 (2), 345–353.
- Haag, I., Luce, A., 2008. The integrated water balance and water temperature model LARSIM-WT. *Hydrol. Process.* 22 (7), 1046–1056.
- Haag, I., Westrich, B., 2002. Processes governing river water quality identified by principal component analysis. *Hydrol. Process.* 16 (16), 3113–3130.
- Hannah, D., Garner, G., 2015. River water temperature in the United Kingdom: changes over the 20th century and possible changes over the 21st century. *Prog. Phys. Geogr.* 39, 68–92.
- Hilldale, R.C., Raff, D., 2008. Assessing the ability of airborne LiDAR to map river bathymetry. *Earth Surf. Process. Landf.* 33 (5), 773–783.
- Hofierka, J., Suri, M., 2002. The solar radiation model for open source GIS: implementation and applications. Proceedings of the Open Source GIS-GRASS Users Conference, pp. 1–19.
- Johnson, S.L., 2004. Factors influencing stream temperatures in small streams: substrate effects and a shading experiment. *Can. J. Fish. Aquat. Sci.* 61 (6), 913–923.
- Johnson, G.T., Watson, I.D., 1984. The determination of view-factors in urban canyons. *J. Clim. Appl. Meteorol.* 23 (2), 329–335.
- Johnson, M.F., Wilby, R.L., 2015. Seeing the landscape for the trees: metrics to guide riparian shade management in river catchments. *Water Resour. Res.* 51 (5), 3754–3769.
- Konarska, J., Lindberg, F., Larsson, A., Thorsson, S., Holmer, B., 2014. Transmissivity of solar radiation through crowns of single urban trees - application for outdoor thermal comfort modelling. *Theor. Appl. Climatol.* 117 (3–4), 363–376.
- Lalot, E., Curie, F., Wawrzyniak, V., Schomburgk, S., Piegay, H., Moatar, F., 2015. Quantification of the Beauce's groundwater contribution to the Loire River discharge using satellite infrared imagery. *Hydrol. Earth Syst. Sci. Discuss.* 12 (2), 2047–2080.
- Lamouroux, N., Pella, H., Vanderbecq, A., Sauquet, E., Lejot, J., 2010. Estimkart 2.0: Une plate-forme de modèles écohydrologiques pour contribuer à la gestion des cours d'eau à l'échelle des bassins français. Version provisoire. Version provisoire. Cemagref, Agence de l'Eau Rhône-Méditerranée-Corse, Onema, Lyon (45 pp.).
- Leach, J., Moore, R., 2010. Above-stream microclimate and stream surface energy exchanges in a wildfire-disturbed riparian zone. *Hydrol. Process.* 24 (17), 2369–2381.
- LeBlanc, R.T., Brown, R.D., FitzGibbon, J.E., 1997. Modeling the effects of land use change on the water temperature in unregulated urban streams. *J. Environ. Manag.* 49 (4), 445–469.
- Lebourgeois, F., Pierrat, J.-C., Perez, V., Piedallu, C., Cecchini, S., Ulrich, E., 2008. Phenological timing in French temperate forests - a study on stands in the Renecofor network. Retrieved from <http://hdl.handle.net/2042/19767>.
- Lee, T.Y., Huang, J.C., Kao, S.J., Liao, L.Y., Tzeng, C.S., Yang, C.H., Kalita, P.K., et al., 2012. Modeling the effects of riparian planting strategies on stream temperature: increasing suitable habitat for endangered Formosan Landlocked Salmon in Shei-Pa National Park, Taiwan. *Hydrol. Process.* 26 (24), 3635–3644.
- Li, G., Jackson, C.R., Krasinski, K.A., 2012. Modeled riparian stream shading: agreement with field measurements and sensitivity to riparian conditions. *J. Hydrol.* 428, 142–151.
- Loinaz, M.C., Davidsen, H.K., Butts, M., Bauer-Gottwein, P., 2013. Integrated flow and temperature modeling at the catchment scale. *J. Hydrol.* 495, 238–251.
- Maderich, V., Helling, R., Bezhenar, R., Brovchenko, I., Jenner, H., Koshebutskyy, V., Kuschan, A., et al., 2008. Development and application of 3D numerical model THREEOX to the prediction of cooling water transport and mixing in the inland and coastal waters. *Hydrol. Process.* 22 (7), 1000–1013.
- Magnuson, J.J., Crowder, L.B., Medvick, P.A., 1979. Temperature as an ecological resource. *Am. Zool.* 19 (1), 331–343.
- Marchand, M., Al-Azri, N., Ombe-Ndeffotsing, A., Wey, E., Wald, L., 2017. Evaluating meso-scale change in performance of several databases of hourly surface irradiation in south-eastern Arabic Peninsula. *Adv. Sci.* Res. 14, 7.
- Michez, A., Piégay, H., Lejeune, P., Claessens, H., 2017. Multi-temporal monitoring of a regional riparian buffer network (>12,000 km) with LiDAR and photogrammetric point clouds. *Journal of Environmental Management Piégay & Lamouroux "Enlarging Spatial and Temporal Scales for Biophysical Diagnosis and Sustainable River Management"*. 202 (Part 2), pp. 424–436.
- Moatar, F., Gailhard, J., 2006. Water temperature behaviour in the river Loire since 1976 and 1881. *Compt. Rendus Geosci.* 338 (5), 319–328.
- Moatar, F., Miquel, J., Poirel, A., 2001. A quality-control method for physical and chemical monitoring data. Application to dissolved oxygen levels in the river Loire (France). *J. Hydrol.* 252 (1–4), 25–36.
- Moore, R.D., Spittlehouse, D.L., Story, A., 2005. Riparian microclimate and stream temperature response to forest harvesting: a review. *J. Am. Water Resour. Assoc.* 41 (4), 813–834.
- Moore, R.D., Leach, J.A., Knudson, J.M., 2014. Geometric calculation of view factors for stream surface radiation modelling in the presence of riparian forest. *Hydrol. Process.* 28 (6), 2975–2986.
- Muller, E., 1995. Phénologie forestière révélée par l'analyse d'images thematic mapper. *C. R. Acad. Sci.* III 318 (9), 993–1003.
- Nash, J.E., Sutcliffe, J.V., 1970. River flow forecasting through conceptual models part I — a discussion of principles. *J. Hydrol.* 10 (3), 282–290.
- Ouellet, V., Secretan, Y., St-Hilaire, A., Morin, J., 2014. Daily averaged 2d water temperature model for the St. Lawrence River. *River Res. Appl.* 30 (6), 733–744.
- Pedersen, N.L., Sand-Jensen, K., 2007. Temperature in lowland Danish streams: contemporary patterns, empirical models and future scenarios. *Hydrol. Process.* 21 (3), 348–358.
- Quintana-Seguí, P., Le Moigne, P., Durand, Y., Martin, E., Habets, F., Baillon, M., Canellas, C., et al., 2008. Analysis of near-surface atmospheric variables: validation of the SAFRAN analysis over France. *J. Appl. Meteorol. Climatol.* 47 (1), 92–107.
- Sattin, M., Milne, R., Deans, J.D., Jarvis, P.G., 1997. Radiation interception measurement in poplar: sample size and comparison between tube solarimeters and quantum sensors. *Agric. For. Meteorol.* 85 (3–4), 209–216.
- Sellers, W.D., 1965. Physical climatology. University of Chicago Press.
- Soudani, K., Hmimina, G., Delpierre, N., Pontailler, J.-Y., Aubinet, M., Bonal, D., Caquet, B., et al., 2012. Ground-based network of NDVI measurements for tracking temporal dynamics of canopy structure and vegetation phenology in different biomes. *Remote Sens. Environ.* 123, 234–245.
- Sridhar, V., Sansone, A.L., LaMarche, J., Dubin, T., Lettenmaier, D.P., 2004. Prediction of stream temperature in forested watersheds. Wiley Online Library.
- Sun, N., Yearsley, J., Voisin, N., Lettenmaier, D.P., 2015. A spatially distributed model for the assessment of land use impacts on stream temperature in small urban watersheds. *Hydrol. Process.* 29 (10), 2331–2345.
- Teti, P., 2006. Stream shade as a function of channel width and riparian vegetation in the BC southern interior. *Streamline Watershed Manag. Bull.* 9, 10–15.
- Thiéry, D., Moutzopoulos, C., 1992. Un modele hydrologique spatialisé pour la simulation de tres grands bassins: le modele EROS formé de grappes de modeles globaux élémentaires. VIIIèmes journées hydrologiques de l'ORSTOM: Régionalisation en hydrologie, application au développement. ORSTOM Editions, pp. 285–295.
- Tisseuil, C., Vrac, M., Grenouillet, G., Wade, A.J., Geyrey, M., Oberdorff, T., Grodwohl, J.-B., et al., 2012. Strengthening the link between climate, hydrological and species distribution modeling to assess the impacts of climate change on freshwater biodiversity. *Sci. Total Environ.* 424, 193–201.
- Torgersen, C.E., Faux, R.N., McIntosh, B.A., Poage, N.J., Norton, D.J., 2001. Airborne thermal remote sensing for water temperature assessment in rivers and streams. *Remote Sens. Environ.* 76 (3), 386–398.
- Tormos, T., Van Looy, K., Villeneuve, B., Kosuth, P., Souchon, Y., 2014. High resolution land cover data improve understanding of mechanistic linkages with stream integrity. *Freshw. Biol.* 59 (8), 1721–1734.
- Tung, C.-P., Lee, T.-Y., Yang, Y.-C., 2006. Modelling climate-change impacts on stream temperature of Formosan landlocked salmon habitat. *Hydrol. Process.* 20 (7), 1629–1649.
- Tung, C.-P., Yang, Y.-C.E., Lee, T.-Y., Li, M.-H., 2007. Modification of a stream temperature model with Beer's law and application to GaoShan Creek in Taiwan. *Ecol. Model.* 200 (1–2), 217–224.
- Valette, L., Piffady, J., Chandresis, A., Souchon, Y., 2012. SYRAH-CE: description des données et modélisation du risque d'altération de l'hydromorphologie des cours d'eau pour l'Etat des lieux DCE. Rapport final, Pôle Hydroécologie des cours d'eau Onema-Irstea Lyon. MALY-LHQ, Lyon.
- Vidal, J.-P., Martin, E., Franchistéguy, L., Baillon, M., Soubeyrou, J.-M., 2010. A 50-year high-resolution atmospheric reanalysis over France with the Safran system. *Int. J. Climatol.* 30 (11), 1627–1644.
- Wawrzyniak, V., Allemand, P., Bailly, S., Lejot, J., Piégay, H., 2017. Coupling LiDAR and thermal imagery to model the effects of riparian vegetation shade and groundwater inputs on summer river temperature. *Sci. Total Environ.* 592 (Supplement C), 616–626.
- Woltemed, C.J., Hawkins, T.W., 2016. Stream temperature impacts because of changes in air temperature, land cover and stream discharge: Navarro River watershed, California, USA. *River Res. Appl.* 32 (10), 2020–2031.







Pierre LOICQ

AGENCE FRANÇAISE  
POUR LA BIODIVERSITÉ  
ÉTABLISSEMENT PUBLIC DE L'ÉTAT

## Caractérisation et modélisation de la température des rivières sur le bassin de la Maine: influence de la végétation rivulaire et des échanges nappe-rivière

### Résumé

La variabilité spatiale de la température des cours d'eau a été analysée à l'échelle régionale sur le bassin la Maine (22350 km<sup>2</sup>), où le climat est relativement homogène. La température a été mesurée à 44 stations localisées sur des ordres de Strahler allant de 2 à 7. Les résultats montrent que cette variabilité est liée à la distance à la source et aux flux de nappe. De là, un modèle empirique a été développé. Il peut prédire la température hebdomadaire de l'eau avec une RMSE de 1,35 °C et un biais moyen de -0,13 °C. Le modèle à base physique T-NET a été appliqué sur le bassin versant de la Maine afin de comprendre ses points forts et ses faiblesses et comment les résoudre. L'impact de la végétation rivulaire sur la température, via son influence sur le rayonnement solaire et infrarouge a été caractérisé à la résolution métrique grâce à des données LiDAR sur 270 km du Loir. Les performances de T-NET sont améliorées par rapport aux méthodes plus simples de caractérisation de l'ombrage et l'effet de refroidissement de la végétation sur la température maximale journalière a été quantifié. Enfin, les flux de nappe calculés sur le bassin du Loir par le modèle Eaudyssée à la résolution kilométrique et au pas de temps journalier ont été injectés dans le modèle T-NET. L'impact sur les performances de T-NET et l'influence thermique de ces flux de nappe ont été analysés.

Mots-clés: modélisation ; régime thermique ; température des rivières ; échelle régionale ; ombrage ; végétation rivulaire ; LiDAR ; Maine ; Loir; flux de nappe ; échanges nappe-rivière ; Eaudyssée

### Abstract

The spatial variability of stream temperature was analysed at the regional scale on the climatically homogeneous Maine catchment (22350 km<sup>2</sup>), thanks to temperature measurements of 44 monitoring stations localised on Strahler orders 2 to 7. This variability was found to be linked to the distance from source and the groundwater fluxes. Based on this finding, an empirical model was developed. It can predict weekly water temperature with a RMSE of 1.35 °C and a mean bias of -0.13 °C. The physically based model T-NET was applied on the Maine catchment in order to understand its strong and weak points and suggest potential methods to solve them. The impact of riparian vegetation on stream temperature, via its influence on solar and longwave downward radiation was characterised at the metric resolution thanks to LiDAR data on 270 km of the Loir River. T-NET's performances are improved compared to simpler shade characterisation methods and the vegetation's cooling effect on maximum daily temperature was quantified. Finally, groundwater fluxes computed on the Loir basin by the Eaudyssée model at the kilometric resolution and the daily time step were injected in T-NET. The impact on T-NET's performances, as well as the thermal influence of these groundwater fluxes were analysed.

Keywords: modelling; thermal regime; stream temperature; regional scale; riparian shading; LiDAR; Loir; Maine; groundwater fluxes; stream-aquifer exchanges; Eaudyssée